



**University of
Nottingham**

UK | CHINA | MALAYSIA

**Developing analytical data-informed statistical models for
predicting the physical stability of drug-polymer solid
dispersions using high-throughput 2D printed arrays**

By: Noha Fawzy Ibraheem Aboelmagd Ghazi ^a

Supervisors: Prof. Clive Roberts ^{a,b}, Dr Jonathan Burley ^a, and Prof. Ian Dryden ^c

***^a School of Pharmacy, University of Nottingham**

***^b School of Life Sciences, University of Nottingham**

***^c Department of Mathematics and Statistics, Florida International University**

Thesis submitted to the University of Nottingham for the degree of

Doctor of Philosophy

School of Pharmacy, University of Nottingham

March 2024

Acknowledgement

In embarking on the pages of acknowledgement, I reflect upon the multitude of individuals whose unwavering support has illuminated the path of my academic journey. Their encouragement, guidance, and camaraderie have been instrumental in bringing this thesis to fruition.

First and foremost, I express my deepest gratitude to my esteemed supervisors. Your profound commitment to fostering academic excellence, coupled with your unwavering support and guidance, has been pivotal to the success of this research. The indelible impact of your mentorship is immeasurable, and I am truly fortunate to have had the privilege of working under your supervision. I want to give a special thanks to Professor Clive Roberts. He has been there for me not only with his scientific guidance but also with his support and encouragement when things got tough. His help has been crucial in making this research meaningful and valuable. I am really grateful for the chance to work with him and for the positive impact he has had on both my studies and personal journey. I extend special thanks to Dr. Jonathan Burley for patiently answering my numerous questions and providing valuable guidance in the development of the model. His expertise and willingness to assist have been crucial to the success of this research. Additionally, I want to express my gratitude to Professor Ian Dryden for dedicating his time to help me grasp the statistical intricacies behind the model. His support at every step has been invaluable, contributing significantly to the depth and quality of this work. I greatly appreciate their dedication and assistance in making this academic journey more enriching and rewarding. I wish to extend my thanks and appreciation to my internal assessor, Dr Andrew Hook, for his expert advice and opinions throughout the project.

My deepest appreciation goes to my family, the pillar of my strength. To my mother, Hanan Tantawy, your endless love and encouragement have fuelled my perseverance. To my amazing brother, Ibraheem Ghazi, and my lovely sister Nada Ghazi, your support has been unwavering. To

my adorable nephew, Malek, and niece, Sila, your joyous presence has been a source of inspiration. A heartfelt thank you to Aunt Mona Tantawy for your continuous support and care.

A special acknowledgement goes to my friend and colleague, George Bebawy, for your invaluable assistance in the realms of 2D printing and your continuous support during the whole journey. A heartfelt acknowledgement goes to Professor Mohammed Youssif for his unwavering support and valuable insights throughout this journey. To my dear friends Kate, Thata, Rebecca, Randa, Rania, Julian, Ramy and Daniel, your friendship and encouragement provided solace during challenging times. Your unwavering support has been a constant source of strength.

To the dedicated technicians and all the staff at the School of Pharmacy, University of Nottingham, your assistance has been pivotal to the smooth progress of my research. Special thanks to Jisun Lm and Geoffrey Rivers in AMB for their crucial contributions to the 3D printing studies.

I extend my heartfelt gratitude to the Egyptian Mission Sector and my home institute, the Faculty of Pharmacy at Mansoura University. Their generous support and unwavering belief in the importance of academic research have been instrumental in successfully completing this thesis. The financial backing provided by the Egyptian Mission Sector has allowed me to dedicate my time and energy to this comprehensive study, and for that, I am sincerely thankful.

In memory of my beloved father, Fawzy Ghazi, whose spirit continues to inspire me. Though he is not physically present, I dedicate this work to his soul, hoping he will be proud of my achievements.

This journey would not have been possible without the collective support and encouragement of these exceptional individuals. I am deeply grateful for the privilege of having such wonderful mentors, family, friends, and colleagues.

Declaration

I hereby declare that the work contained in this thesis titled “Developing analytical data-informed statistical models for predicting the physical stability of drug-polymer solid dispersions using high-throughput 2D printed arrays” is the result of my own work conducted at the School of Pharmacy, University of Nottingham between February 2019 and December 2023 under the supervision of Prof. Clive Roberts, Dr Jonathan Burley and Prof. Ian Dryden.

Abstract

Introduction:

Amorphous solid dispersions (ASDs) offer a promising strategy to address the poor solubility challenges in over 40% of newly discovered active pharmaceutical ingredients (APIs). Despite the potential advantages of solid dispersions, some challenges would hinder the development of ASDs such as scaling up and physical instability that lead to phase segregation and possible further recrystallization of the API, particularly during the storage period. Traditional preparation methods of ASDs as well as analytical techniques to assess formulation stability may require samples on a milligram-to-gram scale. However, whilst a number of drugs and polymers have been studied in the literature, the number of researched APIs and their loading with different polymers is still very limited, and model development is often done for each system in isolation, making it difficult to draw any general conclusions regarding the physicochemical properties of APIs that would be highly correlated to the stability of those ASDs.

Therefore, this thesis aims to combine the use of a novel high-throughput miniaturised screening approach for printing nano-arrays of a relatively larger number of samples than previously reported using a minimal amount of materials in picoliter with statistical modelling of the outcome stability data. That model could correlate the stability of solid dispersion formulations with the physicochemical properties of the utilized APIs. Then to test the predictive power of 2D inkjet printing through 3D inkjet printing, highlighting its utility in anticipating the physical stability of scaled-up drug-polymer dispersions.

Methods:

2-D Microarray Printing for Screening of Pharmaceutical Solid Dispersions. The use of printed nano-arrays in pre-formulation and solid-form screening, employing pico-litres of drugs

with various physicochemical properties is investigated here. The study involves preliminary techniques, such as manual and contact printing, to assess formulation printability, with a subsequent focus on 2D inkjet printing on a nanogram scale. The novelty of the research lies in sample quantity, addressability, and the ease of analysis through exploring a large number of drug-polymer loadings formulations used, around 930 drug/polymer loadings in triplicates (around 2793 loadings) to build an extensive library of drug-polymer combinations. This is much more than has been achieved before in other studies while taking into consideration performing this safely using a minimal (nano-gram) amount of materials. The stability data collected for the prepared ASDs at accelerated conditions for six months is to be used as input in the statistical modelling.

Multiple Linear Regression Modelling for the Stability of Solid Dispersions. Through building an extensive library of formulations developed from 23 different drugs combined within two polymeric matrices sufficient data was gathered to form a statistical-based model. Stability under accelerated conditions served as a critical input for developing multiple linear regression models predicting the stability of amorphous solid dispersions. The models incorporate variables related to the stability of solid dispersions, such as hydrogen bond acceptors, heteroatoms, and oxygen atoms within drug molecules. Rigorous validation through Leave-One-Out Cross-Validation ensures the reliability of the models by confirming the same trend between measured and predicted stability data of different APIs.

3-D Inkjet Printing of Solid Dispersions. This is done to explore the viability of 3D inkjet printing to produce formulations highlighted in the 2D screening with a relatively high drug loading using poorly soluble APIs. The results demonstrate the effectiveness of the 3D printing process in assessing the stability of drug-polymer dispersions. The agreement between 2D and 3D

stability outcomes reinforces the utility of 2D printing in early-stage formulation development, allowing for the anticipation of physical stability in scaled-up dispersions.

Results:

The 2D inkjet printing approach, with its capacity for high-throughput screening, proved to be a valuable tool for assessing drug-polymer miscibility limits and predicting stability outcomes. The extensive library of formulations enabled the development of multiple linear regression models, providing insights into the critical physicochemical properties influencing the stability of amorphous solid dispersions. The 3D inkjet printing results further validated the predictive power of the 2D approach. The formulations exhibited stability consistent with predictions, showcasing the potential for using 2D printing as a reliable tool for early-stage formulation development.

Conclusions:

In conclusion, this thesis introduces a novel approach to solid-dispersion formulation screening. The use of printed nano-arrays and statistical modelling enhances efficiency, minimizes material requirements, and broadens the scope of samples evaluated. The predictive power of 2D inkjet printing is confirmed through 3D inkjet printing, highlighting its utility in anticipating the physical stability of scaled-up drug-polymer dispersions. This work not only advances pharmaceutical formulation but also sets the stage for the practical application of these statistical models in the industry.

Table of Contents

1 Chapter 1: Introduction	1
1.1 The journey of drug discovery and development	1
1.2 Oral drug delivery	2
1.2.1 Biopharmaceutical classification system (BCS) and the Developability classification system (DCS)	3
1.2.2 Poor aqueous solubility	5
1.2.3 Challenges connected with poor solubility	7
1.3 Strategies to overcome problems of poor water solubility	8
1.3.1 Chemical alteration such as prodrugs	9
1.3.2 Crystal modification	10
1.3.2.1 Polymorphs	10
1.3.2.2 Salt formation	11
1.3.2.3 Cocrystal formation	11
1.3.3 Particle size reduction	12
1.3.3.1 Micronisation	12
1.3.3.2 Nanocrystals	13
1.3.4 Cyclodextrin complexation	13
1.3.5 Self-emulsification	14
1.3.6 Amorphous versus crystalline form	14
1.3.7 Amorphous solid dispersion (ASD)	16
1.3.8 Hot melt extrusion (HME)	19
1.3.9 Spray drying	20
1.4 The instability and scale-up problems of the ASD formulations	21
1.5 Support Tools in Formulation Development	22
1.5.1 Predictive models	23
1.5.1.1 Current evaluation approaches	24
1.5.1.2 Theoretical approaches in solid dispersion stability	24
1.5.1.2.1 Hildebrand solubility parameter and Hansen solubility parameter	25
1.5.1.2.2 Flory-Huggins	26
1.5.1.3 Mathematical approaches in solid dispersion stability prediction	27
1.5.1.3.1 Molecular dynamics	27
1.5.1.3.2 Principal Component Analysis (PCA)	28
1.5.1.4 Statistical models	28

1.5.2 High throughput screening (HTS)	30
1.6 Printing Technologies	32
1.6.1 Contact printing	33
1.6.2 Non-contact printing (Inkjet printing)	34
1.6.2.1 Continuous Inkjet Printing.....	35
1.6.2.2 Drop on Demand (DoD) Inkjet Printing.....	36
1.6.2.2.1 Thermal Inkjet Printing.....	37
1.6.2.2.2 Piezoelectric Inkjet Printing.....	38
Advantages of Inkjet Printing.....	39
Challenges of Inkjet printing	39
1.6.3 Pharmaceutical applications of inkjet printing	41
2 Chapter 2: Materials and Methods.....	50
2.1 Drug and polymer selection.....	50
2.1.1 Drug Selection	50
2.1.2 Polymer selection.....	54
2.1.2.1 Polyvinylpyrrolidone-vinyl acetate (PVPVA) (Kollidon®).....	55
2.1.2.2 Hydroxy propyl methyl cellulose acetate succinate (HPMCAS)	55
2.1.2.3 Polyvinyl caprolactam – polyvinyl acetate – polyethylene glycol (PEG) (Soluplus™)	56
2.2 Materials	56
2.3 Instruments.....	58
2.3.1 2-D Inkjet printing	58
2.3.2 Polarised Light Microscopy.....	67
2.3.3 Atomic Force Microscopy (AFM).....	70
2.3.4 Water contact angle measurement (WCA)	71
2.3.5 Stability study of the printed Microarrays	72
2.3.6 3D inkjet printer (Dimatix).....	74
2.3.7 Malvern Rheometer	75
3 Chapter 3: 2-D Microarray Printing for Screening of Pharmaceutical Solid Dispersions.....	76
3.1 Introduction.....	76
3.2 Aims and Objectives.....	78
3.3 Methodology.....	79
3.3.1 Materials (Model Drugs and Polymers).....	79
3.3.2 Substrate analysis.....	80

3.3.2.1	Water contact angle measurement (WCA)	80
3.3.2.2	Measuring the roughness of the gold-coated slides using atomic force microscopy (AFM)	80
3.3.3	Preliminary studies to choose the printing instrument.....	81
3.3.3.1	Hand method (Hamilton Syringe).....	81
3.3.3.2	Contact printing (Pin printing).....	83
3.3.4	Piezoelectric inkjet printing	90
3.3.4.1	Microarray development.	92
3.3.5	Stability Testing Conditions	96
3.3.6	Polarised light microscopy (PLM).....	97
3.3.7	Evaluation of Crystallisation Behavior	97
3.3.8	Drop-Cast preparation of drug/PVPVA dispersion and bulk validation according to the literature	99
3.4	Results and Discussion	100
3.4.1	Water contact angle measurement (WCA)	100
3.4.2	The roughness of the gold-coated slides (Atomic Force Microscopy)	101
3.4.3	Manual deposition technique by Hamilton Syringe.....	103
3.4.4	Contact printer (Pin Printer).....	107
3.4.4.1	Printing some pure APIs as one contact droplet per spot as the smallest amount.	107
3.4.4.2	Printing some pure APIs and polymers at 12 contact droplets per spot	108
3.4.4.3	API/ polymer blend printing and order of printing API and polymer solutions.	109
3.4.5	Crystallisation behaviour following 2D inkjet printing of pure APIs and upon storage	112
3.4.6	Choosing the optimised number of droplets (printed mass) using a 2-D Sciflexarrayer S5 inkjet printer.....	117
3.4.7	Effect of Drug/PVPVA ratio and time on drug crystallisation within the PVPVA matrix	119
3.4.8	Building a library of different APIs in various APIs/PVPVA loadings	122
3.4.9	Miscibility limit comparison for different APIs within PVPVA polymeric matrix ..	128
3.4.10	Miscibility limit comparison for different APIs within the Soluplus polymeric matrix	131
3.4.11	Miscibility limit comparison for three APIs within the HPMCAS polymeric matrix	134
3.4.12	Interactions and stabilization mechanisms in drug-polymer systems.....	135
3.4.13	Drop casting of drug/PVPVA formulations and comparison to the 2D inkjet printing miscibility limits	140

3.4.14 Literature Comparison of API/Polymer Formulations	145
3.5 Conclusion	147
4 Chapter 4: Multiple Linear Regression Modelling for predicting the stability of solid dispersions	150
4.1 Introduction.....	150
4.1.1 Challenges in Predicting Complex Systems	150
4.1.1.1 Statistical models developed for predicting solid dispersion stability.....	151
4.2 Aims and objectives of this chapter	152
4.3 Materials and methods	153
4.3.1 Stability data of the 2D printed microarray formulations	153
4.3.2 Physicochemical properties of APIs	153
4.3.2.1 The variation in the physicochemical properties across the model drugs used in the modelling process	156
4.3.3 Explanation of the modelling process in R script	158
4.3.4 Set-Up of the Model.....	159
4.3.4.1 Setting Up the Environment and Libraries	159
4.3.4.2 Data Collection and Initial Preprocessing.....	159
4.3.4.2.1 Data Sources.....	159
4.3.4.2.2 Reading the Data	160
4.3.4.2.3 Dataset and Selection	160
4.3.4.2.4 Percent of Drugs in Polymer Selection	160
4.3.4.3 Data Transformation and Variable Definitions.....	160
4.3.4.3.1 Definition of Log Stability	160
4.3.4.3.2 Data Exclusion and Inclusion.....	160
4.3.4.4 Modelling Process.....	160
4.3.4.4.1 Initial Modelling and model selection.....	160
4.3.4.4.2 Tabulation of Frequency Results	162
4.3.4.4.3 Forward-Selection and Cross-Validation	162
4.3.4.4.4 Final Model Building	162
4.4 Results and Discussion	162
4.4.1 Using a selection of PVPVA data.....	162
4.4.1.1 Frequency of the variables	162
4.4.1.2 Final Model Choice.....	164
4.4.1.3 Model Performance and Selection	164
4.4.1.4 Coefficients.....	170

4.4.1.5 Effects of setting a non-crystallised drug (i.e. a null result) at 500 days	177
4.4.1.6 Correlation matrix of log stability within PVPVA and predictor variables and the correlation between the variables and each other	178
4.4.1.7 LOOCV for log stability in PVPVA drug loading.....	180
4.4.1.8 Comparative analysis of predicted vs. measured stability across various drug formulations using LOOCV.....	182
4.4.1.8.1 Theophylline.....	182
4.4.1.8.2 Nitrofurantoin.....	183
4.4.1.8.3 Flufenamic acid.....	184
4.4.1.8.4 Tolbutamide	185
4.4.1.8.5 Nifedipine.....	185
4.4.1.8.6 Felodipine.....	186
4.4.1.8.7 Ritonavir.....	187
4.4.1.8.8 Fenofibrate	187
4.4.2 Drugs with Soluplus.....	190
4.4.2.1 Frequency of the variables	190
4.4.2.2 Final Model Choice.....	191
4.4.2.3 Model Performance and Selection	191
4.4.2.4 Coefficients	196
4.4.3 Effects of setting non-crystallised drug log stability at 500 days	203
4.4.3.1 Correlation matrix of log stability within Soluplus and predictor variables and the correlation between the variables and each other	204
4.4.3.2 Analysis of LOOCV for log stability in Soluplus drug loading	206
4.4.3.3 Comparative analysis of predicted vs. measured stability across various drug formulations using LOOCV.....	210
4.4.3.3.1 Theophylline.....	210
4.4.3.3.2 Nitrofurantoin.....	210
4.4.3.3.3 Atenolol.....	212
4.4.3.3.4 Piroxicam	212
4.4.3.3.5 Nifedipine.....	213
4.4.3.3.6 Felodipine.....	214
4.4.3.3.7 Orlistat.....	215
4.4.3.3.8 Aprepitant.....	215
4.4.4 Suggested guidelines for enhancing stability in PVPVA and Soluplus solid dispersions	218
4.5 Conclusions.....	225

5 Chapter 5: Three-Dimensional Inkjet Printing of Solid Dispersions.....	227
5.1 Three-Dimensional (3D) Technology.....	227
5.1.1 Introduction.....	227
5.1.2 3D Printing Technologies in Drug Delivery.....	229
5.1.2.1 Inkjet printing.....	229
5.1.2.1.1 Thermal and Piezoelectric Print Heads in DOD Printing.....	229
5.1.2.1.2 Considerations in Formulation and Process Parameters.....	229
5.1.3 Advantages of 3D Printing in Pharmaceutical Applications.....	231
5.1.3.1 Precise Drug Release Control.....	231
5.1.3.2 Rapid Integration of Production.....	231
5.1.3.3 Personalised Medicine for Special Populations.....	231
5.2 Aims and Objectives.....	232
5.3 Experimental design.....	233
5.3.1 Materials (model drugs and polymers).....	233
5.3.2 Methods:.....	234
5.4 Results and Discussion.....	237
5.4.1 Optimisation of the printing criteria for 3D printed formulation.....	237
5.4.1.1 Inkjet printing progression from droplets to a square single-layer formulation (0.5 mm x 0.5mm).....	237
5.4.1.2 Inkjet printing a 3D square formulation (3mm x 3mm).....	239
5.4.1.3 3D-printed Flurbiprofen/PVPVA formulation.....	240
5.4.2 3D-printed Piroxicam/PVPVA formulation.....	244
5.5 Conclusions.....	248
6 Conclusions and Future Work.....	249
6.1 Conclusions.....	249
6.2 Future work.....	253
7 References.....	256
8 Appendix: Supporting Information (SI).....	i

List of Figures

Figure 1. Drug Discovery Process and timeline.	2
Figure 2. Biopharmaceutics classification system (BCS) and formulation strategies based on the BCS modified from [10].	4
Figure 3. DCS (in blue) by modifying the BCS (in black) for more realistic volumes of fluid available in the GI tract and the compensatory nature of permeability on low solubility. FaSSIF: Fasted State Simulated Intestinal Fluid, Peff: effective permeability. Modified from [8].	5
Figure 4. Schematic diagram shows the different techniques commonly used to address poor water solubility [33].	10
Figure 5. Order of molecules in Amorphous versus crystalline structure.	15
Figure 6. Schematic diagram of free energy versus temperature of a molecule in different states. [83].	16
Figure 7. The figure illustrates three possible drug/polymer solid dispersion structures, with hexagonal figures representing drug molecules and wavy lines depicting polymer chains (A) in a homogeneous drug-polymer solution, polymer chains are random coils that interpenetrate each other and extend through the whole system, while drug molecules are dispersed randomly among the polymer segments (displays the optimal structure of a solid dispersion with the drug molecularly dispersed throughout the polymer matrix) (B) the drug molecules separate from the polymeric matrix and rearranged in the conformation that leads to crystallisation leading to instability of the formulation and (C) an intermediate meta-stable structure where the amorphous drug aggregates are dispersed in a polymer matrix containing drug at its amorphous solubility (displays a system where amorphous drug-rich areas are interspersed within the polymer matrix) [114].	22
Figure 8. Schematic illustration of main types of pins used in contact printing; (a) solid pin, which holds a small volume of ink on its tip, (b) split or quill pin that holds a volume of ink in its slot, allowing multiple spotting per loading. (Adapted from [160]).	33
Figure 9. Schematic illustration of initial uptake (left side) of the solution (ink) from a source plate by A) the printing quill pin or B) the printing nozzle (both controlled by XYZ robotic arm) with subsequent deposition of a small volume to specific locations(right side)[158, 161].	34
Figure 10. Schematic illustration of jetting nozzle (adapted from [166]).	35
Figure 11. A schematic illustration of continuous mode jetting and an image showing temporal droplet formation at the figure's bottom [166].	36
Figure 12. A schematic illustration of demand mode jetting and an image showing temporal droplet formation at the figure's bottom [166].	37
Figure 13. A schematic illustration of a droplet formation at the two modes of DoD printing; A) Piezoelectric inkjet printing, B)Thermal inkjet printing [170].	38
Figure 14. desirable drop formation in piezoelectric inkjet printing and undesirable satellite drop formation [184].	40
Figure 15. Chemical structures of the APIs used in this study [230].	52
Figure 16. Chemical structures of polymers used in this study [233-235].	55
Figure 17. General Schematic of Electrostatic inkjet printing system (modified from [246]).	58
Figure 18. The camera captured piezoelectric droplet ejection from the dispenser head with an internal diameter of 70 μm [247].	59
Figure 19. SciFlexarrayer S5 2D inkjet printer used in this study.	60
Figure 20. The first step of settings for choosing the suitable Probe, the program to run and the Target for the printing process.	61

Figure 21. The Settings for DMF flush through the system by Syringe pump before the nozzle is connected.	62
Figure 22. Droplet optimisation via adjusting voltage and pulse droplet size in the image is 220 picolitre.	63
Figure 23. Target set up for preparation of slide design and microarray spots layout	64
Figure 24. Field set up for the determination of each spot component and the number of droplets to be printed in each to print the required drug-polymer ratios.	65
Figure 25. The final step to run the slide printing as pre-planned in the previous actions.	65
Figure 26. The image at the top shows the vacuum system used for DMF filtration before the printing process, and the one at the bottom shows an example of the impurities detected by the filter.	66
Figure 27. The components of a modern polarised light microscope and how it works [251]	68
Figure 28. Polarised light microscopy used in this study and its components.	69
Figure 29. Schematic diagram of Atomic force microscope AFM [255]	70
Figure 30. Water contact angle equipment used in this study.	72
Figure 31. Microarray storage at 75% RH \pm 5% at 40°C in a stability oven. as an accelerated condition for the stability study.	73
Figure 32. The stability oven used for the accelerated conditions for the physical stability assessment of the printed Microarrays.	73
Figure 33. 3D inkjet printer, the Dimatix, utilised in this study, along with an annotated schematic detailing its key components such as the fiducial camera, ink reservoir, 12-jet Samba cartridge, drop watcher camera, cleaning pad, and substrate position.	74
Figure 34. Malvern Instruments Kinexus Pro Research Rheometer used to measure the viscosity of the ink.	75
Figure 35. Washing and vacuum drying of the pin.	84
Figure 36. Depositing the solution through the pin onto a substrate by making contact controlled by an X-Y-Z robotic arm.	84
Figure 37. Schematic diagram of the printing plan 1 to print 6 replicates of 5 pure APIs.	86
Figure 38. Schematic diagram of the printing plan 2 to print six replicates of five pure APIs and three pure polymers.	87
Figure 39. Schematic diagram of the printing plan 3 to print three replicates of 50% API polymer loading by printing the API solution and the polymer solution separately in a different order. In the first three columns (A, B, C), the API solution was printed first and then the polymer solution in the same amount, while in the other three columns, the polymer was printed first, then the API solution.	88
Figure 40. Schematic diagram of the printing plan 4 to print premixed API/polymer solution in two API loadings (50%, 12.5%). Three replicates of 50% API polymer loading were printed in the first three columns of the first five rows, while three replicates of 12.5% API polymer loading were printed in the second three columns of the first five rows. In the second 5 rows, the pure APIs were printed in 6 replicated as a reference.	90
Figure 41. Schematic representation of steps followed in manufacturing and analysing microarrays, including drug and polymer solutions preparation, pipetting into well-plate, withdrawing drug solution through the printer nozzle and then dispensing at the required amount in the desired pre-located place on the substrate, followed by repeating the same process for the polymer solution to print it onto the printed drug solution droplets.	92

Figure 42. A schematic diagram of the printing plan of APIs, polymers and different API/ polymer loadings by piezoelectric Scienion S5 printer..... 95

Figure 43. A schematic drawing of the slide design is shown on the left side of the figure, as API and polymer were printed as a reference in the top and bottom two rows. In between, API/polymer mixtures were printed in triplicates starting from 5% with 5% w/w increment till 95%. An image of a printed microarray of Estradiol and PVPVA as a model for the APIs used in the study is shown in the middle. On the right side, microscopic images using bright (left) and cross-polarised field (right) of four printed spots are shown as examples of the crystallisation assessment, as the first and third rows (0%, 20%) show no birefringence (no crystallisation) and second and fourth rows (50%, 100%) show the presence of birefringence (crystallisation). Images shown here were taken after 6 months of storage in accelerated conditions (75% relative humidity and 40°C in a stability oven). The dimensions of gold-coated glass slides are (25x75mm²)..... 96

Figure 44. WCA angle measurement of the microscopic glass slide is shown in image (A) around 26.2°, and the WCA of the gold-coated glass slide is shown in image (B) around 79.5° using water as testing liquid. The water needle is shown on the top, and the formed water droplet is on the bottom. 101

Figure 45. AFM topographic images of gold-coated slides (1µm x 1µm area on the left side and 5µm x 5 µm area on the right side)..... 102

Figure 46. The figure shows crystallisation profiles of pure APIs and pure polymers performed by Hamilton syringe with different final deposited masses between 1000 to 5000 ng. All images are reported without (top row) and with (bottom row of each set) cross-polarised filters. Images of all APIs are depicted six months from solvent evaporation while storage in accelerated conditions (75% relative humidity and 40°C in a stability oven). 104

Figure 47. Examples of dried spots of 50% API/polymer loading of different APIs produced by a Hamilton syringe with three polymers. The top section shows 50% APIs/ Soluplus, the middle section shows 50% APIs/ PVPVA, and the bottom section shows 50% APIs/ HPMCAS. All images are reported without (top part of each section) and with (bottom part) cross-polarised filter after storage of the spots in accelerated conditions for 6 months (75% relative humidity and 40°C in stability oven). Final mass around 6000 ng (6 µg). 106

Figure 48. Examples of dried spots of pure five APIs printed by contact printer as one contact per spot depositing a final total mass of around 50 ng. All images are depicted without (top part of each section) and with (bottom part) cross-polarised filter after storage of the spots in accelerated conditions for 6 months (75% relative humidity and 40°C in stability oven). 108

Figure 49. Examples of dried spots of pure five APIs and three pure polymers printed by contact printer as 12 contacts per spot depositing a final total mass of around 600 ng. All images are reported without (top part of each section) and with (bottom part) cross-polarised filter after storage of the spots in accelerated conditions for 6 months (75% relative humidity and 40°C in stability oven). 108

Figure 50. Examples of dried spots of 50% API/HPMCAS loading in different order of API and polymer by a) printing 6 droplets of the API solution first and then 6 droplets of the polymer solution that are shown in the upper part of the figure, while b) printing 6 droplets of the polymer first and then 6 droplets of the API solution is shown on the bottom part of the figure. The final total mass in both cases is around 600 ng. All images are reported without (top part of each section) and with (bottom part) cross-polarised filter after storage of the spots in accelerated conditions for 6 months (75% relative humidity and 40°C in stability oven). 110

Figure 51. Examples of dried spots printed by contact printer as 12 contacts per spot depositing a final total mass of around 600 ng. The first set shows the printing of a premixed 50% API/HPMCAS solution. The middle set shows the printing of a premixed 12.5% API/ HPMCAS solution. The bottom set shows the printing of pure APIs and pure polymer (HPMCAS). All images are reported without (top part of each section) and with (bottom part) cross-polarised filter after storage of the spots in accelerated conditions for 6 months. 111

Figure 52. The figure shows different APIs recrystallisation profiles used in this study (final mass 1000-1100 ng) printed using 2D piezoelectric inkjet printer. All images are reported without (top row) and with (bottom row of each set) cross-polarised filters. Images of all APIs are depicted six months from solvent evaporation while storage in accelerated conditions (75% relative humidity and 40°C in stability oven). 112

Figure 53. The figure shows different APIs recrystallisation profiles at different numbers of printed droplets with different final masses of printed spots starting at 50 droplets (final mass 100-110 ng), 100 droplets (mass 200-220 ng), 200 droplets (mass 400-440 ng), 300 droplets (mass 600-660 ng), 400 droplets (mass 800-880 ng) and 500 droplets (mass 1000-110 ng). All images are reported without (top row) and with (bottom row of each set) cross-polarised filters. Images of all APIs are depicted six months from solvent evaporation while storage in accelerated conditions (75% relative humidity and 40°C in stability oven) 119

Figure 54. An example of an array section depicted by PLM. All the spots are reported with bright field and cross-polarised filters (top and bottom of each section, respectively). Images of all Flurbiprofen/PVPVA (for example, as one of the drugs used in this study) at all of the different ratios (starting from 0% to 100% with a 5% increment) are depicted after 6 months of storage in accelerated conditions (75% relative humidity and 40°C in stability oven). The final mass of individual spots is 1000-1100 ng. 121

Figure 55. Examples of different APIs/PVPVA printed dispersions, starting from 0% to 100% API using 19 APIs and one polymer (PVPVA). All images are reported without cross-polarised filter. All images are reported after storage of the microarrays in accelerated conditions for 6 months (75% relative humidity and 40°C in a stability oven). Final mass 1000-1100 ng. 125

Figure 56. Examples of different APIs/PVPVA printed dispersions using cross-polarised filters, starting from 0% to 100% API using 19 APIs and one polymer (PVPVA). All images are reported after storage of the microarrays in accelerated conditions for 6 months (75% relative humidity and 40°C in a stability oven). Final mass 1000-1100 ng. 128

Figure 57. Examples of different APIs/PVPVA printed dispersions. All images are reported without (top part of each section) and with (bottom part) cross-polarised filter. The top section shows the API/polymer loading ratios with no birefringence (no crystallisation monitored). In contrast, the middle section shows the API/polymer loading ratios that show the start of birefringence detection (start of crystallisation), and the bottom section shows the API/polymer loading ratios that show apparent birefringence detection (crystallisation). Three different ratios for API/polymer loading were displayed to compare the assessment of crystallisation by PLM. All images are reported after storage of the microarrays in accelerated conditions for 6 months (75% relative humidity and 40°C in stability oven). Final mass 1000-1100 ng 129

Figure 58. Examples of different APIs/Soluplus printed dispersions. All images are reported without (top part of each section) and with (bottom part) cross-polarised filter. The top section shows the API/polymer loading ratios with no birefringence (no crystallisation monitored). In contrast, the middle section shows the API/polymer loading ratios that show the start of birefringence detection (start of crystallisation), and the bottom section shows the API/polymer

loading ratios that show apparent birefringence detection (crystallisation). Three different ratios for API/polymer loading were displayed to compare the assessment of crystallisation by PLM. All images are reported after storage of the microarrays in accelerated conditions for 6 months (75% relative humidity and 40°C in stability oven). Final mass 1000-1100 ng. 132

Figure 59. Examples of three APIs/HPMCAS printed dispersions. All images are reported without (top part of each section) and with (bottom part) cross-polarised filter. The top section shows the API/polymer loading ratios with no birefringence (no crystallisation monitored). In contrast, the middle section shows the API/polymer loading ratios that show the start of birefringence detection (start of crystallisation), and the bottom section shows the API/polymer loading ratios that show apparent birefringence detection (crystallisation). Three different ratios for API/polymer loading were displayed to compare the assessment of crystallisation by PLM. All images are reported after storage of the microarrays in accelerated conditions for 6 months (75% relative humidity and 40°C in a stability oven). Final mass 1000-1100 ng. 134

Figure 60. The figure shows plotting the data of the three APIs with API/polymer loading w/w% at which no birefringences were detected (no crystallisation monitored) as the miscibility limit of API within the polymer using three polymers; PVPVA, Soluplus and HPMCAS. 138

Figure 61. The figure shows plotting the data of the different APIs with the limiting concentration (loading %) at which no birefringences were detected (no crystallisation monitored) as the miscibility limit of API within the polymer using 2 polymers; PVPVA and Soluplus. 139

Figure 62. The top row shows the spots by drop cast technique for Flurbiprofen/PVPVA pipetted on gold-coated glass slides as substrate. a) Pure polymer PVPVA (0%), b) 40% Flurbiprofen/PVPVA, c) 45% Flurbiprofen/PVPVA, d) 50% Flurbiprofen/PVPVA, e) Pure Flurbiprofen. (100%). Images were depicted as resembling a small section taken with optical (middle row) and cross-polarised (bottom row). 142

Figure 63. The top row shows the spots by drop cast technique for pure APIs pipetted on gold-coated glass slides as substrate. a) pure Orlistat (0%), b) pure Fenofibrate, c) pure Itraconazole, d) pure Celecoxib. Images were depicted as resembling a small section taken with optical (middle row) and cross-polarised (bottom row). 143

Figure 64. The top row shows the spots by drop cast technique for Nitrofurantoin/PVPVA pipetted on gold-coated glass slides as substrate. a) Pure Nitrofurantoin (0%), b) 10% Nitrofurantoin/PVPVA, c) 15% Nitrofurantoin/PVPVA, d) 25% Nitrofurantoin/PVPVA. Images were depicted as resembling a small section taken with optical (middle row) and cross-polarised (bottom row). 144

Figure 65. The top row shows the spots by drop cast technique for Flufenamic acid/PVPVA pipetted on gold-coated glass slides as substrate. a) Pure Flufenamic acid (0%), b) 40% Flufenamic acid/PVPVA, c) 45% Flufenamic acid/PVPVA, d) 55% Flufenamic acid/PVPVA. Images were depicted as resembling a small section taken with optical (middle row) and cross-polarised (bottom row). 145

Figure 66. The top row shows the spots by drop cast technique for Estradiol/PVPVA pipetted on gold-coated glass slides as substrate. a) Pure Estradiol (0%), b) 25% Estradiol/PVPVA, c) 30% Estradiol/PVPVA, d) 40% Estradiol/PVPVA. Images were depicted as resembling a small section taken with optical (middle row) and cross-polarised (bottom row). 145

Figure 67. Miscibility limit (% at which no birefringence detected) for Itraconazole/PVPVA, Itraconazole/Soluplus, Itraconazole/HPMCAS printed in the present work (blue) and limiting concentration extracted from film-casting previously published data in the

literature (red) are shown in the figure. The same miscibility/compatibility trend was found when comparing the two sets of data, HPMCAS > Soluplus > PVPVA.....	147
Figure 68. Variability in the chemistry of the physicochemical properties of APIs used in this model.....	157
Figure 69. The Percentage of crystallization observed in drug samples at various drug loadings within the two polymer matrices (PVPVA and Soluplus) as within the whole data set. This bar graph illustrates the experimental data collected for multiple drugs, showcasing the frequency of crystallization events as a function of drug loading percentages. Each bar represents the proportion of samples that exhibited crystallization at specified drug loading levels.....	168
Figure 70. Fitted R ² extracted from the multiple linear regression model for the PVPVA data set, using all drug/polymer loadings (5-100% with 5% increment) for 23 employed APIs.	169
Figure 71. Scatter plot of coefficient values for hydrogen bond acceptors (HBA) variable obtained from multiple linear regression analyses across 23 different drugs at varying drug/polymer loadings from 5 to 100% using the data collected from the two polymers.....	171
Figure 72. Scatter plot of coefficient values for the number of Oxygen atoms (nO) variable obtained from multiple linear regression analyses across 23 different drugs at varying drug/polymer loadings from 5 to 100%.....	172
Figure 73. Scatter plot of coefficient values for the number of heteroatoms (nHet) variable obtained from multiple linear regression analyses across 23 different drugs at varying drug/polymer loadings from 5 to 100%.....	173
Figure 74. Scatter plot of coefficient values melting point (mp) variable obtained from multiple linear regression analyses across 23 different drugs at varying drug/polymer loadings from 5 to 100%.....	174
Figure 75. Scatter plot of intercept values obtained from multiple linear regression analyses across 23 different drugs at varying drug/polymer loadings from 5 to 100%.....	175
Figure 76. The correlation matrix displays the pairwise correlations between the predictor variables and log stability within PVPVA. Each cell represents the correlation coefficient between the corresponding variables. These correlations are not derived from the linear regression model. (mp: melting point, nHet: number of heteroatoms, HBA: number of hydrogen bond acceptors and nO: number of oxygen atoms).	179
Figure 77. Comparison of predicted log stability, determined using the LOOCV method based on the multiple linear regression model, versus measured log stability from experimental microarray data for Theophylline (A), Nitrofurantoin (B), Flufenamic Acid (C), and Tolbutamide (D) across a range of drug loadings within the PVPVA polymeric matrix. The blue bars indicate the predicted stability, while the red bars show the measured stability, allowing for an evaluation of the predictive model's accuracy at different drug loadings.	184
Figure 78. Comparison of predicted log stability, determined using the LOOCV method based on the multiple linear regression model, versus measured log stability from experimental microarray data for Nifedipine (A), Felodipine (B), Ritonavir (C), and Fenofibrate (D) across a range of drug loadings within the PVPVA polymeric matrix. The blue bars indicate the predicted stability, while the red bars show the measured stability, allowing for an evaluation of the predictive model's accuracy at different drug loadings.....	186
Figure 79. A fitted r-square was extracted from the multiple linear regression model for the Soluplus data set, using all drug/polymer loadings (5-100% with 5% increment) for 23 employed APIs.....	195

Figure 80. Scatter plot of coefficient values for the number of heteroatoms (nHet) variable obtained from multiple linear regression analyses across 23 different drugs at varying drug/polymer loadings from 5 to 100%.....	196
Figure 81. Scatter plot of coefficient values for hydrogen bond acceptors (HBA) variable obtained from multiple linear regression analyses across 23 different drugs at varying drug/polymer loadings from 5 to 100%.....	197
Figure 82. Scatter plot of coefficient values for the number of Oxygen atoms (nO) variable obtained from multiple linear regression analyses across 23 different drugs at varying drug/polymer loadings from 5 to 100%.....	198
Figure 83. Scatter plot of coefficient values for Water accessible area (ASA) variable obtained from multiple linear regression analyses across 23 different drugs at varying drug/polymer loadings from 5 to 100%. (A^2 is the unit of surface area).....	199
Figure 84. Scatter plot of coefficient values for melting point (mp) variable obtained from multiple linear regression analyses across 23 different drugs at varying drug/polymer loadings from 5 to 100%.	200
Figure 85. Scatter plot of intercept values obtained from multiple linear regression analyses across 23 different drugs at varying drug/polymer loadings from 5 to 100%.	201
Figure 86. The correlation matrix displays the pairwise correlations between the predictor variables and log stability within Soluplus. Each cell represents the correlation coefficient between the corresponding variables. These correlations are not derived from the linear regression model. (mp: melting point, nHet: number of heteroatoms, ASA: accessible water surface area, HBA: number of hydrogen bond acceptors and nO: number of oxygen atoms).	206
Figure 87. Comparison of predicted log stability, determined using LOOCV method based on the multiple linear regression model, versus measured log stability from experimental microarray data for Theophylline (A), Nitrofurantoin (B), Atenolol (C), and Piroxicam (D) across a range of drug loadings within the Soluplus polymeric matrix. The blue bars indicate the predicted stability, while the red bars show the measured stability, allowing for an evaluation of the predictive model's accuracy at different drug loadings.	211
Figure 88. Comparison of predicted log stability, determined using the LOOCV method based on the multiple linear regression model, versus measured log stability from experimental microarray data for Nifedipine (A), Felodipine (B), Orlistat (C), and Aprepitant (D) across a range of drug loadings within the Soluplus polymeric matrix. The blue bars indicate the predicted stability, while the red bars show the measured stability, allowing for an evaluation of the predictive model's accuracy at different drug loadings.	214
Figure 89. The molecular structures of two APIs, Flurbiprofen and Piroxicam, alongside the structure of a polymer, Polyvinylpyrrolidone-vinyl acetate (PVPVA), referred to here as Kollidon VA 64, utilised within this research [232, 233].	234
Figure 90. 3D inkjet printer, the Dimatix, utilised in this study, along with an annotated schematic detailing its key components such as the fiducial camera, ink reservoir, 12-jet Samba cartridge, drop watcher camera, cleaning pad, and substrate position.	235
Figure 91. The stages of 3D printing optimisation, progress using 30% Flurbiprofen/PVPVA from precise droplet deposition (fine-tuning droplet formation) (A) to printing continuous lines (B) to the creation of larger, uniform structures of defined square formulation (0.5mm × 0.5 mm) (C) and finally, square formulations (3mm × 3mm) (D) as shown in the microscopic images at the bright field.	238

Figure 92. Four bright-field microscopic images of the same 3D-printed formulation prepared with a 30% Flurbiprofen/PVPVA mixture. Each image captures the 3D-printed formulation from a different angle, providing a comprehensive view of its structure. The scale bar represents 200 μm .

..... 241

Figure 93. Microscopic images of the same 3D-printed formulation of Flurbiprofen/PVPVA within storage in accelerated stability conditions ($40^{\circ}\text{C} \pm 2^{\circ}\text{C}/75\% \text{RH} \pm 5\% \text{RH}$). The four images on the top (A) are captured in bright fields, and those on the bottom (B) are in polarised light; both sets provide views from different angles to identify any crystalline formations within the structure.

..... 243

Figure 94. Four bright-field microscopic images of the same 3D-printed formulation prepared with a 30% Piroxicam/PVPVA mixture. Each image captures the formulation from a different angle, providing a comprehensive view of its structure. The scale bar represents 200 μm

245

Figure 95. Microscopic images of the same 3D-printed formulation of Piroxicam/PVPVA within storage in accelerated stability conditions ($40^{\circ}\text{C} \pm 2^{\circ}\text{C}/75\% \text{RH} \pm 5\% \text{RH}$). The four images on the top (A) are captured in bright fields, and those on the bottom (B) are in polarised light, both sets provide views from different angles to identify any crystalline formations within the structure.

..... 246

List of Tables

Table 1. Solubility definition in the USP [14]	6
Table 2. Summary of commercially available solid dispersions in oral dosage forms, detailing the trade name, active pharmaceutical ingredients (APIs) included, polymers (carriers) utilized, their various applications, and the manufacturing companies adapted from sources [97-102].	18
Table 3. Examples of inkjet dispensing systems reported in the literature for the study of pharmaceutical printing.	41
Table 4. The calculated physicochemical parameters of the APIs used in this study as calculated from Chemicalize from Chemaxon and their melting points as obtained from ChemSpider [231, 232].	53
Table 5. The composition of slide 1 was performed using Hamilton syringe.	82
Table 6. The composition of slide 2 was performed using Hamilton syringe.	83
Table 7. Design of printing microarrays by Piezoelectric (Sciencion S5) printer, including the number of droplets of API and polymer printed per spot and the nominal mass of each per spot.	94
Table 8. Equilibrium Relative Humidity of selected saturated salt solution [266].	97
Table 9. The table shows the measured roughness of the gold-coated slides by AFM and the calculated average roughness.	102
Table 10. Stability of the printed pure APIs (birefringence detection point) in days during storage for six months in accelerated conditions ($40^{\circ}\text{C} \pm 2^{\circ}\text{C}/75\% \text{RH} \pm 5\% \text{RH}$).	114
Table 11. Comparing crystallisation Behavior Following 2D inkjet printing stored in accelerated conditions for 6 months versus following Spin Coating stored in dry conditions for 7 days.	116
Table 12. Stability of the printed microarrays of each API with PVPVA in API/polymer loading from 5% to 100% with 5% API increment (the last time point in days where no crystals were observed). Microarrays were kept in accelerated conditions ($40^{\circ}\text{C} \pm 2^{\circ}\text{C}/75\% \text{RH} \pm 5\% \text{RH}$) for six months.	130
Table 13. Stability of the printed microarrays of each API with Soluplus in API/polymer loading from 5% to 100% with 5% API increment (the last time point where no crystals were observed represented in days). Microarrays were kept in accelerated conditions ($40^{\circ}\text{C} \pm 2^{\circ}\text{C}/75\% \text{RH} \pm 5\% \text{RH}$) for six months.	133
Table 14. Stability of the printed microarrays of each API with HPMCAS in API/polymer loading from 5% to 100% with 5% API increment (the last time point where no crystals were observed represented in days), stored in accelerated conditions for 6 months. N: no crystallisation was observed for those samples during the whole period of the study.	135
Table 15. Comparison between the three polymers used in this study regarding the number of H-bond donors and acceptors per monomer unit. PVPVA, Soluplus and HPMCAS. The range of HBD and HBA for HPMCAS depends on the grade of HPMCAS, that is L, M or H [101, 273].	136
Table 16. Comparison between the APIs used in this study regarding the number of H-bond donors (HBD) and H-bond acceptors (HBA).	137
Table 17. Comparing the printed volume and deposited mass of two techniques, drop cast method and 2D inkjet printing.	141
Table 18. Nomenclature of the physicochemical properties used in the model.	154
Table 19. The frequency table shows the variability in the physicochemical properties, as appeared in the 20 models (one model at each drug/polymer loading) using PVPVA stability data and drug-polymer loadings from 5-100% for the 23 employed APIs in this study.	163

Table 20. Equations extracted from the model using the PVPVA data set and all drug/polymer loadings 5 to 100%.....	165
Table 21. Summary of the models' equations extracted using the LOOCV and the variables adopted in each equation for each of the 23 APIs used in this study within the PVPVA matrix. Where mp is the melting point, nHet is the number of Hetero atoms, nO is the number of oxygen atoms, HBA is the number of hydrogen bond acceptors, Mref is molar refractivity, and MW is the molecular weight.....	181
Table 22. The frequency table shows the variability in the physicochemical properties, as appeared in the 20 models using Soluplus stability data and drug-polymer loadings from 5-100% for the 23 employed APIs in this study.	190
Table 23. Equations were extracted from the model using the Soluplus data set, and all drug/polymer loadings were 5 to 100%.	192
Table 24. Summary of the models' equations from the LOOCV and the variables adopted in each equation for each of the 23 APIs used in this study within the Soluplus matrix. Where mp is the melting point, nHet is the number of Hetero atoms, HBA is the number of hydrogen bond acceptors, nHet_ring is the number of hetero rings, ASA is the accessible surface area, and nO is the number of oxygen atoms.....	208

Abbreviations

IND	Investigated new drug
NDA	New drug application
NCEs	New chemical entities
USP	United States Pharmacopeia
HTS	High-throughput screening
DMSO	Dimethyl sulfoxide
TPD	Targeted protein degradation
PROTACs	Proteolysis targeting chimaeras
API	Active pharmaceutical ingredients
SEDDS	Self-emulsification drug delivery systems
SMEDDS	Self-micro emulsification drug delivery systems
SNEDDS	Self-nano emulsification drug delivery systems
GIT	Gastrointestinal tract
T _m	Melting point
T _g	Glass transition temperature
ASD	Amorphous solid dispersion
PVP	Polyvinylpyrrolidone
HPMC	Hydroxy propyl methyl cellulose
PEG	Poly ethylene glycol
HPC	Hydroxypropyl cellulose
HPMCAS	Hydroxy propyl methyl cellulose acetate succinate
PVPVA	Poly vinyl pyrrolidone vinyl acetate

HME	Hot melt extrusion
XRPD	X-Ray powder diffraction
DSC	Differential scanning calorimetry
BCS	Biopharmaceutical classification system
DCS	Developability classification system
SLAD	Solubility limited absorbable dose
MD	Molecular dynamics
RH	Relative humidity
DoD	Drop on demand
TIJ	Thermal inkjet
FTIR	Fourier transform infrared
ATR	Attenuated total reflection
DMF	Dimethyl formamide
AFM	Atomic force microscopy
WCA	Water contact angle
PLM	Polarised light microscopy
ICH	International Council for Harmonisation of Technical Requirements for Pharmaceuticals for Human Use
RMS	Root mean square
HBA	Hydrogen bond acceptor
HBD	Hydrogen bond donor
FIH	Flory-Huggins interaction
PCA	Principal component analysis

MLR	Multiple linear regression
BIC	Bayesian information criterion
AIC	Akaike information criterion
MSE	Mean squared error
LOOCV	Leave-one-out cross-validation
CAD	Computer-aided design
PB	Powder bed
FDM	Fused deposition modelling
SLA	Stereolithography
MED	Melt extrusion deposition
SSE	Semi-solid extrusion
PET	Polyethylene terephthalate
SEM	Scanning electron microscopy

1 Chapter 1: Introduction

1.1 *The journey of drug discovery and development*

The process of discovering and developing new drugs is a complex but highly rewarding endeavour, comprising several steps, starting with identifying the drug target and ending with introducing the drug to the market. A company has to screen thousands of compounds before it can take on the task of developing a promising compound. It is always conceivable for a drug candidate to fail at any stage of development for reasons related to quality, safety, toxicity, or effectiveness, which would raise the overall cost of research [1].

Any drug's lifecycle includes four primary phases: drug discovery, drug development, regulatory approval, and manufacturing and marketing, in between them, there are several further stages, as depicted in Figure 1. An average of around six to seven years could be spent on the discovery and preclinical stages and bringing the investigated new drug (IND) to the next step; around another six to seven years could be spent on clinical trials to ensure the medicine is safe for human use. More time (around one and a half to two years) would be essential for the regulatory approval of the new drug application (NDA) to be examined and approved. Further studies and testing from the innovator company would be requested during this process, which may cause a further delay in the drug discovery process [1].

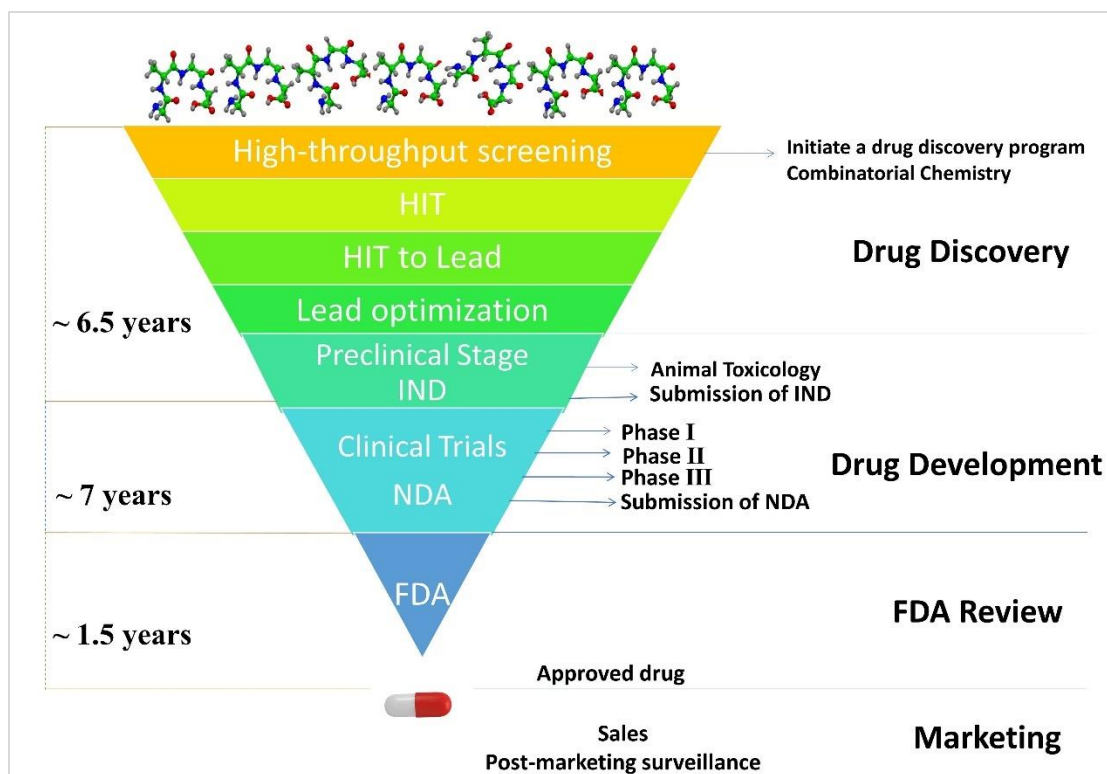


Figure 1. Drug Discovery Process and timeline.

1.2 Oral drug delivery

Following oral administration of a dosage form, the dosage form typically disintegrates into smaller particles in the stomach or intestine, where it dissolves and is then absorbed across the intestinal lining into the bloodstream. The dose, permeability, and water solubility are the main factors affecting the degree of absorption of a drug [2]. Oral drug delivery offers several advantages, including ease of administration, accurate dosing, and flexibility in formulation design. However, challenges such as variability in gastrointestinal conditions, first-pass metabolism in the liver, and patient compliance can affect the efficacy and bioavailability of orally administered drugs. Innovative technologies, such as drug delivery systems designed to improve absorption and control drug release, continue to advance the field of oral drug delivery, enhancing therapeutic outcomes and patient care [3, 4]. Soluble and permeable compounds are entirely released in the gastrointestinal system and can easily pass through the cell membranes (e.g.

enterocytes). High solubility and membrane permeability ensure that a drug has no issues with bioavailability. Otherwise, rigorous formulation studies are necessary [5].

The Biopharmaceutical Classification System (BCS) and the Developability Classification System (DCS) serve as valuable tools in drug development. The BCS categorizes APIs based on solubility and permeability, identifying formulations that may require improvement for optimal absorption.

1.2.1 Biopharmaceutical classification system (BCS) and the Developability classification system (DCS)

The biopharmaceutical classification system (BCS) is used as a support tool to highlight the potential ways to enhance bioavailability in drug development. The APIs have been classified into four categories based on solubility and permeability, as shown in Figure 2. Highly permeable APIs are the ones that are absorbed by humans at a rate of at least 90%. The maximum dosage strength of the API is shown to be soluble in 250 mL of aqueous solution with a pH range of 1-7.5 to meet the criterion for high solubility [6-8]. According to this system, class I is the best candidate to move on with clinical trials because of its high solubility and permeability properties. Particularly for class II APIs, inadequate bioavailability is typically caused by their limited solubility in GI fluids. Depending on the BCS, increasing the API's solubility and rate of dissolution in GI liquids may increase bioavailability. Since class III compounds' solubility is most likely high, their bioavailability depends on the permeability rate (high soluble, low permeable). Poor permeability and solubility characteristics of Class IV components make them unfavourable candidates for therapeutic development. As a result, formulation strategies to improve the solubility and dissolution of BCS class II and IV compounds are gaining more popularity [9].

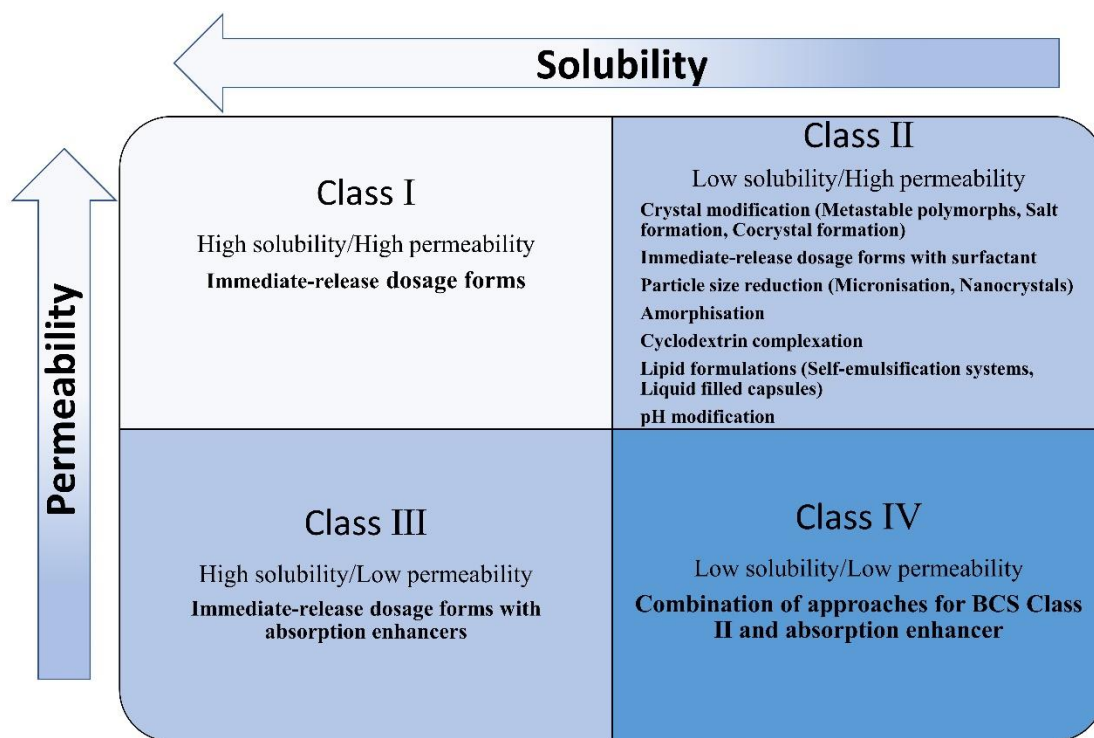


Figure 2. Biopharmaceutics classification system (BCS) and formulation strategies based on the BCS modified from [10].

A revised classification system based on BCS was proposed by Butler and Dressman to make this tool (BCS) more valuable and to enhance its utility in formulation development [8]. They suggested that the standard format of the system is overly cautious in evaluating absorption-limiting solubility and dissolution rate. Therefore, the modified system, named the Developability Classification System (DCS), expands the assessment volume for solubility of a dosage form to 500 mL instead of 250 mL used in the BCS using a fasted-state simulated intestinal fluid as the medium. Additionally, it subdivides class II into two subgroups, IIa and IIb, where IIa indicates dissolution rate limited and IIb indicates solubility limited. The boundary between these subclasses is determined by the solubility-limited absorbable dose (SLAD), calculated based on an estimate of small intestine solubility, fluid volume, and a permeability-dependent multiplier. The DCS more effectively categorises APIs based on characteristics that affect oral absorption. As a result, the

DCS provides a more helpful categorization tool for the issues related to the development of oral products [8].

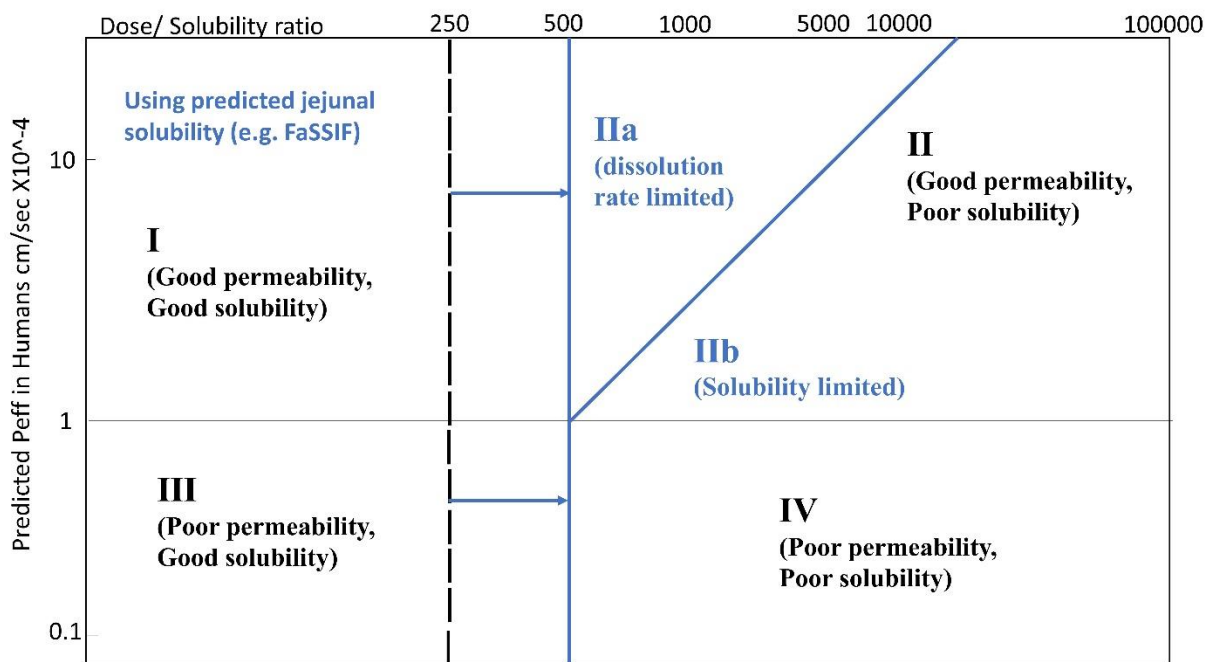


Figure 3. DCS (in blue) by modifying the BCS (in black) for more realistic volumes of fluid available in the GI tract and the compensatory nature of permeability on low solubility. FaSSIF: Fasted State Simulated Intestinal Fluid, Peff: effective permeability. Modified from [8].

1.2.2 Poor aqueous solubility

An important factor affecting bioavailability is aqueous solubility [5]. The property of a solid, liquid, or gaseous chemical substance known as a solute to dissolve in a solid, liquid, or gaseous solvent, forming a homogenous solution of the solute in the solvent, is known as solubility [11, 12]. The extent of solubility varies widely, from being completely miscible (infinitely soluble) like ethanol in water to poorly soluble like silver chloride in water. The term, insoluble is often applied to poorly or very poorly soluble compounds [13]. Solubility happens under dynamic equilibrium as it is the outcome of the simultaneous and opposing processes of dissolution and phase joining (such as the precipitation of solids). The saturation concentration, where adding more solute does not have a further effect on increasing the substance concentration in the solution, can be measured

as the extent of the solubility of that substance in a specific solvent [11, 12]. As shown in Table 1, the United States Pharmacopeia (USP) divides solubility in water in terms of quantification into seven categories that range from highly soluble substances (>1000 mg/ml; class I and III BCS) to essentially insoluble compounds (0.1 mg/ml; II and IV BCS) [14].

Table 1. Solubility definition in the USP [14]

Description forms (solubility definition)	Parts of solvent required for one part of the solute	Solubility range (mg/ml)	Solubility limit (mg/ml)
Very soluble (VS)	<1	>1000	1000
Freely soluble (FS)	From 1 to 10	100–1000	100
Soluble	From 10 to 30	33–100	33
Sparingly soluble (SPS)	From 30 to 100	10–33	10
Slightly soluble (SS)	From 100 to 1000	1–10	1
Very slightly soluble (VSS)	From 1000 to 10,000	0.1–1	0.1
Practically insoluble (PI)	>10.000	<0.1	0.01

Difficulties with solubility and pharmacokinetics under normal physiological conditions frequently lead to expensive failures in the later stages of drug development, which is a significant concern. It is estimated that about 90% of drug molecules face challenges with poor water solubility early in their development. Furthermore, poor water solubility is a primary factor in the bioavailability issues of around 40% of drugs currently on the market [15].

The rise in poorly soluble molecules can be attributed, at least in part, to advancements in combinatorial chemistry and the extensive use of high-throughput screening (HTS) methods. These methods, which are used to screen a large number of drug candidates, tend to focus on optimizing drug potency during the discovery phase [5]. With the introduction of high-throughput techniques, there has been an increase in the average molecular weight and lipophilicity of the compounds tested, leading to decreased solubility [16]. In vitro testing often involves dissolving compounds initially in dimethyl sulfoxide (DMSO) and then in water. This process results in an apparent concentration in water that is higher than the actual equilibrium concentration, leading to misleading data about the compound's water solubility. Although this aids in dissolving

compounds, it can significantly impact biochemical assays and result in the development of low-solubility compounds. Such discrepancies in solubility measurement methods can lead to unforeseen challenges in formulation and delivery when progressing to dosage forms [17]. Guidelines such as Lipinski's 'Rule of Five' could provide insights into where poor solubility could be expected regarding the physicochemical properties of the API. This rule, commonly applied by medicinal chemists during drug discovery, assists in predicting a compound's oral bioavailability and drug properties [18]. The Rule of Five stipulates criteria including lipophilicity (clogP) under 5, molecular weight under 500, no more than 5 hydrogen bond donors, and fewer than 10 hydrogen bond acceptors [19, 20]. According to this rule, a chemical failing to meet two or more criteria is likely to have oral bioavailability issues. The Rule of Five serves as a guideline for identifying key molecular properties important for a drug's absorption, distribution, metabolism, and excretion [20].

In the realm of chemical biology and drug discovery, targeted protein degradation (TPD) marks a new and exciting phase such as the innovative approach of Proteolysis Targeting Chimaeras (PROTACs) that offers promising prospects [21]. However, their inherent high molecular weight and physicochemical properties often result in limited solubility, impacting oral bioavailability [22]. Hence, research into orally deliverable PROTACs is garnering significant interest, with the primary challenge being their low water solubility, a critical factor for lipophilic drugs in oral formulations. Therefore, developing methods to overcome this low solubility is of paramount importance [23, 24].

1.2.3 Challenges connected with poor solubility

Poor solubility commonly negatively impacts the bioavailability of orally administered drugs, and compounds having an aqueous solubility of less than 0.1 mg/mL typically have dissolution-limited

absorption [25]. After oral administration, a lower dissolution rate causes poor bioavailability, hence incomplete release and absorption in the GIT after oral administration. That subsequently results in a decreased therapeutic effect [26].

NCEs with poor aqueous solubility carry an increased risk of failure during the preclinical and clinical phases. A substantial percentage of poorly soluble, highly potent NCEs do not adequately reach the clinical stage due to failure to improve solubility [27, 28]. The efficacy of in vitro assays during the drug development stage may be impacted by the poor solubility of new drug candidates. Several in vitro cell culture experiments are carried out during the drug discovery process to assess several biological characteristics of drug candidates, including efficacy, membrane permeability characteristics, and genotoxicity. A drug's solubility limitation or precipitation in the test medium may produce inaccurate results regarding the drug's in vitro properties. During preclinical development, toxicological studies often require more prolonged exposure than pharmacological or pharmacokinetic studies to verify the drug's safety, so the solubility constraint might potentially affect the quality of data on in vivo toxicity assessments. In clinical application, a pharmacological substance's inadequate bioavailability may have a limited therapeutic potential, resulting in unsatisfactory clinical results [10]. Recently, it has been suggested that formulation development should be done earlier to increase the chance of successfully developing poorly soluble compounds [29, 30].

1.3 *Strategies to overcome problems of poor water solubility*

In pharmaceutical research and drug development, several strategies have been explored to improve the poor water solubility of drug candidates, as shown in Figure 4.

1.3.1 Chemical alteration such as prodrugs

Chemical alteration of drug molecules is regarded as one of the options to enhance the solubility of drug candidates during the lead optimisation phase. Prodrug strategies may potentially increase the aqueous solubility of poorly soluble drugs in water by inserting a polar functional group into the molecule's structure [31]. The use of prodrugs has proven effective in enhancing water solubility compared to the parent drug, offering a valuable strategy to retain promising drug prototypes and expand therapeutic options hindered by poor solubility. Careful selection of the appropriate pro-moiety and linkage type (e.g., ester, amide, carbamate, and phosphate) plays a crucial role in prodrug selectivity, toxicity, and optimal bioconversion. Additionally, the prodrug approach serves as a viable alternative in early drug discovery phases, allowing for modulation of pharmacokinetic properties (absorption, distribution, metabolism, and excretion) and addressing critical issues like poor water solubility during preclinical stages. Most prodrugs are esters and amides due to their activation by esterases and amidases, leading to the release of the parent drug. Amino acids are commonly utilized as water-soluble pro-moieties, significantly improving solubility in water. Other chemical groups like glycol groups (e.g., polyethylene glycol and ethylene glycol) and glycosides are also utilized, albeit to a lesser extent. Although not all FDA-approved prodrugs aim to enhance solubility, several have been specifically designed for this purpose, including tedizolid phosphate, ceftaroline fosamil, and fospropofol disodium. Consequently, the prodrug approach represents a crucial component of rational drug design aimed at improving water solubility [32].

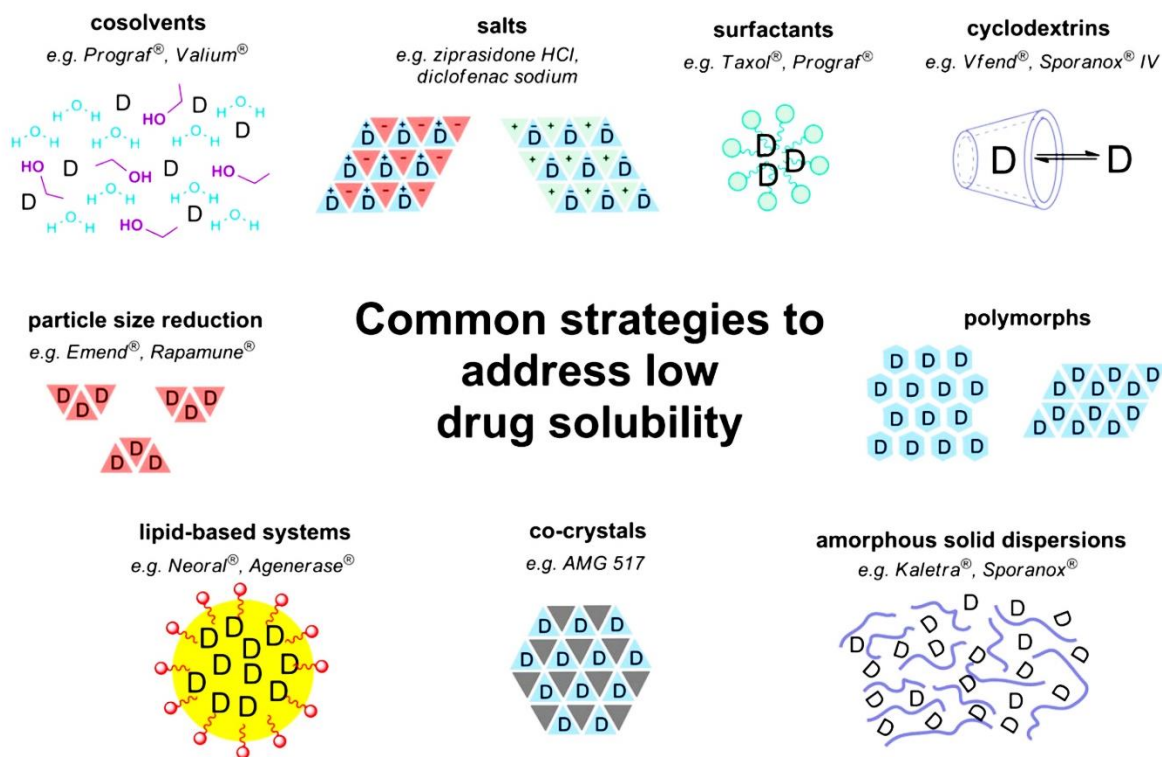


Figure 4. Schematic diagram shows the different techniques commonly used to address poor water solubility [33].

1.3.2 Crystal modification

1.3.2.1 Polymorphs

Polymorphism in crystalline substances describes the phenomenon where materials with identical chemical compositions exhibit different lattice structures and/or molecular conformation [34]. Many drugs are capable of crystallizing into multiple polymorphic forms. Each polymorph displays unique physicochemical properties such as melting point, density, solubility, and stability, which vary based on its energy state. Typically, the solubility of metastable polymorphs is kinetically higher compared to their thermodynamically more stable polymorphs [35]. It has been found that the solubility differences across polymorphs are generally less than 2.0-fold, although occasionally higher ratios can be observed [36]. Although using metastable polymorphs to enhance a drug's dissolution rate is considered a valuable strategy, metastable forms inevitably transform

into the thermodynamically stable form. For consistent bioavailability in oral doses, it is crucial to control the polymorphic transformation of the dosage forms during their production and storage [37].

1.3.2.2 Salt formation

Salt formation is one of the most commonly used techniques in the pharmaceutical industry to improve the dissolution properties of poorly water-soluble basic or acidic APIs [38]. A stable ionic bond can be formed between ionised API and a counter ion when the difference of pKa is greater than 3 [39]. The counter ion-containing salt alters the pH at a salt particle's dissolving surface in the diffusion layer, achieving a higher dissolution rate in the salts compared to the corresponding free forms [38]. Furthermore, the high local concentration achieved by the rapid dissolution of the salt forms can result in much higher concentrations of the drug in solution than non-salts in the local pH microenvironment [40]. For instance, compared to its free acid, tolbutamide's sodium salt form is reported to dissolve in an acidic pH environment 5,000 times faster [41]. Additionally, compared to their free base counterparts, strongly acidic salts of the weakly basic drugs such as ranitidine and chlorpromazine have better GI tract media dissolving characteristics [42]. Various counter ions can be employed; some are typically permitted in all quantities, while others must only be used in limited amounts due to potential toxic effects [43]. For un-ionisable APIs, this approach is ineffective [38].

1.3.2.3 Cocrystal formation

Cocrystals have recently received much attention for their potential to enhance the dissolution rate of poorly water-soluble drugs. Cocrystals are commonly understood to be crystalline substances formed of at least two distinct components with no charge transfer [44]. Pharmaceutical cocrystals are generally made in a stoichiometric ratio from an API and a nontoxic guest molecule (cocrystal former) through hydrogen bonding formation. Cocrystal formation does not include

proton transfer between the API and cocrystal formed, unlike salt formation. In several studies, cocrystal formation has been shown to increase oral bioavailability and dissolution rate [45, 46]. For instance, Amgen's compound (AMG-517) acts as a potent and selective VR1 antagonist in its free base form, yet it is insoluble at physiological pH due to the absence of a pKa value within this range. Creating a cocrystal of AMG 517 with sorbic acid showed an increased dissolution rate in fasted state-simulated intestinal fluid and a 9.4-fold rise in AUC_{0-inf} compared to its free base version following oral administration in dogs [47]. Besides other crystal engineering strategies, such as metastable polymorphs and salt formation, the cocrystal technique offers an alternative method to improve the dissolution rate of drugs with poor solubility, especially for those drug candidates that do not ionize at physiological pH [47].

1.3.3 Particle size reduction

1.3.3.1 Micronisation

The strategy of reducing particle size is frequently employed to enhance the dissolution rate of drugs. Micronization does not increase the equilibrium solubility of the drug itself but it increases the dissolution rate by increasing the surface area to drug ratio by which the active ingredient can dissolve or diffuse from the drug particles [48]. It is theorized that diminishing the particle size to less than 5 μm can lead to a larger surface area and a thinner diffusion layer, thereby speeding up the dissolution rate [49]. The micronisation process has effectively increased the bioavailability of poorly water-soluble drugs like griseofulvin, digoxin, and felodipine [50-52]. Mechanical pulverization of larger drug particles is a standard method to produce micronized particles. Dry milling methods such as jet milling, ball milling, and pin milling are used for this. The smallest particle size achievable with conventional milling methods for solid powders is around 2-3 μm . However, micronisation does not always significantly improve the dissolution rate, as it can lead to the agglomeration of drug particles, potentially decreasing the surface area available for

dissolution. Wetting agents, such as surfactants, would be crucial in this scenario for increasing the effective surface area [10].

1.3.3.2 Nanocrystals

Reducing particle size to the nanometer scale ($<1 \mu\text{m}$) is a promising approach for poorly water-soluble drugs. As previously discussed, this size reduction can increase surface area and decrease the diffusion layer thickness, potentially enhancing the dissolution rate of such drugs [53]. Common methods for producing nanocrystal formulations include wet-milling with beads, high-pressure homogenization, or controlled precipitation [54]. Surfactants and/or hydrophilic polymers are often employed to stabilise nanocrystal suspensions. These drug particles, once nanocrystallized, are dispersed into inert carriers after drying processes like lyophilization or spray drying. Extensive research has been conducted on how nanocrystal technology can boost the oral bioavailability of pharmaceuticals and nutraceuticals [55-68]. Neutral or acidic compounds like danazol [63], cilostazol [57, 68], tranilast [61], and curcumin [64] showed better enhancement in the pharmacokinetic parameters than basic compounds when formulated as a nanocrystal. Some nanocrystal formulations are available now in the market, such as Megace[®] ES, Rapamune[®], Emend[®], and TriCor[®] [10].

1.3.4 Cyclodextrin complexation

Cyclodextrins are oligosaccharides with a relatively hydrophobic inner cavity and a hydrophilic outer surface [69]. Cyclodextrins have been widely used to enhance the properties of poorly soluble drugs, and currently, there are many marketed cyclodextrin-containing solid dosage forms [10]. The physical mixture of the drug with cyclodextrins did not significantly show an increase in drug bioavailability after oral administration. However, bioavailability enhancement has been reported when forming the cyclodextrin-drug inclusion complexes [70].

1.3.5 Self-emulsification

Self-emulsification drug delivery systems (SEDDS) are increasingly utilized to enhance the oral bioavailability of poorly soluble drugs in water, especially those with high lipophilicity. These formulations consist of isotropic mixtures of oil, surfactant, cosolvent, and the drug in solubilized form [71]. These mixtures can rapidly form fine oil-in-water emulsions upon minimal agitation in an aqueous environment. Based on the oil droplet size, SEDDS are classified into self-micro emulsification drug delivery systems (SMEDDS) and self-nano emulsification drug delivery systems (SNEDDS) [72]. SMEDDS produce microemulsions with droplet sizes ranging from 100 to 250 nm, whereas those producing even smaller droplets, less than 100 nm, are categorized as SNEDDS. The quick emulsification of these formulations in the gastrointestinal tract (GIT) can enhance oral bioavailability and lead to a consistent plasma concentration profile. The size of the emulsion droplets is a critical factor influencing the absorption extent of orally administered drugs. Neoral[®], a SNEDDS formulation, is an excellent illustration of the efficiency of using smaller-size droplets; compared to Sandimmune[®], a coarse SMEDDS formulation, Neoral[®] demonstrated higher C_{max} in human trials. The mean peak cyclosporine levels were higher and were achieved significantly earlier with Neoral[®] (C_{max} 790.5 ± 216.5 ng/mL; T_{max} 1.8 ± 1.0 hr) than with Sandimmune[®] (C_{max} 589.4 ± 313 ng/mL, T_{max} 2.5 ± 1.7 hr), implying more rapid and better absorption [73, 74].

1.3.6 Amorphous versus crystalline form

Converting the crystalline drug form into their amorphous counterparts is one of the most promising techniques to enhance the dissolution of poorly soluble drugs compared to other approaches, such as simple micronisation [75] or salt formation [38], which have some limitations. The amorphous state is disordered at the molecular level compared to the crystalline state, as seen in Figure 5. Between 1.1 to 1000-fold variations in solubility have been reported between

amorphous and crystalline forms, which results in increased bioavailability [76, 77]. It is well-known that amorphous pharmaceuticals have better dissolution and thus better bioavailability properties than their crystalline counterparts. A material dissolves due to the breakage of intermolecular bonds caused by water molecules [78]. These advantages, however, can be lost at some point because the high internal energy and improved molecular mobility of amorphous materials also contribute to their higher chemical reactivity and propensity to recrystallise. That would lead to inadequate physical stability, which can occur during formulation, storage, or administration [76, 79-81]. Hence, much focus has been directed on understanding the critical factors affecting recrystallisation and the stability of amorphous forms of drugs.

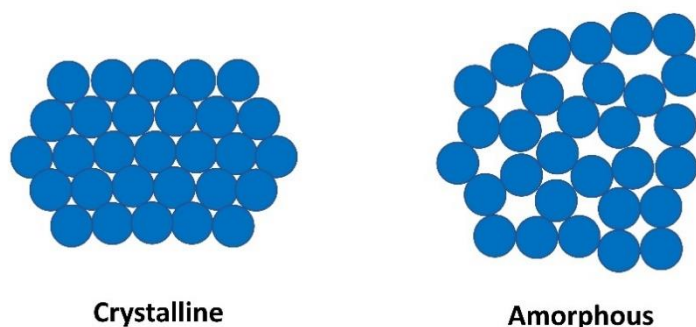


Figure 5. Order of molecules in Amorphous versus crystalline structure.

Amorphous materials frequently transform back into crystals over time because they are thermodynamically unstable. Two separate processes result in crystallisation: nucleation and crystal growth. Crystallisation is characterised by a lag time before stable nuclei are formed, and then these stable nuclei grow to form the crystalline form [82].

A schematic diagram of free energy temperature is shown in Figure 6 [83], which shows that as the temperature rises, the crystal's free energy decreases noticeably until the crystal's melting point (T_m) is reached, where the crystal spontaneously transforms into a liquid. If the produced system is slowly cooled below its T_m and there is enough time for crystal nucleation and crystal growth, the liquid phase will transform into a crystal form depending on the cooling rate of the formed

liquid. In contrast, if the system is quickly cooled and the crystallisation stage is skipped, it will maintain its liquid phase characteristics (supercooled liquid). Additionally, as the system continues to cool, the viscosity of the supercooled liquid rises. Hence, the glassy state will eventually be formed as it can be seen as a distinct discontinuity in the free-energy temperature phase diagram. The term “glass transition temperature” (T_g) refers to a temperature below which amorphous solids exist as a solid material, and above this temperature, it change to a liquid phase [84].

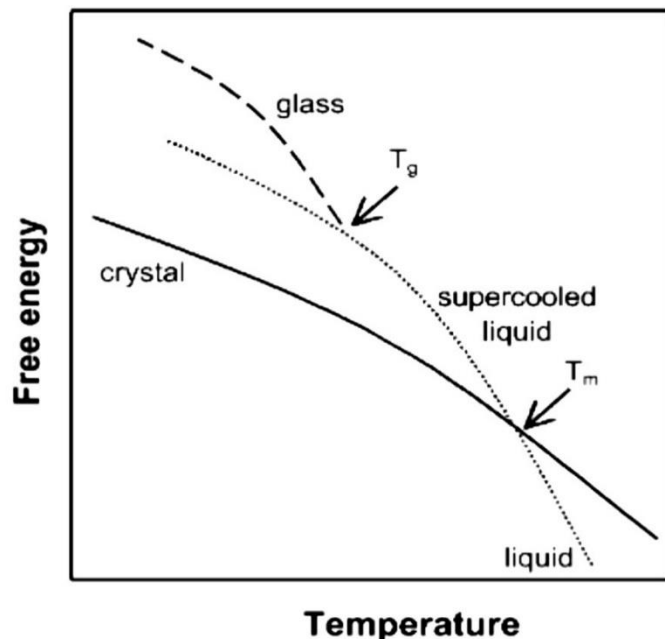


Figure 6. Schematic diagram of free energy versus temperature of a molecule in different states. [83].

1.3.7 Amorphous solid dispersion (ASD)

Amorphous solid dispersion formulations have gained interest in tailoring the physicochemical properties of drugs, such as dissolution and are considered one of the most promising strategies for bioavailability enhancement [26, 85]. Solid dispersions have been used successfully to improve drugs' bioavailability in various marketed products, as summarized in Table 2. Solid dispersions can enhance the dissolution through drug particle size reduction by dispersing the drug as small particles (ordered or amorphous) or as a molecular dispersion (sometimes referred to as a solid

solution) in an inert water-soluble carrier, commonly a hydrophilic polymer [86]. In these scenarios, the surface area of the drug available for solubilization is massively increased. If the drug is in an amorphous state or molecularly dispersed, this also enhances the dissolution rate compared to the crystalline form. The reduction of particle size to nearly a molecular level. As the soluble carrier dissolves, the insoluble drug is exposed to dissolution medium as very fine particles leading to an increase in both surface area and solubilization for fast dissolution and absorption. Formation of amorphous forms of drugs and carriers. The presence of a carrier may also prevent the aggregation of fine drug particles, thereby providing a larger surface area for dissolution [87]. Numerous studies have shown that ASD approaches significantly increase oral absorption [58, 88-95].

Compared to crystalline formulations comprising bulk API or a physical mixture of API and carriers, the ASD techniques exhibited 1.5–82 fold and 1.6–113.5 fold increases in C_{max} and AUC, respectively [10]. 5-lipoxygenase/cyclooxygenase inhibitor with potent anti-inflammatory activity ER- 34122 (Eisai) was reported in the literature as it has limited water solubility (<10 ng/mL). Surprisingly, the C_{max} and AUC values following oral administration of the amorphous solid dispersion formulations in dogs were around 100 times greater than those of the pure drug [96].

Table 2. Summary of commercially available solid dispersions in oral dosage forms, detailing the trade name, active pharmaceutical ingredients (APIs) included, polymers (carriers) utilized, their various applications, and the manufacturing companies adapted from sources [97-102].

Abbreviations include PVP for polyvinyl pyrrolidone, HPMC for hydroxypropyl methylcellulose, PEG for polyethylene glycol, HPC for hydroxypropyl cellulose, HPMCAS for hydroxypropyl methylcellulose acetate succinate and PVPVA for polyvinyl pyrrolidone vinyl acetate.

Trade name	API/ Drug	Polymer Carrier	Class/ Use	Manufacturer
Astagraf XL®	Tacrolimus	HPMC	Immunosuppressant	Astellas Pharma
Belsomra®	Suvorexant	PVPVA	Insomnia	Merck
Braftovi®	Encorafenib	PVPVA	Anti-cancer (colorectal cancer)	Pierre Fabre Medicament
Certican®	Everolimus	HPMC	Immunosuppressant	Novartis
Cesamet™	Nabilone	PVP	Anti-cancer	Valeant Pharmaceuticals
Crestor®	Rosuvastatin	HPMC	Hyperlipidemia	AstraZeneca
Cymbalta®	Duloxetine	HPMCAS	Depression	Lilly
Envarsus	Tacrolimus	HPMC	Immunosuppressant	Rottendorf Pharma GmbH
Epclusa®	Sofosbuvir/ Velpatasvir	PVPVA	Chronic hepatitis C	Gilead Sciences Ireland UC
Erleada®	Apalutamide	HPMCAS	Anti-cancer	Janssen
Fenoglide®	Fenofibrate	PEG 6000	Hyperlipidemia	Valeant Pharmaceuticals
Gris-PEG®	Griseofulvin	PEG 6000	Fungal infection	Valeant Pharmaceuticals
Gris-PEG®	Griseofulvin	PVP	Fungal infection	VIP Pharma
Harvoni®	Ledipasvir/Sofosbuvir	PVPVA	Chronic hepatitis C	Gilead Sciences Ireland UC
Incivek®	Telaprevir	HPMCAS	Chronic Hepatitis C	Vertex
Incivo®	Etravirine	HPMCAS	Chronic Hepatitis C	Janssen Pharmaceuticals
Intelence®	Etravirine	HPMC	Protease inhibitor (AIDS virus)	Tibotec
Isoptin SR®	Verapamil	HPMC/HPC	Hypertension	AbbVie
Kaletra®	Lopinivir and Ritonavir	PVPVA	Protease inhibitor (AIDS virus)	AbbVie Ltd.
Kalydeco®	Ivacaflor	HPMC AS	Cystic fibrosis	Vertex
Lynparza®	Olaparib	PVPVA	Anti-cancer	AstraZeneca
Mavyret™	Glecaprevir/ Pibrentasvir	PVPVA	Chronic hepatitis C	AbbVie
Modigraf®	Tacrolimus	HPMC	Immunosuppressant	Astellas Pharma
Nimotop®	Nimodipine	PEG	Calcium antagonist	Bayer AG
Nivadil®	Nivaldipine	HPMC	Hypertension	Fujisawa Pharmaceuticals Ltd.

Norvir®	Ritonavir	PVP	Protease inhibitor (AIDS virus)	AbbVie
Noxafil®	Posaconazole	HPMCAS	Fungal infection	Merck
Onmel®	Itraconazole	HPMC	Onychomycosis	Merz Pharma
Oriahnn™	Elagolix/ estradiol/ norethindrone acetate	PVPVA	Uterine leiomyomas	AbbVie
Orilissa®	Elagolix	PVP	Endometriosis pain	AbbVie
Orkambi®	Lumacaftor/ Ivacaftor	HPMCAS	Cystic fibrosis	Almac Pharma Services Limited
Rezulin®	Troglitazone	HPMC	Diabetes	Parke Davis Pharmaceuticals
Prograf®	Tacrolimus	HPMC	Immunosuppressant	Astellas Pharma
Symdeko®	Tezacaftor/ Ivacaftor	HPMCAS	Cystic fibrosis	Vertex
Trikafta®	Elexacaftor/ Ivacaftor/ Tezacaftor	HPMCAS	Cystic fibrosis	Vertex
Venclexta®	Venetoclax	PVPVA	lymphocytic leukaemia	AbbVie
Viekira XR™	Dasabuvir/ Ombitasvir/ Paritaprevir/ Ritonavir	PVPVA	Chronic hepatitis C	AbbVie
Zelboraf®	Vemurafenib	HPMC AS	Anti-cancer	Roche
Zepatier®	Elbasvir/ Grazoprevir	PVPVA	Long-term hepatitis C infection	Merck
Zortress®	Everolimus	HPMC	Immunosuppressant	Novartis

Numerous conventional techniques exist for the preparation of amorphous solid dispersion formulations. Techniques such as spray drying, melt extrusion, lyophilization, and using supercritical fluids with polymeric carriers and/or surfactants are employed in developing ASD formulations [26]. Among these, hot melt extrusion and spray drying are the most frequently utilized manufacturing methods. Typically, these processes are relatively straightforward to upscale and effectively create well-mixed dispersions [103, 104].

1.3.8 Hot melt extrusion (HME)

In the HME process, the initial material comprises a blend of the active pharmaceutical ingredient (API) and a polymer carrier. This powder mixture is introduced into the extruder through a hopper.

The extruder typically consists of a lengthy heated barrel housing two screws that either rotate at the same direction or opposite directions. The barrel is heated to a temperature generally above the glass transition temperature (T_g) of the polymer, causing the polymer to soften or melt and enabling dissolution of the API within the polymer matrix. The screws then mix the molten mass to achieve a uniform blend. Depending on the extruder size, the mixture may circulate for a specific duration to ensure thorough mixing. Upon extrusion, the blended material rapidly cools to form a solidified glass, which can undergo further processing such as pelletization or milling [105]. Because HME is more ecologically friendly (solvent-free procedure), and takes less time than spray drying, it is preferable to spray drying for creating ASD formulations [106-110]. The primary drawback of the HME approach is that it should not be used to treat heat-sensitive materials since doing so might result in thermal damage to the materials throughout the production process [107].

1.3.9 Spray drying

One of the techniques most commonly utilised in the formulation of ASD is the spray drying approach. This procedure involves dispersing a polymer and API in a volatile solvent like ethanol, methanol, dichloromethane, or acetonitrile [26, 111, 112]. This solution is delivered into the drying chamber through a nozzle, where it is atomised and sprayed through warm gas or air. The application of heat, which exceeds the solvent's boiling point, facilitates rapid evaporation of the solvent from the solution, resulting in the formation of small, uniform particles of solid dispersion. The particles subsequently dry within the chamber and are collected at the base of the cyclone [111].

In contrast to the HME, which is inadequate for formulating thermosensitive materials, the spray drying process is very convenient for processing thermosensitive materials [107]. Despite this benefit, this process has numerous drawbacks, such as using solvents, which prolongs the time needed to produce formulations and the risks and expenses of employing organic solvents.

Additionally, the product may become entrapped with the leftover solvent, which might affect its stability [99].

1.4 *The instability and scale-up problems of the ASD formulations*

Despite the advantages of solid dispersions, the number of marketed formulations is still not remarkably high because of issues such as scale-up and physical instability of the formulations. Poor scalability during the production process, such as melt extrusion or spray drying, is one of the drawbacks of ASD [26]. The physical instability of amorphous solid dispersions is the main drawback leading to drug-polymer phase segregation and the drug's recrystallisation (hence lowering bioavailability) during storage [113], as shown in Figure 7 [114]. The drug in such formulations may crystallise either during manufacturing (i.e., under the action of mechanical stress) or during storage (i.e. the influence of temperature and humidity stress). Temperature variations can induce physical changes in the solid dispersion. For instance, polymers can soften, and melt, or the drug would recrystallise at elevated temperatures, altering the dispersion's structure and drug release characteristics. Phase transitions, such as amorphous-to-crystalline transitions, can occur, impacting the dispersion's stability and performance [115]. One of the critical issues is the effect of moisture on the stability of solid dispersion, which can result in a reduction in the T_g of the mixture and, as a result, phase separation and crystallisation. ASD formulations often exhibit less chemical and physical stability than the equivalent crystalline solid. The dissolution and oral bioavailability of the drugs in the ASD formulation would decrease when the amorphous form becomes crystalline. The ASD techniques might not be appropriate for amorphous drugs with limited stability [10]. So, developing solid dispersion formulations can be

challenging both due to the long-time scales needed to determine stability and realistic large-scale methods used for preparation [116, 117].

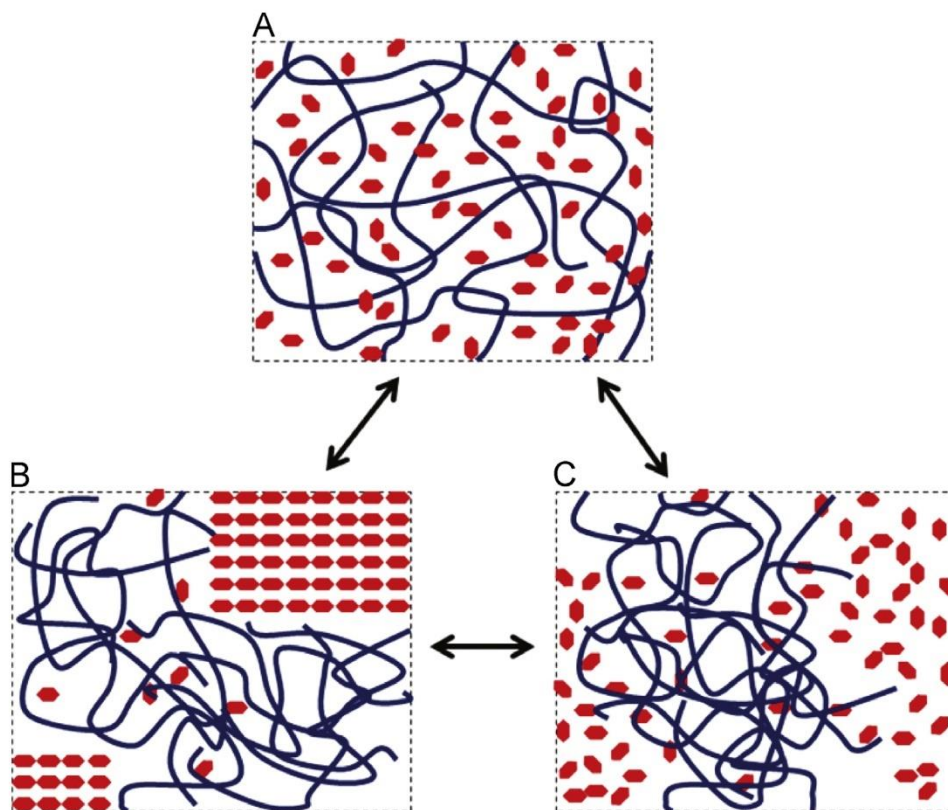


Figure 7. The figure illustrates three possible drug/polymer solid dispersion structures, with hexagonal figures representing drug molecules and wavy lines depicting polymer chains (A) in a homogeneous drug-polymer solution, polymer chains are random coils that interpenetrate each other and extend through the whole system, while drug molecules are dispersed randomly among the polymer segments (displays the optimal structure of a solid dispersion with the drug molecularly dispersed throughout the polymer matrix) (B) the drug molecules separate from the polymeric matrix and rearranged in the conformation that leads to crystallisation leading to instability of the formulation and (C) an intermediate meta-stable structure where the amorphous drug aggregates are dispersed in a polymer matrix containing drug at its amorphous solubility (displays a system where amorphous drug-rich areas are interspersed within the polymer matrix) [114].

1.5 Support Tools in Formulation Development

Due to the high demand for poorly soluble compounds, there is an urgent need to develop the best formulation approaches and the most stable form of poorly soluble drugs. Achieving suitable physical stability of solid dispersions is the most significant obstacle in their development. The carrier polymer itself is a crucial parameter for stability due to the need for miscibility between the drug and the polymer to limit molecular drug mobility and, hence, nucleation/crystallization

processes that lead to physical instability and loss of the desired dissolution enhancement. Assessment in practice is typically applying a single model drug with a small range of polymers for a very limited number of the selected drug: polymer compositions [117]. Using classical analytical techniques such as differential scanning calorimetry (DSC) and X-ray powder diffraction (XRPD) to determine drug stability, recrystallization and hence amorphicity of the drug requires the use of at least milligrams to grams of the sample [116], so are not suitable for strategies that are aiming to limit material use and a high-throughput approach.

A predictive support tool would be highly advantageous to offering early indications of solutions for solubility issues without undertaking numerous experiments with the potential of trial and error. Multiple parameters, such as the appropriate dose, administration route, shelf life, manufacturing technique, and physicochemical characteristics of the drug, would determine the best formulation for each drug. Therefore, it is particularly challenging to choose the best drug formulation. Poor formulation choice can negatively impact the drug development process, resulting in poor clinical data, requiring drug re-formulation and extended clinical trials, or even the project's termination [118]. Currently, various support tools that vary in the level of complexity and effectiveness could be used in the formulation development for poorly soluble drugs. These differ in complexity and efficiency, but most try to predict which route would best suit the API based on selected molecular parameters such as solubility and molecular weight. These tools range from minimal tools and trial-and-error techniques to employing a diverse array of sophisticated tools such as, high-throughput screening, guidance maps, and decision trees to the most complex methods based on computational modelling tools [119].

1.5.1 Predictive models

Predictive models are beneficial tools in the formulation development process. A model can predict the outcomes of specific experiments, such as predicting the stability or

dissolution, decreasing the number of experiments needed and cutting down on the cost and time required for the development process. A model can only be as general as the data set used to build it, which requires a large amount of data.

1.5.1.1 Current evaluation approaches

Due to the high demand for new medicines, there is an urgent need to develop the most appropriate formulation approaches. Currently, the evaluation of the performance of amorphous solid dispersions is reliant on time-consuming and costly stability tests. The mechanism of amorphous solid dispersions' physical stability is poorly understood concerning drug-polymer interactions or polymer-induced changes in molecular mobility [82, 99, 120]. Additionally, although attempts have been reported in the literature, it is not feasible as yet to utilise these factors to forecast long-term amorphous stability [113]. In addition, each experimental method typically requires a substantial amount of carrier-API formulation - potentially not available in early-stage development - and hence cost and in cases of failure. This lengthy cycle needs to be re-evaluated [121, 122]. Assessment in practice is typically based on trial and error evaluations of bulk samples applying a single model drug with a small range of polymers for a very limited number of the selected drug-polymer compositions [117].

1.5.1.2 Theoretical approaches in solid dispersion stability

As the determination of the physical stability of solid dispersions requires time-intensive and unpredictable trial-and-error experiments, various theories regarding stability have been proposed, including the use of solubility parameters and glass transition temperature (T_g) prediction model [123]. However, these theoretical models necessitate a large amount of physicochemical data for each component and a high degree of professional knowledge. Moreover, the predictive capability of these models is limited due to the uncontrolled errors in the mathematical hypothesis arising

from various factors related to data limitations, assumptions, complexity of interactions, and environmental factors such as temperature, humidity, and manufacturing processes [120].

To address this problem various theories and methodologies have emerged to interpret and predict the stability attributes. One of the theories assumes that drugs with a low T_g could be stabilised by polymers with a relatively high T_g due to the anti-plasticizing impact [124, 125]. Kestur and Taylor explored the stabilizing effect of different polymers and discovered that robust and widespread hydrogen bonds were established between polymers and felodipine, promoting stability [126]. Miscibility, solubility parameters, and the Flory-Huggins interaction parameter were leveraged to anticipate drug-polymer miscibility and physical stability [127].

1.5.1.2.1 Hildebrand solubility parameter and Hansen solubility parameter

Historically, thermodynamic and computational analyses are the major research pathways used in the field. The solubility and interaction parameters are frequently used to assess solvents and the substances they solubilize. The Hildebrand solubility parameter is calculated from cohesive energy density [128]. Hildebrand suggested that to dissolve a solute, the solubility parameter has to overcome the intermolecular attraction between the molecules in the solvent [129]. The Hansen parameter, which builds upon the Hildebrand parameter, considers energy from three sources: dispersion forces, dipolar intermolecular force, and hydrogen bonds between molecules [130, 131]. Most solvents display varying degrees of polarity and/or hydrogen bonding, making the Hansen solubility parameter a more precise tool for choosing the appropriate solvent. Nevertheless, this increased precision comes at the cost of added complexity, thereby complicating the process of solvent selection [129]. The solubility parameter and the miscibility between the drug molecules and polymer may be used in pharmaceutical research to predict whether the system is thermodynamically stable [127]. Even though there is no standard point to identify if a drug and a polymer are miscible or immiscible, solubility characteristics are commonly used in the rapid

screening of polymers [132]. The solubility parameters can be either calculated from experimental data combined with relevant theory or interpreted using the group contribution method, which correlates to the miscibility of the drug and polymer [133].

1.5.1.2.2 Flory-Huggins

An alternative theoretical framework is the Flory-Huggins interaction (FHI) parameter, which accounts for polymer chain size when adjusting the enthalpy equation by considering the polymer as a segment to compute its volume fraction [124]. A critical threshold is identified at an interaction parameter value of 0.5, where values below this signify miscibility, while those above indicate immiscibility. Various experimental methods exist for assessing the FHI parameter, including melting point depression, melting annealing, and other thermodynamic parameters [127]. The FHI theory proposes a linear correlation between the interaction parameter and the melting temperature. A phase diagram for drug composition temperature was developed to analyse the phase separation conditions and predict phase behaviour [77]. Another study has projected a three-month stability duration for solid dispersion, underscoring the utility of FHI and miscibility theory in evaluating the stability of solid dispersions [134].

Knopp et al. developed a comparison of various approaches to predict drug-polymer solubility using binary systems consisting of five model drugs (indomethacin, paracetamol, chloramphenicol, celecoxib and felodipine) and polyvinylpyrrolidone/vinyl acetate copolymers (PVPVA) of different monomer weight ratios. Drug-polymer solubility at 25 °C was predicted using the Flory-Huggins model based on data at elevated temperatures using different thermal analysis methods (based on the recrystallization of a supersaturated amorphous solid dispersion and two variations of the melting point depression method). The recrystallization and melting point depression methods accurately predicted solubilities, indicating their potential as a screening tool

if liquid analogues are available. This significant comparative study yielded valuable insights that can be used to pick the most appropriate method for drug-polymer solubility screening [135].

Duarte et al. presented a new screening approach to be used in the early development of spray-dried amorphous solid dispersions. It evaluates thermodynamics, kinetics, and evaporation to predict miscibility estimates of itraconazole in three different polymers (HPMCAS, PVPVA and Eudragit). It differs from most other models in that it considers the impact of the solvent in the system and its evaporation [136]. In addition, compared to other methods (such as using the Flory Huggins theory alone), it can assess a ternary system consisting of a drug, polymer, and solvent by comparing it to a traditional two-component system and taking time-dependent phenomena like solvent evaporation and component mass diffusion into account. The screening process described in this work demonstrated the ability to assess a set of amorphous formulation selections in a computer model, allowing for predicting the most appropriate polymers and identifying the best drug load range to be tested in laboratory experiments [136].

1.5.1.3 Mathematical approaches in solid dispersion stability prediction

1.5.1.3.1 Molecular dynamics

In addition to thermodynamic methods, mathematical techniques have also been employed in solid dispersion research. A "molecular dynamics (MD)" based strategy offers a molecular-level understanding of underlying mechanisms and intermolecular energy contributions [137]. MD simulations provide comprehensive atomic-level structural and energetic information that can help to predict the solubility and miscibility of amorphous drug-excipient solid dispersions [138]. Drug-polymer interactions may be better understood through visualization of the interaction and estimation of that interaction's strength through molecular modelling, which is a powerful addition to the F-H theory [139]. Much progress has been achieved recently using MD to develop model

drug-excipient glasses and understand their solubility/miscibility properties [137, 138, 140, 141]. Amorphous cellulose has been studied using MD by Mazeau et al. [142]. Using fully atomistic MD simulations, Gupta et al. calculated the solubility parameters of the chosen model compounds (drugs, nonpolymeric excipients, and polymeric excipients) [143]. In another study, using MD, Gupta et al. developed an in silico technique to predict the glass transition temperature of amorphous pharmaceuticals and investigate the effect of plasticizers on the T_g [137].

1.5.1.3.2 Principal Component Analysis (PCA)

Another mathematical model employed is principal component analysis (PCA), which was applied to a dataset of 153 drug-solvent combinations to predict the crystallization behaviour of the compounds. Spin coating was used as an effective method for preparing thin drug films and assessing their crystallization rates, which are categorized as rapid (Class I), intermediate (Class II), or slow (Class III). PCA showed distinct differences between Class I and III drugs, suggesting that crystallization tendencies could be predicted based on certain physical and molecular properties of the compounds, such as melting point, glass transition temperature, molecular weight, and the number of rotatable bonds and using an appropriate data set [144].

1.5.1.4 Statistical models

By reducing the time and money spent on trials, models can help speed up the development process and increase performance. A substantial amount of data is required to develop a statistical model, and the model's applicability will be limited to the dataset used. Yet, models may often provide reliable predictions and accurate correlations.

Some models have been developed to predict APIs' glass-forming ability and the stability of the amorphous state [145, 146]. Mahlin and Bergström investigated 50 diverse compound molecules for their glass-forming ability. They suggested a molecular weight cut-off of 300 for quickly predicting the ability to form glass. They found that the ability to form glass was accurately

predicted for 90% of the drugs based solely on their molecular weight. Additionally, drugs with a molecular weight greater than 300 g/mole were typically transformed into their amorphous state (good glass formers) [145]. Prediction of solid dispersion dissolution [147], drug solubility [148, 149], and organic molecule crystallinity [150] are other applications of statistical models in drug development.

Nurzyńska et al. developed a predictive model for the amorphous stability of drugs, particularly poorly water-soluble drugs [151]. They selected 25 neutral molecules with poor solubility from various compounds featuring diverse physicochemical properties and chemical structures. Polarised light microscopy was utilized to monitor the onset of crystallization in amorphous films formed by melting and rapid cooling over six months to assess the physical stability of the amorphous form. This observational data served as the response variable in a statistical model incorporating calculated/predicted or experimentally measured chemical, thermodynamic, and kinetic properties as explanatory variables. Several multiple linear regression models were developed with varying balances between calculated/predicted and measured parameters. The models showed that incorporating measured parameters notably enhances the model's predictive capacity. The most accurate model achieved 82% prediction accuracy, including melting and glass transition temperatures, fusion enthalpy, configurational free energy, lipophilicity, number of hydrogen bond donors, relaxation time, and the carbon-to-heteroatom ratio. Additionally, a simpler model, which only considered molecular weight and fusion enthalpy, still yielded reliable predictions [151].

A similar model was developed by Fridgeirsdottir et al. that included polymers used for solid dispersions [152] with ten weakly soluble drugs, three widely used polymers, and melt extrusion and spray production processes drying used to prepare 60 solid dispersion formulations.

Each formulation underwent a stability study for six months under accelerated conditions of 40°C and 75% relative humidity (RH). Notable variations were observed in the onset of crystallization across the two processing methods and among the different polymers. Several linear regression models were developed to correlate the physicochemical properties of the API with the stability data. These models aimed to identify which combination of processing technique and polymer carrier would most likely result in a stable solid dispersion. Six quantitative statistical models based on multiple linear regression were developed by selecting the most significant physical and chemical factors from a pool of 33 potential variables. Each model corresponded to a specific polymer and processing method combination and demonstrated good stability prediction. The models identified three key trends for formulating sufficiently stable solid dispersions. Specifically, the higher glass transition temperature (T_g) of the drug molecule in solid dispersions, a lower number of hydrogen bond donors, and increased molecular flexibility (indicated by the number of rotatable bonds and ring count) were all factors that contributed to improved stability [152].

1.5.2 High throughput screening (HTS)

During the formulation development process, a set of commonly used excipients is tested with NCE to choose the most suitable excipient. If those fail, there are many more excipients, ratios, and processing conditions to try. The drug candidate cannot progress if no formulation with acceptable physicochemical properties, including dissolution properties, is found. Through HTS, it is possible to test a large number of combinations of excipients or formulations using only a very small quantity of the API, which is extremely valuable, requiring less effort and time than performing larger-scale experiments [153, 154].

Several HTS methods have been utilized to develop formulations for compounds with poor solubility. ALZA Corporation, now owned by Johnson & Johnson, innovated a miniaturized

micro-screening solvent-casting method for quickly preparing and evaluating hundreds of formulations, using only small amounts of compound per formulation tested. In this process, the compound of interest and a range of excipients are dissolved in a chosen solvent like n-propanol and then robotically dispensed into a 96-well microtiter plate. A vacuum centrifuge evaporator is used to evaporate the solvent, leaving a neat formulation comprising 10–40 μg of the substance and 0.4 mg of excipient at the base of each well. Following the addition of an aqueous diluent, the plates are incubated at room temperature. The solubility of each formulation is then determined using either a UV plate reader or HPLC analysis [154].

McDonald et al. developed a high throughput screening approach that employs nanoprecipitation and freeze-drying techniques to identify viable nanosuspensions of the antimicrobial compound triclosan [155]. In that study, 252 formulations containing triclosan were produced and tested. The produced amorphous nanosuspensions, with z-average diameters between 170-290 nm, were freeze-dried and reconstituted in water. Factors such as the concentration of triclosan solution before nanoprecipitation and the concentration of polymer/surfactant influenced the particle size. Nanoparticles made using Pluronic F68 and the cationic surfactant Hyamine exhibited a ten-fold reduction (increased efficacy) in *Escherichia coli*'s inhibitory concentration (IC_{50}) of triclosan compared to an aqueous control, demonstrating an efficient method for generating viable nanosuspensions to improve the water solubility of commercially available bioactive compounds [155].

Shlar et al. developed an innovative high-throughput screening process to identify the most suitable ligands for stabilizing and enhancing the performance of curcumin nanoparticles in aqueous environments [156]. Twenty-eight potential stabilizing ligands were evaluated using the antisolvent precipitation technique. Nitrogen-containing polymers, both cationic and neutral,

showed effective stabilization. In contrast, anionic polysaccharides and most low-molecular-weight compounds were ineffective and led to increased coagulation of curcumin. The selected ligand significantly reduced particle size from 1,200 to 170–230 nm, improved stability, and increased the aqueous concentration of curcumin to up to 1.4 mM. These ligand-protected nanoparticles showed minimal inhibitory concentrations against *Escherichia coli* at 400 or 500 μM [156].

Dai et al. developed a micro-screening approach to rapidly screen various carriers/excipients for solid dispersion formulations with less than 10 mg of API. Seven precipitation inhibitors, nine enteric polymers, and their combinations were investigated. Each formulation was made using an evaporation process, and the solubility of each was determined by dissolving the film in a simulated intestinal fluid [153].

Previous research on HTS has inspired scientists to envision innovative strategies that are more time and resource-efficient than traditional screening methods in industries, notably within the pharmaceutical sector. The prevailing direction in pharmaceuticals emphasizes utilising high-quality, efficient materials that guarantee precise drug delivery. Active ingredients must be administered correctly and in minimal amounts. Consequently, the quest for a robust and reliable method that aligns with these criteria signifies a transformative shift in the pharmaceutical landscape [157].

1.6 *Printing Technologies*

Contact and non-contact printing are considered among the main surface patterning techniques used for microarray development due to their ability to deposit thousands of different molecules onto a substrate in an entirely automated fashion using a smaller amount of materials than other techniques [158].

1.6.1 Contact printing

Contact printing includes using a high-precision robotic arm with X-Y-Z movement to dip a rigid pin in the ink solution, pulling it out, leaving a small volume of liquid on the tip, and then placing the pin down on a solid surface to deposit the liquid on the substrate at the particular location of interest previously set by the software. Solid pins were used for printing small volumes, typically low nanolitres. The size and shape of the resultant spot are controlled by the geometry of the pin, which is either solid or with a slit analogous to an ink quill, as shown in Figure 8. A solid pin is easy to keep clean, making it convenient for transferring proteins and other sticky molecules. A slitted pin can withdraw a larger volume of solution, enabling repeated spotting without re-dipping, as shown in Figure 9A. This may be a huge time saver for long printing runs [158]. The benefits of using pins for a high-density array are their simplicity, robustness, low cost, and small size. Despite the wide range of solutions that this technique could use, the deposited droplet is not readily adjusted. Moreover, the possibility of surface damage due to pin-to-substrate surface direct contact is still a disadvantage of this technique [159].

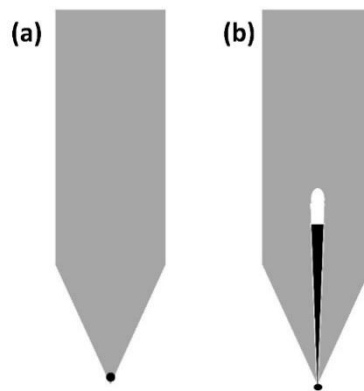


Figure 8. Schematic illustration of main types of pins used in contact printing: (a) solid pin, which holds a small volume of ink on its tip, (b) split or quill pin that holds a volume of ink in its slot, allowing multiple spotting per loading. (Adapted from [160]).

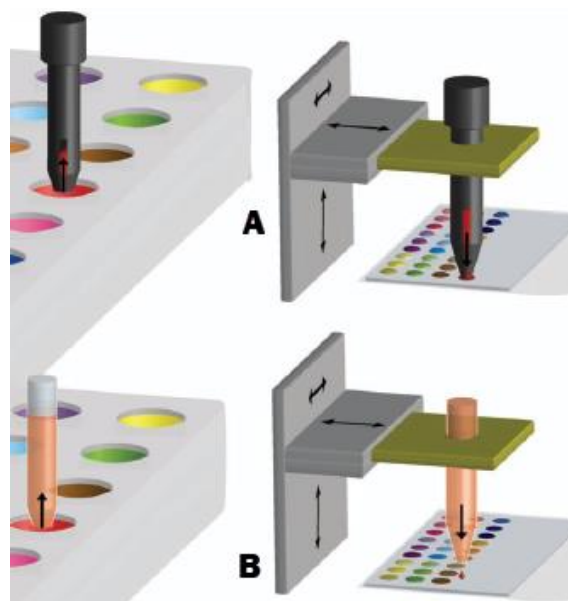


Figure 9. Schematic illustration of initial uptake (left side) of the solution (ink) from a source plate by A) the printing quill pin or B) the printing nozzle (both controlled by XYZ robotic arm) with subsequent deposition of a small volume to specific locations(right side)[158, 161].

1.6.2 Non-contact printing (Inkjet printing)

The non-contact printing technique (also termed “inkjet printing”) encompasses two operation modes: Drop on Demand (DoD) and continuous. Inkjet printing has emerged as an essential technology in many fields of science and industry. One advantage of this method is that it can produce droplets with a consistent shape and volume in nanolitres or picolitres [162] with a high degree of accuracy [160, 163] thanks to its high-productivity software and automation characteristics [164, 165]. Ink-jet printing works by applying force to produce a high-speed liquid stream (jet) that is ejected through a small orifice (nozzle), forming uniformly sized and spaced droplets [162]. A schematic illustration of the jetting nozzle used in piezoelectric inkjet printing is shown in Figure 10. The non-contact printing process involves drawing a solution from a source plate into a nozzle and then ejecting it as droplets of specific sizes in nanoliter or picoliter onto a suitable substrate. The resulting spot size is affected by the droplet volume and the surface energy of the substrate material and the printed solution. Piezoelectric inkjet printing allows precise control over the amount of deposited material and avoids direct contact with the substrate surface [158].

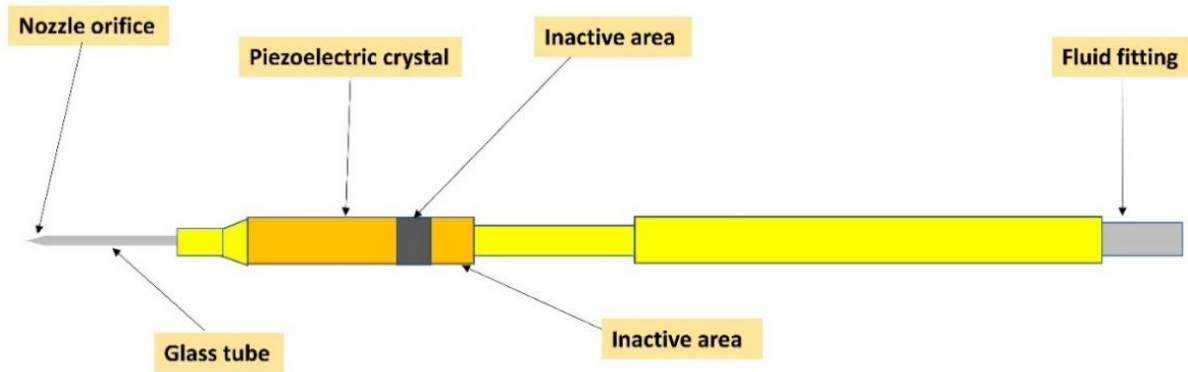


Figure 10. Schematic illustration of jetting nozzle (adapted from [166]).

1.6.2.1 Continuous Inkjet Printing

In continuous-mode printing, droplets are consistently ejected as they are continuously pumped through a nozzle. The printing pattern is achieved by selectively charging some droplets, which are then deflected by an electric field [167]. A liquid jet forms when pressurized fluid is forced through a small opening. Introducing a single frequency disturbance within the appropriate frequency range to the jet via an electromechanical device (transducer) that generates pressure oscillations in the fluid creates droplets with highly uniform size and speed. A charging electrode, positioned near the orifice, imparts a charge to the forming droplet before its separation. If the high-voltage downstream is deactivated, the charged droplets are caught by a catcher cup and redirected back to the liquid reservoir for reuse. Conversely, when a potential is applied to the high-voltage plates, the droplets are directed towards the substrate [166]. Figure 11 provides a schematic representation of continuous-mode jetting.

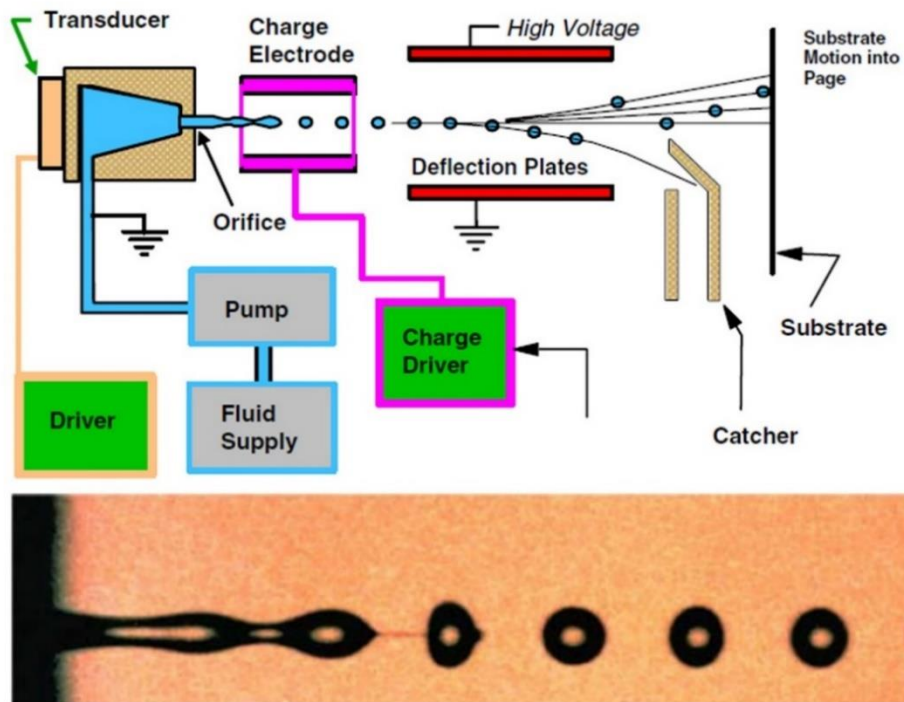


Figure 11. A schematic illustration of continuous mode jetting and an image showing temporal droplet formation at the figure's bottom [166].

1.6.2.2 Drop on Demand (DoD) Inkjet Printing

In contrast, a drop-on-demand ink-jet printer maintains the fluid at ambient pressure, with a transducer creating a drop when needed. The transducer produces pressure waves due to a volumetric change in the fluid. These waves travel to the nozzle, transforming into fluid velocity, and lead to the ejection of a drop from the nozzle, as depicted in Figure 12 [166]. The transducer in these systems may either be a structure that includes piezoelectric materials or a thin-film resistor [168]. Drop-on-demand systems only produce drops when needed, either by superheating the ink until a bubble is formed to expel a drop from the nozzle (thermal ink-jet or bubble jet) or by exciting a piezoelectric material that deforms on the application of a voltage, causing the liquid to be ejected from the printing nozzle as a droplet (piezo ink-jet) [167]. The demand mode has the

advantage of producing smaller drops at lower velocities compared to the continuous mode, and it also minimizes waste and eliminates the need to recirculate the operating fluid.

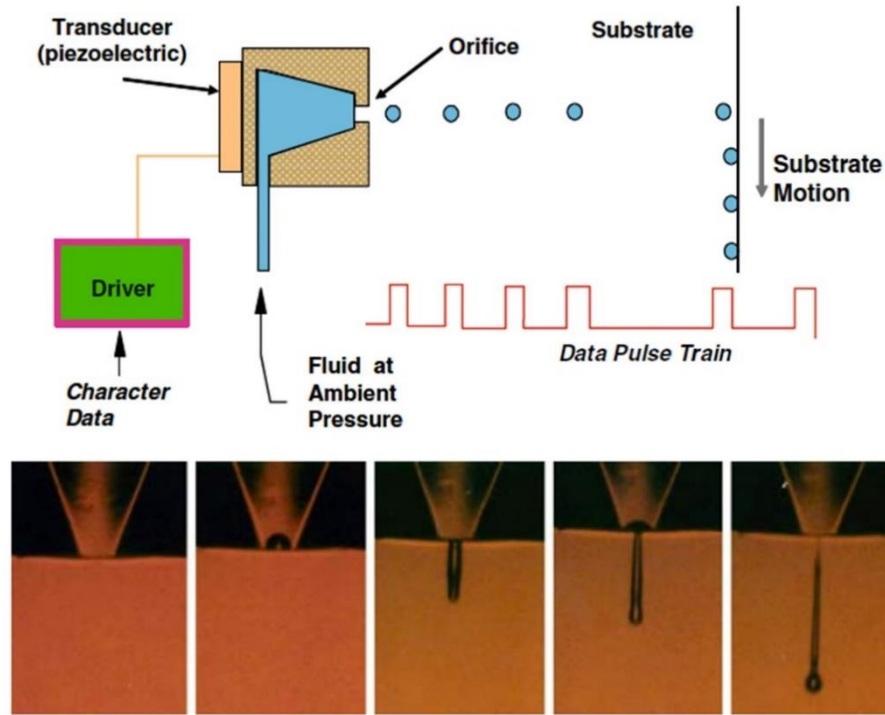


Figure 12. A schematic illustration of demand mode jetting and an image showing temporal droplet formation at the figure's bottom [166].

1.6.2.2.1 Thermal Inkjet Printing

In the thermal inkjet (TIJ) printing process, the setup includes a reservoir holding the liquid to be jetted and a printhead comprising multiple small nozzles replenished with ink from the reservoir. Each nozzle channel is equipped with a thin film resistor. Activating the resistor with an electric current rapidly increases its temperature, causing a vapour bubble of the ink in contact with the resistor to form and expand. This expansion propels the ejection of ink, creating a droplet, as depicted in Figure 13B. Subsequently, the channel is refilled with ink from the reservoir. The ejection process is regulated by the pattern of current pulses, which control the droplet formation. This entire mechanism occurs at a high speed, with the bubble expansion happening in just 3–10s [162] and droplets being ejected at a rate up to 10 ms^{-1} [169-171].

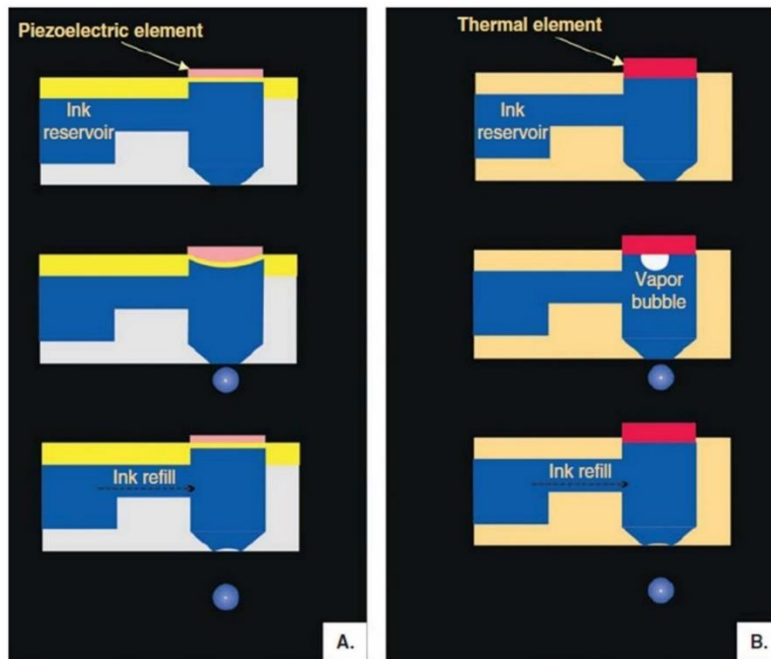


Figure 13. A schematic illustration of a droplet formation at the two modes of DoD printing; A) Piezoelectric inkjet printing, B) Thermal inkjet printing [170].

1.6.2.2.2 Piezoelectric Inkjet Printing

In piezoelectric inkjet printing, the ejection of the droplets is achieved by the action of the transducer, which in this case, is a piezoelectric element that is present in every nozzle usually made from lead zirconate titanate. When the voltage is applied to that piezoelectric element, it deforms as its size or shape changes, creating a pressure wave leading to the ejection of a droplet, as shown in Figure 13A. When the element returns to the starting position, the channel (nozzle) is refilled with the ink from the reservoir [170, 171].

Piezoelectric demand mode technology may generally be more readily adapted to fluid microdispensing applications. As well, it does not subject the fluid to heat stress or shorten the printhead's and fluid's life [168]. Moreover, heat may result in the degradation of the formulation ingredients. Consequently, a piezo-driven dispenser would be more appropriate for applications in drug formulations [172].

Advantages of Inkjet Printing

Demand mode inkjet printing systems generate droplets approximately the same as the droplet generator's orifice diameter. In this mode, small drop diameters and volumes as low as 2 pL would be easy to achieve, offering great potential for highly precise deposition of liquids [169-171]. When the ink is a solution of an API, the amount of drug deposited can be controlled by changing the volume of the jetted solution and/or the concentration of the feed solution [173]. Printing is particularly valuable in reducing the wastage of expensive pharmaceuticals [166]. Due to its versatility, ink-jet printing has been used for various applications, such as the deposition of large human cells [174], the fabrication of cartilage [175], the creation of DNA arrays [176], the deposition of polymers [177], in drug discovery [178] and loading a microneedle array with miconazole [179].

Challenges of Inkjet printing

Inkjet technology has certain benefits over other possibilities, such as relatively small dispensed volumes (10-20 pL per drop), non-contact operation, speed, and relatively high spatial resolution [167, 180]. Nevertheless, dust particles or material aggregates can clog the nozzle's small orifice [181]. Cavitation bubbles [182], undesirable satellite drops [182], the first drop problem [167], nozzle clogging [162, 180, 182] and droplet instability [167, 180] are some of the issues that need to be addressed for each specific ink-print head combination [183].

Developing the inks that could be reliably jetted with this technique is challenging, and some authors classify this task as an art [167]. The number of different materials that may be used in a single printing run is constrained by the difficulty of printing solutions with diverse viscosities and surface energies under the same circumstances [180]. Because several parameters impact proper

droplet formation and uniform deposition of the "ink" onto the substrate, the formulation of "inks" for inkjet printing is quite complicated.

Ink rheological characteristics like viscosity and surface tension are essential. High surface tension is necessary for spherical droplet creation and to prevent ink leakage from the print head when the printer is not in operation. The ink's viscosity should be sufficiently low for effective jetting but high enough to avert unintended jetting, which can result in tail formation and subsequent satellite droplets [204, 205]. These satellite drops, often called "secondary drops," can affect drug deposition location on the substrate, not only affecting the formation of the primary droplet. Drops must land at their predetermined coordinate on the substrate for dosage homogeneity to be guaranteed. A satellite drop might merge with the main drop or land close by on the substrate [205, 206]. Quality printing occurs when ideal ink forms a liquid stream or column post-jetting from the nozzle, leading to a tail that ends in a single primary drop when approaching the substrate, as depicted in Figure 14.

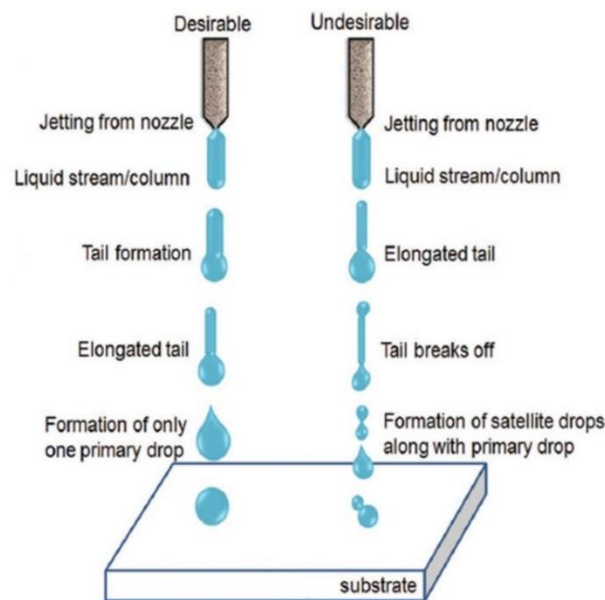


Figure 14. desirable drop formation in piezoelectric inkjet printing and undesirable satellite drop formation [184].

The ink's viscosity and surface tension are also crucial during the refilling stage of the drop generator as the fluid moves through channels into the nozzle [171, 173]. For instance, preferred viscosity and surface tension values for a PIJ printer typically range from 1 to 30 mPa s and 25 to 50 mN/m, respectively [185-187]. Yet, these ideal surface tension and viscosity values vary per device and are often specified by the printer's manufacturer or identified experimentally for a particular device [188].

1.6.3 Pharmaceutical applications of inkjet printing

Using printing technologies to develop drug delivery systems is a relatively new concept that has only been substantially explored in the last decade. This approach stems from the capability to deposit small amounts of liquid precisely and accurately following digital patterns using inkjet technology. As a result, it is possible to achieve extremely accurate placement of drugs and excipients in a desired ratio onto an appropriate substrate in a regulated way, facilitating the production of single or multiple dose forms [170]. Numerous research teams have documented the use of inkjet printing in developing drug delivery systems, as indicated in Table 3.

Table 3. Examples of inkjet dispensing systems reported in the literature for the study of pharmaceutical printing.

Printing system	Purpose and printed pharmaceutical example	Reference
Piezoelectric-driven inkjet (micro-dispenser), JetLab II commercial instrument manufactured by MicroFab Technologies	Coating and loading drug-eluting stents with fenofibrate and a derivative of rapamycin (ABT-578)	[166]
Thermal inkjet printing	Preparation of solid dosage forms of prednisolone using TIJ, using a micropipette for comparison, and characterization of the deposited products.	[169]
Direct-write inkjet technique (MicroFab Technologies Drop-On-Demand)	Producing calcium alginate microcapsules and analyzing the release kinetics within these	[189]

	biopolymer microcapsules for time-dependent drug release	
Piezoelectric inkjet printer Dimatix DMP-2800	Exploring the potential of incorporating APIs (Paracetamol, Caffeine and Theophylline) into porous structures of the substrate using three different substrates	[190]
Piezoelectric inkjet printer with a 90 µm orifice (Gesim A010- 201 PICPIP)	Developing drug formulation to control the drug release using (felodipine) and (polyvinylpyrrolidone [PVP])	[172]
Thermal inkjet printer (Hewlett-Packard Inc)	Preparation of films for oral personalised doses of salbutamol sulphate	[188]
Thermal ink-jet spray freeze-drying (modified Hewlett-Packard Deskjet 340 printer)	Engineering inhalable, excipient-free salbutamol sulphate particles	[191]
Thermal inkjet printer Hewlett-Packard (Deskjet D1660, Hewlett-Packard Inc)	Evaluating the applicability of the different substrates in inkjet-printed drug-delivery systems through deposition of rasagiline mesylate on three model substrates	[192]
Drop on-demand positive displacement pump connected to a nozzle (dropwise additive manufacturing of pharmaceutical products (DAMPP))	Exploration of the use of DoD technology for creating high-potency drug forms, combination drugs with multiple APIs or personalised medicine using Naproxen and PVP K90	[193]
Piezoelectric inkjet printer Dimatix DMP-2800 (Fujifilm Dimatix Inc.,)	Examining the suitability of precise inkjet printing for producing customized dosages of APIs, employing Loperamide hydrochloride and caffeine as model compounds on two different model substrates.	[194]
Piezoelectric inkjet printer Dimatix DMP-2800 printer (Fujifilm Dimatix Inc.)	Formulation of printable dosage forms for piroxicam using polyethylene glycol 400 and understanding the critical	[184]

	parameters for developing such dosage forms	
Inkjet-based micro dosing dispenser head (MD-K-140, microdrop Technologies GmbH, Norderstedt, Germany)	Preparation of Folic acid nanosuspension and testing the capability of inkjet printing to produce personalized medicines.	[195]
Piezoelectric inkjet printer (Dimatix, Santa Clara, CA)	Creating microparticles composed of the drug paclitaxel and the polymer PLGA with precisely defined and controlled shapes.	[196]
Piezoelectric inkjet printer (Sciflexarrayer S5)	Inkjet printing involves three distinct formulations, each containing the drugs felodipine and hydrochlorothiazide along with two polymers, PVP and PLGA, arranged as micro-dot arrays. These arrays are then subjected to individual micro-spot analysis using time-of-flight secondary ion mass spectrometry (ToF-SIMS).	[197]
Piezoelectric inkjet printer (Cluster Technology Corporation)	Manufacturing different size-controlled gel particles using sodium alginate solution	[198]
Thermal Inkjet printer (Pixma iP7250, Canon Inc.)	Investigating the practicality of using colorimetry as an analytical method for quality control, specifically for assessing the content uniformity in printed orodispersible film formulations. These formulations include propranolol hydrochloride in a coloured ink base and are applied on three different edible substrates.	[199]
Thermal desktop inkjet printer Canon Pixma iP3600 (Canon Inc.)	Assessing the feasibility of using a portable colorimetry instrument for quality assurance in printing vitamin B dosages on edible substrates like rice and sugar.	[200]
Piezoelectric inkjet printer	Creating four distinct orodispersible pharmaceutical forms that incorporate two drugs with low	[201]

PixDro LP 50 (Roth & Rau, Eindhoven, Netherlands)	solubility, levothyroxine and prednisolone, printed on two edible materials. This process involves evaluating the stability of the drug inks, assessing the mechanical characteristics, and analyzing the disintegration patterns of the printed units.	
Piezoelectric inkjet printing PixDro LP 50 (Roth&Rau, Netherlands)	Creates a composite therapeutic product that integrates anticancer (paclitaxel) and antiviral (cidofovir) medications into an adhesive film specifically designed for the localized treatment of cervical cancer caused by HPV infection.	[202]
Piezoelectric inkjet printer PixDro LP50 inkjet printer (Roth&Rau, The Netherlands)	Explores the application of electrospun fiber materials in creating inkjet-printed pharmaceutical forms by preparing a single-medication formula with lidocaine hydrochloride and a dual-drug system combining lidocaine hydrochloride and piroxicam, specifically for oromucosal delivery.	[203]
Piezoelectric inkjet printer (Dimatix Materials Printer, DMP2800, FujiFilm Dimatix)	Investigates the use of printed micropatterns that elute antibiotics and calcium as an innovative strategy to inhibit biofilm colony development and support osteogenic cell growth on the surfaces of orthopaedic implants. These micropatterns comprise biphasic calcium phosphate and rifampicin nanoparticles distributed throughout a biodegradable poly (D, L-lactic-co-glycolic) acid (PLGA) matrix.	[204]
Thermal ink-jet spray freeze-drying, modified Hewlett-Packard Deskjet 340 printer	Manufacturing of inhalable particles of terbutaline sulphate and assessing their aerosol properties compared to the commercially available Bricanyl® product.	[205]

XYZ movable inkjet head (Nanoplotter NP 2.1 GeSim, Germany) equipped with a piezo-driven dispenser with a 70 µm orifice (GeSiM nanotip)	Suggests a proficient method for loading a model drug with low solubility into micro-containers through the integration of inkjet printing and supercritical fluid impregnation. The process involves dispensing PVP solutions into micro-containers using inkjet printing, achieving near-zero waste efficiency. Subsequently, ketoprofen is embedded within the polymer matrix utilizing supercritical carbon dioxide as the medium for impregnation.	[206]
---	---	-------

The inkjet printing process has been employed in solid form screening, taking advantage of its capacity to create microscopic droplets of picolitre volumes. Fourier transform infrared (FTIR) spectroscopic imaging with infrared array detectors has emerged as a robust material characterisation method. Chan and Kazarian presented a unique use of FTIR imaging for high-throughput material characterization in a controlled environment [207]. This method included the use of spectroscopic imaging using an attenuated total reflection (ATR)-IR cell, a microdroplet sample deposition system using a microdroplet-on-demand device (AutoDrop, MicroDrop), and a humidity control device inside the cell. By integrating the microdroplet device with the FTIR imaging system, they demonstrated that approximately 100 samples can be analysed simultaneously. Using this method, "chemical snapshots" were obtained from a spatially specified array of several distinct polymer/drug combinations. This technology enabled the direct assessment of material characteristics, which is helpful for high-throughput formulation design and optimization. The array of formulations' simultaneous responses (such as water sorption, crystallisation, etc.) to environmental parameters was investigated. The implications of the given technique vary from smart polymeric materials and sensors to pharmaceutical and biomaterial screening [207].

Considering the potential of drug-polymer dispersions as viable formulations and the significance of exploring diverse techniques dealing with API formulation challenges, it would be advantageous to establish reliable and relatively rapid screening processes that do not necessitate large quantities of the API. This is particularly crucial since ample quantities of the drug are often unavailable in the early stages of drug development.

Regarding screening techniques, Eerdenbrugh and Taylor have created a scaled-down screening approach to examine how effectively 7 polymers can prevent the crystallization of 8 model compounds. They employed 7 drug-polymer ratios for each compound with a distinct polymer, resulting in approximately 392 samples analysed. Films were prepared by rapid evaporation from the solution, applying a spin coating method as 200 μ L drug-polymer solution was spread out the coverslips. Their results were compared to the ones of bulk powders prepared by a rotatory evaporator. Taylor's group concluded that miniaturised screening could be a powerful technique for evaluating drug-polymer chemistry's role in stabilising amorphous solid dispersions [117].

Tanabe et al. developed a nano-spot approach that allows for nanogram-scale evaluation of the crystalline form through some modifications to the nano-spot method previously reported in the literature. This improved nano-spot approach would be applicable for screening API polymorphs or new crystal forms (salts, solvates), not only cocrystals. Additionally, the newly adopted low-frequency Raman spectroscopy made the detection of the crystalline form possible [208].

High-throughput methods such as inkjet printing are among the most promising and pioneering techniques used in screening and formulating different APIs [209, 210]. Inkjet printing is an umbrella term encompassing a wide range of approaches to the digitally controlled formation and placement of small liquid drops [210]. An abundance of versatile materials has been successfully printed by inkjet, including genes [211, 212], cells [213], proteins [214], colloids [215], curable-

antifouling monomers [216], polymers [217], screening of polymer features to assess their suitability with the microarray manufacturing [218] nanomaterials and pharmaceutical formulations [219, 220]. Scoutaris et al. demonstrated for the first time the feasibility of jet dispensing as a high-throughput technology for printing and rapid screening of pharmaceutical cocrystals by exploring a wide range of parameters [221]. Liberski et al. (Bradley's group) established a pioneering link between the high-throughput 2D printing technique and the crystallisation screening of commercial drugs as a high-throughput method for studying polymorphism in small molecules was presented [209]. This technique allowed three small molecule compounds to be screened (in triplicate) with 128 polymers consuming approximately 27 μg of each polymer and a few milligrams (around 3.5 mg) of selected drug compound for the whole experiment.

Inkjet printing technology has been exploited especially in the broad area of new biomaterials [222] and drug discovery, namely, combinatorial chemistry and high-throughput screening [210, 223], but the research in the area of screening amorphous solid dispersion is still limited. In this regard, Taresco et al. [224] proposed a new screening process using 2D inkjet printing that was capable of combining many of the advantages of the previous screening methods, namely, the miniaturisation [117], the addressability, and the high throughput [209]. This approach potentially offers significant efficiency in pharmaceutical formulation screening, with each micro-array experiment requiring 3 up to 6 orders of magnitude lower amounts of sample than conventional screening methods [224].

The choice of polymer carrier and processing method is crucial to ensuring the stability of solid dispersion. The best formulation route for a new drug is still primarily determined by the formulator's expertise and experimental screening assays that might be significantly enhanced by

a knowledge-based computational tool able to predict an optimum formulation technique [225, 226]. Assistance tools can be used to speed up this process, including guidance maps, high throughput screening, and statistical models [119]. There is, hence, the demand for a knowledge-based supportive tool in formulation development that can help formulators determine which formulation route is the best for a given API, which can speed up the development process and reduce the number of trials that need to be done. Although significant work has been done in creating such tools, their accessibility is still relatively restricted [27, 226].

Aims and objectives:

However, whilst a number of drugs and polymers have been studied in the literature, the number of researched APIs and their loading with different polymers is still very limited, and the model development is often done for each system in isolation, making it difficult to draw any general conclusions. **Therefore, the overall aim of this thesis is to:**

- explore the feasibility of employing 2D inkjet printing as a high-throughput screening technique to establish an extensive library of drug-polymer combinations using nanogram amounts of materials. Stability data collected from this extensive library of more than 900 drug-polymer combinations would then be used for the development of a statistical model pinpointing the physicochemical properties of APIs most closely linked to solid dispersion stability providing valuable insights for formulation development and accelerating screening processes.

This would be achieved through the following objectives:

Chapter 3:

- Investigating the feasibility of employing printed nano-arrays with pico-litres of small-molecular weight drugs in pre-formulation and solid-form screening framework to build

an extensive library of various drug and polymer loadings which is a relatively larger number of samples than previously reported.

- Detecting and comparing the range of miscibility limits of each API within two polymeric matrices.
- Developing a miniaturised, high-throughput assay for screening an expanded set of drug-polymer formulations in different drug loading using a 2-D pico-litre inkjet printer, followed by a stability study of the printed microarrays. This is to look at more drug loadings than has been achieved before and to take into consideration performing this safely by using a minimal (nano-gram) amounts of drugs.

Chapter 4:

- Building multiple linear regression models from the generated experimental data set to predict which physicochemical properties of the APIs could be correlated with the stability of formulations and validation of the models.

Chapter 5:

- 3-D inkjet printing of some formulations of APIs within PVPVA polymeric matrix to confirm the screening data generated from the 2-D inkjet printing regarding the miscibility limits within the same polymer.

2 Chapter 2: Materials and Methods

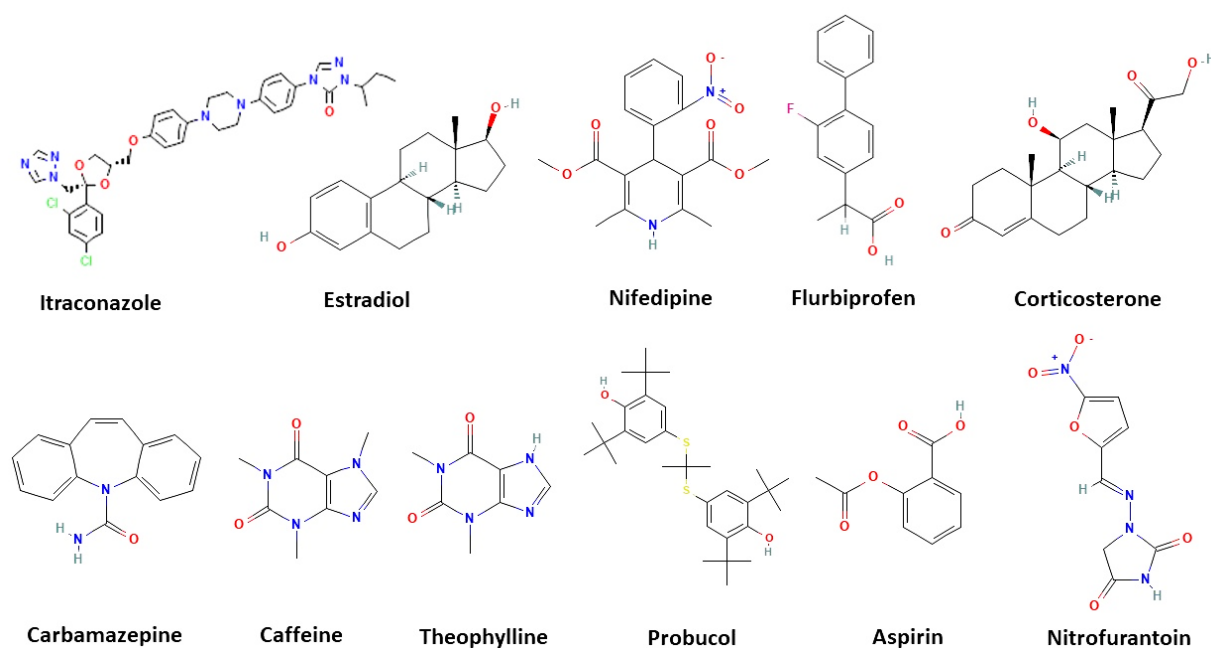
This chapter aims to provide an overview of the materials and the characterisation techniques used in this study. Additionally, it gives explanations for the reason for selecting those materials and analytical methods. A summary of the theory underlying the methods employed and the goals behind their use is clarified. Chapters 3, 4, and 5, the “Materials and Methods” sections, will provide detailed experimental descriptions.

2.1 *Drug and polymer selection*

2.1.1 Drug Selection

Choosing a diverse set of APIs for the study was crucial. The dataset must be as varied as possible to enable general conclusions regarding the stability of solid dispersion and the impact of the APIs’ properties on this. Additionally, since the experimental data was used to create a statistical model, any dataset limitations would restrain the model’s application. However, some practical restrictions to the diversity were required, such as safety, cost, and the sample size still being relatively small (although large compared to any other published study). Three characteristics were considered while determining the restrictions for selecting the APIs. First, most of the used APIs were required to be poorly water-soluble. These limitations were addressed following a similar approach as Nurzyńska et al. [151] and Fridgeirsdottir et al. [152], which generated statistical models that could predict the stability of amorphous APIs. These properties include those with extreme values that may be more likely to crystallise. Those properties and their values included the number of rotatable bonds (nRot) and rings (nRing), which have been reported to correlate with stability [227, 228], and lipophilicity (log P), H-bond donors and acceptors that could be important when considering possible interaction with polymer are displayed in Table 4. Finally, the glass-forming ability of the APIs was considered. Drugs can be classified into three categories

based on their ability to form an amorphous glass and on the stability of the glass state: non-glass formers (Class I), non-stable glass formers (Class II), and stable glass formers (Class III). The drugs used were chosen from these three classes to explore if the inkjet printing technique will provide the same screening compared to the literature, where different sample preparation techniques, such as spin coating and undercooled melt, have been used. Aspirin, Atenolol, Benzocaine, Caffeine, Theophylline, Carbamazepine, Flufenamic acid, Nicotinamide and Tolbutamide are classified as Class I, while Acetaminophen, Celecoxib, Estradiol, Nifedipine, Aprepitant, Orlistat, Piroxicam are classified as Class II. Felodipine, Fenofibrate, Itraconazole, Ketoconazole, Probuco, Ketoprofen and Ritonavir are classified as Class III [144, 146, 229]. The chemical structures of the APIs used in this study are shown in Figure 15.



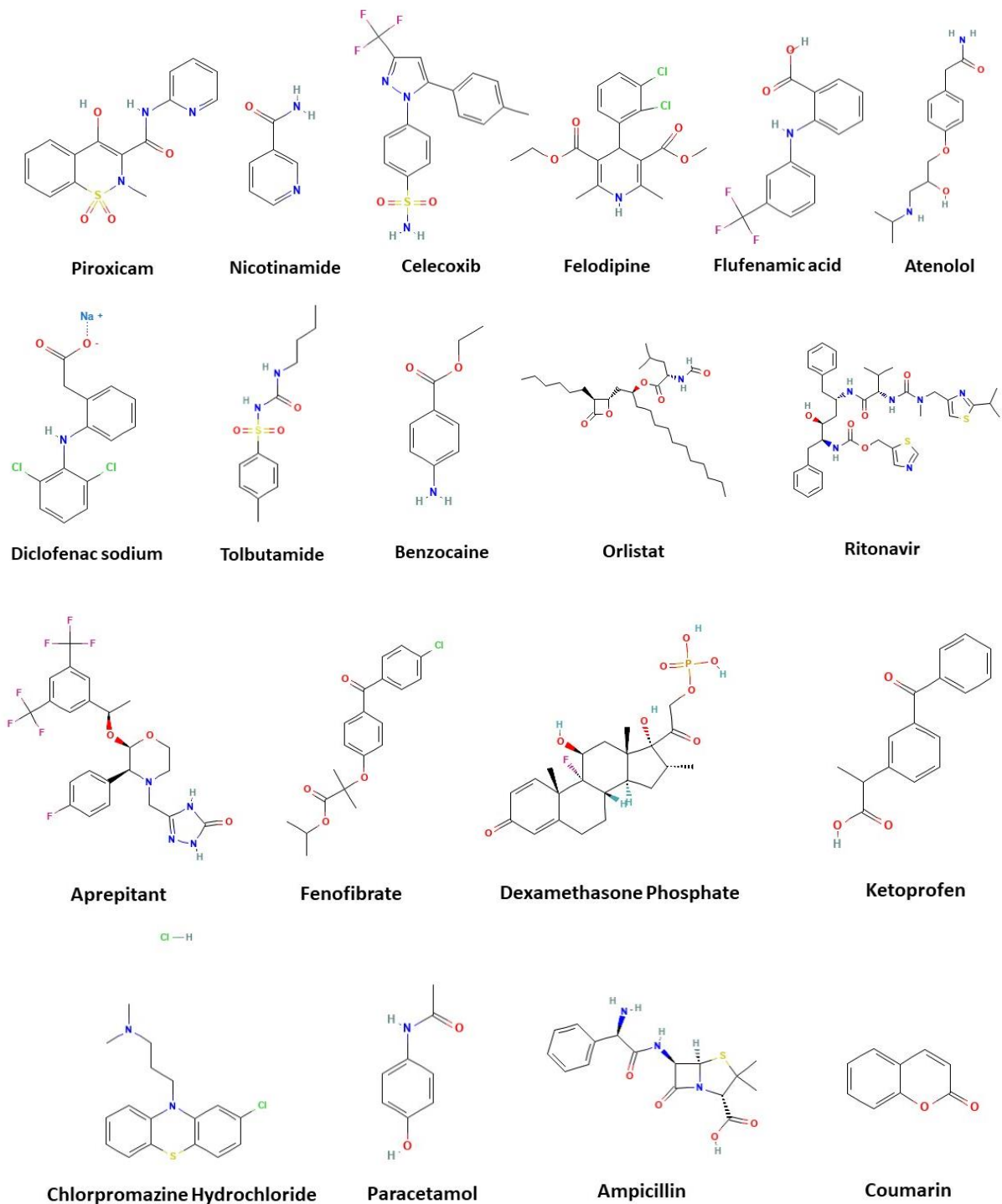


Figure 15. Chemical structures of the APIs used in this study [230].

The program Chemicalize from ChemAxon was used to calculate and predict the physicochemical properties of the different APIs based on the molecular structure of each API [231]. Furthermore,

the melting point of each API has been obtained from ChemSpider [232]. The physicochemical properties are shown in Table 4.

Table 4. The calculated physicochemical parameters of the APIs used in this study as calculated from Chemicalize from Chemaxon and their melting points as obtained from ChemSpider [231, 232].

The following abbreviations are used: MW: molecular weight, logP: lipophilicity, HBA: number of H-bond acceptors, nRing: number of rings, HBD: number of H-bond donors, nAtom: number of atoms, nChir: number of chiral atoms, tPSA: topological polar surface area, ASA: water accessible surface area, HLB: hydrophilicity–lipophilicity balance, nCl: number of chlorine atoms, vdW-SA: van der Waals surface area, vdW-Vol: van der Waals volume, logS0: water solubility in log10 of molar solubility, mp: melting point, nAliphRing: number of aliphatic rings, nArRing: number of aromatic rings, nO: number of oxygen atoms, nC: number of carbon atom, nF: number of fluorine atoms, avPol: average polarizability, nRot: number of nonterminal rotatable bonds, nS: number of sulfur atoms, nHet: number of heteroatoms (atoms other than carbon and hydrogen), nN: number of nitrogen atoms, sp3: number of sp3 carbon atoms, sp2: number of sp2 carbon atoms, nHetRing: number of heteroring, nHeavy: number of heavy atom, logS0 at 7.4: water solubility in log10 of molar solubility at PH 7.4, FSP3: the number of sp3 hybridised carbons/total carbon count, nAsymmetric: number of asymmetric atom, FC: formal charge (the electric charge of an atom in a molecule;), MRef: Molar Refractivity (a measure of the total polarizability of a mole of a substance;), minProjArea: minimum projection area, maxProjArea: maximum projection area, minProjRad: minimum projection radius and maxProjRad: maximum projection radius. logS0 and logS0 at 7.4 of sodium diclofenac: molecule can not be neutralized.

API	Caffeine	Theophylline	Carbamazepine	Piroxicam	Corticosterone	Nitrofurantoin	Diclofenac Sodium	Atenolol	Itraconazole	Nicotinamide	B-Estradiol	Nifedipine	Flurbiprofen	Flufenamic acid	Tolbutamide	Aspirin	Probucol	Celecoxib	Felodipine	Ritonavir	Fenofibrate	Apricitant	Orlistat
HBD	0	1	1	2	2	1	1	3	0	1	2	1	1	2	2	1	2	1	1	4	0	2	1
HBA	3	3	1	5	4	5	3	4	9	2	2	5	2	3	3	3	2	3	3	6	3	6	3
LogP	-0.55	-0.77	2.95	0.39	2.02	-0.22	4.26	0.425	7.311	-0.39	3.75	1.815	3.94	5.25	2.3	1.24	10.57	4.01	3.44	5.22	5.278	4.5	8.11
MW	194.2	180.17	236.27	331.35	346.5	238.2	318.13	266.34	705.6	122.13	272.4	346.34	244.3	281.2	270.35	180	516.8	381	384	721	360.8	534	495.8
mp	236	273	190	199	180	270	288	149	166.2	130	176	173	111	134	129	139	125	158	145	121	81	250	45
nChir	0	0	0	0	7	0	0	0	3	0	5	0	1	0	0	0	0	0	1	4	0	3	4
nHet	6	6	3	8	4	9	5	5	14	3	2	8	3	6	6	4	4	9	7	13	5	14	6
sp2	5	5	15	14	4	7	13	7	22	6	6	12	13	13	7	8	12	15	12	21	14	14	3
sp3	3	2	0	1	17	1	1	7	13	0	12	5	2	1	5	1	19	2	6	16	6	9	26
nAliphRing	0	0	1	1	4	1	0	0	2	0	3	1	0	0	0	0	0	0	1	0	0	1	1
nArRing	2	2	2	2	0	1	2	1	5	1	1	1	2	2	1	1	2	3	1	4	2	3	0
nHet ring	2	2	1	2	0	2	0	0	4	1	0	1	0	0	0	0	0	1	1	2	0	2	1
LogS0 (M) at 7.4	-0.44	-0.82	-3.79	-0.93	-3.68	-3.21	can't be	0.3	-7.72	-0.38	-3.99	-2.9	-1.96	-1.02	-3.38	-1.9	-10.5	-5.5	-4	-6.24	-5.86	-5.3	-9.98
LogS0 (M)	-0.44	-0.96	-3.79	-3.27	-3.68	-3.27	can't be	-1.57	-7.72	-0.38	-3.99	-2.9	-4.24	-4.34	-3.38	-1.9	-10.5	-5.5	-4	-6.24	-5.86	-5.5	-9.99
ASA (A2)	368.4	323.99	370.91	489.16	425.2	416.5	433.35	535.74	992.1	276.72	395.1	533.46	436.5	445.9	554.15	369	874.6	603	581	982	643.5	700	985.3
nAtom	24	21	30	36	55	23	30	41	87	15	44	43	31	30	36	21	83	40	44	98	46	58	88
avPol (A3)	17.87	16.13	26.79	32.56	37.64	19.24	28.92	29.09	71.59	12.28	31.31	33.98	26.96	24.52	27.81	17.2	61.95	36.4	37	75.7	38.18	43	56.15
HLB	12.1	12.39	10.6	19.99	4.34	19	24.27	19.15	5.5	14.5	3.787	19.25	4.74	5.65	11.79	10.1	3.059	10	13.8	19.3	5.73	11	8.07
nC	8	7	15	15	21	8	14	14	35	6	18	17	15	14	12	9	31	17	18	37	20	23	29
nCl	0	0	0	0	0	0	2	0	2	0	0	0	0	0	0	0	0	0	2	0	1	0	0
nF	0	0	0	0	0	0	0	0	0	0	0	0	1	3	0	0	0	3	0	0	0	7	0
nN	4	4	2	3	0	4	1	2	8	2	0	2	0	1	2	0	0	3	1	6	0	4	1
nO	2	2	1	4	4	5	2	3	4	1	2	6	2	2	3	4	2	2	4	5	4	3	5
nS	0	0	0	1	0	0	0	0	0	0	0	0	0	0	1	0	2	1	0	2	0	0	0
nRing	2	2	3	3	4	2	2	1	7	1	4	2	2	2	1	1	2	3	2	4	2	4	1
nRot	0	0	0	2	2	3	4	8	11	1	0	6	3	4	4	3	8	4	6	18	7	8	23
tPSA (A2)	58.44	69.3	46.33	99.6	74.6	118.1	52.16	84.58	100.8	55.98	40.46	107.77	37.3	49.33	75.27	63.6	40.46	78	64.6	146	52.6	75	81.7
vdW-SA (A2)	269.1	235.19	312.24	411.56	543.6	279.9	359.64	440.26	965.4	171.42	436.6	466.23	347.4	348.15	421.08	246	916.6	485	493	1066	533.6	658	925.7
FSP3	0.37	0.29	0	0.07	0.81	0.12	0.07	0.5	0.37	0	0.67	0.29	0.13	0.07	0.42	0.11	0.61	0.12	0.33	0.43	0.3	0.4	0.9
MRef (cm3/mol)	49.83	44.93	71.89	87.04	96	52.11	86.3	73.51	200.4	32.98	79.9	91.61	67.29	67.77	70.27	44.5	159.3	92.2	99.2	195	97.13	127	139.9
nHeavy	14	13	18	23	25	17	20	19	49	9	20	25	18	20	18	13	35	26	25	50	25	37	35
nAsymmetric	0	0	0	0	7	0	0	1	3	0	5	0	1	0	0	0	0	0	1	4	0	3	4
FC	0	0	0	0	0	0	0	0	0	0	0	0	0	0	0	0	0	0	0	0	0	0	0
vdW-Vol (Å3)	164.3	146.69	210.15	267.89	338.5	174.8	234.5	261.34	603.9	108.08	269.7	299.78	219.2	223.8	244.75	155	534.2	299	322	663	325.4	414	529.4
MinProjArea (Å2)	30.01	28.75	40.19	39.47	48.89	31.59	44.3	36.85	99.42	18.73	37.85	57.61	36.95	36.51	51.75	33.3	85.41	58.3	60.7	120	45.12	79	81.63
MaxProjArea (Å2)	61.86	56.51	68.29	94.14	96.43	62.05	77.08	87.58	155.9	44.32	84.51	87.31	72.36	80.4	72.98	56	131	93.3	87.6	163	102.6	115	157.4
MinProjRad (Å)	4.44	4.34	4.48	4.95	4.66	3.76	4.71	4.19	7.02	3.3	4.02	6.22	4.27	4.65	5.08	4.5	6.27	6.19	5.6	8	4.33	6.9	7.66
MAxProjRad (Å)	5.03	4.98	5.76	7.82	7.96	6.97	5.91	9.12	12.51	4.72	7.3	6.46	6.98	6.59	7.24	5.15	8.56	7.33	6.3	9.48	9.72	8.3	13.13

2.1.2 Polymer selection

In this study, the selection of carrier polymers is paramount as the dataset aims to reflect prevalent practices in the formulation of solid dispersions. Furthermore, the use of the statistical models will be limited to the polymers they are based on. Therefore, it was imperative to choose polymers that are representative of those most commonly employed in current solid dispersion technologies. An investigation into commercially available oral dosage forms of solid dispersions in the market indicated a predominant use of different categories of polymers: polyvinyl-based polymers cellulose-derived polymers, and Eudragit and polyethylene glycols (PEGs). Three polymers were chosen in this study as polyvinylpyrrolidone-vinyl acetate copolymer K 28 (PVPVA) (Kollidon[®] VA 64) and hydroxypropyl methylcellulose acetate succinate (HPMCAS-HG) (Aquasolve[™]) which are frequently utilised in marketed solid dispersions, and Soluplus which is the only polymer used here, not currently employed in a marketed formulation. The chemical structures of the polymers are shown in Figure 16. This polymer selection is critical to ensure that the resulting models accurately reflect the current landscape of solid dispersion formulations.

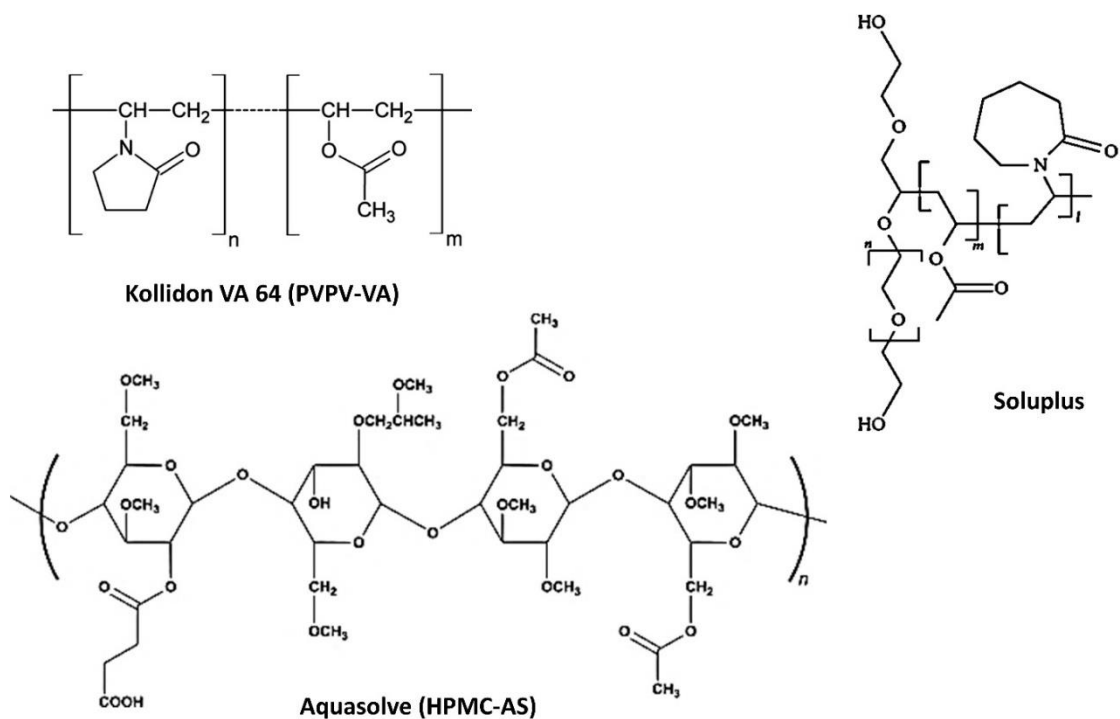


Figure 16. Chemical structures of polymers used in this study [233-235].

2.1.2.1 Polyvinylpyrrolidone-vinyl acetate (PVPVA) (Kollidon®)

PVPVA is a widely used pharmaceutical excipient which is generally considered non-toxic. It is a versatile excipient used for different purposes in drug formulations, such as coating and granulation, as a binder, and as a polymer carrier in ASDs. It is used as a carrier in marketed solid dispersion formulations. PVPVA can be used for immediate and sustained or controlled release when combined with other materials [236, 237]. PVPVA has a moderate glass transition temperature (T_g) of 103°C and is freely soluble in water and polar organic solvents [236].

2.1.2.2 Hydroxy propyl methyl cellulose acetate succinate (HPMCAS)

Hydroxypropyl methylcellulose acetate succinate (HPMCAS) is a highly effective pharmaceutical excipient commercially used to formulate ASD systems. The selection of an appropriate polymer like HPMCAS for ASDs is crucial due to its unique properties as its elevated T_g around 120 °C in

dry conditions, which is fundamentally linked to reduced mobility of drug molecules, thereby contributing significantly to the enhanced physical stability of the ASDs. Its amphiphilic nature complements this stability, enabling efficient interactions with insoluble drug molecules. Soluble in organic solvents such as acetone and methanol, HPMCAS facilitates controllable and economical ASDs processing. Furthermore, its minimal water absorption capacity, even in high humidity conditions, makes it an ideal choice for boosting the stability and effectiveness of pharmaceutical formulations [238].

2.1.2.3 Polyvinyl caprolactam – polyvinyl acetate – polyethene glycol (PEG) (Soluplus™)

Polyvinyl caprolactam (PVC) – polyvinyl acetate (PVA) – polyethene glycol (PEG), or Soluplus™ as it is commercially known, is a relatively new polymer marketed in 2009 by BASF. It is the only polymer used in the study not currently employed in a marketed formulation. It is a graft polymer consisting of three sections: lipophilic, PVC, PVA, and PEG, which are hydrophilic. This amphiphilic nature stabilises poorly water-soluble drugs while remaining water-soluble and forming micelles to further solubilise the drug in the solution. It has a low T_g of 70°C. It is freely soluble in water [104, 239-241]. It was developed to be used in solid dispersions. Moreover, it has also been used for different purposes in granulation and micelles formation [242-244].

2.2 Materials

Nifedipine (CAS 21829-25-4), Celecoxib (CAS 169590-42-5), Fenofibrate (CAS 49562-28-9), Orlistat (CAS 96829-58-2), Flurbiprofen (CAS 5104-49-4), Acetylsalicylic acid (CAS 50-78-2), Caffeine (anhydrous) (CAS 58-08-2), Atenolol (CAS 29122-68-7), Carbamazepine (CAS 298-46-4), Tolbutamide (CAS 64-77-7), Piroxicam (CAS 36322-90-4), Theophylline (CAS 58-55-9),

Flufenamic acid (CAS 530-78-9), Nicotinamide (CAS 98-92-0), Corticosterone (CAS 50-22-6) and Nitrofurantoin (CAS 67-20-9) were purchased from Merck life science UK Ltd. Felodipine (CAS 72509-76-3) was obtained from Carbosynth Ltd, UK Ritonavir (CAS 155213-67-5), Itraconazole (CAS 84625-61-6), and Aprepitant (CAS 170729-80-3) was purchased from Acros Organics, Fisher Scientific UK Ltd. B-Estradiol (CAS 50-28-2) was purchased from AlfaAesar, Thermo Fischer Scientific, UK Probucol (CAS 23288-49-5) was obtained from MP Biomedicals, LLC, France. Diclofenac sodium salt (CAS 15307-79-6) was purchased from MP Biomedicals, LLC, Germany. Dexamethasone phosphate (CAS 2392-39-4), Ketoprofen (CAS 22071-15-4), Chlorpromazine hydrochloride (CAS 69-09-0), Paracetamol (CAS 103-90-2), Ampicillin (CAS 69-53-4), Coumarin (CAS 91-64-5) were purchased from Merck life science UK Ltd. All APIs were of high purity (98–99%) and were used as received without further processing.

The three polymers used in this study were generous gifts from commercial suppliers: Soluplus[®] and Polyvinylpyrrolidone-vinyl acetate copolymer K 28 (PVPVA) (Kollidon[®] VA 64) with molecular weight (45,000–70,000 Da) were received from BASF SE, Germany, while Hydroxyl propyl methyl cellulose acetate succinate (HPMCAS-HG) (Aquasolve[™]) was obtained from Ashland. Sodium chloride (CAS 7647-14-5) was purchased from Acros Organics, Fisher Scientific UK Ltd, to create the 75%RH accelerated condition for microarray slide storage. Dimethylformamide (DMF) >99.5% (CAS 68-12-2) HPLC grade as a solvent for the printing system was obtained from Fisher Scientific UK. Ltd. Dimethyl sulfoxide (DMSO) >99.5% (CAS 67-68-5) was purchased from Sigma Aldrich, France and was used as a common solvent to dissolve all the printable materials and their blends. Polycrystalline gold with 30 nm film thickness on special flat glass 25 × 75 mm² in size, precoated with titanium for better adhesion; roughness < 1 nm) was used as a substrate for the printing and was purchased from George Albert PVD-

Beschichtungen, Silz, Deutschland (Germany). Gold-coated glass slides were chosen as they provide a surface with a higher contact angle than bare glass slides, limiting printed droplet splashing and spreading. 384 well microplates with flat bottoms were purchased from Greiner Bio-One Ltd.

2.3 Instruments

2.3.1 2-D Inkjet printing

Piezoelectric inkjet printing is considered to be convenient for several solvents. It relies on the settings of the pulse and the voltage to generate the electrical vibrations to expand the piezoelectric crystal that then emits a droplet from the capillary (nozzle) [245, 246]. The piezoelectric crystal returns to its normal shape once the number of droplets previously set has been expelled to allow the capillary chamber to be re-filled with the solution to be printed for the following pattern. The nozzle of the printing system and the droplet ejection from the piezoelectric printer are shown schematically in Figure 17 and Figure 18, respectively [246, 247].

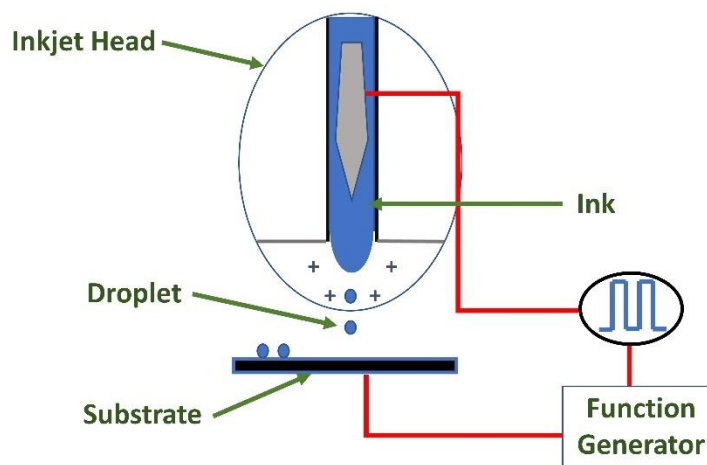


Figure 17. General Schematic of Electrostatic inkjet printing system (modified from [246]).

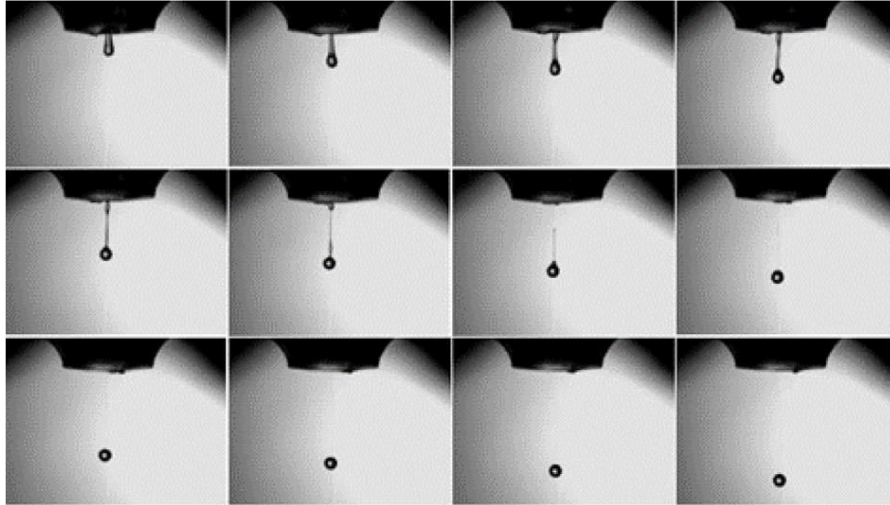


Figure 18. The camera captured piezoelectric droplet ejection from the dispenser head with an internal diameter of 70 μm [247].

Some essential variables should be regarded during the layout of the printing experiment to obtain the best outcomes from drop-on-demand (DoD) printing, such as:

- The viscosity of printing solution. If this is not optimal, satellite droplets may form, leading to liquid stream printing instead of separate droplet printing.
- The solvents for the printing solution, water, DMSO, acetone, and ethanol, have already been utilised as well as the solubility of API, its chemical instability and the time required for solvent evaporation should all be considered [170, 210, 248-250].

A Sciflexarrayer S5, a non-contact piezoelectric depositing printer manufactured by Scienion AG, Germany, was used in this work and shown in Figure 19. The system consists of the following;

- A dispenser head, which encompasses a nozzle connected to a robotic arm, enables it to move in different directions with high flexibility and accuracy.
- A syringe pump, connected to the nozzle, uses suction to take samples and circulate the solvents (dimethyl formamide (DMF), water) to wash the nozzle and the whole system before, through and after the printing process.

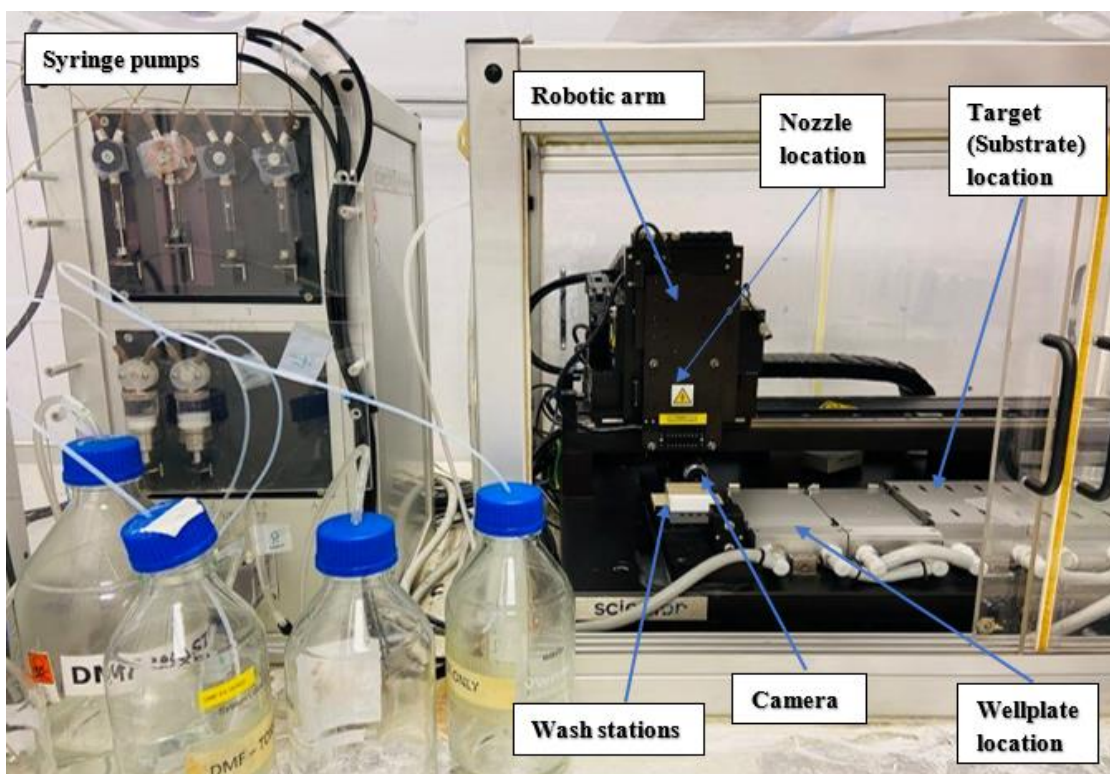


Figure 19. SciFlexarrayer S5 2D inkjet printer used in this study.

Many precautions should be taken into consideration while printing. All the hardware parts are inside a plastic chamber kept under measurable temperature and humidity conditions and in a glass box to minimise contamination. The substrates should be fixed carefully to the holder to avoid attaching and breaking the nozzle head while printing. The hardware parts are operated by integrated software, which manages all the printing steps. The first stage, “Main”, includes choosing the Probe, the target and the run program whose tasks are previously set for the printing process, as shown in Figure 20. Then, DMF as a part of the printer system (used only to wash the nozzle and the whole system before, through and after the printing process) is flushed by the pump syringe through the printer system before the nozzle is connected, as shown in Figure 21. It can control the voltage, and the electrical pulse can be easily tuned to regulate printed droplet size through the next stage, “Nozzle Setup”, to adjust droplet size, as shown in Figure 22. Droplet spacing and microarray fields can be created and modified through the next step, “Target and Field Setup”, as shown in Figure 23 and

Figure 24. Finally, the last step, “Run”, includes determining the slide order to start printing the drug and polymer as pre-planned in the previous steps, as shown in Figure 25.

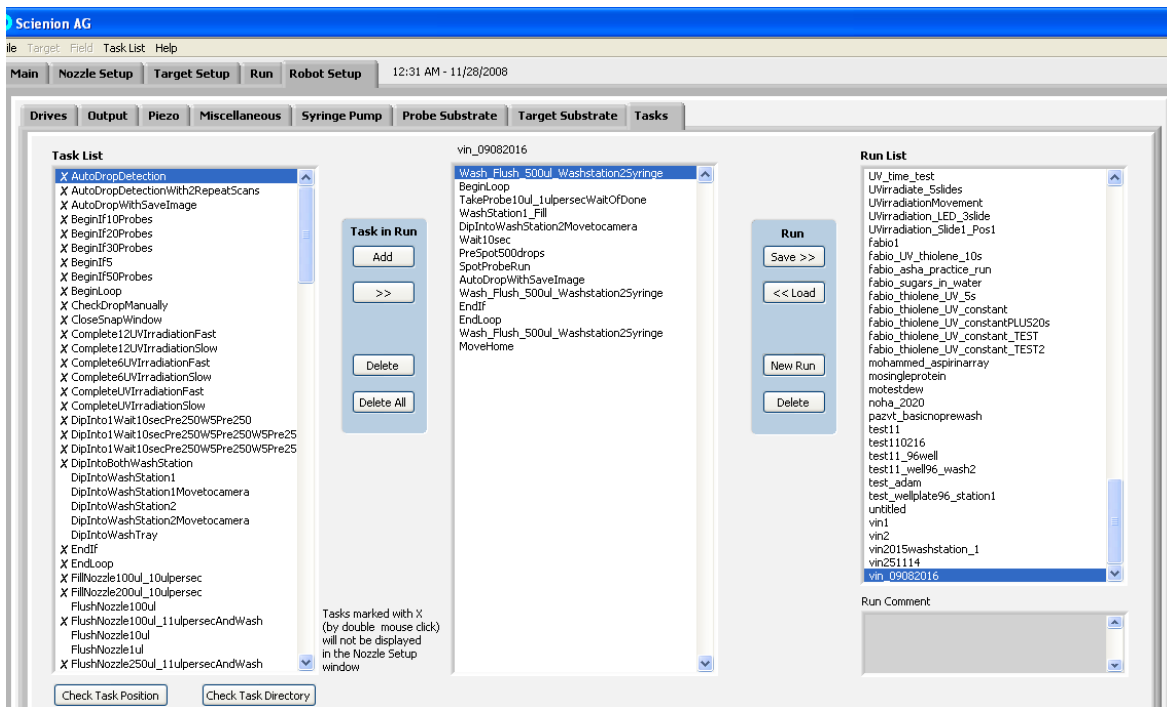
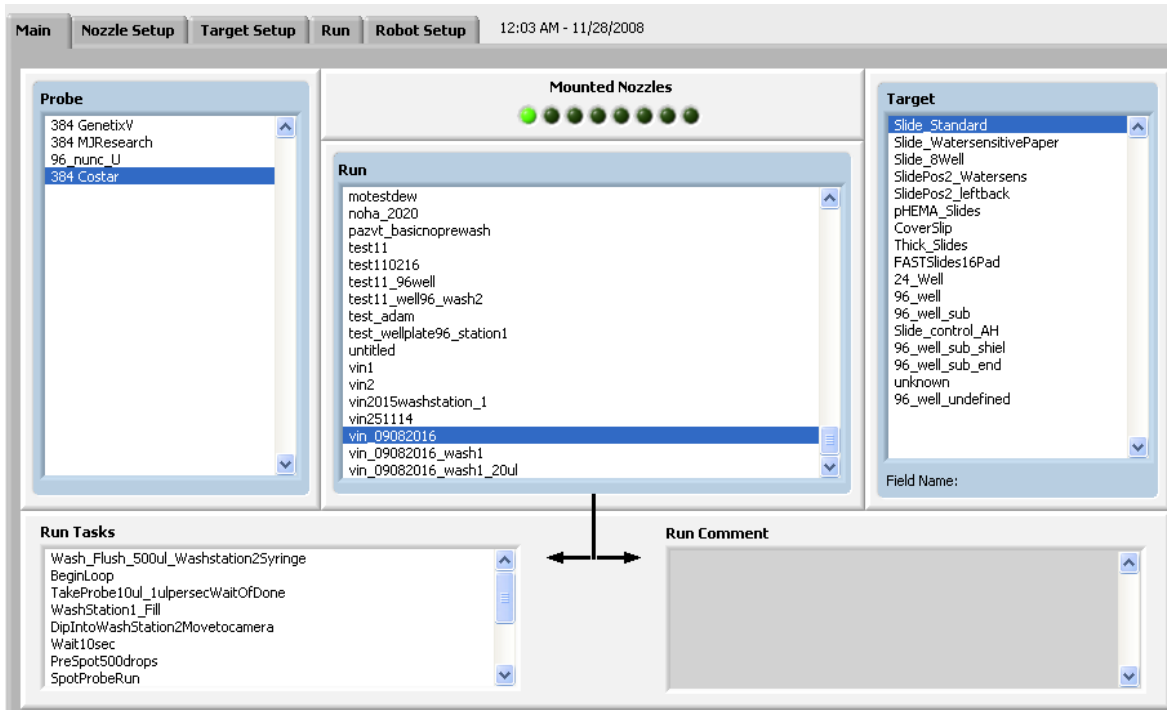


Figure 20. The first step of settings for choosing the suitable Probe, the program to run and the Target for the printing process.

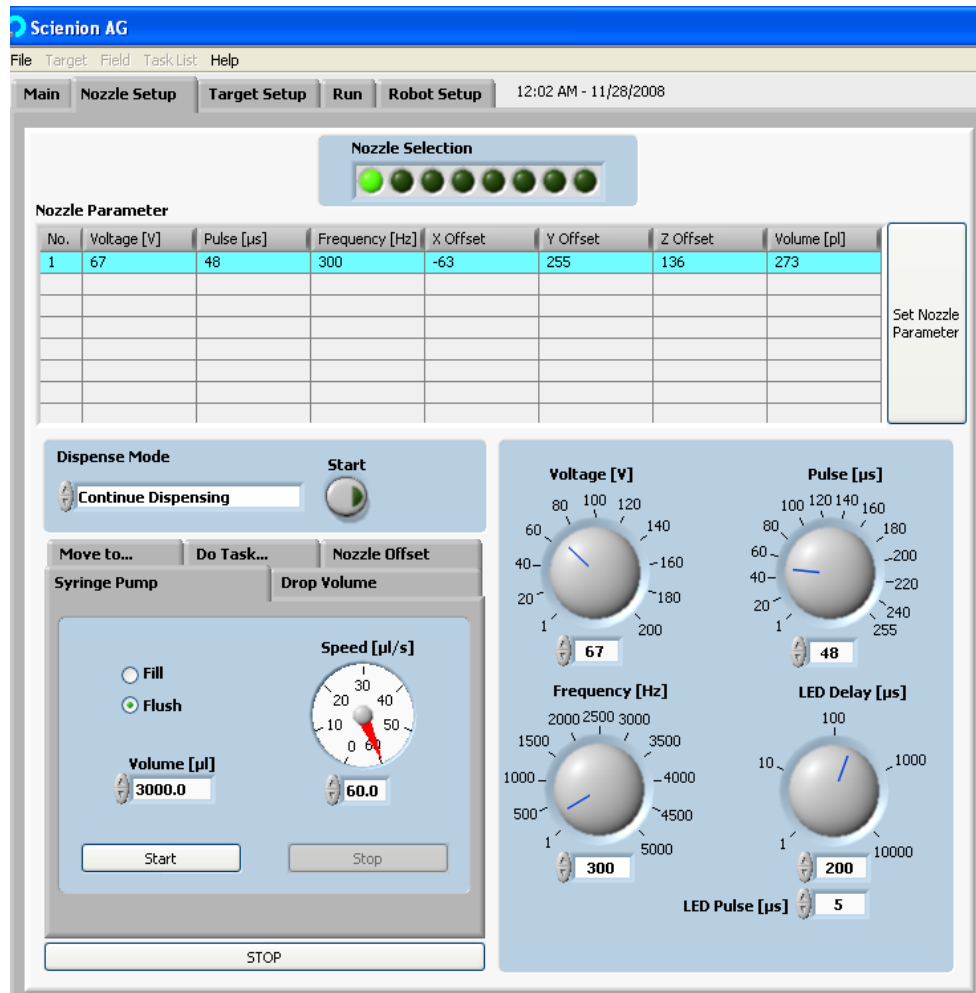


Figure 21. The Settings for DMF flush through the system by Syringe pump before the nozzle is connected.

Main Nozzle Setup Target Setup Run Robot Setup 12:05 AM - 11/28/2008

Nozzle Selection

Nozzle Parameter

No.	Voltage [V]	Pulse [μ s]	Frequency [Hz]	X Offset	Y Offset	Z Offset	Volume [p]
1	67	48	300	-63	255	136	273

Set Nozzle Parameter

Dispense Mode Start

Continue Dispensing

Move to... Do Task... Nozzle Offset

Syringe Pump Drop Volume

Drop Volume Volume [p] 0

3 Accumulations (No. of Cycles) 2 Erosions

25 Maximum No. of Cycles 1.05 Calibration

2 Standard Deviation [%] 0 Average Volume 1.57 μ m/Pixel

0.00 Volume Standard Deviation [%] Manual abort Expired Cycles

STOP

Voltage [V]

67

Pulse [μ s]

48

Frequency [Hz]

300

LED Delay [μ s]

200

LED Pulse [μ s]

5

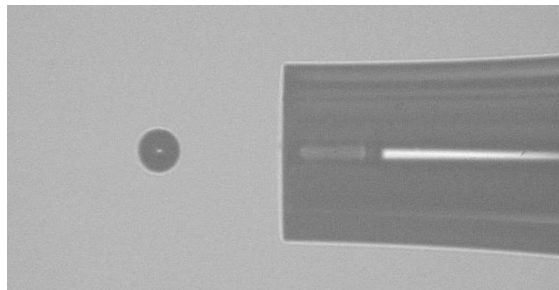


Figure 22. Droplet optimisation via adjusting voltage and pulse droplet size in the image is 220 picolitre.

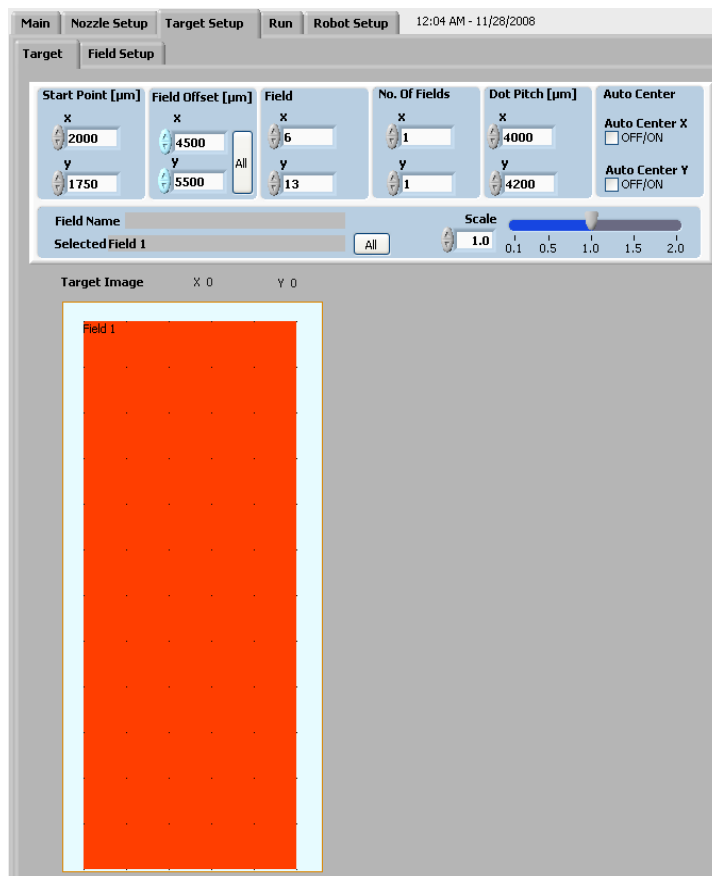


Figure 23. Target set up for preparation of slide design and microarray spots layout

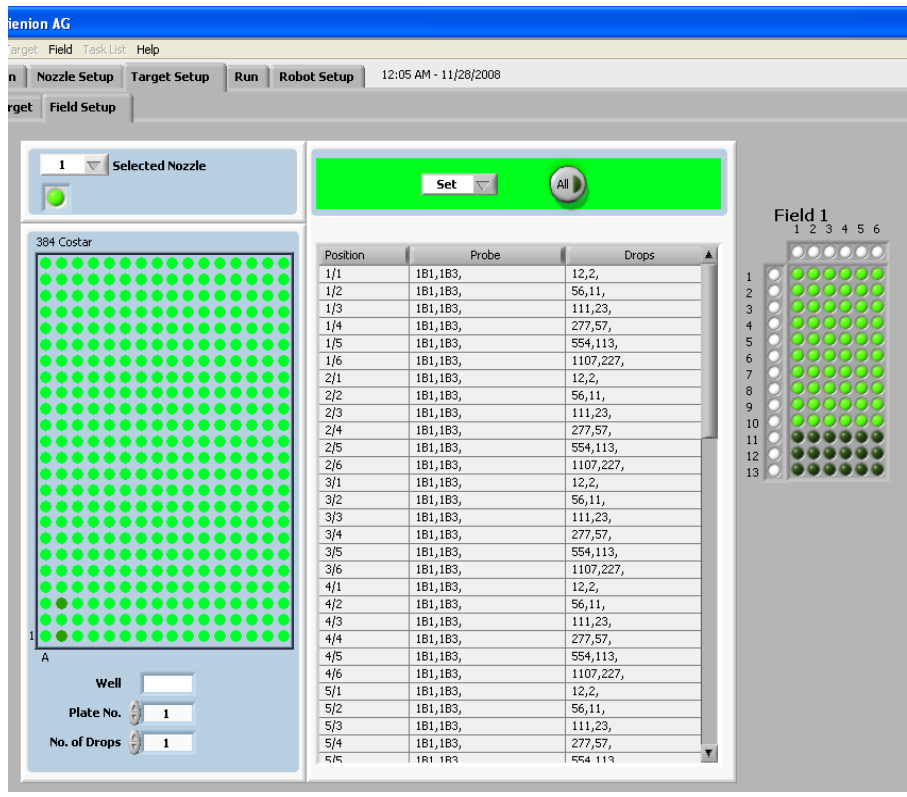


Figure 24. Field set up for the determination of each spot component and the number of droplets to be printed in each to print the required drug-polymer ratios.

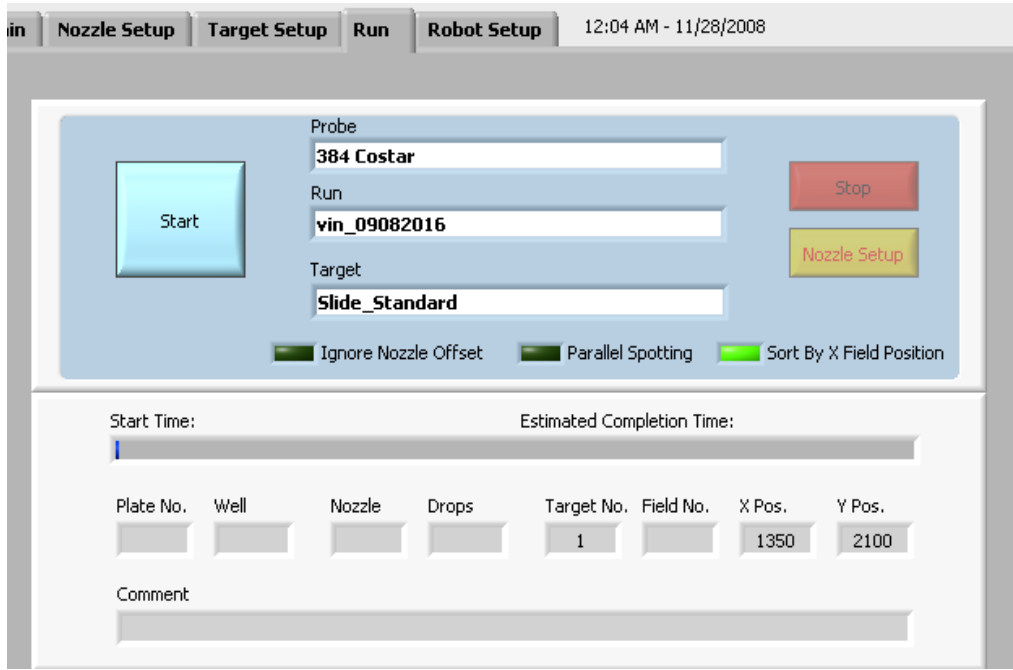


Figure 25. The final step to run the slide printing as pre-planned in the previous actions.

The DMF used in the printer system should be filtered and degassed before being used as a solvent to avoid nozzle blockage and air bubbles that would affect the continuous liquid stream in the system and the efficiency of the printing process. Filtration of DMF is operated in the fume cupboard through a vacuum system connected to a water stream using a Nylon membrane filter GN 0.20 μm , as shown in Figure 26.



Figure 26. The image at the top shows the vacuum system used for DMF filtration before the printing process, and the one at the bottom shows an example of the impurities detected by the filter.

2.3.2 Polarised Light Microscopy

A polarised light microscope is designed to observe and take images of optically anisotropic samples. The microscope includes a polariser placed in the light path before the specimen and an analyser in the optical pathway between the objective posterior aperture and the camera port, as shown in Figure 27. When plane-polarised light interacts with a birefringent (or doubly-refracting) specimen, it creates two distinct wave components, each polarised in a plane perpendicular to the other, resulting in image contrast. The velocities of these parts, known as the ordinary and extraordinary wavefronts, differ and change depending on the direction in which they propagate through the sample. The light components lose phase after departing the specimen, but when travelling through the analyser, they are recombined with constructive and destructive interference. Figure 27 depicts these principles for the wavefront field created by a hypothetical birefringent material [251]

Isotropic samples exhibit the same optical characteristics when probed in all directions. These substances have one refractive index and no restrictions on the vibration direction of the light that passes through them. In contrast, anisotropic samples (e.g., amorphous ones with a degree of order appearing) have optical characteristics that vary with the orientation of incident light with the crystallographic axes. They show a range of refractive indices relying on light's direction through the substance and the vibrational plane coordinates. Anisotropic materials also act as beamsplitters, splitting light beams into two orthogonal components (as illustrated in Figure 27). The polarising microscopy technique exploits the interference of the split light beams when re-united along the same optical path to ensure the presence of anisotropic materials [251].

Although PLM is not a quantitative detection method, it is a sensitive and rapid method which can detect small amounts of crystals in amorphous matrices [114, 117, 252]. Hence, the PLM is the primary approach used in this study for detecting the presence and the onset of crystallisation.

After DMSO evaporation, the printed microarrays were investigated using an Advanced Polarizing microscope, PriorLuxPOL™ with 12V and 30W halogen lamp using variable brightness control to analyse the crystallinity or the amorphicity of the printed spots. Images were viewed and captured with Q-Capture 2.95.0 imaging software, with and without cross-polarisation settings. That showed the physical structure of the microarrays, whether they are crystalline or amorphous arrays [253].

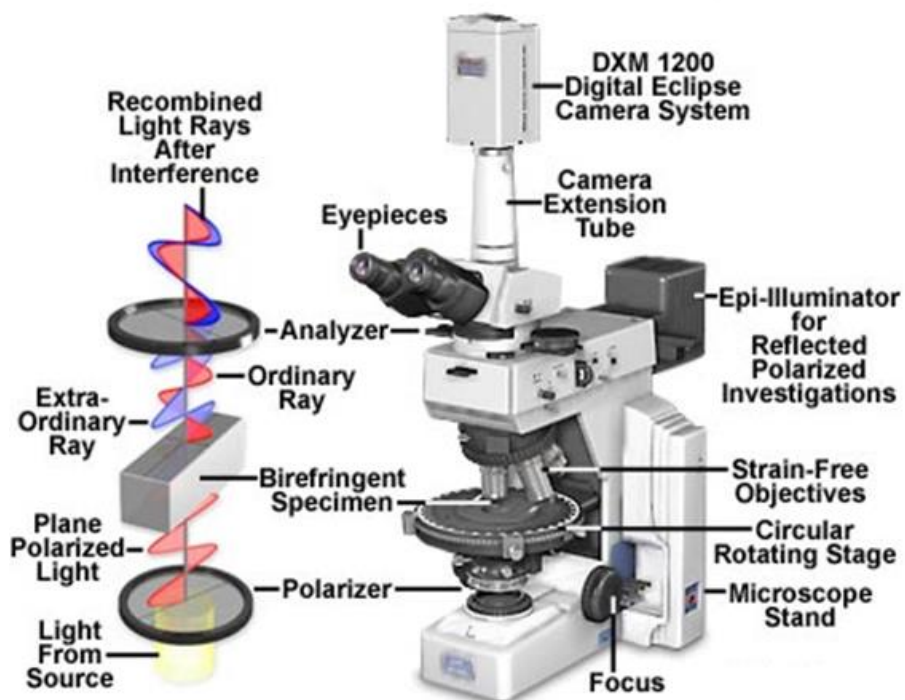


Figure 27. The components of a modern polarised light microscope and how it works [251]

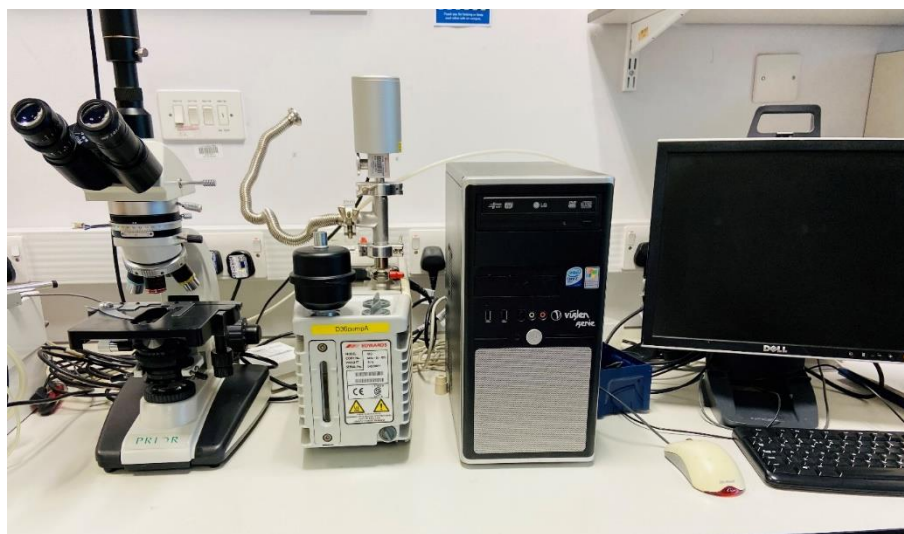
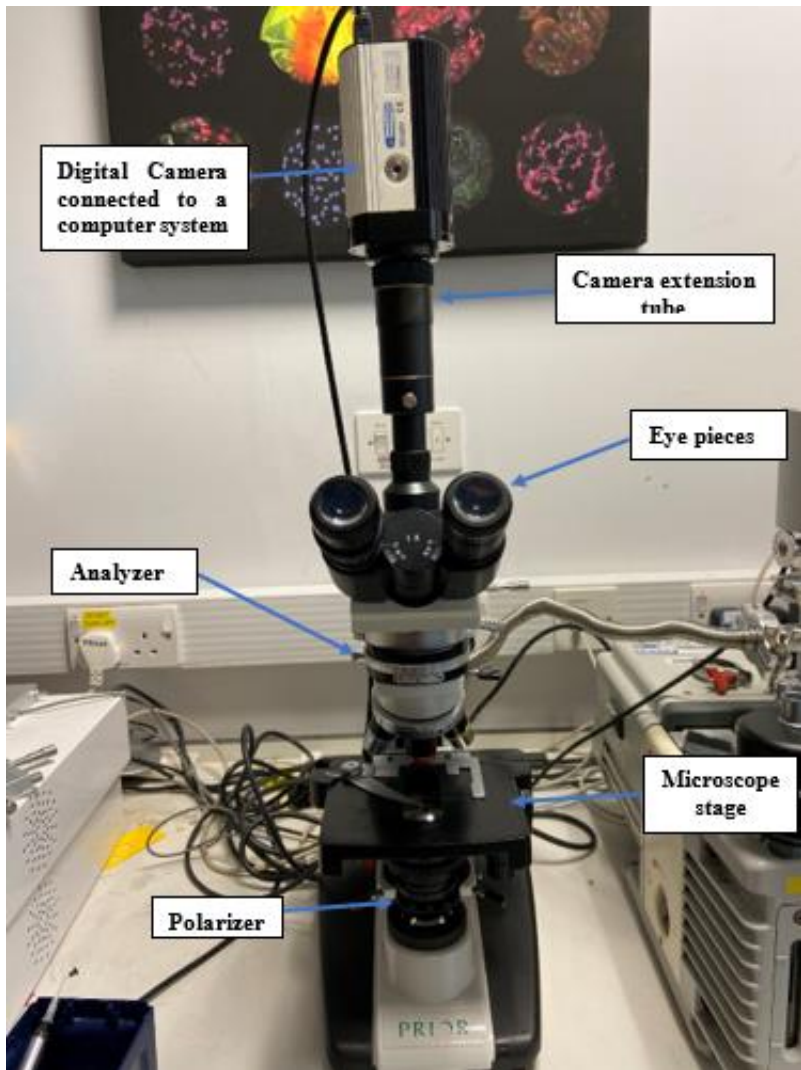


Figure 28. Polarised light microscopy used in this study and its components.

2.3.3 Atomic Force Microscopy (AFM)

At the nano- and microscales, AFM is a versatile technique for surface imaging and localised force/mechanical measurements. Binnig, Quate, and Gerber invented AFM in 1986 [254] as a development from the original probe microscope, and the Scanning Tunnelling Microscope was developed by Binnig and Gerber in 1981. In AFM, a flexible micro-cantilever, typically made from silicon or silicon nitride, is fixed over the sample with the sharp tip pointing towards the surface of interest. A schematic design of a typical AFM setup is shown in Figure 29. A laser source, a scanner, and a position-sensitive quartered photodiode are typically also included in the system. An instrument-based software program (NanoScope Analysis 1.7) controls all these parts.

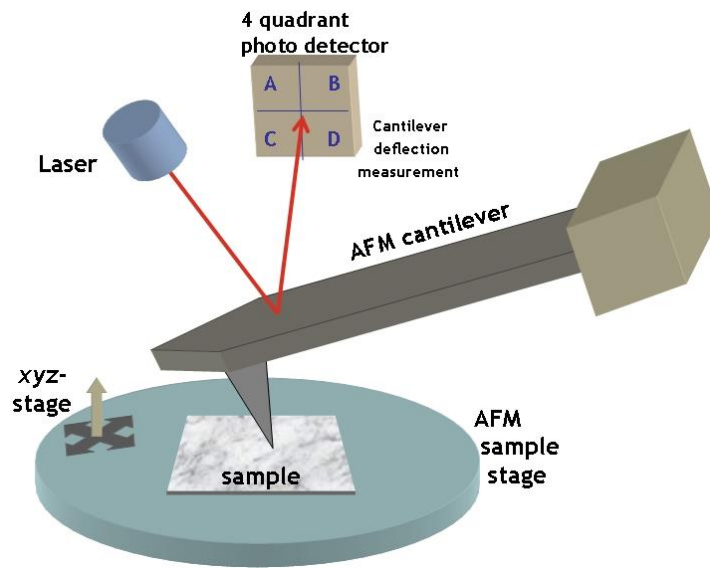


Figure 29. Schematic diagram of Atomic force microscope AFM [255]

The scanner can move in the x, y, and z directions and can be fixed in the AFM's base or head. AFM imaging typically uses one of three fundamental modes: contact mode, intermittent (tapping), or non-contact mode [256]. Here, only the tapping mode was used and discussed. When the cantilever is in tapping mode, it oscillates at a certain (acoustically resonant) frequency, causing the tip to tap a sample's surface at the bottom of each cantilever oscillation. Reducing the

significant lateral force created during contact mode scanning minimises the chance of tip damage. In this study, the tapping mode is employed to image the surface of the substrate (gold-coated slide). The laser beam is focused on the back of the cantilever. The interactions between the tip and the sample surface result in interactions that allow topographic and physical data to be obtained. A quartered photodiode tracks the position of the deflected laser, and the photodetectors measure the variation in light intensities between the bottom and top photodetector quadrants. Changes in the scanner's height are used to form a topographic image of the sample surface [256].

2.3.4 Water contact angle measurement (WCA)

WCA was used to select the optimal substrate for the printing process. The wettability of liquids is often measured using contact angle measurements by placing a liquid droplet onto a substrate. A tangent is then applied to the liquid droplet, and the contact angle can be measured using Young's equation (re-arranged to calculate the cosine of the contact angle) [257]. Poor wettability (high contact angle) is required for the substrate for the printing process as this prevents the spreading of micro-spots during the printing process. It was not possible to determine the contact angle measurements for DMSO on different substrates; therefore, those substrates' contact angle was measured with water.

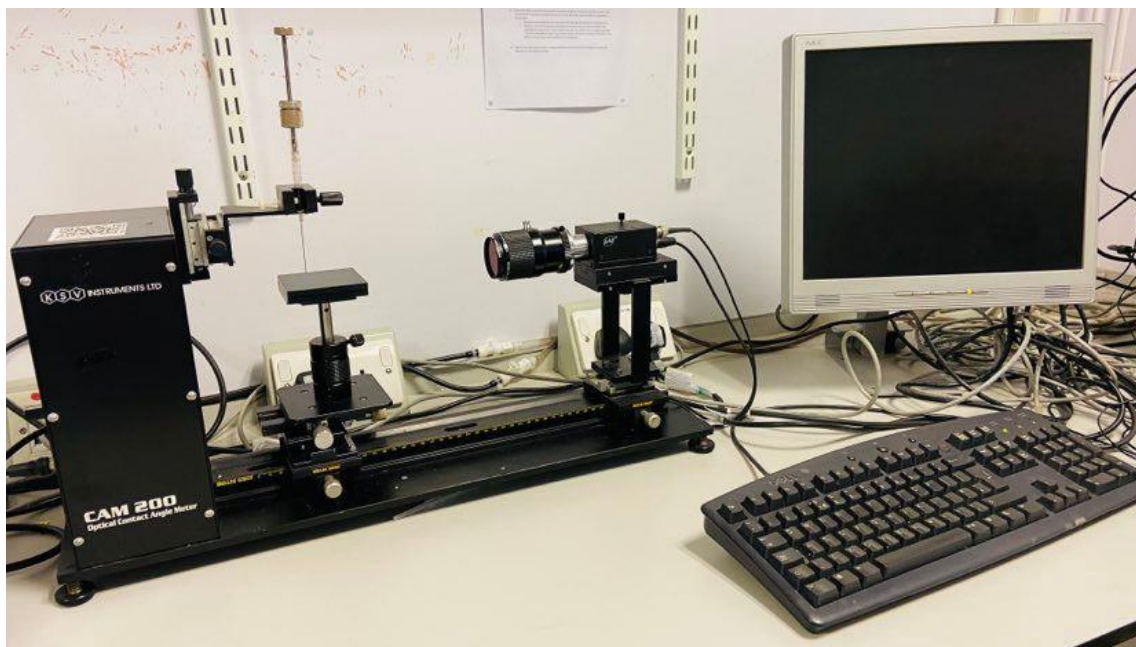


Figure 30. Water contact angle equipment used in this study.

2.3.5 Stability study of the printed Microarrays

A six-month stability study was conducted on all the printed microarrays at accelerated conditions of $40^{\circ}\text{C} \pm 2^{\circ}\text{C}/75\% \text{RH} \pm 5\% \text{RH}$ (relative humidity), as per ICH guidelines [258]. Since solid dispersion dosage forms are often packaged in protective settings and kept at lower temperatures and humidity levels during storage, if no crystallisation of the formulations is seen under such a scenario, they are likely to remain physically stable throughout their shelf life. Storing the microarrays at these harsh accelerated conditions for six months would give a cautious approximation of the solid dispersion's physical stability. The required RH was adjusted by preparing a supersaturation salt solution of Sodium Chloride. To prepare a saturated salt solution, the indicated salt is added to warm (about 40°C) distilled water, stirring until no more salt dissolves. Additional salt is added to ensure an excess of the saturating salt. Then, the saturated solution is cooled to ambient temperature and set for at least 24 hours before use. The solution should cover all salt crystals [259]. The microarray slides were kept in the plastic box containing the supersaturated solution inside a stability oven (Thermo Scientific), as shown in Figure 31 and Figure 32. A data logger,

Thermopro TP49, was used to keep track of the environment. The formulation state, whether amorphous or crystalline, was established before the stability study began using polarised light microscopy to check the presence or absence of birefringence that would interpret crystallisation or amorphicity, respectively. The printed spots were examined daily for the first four weeks and every week for the following six months.



Figure 31. Microarray storage at 75% RH \pm 5% at 40°C in a stability oven. as an accelerated condition for the stability study.



Figure 32. The stability oven used for the accelerated conditions for the physical stability assessment of the printed Microarrays.

2.3.6 3D inkjet printer (Dimatix)

For the 3D printing of formulations in this study, the Fujifilm Dimatix Materials Printer DMP-2850 Series, equipped with a 12-jet Samba cartridge with an approximate 10 pL drop volume, was utilized (as shown in Figure 33). The primary challenge in inkjet printing lies in developing a reliable printable ink that maintains the functionality of the printed formulation. The jetting parameters that could be controlled included the jetting voltage, waveform, frequency, and cartridge heating. The system's drop watcher function allowed for monitoring the jetting behaviour. During the printing, variables like the spacing between drops, the heating of the substrate, and the gap between the print head and the substrate were optimised. Polyethylene terephthalate films were used as a substrate for printing.

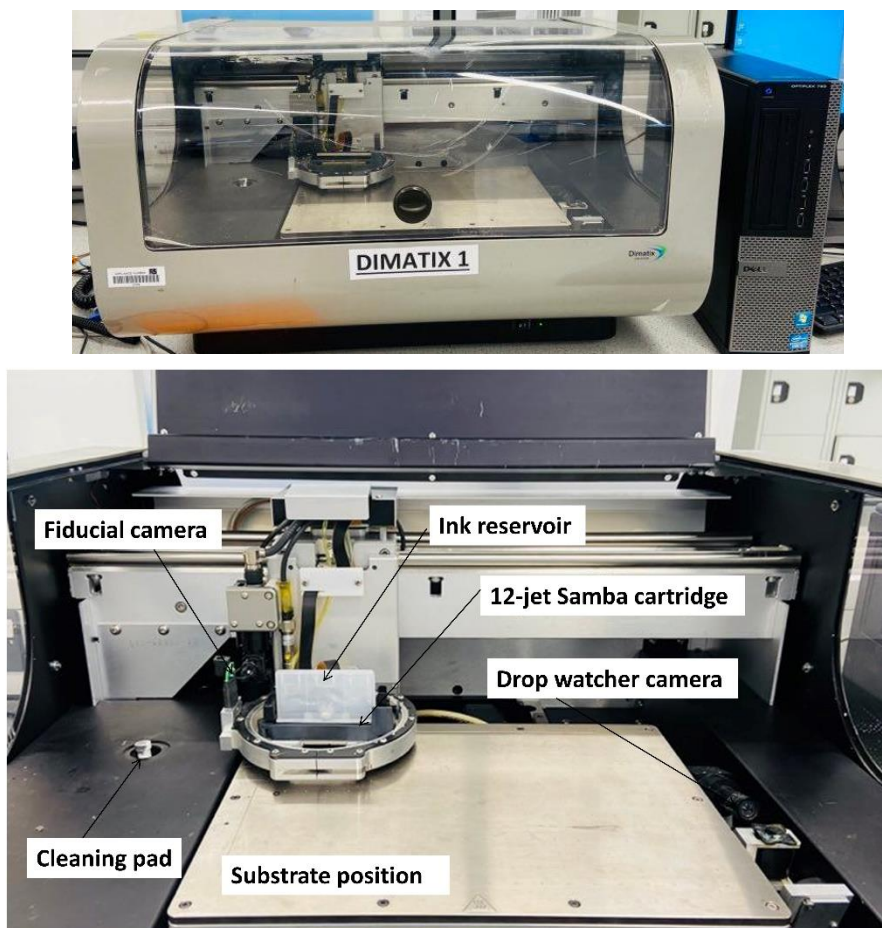


Figure 33. 3D inkjet printer, the Dimatix, utilised in this study, along with an annotated schematic detailing its key components such as the fiducial camera, ink reservoir, 12-jet Samba cartridge, drop watcher camera, cleaning pad, and substrate position.

2.3.7 Malvern Rheometer

The viscosity of the ink is generally accepted in the range between 8 and 15 milliPascal-second (mPa.s) [260]. The viscosity of the ink was characterised using Malvern Instruments Kinexus Pro Research Rheometer (as shown in Figure 34), which was found in the range of 7–9 mPa.s. That was employed using a “cup and bob” configuration to inhibit solvent loss through evaporation. The ink was transferred into the cup using a syringe, and then the bob was lowered into the cup automatically. Viscosity readings were recorded across a range of shear rates, from 1 to 1000 s⁻¹. The readings obtained at a shear rate of 100 s⁻¹ are particularly significant, as they served as a crucial indicator of the dynamic viscosity of the ink during its deposition process. All measurements were conducted in triplicates at a controlled temperature of 25 °C. Measuring ink viscosity at 25°C provides a baseline reference under typical conditions, allowing for standardized comparisons and quality control assessments.



Figure 34. Malvern Instruments Kinexus Pro Research Rheometer used to measure the viscosity of the ink.

3 Chapter 3: 2-D Microarray Printing for Screening of Pharmaceutical Solid Dispersions

3.1 *Introduction*

Solid dispersion formulations have gained interest in tailoring the physicochemical properties of drugs, including the needed increase in drug dissolution and suitable supersaturation conditions in the GIT. Although solid dispersions may be kinetically stable for a while, amorphous drugs may eventually phase separate from solid dispersions depending on their miscibility with polymers and transform to more stable crystalline forms, resulting in shorter shelf life, reduced product performance and lower bioavailability. The carrier polymer itself is also a crucial parameter to achieve suitable physical stability of solid dispersions due to the need for miscibility between the drug and the polymer to limit molecular drug mobility and nucleation/crystallisation processes that lead to physical instability [116, 261].

Numerous variables can affect the miscibility of a drug in a polymeric matrix, such as the chemical nature, molecular weight, viscosity, and T_g of the polymers as well as potential molecular interactions between the drug and the polymer. Understanding the miscibility between drugs and the polymers employed is crucial for successfully developing solid dispersions. Therefore, it is essential to conduct drug-polymer miscibility screening to choose the most appropriate polymeric carriers. It is possible to define drug-polymer miscibility as the ability of the drug to disperse in a polymer matrix and form a single phase without phase separation and drug crystallisation [262].

Assessment in practice is typically based on trial and error evaluations of bulk samples applying a single model drug with a small range of polymers for a very limited number of selected drug/polymer compositions using characterising techniques such as DSC and XRPD that require samples to be prepared on a milligram to gram scale [117]. Given the potential of drug-polymer

dispersions as a suitable formulation and the importance of investigating different techniques dealing with API formulation challenges, it would be helpful to develop reliable and relatively rapid screening processes that do not require large amounts of the drug.

Inkjet printing is among the most promising and pioneering techniques used in screening and formulating different APIs [209, 210]. It is an umbrella term encompassing a wide range of versatile, inexpensive, fully automated approaches to digitally- form and place small liquid drops with high precision onto a surface [210]. An abundance of versatile materials has been successfully printed by inkjet, including genes [211, 212], cells [213], proteins [214], colloids [215], curable-antifouling monomers [216], polymers [217], screening of polymer features to assess their suitability with the microarray manufacturing [218] nanomaterials and pharmaceutical formulations [219, 220]. Inkjet printing technology has been exploited, especially in the broad area of new biomaterials [222] and drug discovery [210, 223], but the research in the area of screening amorphous solid dispersion is still limited.

In this regard, Taresco et al. optimized a new miniaturized, high-throughput assay to screen polymer–drug solid dispersions using a 2-D Inkjet printer [224]. Different drug/polymer loadings using six different drugs and one polymer (PVPVA) were printed and monitored using PLM. A final quantity of 650 ng of materials per printed spot was reported to provide a high correlation of screening compared to the behaviour of the gram scale drug–polymer blend. Once the threshold printed amount required to characterize bulk behaviour was detected, another array was developed to establish a literature comparison of one drug within four commercial polymeric matrices for validation. An average of 390 ng (10 and 50% of drug) in the printed drug/polymer arrays was used in hence < 0.05% sample than a bulk experiment, where around 1.1 g was used, confirming that the screening process was not just high-throughput but also very sparing in the use of precious

material. This approach potentially offers significant efficiency in pharmaceutical formulation screening, with each experiment in the micro-array format requiring from 3 up to 6 orders of magnitude lower amounts of sample than conventional screening methods [224].

3.2 Aims and Objectives

However, whilst a number of drugs and polymers have been studied in the literature, the number of researched APIs and their loading with different polymers is still very limited, and the model development is often done for each system in isolation, making it difficult to draw any general conclusions. **Therefore, the aim of this chapter is:**

- To develop a miniaturised, high-throughput assay for screening around 930 drug/polymer loadings in triplicates, which is much more than has been achieved before while taking into consideration performing this safely using a minimal (nano-gram) amount of drug developing an expanded set of drug-polymer formulations in different drug loadings using a 2-D pico-litre inkjet printer, followed by a stability study of the printed microarrays.

That could be achieved through the following objectives:

- Investigating the feasibility of employing 2D inkjet printing and printed nano-arrays with pico-litres of APIs in pre-formulation and solid-form screening framework
- Developing a miniaturised, high-throughput assay for screening an expanded set of drug-polymer formulations in different drug loading using a 2-D pico-litre inkjet printer for building an extensive library of various drug and polymer loadings which is a relatively larger number of samples than previously reported.
- Stability study of the printed microarrays drug-polymer solid dispersions at accelerated conditions.

- Detecting and comparing the range of miscibility limits of each API within different polymeric matrices and comparing that with the literature.

3.3 Methodology

3.3.1 Materials (Model Drugs and Polymers)

Following a similar approach as Nurzyńska et al. [151] and Fridgeirsdottir et al. [152], APIs with diverse chemistries, including different functional groups with varying molecular weights, were chosen. The structures of model drugs selected for this study are shown in Figure 15 and their physicochemical properties are shown in Table 4 as previously mentioned in Chapter 2. The three polymers were chosen to represent the polymer classes that are most commonly used, as PVPVA and HPMCAS are frequently utilised in marketed solid dispersions, while Soluplus is the only polymer used here, not currently employed in a marketed formulation. They are commercially available, inexpensive, and widely utilised in the literature and the industry. The chemical structures of the three polymers used in this study are shown in Figure 16 in Chapter 2.

3.3.2 Substrate analysis

3.3.2.1 Water contact angle measurement (WCA)

In order to choose a suitable substrate for the printing process, it was necessary to assess the wettability of the substrates by measuring the WCA using a KSV CAM200 (Figure 30 shown in Chapter 2) based on the drop's side view. Substrates (glass slides and gold-coated slides) were cleaned thoroughly to remove any contamination and ensure uniform surface conditions. A drop of distilled water (around 5 μL) was deposited using the syringe on the surface of the glass slide and the gold-coated slide at room temperature at 25°C. The angle measurement is made from images through a digital camera captured by a computer. The software allows digitizing the contour of the drop by processing the images and determining the contact angle by applying a tangent to the liquid droplet and by applying Young's equation (re-arranged to calculate the cosine of the contact angle) [257]. The contact angles measured were compared for both substrates.

3.3.2.2 Measuring the roughness of the gold-coated slides using atomic force microscopy (AFM)

Using Bruker's Dimension Fast-Scan AFM equipment, the topography and roughness of the gold-coated glass slides were investigated at the nanoscale level. The tapping technique was employed in this study to image the topography of the substrates' surface with high resolution. Using an aluminium reflective coating tip MPP-12120 (TAP150A) with a resolution of 256×256 points, AFM measurements were performed in triplicates at 1 μm and 5 μm areas throughout the substrates. NanoScope Analysis, version 1.7, was used to analyse the acquired topographical images of all solid surfaces.

3.3.3 Preliminary studies to choose the printing instrument

3.3.3.1 Hand method (Hamilton Syringe)

As a preliminary study and subject to the availability of the materials, three APIs were used in this experiment, including Estradiol, Nifedipine and Celecoxib and three polymers, including PVPVA, Soluplus and HPMCAS. 10 mg/ml solution of each API and polymer which was below the solubility limit was prepared by weighing and dissolving the material in DMSO, followed by sonication. 10 µl Hamilton[®] syringe (701N) was used for pipetting different volumes of pure APIs and polymers in triplicates on gold-coated glass slides, according to Table 5. The API solution was pipetted on the substrate, followed by the polymer solution on top of the wet API droplet to prepare 50% API/polymer loading spots of 3 APIs with the three polymers, according to

Table 6. The printed spots were left for 24 hr to dry in the printer box to apply the same conditions within all the techniques. The dried spots were monitored by PLM at different time points for three months of storage in accelerated conditions (to be mentioned in detail later in section 2.2.4).

Table 5. The composition of slide 1 was performed using Hamilton syringe.

	A	B	C	D	E	F
1	0.1µl Estradiol	0.1µl Estradiol	0.1µl Estradiol	0.2µl Estradiol	0.2µl Estradiol	0.2µl Estradiol
2	0.3µl Estradiol	0.3µl Estradiol	0.3µl Estradiol	0.4µl Estradiol	0.4µl Estradiol	0.4µl Estradiol
3	0.5µl Estradiol	0.5µl Estradiol	0.5µl Estradiol	0.1µl Nifedipine	0.1µl Nifedipine	0.1µl Nifedipine
4	0.2µl Nifedipine	0.2µl Nifedipine	0.2µl Nifedipine	0.3µl Nifedipine	0.3µl Nifedipine	0.3µl Nifedipine
5	0.4µl Nifedipine	0.4µl Nifedipine	0.4µl Nifedipine	0.5µl Nifedipine	0.5µl Nifedipine	0.5µl Nifedipine
6	0.1µl Celecoxib	0.1µl Celecoxib	0.1µl Celecoxib	0.2µl Celecoxib	0.2µl Celecoxib	0.2µl Celecoxib
7	0.1µl Celecoxib	0.3µl Celecoxib	0.3µl Celecoxib	0.4µl Celecoxib	0.4µl Celecoxib	0.4µl Celecoxib
8	0.5µl Celecoxib	0.5µl Celecoxib	0.5µl Celecoxib	0.1µl Soluplus	0.1µl Soluplus	0.1µl Soluplus
11	0.2µl Soluplus	0.2µl Soluplus	0.2µl Soluplus	0.3µl Soluplus	0.3µl Soluplus	0.3µl Soluplus
12	0.4µl Soluplus	0.4µl Soluplus	0.4µl Soluplus	0.5µl Soluplus	0.5µl Soluplus	0.5µl Soluplus

Table 6. The composition of slide 2 was performed using Hamilton syringe.

	A	B	C	D	E	F
1	0.1µl PVPVA	0.1µl PVPVA	0.1µl PVPVA	0.2µl PVPVA	0.2µl PVPVA	0.2µl PVPVA
2	0.3µl PVPVA	0.3µl PVPVA	0.3µl PVPVA	0.4µl PVPVA	0.4µl PVPVA	0.4µl PVPVA
3	0.5µl PVPVA	0.5µl PVPVA	0.5µl PVPVA	0.1µl HPMCAS	0.1µl HPMCAS	0.1µl HPMCAS
4	0.2µl HPMCAS	0.2µl HPMCAS	0.2µl HPMCAS	0.3µl HPMCAS	0.3µl HPMCAS	0.3µl HPMCAS
5	0.4µl HPMCAS	0.4µl HPMCAS	0.4µl HPMCAS	0.5µl HPMCAS	0.5µl HPMCAS	0.5µl HPMCAS
6	0.3µl Estradiol +0.3µl Soluplus	0.3µl Estradiol +0.3µl Soluplus	0.3µl Estradiol +0.3µl Soluplus	0.3µl Estradiol +0.3µl PVPVA	0.3µl Estradiol +0.3µl PVPVA	0.3µl Estradiol +0.3µl PVPVA
7	0.3µl Estradiol +0.3µl HPMCAS	0.3µl Estradiol +0.3µl HPMCAS	0.3µl Estradiol +0.3µl HPMCAS	0.3µl Nifedipine +0.3µl Soluplus	0.3µl Nifedipine +0.3µl Soluplus	0.3µl Nifedipine +0.3µl Soluplus
8	0.3µl Nifedipine +0.3µl PVPVA	0.3µl Nifedipine +0.3µl PVPVA	0.3µl Nifedipine +0.3µl PVPVA	0.3µl Nifedipine +0.3µl HPMCAS	0.3µl Nifedipine +0.3µl HPMCAS	0.3µl Nifedipine +0.3µl HPMCAS
9	0.3µl Celecoxib +0.3µl Soluplus	0.3µl Celecoxib +0.3µl Soluplus	0.3µl Celecoxib +0.3µl Soluplus	0.3µl Celecoxib +0.3µl PVPVA	0.3µl Celecoxib +0.3µl PVPVA	0.3µl Celecoxib +0.3µl PVPVA
10	0.3µl Celecoxib +0.3µl HPMCAS	0.3µl Celecoxib +0.3µl HPMCAS	0.3µl Celecoxib +0.3µl HPMCAS			

3.3.3.2 Contact printing (Pin printing)

The contact printer was used as another preliminary study to check the printed materials' crystallisation behaviour and the probability of the printer's use in building a library of different drug/polymer loadings. Microarray formation was performed using a contact robot (Biodot) using an XYZ stage (Figure 36). A ceramic pin with a tip diameter of 500 µm (Labnext Inc Xtend Microarray Pin) with around 5 nL uptake volume and deposition volume of approximately 5 nL was used. The pin was loaded into the print head, and gold-coated glass slides were loaded as a substrate. The humidity was maintained at between 30-40%. Typically, 3 to 6 replicates of the same formulation (API or polymer or API/polymer) arrays were printed onto each substrate regarding the pre-set chosen plan (Figure 37, Figure 38, Figure 39 and Figure 40) by the software

(BioDot AxSys). The used pin was washed in DMF between the runs to clean any residues of the previous ink. Then, the pin was washed in a flow bath with agitation, as shown in Figure 35. The printed spots were left overnight to dry in the printer box. The dried spots were monitored by the PLM at different time points for three months of storage in accelerated conditions (to be mentioned in detail later in section 2.2.4).

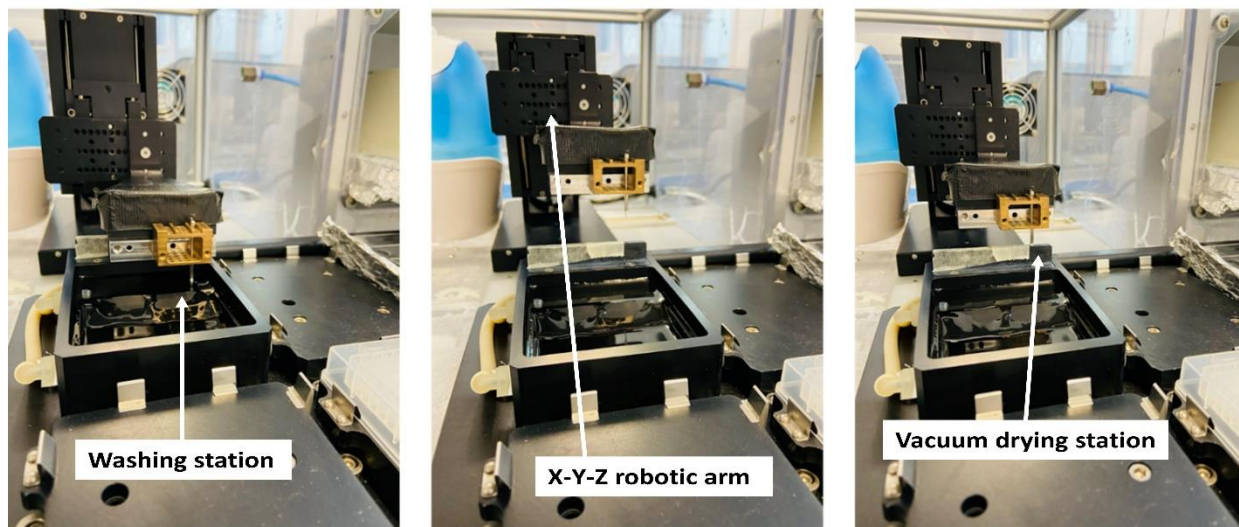


Figure 35. Washing and vacuum drying of the pin.

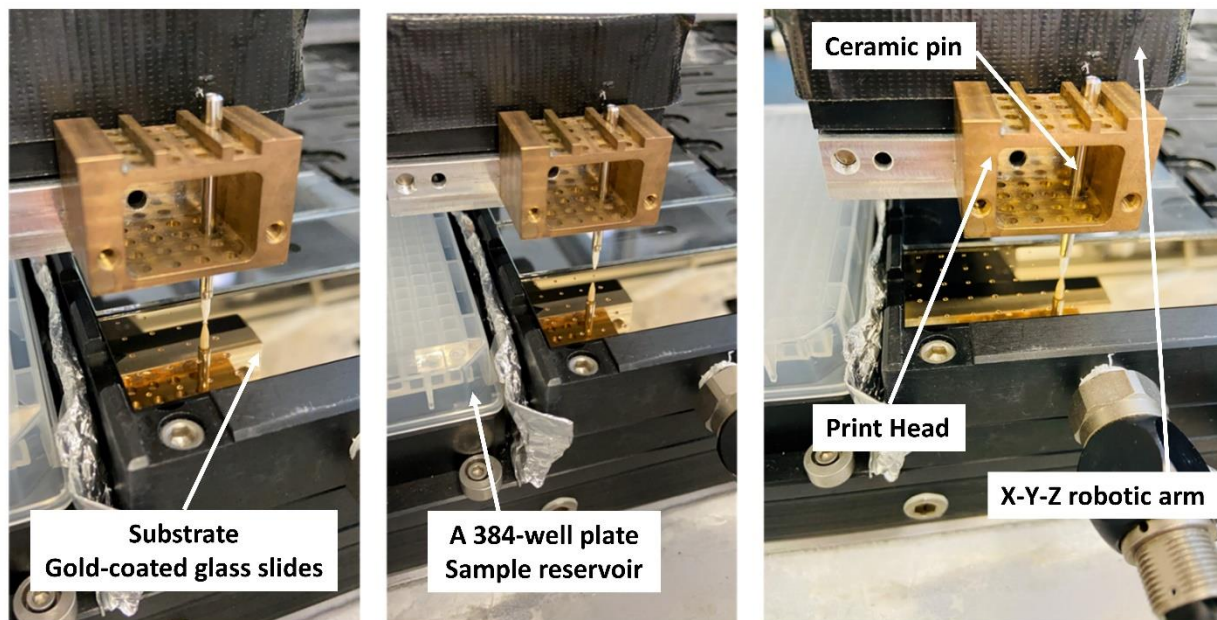


Figure 36. Depositing the solution through the pin onto a substrate by making contact controlled by an X-Y-Z robotic arm.

Microarray development using the contact printer

10 mg/mL solutions were prepared by separately dissolving 10 mg of each API and polymer in 1 mL DMSO and sonicating for 10 minutes. That was best done fresh before each print run to avoid any precipitation of the printed material. 50-60 μ l aliquots were pipetted into a 384-well source plate. The sample was loaded from the source plate into the pin. The pins were lowered into the solutions, held for 5 seconds and then withdrawn. Pins must be blotted before printing to remove excess ink from the outside of the pin. Then, ink delivery occurs from the quilled part of the pin to achieve consistent spot formation.

To evaluate the printability of pure drugs and polymers in drug-polymer dispersions and determine the optimal printing sequence, a systematic experimental approach was implemented. Various plans were devised to test the feasibility of printing pure drugs and polymers, as well as their combinations, using contact printing. Different printing sequences were explored to prepare drug-polymer dispersion spots, assessing the impact of sequence (drug first, polymer first, or simultaneous printing) on dispersion uniformity and stability. The objective was to identify the most effective printing plan for generating an extensive library of drug-polymer formulations at varying loadings.

I. Plan 1.

This plan was designed to assess whether the minimum amount printable using contact printing was sufficient for assessment. The printing process involved making a single contact per spot to deposit one droplet of pure API per spot, resulting in a calculated deposited mass of approximately 50 ng onto the substrate after the evaporation of DMSO. Each API spot was replicated six times to ensure consistency and reliability in the printing process and subsequent analysis (Figure 37).

	Each row has replicates of the same API or polymer or w/w API/polymer loading						
	A	B	C	D	E	F	
1	 50 ng	 50 ng	 50 ng	 50 ng	 50 ng	 50 ng	Estradiol
2	 50 ng	 50 ng	 50 ng	 50 ng	 50 ng	 50 ng	Nifedipine
3	 50 ng	 50 ng	 50 ng	 50 ng	 50 ng	 50 ng	Celecoxib
4	 50 ng	 50 ng	 50 ng	 50 ng	 50 ng	 50 ng	Orlistat
5	 50 ng	 50 ng	 50 ng	 50 ng	 50 ng	 50 ng	Felodipine

Figure 37. Schematic diagram of the printing plan 1 to print 6 replicates of 5 pure APIs.

II. Plan 2.

This plan was designed to assess whether multiple prints using contact printing was a viable approach to produce materials for assessment. The number of contacts made was 12 contacts per spot, producing pure APIs and polymer spots of 12 droplets with a deposited mass of around 600 ng after DMSO evaporation. Six replicates were printed for each API and polymer (Figure 38).

	Each row has replicates of the same API or polymer or w/w API/polymer loading						
	A	B	C	D	E	F	
1	 600 ng	 600 ng	 600 ng	 600 ng	 600 ng	 600 ng	Estradiol
2	 600 ng	 600 ng	 600 ng	 600 ng	 600 ng	 600 ng	Nifedipine
3	 600 ng	 600 ng	 600 ng	 600 ng	 600 ng	 600 ng	Celecoxib
4	 600 ng	 600 ng	 600 ng	 600 ng	 600 ng	 600 ng	Orlistat
5	 600 ng	 600 ng	 600 ng	 600 ng	 600 ng	 600 ng	Felodipine
6	 600 ng	 600 ng	 600 ng	 600 ng	 600 ng	 600 ng	Soluplus
7	 600 ng	 600 ng	 600 ng	 600 ng	 600 ng	 600 ng	PVPVA
8	 600 ng	 600 ng	 600 ng	 600 ng	 600 ng	 600 ng	HPMCAS

Figure 38. Schematic diagram of the printing plan 2 to print six replicates of five pure APIs and three pure polymers.

In order to print API/polymer blends, two techniques were followed;

III. Plan 3.

This plan was designed to assess whether contact printer could be used to achieve in spot mixing of samples. The polymer and the API were printed at the same position on the substrate, as shown in Figure 39. Spots of 50% API/polymer loadings were printed using six contacts of API solution and six contacts of polymer solution per spot, depositing a total mass of around 600 ng in each after solvent evaporation using individual solutions API and HPMCAS polymer of 10 mg/mL. Immediately following the printing of each API in triplicate, and after cleaning and refilling the pin with polymer, the polymer is applied on top of the drug.

Conversely, if the polymer is printed first, the drug is applied in the same manner following the printing of each polymer in triplicate, subsequent to cleaning and refilling the pin with the drug. In the first three columns, the six contacts of API solution were printed first, and then six contacts of polymer were printed on the top at the same position on the substrate. In the second three columns, the six contacts of the polymer solution were printed first, and then six contacts of API were printed on the top of them at the same position. By printing 12 droplets at the same place, the printed mass was 300 ng of drug plus 300 ng of polymer per spot. All were printed in triplicates.

	Each row has triplicates of the same API, polymer or w/w API polymer			Each row has triplicates of the same API, polymer or w/w API polymer			
	A	B	C	D	E	F	
1							50% Estradiol/HPMCAS
	Printing API first			Printing polymer first			
2							50% Nifedipine/HPMCAS
	Printing API first			Printing polymer first			
3							50% Celecoxib/HPMCAS
	Printing API first			Printing polymer first			
4							50% Orlistat /HPMCAS
	Printing API first			Printing polymer first			
5							50% Felodipine/HPMCAS
	Printing API first			Printing polymer first			
6							100% HPMCAS

Figure 39. Schematic diagram of the printing plan 3 to print three replicates of 50% API polymer loading by printing the API solution and the polymer solution separately in a different order. In the first three columns (A, B, C), the API solution was printed first and then the polymer solution in the same amount, while in the other three columns, the polymer was printed first, then the API solution.

IV. Plan 4.

This plan was designed to assess whether contact printing could successfully print pre-mixed samples, which act as a comparison to the Plan 3 printed samples. The drug and polymer were mixed first, and then the mixtures were used as a printing solution in the source well plate, as shown in Figure 40.

- 40 μ l were taken from 10 mg/mL drug solution in DMSO + 40 μ l from 10 mg/mL polymer solution, mixed, placed in the well plate for the five drugs with HPMCAS, then printed in the first three columns 50% drug.
- 10 μ l were taken from 10 mg/mL drug solution in DMSO plus 70 μ l from 10 mg/mL polymer solution, mixed, placed in the well plate for the five drugs with HPMCAS, then printed in the second 3 columns 12.5% drug.
- The pure API solutions were printed in the following five rows as a reference.

	Each row has triplicates of the same API, polymer or w/w API polymer			Each row has triplicates of the same API, polymer or w/w API polymer			
	A	B	C	D	E	F	
1							50% Estradiol/HPMCAS
	50% Estradiol/HPMCAS			12.5% Estradiol/HPMCAS			
2							50% Nifedipine/HPMCAS
	50% Nifedipine/HPMCAS			12.5% Nifedipine/HPMCAS			
3							50% Celecoxib/HPMCAS
	50% Celecoxib/HPMCAS			12.5% Celecoxib/HPMCAS			
4							50% Orlistat /HPMCAS
	50% Orlistat /HPMCAS			12.5% Orlistat /HPMCAS			
5							50% Felodipine/HPMCAS
	50% Felodipine/HPMCAS			12.5% Felodipine/HPMCAS			
7							100% Nifedipine
8							100% Celecoxib
9							100% Orlistat
10							100% Felodipine

Figure 40. Schematic diagram of the printing plan 4 to print premixed API/polymer solution in two API loadings (50%, 12.5%). Three replicates of 50% API polymer loading were printed in the first three columns of the first five rows, while three replicates of 12.5% API polymer loading were printed in the second three columns of the first five rows. In the second 5 rows, the pure APIs were printed in 6 replicated as a reference.

3.3.4 Piezoelectric inkjet printing

The main aim of this study was to compare the miscibility limit of the different APIs within polymeric matrices and to build a library of various API/polymer loadings. That was employed through: 1) Testing the printability and crystallisation behaviour of a relatively large set of 30 APIs. 2) Testing the printability of the polymers and confirming their amorphicity in the pure form. 3) Choosing the APIs would show crystallisation to be printed with the polymers in different

drug/polymer loadings. A miniaturised, high-throughput technique was used to print arrays of different drug-polymer mixtures using a piezoelectric inkjet printer Sciflexarrayer S5, Scienion using a 70 μm orifice nozzle type 2 coating (Scienion, Germany). The droplet size was controlled and optimised by adjusting the voltage and electrical pulse values, which were tuned to prevent the formation of satellite droplets. Using DMSO solutions of 10 mg/mL of pure drug and pure polymer, spots of 500 droplets with an average droplet volume of 200–220 pL with a final deposited mass of 1000-1100 ng were dispensed by adjusting the voltage between 82 to 90 V and the pulse duration between 48 to 58 μs . DMF was used to wash the nozzle between each printing cycle as a part of an automated printing washing program to avoid cross-contamination of the samples. Printed microarrays were stored in the printer chamber overnight at around 25 °C and 55% RH to allow the DMSO to evaporate. DMSO was the solvent of choice in this study for printed microarrays as it has low volatility, thus reducing the likelihood of nozzle clogging [224], and it is a common solvent for many drugs and polymers [263, 264]. The printed microarrays were left overnight in the printer cage to allow the DMSO evaporation. Then, the dried printed spots containing a total final mass of 1000-1100 ng of printed materials were monitored by polarised light microscopy (PLM) (Advanced Polarizing HS1 microscope, Prior LuxPOL™). This instrument has an integrated 30W halogen lamp with variable brightness control polarised light source to detect the presence of birefringence in the printed spots to interpret crystallinity, a routine use in the pharmaceutical field [265].

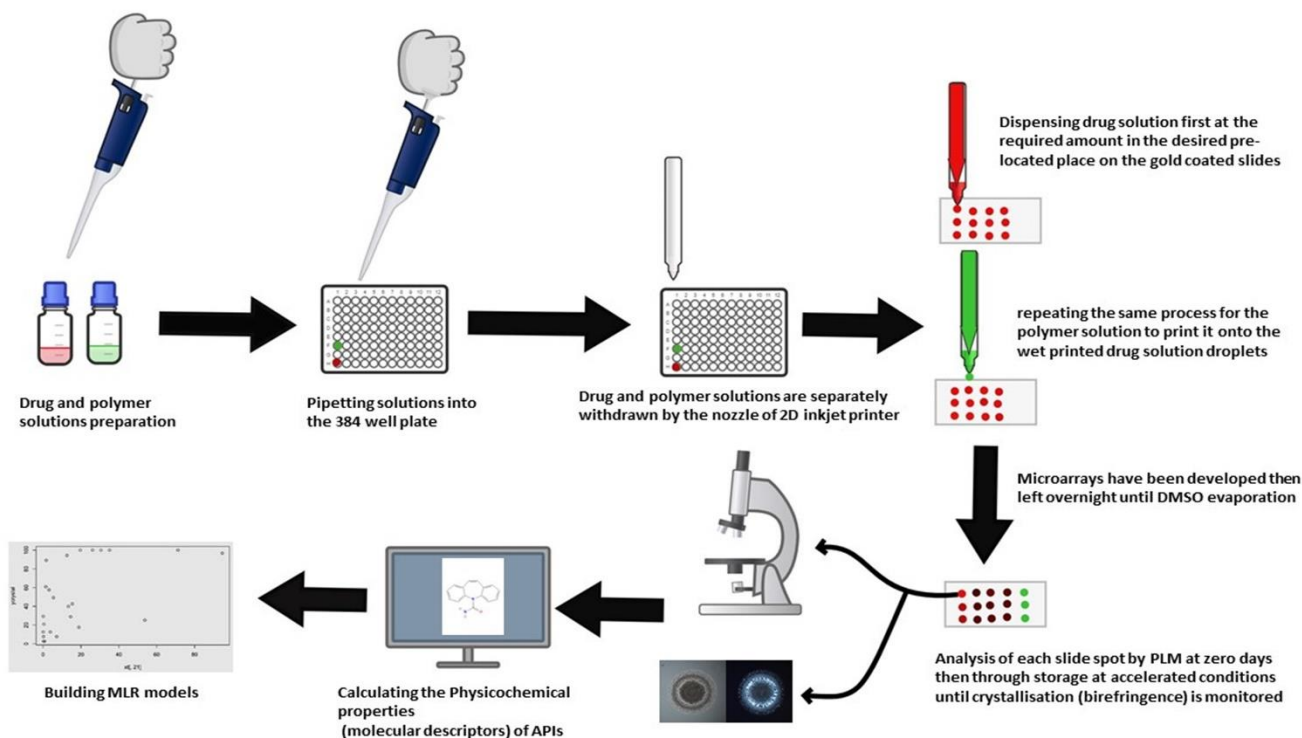


Figure 41. Schematic representation of steps followed in manufacturing and analysing microarrays, including drug and polymer solutions preparation, pipetting into well-plate, withdrawing drug solution through the printer nozzle and then dispensing at the required amount in the desired pre-located place on the substrate, followed by repeating the same process for the polymer solution to print it onto the printed drug solution droplets.

3.3.4.1 Microarray development.

A schematic representation of the sequential steps needed to develop the microarrays is shown in Figure 41. The drug and polymer were dissolved separately in DMSO in scintillation vials to reach a final concentration of 10 mg/mL for each solution. The prepared solutions were sonicated in a water bath at 25°C (room temperature) for 10 minutes to aid the dissolution of both the drug and the polymer. 80 to 100 μL of each stock solution was pipetted into a 384-well plate, which acted as a reservoir for the stock solution. Drug and polymer solutions were printed in a stepwise fashion, firstly dispensing a set volume of drug solution at the desired slide surface location and subsequently dispensing the required amount of polymer solution on the top of a still-wet drug spot. That was achieved using the inkjet printer software Sciflexarrayer (Scienion A, version 2.09.002). Gold-coated slides, supplied by George Albert PVD, were used as substrates due to the

high-water contact angle for the gold surface, which aided the production of well-formed microdots after evaporation of the DMSO. Different masses controlled by different numbers of printed droplets of pure APIs were printed to compare and choose the final number of droplets to be printed for the API/polymer spots. Microarrays were designed using the calculated amounts of each drug solution printed onto the gold-coated slides, subsequently combined with calculated amounts of polymer to give microdots containing different drug/polymer ratios in w/w ranging from 5 to 95% in 5% increments as shown in details in Table 7, Figure 42 and Figure 43. That produced 19 different drug/polymer ratios for each drug/polymer combination in addition to the 0% drug loading (pure polymer) and 100% drug loading (pure drug) printed spots as a reference to investigate how the pure formulation components behaved when printed onto gold-coated slides. Each drug-polymer loading was printed in triplicate. While the droplet is dispensed, the camera connected to the printer can measure the actual volume of the single drop to be printed in picolitres. Depending on the concentration of the printed solution, the actual volume of solution dispensed per droplet is automatically calculated. Consequently, the mass of the drug and polymer in each spot in ng to μg can be readily calculated depending on the number of droplets printed in each spot, as shown in Table 7.

Table 7. Design of printing microarrays by Piezoelectric (Sciencion S5) printer, including the number of droplets of API and polymer printed per spot and the nominal mass of each per spot.

Solution Concentration of API or polymer (mg/mL)	Total Number of Droplets per spot	Final Drug: Polymer Mass				
		Target API concentration wt/wt%	Number of droplets for API per spot	Nominal API mass (ng) Droplet volume 200-220 pl 2.0-2.2 ng in each droplet	Number of droplets for polymer per spot	Nominal Polymer mass (ng) Droplet volume 200-220 pl 2.0-2.2 ng in each droplet
10 mg/ml	500	0	0	0	500	1000
		5	25	50	475	950
		10	50	100	450	900
		15	75	150	425	850
		20	100	200	400	800
		25	125	250	375	750
		30	150	300	350	700
		35	175	350	325	650
		40	200	400	300	600
		45	225	450	275	550
		50	250	500	250	500
		55	275	550	225	450
		60	300	600	200	400
		65	325	650	175	350
		70	350	700	150	300
		75	375	750	125	250
		80	400	800	100	200
		85	425	850	75	150
		90	450	900	50	100
		95	475	950	25	50
100	500	1000	0	0		

	Each row has triplicates of the same w/w drug loading			Each row has triplicates of the same w/w drug loading		
	A	B	C	D	E	F
1	 100%	 100%	 100%	 100%	 100%	 100%
2	 0%	 0%	 0%	 100%	 100%	 100%
3	 5%	 5%	 5%	 10%	 10%	 10%
4	 15%	 15%	 15%	 20%	 20%	 20%
5	 25%	 25%	 25%	 30%	 30%	 30%
6	 35%	 35%	 35%	 40%	 40%	 40%
7	 45%	 45%	 45%	 50%	 50%	 50%
8	 55%	 55%	 55%	 60%	 60%	 60%
9	 65%	 65%	 65%	 70%	 70%	 70%
10	 75%	 75%	 75%	 80%	 80%	 80%
11	 85%	 85%	 85%	 90%	 90%	 90%
12	 95%	 95%	 95%	 0%	 0%	 0%
13	 100%	 100%	 100%	 100%	 100%	 100%

Figure 42. A schematic diagram of the printing plan of APIs, polymers and different API/ polymer loadings by piezoelectric Scienion S5 printer.

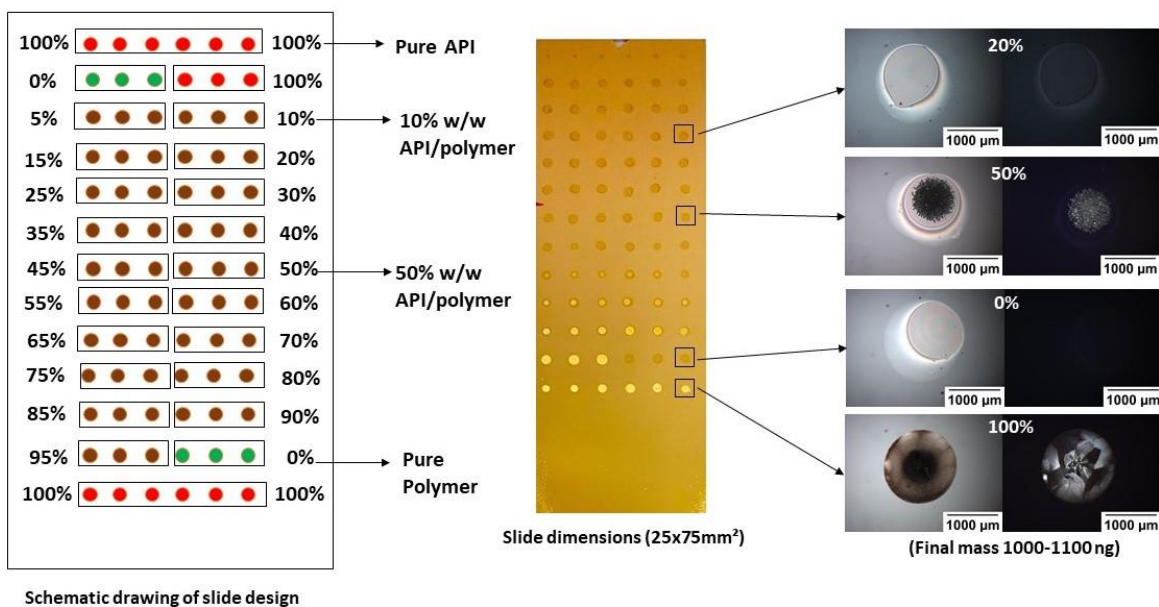


Figure 43. A schematic drawing of the slide design is shown on the left side of the figure, as API and polymer were printed as a reference in the top and bottom two rows. In between, API/polymer mixtures were printed in triplicates starting from 5% with 5% w/w increment till 95%. An image of a printed microarray of Estradiol and PVPVA as a model for the APIs used in the study is shown in the middle. On the right side, microscopic images using bright (left) and cross-polarised field (right) of four printed spots are shown as examples of the crystallisation assessment, as the first and third rows (0%, 20%) show no birefringence (no crystallisation) and second and fourth rows (50%, 100%) show the presence of birefringence (crystallisation). Images shown here were taken after 6 months of storage in accelerated conditions (75% relative humidity and 40°C in a stability oven). The dimensions of gold-coated glass slides are (25x75mm²).

3.3.5 Stability Testing Conditions

Following the International Council for Harmonisation of Technical Requirements for Pharmaceuticals for Human Use (ICH) requirements [266], as shown in Table 8, a six-month stability analysis was carried out on all formulations (printed microarrays) under accelerated conditions (40°C ± 2°C/75% RH ± 5% RH) to monitor the physical stability of different printed microarrays of drug/polymer ratio. The microarray slides were kept in a loosely closed plastic box inside a stability oven, and a data logger, Thermopro TP49, was used to monitor the environment.

Table 8. Equilibrium Relative Humidity of selected saturated salt solution [266].

Temperature (°C)	Lithium Chloride	Potassium Acetate	Magnesium Chloride	Potassium Carbonate	Magnesium Nitrate	Sodium Bromide	Strontium Chloride	Sodium Chloride	Potassium Chloride
10	11.3	23.7	33.5	43.1	57.4	62.2	75.66	75.7	86.8
15	11.3	23.4	33.3	43.2	55.9	60.7	74.13	75.6	85.9
20	11.3	23.1	33.1	43.2	54.4	59.1	72.52	75.5	85.1
25	11.3	22.5	32.8	43.2	52.9	57.6	70.85	75.3	84.3
30	11.3	21.6	32.4	43.2	51.4	56.0	69.12	75.1	83.6
35	11.3	---	32.1	---	49.9	54.6	---	74.9	83.0
40	11.2	---	31.6	---	48.4	53.2	---	74.7	82.3
45	11.2	---	31.1	---	46.9	52.0	---	74.5	81.7
50	11.1	---	30.5	---	45.4	50.9	---	74.4	81.2
55	11.0	---	29.9	---	---	50.2	---	74.4	80.7
60	11.0	---	29.3	---	---	49.7	---	74.5	80.3
65	10.9	---	28.5	---	---	49.5	---	74.7	79.9
70	10.8	---	27.8	---	---	49.7	---	75.1	79.5
75	10.6	---	26.9	---	---	50.3	---	75.6	79.2
80	10.5	---	26.1	---	---	51.4	---	76.3	78.9

3.3.6 Polarised light microscopy (PLM)

The formulation's physical state was investigated before the stability research began using PLM to check the presence or absence of birefringence that would interpret crystallisation or amorphicity, respectively. Within 24 hours of printing at zero time and at various intervals throughout exposure to 40°C/75% RH for six months, the polarised microscopic images of the printed spots of pure drugs and different drug-polymer mixtures were recorded. These were examined every day for the first two weeks and then every week for the following six months. PLM was used to evaluate the stability of the printed samples as samples were regularly checked at the mentioned time intervals for any signs of birefringence and the onset when it started. Printed spots were imaged with and without cross-polarised filters at zero days (after spots were left overnight to allow DMSO evaporation) and then through the prementioned stability points.

3.3.7 Evaluation of Crystallisation Behavior

In this study, the onset of crystallisation of each printed polymer blend was determined from the number of days until the detection of the first obvious birefringence within the PLM spot investigation to be used later in predictive model development. During PLM experiments, birefringence was considered a sign of drug crystallisation from the polymeric matrix. Drug-

polymer miscibility was estimated by determining the ratio of drug to polymer above which birefringence was obviously detected.

The APIs chosen for the current study for drug/polymer dispersions were mainly GFA Class I, which quickly crystallises, providing a meaningful test of the ability of the polymers to stabilise an amorphous form of an API known to have a strong tendency towards crystallisation. Consequently, we may use this estimation of the miscibility limit with confidence when using non glass-forming Class I drugs since it is unlikely that a printed microarray spot that is uniformly amorphous under PLM would contain separate regions of amorphous drug material and polymer if the drug is not able to form a glass in isolation [267]. However, it should be noted that the results represent drug-polymer miscibility at 40°C/75% RH after storage for 6 months, which is a particularly harsh condition given that both the amorphous drug and the polymer would likely absorb significant amounts of moisture at 75% RH, the drug's molecular mobility at 40°C would be higher than at room temperature, and six months of storage is a considerable amount of time for the drug's nucleation. Therefore, various storage settings for microarrays during the drug-polymer miscibility test are possible if required. Storing the microarrays at 40°C/75% RH for six months would give a cautious approximation of the solid dispersion's physical stability. Since solid dispersion dosage forms are often packaged in protective settings and kept at lower temperatures and humidity levels during storage, if no crystallisation of the medication is seen under such a scenario, they are likely to remain physically stable throughout their shelf life.

Van Eerdenburgh and Taylor developed a classification approach to classify the crystallisation behaviour of spots of a variety of compounds semi-quantitatively by PLM [144]. Due to the deposited spot's small size, the entire spot may be seen and evaluated in one snapshot. The ratio of the drug to the polymer corresponds to the first birefringence observed is considered to be the

miscibility limit, i.e. the combination with the lowest drug concentration at which birefringence is first noticed. The miscibility limit is assumed to be the ratio midway between the spots if the classification is not continuous and the designation between adjacent spots changes, for example, from fully amorphous to AACC [267]. Using a film casting method, Parekh et al. previously utilised a similar definition for the miscibility limit [262].

3.3.8 Drop-Cast preparation of drug/PVPVA dispersion and bulk validation according to the literature

To explore the agreement of the behaviour of the printed microarrays with the bulk behaviour, pure drugs, as well as three drug/PVPVA ratios for each drug, were chosen for a scaled-up formulation. Those were selected depending on data collected from the stability data of printed microarrays. An individual solution of 10 mg/ml of Orlistat, Fenofibrate, Itraconazole, and Celecoxib was prepared and pipetted on gold-coated slides as a substrate to investigate the bulk behaviour of pure APIs.

The scaled-up formulations' PVPVA ratios were chosen for each drug depending on the miscibility limit determined through the 2D inkjet printing, below and above the miscibility limit. For example, drop-cast samples were developed for Flurbiprofen by dissolving a final amount of 30 mg of materials in 3 mL of DMSO. Hence, solutions of pure drug, pure PVPVA, and combinations at three drug loading ratios (40%, 45% and 50%) were prepared. For Flufenamic acid, 30 mg was dissolved in 3 mL of DMSO and three drug/polymer combinations were prepared at drug loading ratios (40%, 45% and 55%). For Nitrofurantoin, 100 mg was dissolved in 10 mL DMSO and three drug/polymer combinations were prepared at drug loading ratios (10%, 15% and 25%). For Estradiol, 100 mg was dissolved in 10 mL DMSO and three drug/polymer combinations were prepared at drug loading ratios (25%, 30% and 40%). Since DMSO was the preferred solvent

during the printing process, it was chosen to mimic the printing circumstances. As a result, the DMSO evaporation conditions in bulk studies were comparable to those of printed spot DMSO evaporation. Using a micropipette, 200-250 μL were dropped onto gold-coated glass slides to form large spots of final mass around 2 mg for each solution (drug-polymer mixture), which was done in triplicates. The gold-coated slides were left in the printer cage for 3-4 days to allow complete DMSO evaporation, which took longer than the printed microarray spots due to the scaled-up size of the experiment. Then, the dried drops were analysed by PLM while stored in the same accelerated conditions as the printed microarrays.

3.4 Results and Discussion

Preliminary tests using AFM and WCA were carried out to choose the best substrate for the printing process.

3.4.1 Water contact angle measurement (WCA)

Poor wettability of the substrate would prevent the spreading of micro-spots during the printing process. Due to the available equipment (water syringe), it was not possible to determine the contact angle measurements for dimethyl sulfoxide on different substrates. Therefore, the contact angles of those substrates were measured using water. Figure 44 shows that the wettability of glass microscopic slides with average contact angle measurements (for five replicates) of $26.2^\circ \pm 1.12$ was higher than that of gold-coated slides with average contact angle measurements (for five replicates) of $79.5^\circ \pm 0.41$. According to an explanation in the literature on how reduced surface tension can enhance wettability (the surface tension of DMSO is 42.68 mJ/m^2 compared to the surface tension of water which is 72.70 mJ/m^2 at room temperature) [257, 268], the decision was made to use the gold coated slides which would have poorer wettability, hence, less droplets spreading over the surface than the glass microscopic slides as a substrate.

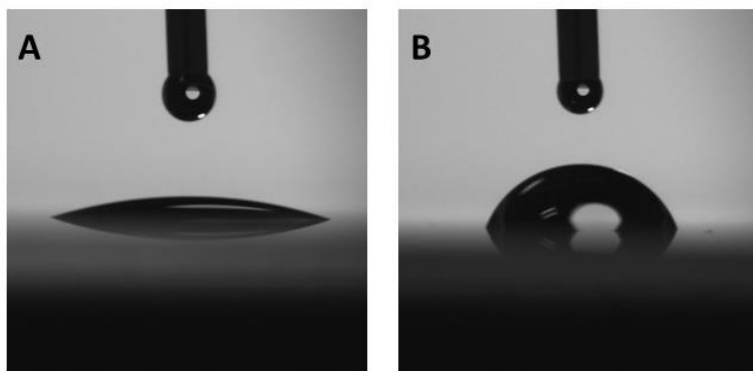


Figure 44. WCA angle measurement of the microscopic glass slide is shown in image (A) around 26.2° , and the WCA of the gold-coated glass slide is shown in image (B) around 79.5° using water as testing liquid. The water needle is shown on the top, and the formed water droplet is on the bottom.

3.4.2 The roughness of the gold-coated slides (Atomic Force Microscopy)

Surface roughness is a known factor that influences contact angle and wetting. Figure 45 shows AFM topographic images of $1\mu\text{m} \times 1\mu\text{m}$ and $5\mu\text{m} \times 5\mu\text{m}$ areas for the chosen substrate, gold-coated slides, as roughness measurements change with image size comparisons were only made between images of similar sizes. The root mean square (RMS) was used here to express the roughness of the surface. As shown in Figure 45 and Table 9 the plain gold surface appears to be smooth, with an RMS value of around $0.4\text{ nm} \pm 0.002$ at both $1\mu\text{m} \times 1\mu\text{m}$ and $5\mu\text{m} \times 5\mu\text{m}$ areas. It can be observed that AFM images of plain gold exhibit quite a homogenous nanoscale granular topography. It was essential to know the degree of roughness of the used substrates before using them as printing substrates. To conclude, the AFM study suggests that the gold-coated slides offer a consistently smooth and homogenous surface at the nanoscale level, validating their selection as a substrate for APIs-polymer interaction studies. The consistency in topography across various sample areas bodes well for their application, ensuring that experimental variables of substrate-induced anomalies are minimized. Hence, these substrates are endorsed for their intended use, with

the expectation that they will contribute to the precision and reliability of the ensuing experimental outcomes.

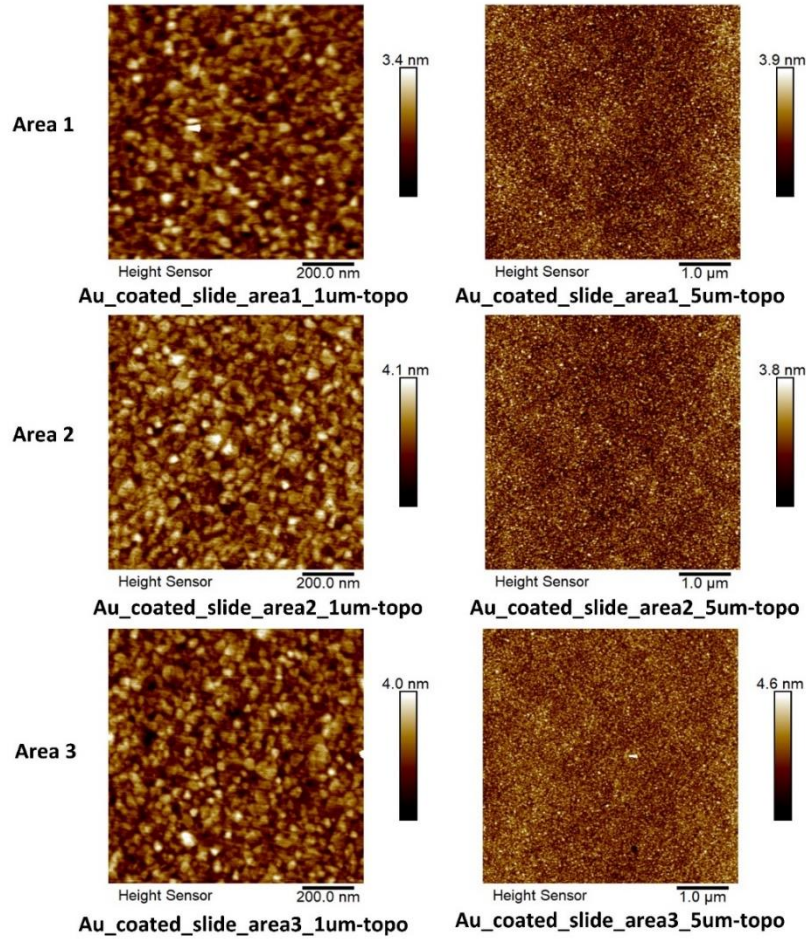


Figure 45. AFM topographic images of gold-coated slides ($1\mu\text{m} \times 1\mu\text{m}$ area on the left side and $5\mu\text{m} \times 5\mu\text{m}$ area on the right side).

Table 9. The table shows the measured roughness of the gold-coated slides by AFM and the calculated average roughness.

	RMS roughness (nm)	Average roughness (nm)
area 1_1µm	0.5	0.4
area 2_1µm	0.6	0.5
area 3_1µm	0.6	0.5
area 1_5µm	0.5	0.4
area 2_5µm	0.5	0.4
area 3_5µm	0.6	0.4

3.4.3 Manual deposition technique by Hamilton Syringe

A 10 μl Hamilton syringe was used as a preliminary step to deposit different amounts of pure APIs, pure polymers and API/polymer blends by dropping the polymer solution on the pre-deposited API solution using the gold-coated slides. Figure 46 presents the crystallisation profiles of pure APIs and pure polymers deposited by this method in different volumes starting from 0.1 μl (depositing amount of around to around 1000 ng) with 0.1 μl increment reaching 0.5 μl (depositing amount of around 5000 ng of printed material). Figure 46 shows the images of the pure APIs and pure polymers depicted six months from solvent evaporation while storage in accelerated conditions. The presence of opaque material and apparent structure in bright-field and birefringence under cross-polars is taken to indicate crystallisation. Spot transparency, lack of prominent structure, and no birefringence are taken to indicate a lack of crystallization and the presence of mainly amorphous material.

Estradiol, Nifedipine and Celecoxib spots of all pipetted volumes from 0.1 μl to 0.5 μl with a calculated deposited mass of approximately 1 to 5 micrograms exhibit obvious birefringence indicating crystallisation. In contrast, the spots of Soluplus, PVPVA and HPMCAS polymers show no birefringence which are taken to indicate a lack of crystallization and the presence of mainly amorphous material [269]. The existence of polymers in the amorphous state is widely reported in the literature [117, 262, 270]. The deposition of different masses confirmed the same results regarding amorphicity/crystallisation in both pure drugs and polymers.

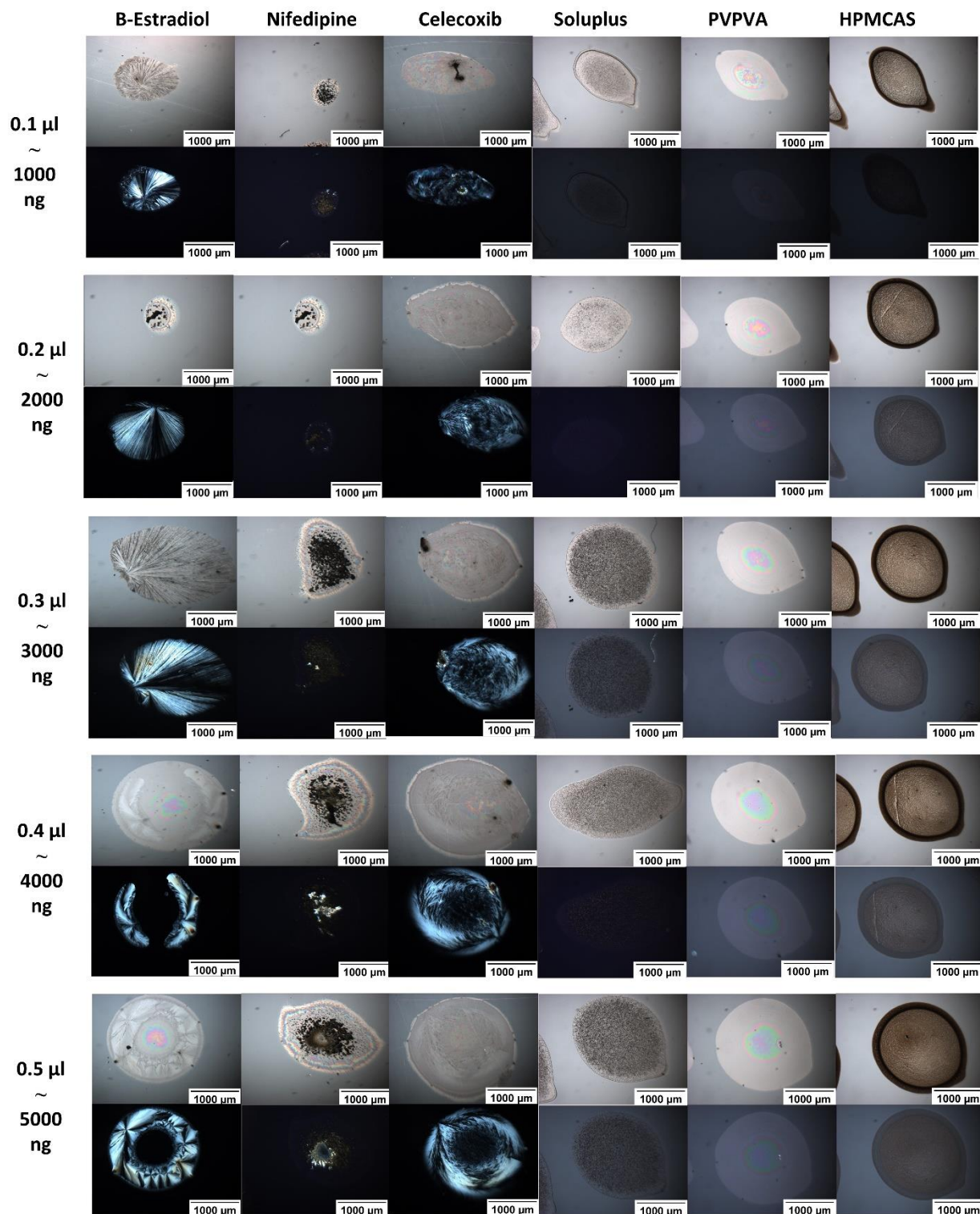


Figure 46. The figure shows crystallisation profiles of pure APIs and pure polymers performed by Hamilton syringe with different final deposited masses between 1000 to 5000 ng. All images are reported without (top row) and with (bottom row of each set) cross-polarised filters. Images of all APIs are depicted six months from solvent evaporation while storage in accelerated conditions (75% relative humidity and 40°C in a stability oven).

Figure 47 shows examples of dried spots of 50% API/polymer loading employed by a Hamilton syringe using the three different polymers. The top section shows 50% APIs/ Soluplus, the middle section shows 50% APIs/ PVPVA, and the bottom section shows 50% APIs/ HPMCAS. All images are reported without and with the cross-polarised filter with a final mass of around 6000 ng (6 μ g) in each spot. In Figure 47, 50% Estradiol/ polymer and Nifedipine/polymer loadings spots showed birefringence in cross-polars, confirming crystallisation in the 50% API/ polymer loading with the three employed polymers (Soluplus, PVPVA and HPMCAS). None of the three polymers was able to inhibit the crystallisation of Estradiol and Nifedipine at 50% loadings, while there was limited crystallisation in the case of 50% Nifedipine/HPMCAS. No birefringence was monitored in the case of 50% Celecoxib with the three polymers. That would confirm the polymer's role in inhibiting the crystallisation in the case of Celecoxib at this ratio.

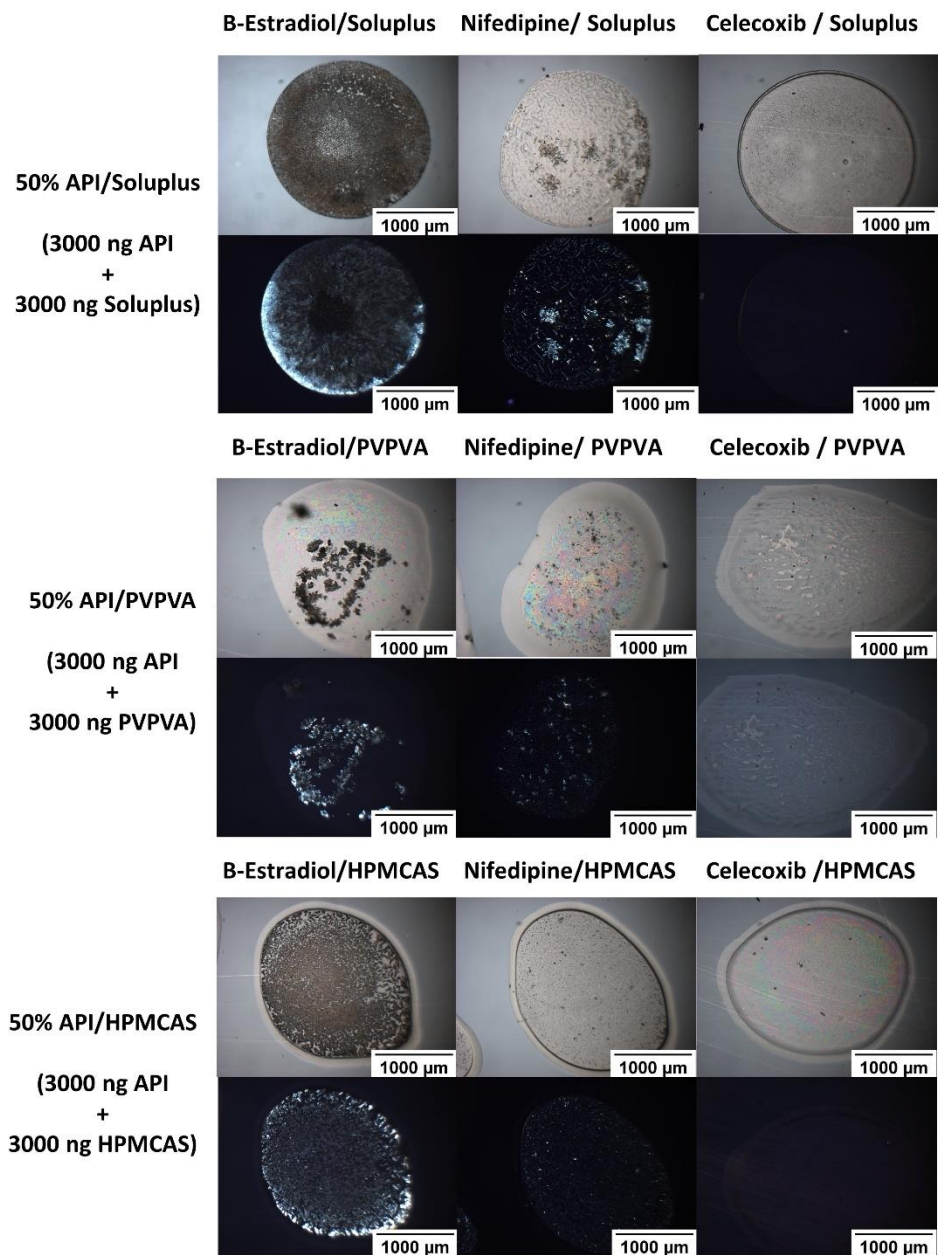


Figure 47. Examples of dried spots of 50% API/polymer loading of different APIs produced by a Hamilton syringe with three polymers. The top section shows 50% APIs/ Soluplus, the middle section shows 50% APIs/ PVPVA, and the bottom section shows 50% APIs/ HPMCAS. All images are reported without (top part of each section) and with (bottom part) cross-polarised filter after storage of the spots in accelerated conditions for 6 months (75% relative humidity and 40°C in stability oven). Final mass around 6000 ng (6 µg).

The manual method performed by the Hamilton syringe was efficient in following up the crystallisation behaviour of the pure APIs (Estradiol, Nifedipine and Celecoxib) and the 50% API/polymer blends of three APIs with three polymers. However, this simple ‘bulk’ technique has some disadvantages, including spreading the pipetted droplets and interference of some droplets with

each other. Additionally, the reproducibility was challenging as the formed spots had different shapes that would create a nonuniform distribution of the API and the polymer in the spot, leading to some variability in the results. The accuracy of the deposited mass of API or polymer in each spot could not be guaranteed as it is susceptible to human error as not always the same droplet volume comes from this pipette when it comes in contact with the slide due to the minimal volume used. Consequently, using this manual technique to build a trustable library of different loadings of different APIs and polymers would be very challenging. Still, it was helpful to show the approach's ability to differentiate the crystallisation/amorphylicity pattern of pure APIs and polymers as well as the 50% drug/polymer loadings using different polymers.

3.4.4 Contact printer (Pin Printer)

3.4.4.1 Printing some pure APIs as one contact droplet per spot as the smallest amount.

Figure 48 shows the dried spots of five pure APIs printed by the contact printer with one contact per spot (one droplet). All images are depicted without and with a cross-polarised filter after storage in accelerated conditions for six months. The final deposited mass of each API in the printed spot was around 50 ng as 10 mg/ml API solution was printed through a pin with a tip diameter of 0.5 mm and a deposition volume of 5 to 20 nL. Estradiol, Nifedipine and Celecoxib showed crystallisation, while Orlistat and Felodipine remained amorphous over six months of storage in accelerated conditions.

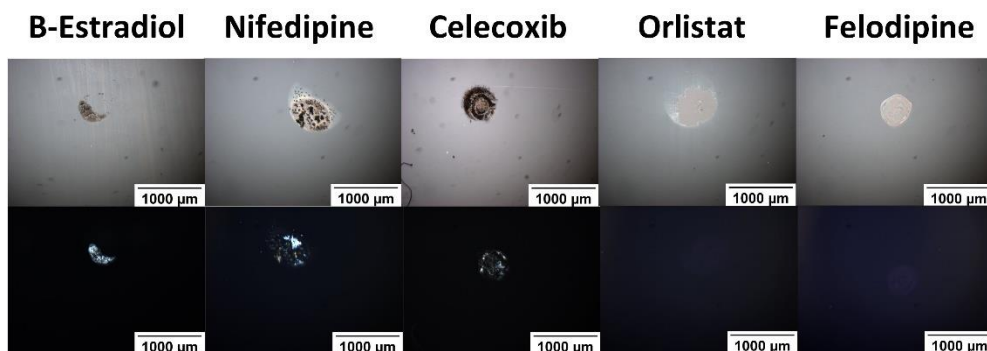


Figure 48. Examples of dried spots of pure five APIs printed by contact printer as one contact per spot depositing a final total mass of around 50 ng. All images are depicted without (top part of each section) and with (bottom part) cross-polarised filter after storage of the spots in accelerated conditions for 6 months (75% relative humidity and 40°C in stability oven).

3.4.4.2 Printing some pure APIs and polymers at 12 contact droplets per spot

Figure 49 shows examples of dried spots of five pure APIs and three pure polymers printed by a contact printer at 12 contacts per spot. All images are reported without and with a cross-polarised filter after storage in accelerated conditions for six months. The final deposited mass of each API or polymer in the printed spot was calculated to be around 600 ng. The presence of birefringence under cross-polars indicates crystallisation for the following APIs: Estradiol, Nifedipine, Celecoxib and Felodipine. In contrast, no birefringence that confirms the amorphicity of the spot was seen in Orlistat and the three polymers: PVPVA, Soluplus and HPMCAS. In this case, Felodipine showed a different crystallisation behaviour than in the pattern of 1 contact droplet per spot (50 ng), indicating the need to consider the number of droplets to be printed as a factor.

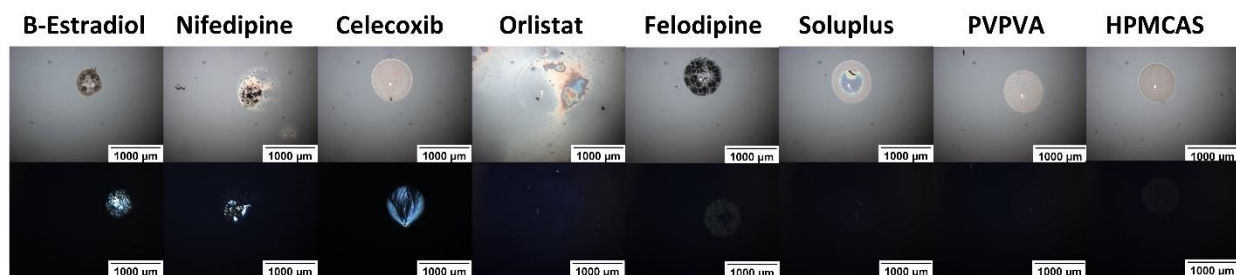


Figure 49. Examples of dried spots of pure five APIs and three pure polymers printed by contact printer as 12 contacts per spot depositing a final total mass of around 600 ng. All images are reported without (top part of each section) and with (bottom part) cross-polarised filter after storage of the spots in accelerated conditions for 6 months (75% relative humidity and 40°C in stability oven).

3.4.4.3 API/ polymer blend printing and order of printing API and polymer solutions

Figure 50 shows the dried spots of 50% API/HPMCAS loading using a different order of API and polymer printing by printing 6 contact droplets of the API solution first and then 6 contact droplets of the polymer solution while the other was printing 6 droplets of the polymer first and then 6 droplets of the API solution. The final calculated total mass per spot is around 600 ng (around 50 ng per contact). All images are reported without (top part of each section) and with (bottom part) cross-polarised filter after six months of storage in accelerated conditions. Birefringences as an indication for crystallisation were detected for 50% Estradiol and Nifedipine with HPMCAS for both printing the API first or the polymer first. No birefringences were observed for the 50% Celecoxib, Orlistat, and Felodipine with HPMCAS in printing either the API or the polymer first. HPMCAS polymer was printed as a reference and showed amorphicity over the six months. Hence, no significant variation was observed when altering the sequence of printing the drug and polymer. This suggests that the order of printing is not a critical factor to consider during the printing process. To ensure consistency in our results, we aimed to confirm whether this sequence could impact outcomes. Given the lack of observed impact, we plan to proceed with the approach of printing the drug followed by the polymer on all slides, thereby minimizing any potential variability in our experimental results.

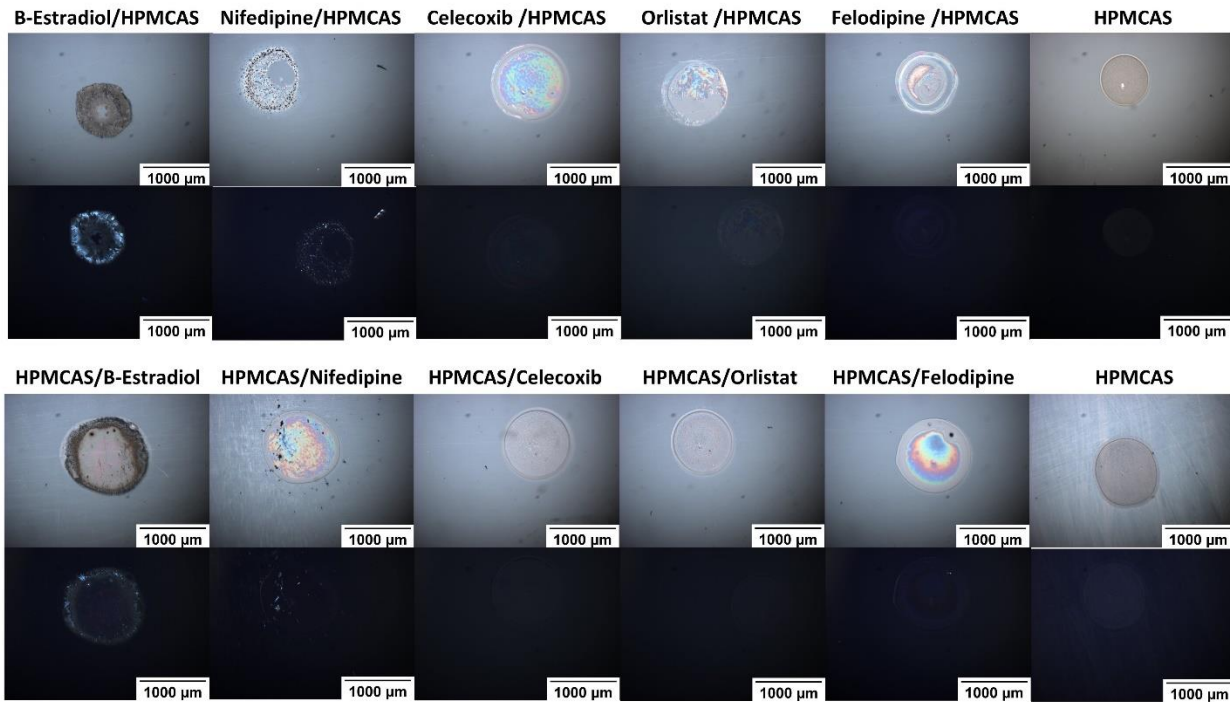


Figure 50. Examples of dried spots of 50% API/HPMCAS loading in different order of API and polymer by a) printing 6 droplets of the API solution first and then 6 droplets of the polymer solution that are shown in the upper part of the figure, while b) printing 6 droplets of the polymer first and then 6 droplets of the API solution is shown on the bottom part of the figure. The final total mass in both cases is around 600 ng. All images are reported without (top part of each section) and with (bottom part) cross-polarised filter after storage of the spots in accelerated conditions for 6 months (75% relative humidity and 40°C in stability oven).

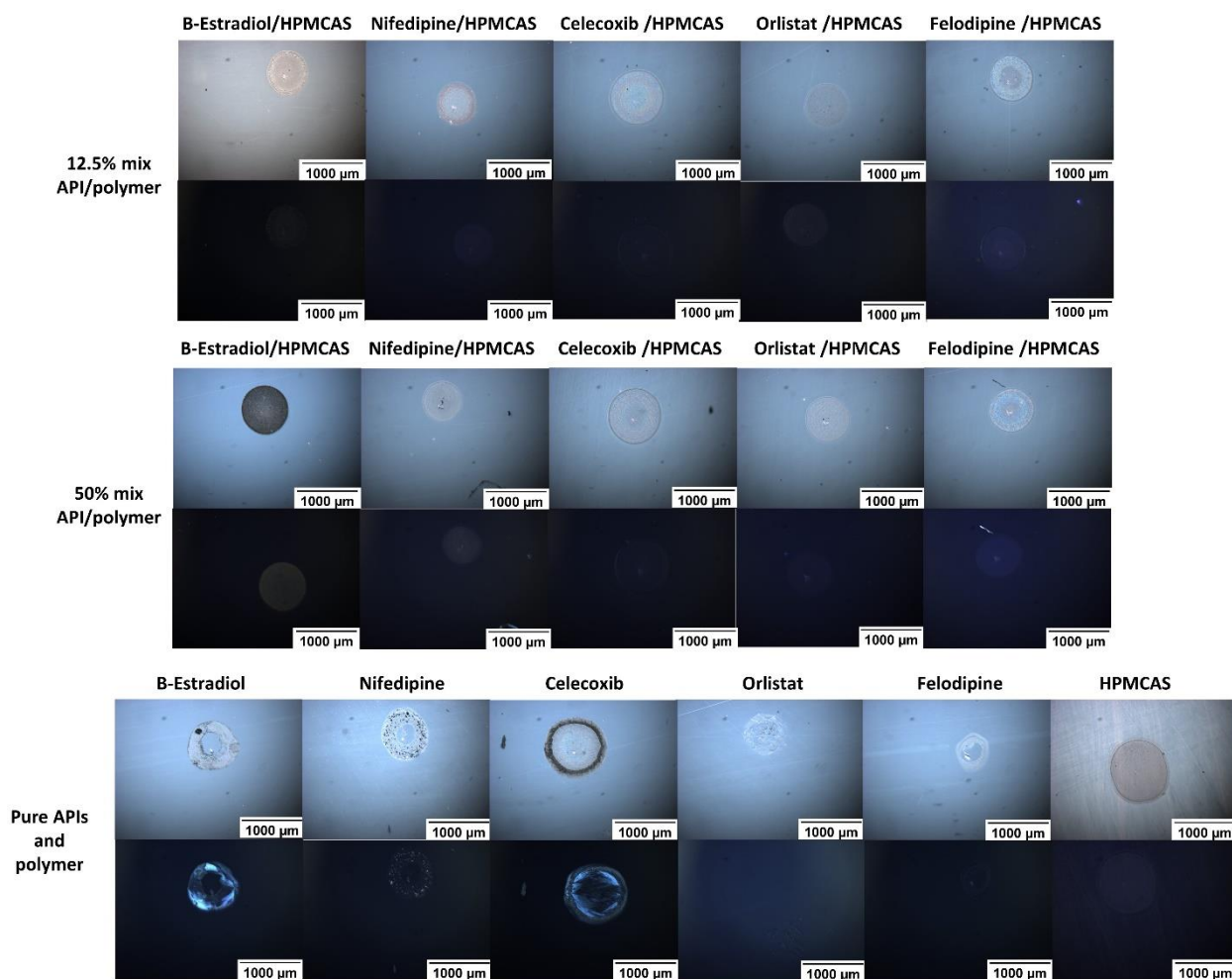


Figure 51. Examples of dried spots printed by contact printer as 12 contacts per spot depositing a final total mass of around 600 ng. The first set shows the printing of a premixed 50% API/HPMCAS solution. The middle set shows the printing of a premixed 12.5% API/ HPMCAS solution. The bottom set shows the printing of pure APIs and pure polymer (HPMCAS). All images are reported without (top part of each section) and with (bottom part) cross-polarised filter after storage of the spots in accelerated conditions for 6 months.

3.4.5 Crystallisation behaviour following 2D inkjet printing of pure APIs and upon storage

Figure 52 presents bright-field and cross-polarised images of all 30 pure drug spots six months after printing, having been stored at 40°C/75 % RH for that time. The images have been arranged with the samples showing opaque spots with obvious structure (bright field) and birefringence (cross-polarised) towards the top of the figure. The spots that are presented as mainly transparent, with little to no structure and no birefringence, are shown towards the bottom of the figure. All twenty (of thirty total) spots which were opaque from visual inspection exhibited clear and obvious birefringence; the ten (of thirty total), which appeared mainly transparent, also showed no birefringence. The presence of birefringence under cross-polars is taken to indicate crystallisation. Likewise, transparency, lack of obvious structure, and no birefringence are taken to indicate a lack of crystallisation and the presence of mainly amorphous material.



Figure 52. The figure shows different APIs recrystallisation profiles used in this study (final mass 1000-1100 ng) printed using 2D piezoelectric inkjet printer. All images are reported without (top row) and with (bottom row of each set) cross-polarised filters. Images of all APIs are depicted six months from solvent evaporation while storage in accelerated conditions (75% relative humidity and 40°C in stability oven).

Images were also collected in the time period between printing and the final examination after six months of storage in accelerated conditions. The first point at which crystallisation was detected is shown in Table 10. Itraconazole, Estradiol, Flurbiprofen, Corticosterone, Carbamazepine, Caffeine, Theophylline, Aspirin, Nitrofurantoin, Piroxicam, Nicotinamide, Flufenamic acid, Atenolol, Diclofenac sodium, Tolbutamide, Benzocaine showed obvious structure, opaqueness and birefringence (signs of crystallisation) in the optical and cross-polarised images through the first day after solvent evaporation. At the same time, Nifedipine showed birefringence through the fifth day after solvent evaporation upon storage in accelerated conditions. Interestingly, Felodipine, Celecoxib, and ProbucoI took extended time in the amorphous state until they showed signs of birefringence, which were detected within 56 days after solvent evaporation while stored in accelerated conditions. In contrast, the following APIs, Orlistat, Ritonavir, Aprepitant, Fenofibrate, Dexamethasone, Ketoprofen, Chlorpromazine, Paracetamol, Ampicillin and Coumarin did not show any signs of crystallisation as they remained transparent during 6 months storage in accelerated conditions. These results agreed with the results obtained from the other classification techniques in the literature [144, 146, 229].

Table 10. Stability of the printed pure APIs (birefringence detection point) in days during storage for six months in accelerated conditions ($40^{\circ}\text{C} \pm 2^{\circ}\text{C}/75\% \text{RH} \pm 5\% \text{RH}$).

Printed pure APIs	Birefringence detection point in days (the exact day when birefringence was detected) within six months
Caffeine	1
Flufenamic acid	1
Tolbutamide	1
Benzocaine	1
Flurbiprofen	1
Carbamazepine	1
Itraconazole	1
Atenolol	1
Probucol	56
Celecoxib	56
Felodipine	56
Fenofibrate	No birefringence detected
Ritonavir	No birefringence detected
Ketoprofen	No birefringence detected
Paracetamol	No birefringence detected
Theophylline	1
Piroxicam	1
Corticosterone	1
Nitrofurantoin	1
Diclofenac sodium	1
Nicotinamide	1
Estradiol	1
Aspirin	1
Nifedipine	5
Chlorpromazine HCl	No birefringence detected
Dexamethasone phosphate	No birefringence detected
Aprepitant	No birefringence detected
Orlistat	No birefringence detected
Ampicillin	No birefringence detected
Coumarin	No birefringence detected

The results presented above can be compared in a limited manner with the work of van Eerdenbrugh et al [144]. We note that the storage conditions employed differed significantly from the utilised storage at $40^{\circ}\text{C}/75\% \text{RH}$ for six months here. In contrast, van Eerdenbrugh reported

results after seven days of storage at room temperature in very dry conditions. We would, therefore, expect that our storage conditions would provide far more opportunity for samples to crystallise compared to van Eerdenburgh's. According to Table 11, the two compound libraries only overlap for 15 compounds of the samples. For samples where crystallisation was not observed after six months, we have complete agreement with van Eerdenburgh, who classified paracetamol, ketoprofen, fenofibrate, and ritonavir as class II or III, i.e. limited or no crystallisation observed after seven days.

For the samples which were observed to crystallise in the present study, the results are more mixed, but this is to be expected given the differences in storage conditions between the two studies. If van Eerdenburgh did not observe crystallisation within seven days for a given sample, it might be that crystallisation did happen at a later point outside this time window, and hence, the present study would potentially differ.

We, therefore, conclude from the data and analyses presented above that the results from miniaturised inkjet printing at ca. 1000 ng are reasonable and representative of results from a related set of samples prepared by spin coating and that there are no apparent discrepancies or areas of concern. We, therefore, undertook the printing of mixed drug-polymer samples, and these results are reported below.

From our printed set of 30 APIs, 16 could be classified as Class I (rapid crystallisation), 4 APIs as Class II (intermediate crystallisation), and 10 as Class III (slow crystallisation) using the classification scheme of van Eerdenburgh. The classification comparison is shown in Table 11. Throughout the investigation, the 10 Class III compounds exhibited no signs of crystallinity. They, therefore, were left out of the subsequent experimental work because, even without the addition of polymers, significant physical stability was predicted during the time frame of the experiment, and

it was not felt that these non-crystallising APIs would provide valuable data for the subsequent model-building.

Table 11. Comparing crystallisation Behavior Following 2D inkjet printing stored in accelerated conditions for 6 months versus following Spin Coating stored in dry conditions for 7 days.

Class I (rapid crystallisation), APIs as Class II (intermediate crystallisation), and Class III (slow crystallisation).

API	GFA classification according to 2D inkjet printing in our study (6 months accelerated conditions)	GFA classification according to Van Edinburgh Spin Coating (7 days dry conditions)
Caffeine	I	I
Flufenamic acid	I	I
Tolbutamide	I	I
Benzocaine	I	I
Flurbiprofen	I	I
Carbamazepine	I	II
Itraconazole	I	III
Atenolol	I	III
Probucof	II	II
Celecoxib	II	III
Felodipine	II	III
Fenofibrate	III	II
Ritonavir	III	III
Ketoprofen	III	III
Paracetamol	III	III
Theophylline	I	
Piroxicam	I	
Corticosterone	I	
Nitrofurantoin	I	
Diclofenac sodium	I	
Nicotinamide	I	
Estradiol	I	
Aspirin	I	
Nifedipine	II	
Chlorpromazine HCl	III	
Dexamethasone phosphate	III	
Aprepitant	III	
Orlistat	III	
Ampicillin	III	

Coumarin	III	
----------	-----	--

3.4.6 Choosing the optimised number of droplets (printed mass) using a 2-D Sciflexarrayer S5 inkjet printer

Figure 53 shows different 20 APIs recrystallisation profiles at various numbers of printed droplets with different final masses of printed spots starting from solutions at 10 mg/mL spots with an average of 100-110 ng for 50 droplets, 200-220 ng for 100 droplets, 400-440 ng for 200 droplets, 600-660 ng for 300 droplets, 800-880 ng for 400 droplets up to 1000-110 ng for 500 droplets. This was done to choose the number of droplets to be used in the following printing plans. All images are reported without and with cross-polarised filters. Images of all APIs are depicted three months from solvent evaporation with storage in accelerated conditions as a preliminary study to choose the number of droplets for the subsequent experimental work. As illustrated in Figure 53, most of the printed APIs at different numbers of droplets showed signs of birefringence which is an indication of crystallization. Despite using a similar final amount of APIs, there was a variation in the final spot sizes between the different printed APIs as they showed recrystallization with a diverse and unique pattern. This may be due to a variation in properties such as the nature of different crystals of the different used APIs. Celecoxib, ProbucoI, and Felodipine spots showed birefringences only at the higher number of printed droplets per spot, possibly due to the preliminary study's short period, which was three months. The spot size at 500 droplets, even after shrinkage of the spots during solvent evaporation, was suitable to be detected at the same magnification for all the used APIs as well as crystallisation was seen at this number of droplets for all pure APIs used in this study. Consequently, the final number of droplets to be used in the API/polymer mixtures would be 500 droplets depositing a final mass of printed spots of around 1000 to 1100 ng.



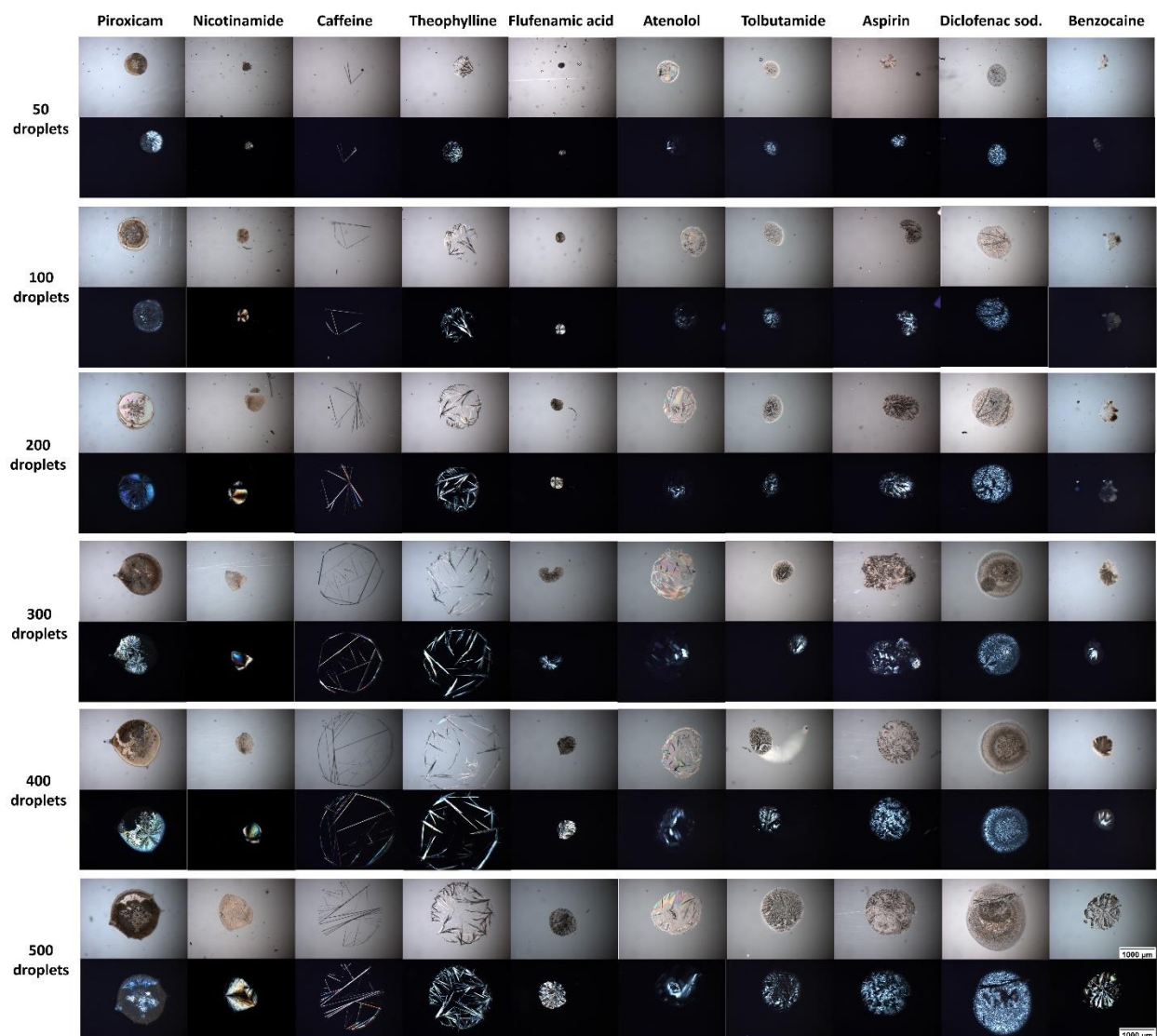


Figure 53. The figure shows different APIs recrystallisation profiles at different numbers of printed droplets with different final masses of printed spots starting at 50 droplets (final mass 100-110 ng), 100 droplets (mass 200-220 ng), 200 droplets (mass 400-440 ng), 300 droplets (mass 600-660 ng), 400 droplets (mass 800-880 ng) and 500 droplets (mass 1000-110 ng). All images are reported without (top row) and with (bottom row of each set) cross-polarised filters. Images of all APIs are depicted six months from solvent evaporation while storage in accelerated conditions (75% relative humidity and 40°C in stability oven)

3.4.7 Effect of Drug/PVPVA ratio and time on drug crystallisation within the PVPVA matrix

All the 19 APIs that showed crystallisation through inkjet printing after six months of storage under challenge conditions were printed in the same scheme, as previously in Figure 43. Flurbiprofen is reported here as a model drug for the drug-polymer printing pattern, as shown in

Figure 54. At the same time, detailed data on crystallisation behaviour and the onset of crystallisation of the remaining 18 APIs can be found in Figures (S1-S18) in the appendix.

Figure 54 presents bright-field and cross-polarised images of spots of 21 Flurbiprofen-PVPVA formulations for compositions 0, 5, 10, ...95, 100 % drug loading six months after printing, having been stored at 40°C/75 % RH within this period. The images have been arranged with the bright field images on the top of each section and the cross-polarised images on the bottom of each section showing opaque/transparent structure (bright field) and presence/absence of birefringence (cross-polarised).

As the w/w loading of Flurbiprofen increases from 0 to 100 %, there is a clear trend for the printed spots to change from visually transparent and unstructured to visually opaque with the appearance of structure. These changes are accompanied by the emergence of birefringence. The spots up to 20 % API loading appear entirely transparent, above this part of the spot appears opaque, and for 95 and 100 % API loading the spots appear wholly opaque. Interestingly, birefringence only emerges for 45 % loading and above despite the appearance of some small opaque areas in the spots for 20 % API loading and above.

The appearance of birefringence is unambiguous evidence of crystallisation in the sample and of API-polymer phase segregation [269]. This is therefore interpreted as an upper estimate of the limit of drug miscibility in the polymer. The small opaque areas for 20-40 % API loadings may indicate phase segregation, but may also just be due to the shape/structure of the spots, drying effects etc. No crystallisation was detected at this range while it was detected above this limit. The PLM used in this study is transmissive microscopy as light travels through the sample, and the transmitted light is collected by the objective lens to form an image. As such, we use the

appearance of birefringence as an unambiguous indication of drug-polymer phase separation and therefore a reliable upper estimate of maximum miscibility of Flurbiprofen in PVPVA.

The same approach was adopted for all 19 formulations with PVPVA; namely, the appearance of birefringence in cross-polarised microscopy images was taken to be an unambiguous indication of drug-polymer phase separation in the ASD formulations. The printed spots were examined daily for the first four weeks and every week for the following six months. The time of appearance of birefringence was recorded for all samples and was used as input for developing a model linking stability (time to crystallisation) with molecular and material properties. These model input data are presented in Table 12, ranked by the number of days and the raw data used to determine the appearance of birefringence are shown in Figures (1S-18S) in the appendix.

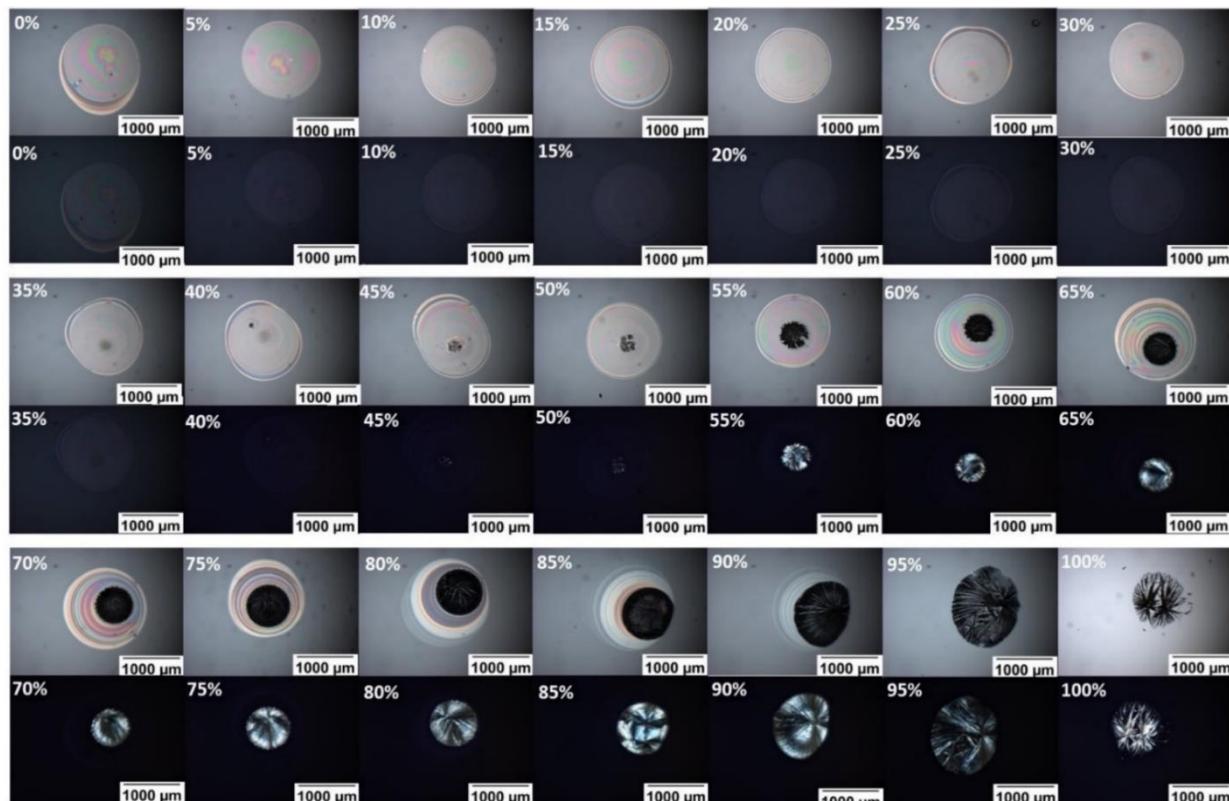


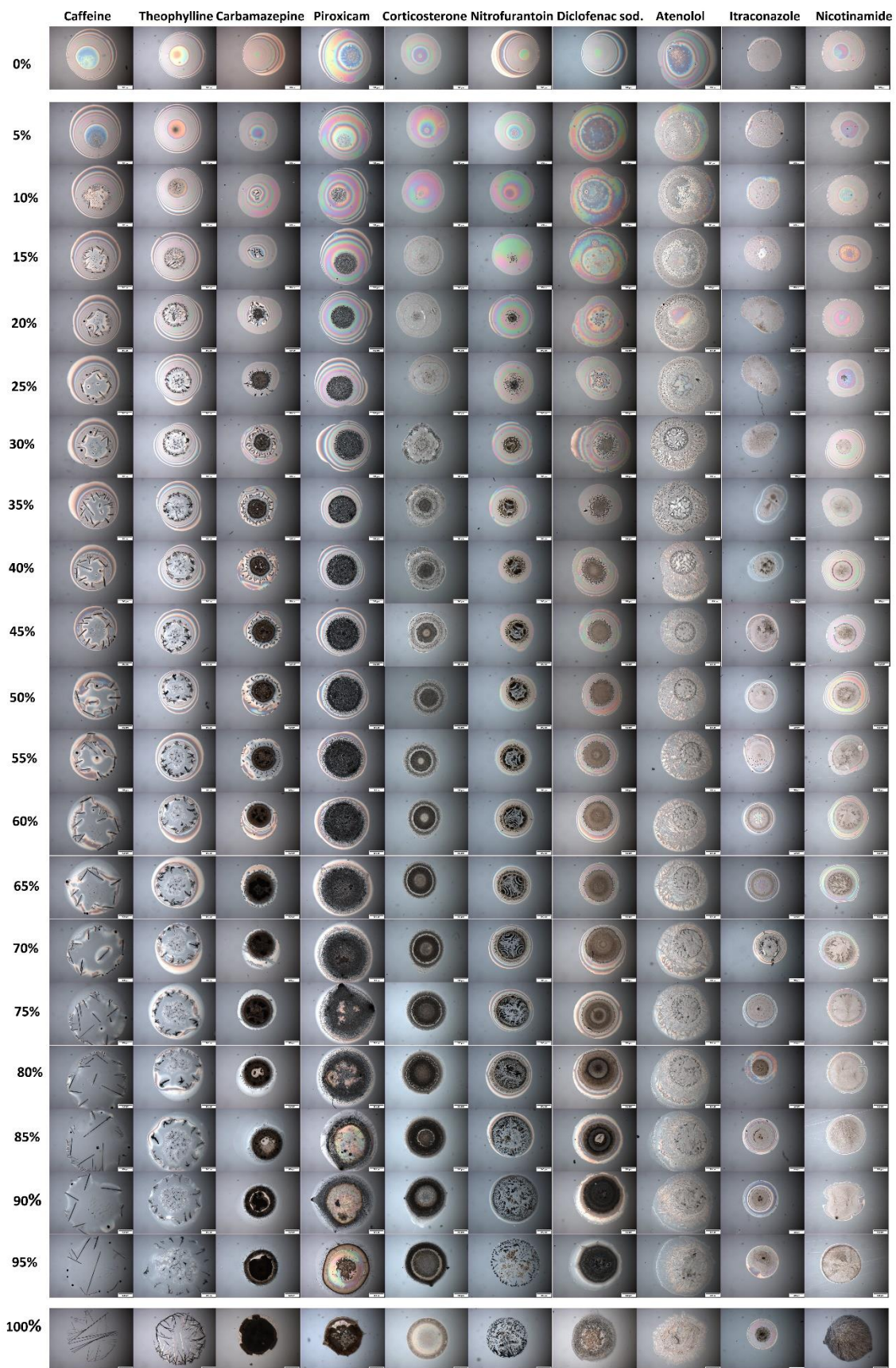
Figure 54. An example of an array section depicted by PLM. All the spots are reported with bright field and cross-polarised filters (top and bottom of each section, respectively). Images of all Flurbiprofen/PVPVA (for example, as one of the drugs used in this study) at all of the different ratios (starting from 0% to 100% with a 5% increment) are depicted after 6 months of storage in accelerated conditions (75% relative humidity and 40°C in stability oven). The final mass of individual spots is 1000-1100 ng.

The trend toward early crystallisation of higher drug loading spots over lower drug loading spots most likely results from the fact that the likelihood of nucleation is a function of the total amount of drug molecules present. In samples with lower drug loading, the physical separation of the drug molecules by polymer will also minimise the likelihood of nucleation. The polymer (PVPVA) did not exhibit any birefringence, indicating its amorphicity, as widely described in the literature, as typical for many polymers [270, 271].

3.4.8 Building a library of different APIs in various APIs/PVPVA loadings

Figure 55 and Figure 56 present a built library of 19 API-PVPVA formulations for compositions 20, 25, 30 ...90, 95% API/PVPVA loading for 19 APIs in addition to the pure polymer in the top row and the pure API in the bottom row as references in each printed slide. Those dispersions were arranged in an ascending order regarding the loading ratio at which birefringences were detected. All the images are depicted in bright-field and cross-polarised. All the images shown were taken six months after printing, having been stored at 40°C/75 % RH within this period.

From the library shown in Figure 56, there is a clear trend for the printed spots to change from visually transparent and unstructured to visually opaque, with the appearance of structure accompanied by the emergence of birefringence as the API loading goes higher. In the same pattern, as discussed in the previous section for Flurbiprofen/PVPVA, the appearance of birefringence could be used as an unambiguous indication of drug-polymer phase separation and, therefore, a reliable upper estimate of maximum miscibility of API in PVPVA. The results of the miscibility limits of all APIs that showed signs of birefringences in the pure form within PVPVA polymer will be discussed in detail in the next section as the summarised figure (Figure 57) for all APIs that showed signs of birefringences in the pure form.



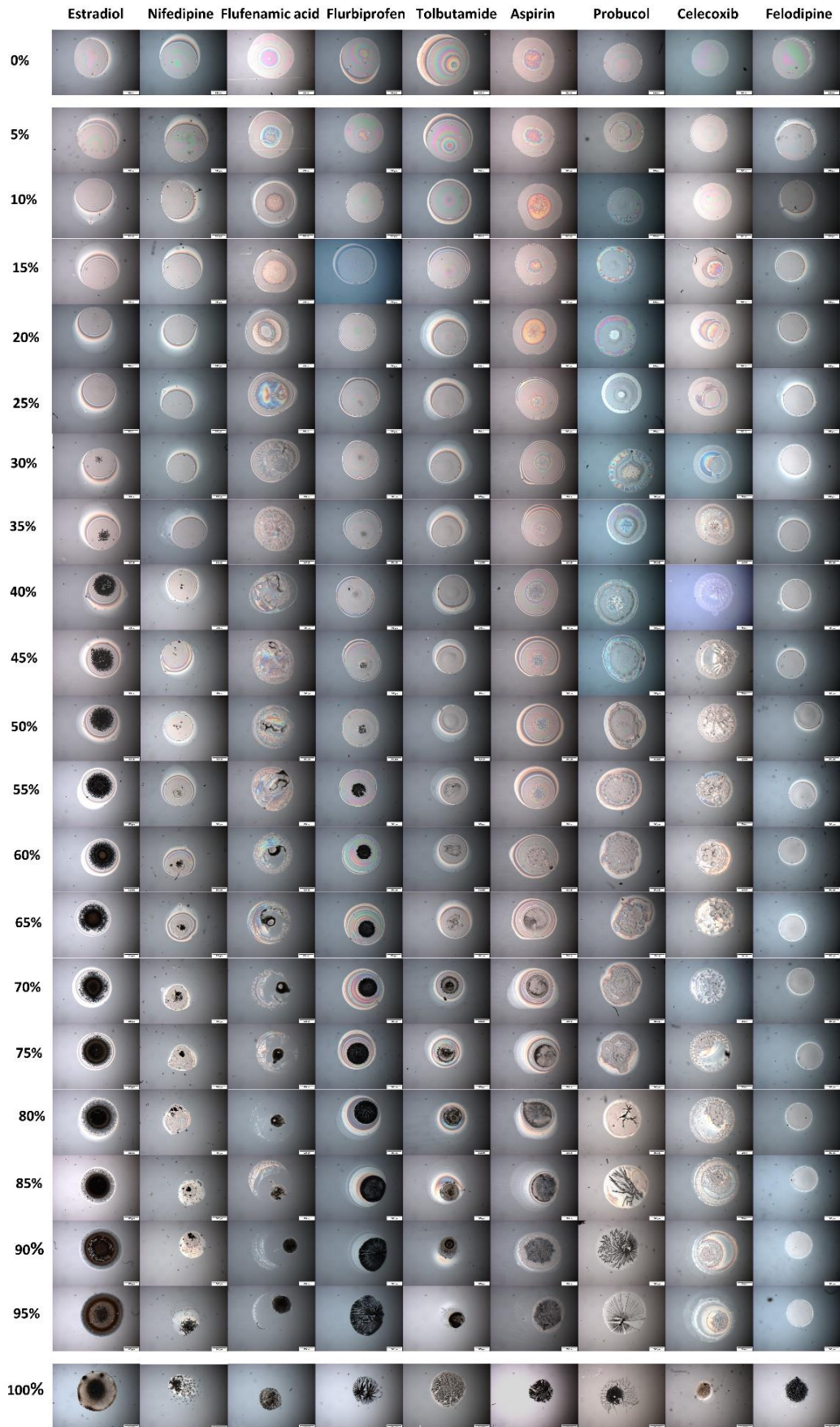
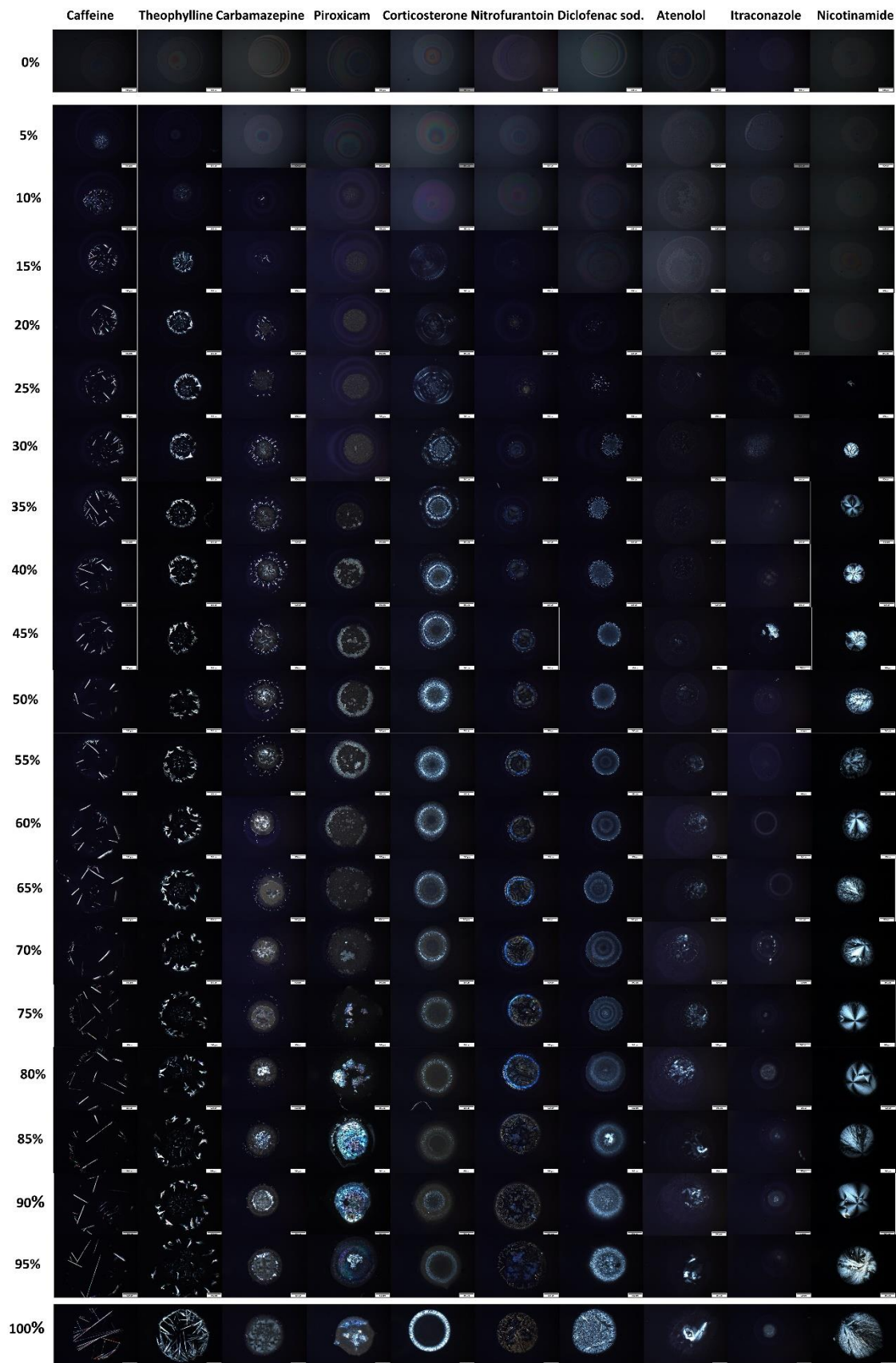


Figure 55. Examples of different APIs/PVPVA printed dispersions, starting from 0% to 100% API using 19 APIs and one polymer (PVPVA). All images are reported without cross-polarised filter. All images are reported after storage of the microarrays in accelerated conditions for 6 months (75% relative humidity and 40°C in a stability oven). Final mass 1000-1100 ng.



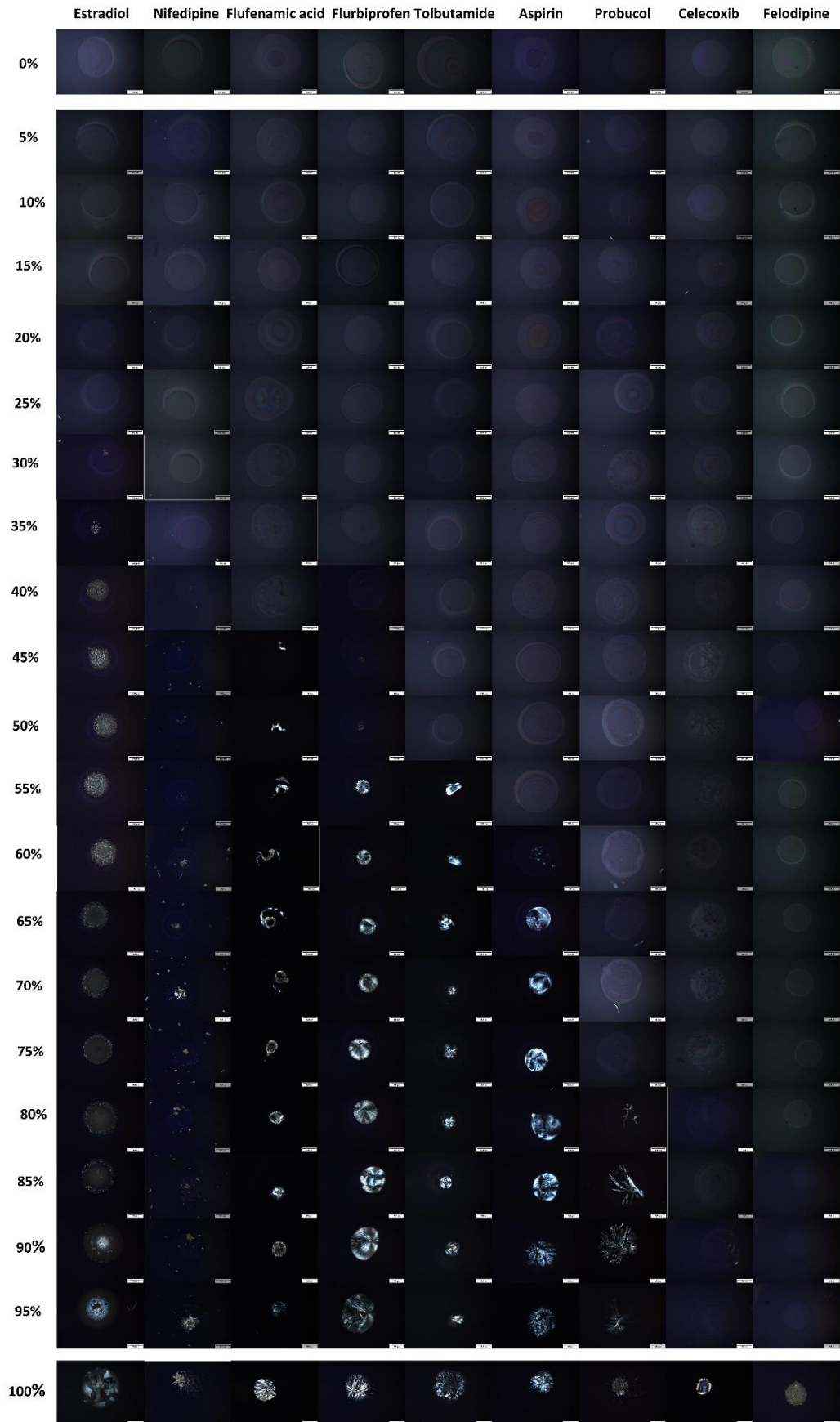


Figure 56. Examples of different APIs/PVPVA printed dispersions using cross-polarised filters, starting from 0% to 100% API using 19 APIs and one polymer (PVPVA). All images are reported after storage of the microarrays in accelerated conditions for 6 months (75% relative humidity and 40°C in a stability oven). Final mass 1000-1100 ng.

3.4.9 Miscibility limit comparison for different APIs within PVPVA polymeric matrix

Figure 57 presents bright-field and cross-polarised images of 3 different API/polymer loading ratios, first with no birefringence (no crystallisation monitored), second ratios that show the start of birefringence detection (start of crystallisation), and finally, ratios that show apparent birefringence detection (crystallisation) six months after printing, having been stored at 40°C/75 %RH for that time. The images have been arranged in ascending order of the displayed drug-polymer ratio. All images are reported without (top part of each section) and with (bottom part) cross-polarised filter. The top section shows the API/polymer loading ratios with no birefringence. In contrast, the middle section shows the API/polymer loading ratios that show the start of birefringence detection, and the bottom section shows the API/polymer loading ratios that show apparent birefringence detection.

Caffeine and theophylline, which have a very similar chemical structure, appeared to crystallise immediately after solvent evaporation at all drug-polymer ratios, even the lowest of 5%. We, therefore, deduce that these actives had a low miscibility limit with the polymer tested here, indicating that the polymer could not stabilise either compound in an amorphous state. Conversely, from GFA Class I, according to our classification, Aspirin and Tolbutamide had a high miscibility limit with PVPVA, and these drugs crystallise only at high drug loadings (>50% and 55%, respectively). From GFA Class II, Celecoxib and Felodipine showed amorphicity at all ratios, even the highest drug-polymer loading at 95%, with a high apparent miscibility limit. Other than those, different APIs showed variable apparent miscibility limits within the polymeric matrices, as seen in Figure 57 and different onsets of crystallisation, as highlighted in Table 12. The microscopic

images of the different drug/polymer loadings for each API can be found in Figures (1S-18S) in the appendix.

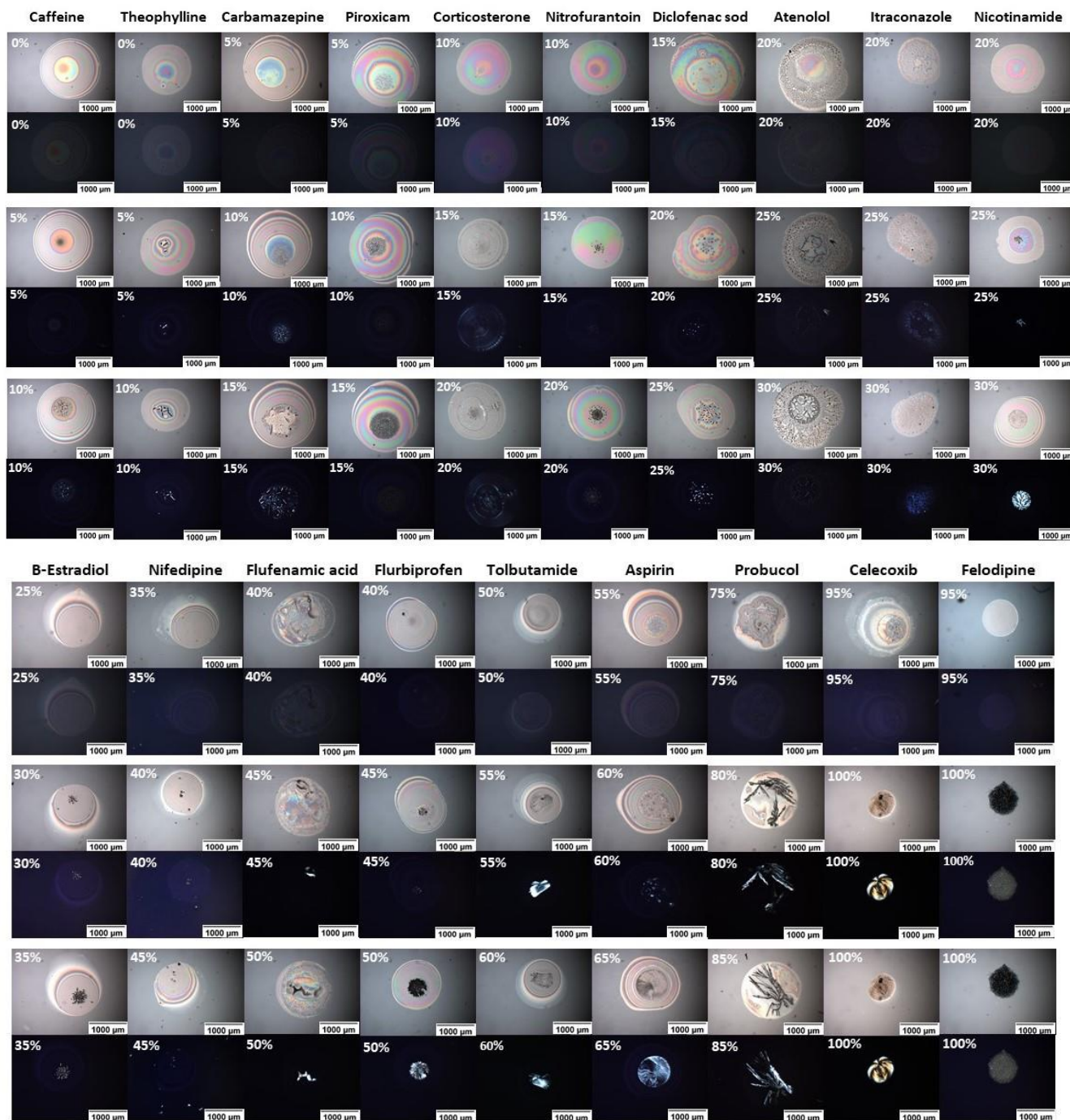


Figure 57. Examples of different APIs/PVPVA printed dispersions. All images are reported without (top part of each section) and with (bottom part) cross-polarised filter. The top section shows the API/polymer loading ratios with no birefringence (no crystallisation monitored). In contrast, the middle section shows the API/polymer loading ratios that show the start of birefringence detection (start of crystallisation), and the bottom section shows the API/polymer loading ratios that show apparent birefringence detection (crystallisation). Three different ratios for API/polymer loading were displayed to compare the assessment of crystallisation by PLM. All images are reported after storage of the microarrays in accelerated conditions for 6 months (75% relative humidity and 40°C in stability oven). Final mass 1000-1100 ng

Table 12. Stability of the printed microarrays of each API with PVPVA in API/polymer loading from 5% to 100% with 5% API increment (the last time point in days where no crystals were observed). Microarrays were kept in accelerated conditions (40°C ± 2°C/75% RH ± 5% RH) for six months.

N: no crystallisation was observed for those samples during the whole period of the study.

API/PVPVA loading w/w%	0	5	10	15	20	25	30	35	40	45	50	55	60	65	70	75	80	85	90	95	100		
Caffeine	N	0	0	0	0	0	0	0	0	0	0	0	0	0	0	0	0	0	0	0	0	0	
Theophylline	N	0	0	0	0	0	0	0	0	0	0	0	0	0	0	0	0	0	0	0	0	0	0
Carbamazepine	N	N	4	3	3	2	2	2	2	2	2	2	2	2	2	2	1	1	0	0	0	0	0
Piroxicam	N	N	4	2	2	2	2	2	2	2	2	2	2	2	2	2	2	2	1	0	0	0	0
Corticosterone	N	N	N	4	4	2	2	2	2	2	2	2	2	2	2	2	2	1	1	0	0	0	0
Nitrofurantoin	N	N	N	3	1	1	0	0	0	0	0	0	0	0	0	0	0	0	0	0	0	0	0
Diclofenac sodium	N	N	N	N	2	2	2	2	2	2	2	2	2	1	1	0	0	0	0	0	0	0	0
Atenolol	N	N	N	N	N	2	1	0	0	0	0	0	0	0	0	0	0	0	0	0	0	0	0
Itraconazole	N	N	N	N	N	55	10	4	2	2	2	2	0	0	0	0	0	0	0	0	0	0	0
Nicotinamide	N	N	N	N	N	3	3	1	1	0	0	0	0	0	0	0	0	0	0	0	0	0	0
Estradiol	N	N	N	N	N	N	72	10	4	2	1	1	1	1	1	1	1	1	0	0	0	0	0
Nifedipine	N	N	N	N	N	N	N	N	138	138	138	138	76	55	55	55	55	12	10	10	4	4	4
Flufenamic acid	N	N	N	N	N	N	N	N	N	1	1	1	0	0	0	0	0	0	0	0	0	0	0
Flurbiprofen	N	N	N	N	N	N	N	N	N	4	2	2	2	2	1	1	0	0	0	0	0	0	0
Tolbutamide	N	N	N	N	N	N	N	N	N	N	N	4	2	2	1	0	0	0	0	0	0	0	0
Aspirin	N	N	N	N	N	N	N	N	N	N	N	N	0	0	0	0	0	0	0	0	0	0	0
Probucol	N	N	N	N	N	N	N	N	N	N	N	N	N	N	N	N	N	81	81	81	72	55	55
Celecoxib	N	N	N	N	N	N	N	N	N	N	N	N	N	N	N	N	N	N	N	N	N	N	55
Felodipine	N	N	N	N	N	N	N	N	N	N	N	N	N	N	N	N	N	N	N	N	N	N	55
Ritonavir	N	N	N	N	N	N	N	N	N	N	N	N	N	N	N	N	N	N	N	N	N	N	N
Fenofibrate	N	N	N	N	N	N	N	N	N	N	N	N	N	N	N	N	N	N	N	N	N	N	N
Aprepitant	N	N	N	N	N	N	N	N	N	N	N	N	N	N	N	N	N	N	N	N	N	N	N
Orlistat	N	N	N	N	N	N	N	N	N	N	N	N	N	N	N	N	N	N	N	N	N	N	N

3.4.10 Miscibility limit comparison for different APIs within the Soluplus polymeric matrix

Figure 58 presents bright-field and cross-polarised images of 3 different API/polymer loading ratios, first with no birefringence, second ratios that show the start of birefringence detection, and finally, ratios that show apparent birefringence detection six months after printing, having been stored at 40 °C/75 %RH for that time. The images have been arranged in ascending order of the displayed drug-polymer ratio. All images are reported without and with cross-polarised filters. Caffeine and theophylline appeared to crystallise immediately after solvent evaporation, even the lowest drug-polymer ratio of 5%, exactly at the same pattern shown previously when printed within the PVPVA matrix. Hence, neither PVPVA nor Soluplus could stabilise any of the compounds in an amorphous state. Conversely, Probuco, Celecoxib and Felodipine showed amorphicity at all ratios, with a very high miscibility limit detected at 95%. In between those, the other APIs showed variable apparent miscibility limits within the Soluplus matrix, as highlighted in Table 13. Soluplus was able to stabilise Carbamazepine only at 5%, while it could stabilise Piroxicam and Nitrofurantoin up to 10% drug loading. Corticosterone and Estradiol showed a miscibility limit of around 20% with Soluplus, whereas Nifedipine and Aspirin showed a higher miscibility limit of 45%. The microscopic images of the different API/Soluplus loadings can be found in Figures (19S-37S) in the appendix.



Figure 58. Examples of different APIs/Soluplus printed dispersions. All images are reported without (top part of each section) and with (bottom part) cross-polarised filter. The top section shows the API/polymer loading ratios with no birefringence (no crystallisation monitored). In contrast, the middle section shows the API/polymer loading ratios that show the start of birefringence detection (start of crystallisation), and the bottom section shows the API/polymer loading ratios that show apparent birefringence detection (crystallisation). Three different ratios for API/polymer loading were displayed to compare the assessment of crystallisation by PLM. All images are reported after storage of the microarrays in accelerated conditions for 6 months (75% relative humidity and 40°C in stability oven). Final mass 1000-1100 ng.

Table 13. Stability of the printed microarrays of each API with Soluplus in API/polymer loading from 5% to 100% with 5% API increment (the last time point where no crystals were observed represented in days). Microarrays were kept in accelerated conditions (40°C ± 2°C/75% RH ± 5% RH) for six months.
N: no crystallisation was observed for those samples during the whole period of the study.

API/Soluplus loading w/w%	0	5	10	15	20	25	30	35	40	45	50	55	60	65	70	75	80	85	90	95	100	
Caffeine	N	0	0	0	0	0	0	0	0	0	0	0	0	0	0	0	0	0	0	0	0	0
Theophylline	N	0	0	0	0	0	0	0	0	0	0	0	0	0	0	0	0	0	0	0	0	0
Carbamazepine	N	N	6	3	3	2	2	2	2	2	2	2	2	1	1	0	0	0	0	0	0	0
Piroxicam	N	N	N	6	2	1	1	1	1	1	1	1	1	1	0	0	0	0	0	0	0	0
Nitrofurantoin	N	N	N	0	0	0	0	0	0	0	0	0	0	0	0	0	0	0	0	0	0	0
Atenolol	N	N	N	N	28	28	0	0	0	0	0	0	0	0	0	0	0	0	0	0	0	0
Corticosterone	N	N	N	N	N	4	2	2	0	0	0	0	0	0	0	0	0	0	0	0	0	0
Estradiol	N	N	N	N	N	2	2	2	2	2	0	0	0	0	0	0	0	0	0	0	0	0
Nicotinamide	N	N	N	N	N	N	2	2	1	1	1	0	0	0	0	0	0	0	0	0	0	0
Diclofenac sodium	N	N	N	N	N	N	1	1	1	1	1	0	0	0	0	0	0	0	0	0	0	0
Tolbutamide	N	N	N	N	N	N	N	1	1	0	0	0	0	0	0	0	0	0	0	0	0	0
Itraconazole	N	N	N	N	N	N	N	54	54	19	6	3	3	3	0	0	0	0	0	0	0	0
Flurbiprofen	N	N	N	N	N	N	N	N	3	2	2	2	2	1	1	1	1	1	0	0	0	0
Flufenamic acid	N	N	N	N	N	N	N	N	N	0	0	0	0	0	0	0	0	0	0	0	0	0
Nifedipine	N	N	N	N	N	N	N	N	N	N	22	19	13	13	13	9	9	9	9	9	9	6
Aspirin	N	N	N	N	N	N	N	N	N	N	1	1	0	0	0	0	0	0	0	0	0	0
Probucol	N	N	N	N	N	N	N	N	N	N	N	N	N	N	N	N	N	N	N	N	N	55
Celecoxib	N	N	N	N	N	N	N	N	N	N	N	N	N	N	N	N	N	N	N	N	N	55
Felodipine	N	N	N	N	N	N	N	N	N	N	N	N	N	N	N	N	N	N	N	N	N	55
Ritonavir	N	N	N	N	N	N	N	N	N	N	N	N	N	N	N	N	N	N	N	N	N	N
Fenofibrate	N	N	N	N	N	N	N	N	N	N	N	N	N	N	N	N	N	N	N	N	N	N
Aprepitant	N	N	N	N	N	N	N	N	N	N	N	N	N	N	N	N	N	N	N	N	N	N
Orlistat	N	N	N	N	N	N	N	N	N	N	N	N	N	N	N	N	N	N	N	N	N	N

3.4.11 Miscibility limit comparison for three APIs within the HPMCAS polymeric matrix

Printing of HPMCAS was very challenging as it was a very viscous polymer, so concentration was used as half of the previous one to avoid nozzle clogging. A 5 mg/mL solution of drugs and polymer was used in the printing process, and the number of droplets of drugs and polymer was adjusted during printing to get the same final drug/polymer loadings as the previous formulations with other polymers. Figure 59 shows bright-field and cross-polarised images of 3 different API/polymer loading ratios, first with no birefringence, then ratios that show the start of birefringence detection and finally, ratios that show apparent birefringence detection six months after printing for only three APIs, stored at accelerated conditions.

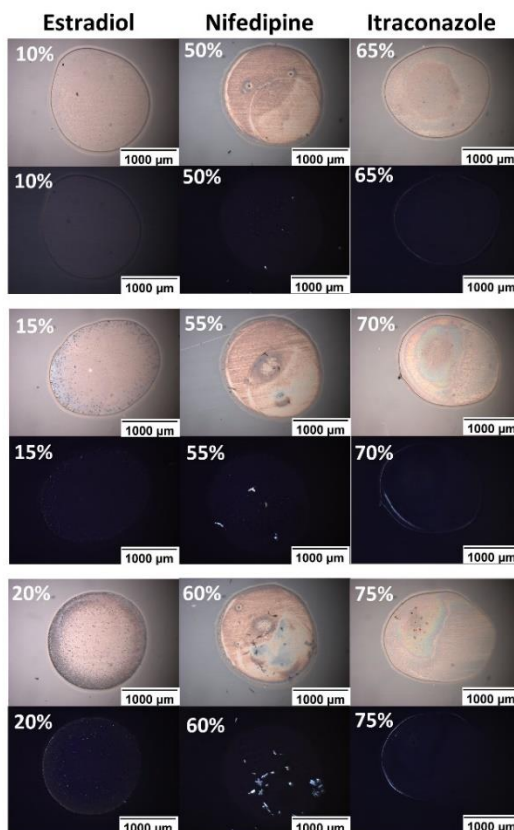


Figure 59. Examples of three APIs/HPMCAS printed dispersions. All images are reported without (top part of each section) and with (bottom part) cross-polarised filter. The top section shows the API/polymer loading ratios with no birefringence (no crystallisation monitored). In contrast, the middle section shows the API/polymer loading ratios that show the start of birefringence detection (start of crystallisation), and the bottom section shows the API/polymer loading ratios that show apparent birefringence detection (crystallisation). Three different ratios for API/polymer loading were displayed to compare the assessment of

crystallisation by PLM. All images are reported after storage of the microarrays in accelerated conditions for 6 months (75% relative humidity and 40°C in a stability oven). Final mass 1000-1100 ng.

The images have been arranged in ascending order of the displayed drug-polymer ratio. Estradiol appeared to crystallise 23 days after solvent evaporation at 15% drug/polymer loading and higher, as highlighted in Table 14. Therefore, the miscibility limit of Estradiol within HPMCAS would be the lowest among the three drugs tested here, while Nifedipine showed a higher miscibility limit within HPMCAS at 50%. In contrast, Itraconazole showed amorphicity at drug/polymer loading up to 65% as the highest apparent miscibility limit within the three APIs. The images of the different API/polymer loadings of the three APIs can be found in Figures (38S-40S) in the appendix.

Table 14. Stability of the printed microarrays of each API with HPMCAS in API/polymer loading from 5% to 100% with 5% API increment (the last time point where no crystals were observed represented in days), stored in accelerated conditions for 6 months. N: no crystallisation was observed for those samples during the whole period of the study.

API/HPMCAS loading w/w%	0	5	10	15	20	25	30	35	40	45	50	55	60	65	70	75	80	85	90	95	100	
Estradiol	N	N	N	22	22	19	19	1	1	1	1	1	1	1	1	1	1	1	1	1	1	0
Nifedipine	N	N	N	N	N	N	N	N	N	N	N	22	6	5	5	4	4	4	4	4	3	3
Itraconazole	N	N	N	N	N	N	N	N	N	N	N	N	N	N	20	5	5	5	5	5	5	0

3.4.12 Interactions and stabilization mechanisms in drug-polymer systems

The interactions between drug and polymer generally encompass four types of interactions: ionic interaction, hydrogen bond, dipole-dipole interaction, and Van der Waals interaction. a) Ionic interaction refers to the strong attraction or repulsion between ionised molecules. b) Hydrogen bonding is the attraction between a lone pair of an electronegative atom (as N, O and F) and a hydrogen atom, it would exist between two similar molecules of the drug or between the drug and polymer. c) Dipole–dipole interaction can occur between two polar molecules; an attraction will develop between a molecule's positive charge site and the negative charge site of another molecule

when two molecules with permanently separated positive and negative charge sites get close to one another. d) Nearly all systems exhibit Van der Waals force, which includes attraction and repulsion between molecules which is considered the weakest interaction among the four types [272]. The typical bond energy and the relative strength of the four types of those interactions can be ordered in the following sequence: ionic interaction > hydrogen bond > dipole-dipole interaction > van der Waals interaction. The ionic interaction is considered the strongest interaction, while the hydrogen bond is the most common interaction between drug and polymer [272].

The physical stability of solid dispersions can be affected by specific interactions between the drug and the polymer. For instance, H-bonds between the polymer and the drug may inhibit crystallisation by limiting the number of drug molecules available in the conformations needed for crystallisation. On the other hand, H-bonding can be formed between similar drug molecules inducing crystallisation. However, crystallisation may be inhibited if more or stronger H-bonds are available between drug and polymer or between amorphous drug-drug than between crystalline drug-drug [99].

Table 15. Comparison between the three polymers used in this study regarding the number of H-bond donors and acceptors per monomer unit. PVPVA, Soluplus and HPMCAS. The range of HBD and HBA for HPMCAS depends on the grade of HPMCAS, that is L, M or H [101, 273].

	PVPVA	Soluplus	HPMCAS
Number of H-bond donors (HBD) per monomer unit	0	0	0 - 6
Number of H-bond acceptors (HBA) per monomer unit	2	3	10 - 28

In our study, functional groups that can act as H-bond acceptors are present in all the three polymers studied here as amide (PVPVA, Soluplus), esters (Soluplus, PVPVA and HPMCAS), and ethers (Soluplus and HPMCAS), while as alcohol and carboxylic acid that can act as H-bond donors could be found only in HPMCAS [117]. The number of H-bond donors and acceptors varies

between the different APIs used here, as the number of H-bond donors ranges between zero and four while H-bond acceptors range between two to nine, as shown in Table 16.

Table 16. Comparison between the APIs used in this study regarding the number of H-bond donors (HBD) and H-bond acceptors (HBA).

API	HBD	HBA
Caffeine	0	3
Theophylline	1	3
Carbamazepine	1	1
Piroxicam	2	5
Corticosterone	2	4
Nitrofurantoin	1	5
Diclofenac sodium	1	3
Atenolol	3	4
Itraconazole	0	9
Nicotinamide	1	2
B-Estradiol	2	2
Nifedipine	1	5
Flurbiprofen	1	2
Flufenamic acid	2	3
Tolbutamide	2	3
Aspirin	1	3
Probucol	2	2
Celecoxib	1	3
Felodipine	1	3
Ritonavir	4	6
Fenofibrate	0	3
Aprepitant	2	6
Orlistat	1	3

If the ability of the drug and polymer to form specific bonds, such as H-bonds, were the only factor influencing the stability of solid dispersions, it would be reasonable to expect that PVPVA and Soluplus would not sufficiently stabilise drugs with no H-bond donors, and so would have the least miscibility limit as no interaction would be possible. In contrast, drugs with a high number of H-bond acceptors would be expected to be more stable in HPMCAS - which has a number of H-bond donor functional groups- than PVPVA and Soluplus which do not have at all. The API/polymer

loading percentage data at which no birefringence was detected within the three polymeric matrices are plotted for the three APIs in Figure 60. Itraconazole, with the highest number of H-bond acceptors, showed the highest miscibility limit within HPMCAS at 65%, which was higher than the miscibility limit within PVPVA (20%) and Soluplus (30%). Conversely, Nifedipine, which has a lower number of hydrogen-bond acceptors (5), demonstrated a lower miscibility limit compared to Itraconazole when formulated with the same polymer (HPMCAS). However, Nifedipine exhibited a higher miscibility limit with HPMCAS compared to its miscibility limits within PVPVA and Soluplus. In contrast, in the case of Estradiol which has a lower number of H-bond acceptors (2), the miscibility limit within HPMCAS was the lowest compared to Itraconazole and Nifedipine. No general conclusion could be confirmed from the HPMCAS data regarding the role of hydrogen bond interaction, as only three APIs were printed within this polymer.

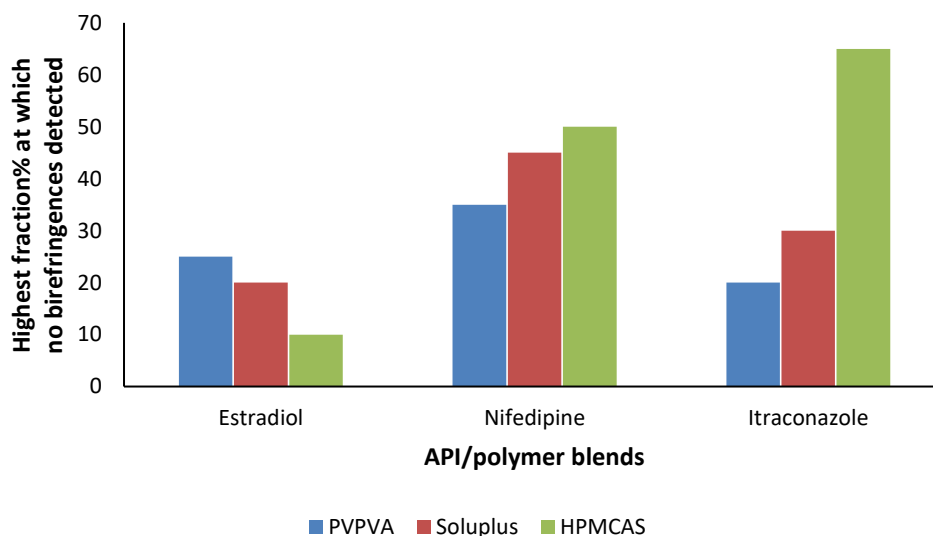


Figure 60. The figure shows plotting the data of the three APIs with API/polymer loading w/w% at which no birefringences were detected (no crystallisation monitored) as the miscibility limit of API within the polymer using three polymers; PVPVA, Soluplus and HPMCAS.

Figure 61 presents the plotted data of the different APIs with API/polymer loading w/w% at which no birefringences were detected (no crystallisation monitored) as the miscibility limit of API in the polymer with two polymers; PVPVA and Soluplus. Caffeine and theophylline appeared to

crystallise immediately after solvent evaporation at all drug-polymer ratios, even the lowest as 5% in the case of printing with both polymers. Carbamazepine, Nitrofurantoin, Flufenamic acid, Celecoxib, and Felodipine showed the same miscibility limit with both polymers at 5%, 10%, 40%, 95%, 95%, respectively). Piroxicam, Corticosterone, Diclofenac sodium, Itraconazole, Nicotinamide, Nifedipine, and ProbucoI showed higher miscibility limits with Soluplus than PVPVA. While Atenolol, Estradiol, Flurbiprofen, Tolbutamide, and Aspirin showed higher miscibility limits with PVPVA than Soluplus.

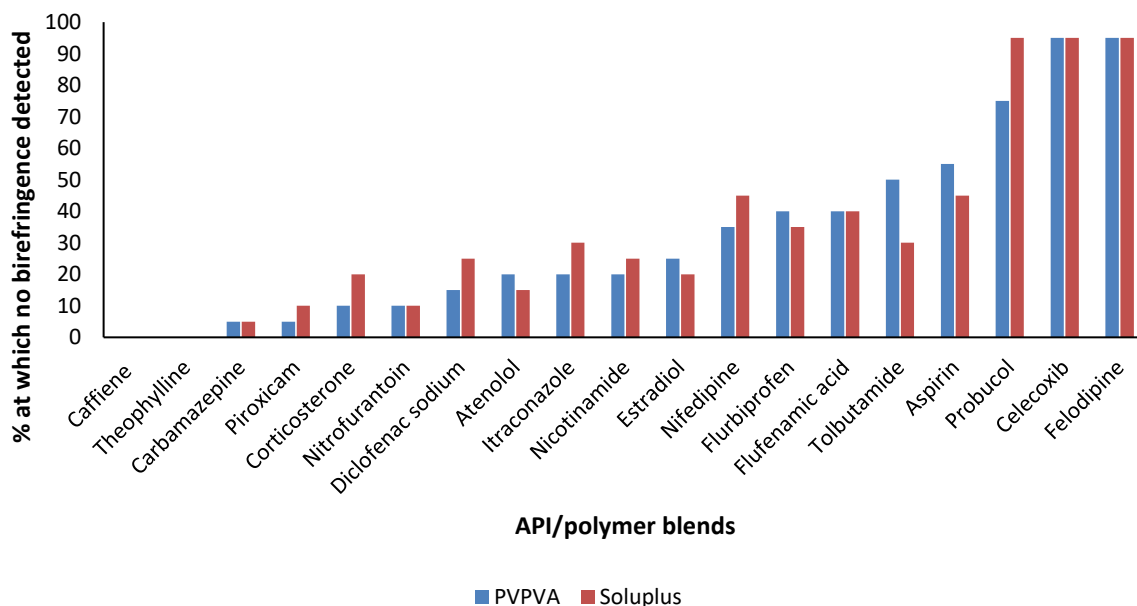


Figure 61. The figure shows plotting the data of the different APIs with the limiting concentration (loading %) at which no birefringences were detected (no crystallisation monitored) as the miscibility limit of API within the polymer using 2 polymers; PVPVA and Soluplus.

Itraconazole and Caffeine, which have zero H-bond donors, showed different miscibility limits as the two polymers were not able to stabilise the Caffeine. In contrast, the miscibility limits were around 20% and 30% within PVPVA and Soluplus, respectively, in the case of Itraconazole. At the same time, Theophylline followed the same pattern of miscibility as Caffeine within the two polymers despite having one H-bond donor. Atenolol, which has the highest number of H-bond donors, which is three and was expected to have the highest miscibility limit showed low

miscibility limits at 20% and 15% within PVPVA and Soluplus, respectively. Additionally, both Celecoxib and Felodipine showed the highest miscibility limits despite having only one H-bond donor. Therefore, it is evident that stability is affected by some properties other than just the interaction between a drug and a polymer, although it is clearly an important factor.

3.4.13 Drop casting of drug/PVPVA formulations and comparison to the 2D inkjet printing miscibility limits

To assess inkjet printing as a screening/predictive technique to identify useful drug-polymer formulations suitable as solid dispersions, three drug/polymer ratios at the apparent miscibility limit and below and above were selected to be further analysed for all the drugs at a milligram scale. This study aimed to confirm the feasibility of using 2D inkjet printing to screen the miscibility limit of a drug/polymer library with minimal API quantities at the nanogram scale, thereby obtaining comparable results to those achievable at the milligram scale. Flurbiprofen, Itraconazole, Celecoxib, Flufenamic acid, Nitrofurantoin, and Estradiol were examples of pure drugs that showed crystallisation behaviour upon storage. In contrast, Orlistat and Fenofibrate showed no crystallisation within the micro-array experiment. This selection of drugs and ratios aims to comprehensively evaluate the predictive capabilities of inkjet printing in identifying the miscibility limits of those

Figure 62 represents the drop-casted samples in the top row and then bright-field and cross-polarised images of drop-casted three Flurbiprofen-PVPVA loadings and pure Flurbiprofen and PVPVA six months after printing, stored at 40 °C/75 %RH. The microscopic images were arranged as the ones depicted by a bright field in the middle row and a cross-polarised field at the bottom. As shown in Figure 62, no evidence of birefringence was found for the pure polymer and the 40% drug/polymer ratio, which matched the observation with the printed microarrays, as previously

shown in Figure 54. The PLM observation showed clear evidence of birefringence at 45% and 50% w/w ratios and the pure Flurbiprofen in the drop-cast samples. This was in good agreement with the printed sample observations. The ability of PVPVA to inhibit the crystallisation of Flurbiprofen was confirmed at both the nanogram and milligram scale at 40% drug loading and less. For the 40% drug/polymer ratio, for example, the deposited mass of the printed spots by 2D inkjet printing as a miniaturised approach was 400 ng drug and 600 ng polymer, while for by drop cast method was 0.8 mg drug and 1.2 mg polymer. The calculated deposited masses for drop-casted and printed samples are illustrated in Table 17.

Table 17. Comparing the printed volume and deposited mass of two techniques, drop cast method and 2D inkjet printing.

Formulation	Drop cast technique (Pipetted volume is 170-200 µl)		2D inkjet printing (500 droplets, droplet size is 200-220 pL)			
	Deposited mass (Around 2mg in total)		Printed volume (Around 0.1 µl in total)		Deposited mass (around 1000 ng in total)	
	Drug	Polymer	Drug	Polymer	Drug	Polymer
Pure drug	2 mg	0	0.1 µl	0	1000 ng (1 µg)	0
Pure polymer	2 mg	0	0.1 µl	0	1000 ng (1 µg)	0
40% Flurbiprofen/PVPVA	0.8 mg	1.2 mg	40 nL	60 nL	400 ng	600 ng
45% Flurbiprofen/PVPVA	0.9 mg	1.1 mg	45 nL	55 nL	450 ng	550 ng
50% Flurbiprofen/PVPVA	1 mg	1 mg	50 nL	50 nL	500 ng	500 ng
10%Nitrofurantoin/PVPVA	0.2 mg	1.8 mg	10 nL	90 nL	100 ng	900 ng
15%Nitrofurantoin/PVPVA	0.3 mg	1.7 mg	15 nL	85 nL	150 ng	850 ng
25%Nitrofurantoin/PVPVA	0.5 mg	1.5 mg	25 nL	75 nL	250 ng	750 ng
40% Flufenamic acid/PVPVA	0.8 mg	1.2 mg	40 nL	60 nL	400 ng	600 ng
45% Flufenamic acid/PVPVA	0.9 mg	1.1 mg	45 nL	55 nL	450 ng	550 ng
55% Flufenamic acid/PVPVA	1.1 mg	0.9 mg	55 nL	45 nL	550 ng	450 ng
25% Estradiol/PVPVA	0.5 mg	1.5 mg	25 nL	75 nL	250 ng	750 ng
30% Estradiol/PVPVA	0.6 mg	1.4 mg	30 nL	70 nL	300 ng	700 ng

40% Estradiol/PVPVA	0.8 mg	1.2 mg	40 nL	60 nL	400 ng	600 ng
---------------------	--------	--------	-------	-------	--------	--------

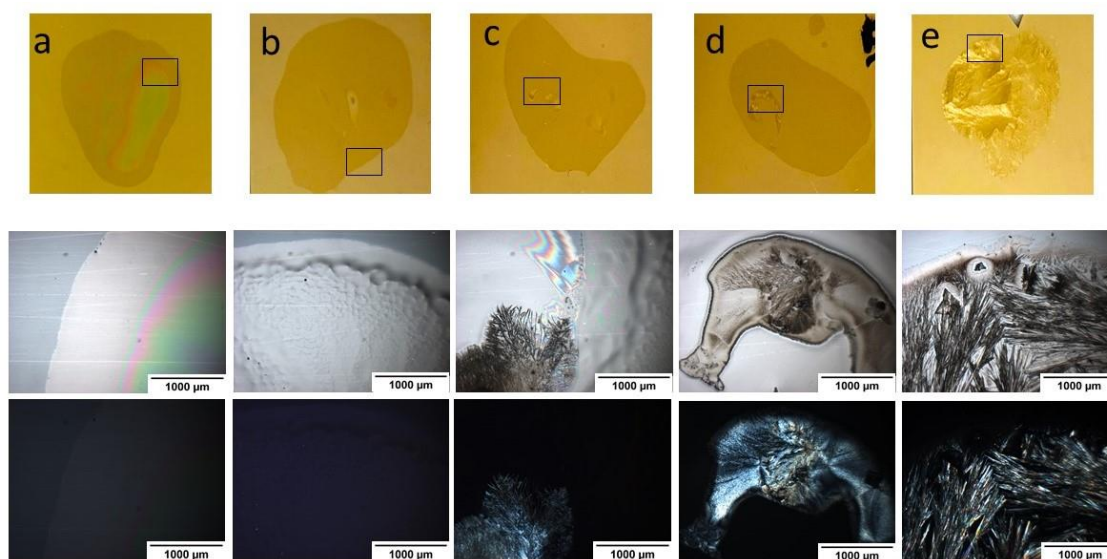


Figure 62. The top row shows the spots by drop cast technique for Flurbiprofen/PVPVA pipetted on gold-coated glass slides as substrate. a) Pure polymer PVPVA (0%), b) 40% Flurbiprofen/PVPVA, c) 45% Flurbiprofen/PVPVA, d) 50% Flurbiprofen/PVPVA, e) Pure Flurbiprofen. (100%). Images were depicted as resembling a small section taken with optical (middle row) and cross-polarised (bottom row).

Figure 63 represents the drop-casted samples and the microscopic images for four pure APIs; Orlistat, fenofibrate, Celecoxib and Itraconazole. In the same manner as Flurbiprofen-PVPVA, Figure 64, Figure 65, and Figure 66 represent the drop-casted samples of pure API and three different API/polymer loadings for Nitrofurantoin, Flufenamic acid and Estradiol, respectively. No evidence for crystallisation was found in the pure drop-casted Fenofibrate and Orlistat. In contrast, birefringences were detected in the pure Itraconazole, Celecoxib, Nitrofurantoin, Flufenamic acid and Estradiol drop-casted samples. That agrees with the 2D printing results, as shown in Figure 52, that required around three orders of magnitude lower amounts of sample than the drop Cast method used here.

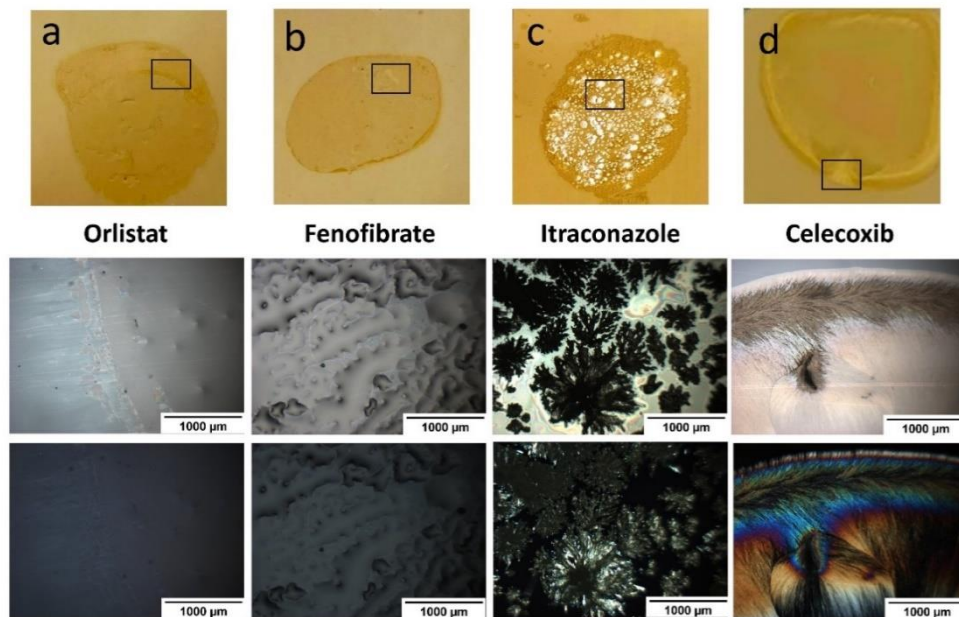


Figure 63. The top row shows the spots by drop cast technique for pure APIs pipetted on gold-coated glass slides as substrate. a) pure Orlistat (0%), b) pure Fenofibrate, c) pure Itraconazole, d) pure Celecoxib. Images were depicted as resembling a small section taken with optical (middle row) and cross-polarised (bottom row).

Figure 64 shows no evidence of birefringence for the 10% drug/polymer ratio of Nitrofurantoin, which matched the observation with the printed microarrays (Figure 57). The PLM observation showed clear evidence of birefringence at 15% and 25% ratios and the pure Nitrofurantoin in the drop-cast samples. As presented in Figure 65, no evidence of birefringence was found for the 40% drug/polymer ratio of Flufenamic acid, which matched the observation with the printed microarrays, as previously shown in Figure 57. The PLM observation showed clear evidence of birefringence at 45% and 55% ratios and the pure Flufenamic acid in the drop-cast samples. As shown in Figure 66, no evidence of birefringence was found for the 25% drug/polymer ratio of Estradiol, which matched the observation with the printed microarrays, as previously shown in Figure 57. At 30% and 40% ratios and pure Estradiol in the drop-cast samples, the PLM observation showed clear evidence of birefringence. All the results for the drop-casted samples for the pure APIs and the different API/polymer ratios mirrored the printed sample observations well. By comparing the crystallisation results at both the nano- and milligram scales, 2D inkjet printing

as a miniaturisation technique may offer significant efficiency in pharmaceutical formulation screening, with each experiment in the nano micro-array format requiring at least three orders of magnitude lower amounts of sample than even thin-film screening methods.

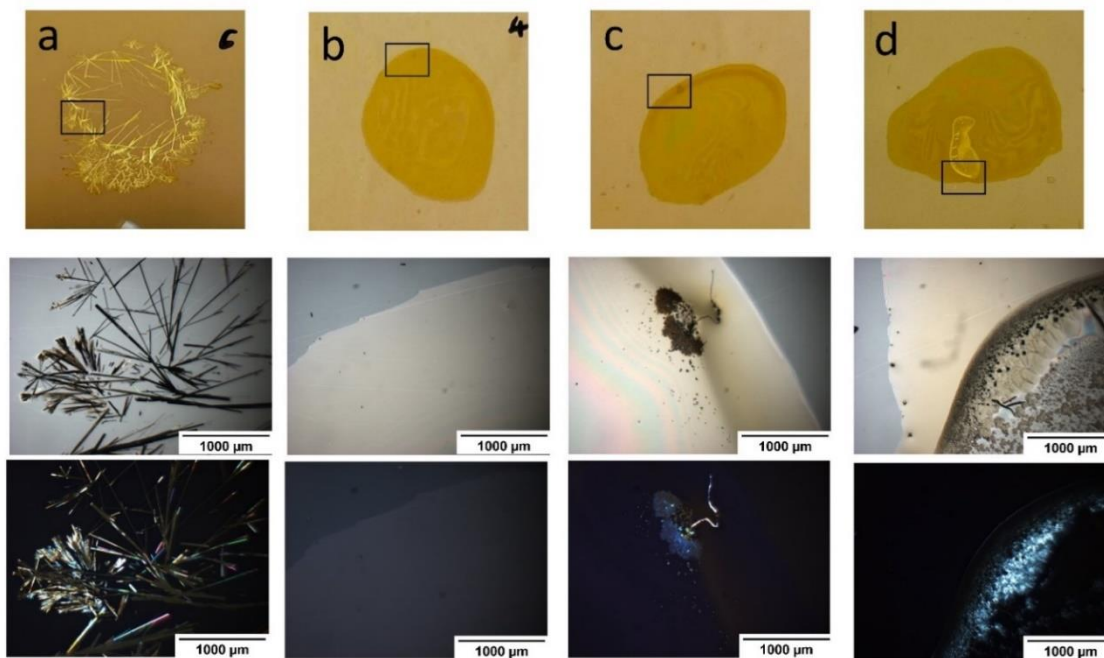


Figure 64. The top row shows the spots by drop cast technique for Nitrofurantoin/PVPVA pipetted on gold-coated glass slides as substrate. a) Pure Nitrofurantoin (0%), b) 10% Nitrofurantoin/PVPVA, c) 15% Nitrofurantoin/PVPVA, d) 25% Nitrofurantoin/PVPVA. Images were depicted as resembling a small section taken with optical (middle row) and cross-polarised (bottom row).

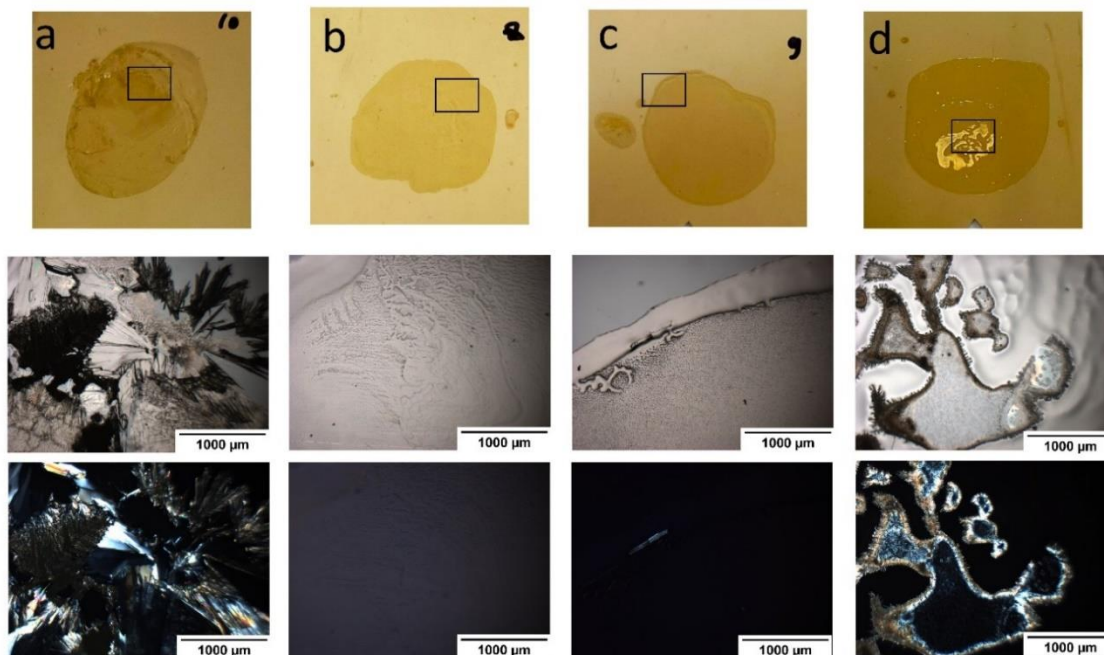


Figure 65. The top row shows the spots by drop cast technique for Flufenamic acid/PVPVA pipetted on gold-coated glass slides as substrate. a) Pure Flufenamic acid (0%), b) 40% Flufenamic acid/PVPVA, c) 45% Flufenamic acid/PVPVA, d) 55% Flufenamic acid/PVPVA. Images were depicted as resembling a small section taken with optical (middle row) and cross-polarised (bottom row).

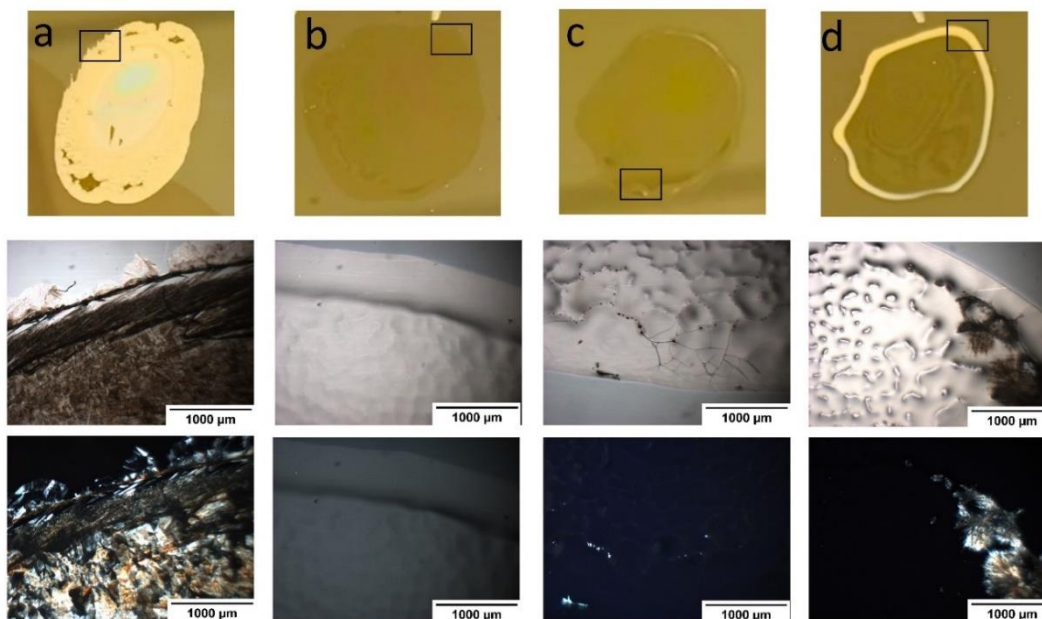


Figure 66. The top row shows the spots by drop cast technique for Estradiol/PVPVA pipetted on gold-coated glass slides as substrate. a) Pure Estradiol (0%), b) 25% Estradiol/PVPVA, c) 30% Estradiol/PVPVA, d) 40% Estradiol/PVPVA. Images were depicted as resembling a small section taken with optical (middle row) and cross-polarised (bottom row).

3.4.14 Literature Comparison of API/Polymer Formulations

A comparison with literature was made to the results of 2D inkjet printed microarrays of Flufenamic acid microarrays with PVPVA as well as Itraconazole with three polymers; PVPVA, Soluplus and HPMCAS. Both were used to match some formulations and weight ratios reported in the literature produced by spin coating and film casting, respectively, to further test the reported high-throughput nano-miniaturised method and compare it with the already well-established literature [117, 262]. The resulting dry spots of Flufenamic acid in the polymeric matrix in the micro-array format that showed an apparent miscibility limit of 45% (w/w) were compared to previously published outcomes obtained by spin coating, which suggested a miscibility limit of around 60% [117]. The printed spots of Itraconazole/PVPVA blends showed a miscibility limit at 25% (w/w), which were compared to the previously published results obtained by a film-casting

technique that showed that Itraconazole was miscible with PVPVA up to 2:8 (w/w) drug to polymer ratio and crystallisation of the drug was detected for 3:7 (w/w) drug to polymer ratio [262]. The printed spots of Itraconazole/Soluplus blends showed a miscibility limit at 30% (w/w), which were compared to the previously published results obtained by the film-casting technique that showed that Itraconazole was miscible with Soluplus up to 3:7 (w/w) drug to polymer ratio, while the 4:6 (w/w) ratio displayed slight birefringence [262]. Additionally, the printed spots of Itraconazole/HPMCAS blends showed a higher miscibility limit at 65% (w/w), which were compared to the previously published results obtained by the film-casting technique that showed that Itraconazole was miscible with Soluplus up to 6:4 (w/w) drug to polymer ratio and birefringence was observed at 7:3 (w/w) and higher drug/polymer ratios [262].

The miscibility limit of printed spots of Itraconazole within the three polymers was plotted against the values of the miscibility limit reported in the literature and presented in Figure 67 to simplify the drug-polymer compatibility rank and to easily evaluate differences concerning the published data. The same miscibility trend, HPMCAS > Soluplus > PVPVA, was found both in the experimental results collected in the present study and the previously published data [262]. The hydrogen bonding between the drug and polymer molecules may play a significant role in the stability of solid dispersion and consequently this trend, but there also may be other factors that need to be investigated.

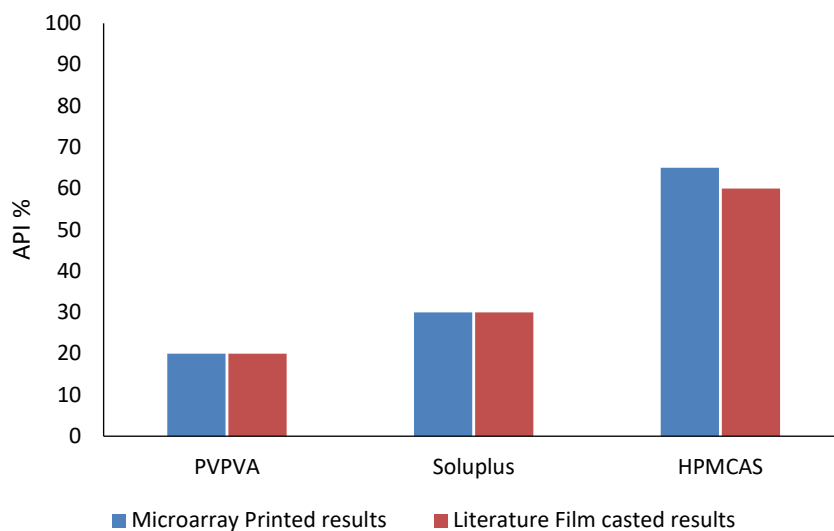


Figure 67. Miscibility limit (% at which no birefringence detected) for Itraconazole/PVPVA, Itraconazole/Soluplus, Itraconazole/HPMCAS printed in the present work (blue) and limiting concentration extracted from film-casting previously published data in the literature (red) are shown in the figure. The same miscibility/compatibility trend was found when comparing the two sets of data, HPMCAS > Soluplus > PVPVA.

Therefore, there is good agreement between the micro-array apparent drug-in-polymer miscibility and previous literature based on more bulk-like methods, at least where such comparisons can be meaningfully made. The amount of material needed for analysis and prediction using the micro-array approach is perhaps the key benefit of the current study, in addition to the other advantages of saving precious or newly synthesized compounds and reducing the assay space to just a few slides. In reality, for each drug/polymer ratio formulation, a maximum of 3 μg was deposited using the micro-array approach against an approximate value of 5–15 mg following the drop-casting methodology in the Taylor group papers [117, 144].

3.5 Conclusion

The current work has demonstrated for the first time the feasibility of employing printed nano-arrays with pico-litres of small-molecular weight drugs in the framework of pre-formulation and solid-form screening to build an extensive library of different drug and polymer loadings. The

range of miscibility limits of drugs within the various polymeric matrices was able to be detected and compared.

Different techniques with varying printing plans were employed as preliminary steps, such as the manual method and contact printing, to test the printability of the used drugs and polymers. The results of the 2D inkjet printing using a nanogram scale agreed with the results of the preliminary techniques. The results from the 2D printed arrays were confirmed to be similar for the pure drugs and the miscibility limit range of the drugs within PVPVA polymeric matrices compared to the drop cast technique. The miscibility trend for one of the used APIs (Itraconazole) within three polymeric matrices was found to be the same (HPMCAS > Soluplus > PVPVA) in both experimental results collected in the present study and the previously published data [262].

Even though only relatively few drugs and polymers were employed in the present study, the novelty in our research here would be the number of drug-polymer loadings formulations used, which is around 930 drug/polymer loadings (around 2793 loadings in triplicates) which are much more than has been achieved before in other studies while taking into consideration performing this safely using a minimal (nano-gram) amount of materials. 400-500 spots can easily fit on a single microscope slide and can be produced at a pace of about 1000 spots per hour. In around 45 minutes, PLM analysis and taking a record of a single slide might be completed. 2D inkjet printing techniques might be exploited to save precious or unknown/newly synthesised organic compounds, reduce the assay space to just a few slides, and facilitate much more rapid sample preparation and analysis. When all factors are considered, inkjet printing satisfies the primary requirements for a high-throughput-miniaturised screening approach, not only in drug-solid dispersion but in all those areas where crystallisation needs to be assessed. These factors include tailored flexibility in terms of materials and solvents adopted, [171] high degrees of automation,

speed of execution, [192] combined with low error [188] and wastage, [210] and inkjet printing thoroughly meets all characteristics and demands for a high-throughput. 2D inkjet printing, while offering these advantages, it does have some limitations. These include constraints related to ink viscosity, as high viscosity can cause nozzle clogging and low viscosity can result in poor droplet formation. Material compatibility is also a consideration, as not all materials are suitable for inkjet printing without careful formulation adjustments.

Bearing in mind the different timescales of the different evaluation methods, plus the versatile techniques, the similarity in crystallisation tendency of the various compounds is remarkable and has important practical implications. It is worth noting that predicting formulations at this stage is not obvious, that the APIs with high or low crystallisation do not follow an obvious chemical pattern and so some more in-depth modelling is required. The high volume of data derived from this 2D array approach is ideal to better develop models that can predict the stability of solid dispersion (API/polymer blend) depending on the APIs' physicochemical properties, as will be explored later in this thesis.

4 Chapter 4: Multiple Linear Regression Modelling for predicting the stability of solid dispersions

4.1 *Introduction*

4.1.1 Challenges in Predicting Complex Systems

There are multiple physical and chemical properties that determines whether a drug-polymer combination will form an amorphous solid dispersion [274]. Modelling has been explored as an approach to allow in silico prediction of optimal drug-polymer formulations from the physicochemical properties of the drug/polymer [275]. A number of theoretical frameworks have been developed that attempt to describe this complex system. In earlier theoretical frameworks, certain thermodynamic parameters were defined as the description of complex systems. These theoretical models offered some insight into solid dispersions yet faced challenges in accurately predicting the behavior of complex systems in actual experimental scenarios, as they were predicated on ideal conditions [120]. In contrast, mathematical models typically aim at outcomes tied to the properties of SD systems, such as the potential for amorphous molecular solid dispersion and the crystallization propensity of compounds. Consequently, while previous theoretical and statistical models could elucidate some correlations between thermodynamic or other physicochemical parameters and physical stability, their predictive capacity remains constrained when applied to complex systems under actual experimental conditions [120].

During the formulation development process, the availability of predictive models is highly advantageous as by reducing the time and money spent on trials, models can help speed up the development process. A substantial amount of data is required to develop a statistical model, and the model's applicability will be limited to the dataset used. Yet, models may often provide reliable predictions and accurate correlations. Some models have been developed to predict APIs' glass-

forming ability and the stability of the amorphous state [145, 146]. Prediction of solid dispersion dissolution [147], drug solubility [148, 149], and crystallisation of organic molecules [150] are other applications of statistical models in medicine development.

4.1.1.1 Statistical models developed for predicting solid dispersion stability

A predictive model of the drugs' amorphous stability, focusing on poorly water-soluble compounds, was developed by Nurzyńska et al. [151]. From a large library of available compounds, 25 neutral, poorly soluble molecules with various physicochemical properties and chemical structures were chosen. PLM was used to evaluate the amorphous form's physical stability over six months by tracking the beginning of crystallisation in amorphous films created by melting and quench-cooling. The data were employed as a response variable in a statistical model using calculated/predicted or measured chemical, thermodynamic, and kinetic properties as explanatory factors. Several multiple linear regression models were developed with varying balances between calculated/predicted and measured parameters. It has been demonstrated that the inclusion of measured parameters significantly improves the model's predictive ability of the model. The best model had an 82% prediction accuracy and had the following parameters: melting and glass transition temperatures, the fusion enthalpy, the configurational free energy, the lipophilicity, the number of hydrogen bond donors, the relaxation time, and the ratio of carbon to heteroatoms. A simpler model that only included two easily obtainable parameters, molecular weight and fusion enthalpy, also produced good predictions [151].

A similar model was developed by Fridgeirsdottir et al. using 60 solid dispersion formulations developed from ten poorly soluble drugs, three widely used polymers using two methods of preparation: hot melt extrusion and spray drying at 10% w/w drug-polymer loading in gram scale

[152]. A six-month stability study of each formulation was conducted under accelerated conditions at 40 °C and 75%RH. There were significant differences in the onset of crystallization between the two processing techniques and the different polymers for each drug. Several linear regression models were built to correlate the physicochemical characteristics of the API with the stability data. These models were designed to show which processing technique and polymer carrier combination were the most likely to produce a stable solid dispersion. Based on selecting the most influencing independent physical and chemical parameters from a set of 33 potential factors, six quantitative statistical multiple linear regression-based models were built, one model for each combination of polymer and processing method, with good predictability of stability. From these models, three general trends are provided for the formulation of adequately stable solid dispersions. In particular, the drug molecule's higher T_g of solid dispersions, fewer H-bond donors, and higher molecular flexibility (such as rotatable bonds and ring count) were all associated with enhanced stability [152].

4.2 Aims and objectives of this chapter

However, to date, only a limited number of models have been able to predict the stability of solid dispersions that have been derived from a limited set of experimental data.

Therefore, the aim of this chapter is to:

- build a statistical predictive model for the physical stability of solid dispersions using multiple linear regression based on experimental data obtained from micro-arrays fabricated through pico-litre 2D inkjet printing. This model could highlight the physicochemical properties of the APIs that are highly correlated to the stability of the solid dispersions. Hence, this model is expected to allow formulators to readily identify likely formulations for new and existing amorphous solid dispersion.

This could be achieved through the following objectives:

- Building multiple linear regression models using the experimental stability data collected at accelerated conditions (natural log of the stability (onset of crystallisation)) of around 900 drug-polymer loadings in triplicates and the physicochemical properties of 23 drugs.
- Testing the multicollinearity of the physicochemical parameters of the used APIs.
- Validation of the model predictivity and reliability through Leave One Out Cross Validation.
- Comparing the predicted stability to the measured experimental ones for each API within the two polymeric matrices.
- Pinpointing of the physicochemical properties of APIs that are highly correlated to the stability of the amorphous solid dispersion. That would provide valuable insights for amorphous solid dispersion formulation development in the industry.

4.3 *Materials and methods*

4.3.1 Stability data of the 2D printed microarray formulations

Stability data was a record of when, in days, a given formulation exhibited textured opaque areas in transmitted light microscopy, producing birefringence in cross-polarised optical microscopy (i.e., the onset of crystallisation). This data was inputted into the multiple linear regression (MLR) workflow as a natural log of days to crystallisation (number of days + 1).

4.3.2 Physicochemical properties of APIs

The program Chemicalize from ChemAxon was used to calculate the physicochemical properties of the different APIs based on the molecular structure of each API [231]. Furthermore, the melting point of each API was obtained from ChemSpider [232]. The parameters included in the modelling process and their abbreviations are shown in Table 18. The selection of parameters for the

modelling process was based on careful consideration of physicochemical properties that are known to influence the behaviour, interactions, and characteristics of molecules in pharmaceutical and chemical contexts as well as the parameters used in other modelling on smaller datasets in the literature [151, 152].

Table 18. Nomenclature of the physicochemical properties used in the model.

Nomenclature	Physicochemical property	Nomenclature	Physicochemical property
MW	molecular weight	nC	number of carbon atoms
logP	lipophilicity	nF	number of fluorine atoms
HBA	number of H-bond acceptors	avPol	average polarizability
HBD	number of H-bond donors	nRot	number of nonterminal rotatable bonds
nRing	number of rings	nS	number of sulphur atoms
nAtom	number of atoms	nHet	number of heteroatoms (atoms other than carbon and hydrogen)
nChir	number of chiral atoms	nN	number of nitrogen atoms
tPSA	topological polar surface area	sp3	number of sp ³ carbon atoms
ASA	water accessible surface area	MRef	Molar Refractivity
HLB	hydrophilicity–lipophilicity balance	sp2	number of sp ² carbon atoms
nCl	number of chlorine atoms	nHeavy	number of heavy atoms
vdW-SA	van der Waals surface area	logS0 at 7.4	water solubility in log ₁₀ of molar solubility at pH 7.4
vdW-Vol	van der Waals volume	FSP3	the number of sp ³ hybridised carbons/total carbon count
logS0	water solubility in log ₁₀ of molar solubility	nAsymmetric	number of asymmetric atoms
mp	melting point	FC	formal charge (the electric charge of an atom in a molecule)
nAliphRing	number of aliphatic rings	minProjArea	Minimum projection area
nArRing	number of aromatic rings	maxProjArea	Maximum projection area
nO	number of oxygen atoms	minProjRad	Minimum projection radius
		maxProjRad	Maximum projection radius

Because not all APIs have values for the strongest acidic pKa and because missing values are not allowed throughout the modelling, this property was not used. LogS₀ of the drug "Diclofenac sodium" had placeholder text "the molecule cannot be neutralized," which was replaced with zeros for computational purposes. The physicochemical properties used and their values are listed in Table 4 in Chapter 2.

4.3.2.1 The variation in the physicochemical properties across the model drugs used in the modelling process

The selection of the drugs was intended to cover as wide a variety of chemistry and physicochemical properties to ensure as much diversity in the data gathered from modelling as possible, within the constraints of safe-to-use compounds and cost. For example, molecular weight ranged from 122.1 g/mol for Nicotinamide to 720.9 g/mol for Ritonavir. The number of hydrogen bond donors ranged from 0 for Caffeine, Fenofibrate and Itraconazole to 4 for Ritonavir. The number of hydrogen bond acceptors ranged from 1 for Carbamazepine, 4 for Atenolol to 9 for Itraconazole. The melting point ranged widely between 45°C for orlistat and 81°C for fenofibrate, reaching 273°C for Theophylline and 288°C for Diclofenac sodium. The number of heteroatoms ranged from 2 for Estradiol to 14 for Aprepitant and Itraconazole. The number of Oxygen ranged from 1 for Nicotinamide and Carbamazepine to 6 for Nifedipine. Lipophilicity (logP) ranged from -0.77 for Theophylline to 10.57 for Probucol. An example of the variability in the chemistry of the APIs used in this model can be seen in Figure 68.

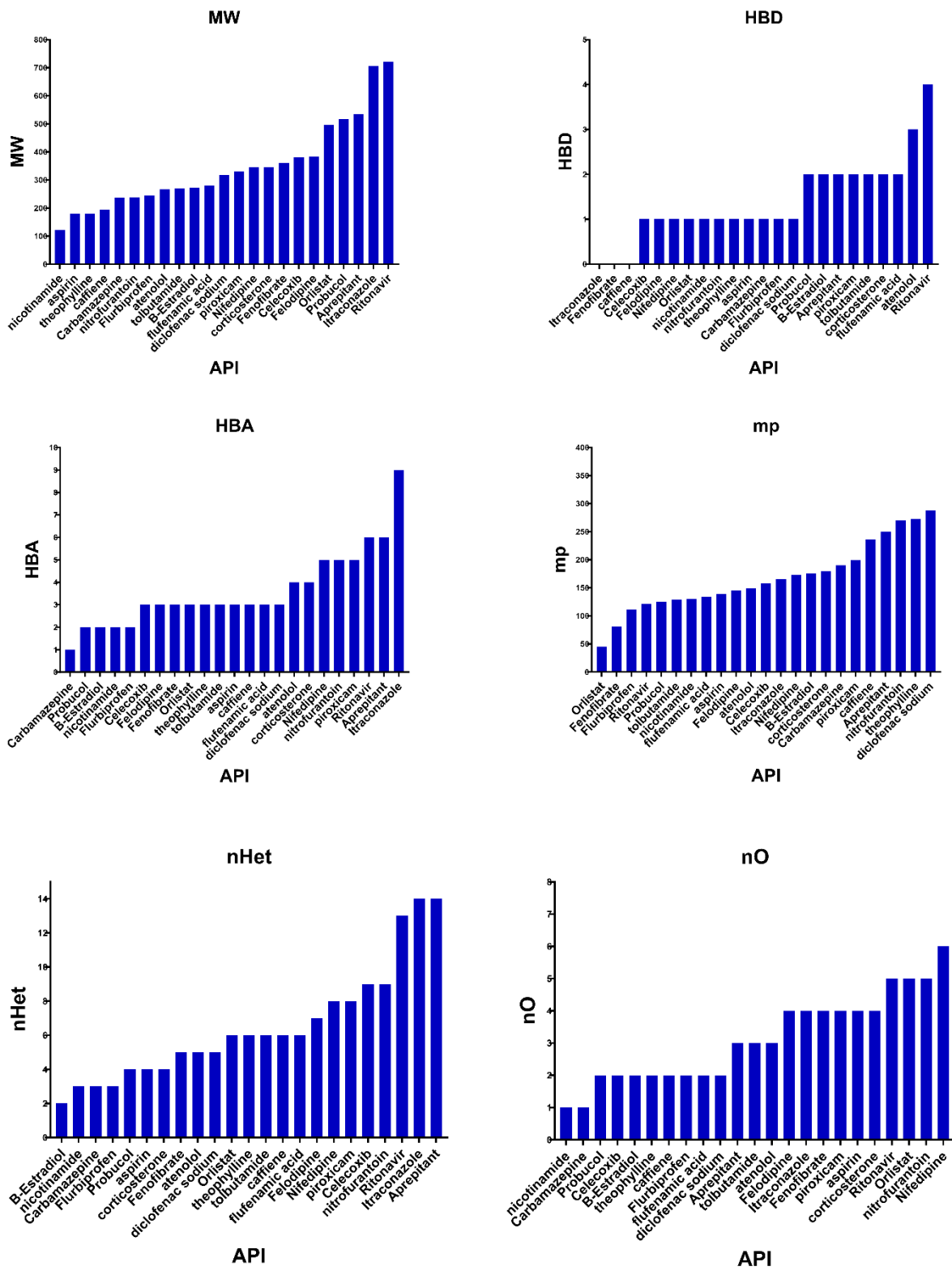


Figure 68. Variability in the chemistry of the physicochemical properties of APIs used in this model.

4.3.3 Explanation of the modelling process in R script

R and R Studio (version 1.0.143) were employed as tools to construct multiple linear regression (MLR) models to fit the experimental dataset. Specifically, calculated and predicted molecular parameters were employed as input variables in the regression models. This analytical approach involved the utilization of statistical modelling techniques and entailed combining data obtained from an accelerated stability study conducted over six months with the computed physicochemical attributes of the APIs. The physicochemical properties of the polymer are not included in our modelling process. Within this framework, MLR models were developed. A MLR model is a statistical technique used to understand the relationship between one dependent variable and two or more independent variables [276]. MLR assumes a linear relationship between the variables, meaning that the change in the dependent variable is expected to be a linear combination of the changes in the independent variables. In MLR, each independent variable is assigned a coefficient that quantifies its influence on the dependent variable. The model also includes an intercept term, representing the value of the dependent variable when all independent variables are zero.

For the outcome variable, a logarithmic transformation was used, applying the natural logarithm to the stability (stability in days + 1) and this is usually used to avoid long values unduly biasing the model. This transformation was implemented to mitigate issues related to zero values. To facilitate the selection of covariates for our regression models, the "leaps" package within R was harnessed. Employing exhaustive selection, a search was carried out to identify the most influential predictors, but the maximum number of covariates in each model was limited to three. To circumvent the challenge of linear dependency among covariates, the selected parameters were subjected to an assessment of intercorrelation. Whenever the correlation coefficient exceeded a threshold of 0.9, indicating a high level of multicollinearity, additional iterations of parameter selection were performed. Subsequently, these three parameters were leveraged to construct a

regression model, thus establishing a linkage between the physicochemical properties of the APIs and the natural logarithm of the measured stability of the solid dispersion formulation (the onset of crystallisation of the printed spots), which is representative of the time until the onset of crystallization.

4.3.4 Set-Up of the Model

4.3.4.1 Setting Up the Environment and Libraries

At the commencement of the analytical framework, the environment was initialized, focusing on configuring the knitr chunk options for optimal code chunk display (knitr is the engine in R Studio which creates the “dynamic” part of R reports and allows integration of R code into other formats, such as excel). These are sections in a document where the R code was entered. When creating the final report, the knitr function runs this code and adds the results, such as graphs or tables, into the report.

The primary dataset, saved in a .csv format after preliminary cleaning, consisted of three columns: the specific drug, its proportional mixture with the polymer, and the log stability. For instances where a drug failed to crystallize within the observed timeframe, a default value of 500 days for stability was used. While other values like 1000 or 10000 are potential alternatives, their potential implications on the analysis will be further discussed.

4.3.4.2 Data Collection and Initial Preprocessing

4.3.4.2.1 Data Sources

The obtained comprehensive dataset comprises 23 distinct drugs with 38 accompanying columns detailing their physicochemical attributes, all sourced from ChemAxon. Following this, the leaps library for statistical modelling was integrated. The collated data originated from two discrete .csv files, each symbolizing a batch of drugs mixed with a particular polymer: PVPVA or Soluplus.

4.3.4.2.2 Reading the Data

To assimilate this data into our workspace, the `read.csv` function facilitated the translation of these files into two distinct data frames: `fulldat.PVPVA` and `fulldat.soluplus`.

4.3.4.2.3 Dataset and Selection

An interactive module was embedded within the script, offering a choice among three datasets: **1)** PVPVA, **2)** Soluplus, or **3)** a combined set of PVPVA and Soluplus.

4.3.4.2.4 Percent of Drugs in Polymer Selection

Another interactive dimension of the script empowers users to select the range of drug percentages they wish to incorporate into the analysis. The options available are **1)** fixed percentages of 5, 10, 15, 20), **2)** a range of 5-50 in 5% increments, **3)** 5-100 in 5% increments, and **4)** 55-100 in 5% increments.

4.3.4.3 Data Transformation and Variable Definitions

4.3.4.3.1 Definition of Log Stability

The focal variable, log stability, is formulated as $\log_{\text{stability}} = \log_e(\text{days} + 1)$. Here, "days" represents the recorded time for crystallization obtained from the preceding chapter.

4.3.4.3.2 Data Exclusion and Inclusion

Post-data refinement, the dataset excluded columns that were either drug names or the all-zero column (FC). The polished dataset was subsequently stored as the data frame, `moldata`.

4.3.4.4 Modelling Process

The subsequent steps for the development of MLR models were followed:

4.3.4.4.1 Initial Modelling and model selection

The leaps library, coupled with the *regsubsets* function in R, was instrumental here. Notably, drug loadings at 0% were explicitly excluded, as using these descriptors to model pure polymer stability is impractical.

In R, the *regsubsets* function is part of the leaps package and is used for exhaustive search subset selection. It is employed to identify the best set of variables for an optimal linear regression model from a given set of predictors. This function assesses all possible models that can be constructed from the predictors and evaluates them based on several key metrics, such as the adjusted R^2 , BIC (Bayesian Information Criterion), and AIC (Akaike Information Criterion) to ascertain the robustness and suitability of our regression models. R^2 measures the proportion of the discrepancy in the dependent variable that is predictable from the independent variables, like a score that tells how well the model's predictions match the actual data. If R^2 is 1, the match is perfect, but if it is 0, the model does not match the data at all. It is hence a statistical indicator of the goodness of fit for the model. BIC and AIC are both ways to judge how good a statistical model is.

The results from the models fitted for each percentage are presented. To mitigate the risk of overfitting, especially given the relatively limited number of drugs (i.e. 23), our models were restricted to a maximum of four variables (comprising three variables and an intercept). Key statistical metrics like R^2 , BIC, and AIC were computed. Only variables with a t-ratio greater than 2 are retained. The t-ratio is a way to show if the investigated response/effect is likely to be real or just happened by chance. It is calculated by taking the size of the effect looked at and dividing it by how much this effect varies. A higher t-ratio means there is a higher chance that the effect is real. If the t-ratio is greater than 2, the effect will likely be real and not just due to random chance. The best model with a maximum of four variables was established for each drug loading percentage in the polymer. The coefficients in the model are shown. Different properties are

included in the model for different percentages of drug/polymer. The variables present in many models were considered as likely, indicating that these variables have linear associations with log stability over a range of percentages.

4.3.4.4.2 Tabulation of Frequency Results

Following the modelling, the output from the model selection step was organized and ranked by the frequency of terms appearing. That facilitated easy identification of the most recurrent terms.

4.3.4.4.3 Forward-Selection and Cross-Validation

A forward-selection strategy was executed to construct a model that elucidated all formulations based on percentage-loading. A leave-one-out cross-validation technique (LOOCV) was adopted to identify the best model, referred to as the “ML model”.

4.3.4.4.4 Final Model Building

The derived “ML model” was then applied to all data using a multiple linear regression approach, ensuring that while the terms remained constant, the coefficients were allowed variation based on composition.

4.4 Results and Discussion

4.4.1 Using a selection of PVPVA data

4.4.1.1 Frequency of the variables

Twenty multiple linear regression models, one model for each drug/polymer were developed. Looking for variables that are present in many of the models, as these should indicate that the variables have associations with log stability over a range of percentages. The selection of variables from the PVPVA data spanning drug-polymer loadings from 5-100% at 5% increments showed various frequencies in the MLR model. Table 19 summarizes the frequency of each of

these physicochemical properties. It is evident that certain properties, such as HBA, nHet, and nO, were more frequently incorporated into the models than others, such as nN, nAtom, and vdW.SA.

Table 19. The frequency table shows the variability in the physicochemical properties, as appeared in the 20 models (one model at each drug/polymer loading) using PVPVA stability data and drug-polymer loadings from 5-100% for the 23 employed APIs in this study.

Physicochemical property	Frequency of each variable as appeared in the 20 models
HBA	11
nHet	10
nO	10
mp	6
ASA	4
MRef	4
MW	4
MAxProjRad	3
nHet.ring	3
vdW.Vol	3
FSP3	2
LogS0 at.7.4	2
MaxProjArea	2
MinProjArea	2
nAliphRing	2
avPol	1
nAtom	1
nHeavy	1
nN	1
vdW.SA	1

The frequency with which physicochemical properties appeared in the MLR models offers insights into their potential significance or influence on drug stability. For instance:

- High-frequency properties: HBA, nHet, and nO were the most frequent, appearing in more than half of the models. That suggests that these properties may have a significant impact on the stability of drugs in PVPVA.
- Medium-frequency properties: Properties such as mp, ASA, MRef, and MW have a moderate appearance. They may play a secondary role in influencing ASD stability.

- Low-frequency properties: Those appearing once or twice, like avPol, nAtom, and vdW.SA might have a lesser or specific role in determining stability, or their influence could be conditional based on other factors.

4.4.1.2 Final Model Choice

Using the data collected for all the compositions, we tried to develop one equation that is the best to represent our model. The best model for the PVPVA dataset, chosen for minimizing the MSE, is characterized by the following equation:

$$\log\text{stability} = \text{intercept} + c_1 \times n\text{Het} + c_2 \times \text{HBA} + c_3 \times n\text{O} + c_4 \times mp$$

as:

- HBA represents the number of hydrogen bond acceptors.
- nHet is the number of heteroatoms.
- nO is the number of oxygen atoms.
- mp is the melting point.
- c_1 , c_2 , c_3 and c_4 are the coefficients for each variable.

4.4.1.3 Model Performance and Selection

Mean squared error (MSE) is a widely used measure for evaluating the accuracy of a predictive model. It is a key metric for assessing how well a predictive model performs, especially in regression analysis. That is achieved by calculating the distances between the points and the regression line (referred to as "errors") and then squaring these distances. Squaring the distances serves the purpose of eliminating any negative values. MSE is calculated as the average of the squares of the errors [277]. The model's performance was evaluated through LOOCV, yielding a MSE of 3.711. The "error" in our study is the difference between the measured log stability values and the predicted log stability values generated by the model. A lower MSE value indicates a better

fit of the model to the data (i.e., the predictions are closer to the actual /measured values). However, MSE is sensitive to outliers because of the squaring part of the formula.

This model was selected after extensive testing and fitting to subsets of data for different drug loadings. The representative equation for each drug/polymer loading and the adjusted R² values are detailed in Table 20 and illustrated in Figure 70. This approach underscores the aim to establish a dependable model for predicting the log stability of various drug compositions.

Table 20. Equations extracted from the model using the PVPVA data set and all drug/polymer loadings 5 to 100%.

Drug/polymer loading	Equation	Adjusted R ²
5	logstability= 6.996475 +0.246874 HBA -0.059707 nHet + 0.108801 nO -0.012858 mp	0.1906
10	logstability= 6.719668 +0.191279 HBA +0.02490 nHet + 0.130794 nO -0.016460 mp	0.2197
15	logstability= 8.506367+0.122059 HBA +0.138404 nHet -0.258290 nO -0.024924 mp	0.3289
20	logstability= 9.476716 -0.148043 HBA +0.311623 nHet -0.265762 nO -0.033630 mp	0.5874
25	logstability= 7.794643 -0.992177 HBA +0.591371 nHet +0.227512 nO -0.028057 mp	0.5338
30	logstability= 7.704040 -1.270611 HBA+ 0.699285 nHet+ 0.310144 nO -0.028329 mp	0.6001
35	logstability= 7.802053 -1.482707 HBA+ 0.786873 nHet + 0.332984 nO -0.028699 mp	0.6241
40	logstability= 6.272624 -1.775292 HBA+ 0.921450 nHet + 0.575989 nO -0.025085 mp	0.6546

45	logstability= 3.690459 -1.865890 HBA+ 0.936704 nHet+ 0.948554 nO -0.018149 mp	0.6354
50	logstability= 3.376875 -1.900602 HBA+ 0.959294 nHet + 0.992693 nO -0.017569 mp	0.6343
55	logstability= 2.869633 -1.851043 HBA+0.972986 nHet + 0.918478 nO -0.016115 mp	0.6187
60	logstability= 2.738579 -2.057051 HBA+ 1.050360 nHet + 0.903640 nO -0.014844 mp	0.6217
65	logstability= 2.816804 -2.055402 HBA+ 1.056535 nHet+ 0.885434 nO -0.015492 mp	0.6278
70	logstability= 2.579960 -2.072312 HBA+1.101958 nHet+ 0.819226 nO -0.014995 mp	0.6342
75	logstability= 2.583526 -2.057554 HBA+ 1.099058 nHe + 0.830711 nO -0.015733 mp	0.6321
80	logstability= 1.852182 -2.018366 HBA+ 1.100582 nHet+ 0.900466 nO -0.014425 mp	0.6629
85	logstability= 2.287267 -2.029673 HBA+1.142115 nHet + 0.711278 nO -0.015562 mp	0.6782
90	logstability= 2.085831 -2.002394 HBA+ 1.146997 nHet+ 0.724524 nO -0.015922 mp	0.6867
95	logstability= 2.263351 -2.069877 HBA+ 1.181978 nHet + 0.696395 nO -0.016566 mp	0.691
100	logstability= 2.154057 -1.843040 HBA+ 1.074906 nHet+ 0.628304 nO -0.016293 mp	0.6749

Each row in Table 20 represents a specific outcome of the overarching MLR model tailored for varying drug-in-polymer loadings. Though the structural format of the model remains consistent

(i.e., log stability as a function of HBA, nHet, nO, and mp), each drug loading value has its own set of coefficients reflecting the unique contribution of the physicochemical properties at each drug loading.

Figure 69 shows the percentage of samples that showed crystallization within the experimental dataset that encompasses results from experiments conducted with 23 drugs, each at 20 different drug-polymer loadings in triplicate and using two different polymers at different drug loadings from 5 to 100 w/w% (representing all the data that will be used in the model for all APIs within the two polymers). The figure shows that as the drug loading increases, so does the percentage of samples that crystallise, as would be expected due to the increased statistical likelihood of drug molecules to nucleate within the dispersion given a certain level of molecular mobility. Starting with the lowest percentage (around 5%) of samples that showed crystallization at 5% drug loading, the trend increases steadily, reaching around 80% of samples showing crystallization at 100%.

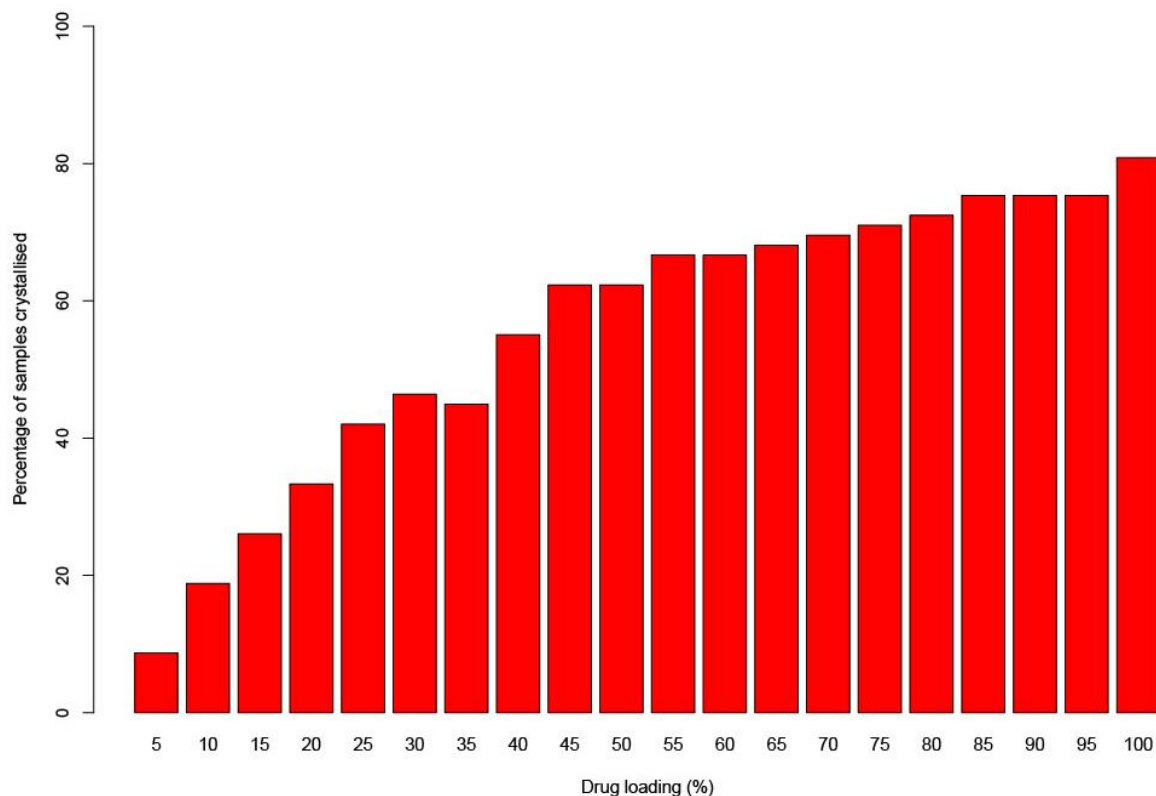


Figure 69. The Percentage of crystallization observed in drug samples at various drug loadings within the two polymer matrices (PVPVA and Soluplus) as within the whole data set. This bar graph illustrates the experimental data collected for multiple drugs, showcasing the frequency of crystallization events as a function of drug loading percentages. Each bar represents the proportion of samples that exhibited crystallization at specified drug loading levels.

Figure 70 shows the fitted R^2 extracted from the multiple linear regression model for the PVPVA data set, using all drug/polymer loadings (5-100% with 5% increment) for 23 employed APIs. The adjusted R-squared values offer valuable insights into the model's predictability across different drug/polymer loadings. At the outset, with lower drug loadings (around 5%), the model has an adjusted R-squared value of 0.19, indicating that nearly 19% of the variability in the log stability is captured by the model. As we transition to higher drug loadings, the adjusted R^2 values exhibit a consistent increase, culminating at a value of 0.69 at 95% loading. That implies that for formulations with 95% drug loading, the model can account for approximately 69% of the variability in log stability. As the model is sensitive to the effects of molecular interactions within a dispersion, as the number of drug molecules increases with loading it is reasonable that the

models are able to fit experimental outcomes to a greater extent. Additionally, it could be that at higher drug loading we have more actual data in numbers which are different among the different loadings instead of (N as no crystallization). In addition, if a threshold of drug loading is exceeded (e.g. maximum solubility of drug in the polymer) either locally or in the bulk then processes related to physical instability will change and provide an additional impact on the model.

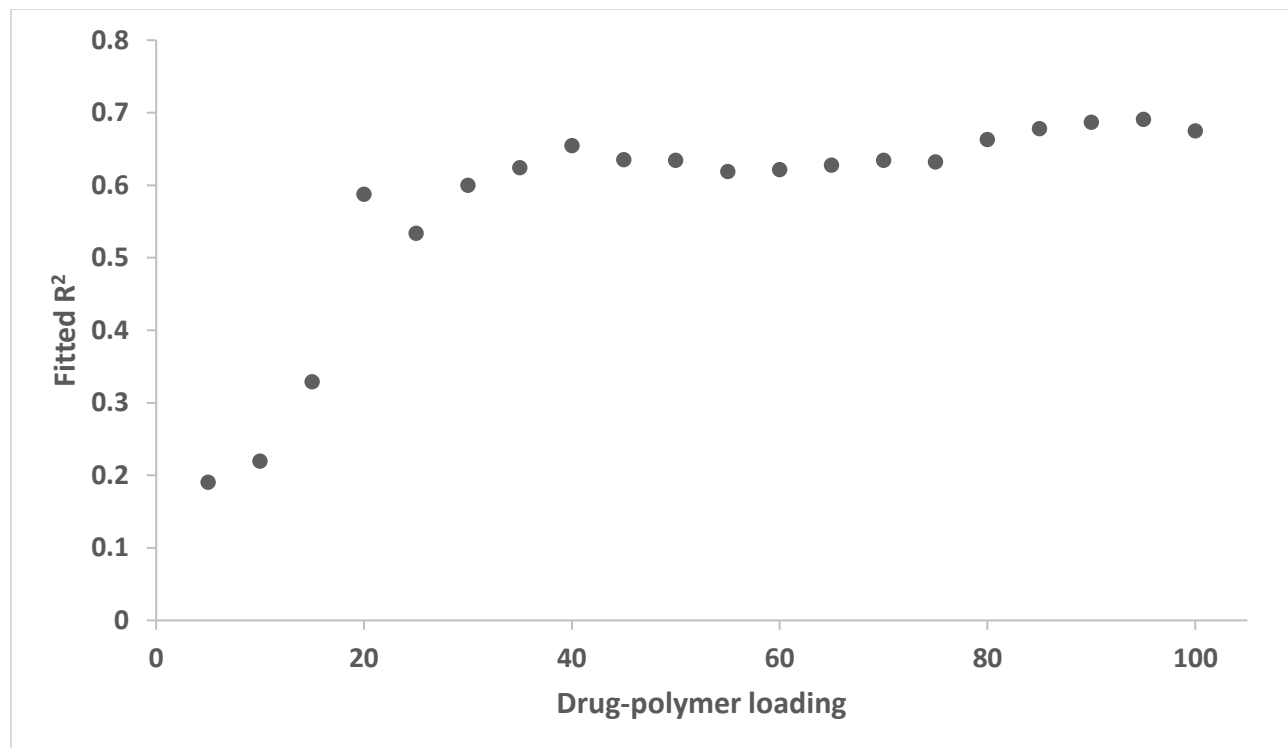


Figure 70. Fitted R² extracted from the multiple linear regression model for the PVPVA data set, using all drug/polymer loadings (5-100% with 5% increment) for 23 employed APIs.

To a degree, this mirrors the higher propensity for recrystallization – as ascertained from the experimental data collected - of these formulations compared to their lower-loaded counterparts, as shown in Figure 69. The adjusted R² values serve as a metric for the model's goodness of fit. Across the drug/polymer loading spectrum, these values show a consistent increase, peaking at 95% drug loading. The four variables were chosen as they showed the highest frequency while developing the model and we entered that condition in the R script.

4.4.1.4 Coefficients

Figure 71 to Figure 75 show the fluctuation in coefficients for the key model parameters as a function of drug loading in the formulations. That enables an understanding of how different descriptors contribute to log stability at various drug loadings. The coefficients vary in a reasonably regular manner as a function of composition.

- **Hydrogen bond acceptors (HBA):** The coefficient is a function of drug loading as the stability results collected at each API/ polymer loading for all the APIs differ, hence the coefficient extracted differs. As shown in Figure 71, the contribution of hydrogen bond acceptors (HBA) is very low in magnitude in the range of 5-20 % drug loading, after which it rapidly becomes more prominent but in a negative value up to around 40%, above which the contribution of this term remains relatively constant. Since the coefficient grows in magnitude, it suggests that HBA increasingly negatively affects (negatively correlated) the stability of ASD at higher drug loadings, presumably when exceeds the solubility limit of the drug in the polymer.

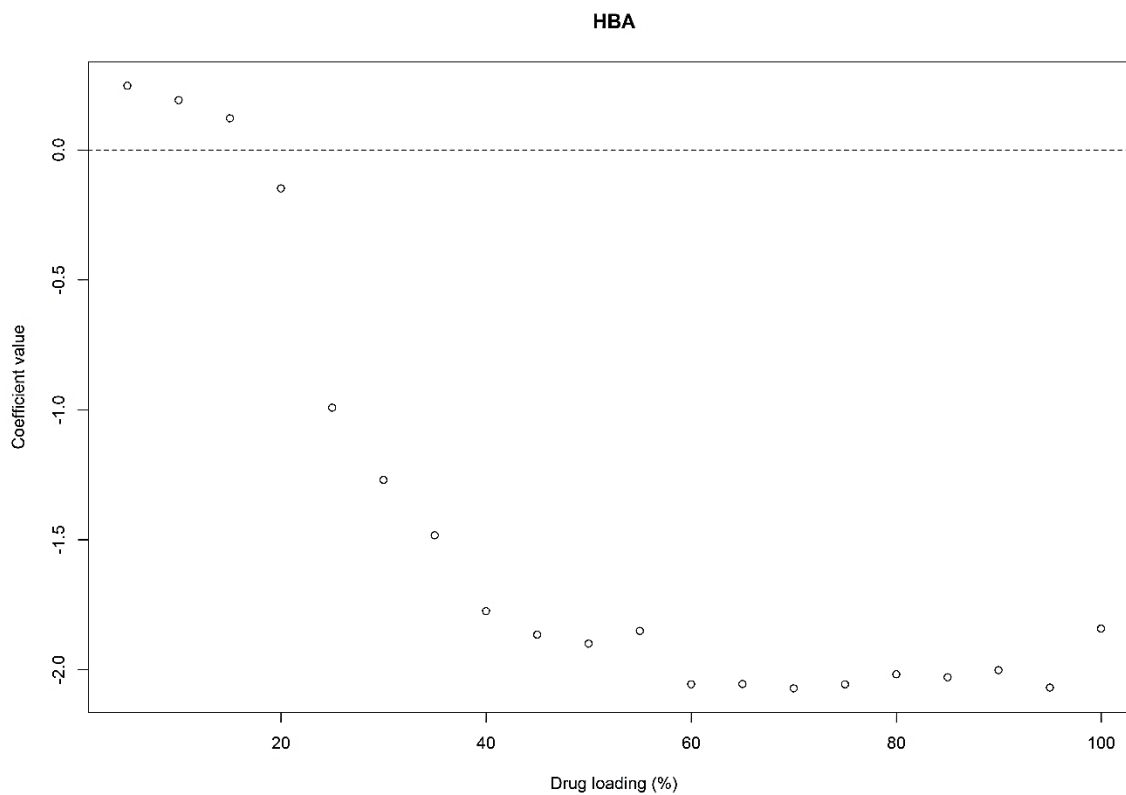


Figure 71. Scatter plot of coefficient values for hydrogen bond acceptors (HBA) variable obtained from multiple linear regression analyses across 23 different drugs at varying drug/polymer loadings from 5 to 100% using the data collected from the two polymers.

- The number of Oxygen atoms (nO):** As shown in Figure 72, the number of oxygen atoms in a given drug molecule has a near-zero contribution to stability at low drug loadings (0 to perhaps 35% loading), above which it becomes a positive correlation. The rise in coefficient indicates that having more oxygen atoms is positively linked to the stability of the ASD.

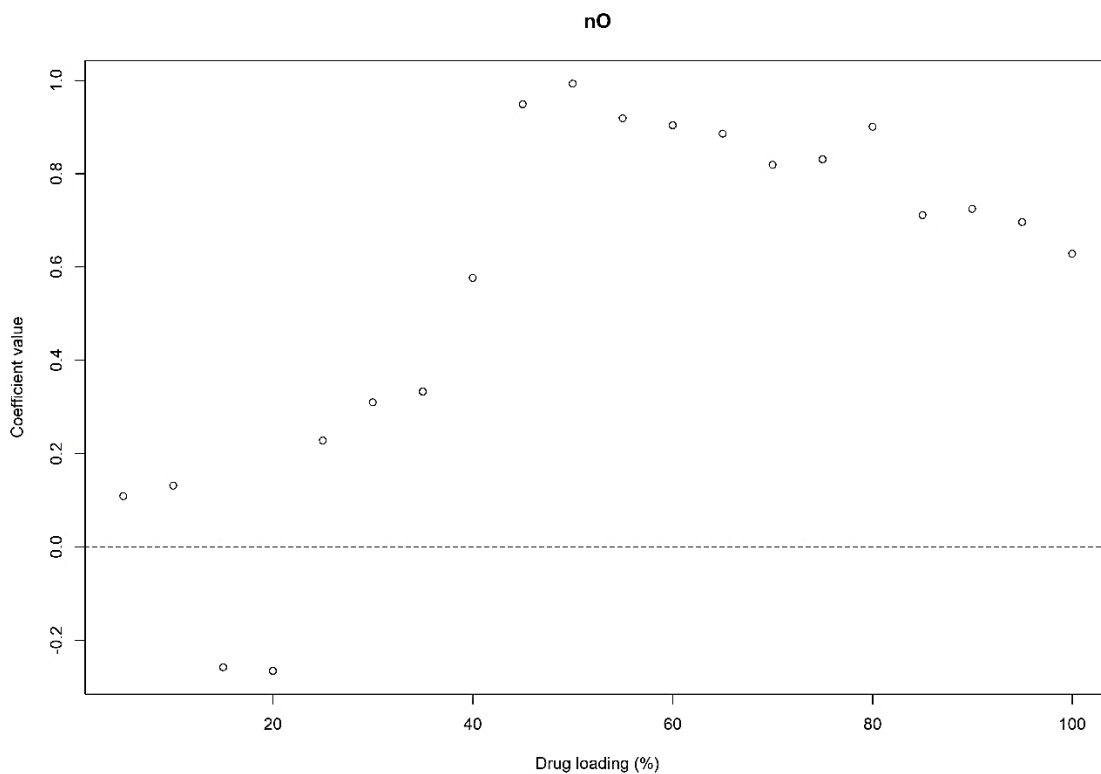


Figure 72. Scatter plot of coefficient values for the number of Oxygen atoms (nO) variable obtained from multiple linear regression analyses across 23 different drugs at varying drug/polymer loadings from 5 to 100%.

- The number of heteroatoms (nHet):** As shown in Figure 73, the contribution of the number of heteroatoms (nHet) is very low in magnitude in the range of 5-20% drug loading, after which it rapidly becomes larger above 20%, increasing up to around 60%, above which the contribution of this term remains relatively constant. The number of heteroatoms in the drug molecule has a rapidly increasing (and positive) effect on the stability of ASD formulations up to about 40% drug loading, implying that the increased number of heteroatoms in drug molecules enhances the stability of ASDs.

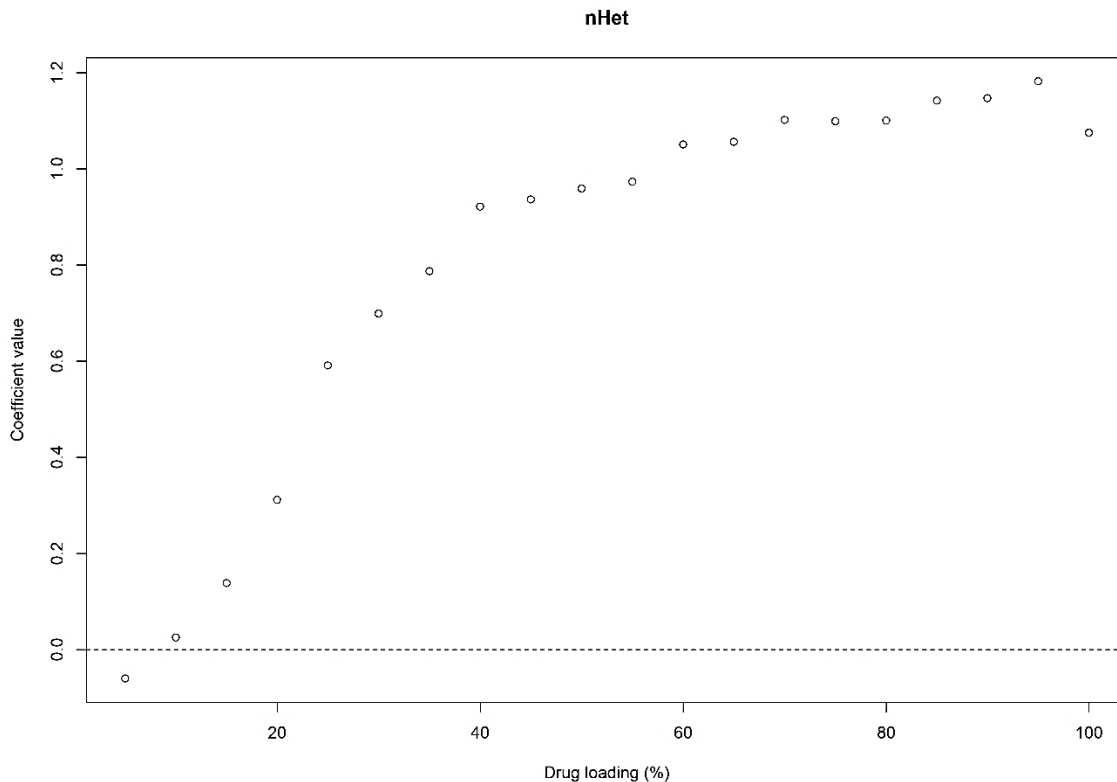


Figure 73. Scatter plot of coefficient values for the number of heteroatoms (nHet) variable obtained from multiple linear regression analyses across 23 different drugs at varying drug/polymer loadings from 5 to 100%.

- Melting point (mp):** As shown in Figure 74, the scatter plot displays the relationship between drug loading percentages and the coefficient values for the mp of various drugs within a polymer matrix. The coefficient values range from just below 0 to slightly negative values as drug loading increases from 0% to around 60%. After 60% drug loading, the coefficient values are around the zero line, suggesting negligible influence. While the coefficient values for the melting point are negative, they are relatively small in magnitude, especially when compared to some of the other variables. However, this results from the data used for the melting point being of a greater magnitude than the other data, which is also considered for the equation for log stability. As the values are not so close to zero as to be considered negligible for all loadings, mainly up to 60% drug loading, where the melting point negatively influences stability. This suggests that (from our data and analysis) low melting point drugs tend to be more stable in ASD formulations in PVPVA

formulations than drugs with higher melting points for typical pharmaceutical loadings (5-25 %).

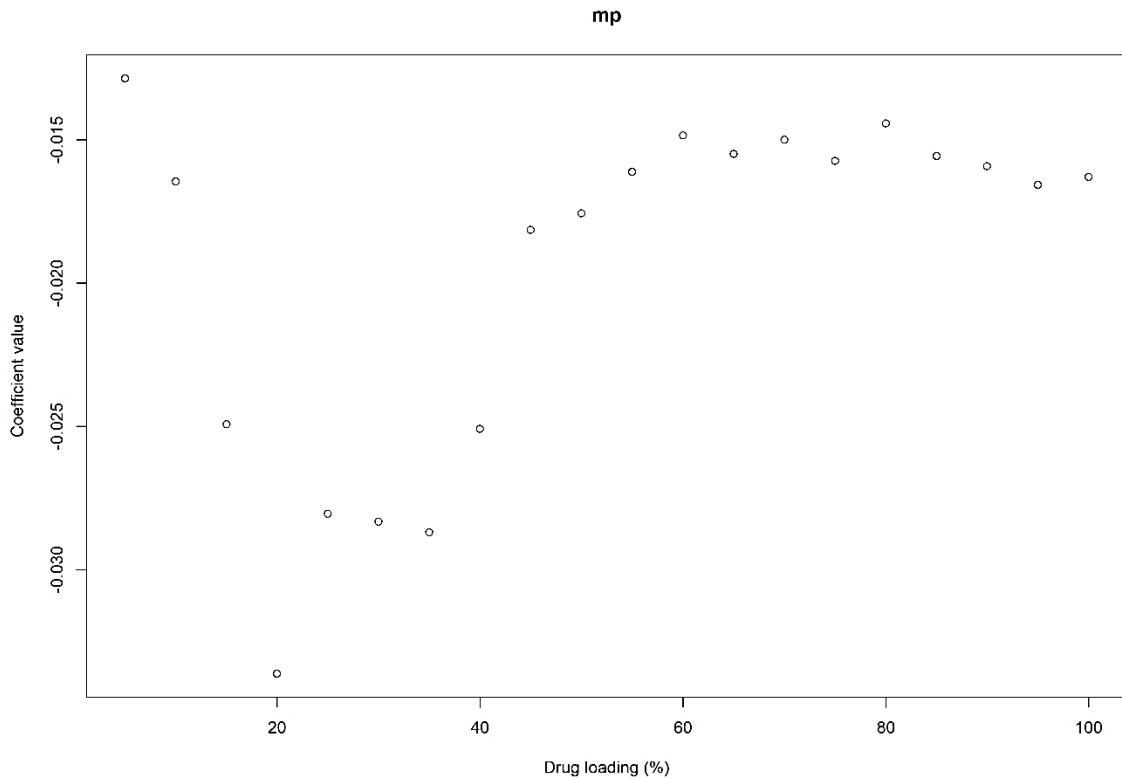


Figure 74. Scatter plot of coefficient values melting point (mp) variable obtained from multiple linear regression analyses across 23 different drugs at varying drug/polymer loadings from 5 to 100%.

- **Intercept:** Figure 75 presents a distinct change in intercept as a function of drug loading. The intercept shows high values at lower drug loadings; then, there is a marked shift to a lower intercept plateau above 40% drug loading. The drop in the values of the intercept is because more samples crystallize at higher drug loadings, so the intercept would not be so high (as the log-stability numbers are lower due to the drugs that crystallize).

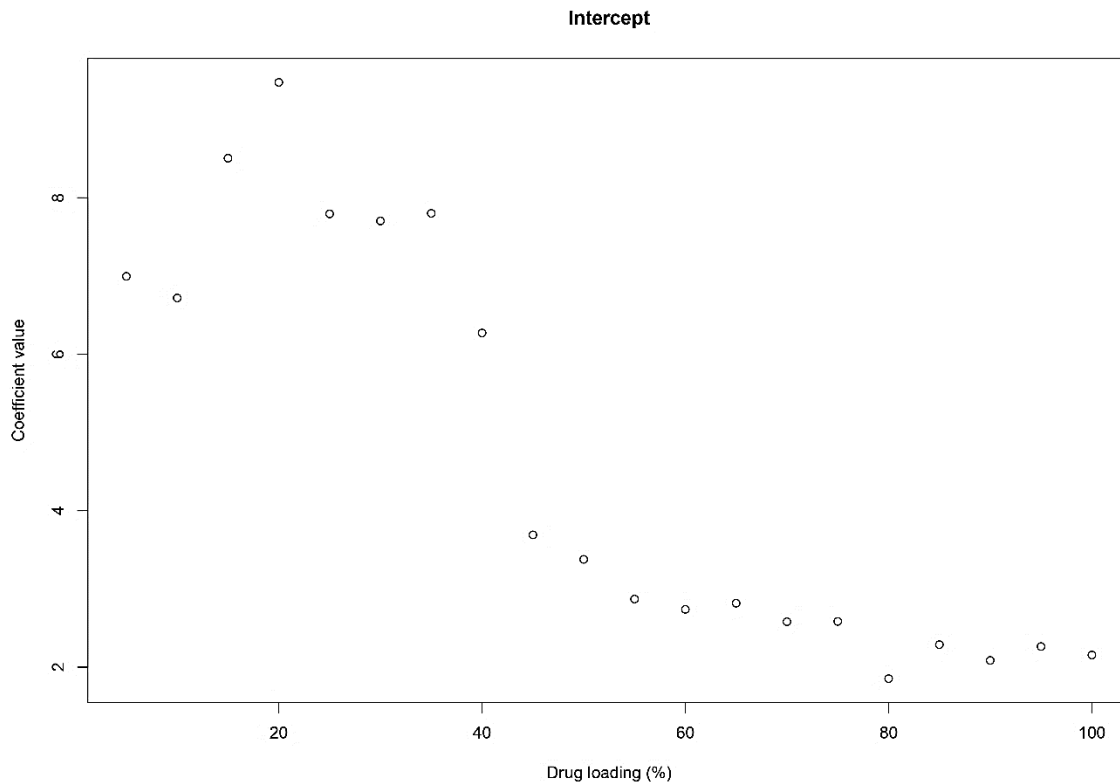


Figure 75. Scatter plot of intercept values obtained from multiple linear regression analyses across 23 different drugs at varying drug/polymer loadings from 5 to 100%.

Key Insights:

1. **HBA** becomes increasingly negative with drug loading, making it a significant factor in decreasing stability as drug loading increases. One plausible interpretation of the negative coefficient associated with drug HBAs could be the potential for repulsive interactions between the HBAs on the drug molecules and those on the polymer. Such repulsion could arise due to the electrostatic nature of the HBA groups, which are electron-rich regions that could resist being close to each other due to electron cloud repulsion. This HBA-HBA repulsion might disrupt the uniform dispersion of the drug within the polymer matrix, leading to phase separation or aggregation of the drug molecules. As the drug loading increases, the concentration of HBAs within the formulation rises, potentially exacerbating these repulsive interactions. This could culminate in the formation of drug-rich domains

within the ASD, which are more prone to crystallization, thereby reducing the overall stability of the dispersion.

2. **nO** has a late-emerging positive correlation effect, suggesting it might enhance stability in higher drug loadings, possibly due to their impact on the electronic distribution and the interactions within the polymer matrix.
3. **nHet** has a strong positive effect on stability, especially in the mid and higher drug loading range. This could be attributed to increased molecular flexibility and a reduced tendency for crystalline alignment.
4. **mp**: Lower melting points (more negative values (zero towards the top of the figure)) seem beneficial for stability, especially in lower drug loadings. A lower melting point suggests a lower intra-molecular bonding in the crystal structure and hence a lower energy gain for crystallisation within the matrix and hence improved stability.

As stated in terms of typical pharmaceutical use, drug loadings of 5-20 % w/w in solid dispersions are typical (i.e. below the solubility limit), and for these loadings, our model suggests from the values of coefficients and the significance of each parameter at each single drug/polymer loading obtained from running the script

1. HBA is relatively less important
2. nO is relatively less important
3. Low values of mp lead to better stability when formulated with PVPVA
4. nHet correlates positively with stability, especially between 15-20% drug-loading.

For drug loadings here above 20 or 25%, which represent more concentrated pharmaceutical formulations, our analysis of the data suggests the following:

1. The number of HBAs correlates negatively with the stability of formulations.

2. The presence of oxygen atoms correlates positively with the stability of the formulations
3. mp is relatively less important
4. nHet correlates positively with stability, especially at higher drug loadings.

The model parameters and R^2 values indicate that the model is most appropriate for predicting the stability of high drug loadings (above ca. 40%) rather than lower drug loadings. Therefore, the model-building process was repeated, using only input data from 5 to 20 and 5 to 50 % drug loading. However, the 5 to 20 % input data yielded a model with no consistent trends or features in which the values of the various coefficients were scattered around zero, suggesting that data capable of differentiation of stability behaviour at these loadings had not been determined in this specific study.

4.4.1.5 Effects of setting a non-crystallised drug (i.e. a null result) at 500 days

To investigate whether describing the formulations that did not show crystallisation as having a stability of a nominal 500 days (ca. 1.5 years) was adversely affecting the ML output, modelling trials were run with the non-crystallising drug stability set at 1000 days (ca. 2.7 years), 10,000 days (ca. 27 years) and 100,000 days (ca. 273 years). Results were compared with the output from the 500-day-based models.

When comparing results from baseline stability of 500 days to other extended stabilities (1000 days, 10,000 days, and 100,000 days), it was observed that the model's selected parameters remained consistent. Namely, HBA, nO, nHet, and mp were the recurrently chosen descriptors. This suggests that assigning different stability values to non-crystallized formulations within the tested stability range does not significantly alter the key model parameters and 500 days was a reasonable choice. However, it is worth noting that while the variables selected remained

consistent, the exact coefficient values, predictive performance, and model dynamics might exhibit variations based on the assigned stability durations.

4.4.1.6 Correlation matrix of log stability within PVPVA and predictor variables and the correlation between the variables and each other

Figure 76 presents a matrix depicting the pairwise correlations between several predictor variables (mp, nHet, HBA and nO) and the 'log stability' variable. This matrix serves as a preliminary examination tool to discern the relationships between the variables before regression analysis.

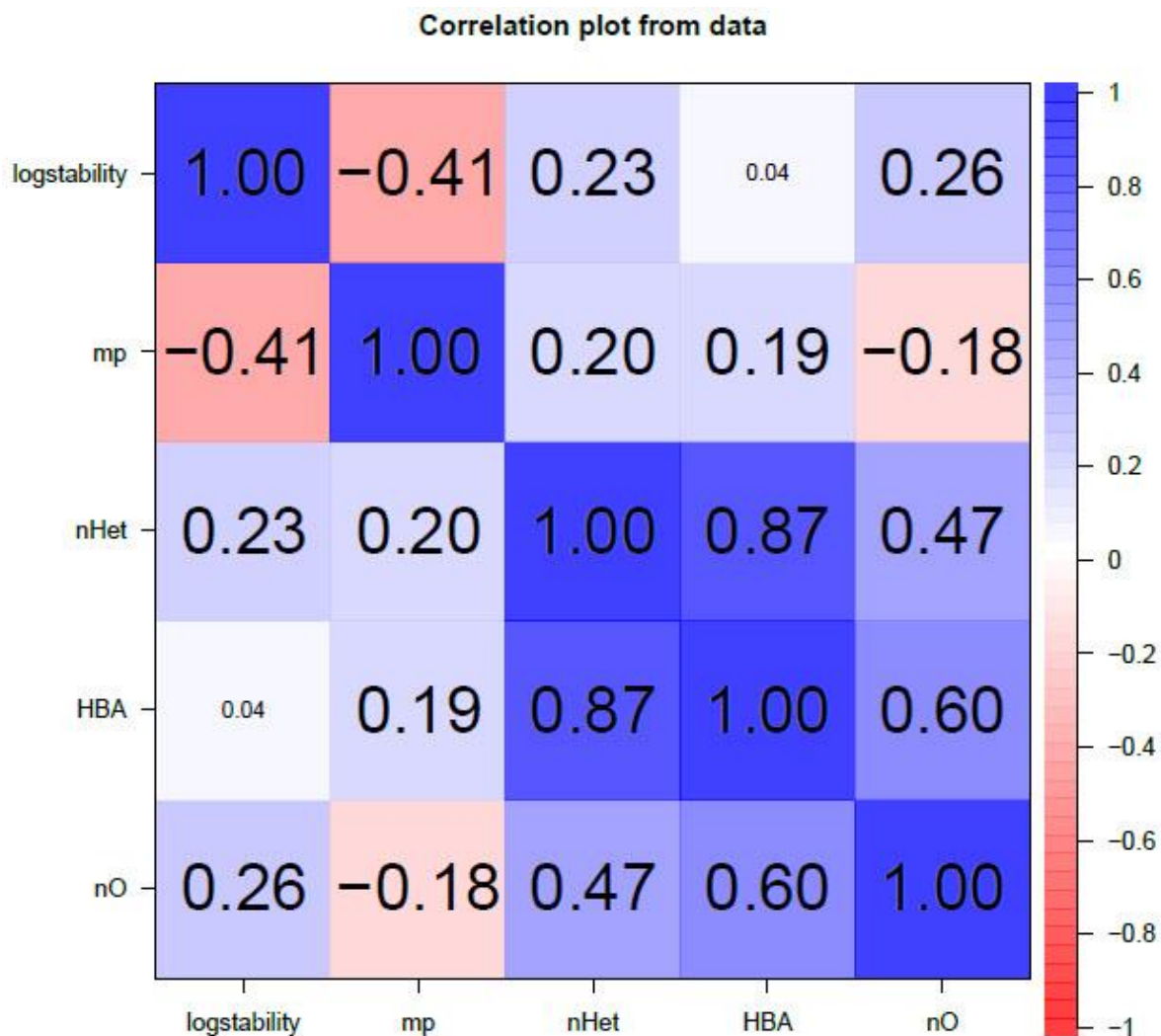


Figure 76. The correlation matrix displays the pairwise correlations between the predictor variables and log stability within PVPVA. Each cell represents the correlation coefficient between the corresponding variables. These correlations are not derived from the linear regression model. (mp: melting point, nHet: number of heteroatoms, HBA: number of hydrogen bond acceptors and nO: number of oxygen atoms).

The matrix utilizes a colour gradient where deep blue indicates a positive correlation near +1, deep red indicates a negative correlation near -1, and white shows no or minimal correlation. This gradient provides a visual means to discern the strength and direction of each correlation. The numerical values within each cell are the actual correlation coefficients, ranging between -1 and +1. A value of 1 or -1 indicates a perfect linear relationship, whereas a value closer to 0 suggests little to no linear correlation.

High correlation values, whether positive or negative, can suggest potential multicollinearity if these variables are used together in a regression model. Multicollinearity can make it difficult to discern the individual effect of each predictor on the response variable. Therefore, these correlations offer initial insights into which variables need further scrutiny or consideration when building regression models.

Log stability shows a negative correlation of -0.41, with mp suggesting a negative, while a correlation of 0.23 indicates a weak positive relationship. In addition, log stability shows a very weak correlation of 0.04 with HBA, which is almost negligible, and a correlation of 0.26, suggesting a weak positive relationship with nO.

The mp exhibits weak positive correlations with nHet (0.20) and HBA (0.19) and a weak negative correlation with nO (-0.18), while nHet and HBA show a strong positive correlation (0.87), indicating. The nHet also has a moderate positive correlation with nO (0.47), while HBA and nO display a moderate positive correlation (0.60).

Upon evaluating the correlation matrix, the variables demonstrate varying degrees of association, none of which approach values suggest multicollinearity. The highest correlation observed does

not breach the critical threshold commonly considered in multiple linear regression analyses, around 0.9. Thus, given their interrelationships, these variables appear well-suited for inclusion in the multiple linear regression model, ensuring the results are robust and reliable.

All correlations in this matrix are just linear (not done by multiple linear regression), meaning they describe the strength and direction of a straight-line relationship between two variables. However, actual interactions and correlations could be more complex when all variables are considered simultaneously in a regression framework to capture non-linear associations. This has been developed using multiple linear regression in our study.

4.4.1.7 LOOCV for log stability in PVPVA drug loading

The LOOCV approach was utilized to assess the accuracy and reliability of our model [278]. This approach involves sequentially removing the data for a single drug and applying the model to the remaining dataset. The omitted drug's data was then used to validate the model. This process was repeated for each drug in the dataset, ensuring a robust evaluation of the model's performance. Results from the LOOCV are summarized in Table 21.

Each drug has an associated equation that predicts its log stability based on different variables.

The overarching model equation used in this study was

$$\log\text{stability} = \text{intercept} + c_1 \times n\text{Het} + c_2 \times \text{HBA} + c_3 \times n\text{O} + c_4 \times mp$$

This equation served as the baseline against which individual drug equations were compared.

Across all drugs, various variables were tested for their contribution to the model's predictive power. HBA, nHet, nO, and mp were the most frequently included variables across drug-specific equations. The presence (indicated by TRUE) or absence (indicated by FALSE) of each variable for a specific drug denotes its significance for that drug's log stability prediction within the model.

Table 21. Summary of the models' equations extracted using the LOOCV and the variables adopted in each equation for each of the 23 APIs used in this study within the PVPVA matrix. Where mp is the melting point, nHet is the number of Hetero atoms, nO is the number of oxygen atoms, HBA is the number of hydrogen bond acceptors, Mref is molar refractivity, and MW is the molecular weight.

Drug name	Equation	HBA?	mp?	nHet?	nO?
Aprepitant	logstability ~ HBA + nHet + nO + mp	TRUE	TRUE	TRUE	TRUE
Orlistat	logstability ~ HBA + ASA + nHet + nO + mp + maxProjArea + MRef + MW	TRUE	TRUE	TRUE	TRUE
Nifedipine	logstability ~ HBA + MW+ ASA + MRef + mp	TRUE	TRUE	FALSE	FALSE
Estradiol	logstability ~ HBA + nHet + nO + mp	TRUE	TRUE	TRUE	TRUE
Felodipine	logstability ~ HBA + nHet + mp	TRUE	TRUE	TRUE	FALSE
Fenofibrate	logstability ~ nHet + HBA + mp + nArRing + MinProjRad + MW + maxProjrad	TRUE	TRUE	TRUE	FALSE
Celecoxib	logstability ~ HBA + MW + nO + MRef+ mp	TRUE	TRUE	FALSE	TRUE
Probucol	logstability ~ HBA + nHet + MRef+ MW + mp	TRUE	TRUE	TRUE	FALSE
Ritonavir	logstability ~ HBA+ nHet + MW + mp + nO + MRef	TRUE	TRUE	TRUE	TRUE
Itraconazole	logstability ~ mp + HBD + MaxProjArea + MW	FALSE	TRUE	FALSE	FALSE
Nicotinamide	logstability ~ HBA+ nHet + MW + nO + mp	TRUE	TRUE	TRUE	TRUE
Nitrofurantoin	logstability ~ nHet + HBA+ Log S0 at 7.4 + nO	TRUE	FALSE	TRUE	TRUE
Piroxicam	logstability ~ HBA + nHet + mp + Mref + MW	TRUE	TRUE	TRUE	FALSE
Theophylline	logstability ~ HBA + nHet + mp	TRUE	TRUE	TRUE	FALSE
Tolbutamide	logstability ~ HBA + nHet + ASA + mp	TRUE	TRUE	TRUE	FALSE
Aspirin	logstability ~ HBA + nHet + ASA + mp + MW + MRef + MaxProjArea	TRUE	TRUE	TRUE	FALSE
Atenolol	logstability ~ HBA+ nHet + Log S0 at 7.4 + mp + Mref + MW + nHetRing	TRUE	TRUE	TRUE	FALSE
Caffeine	logstability ~ HBA + nHet + mp + ASA + Mref + MW	TRUE	TRUE	TRUE	FALSE
Carbamazepine	logstability ~ nHet + HBA + nO + MinProjArea + nCl + mp + nAtom + nC	TRUE	TRUE	TRUE	TRUE
Corticosterone	logstability ~ HBA + nHet + mp + Mref + MW + nO	TRUE	TRUE	TRUE	TRUE
Flufenamic acid	logstability ~ HBA + nHet + mp	TRUE	TRUE	TRUE	FALSE
Flurbiprofen	logstability ~ HBA + nHet + mp+ ASA+ Mref+ MW+ MaxProjRad	TRUE	TRUE	TRUE	FALSE
Diclofenac sodium	logstability ~ HBA + nHet + ASA + MinProjArea + mp + MW + nAtom + nO + avPol	TRUE	TRUE	TRUE	TRUE
Frequency		22	22	20	10
Model equation	logstability ~ HBA + nHet + nO + mp	HBA	mp	nHet	nO

For instance, Carbamazepine and Diclofenac sodium incorporate all the variables in the overarching model, with additional variables for a more precise prediction. In contrast, drugs such as Fenofibrate and Celecoxib exclude one or more variables from the general model, indicating a different interaction pattern within the PVPVA polymer loading.

The last row of Table 21 provides a count of how often each variable appeared as significant across all drug equations. For example, the variable HBA was significant in 22 out of the total number of drugs tested, suggesting its significant importance in log stability predictions for drugs within the PVPVA polymer.

The LOOCV approach provided valuable insights into variables' individual and collective significance in predicting log stability for various drugs in the context of PVPVA polymer loading.

The variability in drug equations underscores the importance of considering drug-specific interactions and characteristics when predicting their stability. The consistent appearance of certain variables across multiple drugs also highlights these factors' potential generalizability and importance in a broader context.

4.4.1.8 Comparative analysis of predicted vs. measured stability across various drug formulations using LOOCV

Figure 77 and Figure 78 present a comprehensive comparison of the log stability predicted using multiple linear regression and LOOCV versus the experimentally measured log stability for eight distinct drugs that showed different crystallisation behaviours experimentally within the PVPVA polymeric matrix.

4.4.1.8.1 Theophylline

Figure 77 (A) shows the predicted log stability versus the measured for Theophylline/PVPVA across different loadings. The measured log stability for Theophylline (which is the same in the case of Caffeine) indicates immediate crystallization at all drug/polymer loadings from 5% to

100%. Hence, Theophylline, as a dispersion in PVPVA, is highly unstable across all loadings. In contrast, the predicted log stability for Theophylline starts with a pronouncedly high value for the lower drug/polymer loadings. Then, a rapid decline in predicted stability is observed at around 20% loading, gradually reducing further as the drug loading increases. Mostly, the immediate crystallization observed across all drug loadings in those APIs that produced zero values of the measured stability created some notable discrepancies against predicted values. This discrepancy suggests that the prediction model may not be reliable for Theophylline and Caffeine or may need further refinement and calibration.

4.4.1.8.2 Nitrofurantoin

Figure 77 (B) shows the predicted log stability versus the measured for Nitrofurantoin/PVPVA across different loadings. The measured log stability begins with high values at lower drug/polymer loadings, suggesting highly stable formulations. However, as the drug/polymer loading increases, there is a noticeable dip in log stability. Specifically, at loadings around 25% and onwards, the measured stability drops to zero. The predicted stability for Nitrofurantoin begins at elevated levels, particularly at lower drug/polymer loadings. As the loading increases, the predicted stability decreases, consistent with the experimental data, although showing a gradual decrease rather than the sharp drop seen experimentally.

Nevertheless, it is encouraging to note a similar trend in both the predicted and measured data. This suggests that whilst the model might not accurately predict the exact magnitude of stability (due to the sudden onset of crystallization seen in the physical system), it successfully captures the overarching trend of stability across varying drug/polymer loadings.

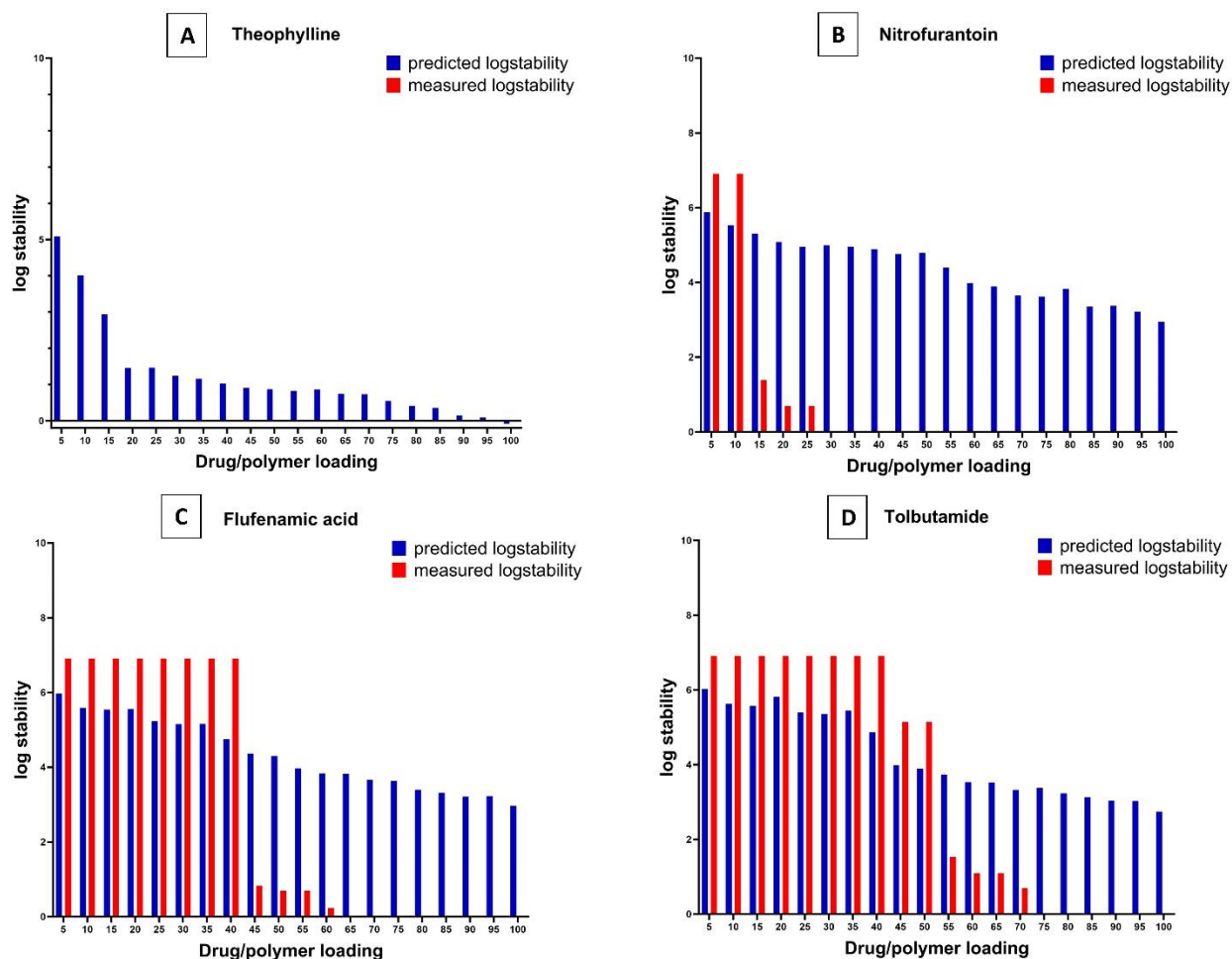


Figure 77. Comparison of predicted log stability, determined using the LOOCV method based on the multiple linear regression model, versus measured log stability from experimental microarray data for Theophylline (A), Nitrofurantoin (B), Flufenamic Acid (C), and Tolbutamide (D) across a range of drug loadings within the PVPVA polymeric matrix. The blue bars indicate the predicted stability, while the red bars show the measured stability, allowing for an evaluation of the predictive model's accuracy at different drug loadings.

4.4.1.8.3 Flufenamic acid

Figure 77 (C) shows the predicted log stability versus the measured for Flufenamic acid/PVPVA across different loadings. Pronounced stability is observed at lower loadings for the measured log stability, represented by the red bars. However, from 65% loading onwards, the values drop sharply to zero due to crystallization at these loadings. As for Nitrofurantoin, the predicted log stability of Flufenamic shows a more gradual decrease as the loading percentage increases, without

the abrupt drop to zero as seen in the measured values. Still, it shows the same trend of decreasing stability of the formulations as the drug/polymer increases.

4.4.1.8.4 Tolbutamide

Figure 77 (D) shows the predicted log stability versus the measured for Tolbutamide/PVPVA across different loadings. For Tolbutamide's log stability within the PVPVA polymeric matrix, the measured values show a trend of consistently high stability at lower drug/polymer loadings, progressively declining as the loading increases, notably after 70%, sharply dropping towards minimal stability towards 100% loading. Meanwhile, the predicted values for tolbutamide follow a broadly similar pattern with measured stability values. At lower drug/polymer loadings, the predicted values indicate a stable environment, and akin to the measured values, they also show a reduction in stability as the loading intensifies.

4.4.1.8.5 Nifedipine

Figure 78 (A) shows the predicted log stability versus the measured for Nifedipine/PVPVA across different loadings. The measured stability of Nifedipine, as shown by the red bars, starts at high values for the lowest drug/polymer loading. As the drug/polymer loading increases, there is a general decreasing trend in the stability. The stability notably diminishes by the higher end of the drug/polymer loading spectrum.

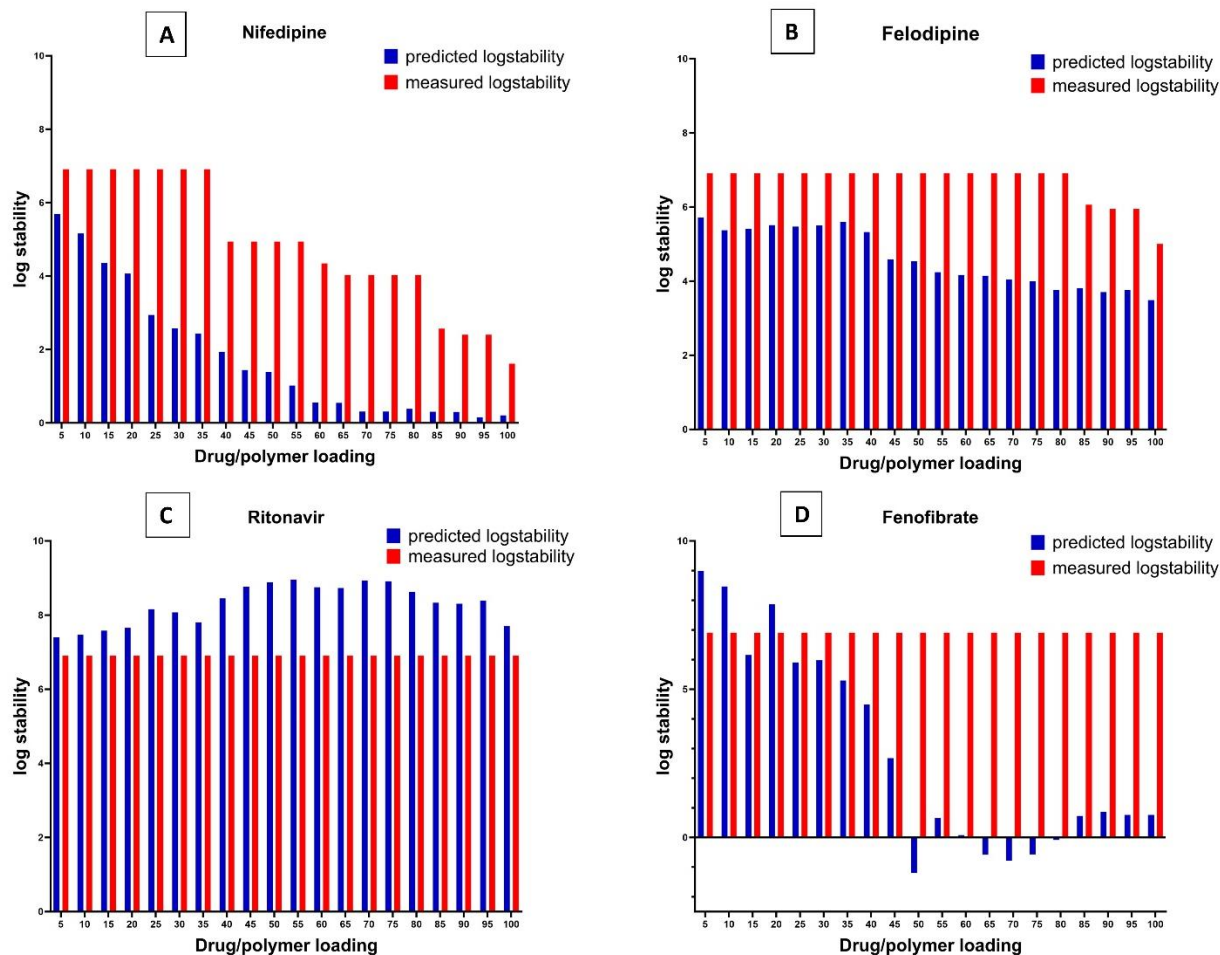


Figure 78. Comparison of predicted log stability, determined using the LOOCV method based on the multiple linear regression model, versus measured log stability from experimental microarray data for Nifedipine (A), Felodipine (B), Ritonavir (C), and Fenofibrate (D) across a range of drug loadings within the PVPVA polymeric matrix. The blue bars indicate the predicted stability, while the red bars show the measured stability, allowing for an evaluation of the predictive model's accuracy at different drug loadings.

The predicted stability, depicted by the blue bars, begins at a high level, mirroring the measured data for the lowest drug/polymer loading. As we progress to higher loadings, the predicted stability decreases, showing a similar descending trend.

The overall declining trend between the measured and predicted stability values indicates the model's capability to reproduce the behaviour of Nifedipine with varying drug/polymer loadings.

4.4.1.8.6 Felodipine

Figure 78 (B) shows the predicted log stability versus the measured for Felodipine/PVPVA across different loadings. The measured stability of Felodipine displays a consistently high value for drug

loadings, ranging from 5% to 80%. This indicates that no crystallization was observed within this range. There is a notable drop in stability from 85% to 95% and an even more pronounced drop after 95%. The predicted stability shows a consistently high value at the lower drug loadings. However, starting from 45%, a decline in stability begins, becoming more pronounced but not too sharp as drug loading further increases.

The measured and predicted data consistently display high stability at the lower drug loadings.

4.4.1.8.7 Ritonavir

Figure 78 (C) shows the predicted log stability versus the measured for Ritonavir/PVPVA across different loadings. The measured log stability for Ritonavir appears to be relatively consistent throughout the drug/polymer loadings range. It maintains a high stability across most loadings, as no crystallisation was monitored, even in the case of pure Ritonavir. There are no significant decreases in stability observed across the drug loading range. The predicted log stability for Ritonavir remains at elevated levels throughout all drug loadings. However, it does exhibit some fluctuations. Despite these variations, the predicted values tend to overestimate stability compared to the measured data, although they follow a similar trend. The measured and predicted data for Ritonavir show consistent high stability across drug/polymer loadings.

4.4.1.8.8 Fenofibrate

Figure 78 (D) shows the predicted log stability versus the measured for Fenofibrate/PVPVA across different loadings. The stability of Fenofibrate appears consistently high across all drug loadings. The predicted stability shows fluctuations throughout the drug loadings. It remains high up to 45% loading, with substantial fluctuations between 50% and 80%, and then displays a diminishing stability trend from 85% to 100%. While the model's predictions align with the measured values

at lower loadings, the resemblance deviates significantly after 45%. The model fails to accurately mirror the consistently high measured stability, especially in the higher loadings.

Analysing the eight representative drugs within the PVPVA polymeric matrix has provided key insights into the prediction model's capabilities and limitations. Several consistent observations emerged across multiple drugs:

- **Uniform Stability Values:** The observation of uniformly high stability across multiple drug/polymer loadings for a range of drugs, including Ritonavir, Fenofibrate, Aprepitant, Orlistat, Felodipine, Probuco, and Celecoxib, highlights a specific trend that might have impacted the predictive accuracy of our model. The similar high stability results for most of these drug-polymer combinations provided limited variability in the dataset. This lack of variation could be a key reason why the model's predictions did not closely align with the measured stability values. In scenarios where no crystallization was detected, this consistent pattern of high stability across different drug/polymer loadings might have contributed to the model's challenges in distinguishing between subtly different stability outcomes. Essentially, the model's ability to accurately predict was likely hindered by the homogeneity in the data, as models generally require a range of outcomes to learn and predict effectively.
- **Capturing Overarching Trends:** In cases like Flufenamic acid, Tolbutamide, Nifedipine, Nitrofurantoin, Atenolol, Nicotinamide, Diclofenac sodium, Flurbiprofen, Aspirin, Carbamazepine, Estradiol, Piroxicam and Corticosterone, the predictive model captures the overarching trend of stability, even if it did not precisely mirror exact stability values. The good predictive capability of the developed model can be primarily attributed to the diverse range of stability values observed across various drug-polymer loadings. These

values represent a spectrum of stability scenarios, which are not relatively shifted towards immediate crystallization or being highly stable. This variation in stability data enhances the robustness and accuracy of our predictive model.

- **Immediate Crystallization Phenomenon:** The observed immediate crystallization of drugs such as Theophylline and Caffeine across all drug loadings presented significant challenges for the predictive accuracy of our model. This phenomenon, where the measured stability values were consistently zero for all drug-polymer loadings, resulted in a uniformity that created notable discrepancies between the actual and predicted stability values. This uniform zero stability measurement across different loadings did not provide the variability needed for the model to effectively learn and predict diverse stability outcomes, leading to these challenges in its predictive capacity.

4.4.2 Drugs with Soluplus

4.4.2.1 Frequency of the variables

The selection of physicochemical properties from the Soluplus data spanning drug-polymer loadings from 5-100% at 5% increments showed a range of frequencies in the MLR model. Table 22 summarizes the frequency of each of these physicochemical properties. It could be seen that certain properties, such as nHet, HBA, nO, ASA and mp, were more frequently incorporated into the models than others.

Table 22. The frequency table shows the variability in the physicochemical properties, as appeared in the 20 models using Soluplus stability data and drug-polymer loadings from 5-100% for the 23 employed APIs in this study.

Physicochemical property	Frequency of each variable as appeared in the 20 models
nHet	13
HBA	12
nO	12
ASA	11
mp	5
Fsp3	3
LogP	3
nHet.ring	3
avPol	2
LogS0	2
MinProjRad	2
Sp3	2
LogS0 at 7.4	1
MaxProjRad	1
MinProjArea	1
Mref	1
nAliphRing	1
nAtom	1
nN	1
tpSA	1

The frequency with which physicochemical properties appeared in the MLR models offers insights into their potential significance or influence on drug stability. For instance:

- High-frequency properties: HBA, nHet, nO and ASA were the most frequent, appearing in more than half of the models. That suggests that these properties may significantly impact the stability of drugs within the Soluplus matrix. The same properties appeared at the highest frequency in the models developed using the PVPVA dataset.
- Medium-frequency properties: Properties such as mp, Fsp3, logP and nHet.ring have a moderate appearance. They may play a secondary role in influencing drug stability.
- Low-frequency properties: Those appearing once or twice, like avPol, logS0, minProjRad and nAtom might have a lesser or specific role in determining stability, or their influence could be conditional based on other factors.

4.4.2.2 Final Model Choice

The best model for the Soluplus dataset, chosen for minimizing the cross-validation MSE, is characterized by the following equation:

$$\log\text{stability} = \text{intercept} + c_1 \times \text{nHet} + c_2 \times \text{HBA} + c_3 \times \text{nO} + c_4 \times \text{ASA} + c_5 \times \text{mp}$$

as:

- HBA represents the number of hydrogen bond acceptors.
- nHet is the number of heteroatoms.
- nO is the number of oxygen atoms.
- ASA is the water-accessible surface area
- mp is the melting point.
- c_1 , c_2 , c_3 , c_4 and c_5 are the coefficients for the variables.

4.4.2.3 Model Performance and Selection

The model's performance, evaluated through LOOCV, yielded an MSE of approximately 4.0799.

The "error" in the study is the difference between the measured log stability values and the

predicted log stability values generated by the model. A lower MSE value indicates a better fit of the model to the data (i.e., the predictions are closer to the actual /measured values). However, MSE is sensitive to outliers because of the squaring part of the formula.

This model was selected after extensive testing and fitting to subsets of data for different drug loadings. The representative equation for each drug/polymer loading and the adjusted R² values are detailed in Table 23 and illustrated in Figure 79. This comprehensive approach underscores the aim to establish a dependable model for predicting the log stability of various drug compositions.

Table 23. Equations were extracted from the model using the Soluplus data set, and all drug/polymer loadings were 5 to 100%.

Drug/polym er loading	Equation	Adjusted R ²
5	logstability= 6.904478 - 0.066308 nHet + 0.246153 HBA + 0.108606 nO + 0.000154 ASA - 0.012543 mp	0.1779
10	logstability= 6.392930 - 0.102272 nHet + 0.459472 HBA + 0.212930 nO - 0.000213 ASA - 0.014521 mp	0.2771
15	logstability= 8.055358 - 0.146929 nHet + 0.538595 HBA - 0.319920 nO + 0.001531 ASA - 0.023051 mp	0.3704
20	logstability= 6.722228 + 0.163601 nHet - 0.190217 HBA - 0.185869 nO + 0.002556 ASA - 0.019877 mp	0.3323
25	logstability= 6.579584 + 0.408126 nHet - 0.436831 HBA - 0.122492 nO + 0.001667 ASA - 0.023196 mp	0.3962
30	logstability= 8.192919 + 0.649435 nHet - 0.635919 HBA + 0.036673 nO - 0.000747 ASA - 0.035003 mp	0.6588
35	logstability= 8.277985 + 0.808015 nHet - 1.033161 HBA + 0.129317 nO - 0.001589 ASA - 0.033944 mp	0.5646
40	logstability= 2.326668 + 0.767811 nHet - 1.341784 HBA + 0.595642 nO + 0.002769 ASA - 0.016829 mp	0.5828
45	logstability= -0.718375 + 0.674292 nHet - 1.565819 HBA + 0.820713 nO + 0.005679 ASA - 0.006133 mp	0.6111

50	logstability= 0.475585 + 0.772708 nHet - 1.725074 HBA + 0.460044 nO + 0.005684 ASA - 0.008204 mp	0.6239
55	logstability= -1.468648 + 0.799246 nHet - 1.928795 HBA + 0.583463 nO + 0.007528 ASA - 0.003160 mp	0.772
60	logstability= -0.635987 + 0.807753 nHet - 1.887381 HBA + 0.476389 nO + 0.007124 ASA - 0.005803 mp	0.7313
65	logstability= -1.725031 + 0.812978 nHet - 1.933247 HBA + 0.534638 nO + 0.007864 ASA - 0.002758 mp	0.7799
70	logstability= -0.763022 + 0.870485 nHet - 2.173013 HBA + 0.581958 nO + 0.007213 ASA - 0.004297 mp	0.7365
75	logstability= -0.906745 + 0.865665 nHet - 2.146650 HBA + 0.590819 nO + 0.007262 ASA - 0.004459 mp	0.7288
80	logstability= 0.095617 + 0.874284 nHet - 2.201381 HBA + 0.488665 nO + 0.006998 ASA - 0.005858 mp	0.6767
85	logstability= -1.793873 + 0.870811 nHet - 2.174307 HBA + 0.639040 nO + 0.007778 ASA - 0.002045 mp	0.7693
90	logstability= -1.912472 + 0.872332 nHet - 2.181690 HBA + 0.667993 nO + 0.007769 ASA - 0.001749 mp	0.7684
95	logstability= -1.022289 + 0.864255 nHet - 2.138428 HBA + 0.592750 nO + 0.007325 ASA - 0.004290 mp	0.7248
100	logstability= -1.888800 + 0.781680 nHet - 1.881721 HBA + 0.651467 nO + 0.006722 ASA - 0.002450 mp	0.7658

Each row in the table represents a specific instantiation of our overarching MLR model tailored for varying drug/polymer loadings. Though the structural format of the model remains consistent (i.e., log stability as a function of HBA, nHet, nO, ASA and mp), each drug loading value has its own set of coefficients reflecting the unique contribution of the physicochemical properties at individual drug loadings.

The adjusted R^2 values presented in the scatter plot in Figure 79 offer valuable insights into the model's predictability across varying drug/polymer loadings. The data begins with lower R^2 values at lower drug/polymer loadings, suggesting that the variability in the response is less explained by the predictor in these initial formulations. This started with minimal drug loadings (5%); the model suggests that nearly 18% of the variability in log stability is accounted for. This percentage significantly increases as drug loadings rise, marking a clear trend in the model's heightened ability to predict log stability. There is a noticeable increase in the R^2 value as drug/polymer loading transitions from 5% to around 60%. This increasing trend indicates that as the drug/polymer loading increases, the model's ability to capture the variability in the data improves significantly, as was seen for PVPVA. After approximately 60% drug/polymer loading, there is a slight fluctuation in the R^2 values. Still, it remains relatively high, suggesting a robust predictive capacity of the model for these higher drug/polymer loadings. Although the R^2 values exhibit fluctuations around the 60% to 80% drug/polymer loading range, the trend remains largely consistent, without any drastic drops, pointing to the relatively stable predictive performance of the model in this range. Towards the higher end of the drug/polymer loading scale (around 90%-100%), the R^2 values appear to stabilize without a pronounced increase or decrease.

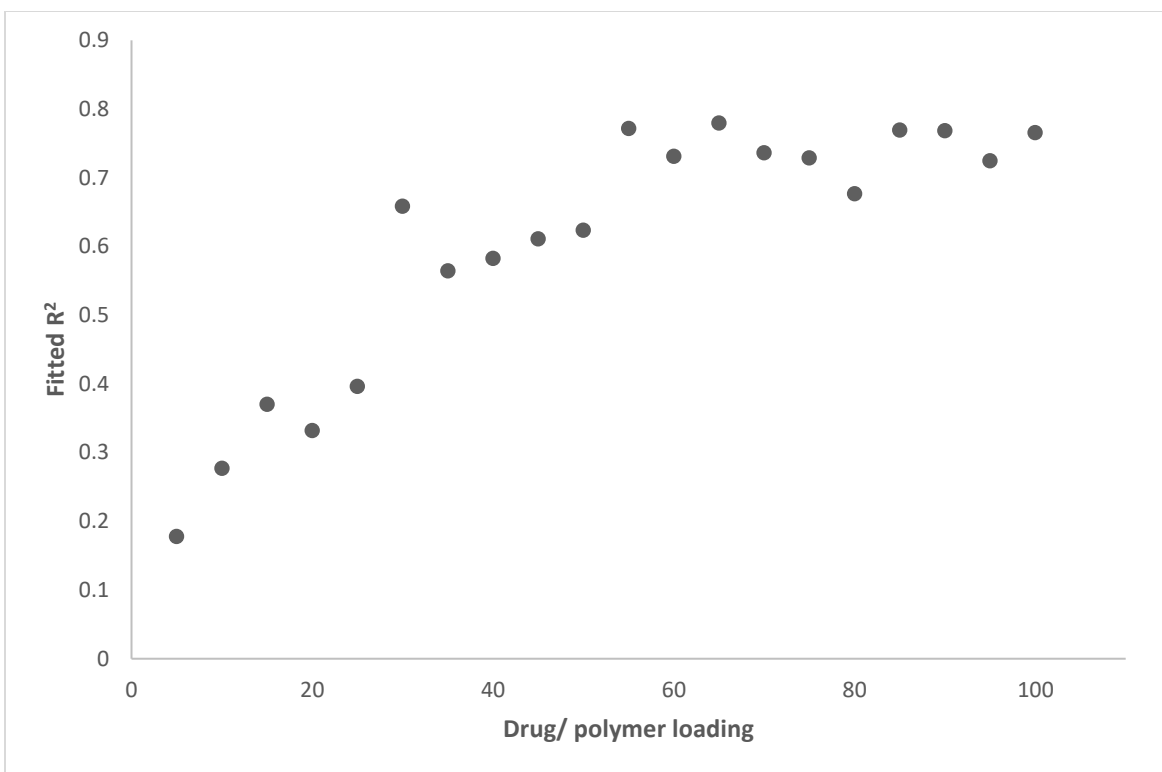


Figure 79. A fitted r -square was extracted from the multiple linear regression model for the Soluplus data set, using all drug/polymer loadings (5-100% with 5% increment) for 23 employed APIs.

The scatter plot portrays a consistent upward trend in R^2 values as drug/polymer loading increases, while there are observed fluctuations in specific intervals. The model's predictive capability is shown to be high, particularly for high drug/polymer loadings.

Another noteworthy observation is the behaviour of high-loading formulations, especially those that approach pure drug compositions. The model more accurately represents these formulations. Experimental data further corroborate these findings. It is observed that formulations with higher drug loadings display an increased propensity for recrystallization. This observation accentuates the robustness of the model, especially at elevated loadings, and the peak goodness-of-fit observed at around 95% drug loading serves as a testament to this robustness.

4.4.2.4 Coefficients

Figure 80 to Figure 85 show the fluctuation in coefficients for the key model parameters as a function of drug loading in the formulations. This enables an understanding of how different descriptors contribute to log stability at various drug loadings. All coefficients vary in a reasonably regular manner as a function of composition. The importance of the compositions (as measured by their coefficient in the model) varies as a function of composition.

- **The number of heteroatoms (nHet):** As shown in Figure 80, the number of heteroatoms in the drug molecule has a rapidly increasing (and positive) effect on the stability of ASD formulations up to about 40% drug loading, implying that increased heteroatoms in drug molecules enhance stability.

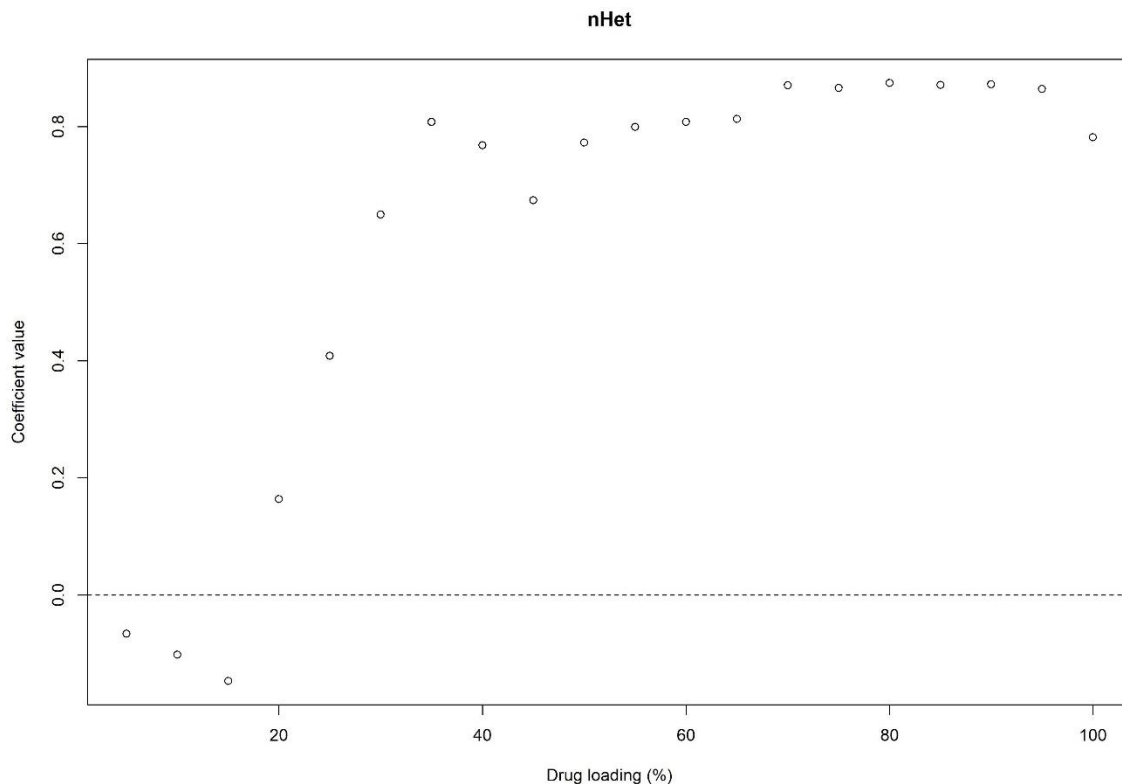


Figure 80. Scatter plot of coefficient values for the number of heteroatoms (nHet) variable obtained from multiple linear regression analyses across 23 different drugs at varying drug/polymer loadings from 5 to 100%.

- **The number of hydrogen bond acceptors (HBA):** As shown in Figure 81, the contribution of hydrogen bond acceptors (HBA) is minimal positive in the range of 5-20 %

drug loading, after which it rapidly becomes larger beyond the solubility limit of the drug in the polymer, in absolute value up to around 60%, above which the contribution of this term remains relatively constant. This progression in magnitude implies an increasing adverse impact of HBA on stability especially at higher drug loadings.

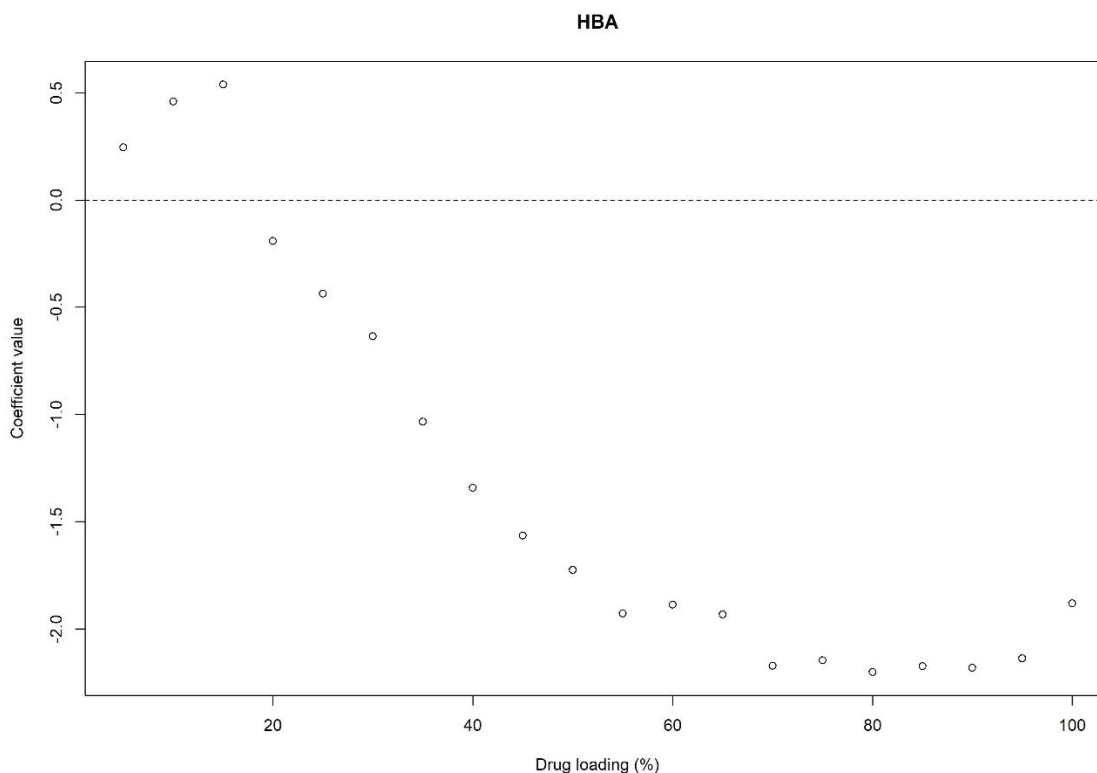


Figure 81. Scatter plot of coefficient values for hydrogen bond acceptors (HBA) variable obtained from multiple linear regression analyses across 23 different drugs at varying drug/polymer loadings from 5 to 100%.

- The number of Oxygen atoms (nO):** As shown in Figure 82, the number of oxygen atoms in a given drug molecule has a near-zero contribution to stability at low drug loadings (0 to perhaps 35 % loading), above which it becomes a positive correlation. The rise in coefficient indicates that having more oxygen atoms is positively linked to the stability of ASD as drug loading increases.

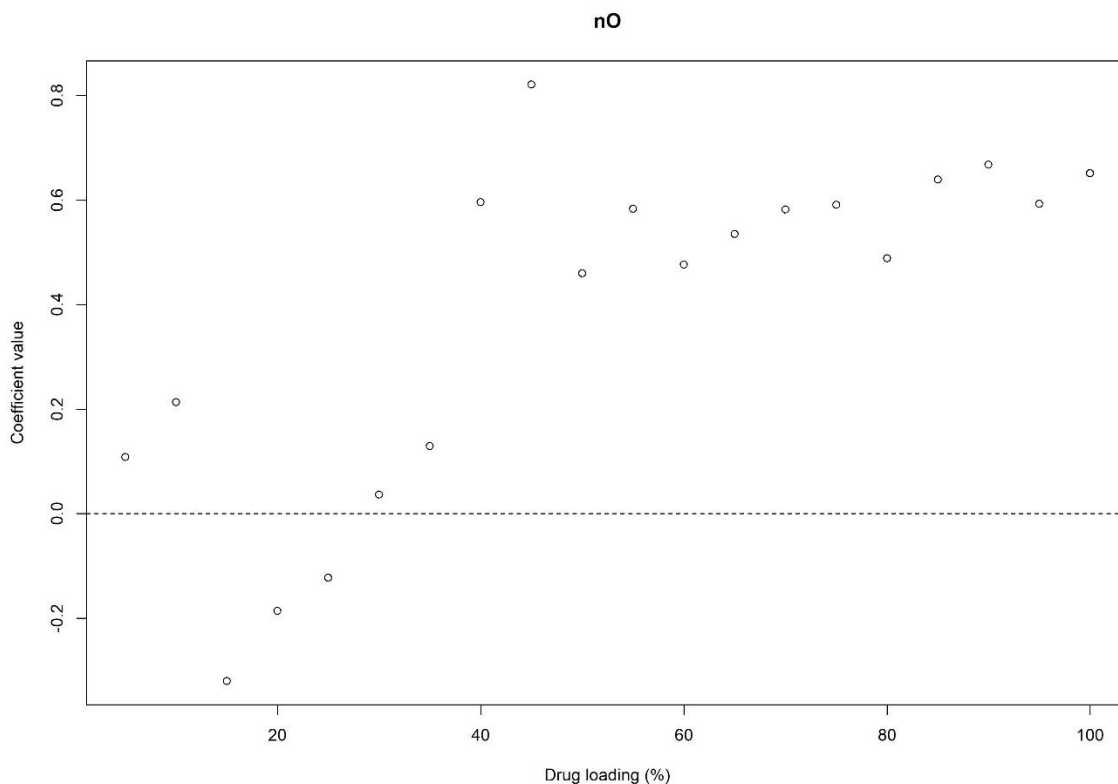


Figure 82. Scatter plot of coefficient values for the number of Oxygen atoms (nO) variable obtained from multiple linear regression analyses across 23 different drugs at varying drug/polymer loadings from 5 to 100%.

- Water accessible surface area (ASA):** As shown in Figure 83, the coefficients for ASA are consistently positive across the range of drug loadings, although the magnitude of these coefficients is very small. Despite the small coefficients, the actual ASA values for the drugs involved in the study are reportedly very high. Therefore, even small coefficients may represent a significant effect on stability when applied to the high ASA values. This implies that the ASA, while represented by small coefficients in the model, could still have a meaningful impact on the stability of the ASDs due to the large magnitude of the ASA values themselves. In terms of its relation to stability, the positive sign of the coefficients suggests that a larger ASA is associated with increased stability within the model's predictions. The presence of a positive correlation, irrespective of the small coefficient values, indicates that larger water-accessible surface areas of the drug molecules could be beneficial to the stability of the ASDs.

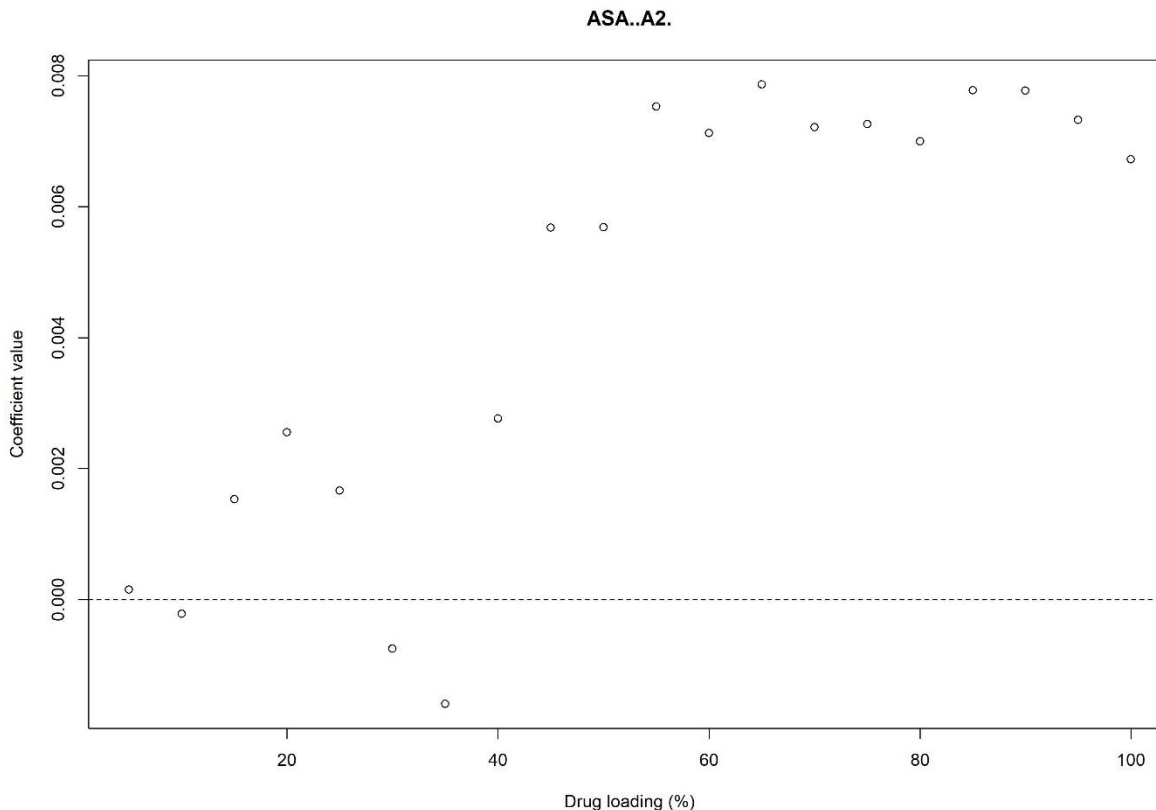


Figure 83. Scatter plot of coefficient values for Water accessible area (ASA) variable obtained from multiple linear regression analyses across 23 different drugs at varying drug/polymer loadings from 5 to 100%. (A^2 is the unit of surface area).

- Melting point (mp):** As shown in Figure 84, the coefficient values range from just below 0 to slightly negative values as drug loading increases from 0% to around 60%. After 60% drug loading, the coefficient values hover around the zero line, suggesting negligible influence. The data shows that the influence of melting point on stability diminishes after 60% drug loading, where coefficients approach zero, indicating that melting point has a limited role in this higher loading range. For typical pharmaceutical formulations, which often feature drug loadings between 5% and 25%, the negative correlation suggests that drugs with lower melting points are associated with more stable ASDs in the polymer matrix used, in this case, Soluplus. It is important to note that the relative contribution of the melting point to the model's predictive capability cannot be determined solely by the

magnitude of its coefficient. Since melting points are inherently high, even a small coefficient, when multiplied by the actual melting point value, can result in a significant term within the model. However, the values are not so close to zero as to be considered negligible for all drug loadings. Mainly up to 60% drug loading, the melting point has a negative influence on stability, even if it is not a strong one. This suggests that (from our data and analysis) low melting point drugs tend to be more stable as ASD formulations in Soluplus formulations than drugs with higher melting points for typical pharmaceutical loadings (5-25%).

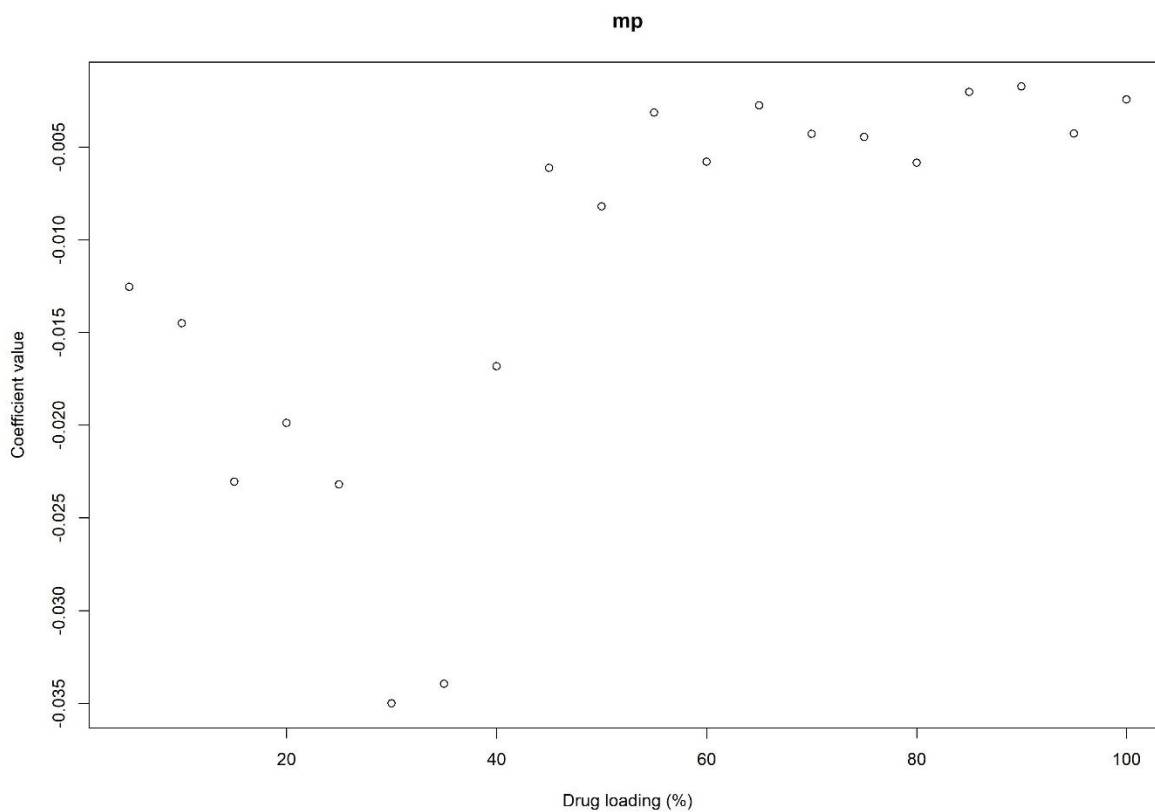


Figure 84. Scatter plot of coefficient values for melting point (mp) variable obtained from multiple linear regression analyses across 23 different drugs at varying drug/polymer loadings from 5 to 100%.

- **Intercept:** As shown in Figure 85, the intercept does show a trend of higher values and then drops to zero and below at the higher drug loadings. The drop in the values of the intercept would be just because more samples crystallize at higher drug loadings, so the

intercept would not be so high (as the log-stability numbers are lower due to the drugs that crystallize).

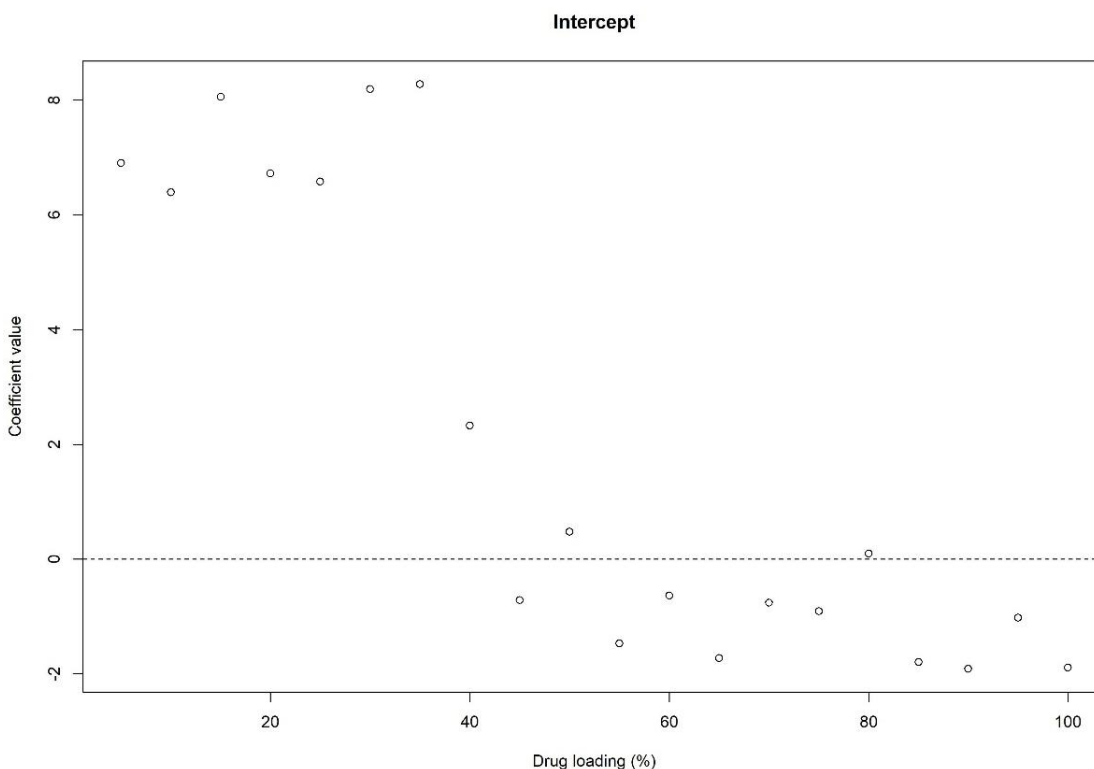


Figure 85. Scatter plot of intercept values obtained from multiple linear regression analyses across 23 different drugs at varying drug/polymer loadings from 5 to 100%.

Key Insights:

- **nHet** has a strong positive effect on stability, especially in the mid and higher drug loading range. This could be attributed to increased molecular flexibility and a reduced tendency for crystalline alignment.
- **HBA** becomes increasingly negative, making it a significant factor in decreasing the stability of ASD as drug loading increases, presumably when exceeds the solubility limit of the drug in the polymer. This may be attributed to the electrostatic repulsion between the drug's HBA groups and the polymer's HBA groups, disrupting the even distribution of the drug, and leading to possible drug clustering and phase separation. Such segregation may foster crystalline areas, thereby diminishing the stability of the ASD.

- **nO** has a late-emerging positive effect, suggesting it might enhance stability in higher drug loadings, possibly due to their impact on the electronic distribution and the interactions within the polymer matrix.
- **ASA** has a positive impact on stability, especially in the higher drug loading range.
- **mp**: as before lower melting points (more negative values) are beneficial for stability, especially in lower drug loadings.

Applying to different drug loadings:

In terms of typical pharmaceutical use (i.e. below the solubility limit), drug loadings of 5-20 % are the norm for ASD-based formulations, and for these loadings, our model suggests that:

- nHet correlates negatively with stability below 20% loading.
- HBA is relatively less important and correlates positively with stability below 20% loading.
- nO is relatively less important
- ASA is relatively less important
- Low values of mp lead to better stability when formulated with Soluplus.

For drug loadings above 20 or 25%, our analysis from the image suggests the following:

- nHet correlates positively with stability.
- HBA correlates negatively with the stability of formulations.
- The presence of Oxygen atoms correlates positively with the stability of the formulations.
- ASA correlates positively especially above 60% drug loadings, with very minimal effect.
- mp is relatively less important.

The model parameters and R^2 values indicate that the model is appropriate for predicting the stability of high drug loadings (above ca. 40%) rather than the lower drug loading, which tends to be used in pharmaceutical formulation. Therefore, the model-building process was repeated, using only input data from 5 to 20 and 5 to 50 % drug loading. The 5 to 20 % input data yielded an uninspiring model in which the values of the various coefficients were scattered around zero.

4.4.3 Effects of setting non-crystallised drug log stability at 500 days

To investigate whether describing the formulations which did not show crystallisation as having a stability of 500 days (ca. 1.5 years) was adversely affecting the ML output, modelling trials were run with the non-crystallised drug stability set at 1000 days (ca. 2.7 years), 10,000 days (ca. 27 years) and 100,000 days (ca. 273 years). Results were compared with the output from the 500-day description.

For speed of calculation, a subset of variables was employed. With non-crystallised drugs set at 1000 days stability, the ML model derived for log stability comprised HBA, ASA, nHet and mp, whereas with this set at 10,000 days and at 100,000 days, the ML model arrived at comprised HBA, ASA, nHet and mp.

When comparing results from baseline stability of 500 days to other extended stabilities (1000 days, 10,000 days, and 100,000 days), it was observed that the model's selected parameters remained consistent. Namely, HBA, ASA, nHet, and mp were the recurrently chosen descriptors. This suggests that assigning different stability values to non-crystallized formulations within the tested stability range does not drastically alter the key model parameters. In other words, it remains a justifiable and reasonable choice without exerting undue influence on the machine learning model's outputs. This suggests that using a nominal 500 days to describe the stability of non-

crystallised formulations is reasonable or does not significantly impact modelling. However, it is worth noting that while the variables selected remained consistent, the exact coefficient values, predictive performance, and model dynamics might exhibit variations based on the assigned stability durations.

4.4.3.1 Correlation matrix of log stability within Soluplus and predictor variables and the correlation between the variables and each other

Figure 86 showcases an illustrative matrix that conveys the pairwise correlations among selected predictor variables (mp, nHet, ASA, HBA, and nO) and the log stability. This matrix acts as an initial diagnostic tool, providing a foundation for understanding the variables' dynamics before going into the depth of regression analysis. The matrix employs a colour scale where deep blue signifies a strong positive correlation near +1, while deep red symbolizes a strong negative correlation near -1. A white indicates negligible or no correlation. This colour differentiation offers an immediate visual comprehension of the correlation between strength and direction. Each cell provides a precise correlation coefficient between -1 and +1. A coefficient of 1 or -1 conveys a perfect linear correlation, whereas values near 0 indicate a weak or no linear relationship. The data shows that log stability is inversely correlated with mp at -0.40, while it has a positive correlation of 0.25 with nHet and ASA (0.51). Additionally, log stability has an almost insignificant correlation with HBA at 0.07 and a weak positive correlation of 0.23 with nO.

Regarding the variables, mp displays a weak positive correlation with nHet (0.20) and HBA (0.19) and a negative correlation with nO (-0.18) and with ASA (-0.45). A notable strong positive alignment exists between nHet and HBA (0.87). Further, nHet demonstrates moderate positive associations with both nO (0.47) and ASA (0.59). HBA and nO share a moderate positive correlation (0.60), while ASA and HBA possess a correlation of 0.52.

Upon examining the matrix, the variables display varying degrees of association without indicating significant multicollinearity issues. The highest correlation noted stays within accepted limits for multiple linear regression analyses. Therefore, considering their relationships, these predictors are suitable for inclusion in the multiple linear regression model, ensuring the reliability and robustness of the model.

It is important to highlight that this matrix primarily outlines linear correlations between two variables. However, the relationships between all the variables might reveal more complex patterns. Our study further explores this, employing a comprehensive multiple linear regression approach.

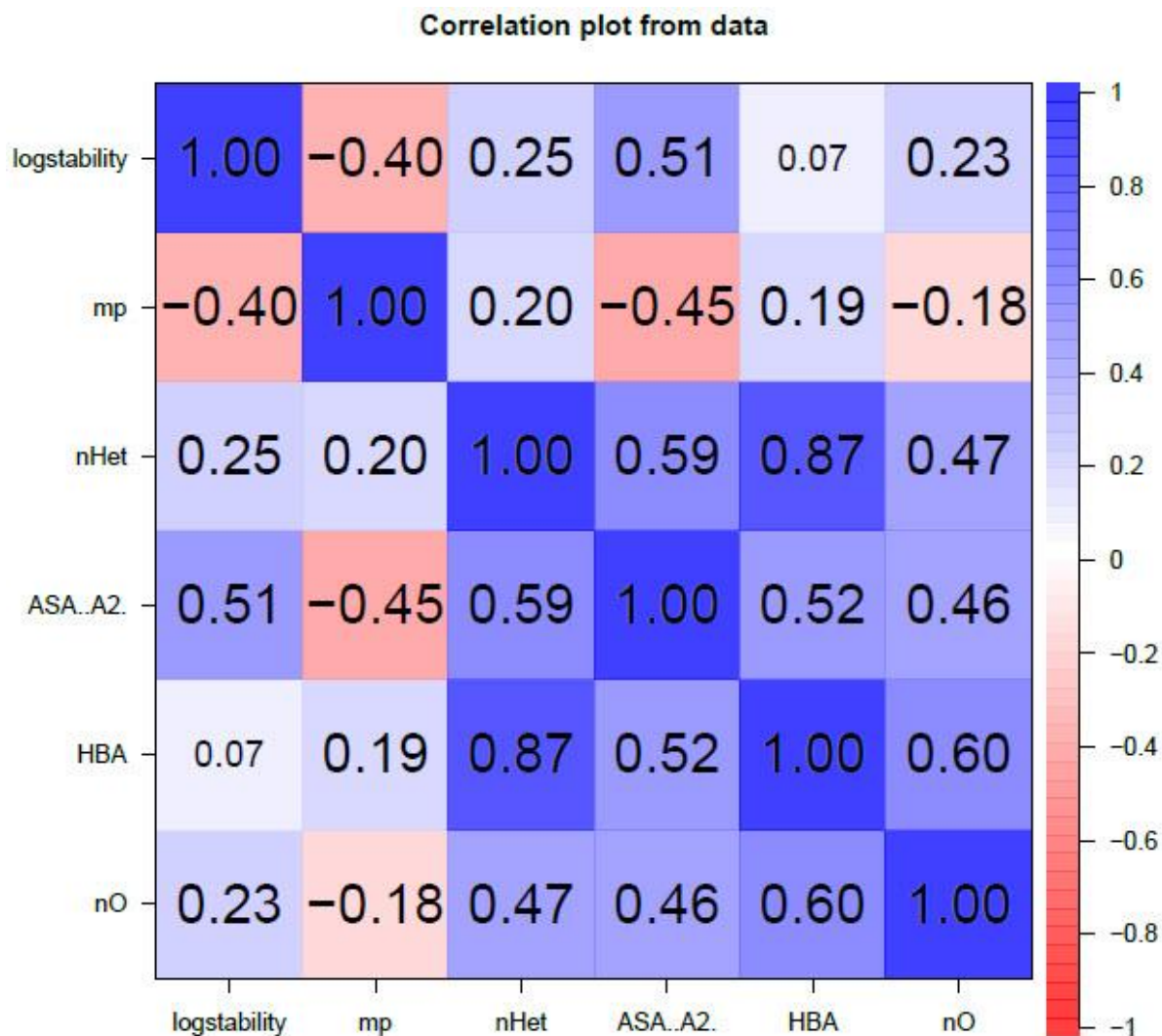


Figure 86. The correlation matrix displays the pairwise correlations between the predictor variables and log stability within Soluplus. Each cell represents the correlation coefficient between the corresponding variables. These correlations are not derived from the linear regression model. (mp: melting point, nHet: number of heteroatoms, ASA: accessible water surface area, HBA: number of hydrogen bond acceptors and nO: number of oxygen atoms).

4.4.3.2 Analysis of LOOCV for log stability in Soluplus drug loading

To ensure the reliability and accuracy of the predictive model for the log stability of drugs combined with Soluplus polymer, the LOOCV technique was employed. Table 24 offers a comprehensive snapshot of the interplay of various variables in dictating the log stability of drugs in a Soluplus polymer environment.

Each drug has an associated equation that predicts its log stability based on different variables.

The overarching model equation used in this study was

$$\log\text{stability} = \text{intercept} + c_1 \times n\text{Het} + c_2 \times \text{HBA} + c_3 \times n\text{O} + c_4 \times \text{ASA} + c_5 \times mp$$

This equation served as the baseline against which individual drug equations were compared. Across all drugs, various variables were tested for their contribution to the model's predictive power. Certain variables recur with higher frequency across the different drug equations. Most notably, nHet, HBA, ASA, and mp emerge as the stalwarts. Their recurring presence underscores their pivotal role in influencing log stability. The table employs the labels 'TRUE' and 'FALSE' as quick visual indicators. The presence (indicated by TRUE) or absence (indicated by FALSE) of each variable for a specific drug denotes its significance for that drug's log stability prediction within the Soluplus polymer loading context. The variable 'nHet_ring' represents the number of hetero rings in a drug. Its sporadic presence suggests that while it is essential for some drugs, it does not play a universal role across all. Despite its place in the general equation, 'nO' is notably absent in most individual drug equations, appearing only once. This indicates that while oxygen atoms might influence the stability on a broader scale, they do not hold a consistent significance across individual drugs. For only one drug, it is flagged as 'TRUE'; oxygen atoms play a substantial role in determining stability. However, for the majority of other drugs, its influence is either minimal or entirely negligible.

Table 24. Summary of the models' equations from the LOOCV and the variables adopted in each equation for each of the 23 APIs used in this study within the Soluplus matrix. Where mp is the melting point, nHet is the number of Hetero atoms, HBA is the number of hydrogen bond acceptors, nHet_ring is the number of hetero rings, ASA is the accessible surface area, and nO is the number of oxygen atoms.

Drug name	Equation	HBA?	nHet?	ASA?	mp?	nO?
Aprepitant	logstability ~ HBA + mp+ nHet + ASA + Log P+ nO	TRUE	TRUE	TRUE	TRUE	TRUE
Orlistat	logstability ~ HBA + nHet + ASA + mp	TRUE	TRUE	TRUE	TRUE	FALSE
Nifedipine	logstability ~ HBA + nHet + ASA + mp+ nHet_ring	TRUE	TRUE	TRUE	TRUE	FALSE
Estradiol	logstability ~ nHet + HBA + ASA + mp	TRUE	TRUE	TRUE	TRUE	FALSE
Felodipine	logstability ~ HBA + nHet + ASA + mp	TRUE	TRUE	TRUE	TRUE	FALSE
Fenofibrate	logstability ~ nHet + HBA + nAtom+ nHet_ring + mp	TRUE	TRUE	FALSE	TRUE	FALSE
Celecoxib	logstability ~ ASA + HBA + nHet + mp+ nHet_ring	TRUE	TRUE	TRUE	TRUE	FALSE
Probuco	logstability ~ ASA + nHet + HBA + mp + AvPol + MW	TRUE	TRUE	TRUE	TRUE	FALSE
Ritonavir	logstability ~ HBA + nAtom+MRef + vdW_Vol+ mp	TRUE	FALSE	FALSE	TRUE	FALSE
Itraconazole	logstability ~ mp + MW + HBD + MaxProjArea	FALSE	FALSE	FALSE	TRUE	FALSE
Nicotinamide	logstability ~ HBA + ASA + nHet + nHet_ring	TRUE	TRUE	TRUE	FALSE	FALSE
Nitrofurantoin	logstability ~ HBA + nHet + ASA	TRUE	TRUE	TRUE	FALSE	FALSE
Piroxicam	logstability ~ nHet + HBA + ASA+mp+ nHet_ring+FSp3	TRUE	TRUE	TRUE	TRUE	FALSE
Theophylline	logstability ~ nHet + HBA + ASA	TRUE	TRUE	TRUE	FALSE	FALSE
Tolbutamide	logstability ~ ASA + nHet + HBA + mp	TRUE	TRUE	TRUE	TRUE	FALSE
Aspirin	logstability ~ nHet + HBA + ASA + mp+ nHet_ring	TRUE	TRUE	TRUE	TRUE	FALSE
Atenolol	logstability ~ HBA + nHet + ASA	TRUE	TRUE	TRUE	FALSE	FALSE
Caffeine	logstability ~ HBA + nHet + ASA	TRUE	TRUE	TRUE	FALSE	FALSE
Carbamazepine	logstability ~ nHet + HBA + nC	TRUE	TRUE	FALSE	FALSE	FALSE
Corticosterone	logstability ~ nHet + HBA + ASA + mp+ nHet_ring	TRUE	TRUE	TRUE	TRUE	FALSE
Flufenamic acid	logstability ~ HBA + nHet + ASA + mp	TRUE	TRUE	TRUE	TRUE	FALSE
Flurbiprofen	logstability ~ nHet + HBA + ASA + mp	TRUE	TRUE	TRUE	TRUE	FALSE
Diclofenac sodium	logstability ~ HBA + nHet + ASA + mp	TRUE	TRUE	TRUE	TRUE	FALSE
Frequency		22	21	20	17	1
Model equation	logstability~ nHet + HBA + nO + ASA + mp	HBA	nHet	ASA	mp	nO

For instance, drugs like Estradiol, Felodipine, and Tolbutamide closely align with the overarching model equation by incorporating almost all its variables. This reflects their comprehensive resonance with the general predictive framework. On the other hand, drugs such as Itraconazole and Ritonavir chart their own course by excluding one or more variables present in the primary model. This underlines their individualistic interaction patterns when integrated within the Soluplus polymeric matrix. This understanding, derived from the LOOCV approach, emphasizes the importance of tailoring predictions based on specific drug properties and interactions, especially when working with the Soluplus polymer.

4.4.3.3 Comparative analysis of predicted vs. measured stability across various drug formulations using LOOCV

Figure 87 and Figure 88 comprehensively compare the predicted log stability using multiple linear regression and LOOCV versus the experimentally measured log stability for eight distinct drugs that showed different crystallisation behaviours experimentally within the Soluplus polymeric matrix.

4.4.3.3.1 Theophylline

Figure 87 (A) shows the plotting of the predicted log stability versus the measured ones for Theophylline/Soluplus across different loadings. The measured log stability for Theophylline (which is the same in the case of Caffeine) indicates immediate crystallization at all drug/polymer loadings from 5% to 100%. This signifies that Theophylline is highly unstable across all drug/polymer loadings. On the other hand, the predicted log stability for Theophylline starts with a pronouncedly high value for the lower drug/polymer loadings. Then, a decline in predicted values is observed as the drug loading increases. The predicted stability gradually diminishes as the drug loading increases to 100%.

This discrepancy suggests that the prediction model is not reliable for Theophylline and Caffeine or may need further refinement and calibration.

4.4.3.3.2 Nitrofurantoin

Figure 87 (B) plots the predicted log stability versus the measured ones for Nitrofurantoin/Soluplus across different loadings. At the very low drug/polymer loadings, specifically at 5 and 10, Nitrofurantoin exhibits high measured log stability when combined with Soluplus, indicating optimal stability at these loadings. Above the 10% drug loading, instantaneous crystallization was detected, so stability dropped to zero beyond this point, and this has been detected for the higher

drug loadings. The predicted log stability commences with elevated values at lower drug/polymer loadings. A gradual decline is observed as the loading increases and nearly diminishes from 65% to 100%.

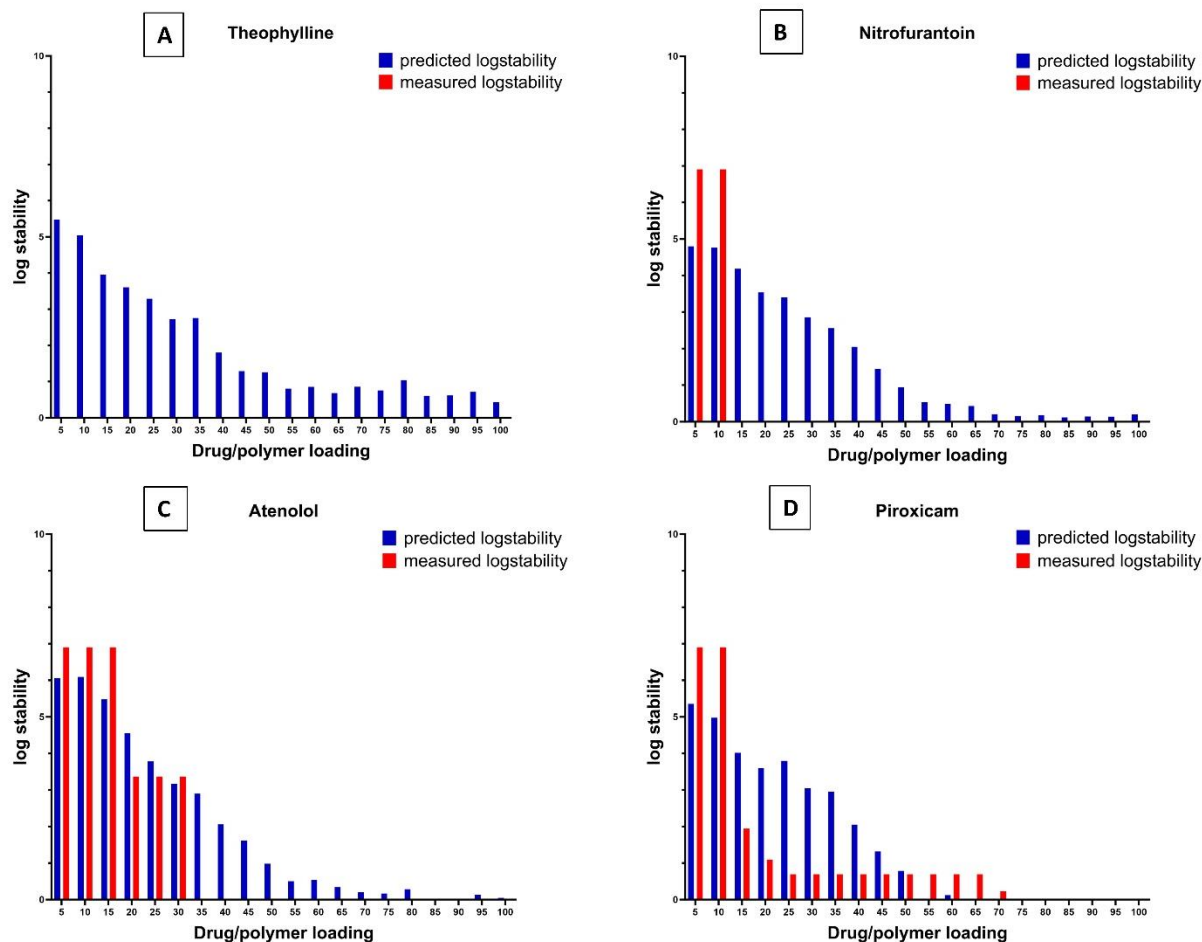


Figure 87. Comparison of predicted log stability, determined using LOOCV method based on the multiple linear regression model, versus measured log stability from experimental microarray data for Theophylline (A), Nitrofurantoin (B), Atenolol (C), and Piroxicam (D) across a range of drug loadings within the Soluplus polymeric matrix. The blue bars indicate the predicted stability, while the red bars show the measured stability, allowing for an evaluation of the predictive model's accuracy at different drug loadings.

For loadings up to 10, both the predicted and measured data align closely, indicating the model's accuracy in this range. However, beyond this point, the model fails to predict the immediate crystallization seen in the measured data. Nonetheless, the model does capture the general trend of declining stability with increased loadings, even if it does not account for the sharp crystallization

event. The model's consistency in following the declining stability trend across varying drug/polymer loadings shows its robustness. It might not pin down every exact data point, but it grasps the general relationship effectively.

4.4.3.3.3 *Atenolol*

Figure 87 (C) plots the predicted log stability versus the measured ones for Atenolol/Soluplus across different loadings. The measured log stability shows a high stability at 5-30% drug/polymer loadings, while a sharp decline to zero indicates immediate crystallisation for all loadings above 30% to 100%. The predicted log stability values are quite close to those measured in the 5-30% range, while above 30%, the decline is not as sharp as in the measured ones.

Both the predicted and actual values display a consistent downtrend in stability with increasing drug/polymer loading, indicative of a similar underlying response to compositional changes. This coherent trend between the predicted and measured data strengthens the model's predictivity, as it reflects the general behaviour of the system despite the variability at higher loadings. The alignment of these trends, particularly at lower drug/polymer ratios, underscores the model's utility in forecasting formulation stability in early-stage pharmaceutical development.

4.4.3.3.4 *Piroxicam*

Figure 87 (D) shows the plotting of the predicted log stability versus the measured ones for Piroxicam/Soluplus across different loadings. Measured log stability shows an initial high stability at minimal drug/polymer loadings of 5-10%. However, there is a noticeable decline in stability from 15% to 70% drug/polymer loading, followed by a transition to minimal stability, indicative of immediate crystallisation, for loadings above 70%, extending to 100%. Predicted log stability mirrors this trend, starting high and gradually diminishing as loading increases, reaching near zero at 60% and above.

The figure shows a clear decrease in stability as the drug/polymer loading increases. Both predicted and measured values align closely, which suggests the model reliably captures the stability trend across the range of loadings. The consistent decrease, matched in both the predictions and measurements, signals that the model has good predictability, effectively mirroring the actual behaviour of Piroxicam formulations. This reliability, even with the potential immediate crystallization post solvent evaporation, is critical for anticipating formulation stability, aiding in the optimization of pharmaceutical development.

4.4.3.3.5 Nifedipine

Figure 88 (A) shows the plotting of the predicted log stability versus the measured ones for Nifedipine/Soluplus across different loadings. The measured log stability commences with high values at drug/polymer loadings between 5 – 45 % and then shows a significant decline as the loading increases above 45% to 100% (pure drug). The predicted log stability starts high at low drug loadings, then starts to decrease at 15% drug loading and experiences a decline as the loading increases up to 100%

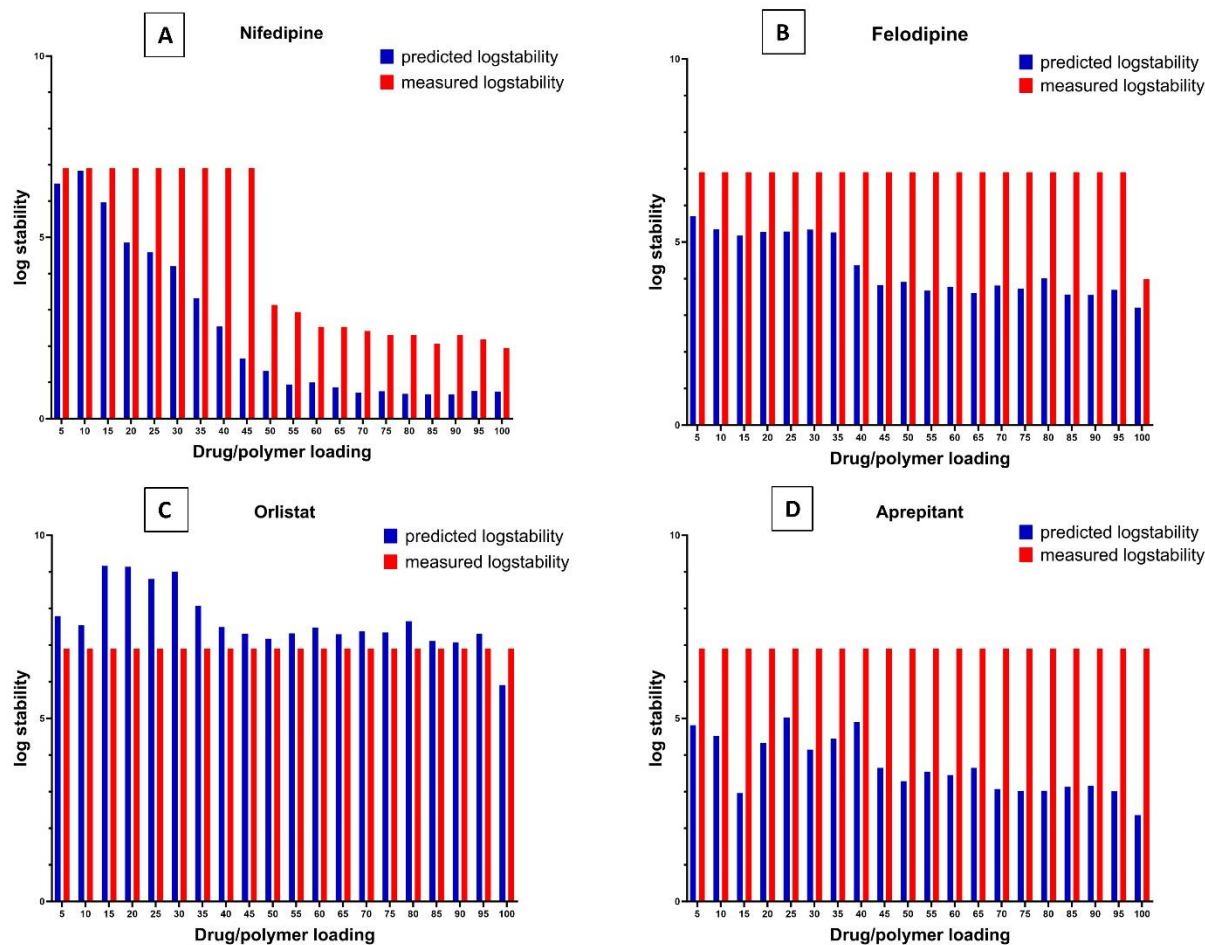


Figure 88. Comparison of predicted log stability, determined using the LOOCV method based on the multiple linear regression model, versus measured log stability from experimental microarray data for Nifedipine (A), Felodipine (B), Orlistat (C), and Aprepitant (D) across a range of drug loadings within the Soluplus polymeric matrix. The blue bars indicate the predicted stability, while the red bars show the measured stability, allowing for an evaluation of the predictive model's accuracy at different drug loadings.

This consistency in the decreasing trend between the measured and predicted stabilities underscores the model's effectiveness in predicting Nifedipine's stability across a range of Soluplus polymer loadings. Despite the difference in the drug loading at which stability started to decrease, the overall correlation suggests the model's predictive reliability.

4.4.3.3.6 Felodipine

Figure 88 (B) shows the plotting of the predicted log stability versus the measured ones for Felodipine/Soluplus across different loadings. The measured log stability maintains consistently high values across all drug/polymer loadings, with an accurately detected stability value (onset of

crystallisation) at 100% (pure drug). This suggests the absence of crystallization, indicating high stability throughout. On the other hand, the predicted log stability exhibits variability and underestimation compared to the measured data while still relatively high.

The fluctuation and underprediction of values might imply that the predictive model lacks accuracy, potentially due to the absence of measured variability in stability across drug/polymer loadings, which could have provided very similar data to be entered into the model. This stability pattern strengthens the need for model refinement to accommodate scenarios with uniformly high stability measurements.

4.4.3.3.7 *Orlistat*

Figure 88 (C) shows the plotting of the predicted log stability versus the measured ones for Orlistat/Soluplus across different loadings. The measured log stability exhibits uniformity across all drug loadings, even the pure drug, indicating no crystallization was detected experimentally, and Orlistat has consistently high stability. The predicted log stability closely aligns with the measured data, with relatively high and similar values but in a fluctuating trend, sometimes slightly overestimating the measured stability. This near-parallel trend between predicted and measured stabilities suggests the model is generally effective in capturing the stability profile for Orlistat as very high stability. However, occasional overestimations highlight areas where model refinement could further enhance accuracy.

4.4.3.3.8 *Aprepitant*

Figure 88 (D) shows the plotting of the predicted log stability versus the measured ones for Aprepitant/Soluplus across different loadings. The measured log stability is consistently high across all drug/polymer loadings, even for the pure drug (100%), suggesting that the drug remains stable in the polymer matrix at all loadings tested, with no signs of crystallization. On the other

hand, the predicted log stability varies significantly, showing several instances where the prediction is substantially lower than the measured stability. This discrepancy suggests that the model used to predict stability might not fully account for certain interactions or conditions that maintain the stability of Aprepitant in the polymer matrix. The model may need refinement to improve its predictive accuracy, particularly at certain drug/polymer loadings where its predictions are markedly off from what is observed.

Analysing the eight representative drugs within the Soluplus polymeric matrix has provided insights into the prediction model's performance and its potential for refinement. Consistent observations across the drugs include:

- **Uniform Stability Values:** Many drugs, such as Ritonavir, Fenofibrate, Aprepitant and Orlistat, as well as Felodipine, Probucof and Celecoxib, showed a trend of uniform high stability across multiple drug/polymer loadings. That highlights a specific trend that might have impact on the predictive accuracy of our model. The similar high stability results for most of these drug-polymer combinations provided limited variability in the dataset. This lack of variation could be a key reason why the model's predictions did not closely align with the measured stability values. In scenarios where no crystallization was detected, this consistent pattern of high stability across different drug/polymer loadings might have contributed to the model's challenges in distinguishing between subtly different stability outcomes. Essentially, the model's ability to accurately predict was likely hindered by the homogeneity in the data, as models generally require a range of outcomes to learn and predict effectively.
- **Capturing Overarching Trends:** In cases like Flufenamic acid, Tolbutamide, Nifedipine, Nitrofurantoin, Atenolol, Nicotinamide, Aspirin, Carbamazepine, Estradiol, Piroxicam and

Corticosterone, the predictive model captures the overarching trend of stability, even if it did not precisely mirror exact stability values. The strong predictive capability of our model can be primarily attributed to the diverse range of stability values observed across various drug-polymer loadings. These values represent a spectrum of stability scenarios, which are not relatively shifted towards immediate crystallization or are highly stable. This variation in stability data enhances the robustness and accuracy of our predictive model.

- **Immediate Crystallization Phenomenon:** The observed immediate crystallization of drugs such as Theophylline and Caffeine across all drug loadings presented significant challenges for the predictive accuracy of our model. This phenomenon, where the measured stability values were consistently zero for all drug-polymer loadings, resulted in a uniformity that created notable discrepancies between the actual and predicted stability values. This uniform zero stability measurement across different loadings did not provide the variability needed for the model to effectively learn and predict diverse stability outcomes, leading to these challenges in its predictive capacity.

In the context of PVPVA, twenty distinct models were generated, each corresponding to different drug loadings. These models incorporated four pivotal variables: the number of hydrogen bond acceptors (HBA), the number of heteroatoms (nHet), the number of oxygen atoms (nO), and the melting point (mp). In contrast, the models of Soluplus included one additional variable, the water-accessible surface area (ASA).

This model underscores the importance of recognizing the nuances in stability data, especially when crystallization data presents itself uniformly, to improve model accuracy and reliability further.

4.4.4 Suggested guidelines for enhancing stability in PVPVA and Soluplus solid dispersions

The comprehensive analysis of data, encompassing 23 drugs formulated within two distinct polymer matrices, PVPVA and Soluplus, and covering a broad spectrum of drug loadings and physicochemical properties, has helped elucidate the complex nature of stability in solid dispersions. Despite the inherent complexity and variability of the models, this analysis has allowed for the identification of overarching trends and significant correlations that influence stability.

A critical aspect of this study involved the application of LOOCV for each polymer matrix. This methodical approach entailed excluding data corresponding to one drug at a time, thereby assessing the robustness and consistency of the model's predictive capability. Notably, for the PVPVA polymer, the variables that consistently emerged across all drug formulations, as indicated by their highest frequency of appearance, mirrored those identified in the multiple linear regression model. A similar pattern was observed in the Soluplus models.

Hence, it can be concluded that the following parameters correlate with increased stability of the solid dispersions within the two polymeric matrices used in this study:

- 1. Decreased number of hydrogen bond acceptors (HBA)**

The analysis in our model indicates that the number of HBA in a drug molecule plays a significant role in the stability of solid dispersions with PVPVA and Soluplus. Several studies have investigated the significance of hydrogen bonding interactions in influencing the thermodynamic activity and dynamic characteristics of drugs and polymers in their mixtures [279, 280]. Xiang and Anderson investigated the molecular structure of ASDs of ibuprofen (IBP) in different polymeric mixtures using molecular dynamics simulations [281]. Extensive hydrogen bonding among IBP molecules was observed, resulting in various configurations such as dimers and chains. Hydrogen

bonding between IBP and polyvinyl pyrrolidone (PVP) in amorphous dispersions was shown to compete with IBP-IBP hydrogen bonding due to the carbonyl hydrogen bond acceptors in the polymer. This disruption of IBP-IBP hydrogen bonds is more pronounced in IBP-PVP dispersions than in the other polymers used, PVPVA and PVA [281]. Another study compared the effects of intermolecular hydrogen bonds between drug and polymer on the stability of ASDs prepared by spray drying for 60 days using six model drugs exhibiting fast, moderate, and slow crystallization tendencies and PVPVA polymer [282]. It highlighted that hydrogen bonds have varying degrees of effects, with the most significant impact observed in ASDs containing drugs with a moderate crystallization tendency. The study suggests that hydrogen bonds not only enhance stability but also influence drug loading capacity in ASDs [282]. Kesteur et al. investigated the influence of different polymers on the crystal growth rates of two diverse organic drug molecules, bifonazole and nimesulide, through the potential varying hydrogen bonding interactions with polymers between the two compounds [283]. Nimesulide exhibited a complicated hydrogen bonding pattern, forming both intramolecular and intermolecular hydrogen bonds. This pattern influenced its crystallization behaviour. They concluded that the choice of polymer to delay crystallization depends on the drug compound's chemistry and the competition between the groups in the drug and those present in the polymer. Polymers reduced the growth rates of both drugs used, but the extent of crystal growth inhibition varied among polymers. Therefore, the availability of hydrogen bonding groups appears to be a factor in a polymer's effectiveness in addition to the drug's chemistry [283].

Numerous studies have also discussed the significant impact of hydrogen bonding on the miscibility of drugs within a polymer matrix. However, the stability of solid dispersions concerning hydrogen bonding has not been addressed in these studies. Fridgeirsdottir et al.

developed six statistical MLR-based models using one drug/polymer loading (10% w/w) of 10 APIs with three polymers through two manufacturing methods [152]. They investigated the correlation of hydrogen bonding in the drug molecules with the stability of ASD, as increased stability correlates with a decreased number of HBDs in the drug molecule [152].

In our study, an increasing number of HBA correlates negatively with stability in all drugs used, at mid (ca. 40%) to higher drug loadings, particularly in high-drug loading scenarios when formulated with PVPVA or Soluplus polymer. Despite both PVPVA and Soluplus having HBA sites, the presence of these sites in the carrier polymer does not automatically lead to hydrogen bonding with the drug. That is a reasonable assertion, as the formation of hydrogen bonds depends on the compatibility and spatial arrangement of HBD (hydrogen bond donors) and HBA sites between the drug and the polymer. Increasing drug loadings (decreasing the polymer loading), may result in increasing the availability of the hydrogen bond donors/acceptors in the drug, which in turn may lead to bonding either between drug molecules or between the drug and water, both resulting in crystallization and reduced stability. This trend highlights the importance of hydrogen bonding interactions in influencing stability, with a higher number of HBA potentially leading to crystallization and decreased stability.

2. Increased number of heteroatoms (nHet):

From our analysis, the presence of heteroatoms (nHet) in the drug molecule exhibits a strong positive effect on the stability of ASD formulations, especially in mid to high-drug loading ranges. Heteroatoms are atoms in a molecule that are not carbon or hydrogen, typically elements like oxygen, nitrogen, sulfur, etc. An increase in the number of those atoms in a molecular structure can lead directly to a rise in the number of heteroatoms as illustrated in Table 4 (Chapter 2).

Heteroatoms like oxygen and nitrogen are highly electronegative, and their presence can significantly alter the electronic distribution, creating regions of partial negative charge that interact favourably with the polymer matrix in ASDs. These interactions could stabilize the amorphous form by preventing the molecules from aligning into a crystalline structure, so consequently could decrease the chance of nucleation and crystallisation. Additionally, heteroatoms can act as hydrogen bond acceptors, enhancing hydrogen bonding interactions within the drug-polymer matrix, thus creating a more interconnected and stable network that resists crystallization. The presence of multiple heteroatoms can also lead to a variety of intermolecular forces, including dipole-dipole interactions and hydrogen bonding, which help maintain the disordered amorphous state and reduce the likelihood of molecular alignment necessary for nucleation and crystal growth, thereby enhancing ASD stability.

When the linear correlation between the number of heteroatoms (nHet) and the number of oxygen (nO) - which resemble a part of the number of heteroatoms - was tested as shown in the matrices for the data sets of the solid dispersion within the two polymers (Figure 76 and Figure 86), a correlation coefficient of 0.47 was found. This value is below the threshold typically used to determine multicollinearity. The moderate correlation between nHet and nO indicates that these variables are not highly correlated to the extent of excluding one from further analysis. Rather, this finding suggests that nHet and nO represent distinct aspects of molecular structure that independently contribute to the stability of solid dispersions. Each variable likely plays a unique role, highlighting different chemical characteristics relevant to the observed properties of the dispersions.

A comprehensive model was developed by Mahlin et al. utilizing partial least squares projection to latent structure discriminant analysis (PLS-DA) based on the glass-forming capabilities of 16

pharmaceutical compounds underscores the positive impact of electronegative heteroatoms on the ability to form and maintain an amorphous state. The results showed that characteristics like branched carbon skeletons, molecular asymmetry, and distribution of electronegative atoms positively influence this ability [227].

As the nHet was the parameter that appeared as one of the highest frequencies when running the model using MLR as well as appeared in the model equation when all stability data for all drug-polymer loadings for two polymeric matrices were used, the nHet can affect the stability by decreasing the chance of molecular alignment into a crystalline structure.

3. Increased number of Oxygen atoms (nO)

In the analysis presented, an increasing number of oxygen atoms in the compound was found to correlate positively with the stability of the ASD, especially at mid to higher drug loadings. Drugs with higher nO counts may lead to more stable solid dispersions, particularly in high-drug loading scenarios when formulated with PVPVA or Soluplus polymer. The number of Oxygen atoms is related to the number of heteroatoms (nHet). However, nO and nHet were not highly correlated (0.47), as shown in Figure 86, to the extent of excluding one of them due to multicollinearity [284]. The number of oxygen atoms (nO) in a molecule is indeed related to its role as a hydrogen bond acceptor (HBA), but it is not solely responsible for determining whether a molecule acts as an HBA. While oxygen atoms can participate in hydrogen bonding interactions by accepting hydrogen bonds, the overall capability of a molecule to act as an HBA depends on its specific chemical structure and functional groups. In the context of solid dispersions and drug-polymer interactions, the presence of oxygen atoms can contribute to hydrogen bonding interactions with other molecules, including polymers. However, other factors such as the arrangement of these

oxygen atoms within the molecule, the availability of lone pairs of electrons, and the overall molecular geometry also play critical roles in determining the molecule's ability to act as an HBA. When the linear correlation between the number of oxygen atoms (nO) and the number of hydrogen bond acceptors (HBA) was tested as shown in the matrices for the data sets of the solid dispersion within the two polymers, a correlation coefficient of 0.6 was found. This value is below the threshold typically used to determine multicollinearity, which is why nO and HBA were not highly correlated to the extent of excluding one of them from our analysis. The moderate correlation suggests that while there is some association between these factors, they represent distinct aspects of molecular structure that independently contribute to the stability of solid dispersions.

Therefore, while the number of oxygen atoms (nO) is an important molecular characteristic that can influence hydrogen bonding interactions and stability in solid dispersions, it is not solely considered an independent factor for being a hydrogen bond acceptor. The overall molecular structure and electronic properties of the molecule must be considered to fully understand its role in hydrogen bonding and stability within drug-polymer systems.

The direct correlation between the number of Oxygen atoms and the stability of solid dispersion has not been discussed in the literature, but Oxygen is a highly electronegative element. The presence of multiple oxygen atoms in a drug molecule can influence its electronic distribution. This altered electron distribution can affect the drug's interactions within the polymer matrix in the solid dispersion. Mahlin et al. developed a comprehensive model based on the glass-forming capabilities of 16 pharmaceutical compounds and proved that characteristics like branched carbon skeletons, molecular asymmetry, and distribution of electronegative atoms positively influence their ability to form a glassy state [227]. Moore et al. investigated the co-solidification of 12

compounds with PVPVA polymer using melt-quenching. For all 12 compounds, molecular descriptor indices were calculated using their crystallographic structures. Logistic regression was then used to determine the correlation between these molecular descriptors and the potential for forming amorphous molecular solid dispersions. The relationship between the atomic mass-weighted third-order R autocorrelation index (R3m) index and the probability of successful solid dispersion formation is positive. This means that as the R3m index increases, the likelihood of the successful formation of solid dispersions also increases. The R3m index considers factors like the arrangement of electronegative atoms and their interatomic distances within a molecule. A higher R3m value indicates a molecular structure where electronegative atoms are positioned around the molecule's periphery in a way that minimizes their interatomic distances. This structural attribute positively correlates with an increased probability of forming successful solid dispersions when combined with polymers like PVPVA [285].

4. Decreased value of the melting point (mp):

The analysis suggests that lower melting points contribute to better stability in solid dispersions, particularly at lower drug loadings (5-25%). While the coefficient values for the melting point are negative, they are relatively small in magnitude, especially when compared to some of the other variables. However, this results from the data used for the melting point being of a greater magnitude than the other data, which is also considered for the equation for log stability. Drugs with lower melting points exhibit weaker intramolecular interactions, allowing for better dispersion within the polymer matrix. The stability of drugs in ASDs, particularly with lower melting points, could be influenced by favourable intermolecular interactions with polymer matrices. This suggests that low melting point drugs tend to be more stable as ASD formulations

within both polymeric matrices than drugs with higher melting points, particularly for typical pharmaceutical loadings (5-25%).

5. **An increased value of water-accessible surface area of drug molecule:**

An increased value of water-accessible surface area (ASA) at the molecular level plays a critical role in achieving stability of solid dispersions. The model suggests that drug molecules with higher ASA achieved higher stability of their solid dispersions. A larger ASA would allow for more extensive intermolecular interactions between the drug and the polymer. These interactions could include van der Waals forces and dipole-dipole interactions, which can help stabilize the amorphous form of the drug within the polymer matrix. Drugs with a larger ASA might disperse more uniformly in the polymer during the manufacturing process. This uniform dispersion is key to achieving a stable ASD because it prevents the formation of drug-rich and drug-poor regions, which can lead to instability and heterogeneity in the final product.

4.5 **Conclusions**

Our study has examined the stability of solid dispersions within two polymeric matrices, PVPVA and Soluplus, utilizing an extensive dataset comprising 23 drugs characterized by diverse physicochemical properties. The analytical approach was anchored in constructing MLR models for each polymer. These models were uniquely developed based on a unique number of formulations using varying drug/polymer loadings, encapsulating the critical variables that would be correlated with the stability of ASD, such as HBA, nHet and nO in the drug molecule. The general guidelines can be concluded that higher stability of solid dispersions can be correlated with:

- the decreased number of hydrogen bond acceptors
- the increased number of heteroatoms

- the increased number of Oxygen atoms
- the decreased melting point
- the decreased accessible surface area

A distinguishing aspect of this study was the application of LOOCV as a robust method for model validation. Remarkably, the results of the predicted log stability from the MLR models showed commendable agreement with the experimentally measured stability outcomes.

Such an analytical methodology, blending comprehensive data analysis with sophisticated validation techniques, has yielded profound insights into the stability mechanisms governing solid dispersions in the chosen polymers. This fusion of empirical data with advanced statistical modelling has not only reinforced the credibility of the study's findings but has also contributed significantly to the nuanced understanding of stability factors in pharmaceutical solid dispersions. The promising results obtained in this study indicate a significant potential for applying knowledge-based computational models in the field of pharmaceutical formulation development. The models developed through our research could serve as valuable resources for guiding the early stages of formulation design.

However, to enhance the reliability of these models for such purposes, additional extensive data would be required to enhance their predictability and robustness. Additionally, external validation would be very beneficial to minimize the risk of model overfitting. By addressing these aspects, the models can be refined and positioned as more robust and reliable tools, paving the way for their practical application in pharmaceutical development.

5 Chapter 5: Three-Dimensional Inkjet Printing of Solid Dispersions

5.1 *Three-Dimensional (3D) Technology*

5.1.1 Introduction

The application of three-dimensional (3D) printing is far-reaching, impacting sectors such as automotive, construction, aerospace, and, notably, the medical sector. More specifically, in pharmaceuticals, 3D printing has experienced a significant surge in interest and development [286, 287]. This is attributable to the technology's ability to offer unprecedented flexibility in medicine design, including structuring complex 3D shapes within medications, customising drug dosages and combinations, and accelerating manufacturing and prototyping [288]. These capabilities enable precise control over drug release, catering to various clinical needs. Moreover, 3D printing in pharmaceuticals allows for a high degree of personalisation, adapting drugs to the specific requirements of individual patients. This personalisation, combined with the significant reduction in the time required for formulation development, could drive a paradigm shift in pharmaceutical manufacturing [289-291]. 3D printing, also known as additive manufacturing, is a process in which a design is created using computer-aided design (CAD) software, segmented into slices, and sent to a printer. The printer then builds the final three-dimensional object layer by layer, following the concept of additive layer construction [292, 293].

The evolution of 3D printing technology has given rise to a plethora of specialised techniques. These methods vary widely in their approach, ranging from the type of materials used to the mechanisms of layer deposition and the characteristics of the final product. In response to this diversity, the American Society for Testing and Materials has categorised 3D printing technologies

into seven distinct types based on their underlying technical principles. These include material extrusion, binder jetting, powder bed fusion, vat photo-polymerisation, material jetting, directed energy deposition, and sheet lamination, each offering unique advantages and applications [294, 295].

Illustrating the versatility of 3D printing in pharmaceutical research, the technology has been employed in manufacturing a diverse range of medicinal products. These include immediate-release and controlled-release tablets, dispersible films, microneedles for painless transdermal drug delivery, implants for sustained drug release, and transdermal patches for topical administration [296].

The 3D-printed drug industry has been evolving for over twenty years. It began in 1996 when the US-based Therics licensed the powder bed (PB) 3D-printing technology from the Massachusetts Institute of Technology, establishing the first 3D-printed drug company. In a pivotal turn, Apria Pharmaceuticals acquired the PB technology in 2003 and, after a decade of development, created the innovative ZipDose technology. This led to the 2015 launch of Spritam®, the first FDA-approved 3D-printed medicine, igniting a surge in research within this field [297]. Post-2015, the sector witnessed numerous specialised 3D-printed drug companies emerging. Developing medicines requires a multidisciplinary approach involving mechanical engineering, pharmacy, materials science, software, and information engineering expertise. Additionally, the industry works within stringent pharmaceutical regulations, adding to the complexity of development. Currently, the global 3D-printed drug market is still in its nascent stage. Several pharmaceutical firms are actively working to advance and introduce new 3D-printed medications. Those companies are primarily based in Europe, the US, and China. These focus on two main application areas: large-scale production and personalised drug delivery [297].

In the context of the work presented in this thesis, this chapter presents an initial assessment of 3D printing in medicine manufacturing, as might be done by scaling up from the screening and modelling studies previously presented in this work.

5.1.2 3D Printing Technologies in Drug Delivery

5.1.2.1 Inkjet printing

Inkjet printing, derived from Lord Rayleigh's instability theory (1878), described the transformation of a liquid stream into droplets [298]. This theory has been instrumental in developing continuous jet (CJ) and drop-on-demand (DOD) printing, as used in conventional desktop printers [292]. Continuous jet printing uses pressurised flow to produce a steady stream of droplets, which are charged and directed onto a substrate or disposed of for recirculation. Conversely, DOD printing, known for its precision and efficiency, generates droplets ranging from 1–100 pL at high speeds as needed [299].

5.1.2.1.1 Thermal and Piezoelectric Print Heads in DOD Printing

In DOD printing, thermal (bubble) and piezoelectric methods are common. Thermal print heads employ a resistor that heats rapidly upon receiving electrical pulses, creating a vapour bubble that propels ink out and draws more ink into the chamber. Though this method risks thermal degradation, its short duration and minimal contact area generally mitigate this. However, the need for volatile solvents could limit its pharmaceutical applications [171]. Piezoelectric print heads use a piezoelectric element to generate mechanical movement and create pressure waves that eject fluid from the nozzle. This method, avoiding heat generation, offers better control over droplet formation, making it more suitable for drug development [300].

5.1.2.1.2 Considerations in Formulation and Process Parameters

3D inkjet printing encompasses three main aspects: droplet formation, droplet impact and spreading, and drying or solidification. Most pharmaceutical DOD printing utilises piezoelectric actuation to avoid the need for volatile materials required by thermal methods. Factors like fluid viscosity, density, and surface tension can influence droplet formation. Dimensionless values like Reynolds (Re), Weber (We), and Ohnesorge (Oh) numbers help predict fluid behaviour, determining stable drop generation and sufficient energy for droplet ejection. Printable fluids generally fall within Z (the inverse of Oh) values of 1–10 [301].

In 3D printing jetting approaches, the standoff distance, the distance between the nozzle and substrate, is critical. Typically, this is set to 2-3 mm in piezoelectric systems to minimise airflow effects while allowing proper droplet formation [301]. Droplet behaviour varies based on the substrate: on non-porous surfaces, it depends on droplet volume and contact angle, while on porous surfaces, like powder beds, it also involves fluid infiltration [299, 302].

The process of drying or solidification significantly affects the characteristics of the ultimate printed medication form. Typically, this involves the evaporation of solvents, with the evaporation rate being dependent on the chosen solvent system. For instance, this solvent evaporation phase can be strategically manipulated by employing a polymer-API-solvent mixture as the printing ink, forming an amorphous solid dispersion once the droplet dries [172, 193]. Such a technique not only enables the formulation of drugs with poor solubility but also allows for the creation of medications in extremely low dosages, thanks to the precise delivery capabilities of inkjet print heads. Nevertheless, there is a potential for the API to recrystallise from the printing fluid, which might alter the mechanical properties and release dynamics of the dosage form. Therefore, it is crucial to investigate the physical stability of the printed API [301].

5.1.3 Advantages of 3D Printing in Pharmaceutical Applications

5.1.3.1 Precise Drug Release Control

Tablets represent the predominant solid oral dosage form, comprising 70% of the production of all dosage forms [303]. Traditional tablet manufacturing by power compression, despite its cost-effectiveness, often lacks innovation and flexibility in creating personalised medications. 3D printing, in contrast, excels in developing controlled-release medications that ensure precise drug release, minimising side effects and maximising efficacy [304]. This technology facilitates the creation of complex preparations combining different drugs and intricate designs.

5.1.3.2 Rapid Integration of Production

Standard pharmaceutical manufacturing, designed for mass production, typically lacks the flexibility needed for rapid changes in drug varieties. 3D printing technology, with its compact and automated setup, simplifies production changes, making it ideal for multi-drug manufacturing. In drug development phases, 3D printing proves cost-effective for small-scale, customised production, which is crucial under tight time and resource constraints. This efficiency is evident in Merck's use of 3D printing to expedite clinical trials, significantly reducing development time and API usage [305].

5.1.3.3 Personalised Medicine for Special Populations

In addressing the medication needs of particular groups, like children and the elderly, 3D printing offers significant benefits. For children, this technology can produce low doses and improve the appearance and taste of the medications to enhance compliance [306-308]. For the elderly, especially those with swallowing difficulties, 3D printing can create porous forms that are easier to ingest. It also enables the combination of multiple drugs into a single tablet, reducing the risks

of medication errors and increasing effectiveness. Additionally, 3D-printed drugs can be customised with special shapes or symbols to assist visually impaired patients [309-311].

Finally, the advancement of 3D printing in the pharmaceutical industry marks a significant leap towards personalised medicine. By leveraging statistical modelling of data derived from 2D printed formulations, researchers can better understand the physicochemical properties of drugs, allowing for more precise customisation of medications. The technology's ability to adapt medicines based on individual patient profiles, considering factors like age, health conditions, and specific physiological responses, is revolutionary. The intricate control over drug composition, dosage, and release mechanisms, guided by comprehensive data analysis, ensures that each medication is optimally tailored for maximum efficacy and safety. Thus, 3D printing stands at the forefront of a new era in healthcare, where personalised medicine is not just a possibility but a practical reality, transforming the approach to treatment and patient care.

5.2 Aims and Objectives

In this chapter, the aim is to explore the viability of 3D inkjet printing in producing relatively high drug-loading formulations (30%) and to investigate the predictive accuracy of 2D printed microarray studies in predicting the miscibility of drug-polymer dispersions and the physical stability of pharmaceutical products in 3D printing processes.

That could be achieved through the following objectives:

- Assessing the feasibility of 3D inkjet printing towards developing formulations using Flurbiprofen and Piroxicam as model drugs within the PVPVA polymer matrix at a strategic drug loading (30%).

- Characterisation of 3D-printed formulations for signs of crystallisation during physical stability study in accelerated conditions as the conditions used for the 2D printed microarrays.
- Comparing the results of 3D printing with the predictions from 2D printed microarray studies, focusing on the physical stability data and miscibility of drug-polymer dispersions.

These aims and objectives integrate the insights gained from the 2D inkjet printing, specifically in terms of drug-polymer miscibility and crystallisation trends, to inform and guide the exploration and evaluation of 3D printing techniques in the context of pharmaceutical development. The results from this study would contribute to a deeper understanding of the parameters critical to the scalability of 3D-printed pharmaceuticals and the preservation of their physical stability during the transition from 2D to 3D printing.

5.3 *Experimental design*

5.3.1 Materials (model drugs and polymers)

Flurbiprofen and Piroxicam were purchased from Merck Life Sciences UK Ltd. The polymer used in this study, Polyvinylpyrrolidone-vinyl acetate copolymer K 28 (PVPVA) (Kollidon[®] VA 64) with molecular weight (45,000–70,000 Da), which is frequently utilised in marketed solid dispersion formulations was received as a generous gift from its commercial supplier from BASF SE, Germany. The chemical structures of the APIs and polymers are shown in Figure 89. Sodium chloride was purchased from Acros Organics, Fisher Scientific UK Ltd, to create the 75%RH accelerated condition for storing the printed samples. Dimethyl sulfoxide (DMSO) > 99.5% was purchased from Sigma Aldrich, France, and used as a common solvent to dissolve all the drugs and the polymer. Polyethylene terephthalate PET Sheets were used as a substrate.

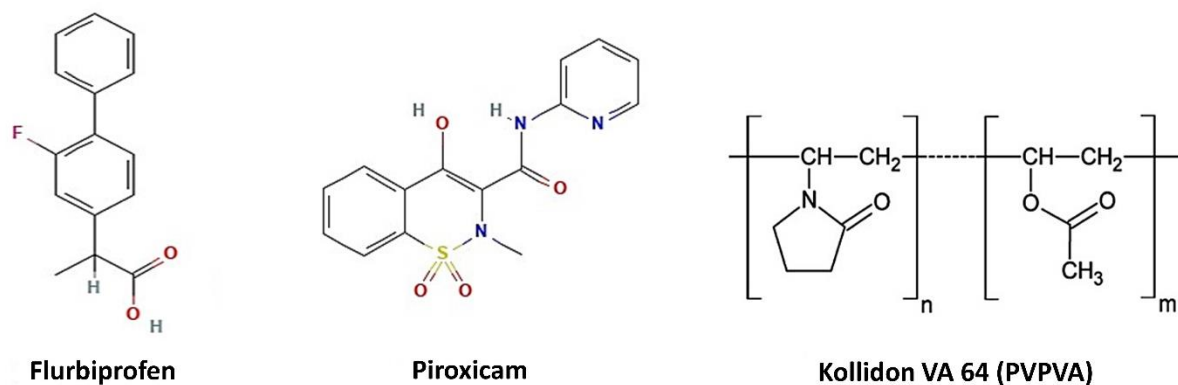


Figure 89. The molecular structures of two APIs, Flurbiprofen and Piroxicam, alongside the structure of a polymer, Polyvinylpyrrolidone-vinyl acetate (PVPVA), referred to here as Kollidon VA 64, utilised within this research [232, 233].

5.3.2 Methods:

In this study, a Fujifilm Dimatix Materials Printer DMP-2850 Series equipped with a 12-jet Samba cartridge (~10 pL drop volume) was used for the 3D printing of Flurbiprofen/Polyvinylpyrrolidone-vinyl acetate (PVPVA) formulations. The instrument is shown in Figure 90. The printing solution, composed of Flurbiprofen and PVPVA in a ratio of 200 mg to 460 mg in dimethyl sulfoxide (DMSO), was prepared to achieve an approximate 30% drug loading. The critical challenge for inkjet printing is the development of a reliable printable ink that can also maintain the functionality of printed formulation. The viscosity of the ink is generally accepted in the range between 8 and 15 milliPascal-second (mPa.s) [260]. The viscosity of the ink was characterised using Malvern Instruments Kinexus Pro Research Rheometer (shown in Figure 34, Chapter 2), which was found in the range of 7–9 mPa.s. That was employed using a ‘cup and bob’ configuration to inhibit solvent loss through evaporation. The ink was transferred into the cup using a syringe, and then the bob was lowered into the cup automatically. Viscosity readings were recorded across a range of shear rates, from 1 to 1000 s⁻¹. Notably, the readings obtained at a shear rate of 100 s⁻¹ are particularly significant, as they served as a crucial indicator of the ink's viscosity during its deposition process. Inks containing the drug and polymer were passed through a 0.45-micron

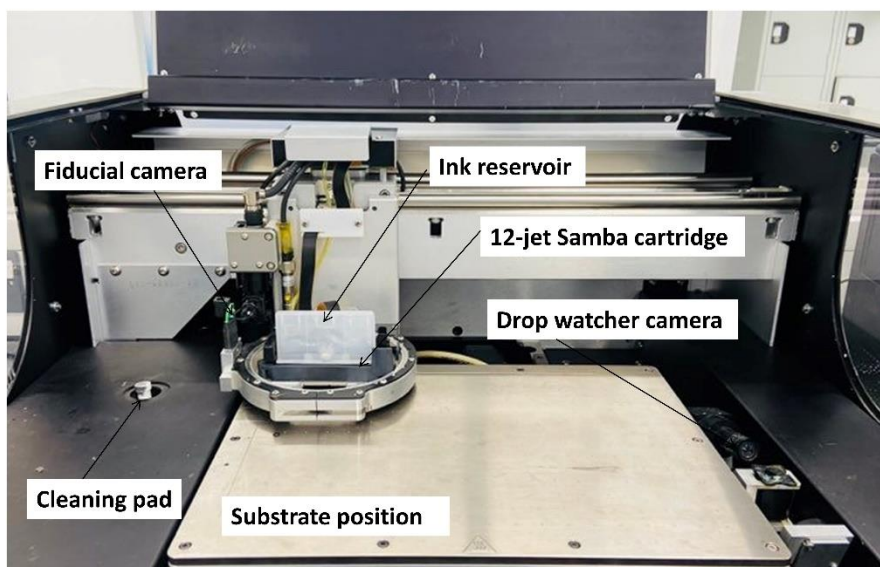


Figure 90. 3D inkjet printer, the Dimatix, utilised in this study, along with an annotated schematic detailing its key components such as the fiducial camera, ink reservoir, 12-jet Samba cartridge, drop watcher camera, cleaning pad, and substrate position.

filter to eliminate any large particles and then loaded into the printer cartridge using a syringe. The jetting parameters that could be controlled included the jetting voltage, waveform, frequency, and cartridge heating. The system's drop watcher function allowed for monitoring the jetting behaviour. During the printing, variables like the spacing between drops, the heating of the substrate, and the gap between the print head and the substrate could be varied. The printer settings were adjusted, with the cartridge temperature maintained at 40°C and the substrate temperature at 60°C, optimising the conditions for the inkjet printing process. The formulations were printed onto a polyethylene terephthalate (PET) film substrate. The printing procedure involved creating various designs, including a 5×5 droplet matrix, a 5 mm length and 0.1 mm width linear structure,

and two square configurations with dimensions of 0.5 mm × 0.5 mm and 3 mm × 3 mm, respectively.

Following the printing process, different substrate temperatures were tested regarding the drying phase and it was optimised at 60°C to ensure proper solvent evaporation and solidification of the formulation in its final form and multiple-layer printing. Throughout the study, strict adherence to safety protocols, particularly in handling DMSO and APIs, was conducted.

Following the established protocol used for Flurbiprofen/PVPVA formulations, the same methodological approach was applied to preparing Piroxicam/Polyvinylpyrrolidone-vinyl acetate (PVPVA) formulations. Utilising the same equipment settings, including the dimatix inkjet printer with a 12-jet Samba cartridge and maintaining identical temperature controls for both the cartridge and substrate, ensuring a consistent formulation preparation approach. The printing and post-printing procedures, including the drying phase and quality assessments, were replicated in line with the previously established method. This consistent approach allowed for the effective adaptation of the technique to the Piroxicam/PVPVA formulations, demonstrating the versatility and reliability of the method in producing varied pharmaceutical formulations.

Following the preparation of the 3D printed formulations, a short-term stability analysis (3 months) was carried out on the formulations under accelerated conditions (40°C ± 2°C/75% RH ± 5% RH) to monitor the physical stability of different 3D printed formulations. The 3D printed formulations were kept in a loosely closed plastic box inside a stability oven, and a data logger, Thermopro TP49, was used to monitor the environment. Polarised light microscopy (Advanced Polarizing microscope, PriorLuxPOL™) was used to analyse the printed formulations monitored directly after solvent evaporation and during the stability study. This instrument has an integrated

30W halogen lamp with variable brightness control polarised light source to detect the presence of birefringence in the printed samples to interpret crystallinity.

5.4 Results and Discussion

The results presented in this chapter represent preliminary data in the study of 3D printing applications for pharmaceutical formulations providing insights into the potential of the application technology in solid dispersion formulations.

In this study, two different drugs, Flurbiprofen and Piroxicam, were selected for their distinct physicochemical properties. PVPVA was chosen as the polymer matrix due to its more consistent performance compared to Soluplus regarding stability prediction of higher numbers of APIs used in this study, as indicated by our developed statistical model, as discussed in Chapter 4, which evaluated the stability of solid dispersions and their efficacy in inhibiting drug crystallisation. Both drugs were incorporated into the formulations at a 30% w/w drug loading concentration. This concentration was strategic; for Flurbiprofen, it is below the drug's miscibility limit with PVPVA and hence expected to promote stability and prevent crystallisation. In contrast, the concentration was above the miscibility limit for Piroxicam, presenting a challenging scenario for assessing the crystallisation behaviour in 3D-printed formulations.

5.4.1 Optimisation of the printing criteria for 3D printed formulation

5.4.1.1 Inkjet printing progression from droplets to a square single-layer formulation (0.5 mm x 0.5mm)

In the process of optimising the conditions for a 3D printer tailored for pharmaceutical use, we progressed systematically from printing discrete droplets to larger continuous forms. The initial phase involved the deposition of single droplets to fine-tune the printer settings, mainly focusing

on the solution's viscosity and operational temperatures. The microscopic images in the bright field displayed in Figure 91 illustrate the sequence of the experimental printing.

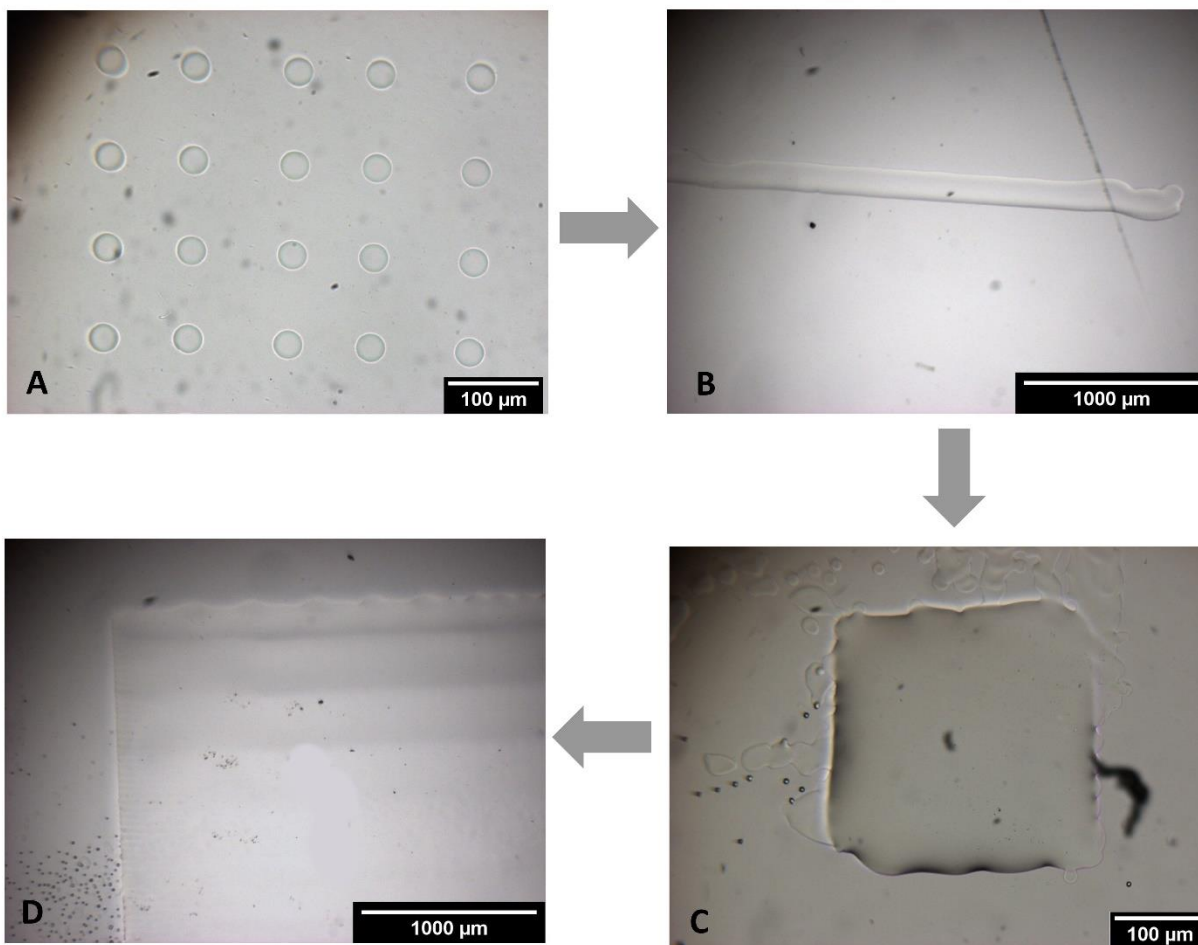


Figure 91. The stages of 3D printing optimisation, progress using 30% Flurbiprofen/PVPVA from precise droplet deposition (fine-tuning droplet formation) (A) to printing continuous lines (B) to the creation of larger, uniform structures of defined square formulation (0.5mm × 0.5 mm) (C) and finally, square formulations (3mm × 3mm) (D) as shown in the microscopic images at the bright field.

Figure 91 (Image 4a) shows a grid of well-defined droplets, indicating the successful calibration of the printer's droplet ejection system. The droplets' uniformity in size and shape suggests that the solution's viscosity and the printer's temperature settings were within the optimal range for this inkjet printer. This initial success was crucial as it provided the confidence to proceed with more complex structures. Figure 91 (Image 4b) demonstrates a uniform linear structure of 5 mm length

and 0.1 mm width. Hence, the continuity of printing and the behaviour of the solution over a larger printed area were verified.

Despite the Z dimension (height or thickness) of our 3D formulation not being directly measured, the successful printing of satisfactory droplets and lines resulted in a final printed structure with dimensions of 0.5 mm × 0.5 mm in the XY plane. The formulation consisted of one layer of material that were exceptionally thin, beyond the limit of practical measurement. The emphasis was placed on achieving optimal printing quality and dimensional accuracy in the XY plane rather than the Z dimension due to the extremely thin nature of the layers. Figure 91 (Image 4c) shows a square structure with well-defined edges and a uniform surface, confirming that the printing parameters set for smaller-scale structures were effective. This was a significant milestone, as it demonstrates the ability to fabricate a formulation on a micro-scale, a requirement for precision medicine and targeted drug delivery.

Encouraged by these results, we scaled up the printing to produce a larger 3D printed formulation with 3 mm × 3 mm dimensions. Figure 91 (Image 4d) shows the larger 3D-printed formulation with relatively straight edges and a homogeneous surface, suggesting that the printing conditions were successfully scaled. However, some irregularities are observed at the edges, indicating a need for further refinement of the printing parameters to achieve the desired precision at larger scales. In conclusion, the progression from droplet to line to square structures is a primary step for ensuring the quality of the larger printed structure is demonstrated and could ultimately lead to the successful 3D printing of a viable formulation.

5.4.1.2 Inkjet printing a 3D square formulation (3mm x 3mm)

Following the successful printing of a single-layer formulation, a 3D formulation with dimensions of 3 mm × 3 mm was printed, focusing on achieving precise printing outcomes within the XY

plane. Five layers were printed successively and then the formulation was left to dry overnight to allow any solvent residues to evaporate. The formulation consisted of multiple layers, each of which was exceedingly thin and not practical to remove the final formulation from the polyethylene terephthalate sheet to be measured directly in the Z dimension. Despite the challenge of measuring the Z dimension due to the thinness of the layers, the primary emphasis was on ensuring optimal printing quality and dimensional accuracy in the XY plane. The aim was to ascertain whether the behaviours observed in 2D printing would be consistent and reproducible when transitioning to a more complex, preliminary 3D structure as required for real-world pharmaceutical products.

5.4.1.3 3D-printed Flurbiprofen/PVPVA formulation

Figure 92 represents a series of microscopic images detailing the morphological characteristics of one 3D-printed formulation composed of a Flurbiprofen and PVPVA drug-polymer mixture printed in 5 layers. The 3D printed formulation, with dimensions of 3 mm by 3 mm, is imaged at various areas to provide a comprehensive view of its structure immediately after solvent evaporation, a critical moment for assessing the risk of crystallisation.

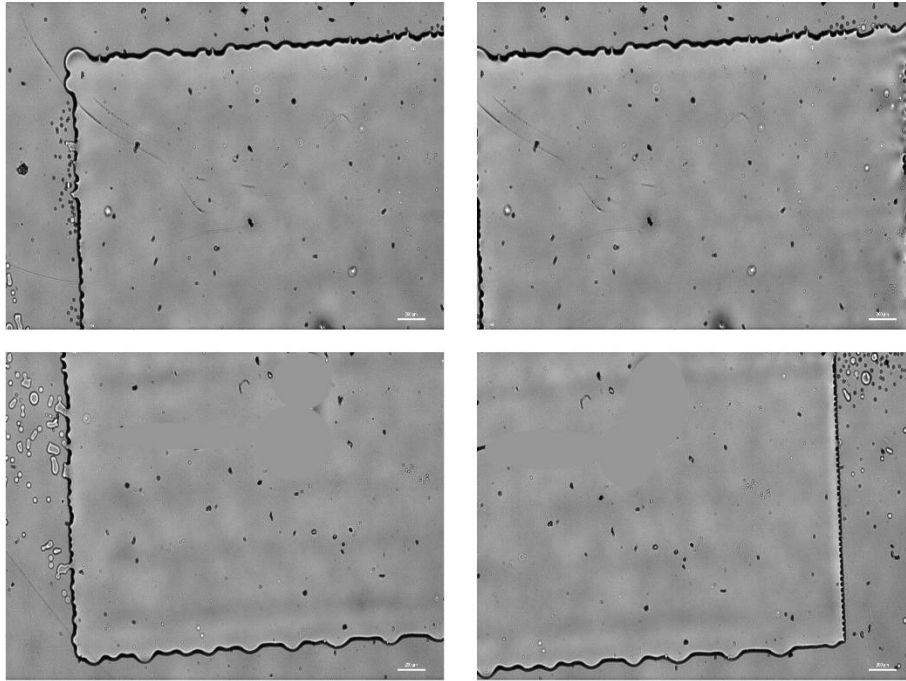


Figure 92. Four bright-field microscopic images of the same 3D-printed formulation prepared with a 30% Flurbiprofen/PVPVA mixture. Each image captures the 3D-printed formulation from a different angle, providing a comprehensive view of its structure. The scale bar represents 200 μm .

An examination of the images in Figure 92 reveals that the 3D-printed formulation retained its integrity post-printing, with no visible signs of stress or shear-induced defects, which could lead to heterogeneity within the formulation.

The maintenance of a homogenous surface suggest that the printing conditions - including temperature settings and solution viscosity - were sufficiently optimised to prevent disruption in the drug-polymer behaviour during the printing process. The conditions were conducive to maintaining the drug in a stable dispersion within the polymer matrix without inducing crystallisation.

These findings are consistent with observations from our previous work involving 2D-printed microarrays of the same drug-polymer dispersion. The resemblance between the 2D microarrays and the 3D printed formulation regarding the absence of crystallisation indicates that the 2D printing process serves as a reliable predictive tool for larger-scale printing. This suggests that the

2D printing technique developed here is not only time and material-efficient but also an accurate method for predicting the behaviour of drug-polymer dispersions in 3D printed forms. Such predictability is crucial for scaling up the manufacturing process while ensuring the quality and stability of the pharmaceutical product.

Figure 93 depicts a sequence of images displaying a 3D-printed formulation of 30% Flurbiprofen/PVPVA after three months of storage under accelerated stability conditions ($40^{\circ}\text{C} \pm 2^{\circ}\text{C}/75\% \text{RH} \pm 5\% \text{RH}$). The images were captured using a polarised light microscope to identify any potential birefringence, which indicates crystalline formation within the drug-polymer matrix. The top set of images (Figure 93 (A)) presents the samples in a bright field, while those at the bottom set (Figure 93 (B)) show the corresponding polarised field.

Upon examination using the cross-polarised field, the 3D-printed formulation exhibits no signs of birefringence, confirming the absence of crystallisation even after extended storage under challenging conditions. This observation is consistent across all the images, suggesting a stable drug dispersion within the polymer matrix over the test period. The maintenance of the amorphous state under accelerated stability conditions is particularly noteworthy as it underlines the robustness of the formulation, reinforcing the notion that the 3D-printed matrix has successfully preserved the drug's amorphous form, as would be predicted from the 2D printing stability modelling. The lack of crystallisation in these 3D printed formulations mirrors the results previously obtained from 2D printed microarrays. Considering the 30% drug loading used in both 2D and 3D formulations, which is below the miscibility limit for the drug, the absence of crystallisation aligns with expectations. These findings suggest that the drug-polymer dispersion remains stable and below the threshold at which the drug typically begins to crystallise.

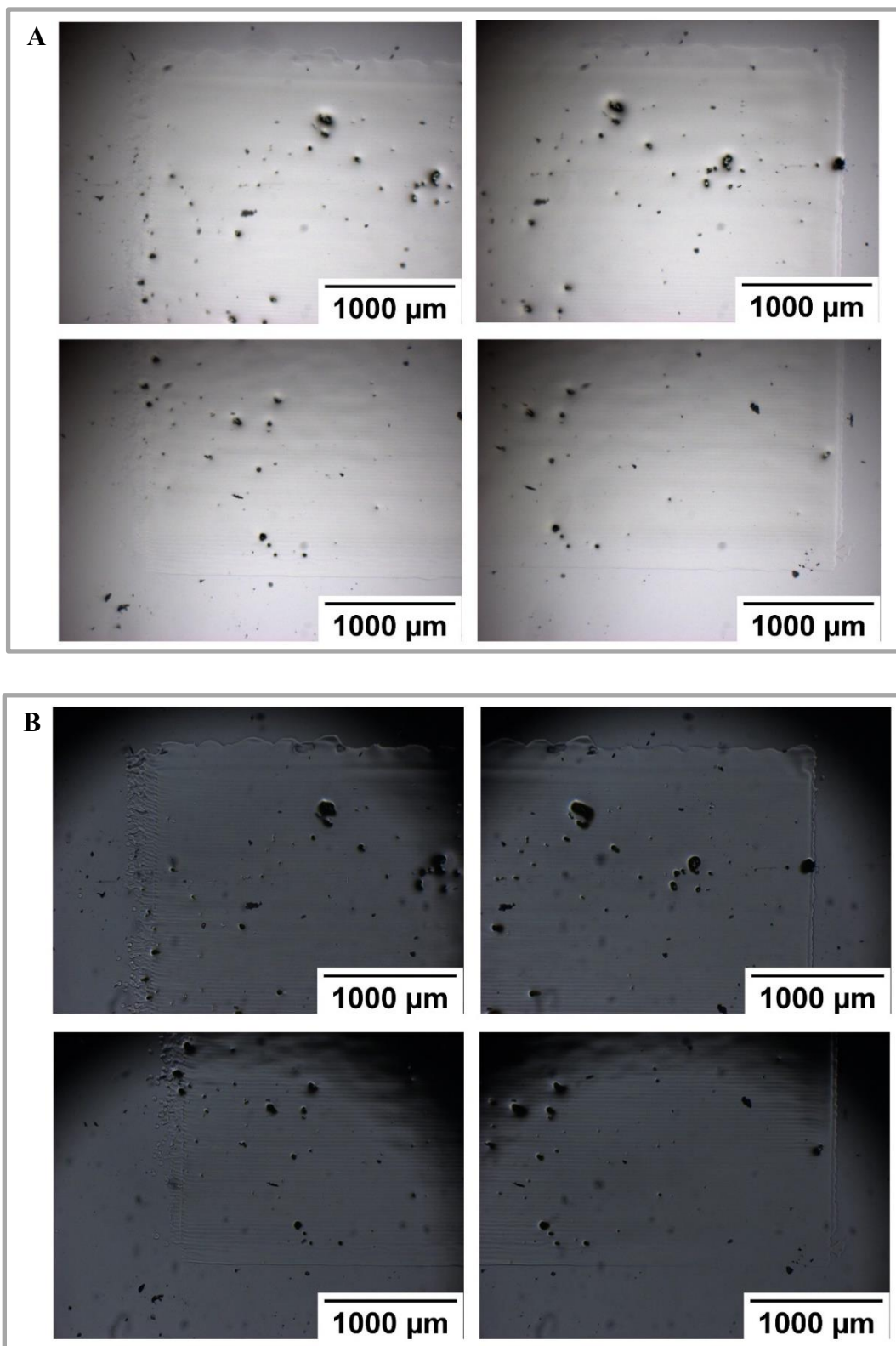


Figure 93. Microscopic images of the same 3D-printed formulation of Flurbiprofen/PVPVA within storage in accelerated stability conditions ($40^{\circ}\text{C} \pm 2^{\circ}\text{C}/75\% \text{RH} \pm 5\% \text{RH}$). The four images on the top (A) are captured in bright fields, and those on the bottom (B) are in polarised light; both sets provide views from different angles to identify any crystalline formations within the structure.

Polarised light microscopy (PLM) represents a tool for the detailed analysis of the solid-state properties of ASDs. PLM's capability to rapidly assess the amorphous nature of pharmaceutical compounds makes it an essential component in the characterisation of ASDs [312]. Thabet et al. demonstrated the continuous inkjet printing of enalapril maleate into orodispersible films. They utilised PLM to monitor the crystallisation process [313]. Cader et al. employed a Fujifilm Dimatix printer to create tablets using a water-based ink formulation composed of polyvinylpyrrolidone and thiamine hydrochloride. The study demonstrated the effective use of this technology in achieving a consistent drug loading and ensuring the drug was in its preferred polymorphic phase. Crucially, the study observed phase separation during the printing and drying process, which was indicative of crystal growth in the formulation. The presence of thiamine hydrochloride crystals suspended in polyvinylpyrrolidone was confirmed through cross-polarised imaging, providing valuable data for understanding crystallisation dynamics [296].

5.4.2 3D-printed Piroxicam/PVPVA formulation

Figure 94 displays images of the 3D-printed formulation containing a 30% Piroxicam and PVPVA drug-polymer mixture, each 3 mm by 3 mm in size, imaged immediately after solvent evaporation to assess crystallisation risk. The formulation shows on printing no signs of crystallisation, with clear surfaces and well-defined edges, indicating a stable dispersion of the drug within the polymer matrix. These results mirror the previous findings with Flurbiprofen, demonstrating that the optimised printing conditions effectively maintained the drug's physical stability.

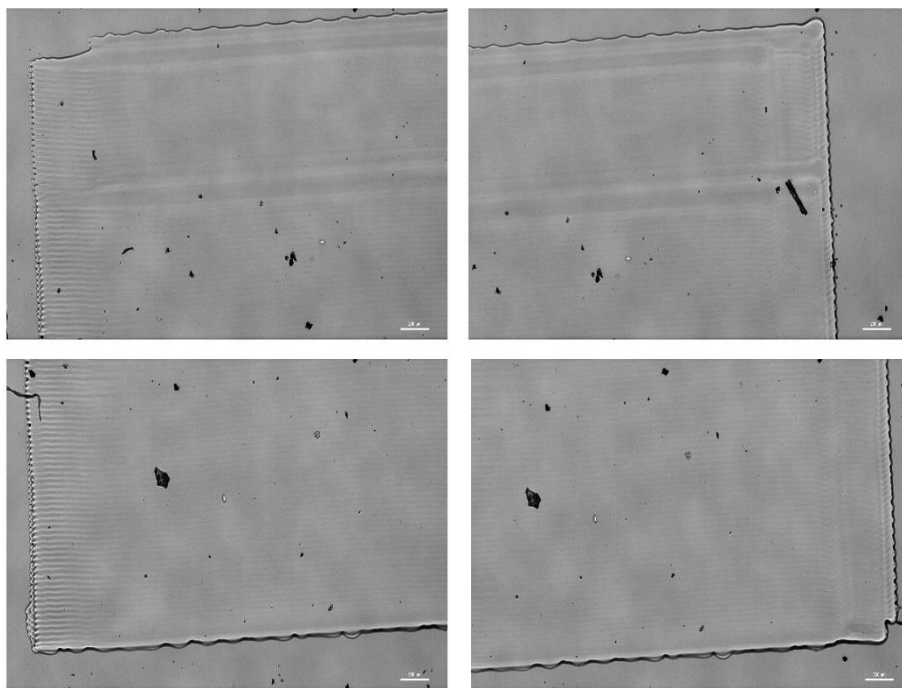


Figure 94. Four bright-field microscopic images of the same 3D-printed formulation prepared with a 30% Piroxicam/PVPVA mixture. Each image captures the formulation from a different angle, providing a comprehensive view of its structure. The scale bar represents 200 μm .

The images presented in Figure 95 demonstrate the stability outcomes of a 3D-printed formulation prepared with a Piroxicam and PVPVA drug-polymer mixture after three months of storage in a stability oven under accelerated conditions ($40^{\circ}\text{C} \pm 2^{\circ}\text{C}/75\% \text{RH} \pm 5\% \text{RH}$). Using a polarised light microscope, Figure 95 (A) displays the samples in a bright field, while Figure 95 (B) shows the samples in polarised light.

In the polarised field, there is a distinct presence of birefringence, indicative of crystallisation within the formulation. This is in contrast to the initial observations post-printing, where no immediate crystallisation was noted. The crystallisation observed aligns with the anticipated behaviour of the Piroxicam/PVPVA formulations, given that the 30% drug loading exceeds the miscibility limit of the drug with the polymer.

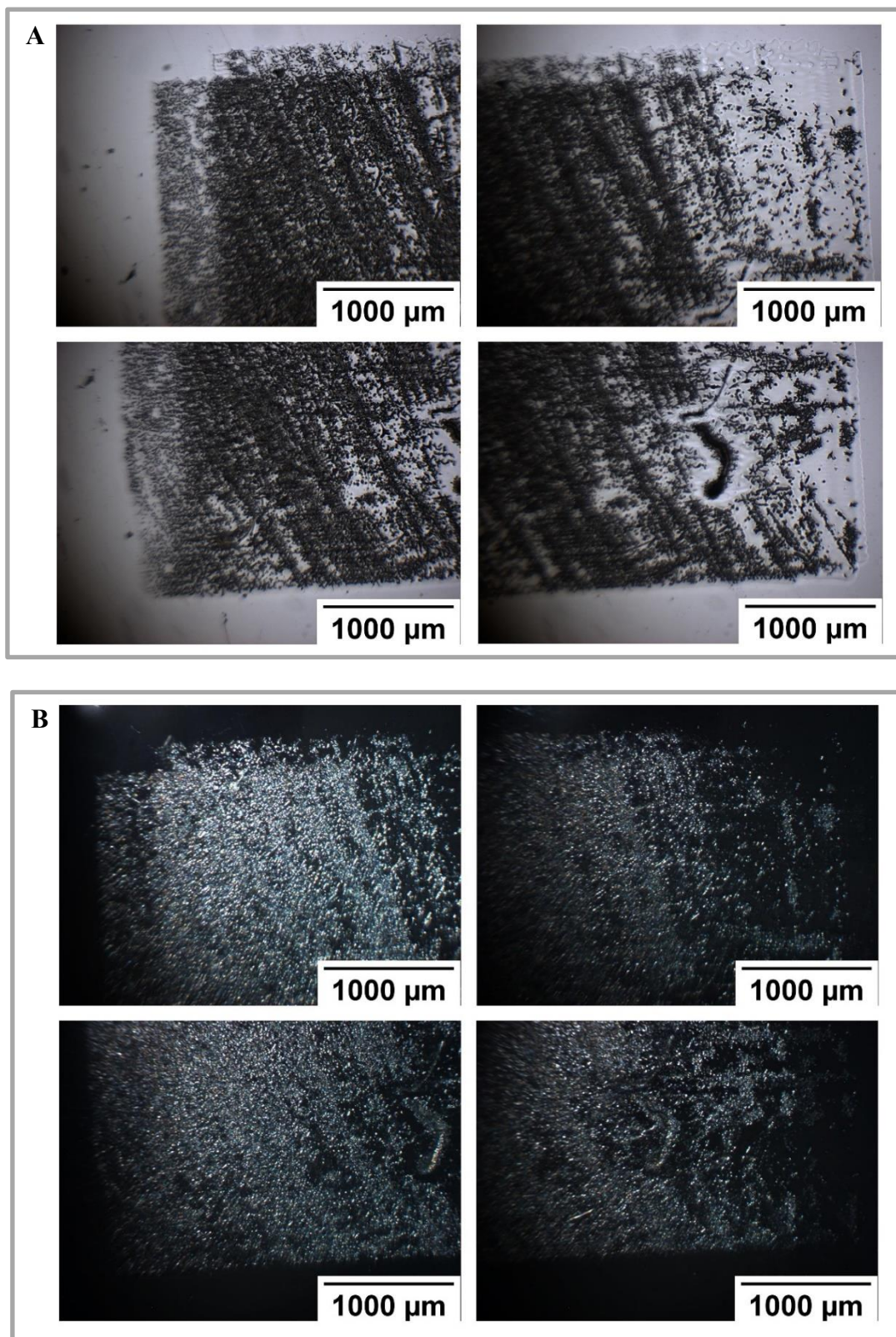


Figure 95. Microscopic images of the same 3D-printed formulation of Piroxicam/PVPVA within storage in accelerated stability conditions ($40^{\circ}\text{C} \pm 2^{\circ}\text{C}/75\% \text{RH} \pm 5\% \text{RH}$). The four images on the top (A) are captured in bright fields, and those on the bottom (B) are in polarised light, both sets provide views from different angles to identify any crystalline formations within the structure.

These findings also correlate with the behaviour observed in our 2D printed microarrays, where crystallisation was expected and occurred under similar storage conditions. This crystallisation upon storage, despite the absence of immediate crystallisation post-printing, confirms that while optimising 3D printing conditions can minimise immediate drug-polymer interaction disturbances, it does not alter the fundamental physicochemical properties of the drug-polymer mixture. Crystallisation is thus governed by the drug's inherent solubility and miscibility characteristics within the polymer matrix, manifesting over time under storage conditions.

A study by Farhan et al. investigated the formulations of 30% w/w spray-dried solid dispersions Flurbiprofen, Ketoprofen, and Piroxicam, using PVPVA as the drug carrier [314]. They demonstrated that fully amorphous solid dispersion systems were successfully produced for Flurbiprofen and ketoprofen with PVPVA, indicated by the absence of any melting endothermic peak in Differential Scanning Calorimetry and the lack of characteristic crystalline peaks in X-ray Powder Diffraction analysis. In contrast, the piroxicam-PVPVA system displayed crystallisation, as evidenced by crystalline peaks in XRPD and the presence of a melting endotherm in DSC. The findings from this study can support the observations in our research, where Flurbiprofen with PVPVA did not show any crystallisation at a 30% drug loading, aligning with the results in this study. Similarly, the observation of crystallisation in Piroxicam with PVPVA solid dispersion at 30% drug loading in our research is also mirrored in this study. The consistent behaviour of crystallisation tendencies of Flurbiprofen and Piroxicam in similar conditions align closely with our observations. In conclusion, the insights gained from the Farhan et al. study provide valuable support to our research findings, particularly in the context of 3D-printed pharmaceutical forms.

5.5 Conclusions

This preliminary study has substantiated the potential of inkjet 3D printing to successfully demonstrate the feasibility of fabricating formulations with a high drug load (30% w/w) using poorly soluble APIs - Flurbiprofen and Piroxicam - within a PVPVA polymeric matrix. The consistency observed between the crystallisation phenomena in 3D printed formulations and 2D microarray data underscores the effectiveness of 2D printing as a predictive tool for transitioning to 3D printing processes. This study emphasises the significance of 2D printing in the preliminary stages of formulation development, as it aids in predicting the physical stability of larger-scale drug-polymer mixtures.

Most importantly, in the context of this thesis, the stability outcomes of the 3D-printed solid dispersions are consistent with the stability modelling from the 2D array method developed here.

6 Conclusions and Future Work

6.1 *Conclusions*

The success and stability of solid dispersion formulations depend significantly on choosing suitable polymer carriers and processing methods. This selection process, usually based on the formulator's knowledge, sometimes supported by experimental tests and/or modelling, could be greatly enhanced - as explored in this work - by using more rapid processes, capable of using minimal amounts of drug and informing more reliable modelling.

The primary objective of this thesis is to develop a comprehensive statistical model that effectively correlates the stability of solid dispersion formulations with the physicochemical properties of the APIs and polymers employed. This model aspires to utilise a resource-efficient approach, minimising the material requirements typically associated with formulation development. Additionally, it aims to evaluate a broader spectrum of samples compared to conventional methods, thereby enhancing the robustness and applicability of the findings.

The feasibility of employing printed nano-arrays with pico-litres amounts of drugs with various physicochemical properties in the framework of pre-formulation and solid-form screening was investigated. This enabled the building of an extensive library of different drug and polymer loadings, which facilitated the identification and comparison of drugs' miscibility limits within different polymeric matrices.

Various preliminary techniques, such as manual and contact printing, were utilised to assess the printability of the drugs and polymers into addressable arrays and to choose the most convenient printing technique for our study. The findings from those techniques aligned with the results from the 2D inkjet printing conducted on a nanogram scale. Notably, the outcomes of the 2D printed arrays corresponded with those observed using a drop cast technique, especially concerning the

pure drugs and their miscibility limits within PVPVA polymeric matrices. The miscibility trend of Itraconazole within three polymeric matrices (HPMCAS, Soluplus, PVPVA) paralleled both the experimental results of this study and previously published data.

The novelty of this study lies in sample quantity, addressability, ease of analysis and the number of drug-polymer loading formulations explored, numbering approximately 930 combinations, significantly surpassing previous efforts, and ensuring safety with the minimal use of materials. With the capacity to fit 400-500 spots on a single microscope slide and the ability to produce roughly 1000 spots per hour, this method showcases efficiency. The slide analysis via PLM can be completed in about 45 minutes (manually and clearly could be done more quickly automatically), making it a swift process.

The 2D inkjet printing approach offers considerable advantages in conserving valuable and/or newly synthesised organic compounds, condensing the assay space, and expediting sample preparation and analysis. Inkjet printing provides a high-throughput and miniaturised screening technique with adaptability, a high level of automation, quick execution, low error rate, and minimal waste.

Despite the varied timescales and techniques used, the consistency in crystallisation tendencies observed across different compounds is noteworthy. This high volume of data from the 2D array approach was instrumental in developing statistical models that can predict the stability of solid dispersions based on the physicochemical properties of APIs. This research underscores the potential of inkjet printing as a valuable tool in the field of drug-solid dispersion and beyond, where assessing crystallisation is crucial.

The investigation built upon the extensive library of formulations developed from 23 different drugs combined within two polymeric matrices, PVPVA and Soluplus, with varying drug loadings.

Those formulations were monitored in a stability study under accelerated conditions to detect the onset of crystallisation. This stability data served as the critical input for developing multiple linear regression models, which aimed to predict the stability of amorphous solid dispersions.

The models integrated critical variables associated with the stability of amorphous solid dispersions, such as the number of hydrogen bond acceptors, heteroatoms, and oxygen atoms within the drug molecules. Key insights from the study illuminated the influences on the stability of solid dispersions:

- The number of hydrogen bond acceptors (HBAs) in a drug molecule exhibited a negative correlation with the stability of its solid dispersion, underscoring the pivotal role of drug-polymer and drug-drug interactions in the crystallisation process.
- The presence of heteroatoms generally enhanced the stability of ASD formulations, particularly at mid to high-drug loadings, likely due to their contribution to molecular flexibility and disruption of crystalline structures.
- A higher count of oxygen atoms within the drug molecule was positively linked to stability, possibly reflecting their impact on electronic distribution and intermolecular interactions in the polymer matrix.
- A decreased value of melting point drugs would lead to the formation of more stable ASD formulations within both polymeric matrices than drugs with higher melting points, particularly for typical pharmaceutical loadings (5-25%).
- An increased water Accessible surface area of the drug molecule is found to be associated with the increased stability of amorphous solid dispersion.

A cornerstone of the study was the rigorous validation of the developed models through LOOCV, yielding results that closely matched the trend of the experimentally measured stability.

The fusion of detailed data analysis with such meticulous validation practices has not only underpinned the reliability of our findings but has also enriched the understanding of stability dynamics in ASDs.

Moving forward, expanding data and external validation will be critical to refine these models, enhancing their predictive accuracy and applicability in pharmaceutical development.

This thesis demonstrated the viability of 3D inkjet printing to produce formulations with a high drug load (30% by weight), focusing on two poorly soluble APIs, Flurbiprofen and Piroxicam, using a PVPVA polymer matrix.

Our findings reveal that the 3D printing process has been optimised to effectively assess the stability of drug-polymer dispersions. The 3D-printed Flurbiprofen/PVPVA formulations exhibited no signs of crystallisation post-printing, with clean surfaces and sharp edges, mirroring the results seen with 2D-printed microarrays. This correlated with 2D printing as a reliable predictor for the outcomes of 3D printing processes. While the Piroxicam/PVPVA formulation initially showed a stable dispersion, crystallisation was observed after three months under accelerated storage conditions. These observations underscore the significance of accounting for the long-term stability of drug-polymer combinations and suggest that 2D printing could be an invaluable predictive tool for assessing the physical stability of pharmaceutical products over time. To sum up, in this thesis, a novel work employing printed nano-arrays with pico-litres of diverse drugs was presented, facilitating the creation of an extensive library of drug and polymer loadings. This enabled a comprehensive comparison of drugs' miscibility limits within various polymers. The precision and efficiency of 2D inkjet printing, alongside its ability to conserve valuable resources, show its suitability for high-throughput and miniaturised screening methods.

Upon this foundation, an extensive library to monitor formulations for crystallisation under accelerated conditions was used to build multiple linear regression statistical models that detected the main physicochemical properties in the drug molecule influencing the stability of amorphous solid dispersions like hydrogen bond acceptors, heteroatoms, and oxygen atoms.

The predictive power of 2D printing was confirmed by using 3D inkjet printing to produce relatively high drug load tablets using poorly soluble APIs. The monitoring of crystallisation in the 3D printed formulation, which was consistent with the 2D microarray data, demonstrates the reliability of 2D printing as a predictive tool for upscaling to 3D printing. The agreement between the 2D and 3D stability outcomes reinforces the utility of 2D printing in early-stage formulation development, enabling the anticipation of the physical stability of scaled-up drug-polymer dispersions.

Overall, this thesis not only advances the field of pharmaceutical formulation but also sets the stage for the future refinement and practical application of these computational models in the industry.

6.2 *Future work*

Expanding the dataset to include a broader and more diverse range of APIs and polymers presents a significant opportunity for future research. It would be valuable to explore additional polymers with varied chemistry, including those with hydrogen-bonding donation capabilities. This exploration would aid in advancing the statistical modelling process and identifying additional descriptors that influence the stability of ASDs. Although our current dataset already surpasses previous studies in scale, extending this to encompass more diverse combinations of APIs with more variant physicochemical properties and crystallisation behaviour as well as polymers that are widely used in the pharmaceutical industry would enable more general conclusions about the

stability of solid dispersions and would allow for a more comprehensive understanding of the physical stability of solid dispersion combinations.

Expanding and diversifying the dataset is a crucial next step that could be considered in future work. The current models show promise, but their reliability and predictive power can be significantly improved with a more extensive dataset. By incorporating additional data, you can reduce the impact of outlier exclusion in LOOCV and potentially enable the use of separate training and test sets for model validation, a methodology that is more robust and indicative of a model's predictive capabilities in real-world scenarios.

Such an expanded dataset would not only provide a more robust foundation for our statistical models but also enhance the predictive accuracy and applicability of our findings in the pharmaceutical field. This approach aligns well with the industry's shift towards personalised medicine, where understanding the different API-polymer interactions is crucial for developing tailored drug formulations.

Conducting release studies and other quality control studies of the printed 3D formulations would offer critical insights into these drug delivery systems' release profiles and efficacy. This aspect is crucial for assessing the practical applicability of 3D-printed pharmaceuticals. Additionally, incorporating more advanced characterisation techniques, such as Raman spectroscopy, ToF-SIMS and scanning electron microscopy (SEM), would provide a deeper understanding of the microstructure and physicochemical properties of the printed formulations. These techniques will be instrumental in elucidating the mechanisms behind drug-polymer interactions and stability, thereby refining the predictive models further.

Future work should also focus on scaling up the research findings for practical, real-world applications in pharmaceutical manufacturing, considering the regulatory and commercial aspects of bringing such innovative drug formulations to market.

By broadening the scope of the research in these directions, our study will not only contribute significantly to the field of pharmaceutical formulation but also pave the way for the practical application of these advanced technologies in drug development and manufacturing. That could lead to the development of more effective, stable, and safe medicine products, ultimately benefiting the field of pharmaceutical sciences and patient care.

7 References

1. Raghavendra, M., J.R. Raj, and A. Seetharaman, A study of decrease in R&D spending in the pharmaceutical industry during post-recession. *International Journal of Academic Research*, 2012. 4(5).
2. Duchowicz, P.R. and E.A. Castro, QSPR studies on aqueous solubilities of drug-like compounds. *International journal of molecular sciences*, 2009. 10(6): p. 2558-2577.
3. Ikegami, K., K. Tagawa, and T. Osawa, Bioavailability and in vivo release behavior of controlled-release multiple-unit theophylline dosage forms in beagle dogs, cynomolgus monkeys, and göttingen minipigs. *Journal of pharmaceutical sciences*, 2006. 95(9): p. 1888-1895.
4. Charman, S.A. and W.N. Charman, Oral Modified-Release Delivery Systems, in *Modified-release drug delivery technology*. 2002, CRC Press. p. 25-34.
5. Wang, J. and T. Hou, Recent advances on aqueous solubility prediction. *Combinatorial chemistry & high throughput screening*, 2011. 14(5): p. 328-338.
6. Amidon, G.L., et al., A theoretical basis for a biopharmaceutic drug classification: the correlation of in vitro drug product dissolution and in vivo bioavailability. *Pharmaceutical research*, 1995. 12: p. 413-420.
7. Bergström, C.A., et al., Is the full potential of the biopharmaceutics classification system reached? *European Journal of Pharmaceutical Sciences*, 2014. 57: p. 224-231.
8. Butler, J.M. and J.B. Dressman, The developability classification system: application of biopharmaceutics concepts to formulation development. *Journal of pharmaceutical sciences*, 2010. 99(12): p. 4940-4954.
9. Savolainen, M., et al., Better understanding of dissolution behaviour of amorphous drugs by in situ solid-state analysis using Raman spectroscopy. *European journal of pharmaceutics and biopharmaceutics*, 2009. 71(1): p. 71-79.
10. Kawabata, Y., et al., Formulation design for poorly water-soluble drugs based on biopharmaceutics classification system: basic approaches and practical applications. *International journal of pharmaceutics*, 2011. 420(1): p. 1-10.
11. Lachman, L., H. Lieberman, and J. Kanig, *The Theory and Practice of Industrial Pharmacy*, Lea and Febiger. Philadelphia, USA, 1986.
12. Savjani, K.T., A.K. Gajjar, and J.K. Savjani, Drug solubility: importance and enhancement techniques. *International Scholarly Research Notices*, 2012. 2012.
13. Clugston, M. and R. Flemming, *Advanced chemistry*. 2000: Oxford university press.
14. Stegemann, S., et al., When poor solubility becomes an issue: from early stage to proof of concept. *European journal of pharmaceutical sciences*, 2007. 31(5): p. 249-261.
15. Loftsson, T. and M.E. Brewster, Pharmaceutical applications of cyclodextrins: basic science and product development. *Journal of pharmacy and pharmacology*, 2010. 62(11): p. 1607-1621.
16. Paolini, G.V., et al., Global mapping of pharmacological space. *Nature biotechnology*, 2006. 24(7): p. 805-815.
17. Llinàs, A., R.C. Glen, and J.M. Goodman, Solubility challenge: can you predict solubilities of 32 molecules using a database of 100 reliable measurements? *Journal of chemical information and modeling*, 2008. 48(7): p. 1289-1303.
18. Leeson, P., Chemical beauty contest. *Nature*, 2012. 481(7382): p. 455-456.

19. Lipinski, C.A., Drug-like properties and the causes of poor solubility and poor permeability. *Journal of pharmacological and toxicological methods*, 2000. 44(1): p. 235-249.
20. Lipinski, C.A., et al., Experimental and computational approaches to estimate solubility and permeability in drug discovery and development settings. *Advanced drug delivery reviews*, 2012. 64: p. 4-17.
21. Nalawansa, D.A. and C.M. Crews, PROTACs: an emerging therapeutic modality in precision medicine. *Cell chemical biology*, 2020. 27(8): p. 998-1014.
22. Benowitz, A.B., P.T. Scott-Stevens, and J.D. Harling, Challenges and opportunities for in vivo PROTAC delivery. *Future Medicinal Chemistry*, 2022. 14(3): p. 119-121.
23. Repka, M.A., et al., Applications of hot-melt extrusion for drug delivery. *Expert opinion on drug delivery*, 2008. 5(12): p. 1357-1376.
24. Van den Mooter, G., The use of amorphous solid dispersions: A formulation strategy to overcome poor solubility and dissolution rate. *Drug Discovery Today: Technologies*, 2012. 9(2): p. e79-e85.
25. Hörter, D. and J. Dressman, Influence of physicochemical properties on dissolution of drugs in the gastrointestinal tract. *Advanced drug delivery reviews*, 2001. 46(1-3): p. 75-87.
26. Vasconcelos, T., B. Sarmiento, and P. Costa, Solid dispersions as strategy to improve oral bioavailability of poor water soluble drugs. *Drug discovery today*, 2007. 12(23-24): p. 1068-1075.
27. DeBoyace, K. and P.L. Wildfong, The application of modeling and prediction to the formation and stability of amorphous solid dispersions. *Journal of Pharmaceutical Sciences*, 2018. 107(1): p. 57-74.
28. Branchu, S., et al., A decision-support tool for the formulation of orally active, poorly soluble compounds. *European journal of pharmaceutical sciences*, 2007. 32(2): p. 128-139.
29. Ku, M.S. and W. Dulin, A biopharmaceutical classification-based Right-First-Time formulation approach to reduce human pharmacokinetic variability and project cycle time from First-In-Human to clinical Proof-Of-Concept. *Pharmaceutical development and technology*, 2012. 17(3): p. 285-302.
30. Hariharan, M., et al., Reducing the time to develop and manufacture formulations for first oral dose in humans. *Pharmaceutical technology (2003)*, 2003. 27(10): p. 68-84.
31. Stella, V.J. and K.W. Nti-Addae, Prodrug strategies to overcome poor water solubility. *Advanced drug delivery reviews*, 2007. 59(7): p. 677-694.
32. Jornada, D.H., et al., The prodrug approach: A successful tool for improving drug solubility. *Molecules*, 2015. 21(1): p. 42.
33. Williams, H.D., et al., Strategies to address low drug solubility in discovery and development. *Pharmacological reviews*, 2013. 65(1): p. 315-499.
34. Rodríguez-Spong, B., et al., General principles of pharmaceutical solid polymorphism: a supramolecular perspective. *Advanced drug delivery reviews*, 2004. 56(3): p. 241-274.
35. Blagden, N., et al., Crystal engineering of active pharmaceutical ingredients to improve solubility and dissolution rates. *Advanced drug delivery reviews*, 2007. 59(7): p. 617-630.
36. Pudipeddi, M. and A.T. Serajuddin, Trends in solubility of polymorphs. *Journal of pharmaceutical sciences*, 2005. 94(5): p. 929-939.

37. Zhang, G.G., et al., Phase transformation considerations during process development and manufacture of solid oral dosage forms. *Advanced drug delivery reviews*, 2004. 56(3): p. 371-390.
38. Serajuddin, A.T., Salt formation to improve drug solubility. *Advanced drug delivery reviews*, 2007. 59(7): p. 603-616.
39. Childs, S.L., G.P. Stahly, and A. Park, The salt– cocrystal continuum: the influence of crystal structure on ionization state. *Molecular pharmaceuticals*, 2007. 4(3): p. 323-338.
40. Badawy, S.I.F. and M.A. Hussain, Microenvironmental pH modulation in solid dosage forms. *Journal of pharmaceutical sciences*, 2007. 96(5): p. 948-959.
41. Makary, P., Principles of salt formation. *UK J Pharm Biosci [Internet]*. 2014 [cited 2017 Mar 15]; 2 (4): 1–4.
42. Kumar, L., A. Amin, and A.K. Bansal, Salt selection in drug development. *Pharmaceutical Technology*, 2008. 3(32).
43. Amidon, G.E., X. He, and M.J. Hageman, Physicochemical Characterization and Oral Dosage Form Selection Based on the Biopharmaceutics classification system. *Burger's Medicinal Chemistry and Drug Discovery*, 2003: p. 25-62.
44. Schultheiss, N. and A. Newman, Pharmaceutical cocrystals and their physicochemical properties. *Crystal growth and design*, 2009. 9(6): p. 2950-2967.
45. Jung, M.-S., et al., Bioavailability of indomethacin-saccharin cocrystals. *Journal of pharmacy and pharmacology*, 2010. 62(11): p. 1560-1568.
46. McNamara, D.P., et al., Use of a glutaric acid cocrystal to improve oral bioavailability of a low solubility API. *Pharmaceutical research*, 2006. 23: p. 1888-1897.
47. Bak, A., et al., The co-crystal approach to improve the exposure of a water-insoluble compound: AMG 517 sorbic acid co-crystal characterization and pharmacokinetics. *Journal of pharmaceutical sciences*, 2008. 97(9): p. 3942-3956.
48. Khadka, P., et al., Pharmaceutical particle technologies: An approach to improve drug solubility, dissolution and bioavailability. *Asian journal of pharmaceutical sciences*, 2014. 9(6): p. 304-316.
49. Mosharraf, M. and C. Nyström, The effect of particle size and shape on the surface specific dissolution rate of micro-sized practically insoluble drugs. *International journal of pharmaceuticals*, 1995. 122(1-2): p. 35-47.
50. Atkinson, R., et al., Effect of particle size on blood griseofulvin-levels in man. *Nature*, 1962. 193: p. 588-589.
51. Jounela, A., P. Pentikäinen, and A. Sothmann, Effect of particle size on the bioavailability of digoxin. *European journal of clinical pharmacology*, 1975. 8: p. 365-370.
52. Scholz, A., et al., Influence of hydrodynamics and particle size on the absorption of felodipine in labradors. *Pharmaceutical research*, 2002. 19: p. 42-46.
53. Müller, R.H. and K. Peters, Nanosuspensions for the formulation of poorly soluble drugs: I. Preparation by a size-reduction technique. *International journal of pharmaceuticals*, 1998. 160(2): p. 229-237.
54. Shegokar, R. and R.H. Müller, Nanocrystals: industrially feasible multifunctional formulation technology for poorly soluble actives. *International journal of pharmaceuticals*, 2010. 399(1-2): p. 129-139.
55. Hanafy, A., et al., Pharmacokinetic evaluation of oral fenofibrate nanosuspensions and SLN in comparison to conventional suspensions of micronized drug. *Advanced drug delivery reviews*, 2007. 59(6): p. 419-426.

56. Hecq, J., et al., Preparation and in vitro/in vivo evaluation of nano-sized crystals for dissolution rate enhancement of ucb-35440-3, a highly dosed poorly water-soluble weak base. *European journal of pharmaceuticals and biopharmaceutics*, 2006. 64(3): p. 360-368.
57. Jinno, J.-i., et al., In vitro–in vivo correlation for wet-milled tablet of poorly water-soluble cilostazol. *Journal of Controlled Release*, 2008. 130(1): p. 29-37.
58. Fakes, M.G., et al., Enhancement of oral bioavailability of an HIV-attachment inhibitor by nanosizing and amorphous formulation approaches. *International journal of pharmaceuticals*, 2009. 370(1-2): p. 167-174.
59. Jia, L., et al., Effect of nanonization on absorption of 301029: ex vivo and in vivo pharmacokinetic correlations determined by liquid chromatography/mass spectrometry. *Pharmaceutical research*, 2002. 19: p. 1091-1096.
60. Jia, L., et al., Carbendazim: disposition, cellular permeability, metabolite identification, and pharmacokinetic comparison with its nanoparticle. *Journal of pharmaceutical sciences*, 2003. 92(1): p. 161-172.
61. Kawabata, Y., et al., Novel crystalline solid dispersion of tranilast with high photostability and improved oral bioavailability. *European journal of pharmaceutical sciences*, 2010. 39(4): p. 256-262.
62. Kondo, N., et al., Improved oral absorption of a poorly water-soluble drug, HO-221, by wet-bead milling producing particles in submicron region. *Chemical and pharmaceutical bulletin*, 1993. 41(4): p. 737-740.
63. Liversidge, G.G. and K.C. Cundy, Particle size reduction for improvement of oral bioavailability of hydrophobic drugs: I. Absolute oral bioavailability of nanocrystalline danazol in beagle dogs. *International journal of pharmaceuticals*, 1995. 125(1): p. 91-97.
64. Onoue, S., et al., Formulation design and photochemical studies on nanocrystal solid dispersion of curcumin with improved oral bioavailability. *Journal of pharmaceutical sciences*, 2010. 99(4): p. 1871-1881.
65. Sylvestre, J.-P., et al., Nanonization of megestrol acetate by laser fragmentation in aqueous milieu. *Journal of controlled release*, 2011. 149(3): p. 273-280.
66. Xia, D., et al., Effect of crystal size on the in vitro dissolution and oral absorption of nitrendipine in rats. *Pharmaceutical research*, 2010. 27: p. 1965-1976.
67. Wu, Y., et al., The role of biopharmaceutics in the development of a clinical nanoparticle formulation of MK-0869: a Beagle dog model predicts improved bioavailability and diminished food effect on absorption in human. *International journal of pharmaceuticals*, 2004. 285(1-2): p. 135-146.
68. Jinno, J.-i., et al., Effect of particle size reduction on dissolution and oral absorption of a poorly water-soluble drug, cilostazol, in beagle dogs. *Journal of controlled release*, 2006. 111(1-2): p. 56-64.
69. Loftsson, T. and M.E. Brewster, Pharmaceutical applications of cyclodextrins. 1. Drug solubilization and stabilization. *Journal of pharmaceutical sciences*, 1996. 85(10): p. 1017-1025.
70. Brewster, M.E. and T. Loftsson, Cyclodextrins as pharmaceutical solubilizers. *Advanced drug delivery reviews*, 2007. 59(7): p. 645-666.
71. Gursoy, R.N. and S. Benita, Self-emulsifying drug delivery systems (SEDDS) for improved oral delivery of lipophilic drugs. *Biomedicine & pharmacotherapy*, 2004. 58(3): p. 173-182.

72. Kohli, K., et al., Self-emulsifying drug delivery systems: an approach to enhance oral bioavailability. *Drug discovery today*, 2010. 15(21-22): p. 958-965.
73. Mueller, E.A., et al., Improved dose linearity of cyclosporine pharmacokinetics from a microemulsion formulation. *Pharmaceutical research*, 1994. 11: p. 301-304.
74. van Mourik, I.D., M. Thomson, and D.A. Kelly, Comparison of pharmacokinetics of Neoral and Sandimmune in stable pediatric liver transplant recipients. *Liver transplantation and surgery*, 1999. 5(2): p. 107-111.
75. Kesisoglou, F., S. Panmai, and Y. Wu, Nanosizing—oral formulation development and biopharmaceutical evaluation. *Advanced drug delivery reviews*, 2007. 59(7): p. 631-644.
76. Hancock, B.C. and M. Parks, What is the true solubility advantage for amorphous pharmaceuticals? *Pharmaceutical research*, 2000. 17: p. 397-404.
77. Huang, L.-F. and W.-Q.T. Tong, Impact of solid state properties on developability assessment of drug candidates. *Advanced drug delivery reviews*, 2004. 56(3): p. 321-334.
78. Graeser, K.A., et al., Correlating thermodynamic and kinetic parameters with amorphous stability. *European journal of pharmaceutical sciences*, 2009. 37(3-4): p. 492-498.
79. Hancock, B.C. and G. Zografi, Characteristics and significance of the amorphous state in pharmaceutical systems. *Journal of pharmaceutical sciences*, 1997. 86(1): p. 1-12.
80. Kaushal, A.M., P. Gupta, and A.K. Bansal, Amorphous drug delivery systems: molecular aspects, design, and performance. *Critical Reviews™ in Therapeutic Drug Carrier Systems*, 2004. 21(3).
81. Aaltonen, J. and T. Rades, Commentary: Towards physico-relevant dissolution testing: The importance of solid-state analysis in dissolution. *Dissolut. Technol*, 2009. 16: p. 47-54.
82. Laitinen, R., et al., Emerging trends in the stabilization of amorphous drugs. *International journal of pharmaceutics*, 2013. 453(1): p. 65-79.
83. Byrn, S.R., G. Zografi, and X.S. Chen, *Solid-state properties of pharmaceutical materials*. 2017: John Wiley & Sons.
84. Newman, A. and G. Zografi, Commentary: considerations in the measurement of glass transition temperatures of pharmaceutical amorphous solids. *Aaps Pharmscitech*, 2020. 21: p. 1-13.
85. Craig, D.Q., The mechanisms of drug release from solid dispersions in water-soluble polymers. *International journal of pharmaceutics*, 2002. 231(2): p. 131-144.
86. Leuner, C. and J. Dressman, Improving drug solubility for oral delivery using solid dispersions. *European journal of Pharmaceutics and Biopharmaceutics*, 2000. 50(1): p. 47-60.
87. Konno, H., et al., Effect of polymer type on the dissolution profile of amorphous solid dispersions containing felodipine. *European journal of pharmaceutics and biopharmaceutics*, 2008. 70(2): p. 493-499.
88. Chen, Y., et al., Enhancing the bioavailability of ABT-963 using solid dispersion containing Pluronic F-68. *International journal of pharmaceutics*, 2004. 286(1-2): p. 69-80.
89. CHIBA, Y., et al., Improvement of dissolution and bioavailability for mebendazole, an agent for human echinococcosis, by preparing solid dispersion with polyethylene glycol. *Chemical and pharmaceutical bulletin*, 1991. 39(8): p. 2158-2160.
90. Dannenfelser, R.-M., et al., Development of clinical dosage forms for a poorly water soluble drug I: application of polyethylene glycol–polysorbate 80 solid dispersion carrier system. *Journal of pharmaceutical sciences*, 2004. 93(5): p. 1165-1175.

91. Fukushima, K., et al., Pharmaceutical approach to HIV protease inhibitor atazanavir for bioavailability enhancement based on solid dispersion system. *Biological and Pharmaceutical Bulletin*, 2007. 30(4): p. 733-738.
92. He, X., et al., Comparison of spray freeze drying and the solvent evaporation method for preparing solid dispersions of baicalein with Pluronic F68 to improve dissolution and oral bioavailability. *AAPS PharmSciTech*, 2011. 12: p. 104-113.
93. Joshi, H.N., et al., Bioavailability enhancement of a poorly water-soluble drug by solid dispersion in polyethylene glycol–polysorbate 80 mixture. *International journal of pharmaceuticals*, 2004. 269(1): p. 251-258.
94. Kai, T., et al., Oral absorption improvement of poorly soluble drug using solid dispersion technique. *Chemical and pharmaceutical bulletin*, 1996. 44(3): p. 568-571.
95. Kennedy, M., et al., Enhanced bioavailability of a poorly soluble VR1 antagonist using an amorphous solid dispersion approach: a case study. *Molecular pharmaceuticals*, 2008. 5(6): p. 981-993.
96. Kushida, I., M. Ichikawa, and N. Asakawa, Improvement of dissolution and oral absorption of ER-34122, a poorly water-soluble dual 5-lipoxygenase/cyclooxygenase inhibitor with anti-inflammatory activity by preparing solid dispersion. *Journal of pharmaceutical sciences*, 2002. 91(1): p. 258-266.
97. Bhujbal, S.V., et al., Pharmaceutical amorphous solid dispersion: A review of manufacturing strategies. *Acta Pharmaceutica Sinica B*, 2021. 11(8): p. 2505-2536.
98. Alshehri, S., et al., Potential of solid dispersions to enhance solubility, bioavailability, and therapeutic efficacy of poorly water-soluble drugs: newer formulation techniques, current marketed scenario and patents. *Drug delivery*, 2020. 27(1): p. 1625-1643.
99. Janssens, S. and G. Van den Mooter, Physical chemistry of solid dispersions. *Journal of Pharmacy and Pharmacology*, 2009. 61(12): p. 1571-1586.
100. Tran, P., et al., Overview of the manufacturing methods of solid dispersion technology for improving the solubility of poorly water-soluble drugs and application to anticancer drugs. *Pharmaceutics*, 2019. 11(3): p. 132.
101. Teja, S.B., et al., Drug-excipient behavior in polymeric amorphous solid dispersions. *Journal of Excipients and Food Chemicals*, 2016. 4(3): p. 1048.
102. Kalia, A. and M. Poddar, Solid dispersions: an approach towards enhancing dissolution rate. *Int j pharm pharm sci*, 2011. 3(4): p. 9-19.
103. Singh, A. and G. Van den Mooter, Spray drying formulation of amorphous solid dispersions. *Advanced drug delivery reviews*, 2016. 100: p. 27-50.
104. Crowley, K. and A. Gryczke, Hot melt extrusion of amorphous solid dispersions. *Pharmaceutical Sciences Encyclopedia: Drug Discovery, Development, and Manufacturing*, 2010: p. 1-23.
105. Pouton, C.W., Formulation of poorly water-soluble drugs for oral administration: physicochemical and physiological issues and the lipid formulation classification system. *European journal of pharmaceutical sciences*, 2006. 29(3-4): p. 278-287.
106. Patil, H., R.V. Tiwari, and M.A. Repka, Hot-melt extrusion: from theory to application in pharmaceutical formulation. *Aaps Pharmscitech*, 2016. 17: p. 20-42.
107. Qi, S., et al., Characterisation of solid dispersions of paracetamol and EUDRAGIT® E prepared by hot-melt extrusion using thermal, microthermal and spectroscopic analysis. *International journal of pharmaceuticals*, 2008. 354(1-2): p. 158-167.

108. Chokshi, R.J., et al., Characterization of physico-mechanical properties of indomethacin and polymers to assess their suitability for hot-melt extrusion processes as a means to manufacture solid dispersion/solution. *Journal of pharmaceutical sciences*, 2005. 94(11): p. 2463-2474.
109. Sarode, A.L., et al., Hot melt extrusion (HME) for amorphous solid dispersions: predictive tools for processing and impact of drug–polymer interactions on supersaturation. *European Journal of Pharmaceutical Sciences*, 2013. 48(3): p. 371-384.
110. Dhumal, R.S., et al., Cocrystallization and simultaneous agglomeration using hot melt extrusion. *Pharmaceutical research*, 2010. 27: p. 2725-2733.
111. Paudel, A., et al., Manufacturing of solid dispersions of poorly water soluble drugs by spray drying: formulation and process considerations. *International journal of pharmaceutics*, 2013. 453(1): p. 253-284.
112. Paudel, A. and G. Van den Mooter, Influence of solvent composition on the miscibility and physical stability of naproxen/PVP K 25 solid dispersions prepared by cosolvent spray-drying. *Pharmaceutical research*, 2012. 29: p. 251-270.
113. Kawakami, K., T. Usui, and M. Hattori, Understanding the glass-forming ability of active pharmaceutical ingredients for designing supersaturating dosage forms. *Journal of pharmaceutical sciences*, 2012. 101(9): p. 3239-3248.
114. Huang, Y. and W.-G. Dai, Fundamental aspects of solid dispersion technology for poorly soluble drugs. *Acta Pharmaceutica Sinica B*, 2014. 4(1): p. 18-25.
115. Kothari, K., V. Ragoonanan, and R. Suryanarayanan, Influence of molecular mobility on the physical stability of amorphous pharmaceuticals in the supercooled and glassy states. *Molecular pharmaceutics*, 2014. 11(9): p. 3048-3055.
116. Vo, C.L.-N., C. Park, and B.-J. Lee, Current trends and future perspectives of solid dispersions containing poorly water-soluble drugs. *European journal of pharmaceutics and biopharmaceutics*, 2013. 85(3): p. 799-813.
117. Van Eerdenbrugh, B. and L.S. Taylor, Small scale screening to determine the ability of different polymers to inhibit drug crystallization upon rapid solvent evaporation. *Molecular pharmaceutics*, 2010. 7(4): p. 1328-1337.
118. Harris, R., Formulation strategies for ‘first-into-man’ Studies. *Innov Pharm Technol*, 2011. 38: p. 72-75.
119. Fridgeirsdottir, G.A., et al., Support tools in formulation development for poorly soluble drugs. *Journal of Pharmaceutical Sciences*, 2016. 105(8): p. 2260-2269.
120. Han, R., et al., Predicting physical stability of solid dispersions by machine learning techniques. *Journal of Controlled Release*, 2019. 311: p. 16-25.
121. Hu, Q., et al., Highly efficient miniaturized coprecipitation screening (MiCoS) for amorphous solid dispersion formulation development. *International journal of pharmaceutics*, 2013. 450(1-2): p. 53-62.
122. Shanbhag, A., et al., Method for screening of solid dispersion formulations of low-solubility compounds—miniaturization and automation of solvent casting and dissolution testing. *International journal of pharmaceutics*, 2008. 351(1-2): p. 209-218.
123. Lu, J., et al., Solid-state characterization of Felodipine–Soluplus amorphous solid dispersions. *Drug development and industrial pharmacy*, 2016. 42(3): p. 485-496.
124. Marsac, P.J., T. Li, and L.S. Taylor, Estimation of drug–polymer miscibility and solubility in amorphous solid dispersions using experimentally determined interaction parameters. *Pharmaceutical research*, 2009. 26: p. 139-151.

125. Oksanen, C.A. and G. Zografi, The relationship between the glass transition temperature and water vapor absorption by poly (vinylpyrrolidone). *Pharmaceutical research*, 1990. 7: p. 654-657.
126. Kestur, U.S. and L.S. Taylor, Role of polymer chemistry in influencing crystal growth rates from amorphous felodipine. *CrystEngComm*, 2010. 12(8): p. 2390-2397.
127. Marsac, P.J., S.L. Shamblin, and L.S. Taylor, Theoretical and practical approaches for prediction of drug–polymer miscibility and solubility. *Pharmaceutical research*, 2006. 23: p. 2417-2426.
128. Hildebrand, J.H., Factors determining solubility among non-electrolytes. *Proceedings of the National Academy of Sciences*, 1950. 36(1): p. 7-15.
129. Welker, R.W., Basics and sampling of particles for size analysis and identification, in *Developments in surface contamination and cleaning*. 2012, Elsevier. p. 1-80.
130. Greenhalgh, D.J., et al., Solubility parameters as predictors of miscibility in solid dispersions. *Journal of pharmaceutical sciences*, 1999. 88(11): p. 1182-1190.
131. Rowe, R., Adhesion of film coatings to tablet surfaces—a theoretical approach based on solubility parameters. *International Journal of Pharmaceutics*, 1988. 41(3): p. 219-222.
132. Forster, A., et al., Selection of excipients for melt extrusion with two poorly water-soluble drugs by solubility parameter calculation and thermal analysis. *International journal of pharmaceutics*, 2001. 226(1-2): p. 147-161.
133. Hoy, K., New values of the solubility parameters from vapor pressure data. *Journal of paint technology*, 1970. 42(541): p. 76-118.
134. Lu, J., et al., Investigation of phase diagrams and physical stability of drug–polymer solid dispersions. *Pharmaceutical development and technology*, 2015. 20(1): p. 105-117.
135. Knopp, M.M., et al., Comparative study of different methods for the prediction of drug–polymer solubility. *Molecular pharmaceutics*, 2015. 12(9): p. 3408-3419.
136. Duarte, Í., et al., Screening methodologies for the development of spray-dried amorphous solid dispersions. *Pharmaceutical research*, 2015. 32: p. 222-237.
137. Gupta, J., C. Nunes, and S. Jonnalagadda, A molecular dynamics approach for predicting the glass transition temperature and plasticization effect in amorphous pharmaceuticals. *Molecular pharmaceutics*, 2013. 10(11): p. 4136-4145.
138. Xiang, T.-X. and B.D. Anderson, Molecular dynamics simulation of amorphous indomethacin-poly (vinylpyrrolidone) glasses: solubility and hydrogen bonding interactions. *Journal of pharmaceutical sciences*, 2013. 102(3): p. 876-891.
139. Maniruzzaman, M., et al., Molecular modeling as a predictive tool for the development of solid dispersions. *Molecular pharmaceutics*, 2015. 12(4): p. 1040-1049.
140. Huynh, L., et al., Predicting the solubility of the anti-cancer agent docetaxel in small molecule excipients using computational methods. *Pharmaceutical research*, 2008. 25: p. 147-157.
141. Yang, H., et al., Molecular dynamics simulation studies of binary blend miscibility of poly (3-hydroxybutyrate) and poly (ethylene oxide). *Polymer*, 2004. 45(2): p. 453-457.
142. Mazeau, K. and L. Heux, Molecular dynamics simulations of bulk native crystalline and amorphous structures of cellulose. *The Journal of Physical Chemistry B*, 2003. 107(10): p. 2394-2403.
143. Gupta, J., et al., Prediction of solubility parameters and miscibility of pharmaceutical compounds by molecular dynamics simulations. *The Journal of Physical Chemistry B*, 2011. 115(9): p. 2014-2023.

144. Van Eerdenbrugh, B., J.A. Baird, and L.S. Taylor, Crystallization tendency of active pharmaceutical ingredients following rapid solvent evaporation—classification and comparison with crystallization tendency from under cooled melts. *Journal of pharmaceutical sciences*, 2010. 99(9): p. 3826-3838.
145. Mahlin, D. and C.A. Bergström, Early drug development predictions of glass-forming ability and physical stability of drugs. *European Journal of Pharmaceutical Sciences*, 2013. 49(2): p. 323-332.
146. Alhalaweh, A., et al., Computational predictions of glass-forming ability and crystallization tendency of drug molecules. *Molecular Pharmaceutics*, 2014. 11(9): p. 3123-3132.
147. Medarević, D.P., et al., Combined application of mixture experimental design and artificial neural networks in the solid dispersion development. *Drug development and industrial pharmacy*, 2016. 42(3): p. 389-402.
148. Palmer, D.S., et al., Random forest models to predict aqueous solubility. *Journal of chemical information and modeling*, 2007. 47(1): p. 150-158.
149. Fagerberg, J.H., et al., Computational prediction of drug solubility in fasted simulated and aspirated human intestinal fluid. *Pharmaceutical research*, 2015. 32: p. 578-589.
150. Bhardwaj, R.M., et al., A random forest model for predicting the crystallisability of organic molecules. *CrystEngComm*, 2015. 17(23): p. 4272-4275.
151. Nurzyńska, K., et al., Long-term amorphous drug stability predictions using easily calculated, predicted, and measured parameters. *Molecular pharmaceutics*, 2015. 12(9): p. 3389-3398.
152. Fridgeirsdottir, G.A., et al., Multiple linear regression modeling to predict the stability of polymer–drug solid dispersions: comparison of the effects of polymers and manufacturing methods on solid dispersion stability. *Molecular pharmaceutics*, 2018. 15(5): p. 1826-1841.
153. Dai, W.-G., et al., Advanced screening assays to rapidly identify solubility-enhancing formulations: high-throughput, miniaturization and automation. *Advanced drug delivery reviews*, 2008. 60(6): p. 657-672.
154. Dai, W.-G., et al., Parallel screening approach to identify solubility-enhancing formulations for improved bioavailability of a poorly water-soluble compound using milligram quantities of material. *International journal of pharmaceutics*, 2007. 336(1): p. 1-11.
155. McDonald, T.O., et al., High-throughput nanoprecipitation of the organic antimicrobial triclosan and enhancement of activity against *Escherichia coli*. *Journal of Materials Chemistry B*, 2013. 1(35): p. 4455-4465.
156. Shlar, I., et al., High-throughput screening of nanoparticle-stabilizing ligands: Application to preparing antimicrobial curcumin nanoparticles by antisolvent precipitation. *Nano-Micro Letters*, 2015. 7: p. 68-79.
157. Voura, C., et al., Printable medicines: a microdosing device for producing personalized medicines. *Pharmaceutical Technology Europe*, 2011. 23(1).
158. Davies, M.C., et al., High throughput surface characterization: a review of a new tool for screening prospective biomedical material arrays. *Journal of drug targeting*, 2010. 18(10): p. 741-751.
159. Austin, J. and A.H. Holway, Contact printing of protein microarrays. *Protein Microarrays: Methods and Protocols*, 2011: p. 379-394.

160. Rose, D., Microdispensing technologies in drug discovery. *Drug discovery today*, 1999. 4(9): p. 411-419.
161. Hook, A.L., et al., Polymer microarrays for high throughput discovery of biomaterials. *JoVE (Journal of Visualized Experiments)*, 2012(59): p. e3636.
162. Le, H.P., Progress and trends in ink-jet printing technology. *Journal of Imaging Science and Technology*, 1998. 42(1): p. 49-62.
163. Lemmo, A.V., D.J. Rose, and T.C. Tisone, Inkjet dispensing technology: applications in drug discovery. *Current Opinion in Biotechnology*, 1998. 9(6): p. 615-617.
164. Arrabito, G. and B. Pignataro, Inkjet printing methodologies for drug screening. *Analytical chemistry*, 2010. 82(8): p. 3104-3107.
165. Zheng, Q., et al., Application of inkjet printing technique for biological material delivery and antimicrobial assays. *Analytical Biochemistry*, 2011. 410(2): p. 171-176.
166. Tarcha, P.J., et al., The application of ink-jet technology for the coating and loading of drug-eluting stents. *Annals of biomedical engineering*, 2007. 35: p. 1791-1799.
167. Lee, E.R., *Microdrop generation*. 2018: CRC press.
168. Cooley, P., D. Wallace, and B. Antohe, Applications of ink-jet printing technology to BioMEMS and microfluidic systems. *JALA: Journal of the Association for Laboratory Automation*, 2002. 7(5): p. 33-39.
169. Meléndez, P.A., et al., Thermal inkjet application in the preparation of oral dosage forms: dispensing of prednisolone solutions and polymorphic characterization by solid-state spectroscopic techniques. *Journal of pharmaceutical sciences*, 2008. 97(7): p. 2619-2636.
170. Kolakovic, R., et al., Printing technologies in fabrication of drug delivery systems. *Expert opinion on drug delivery*, 2013. 10(12): p. 1711-1723.
171. Alomari, M., et al., Personalised dosing: Printing a dose of one's own medicine. *International journal of pharmaceutics*, 2015. 494(2): p. 568-577.
172. Scoutaris, N., et al., Inkjet printing as a novel medicine formulation technique. *Journal of controlled release*, 2011. 156(2): p. 179-185.
173. Bohórquez, J.H., et al., Laser-comparable inkjet text printing. *Hewlett Packard Journal*, 1994. 45: p. 9-9.
174. Wilson Jr, W.C. and T. Boland, Cell and organ printing 1: protein and cell printers. *The Anatomical Record Part A: discoveries in molecular, cellular, and evolutionary biology*, 2003. 272(2): p. 491-496.
175. Cui, X., et al., Human cartilage tissue fabrication using three-dimensional inkjet printing technology. *JoVE (Journal of Visualized Experiments)*, 2014(88): p. e51294.
176. Okamoto, T., T. Suzuki, and N. Yamamoto, Microarray fabrication with covalent attachment of DNA using bubble jet technology. *Nature biotechnology*, 2000. 18(4): p. 438-441.
177. De Gans, B.J., P.C. Duineveld, and U.S. Schubert, Inkjet printing of polymers: state of the art and future developments. *Advanced materials*, 2004. 16(3): p. 203-213.
178. Zhu, X., et al., Recent advances in inkjet dispensing technologies: applications in drug discovery. *Expert Opinion on Drug Discovery*, 2012. 7(9): p. 761-770.
179. Boehm, R.D., et al., Inkjet printing for pharmaceutical applications. *Materials Today*, 2014. 17(5): p. 247-252.
180. Calvert, P., Inkjet printing for materials and devices. *Chemistry of materials*, 2001. 13(10): p. 3299-3305.

181. Tekin, E., B.-J. de Gans, and U.S. Schubert, Ink-jet printing of polymers—from single dots to thin film libraries. *Journal of Materials Chemistry*, 2004. 14(17): p. 2627-2632.
182. Burgold, J., et al., Evolution and Operating Experiences with Different Drop-On-Demand Systems. *Macromolecular rapid communications*, 2005. 26(4): p. 265-280.
183. Di Risio, S. and N. Yan, Piezoelectric ink-jet printing of horseradish peroxidase: effect of ink viscosity modifiers on activity. *Macromolecular Rapid Communications*, 2007. 28(18-19): p. 1934-1940.
184. Rajjada, D., et al., A step toward development of printable dosage forms for poorly soluble drugs. *Journal of pharmaceutical sciences*, 2013. 102(10): p. 3694-3704.
185. Huang, Q., W. Shen, and W. Song, Synthesis of colourless silver precursor ink for printing conductive patterns on silicon nitride substrates. *Applied surface science*, 2012. 258(19): p. 7384-7388.
186. Jang, D., D. Kim, and J. Moon, Influence of fluid physical properties on ink-jet printability. *Langmuir*, 2009. 25(5): p. 2629-2635.
187. Sun, J.M., X.F. Wei, and B.Q. Huang. Influence of the viscosity of edible ink to piezoelectric ink-jet printing drop state. in *Applied Mechanics and Materials*. 2012. Trans Tech Publ.
188. Buanz, A., et al., Preparation of personalized-dose salbutamol sulphate oral films with thermal ink-jet printing. *Pharmaceutical research*, 2011. 28(10): p. 2386-2392.
189. Desai, S., et al., Understanding release kinetics of biopolymer drug delivery microcapsules for biomedical applications. *Materials Science and Engineering: B*, 2010. 168(1-3): p. 127-131.
190. Sandler, N., et al., Inkjet printing of drug substances and use of porous substrates-towards individualized dosing. *Journal of pharmaceutical sciences*, 2011. 100(8): p. 3386-3395.
191. Mueannoom, W., et al., Thermal ink-jet spray freeze-drying for preparation of excipient-free salbutamol sulphate for inhalation. *European Journal of Pharmaceutics and Biopharmaceutics*, 2012. 80(1): p. 149-155.
192. Genina, N., et al., Evaluation of different substrates for inkjet printing of rasagiline mesylate. *European Journal of Pharmaceutics and Biopharmaceutics*, 2013. 85(3): p. 1075-1083.
193. Hirshfield, L., et al., Dropwise additive manufacturing of pharmaceutical products for solvent-based dosage forms. *Journal of pharmaceutical sciences*, 2014. 103(2): p. 496-506.
194. Genina, N., et al., Behavior of printable formulations of loperamide and caffeine on different substrates—Effect of print density in inkjet printing. *International journal of pharmaceutics*, 2013. 453(2): p. 488-497.
195. Pardeike, J., et al., Nanosuspensions as advanced printing ink for accurate dosing of poorly soluble drugs in personalized medicines. *International journal of pharmaceutics*, 2011. 420(1): p. 93-100.
196. Lee, B.K., et al., Fabrication of drug-loaded polymer microparticles with arbitrary geometries using a piezoelectric inkjet printing system. *International journal of pharmaceutics*, 2012. 427(2): p. 305-310.
197. Scoutaris, N., et al., ToF-SIMS analysis of chemical heterogenities in inkjet micro-array printed drug/polymer formulations. *Journal of Materials Science: Materials in Medicine*, 2012. 23: p. 385-391.

198. Iwanaga, S., et al., Facile fabrication of uniform size-controlled microparticles and potentiality for tandem drug delivery system of micro/nanoparticles. *Colloids and Surfaces B: Biointerfaces*, 2013. 109: p. 301-306.
199. Vakili, H., et al., Application of a colorimetric technique in quality control for printed pediatric orodispersible drug delivery systems containing propranolol hydrochloride. *International Journal of Pharmaceutics*, 2016. 511(1): p. 606-618.
200. Wickström, H., et al., Colorimetry as quality control tool for individual inkjet-printed pediatric formulations. *AAPS PharmSciTech*, 2017. 18: p. 293-302.
201. Vakili, H., et al., Application of a handheld NIR spectrometer in prediction of drug content in inkjet printed orodispersible formulations containing prednisolone and levothyroxine. *International Journal of Pharmaceutics*, 2017. 524(1-2): p. 414-423.
202. Varan, C., et al., Inkjet printing of antiviral PCL nanoparticles and anticancer cyclodextrin inclusion complexes on bioadhesive film for cervical administration. *International journal of pharmaceutics*, 2017. 531(2): p. 701-713.
203. Palo, M., et al., Development of oromucosal dosage forms by combining electrospinning and inkjet printing. *Molecular pharmaceutics*, 2017. 14(3): p. 808-820.
204. Gu, Y., et al., Inkjet printed antibiotic-and calcium-eluting bioresorbable nanocomposite micropatterns for orthopedic implants. *Acta biomaterialia*, 2012. 8(1): p. 424-431.
205. Sharma, G., et al., In vitro characterisation of terbutaline sulphate particles prepared by thermal ink-jet spray freeze drying. *International journal of pharmaceutics*, 2013. 447(1-2): p. 165-170.
206. Marizza, P., et al., Polymer-filled microcontainers for oral delivery loaded using supercritical impregnation. *Journal of Controlled Release*, 2014. 173: p. 1-9.
207. Chan, K.A. and S.G. Kazarian, Fourier transform infrared imaging for high-throughput analysis of pharmaceutical formulations. *Journal of combinatorial chemistry*, 2005. 7(2): p. 185-189.
208. Tanabe, Y., et al., Screening a trace amount of pharmaceutical cocrystals by using an enhanced nano-spot method. *European Journal of Pharmaceutics and Biopharmaceutics*, 2019. 136: p. 131-137.
209. Liberski, A.R., et al., Screening for polymorphs on polymer microarrays. *Journal of combinatorial chemistry*, 2008. 10(1): p. 24-27.
210. Daly, R., et al., Inkjet printing for pharmaceutics—a review of research and manufacturing. *International journal of pharmaceutics*, 2015. 494(2): p. 554-567.
211. Heller, M.J., DNA microarray technology: devices, systems, and applications. *Annual review of biomedical engineering*, 2002. 4(1): p. 129-153.
212. Venkatasubbarao, S., Microarrays—status and prospects. *TRENDS in Biotechnology*, 2004. 22(12): p. 630-637.
213. Umez, S., et al., Fundamental characteristics of printed cell structures utilizing electrostatic inkjet phenomena. *Sensors and Actuators A: Physical*, 2011. 166(2): p. 251-255.
214. Lee, B.H. and T. Nagamune, Protein microarrays and their applications. *Biotechnology and Bioprocess Engineering*, 2004. 9(2): p. 69-75.
215. Hauschild, S., et al., Direct preparation and loading of lipid and polymer vesicles using inkjets. *Small*, 2005. 1(12): p. 1177-1180.
216. Hook, A.L., et al., High throughput methods applied in biomaterial development and discovery. *Biomaterials*, 2010. 31(2): p. 187-198.

217. Mant, A., et al., Polymer microarrays: identification of substrates for phagocytosis assays. *Biomaterials*, 2006. 27(30): p. 5299-5306.
218. Hook, A.L., et al., Analysis and prediction of defects in UV photo-initiated polymer microarrays. *Journal of Materials Chemistry B*, 2013. 1(7): p. 1035-1043.
219. Cheow, W.S., T.Y. Kiew, and K. Hadinoto, Combining inkjet printing and amorphous nanonization to prepare personalized dosage forms of poorly-soluble drugs. *European Journal of Pharmaceutics and Biopharmaceutics*, 2015. 96: p. 314-321.
220. Hsu, H.Y., et al., Drop printing of pharmaceuticals: Effect of molecular weight on PEG coated-naproxen/PEG 3350 solid dispersions. *AIChE Journal*, 2015. 61(12): p. 4502-4508.
221. Scoutaris, N., et al., Jet dispensing as a high throughput method for rapid screening and manufacturing of cocrystals. *CrystEngComm*, 2016. 18(27): p. 5079-5082.
222. Anderson, D.G., S. Levenberg, and R. Langer, Nanoliter-scale synthesis of arrayed biomaterials and application to human embryonic stem cells. *Nature biotechnology*, 2004. 22(7): p. 863-866.
223. Scoutaris, N., S. Ross, and D. Douroumis, Current trends on medical and pharmaceutical applications of inkjet printing technology. *Pharmaceutical research*, 2016. 33(8): p. 1799-1816.
224. Taresco, V., et al., Rapid Nanogram Scale Screening Method of Microarrays to Evaluate Drug-Polymer Blends Using High-Throughput Printing Technology. *Molecular pharmaceutics*, 2017. 14(6): p. 2079-2087.
225. Kuentz, M., R. Holm, and D.P. Elder, Methodology of oral formulation selection in the pharmaceutical industry. *European Journal of Pharmaceutical Sciences*, 2016. 87: p. 136-163.
226. Bergström, C.A., W.N. Charman, and C.J. Porter, Computational prediction of formulation strategies for beyond-rule-of-5 compounds. *Advanced drug delivery reviews*, 2016. 101: p. 6-21.
227. Mahlin, D., et al., Toward in silico prediction of glass-forming ability from molecular structure alone: a screening tool in early drug development. *Molecular pharmaceutics*, 2011. 8(2): p. 498-506.
228. Alhalaweh, A., et al., Physical stability of drugs after storage above and below the glass transition temperature: Relationship to glass-forming ability. *International journal of pharmaceutics*, 2015. 495(1): p. 312-317.
229. Baird, J.A., B. Van Eerdenbrugh, and L.S. Taylor, A classification system to assess the crystallization tendency of organic molecules from undercooled melts. *Journal of pharmaceutical sciences*, 2010. 99(9): p. 3787-3806.
230. Drug bank <https://www.drugbank.com/>.
231. ChemAxon/Chemicalize <https://chemicalize.com/app/calculation> (accessed 06/10/2022).
232. Royal Society of Chemistry. ChemSpider <http://www.chemspider.com/>.
233. Lehmkemper, K., et al., Long-term physical stability of PVP-and PVPVA-amorphous solid dispersions. *Molecular pharmaceutics*, 2017. 14(1): p. 157-171.
234. Pignatello, R., et al., Soluplus® polymeric nanomicelles improve solubility of BCS-class II drugs. *Drug Delivery and Translational Research*, 2022. 12(8): p. 1991-2006.
235. Brady, J., et al., Polymer properties and characterization, in *Developing solid oral dosage forms*. 2017, Elsevier. p. 181-223.
236. Rowe, R.C., P. Sheskey, and M. Quinn, *Handbook of pharmaceutical excipients*. 2009: Libros Digitales-Pharmaceutical Press.

237. Buehler, V., Kollidon. Polyvinylpyrrolidone excipients for the pharmaceutical industry, 2008. 9.
238. Friesen, D.T., et al., Hydroxypropyl methylcellulose acetate succinate-based spray-dried dispersions: an overview. *Molecular pharmaceuticals*, 2008. 5(6): p. 1003-1019.
239. Soulairol, I., et al., Spray-dried solid dispersions of nifedipine and vinylcaprolactam/vinylacetate/PEG6000 for compacted oral formulations. *International journal of pharmaceutics*, 2015. 481(1-2): p. 140-147.
240. BASF. Technical information Soluplus 1-8. 2010; Available from: www.pharma-ingredients.basf.com.
241. Lu, X., R. Wenslow, and A. Newman, *Monographs on polymers and surfactants. Pharmaceutical Sciences Encyclopedia: Drug Discovery, Development, and Manufacturing*, 2010: p. 1-22.
242. Bernabeu, E., et al., Novel Soluplus®—TPGS mixed micelles for encapsulation of paclitaxel with enhanced in vitro cytotoxicity on breast and ovarian cancer cell lines. *Colloids and Surfaces B: Biointerfaces*, 2016. 140: p. 403-411.
243. Li, P., H.M. Nielsen, and A. Müllertz, Impact of lipid-based drug delivery systems on the transport and uptake of insulin across Caco-2 cell monolayers. *Journal of pharmaceutical sciences*, 2016. 105(9): p. 2743-2751.
244. Jin, X., et al., Soluplus® micelles as a potential drug delivery system for reversal of resistant tumor. *Biomedicine & Pharmacotherapy*, 2015. 69: p. 388-395.
245. Wickström, H., et al., Improvement of dissolution rate of indomethacin by inkjet printing. *European Journal of Pharmaceutical Sciences*, 2015. 75: p. 91-100.
246. Rahman, K., et al., Simulation of droplet generation through electrostatic forces. *Journal of mechanical science and technology*, 2010. 24(1): p. 307-310.
247. Palmer, D., et al., Printing particles: A high-throughput technique for the production of uniform, bioresorbable polymer microparticles and encapsulation of therapeutic peptides. *Chemical Engineering Science*, 2017. 166: p. 122-129.
248. HILGERT, E., *Development of pharmaceutical ink formulations with silica nanoparticles for inkjet printing*. 2015, ÅBO AKADEMI UNIVERSITY.
249. Wijshoff, H., Drop dynamics in the inkjet printing process. *Current opinion in colloid & interface science*, 2018. 36: p. 20-27.
250. Du, Z., X. Yu, and Y. Han, Inkjet printing of viscoelastic polymer inks. *Chinese Chemical Letters*, 2018. 29(3): p. 399-404.
251. JoVE Science Education Database. *General Laboratory Techniques. Introduction to Light Microscopy*. *Journal of Visualized Experiments*, Cambridge, MA, doi: 10.3791/5041 (2014). <https://www.socmucimm.org/news-media/introduction-to-light-microscopy/>.
252. Davis, M.T., et al., Amorphous solid dispersions of BCS class II drugs: a rational approach to solvent and polymer selection. *Chemical Engineering Research and Design*, 2016. 110: p. 192-199.
253. Seefeldt, K., et al., Crystallization pathways and kinetics of carbamazepine–nicotinamide cocrystals from the amorphous state by in situ thermomicroscopy, spectroscopy, and calorimetry studies. *Journal of pharmaceutical sciences*, 2007. 96(5): p. 1147-1158.
254. Binnig, G., C.F. Quate, and C. Gerber, Atomic force microscope. *Physical review letters*, 1986. 56(9): p. 930.
255. Atomic force microscope https://simple.wikipedia.org/wiki/Atomic_force_microscope. Wikipedia, 2018.

256. Jalili, N. and K. Laxminarayana, A review of atomic force microscopy imaging systems: application to molecular metrology and biological sciences. *Mechatronics*, 2004. 14(8): p. 907-945.
257. Šuly, P., et al., Poly (vinyl alcohol): formulation of a polymer ink for the patterning of substrates with a drop-on-demand inkjet printer. *Materiali in tehnologije*, 2017.
258. Guideline, I., Stability testing of new drug substances and products. Q1A (R2), current step, 2003. 4(1-24).
259. Blaine, R., Humidity fixed points. TA Instruments, 2004.
260. Magdassi, S., *The chemistry of inkjet inks*. 2009: World scientific.
261. Li, B., et al., Both solubility and chemical stability of curcumin are enhanced by solid dispersion in cellulose derivative matrices. *Carbohydrate polymers*, 2013. 98(1): p. 1108-1116.
262. Parikh, T., et al., Application of film-casting technique to investigate drug-polymer miscibility in solid dispersion and hot-melt extrudate. *Journal of pharmaceutical sciences*, 2015. 104(7): p. 2142-2152.
263. Bastin, R.J., M.J. Bowker, and B.J. Slater, Salt selection and optimisation procedures for pharmaceutical new chemical entities. *Organic Process Research & Development*, 2000. 4(5): p. 427-435.
264. Balbach, S. and C. Korn, Pharmaceutical evaluation of early development candidates “the 100 mg-approach”. *International Journal of Pharmaceutics*, 2004. 275(1-2): p. 1-12.
265. Newman, A., *Pharmaceutical Amorphous Solid Dispersions*. Wiley; New York, 2015: p. 193.
266. Greenspan, L., Humidity fixed points of binary saturated aqueous solutions. *Journal of research of the National Bureau of Standards. Section A, Physics and chemistry*, 1977. 81(1): p. 89.
267. Turpin, E.R., et al., In silico screening for solid dispersions: The trouble with solubility parameters and χ_{FH} . *Molecular pharmaceutics*, 2018. 15(10): p. 4654-4667.
268. Kwok, D., et al., Contact angle measurements and contact angle interpretation. 1. Contact angle measurements by axisymmetric drop shape analysis and a goniometer sessile drop technique. *Langmuir*, 1997. 13(10): p. 2880-2894.
269. Echaliier, A., et al., Assessing crystallization droplets using birefringence. *Acta Crystallographica Section D: Biological Crystallography*, 2004. 60(4): p. 696-702.
270. Qian, F., et al., Solution behavior of PVP-VA and HPMC-AS-based amorphous solid dispersions and their bioavailability implications. *Pharmaceutical research*, 2012. 29(10): p. 2766-2776.
271. Wlodarski, K., et al., Physical stability of solid dispersions with respect to thermodynamic solubility of tadalafil in PVP-VA. *European Journal of Pharmaceutics and Biopharmaceutics*, 2015. 96: p. 237-246.
272. Li, Y., et al., Interactions between drugs and polymers influencing hot melt extrusion. *Journal of Pharmacy and Pharmacology*, 2014. 66(2): p. 148-166.
273. Sarabu, S., et al., Hypromellose acetate succinate based amorphous solid dispersions via hot melt extrusion: Effect of drug physicochemical properties. *Carbohydr Polym*, 2020. 233: p. 115828.
274. Krasnyuk, I., et al., Influence of Polymers on the Physicochemical Properties of Benzonal in Solid Dispersions. *Moscow University Chemistry Bulletin*, 2020. 75: p. 388-390.

275. He, R., et al., Impact of Processing Methods on the Physico-chemical Properties of Posaconazole Amorphous Solid Dispersions. *Pharmaceutical Research*, 2024. 41(1): p. 141-151.
276. <https://www.scribbr.com/statistics/multiple-linear-regression/>, (Accessed 12/12/2023).
277. <https://www.statisticshowto.com/probability-and-statistics/statistics-definitions/mean-squared-error/>, (Accessed 12/12/2023).
278. Shi, Y., Support vector regression-based QSAR models for prediction of antioxidant activity of phenolic compounds. *Scientific reports*, 2021. 11(1): p. 8806.
279. Teja, S.B., et al., Drug-excipient behavior in polymeric amorphous solid dispersions. *Journal of Excipients and Food Chemicals*, 2016. 4(3).
280. Kothari, K., V. Ragoonanan, and R. Suryanarayanan, The role of drug–polymer hydrogen bonding interactions on the molecular mobility and physical stability of nifedipine solid dispersions. *Molecular pharmaceutics*, 2015. 12(1): p. 162-170.
281. Xiang, T.-X. and B.D. Anderson, Effects of molecular interactions on miscibility and mobility of ibuprofen in amorphous solid dispersions with various polymers. *Journal of pharmaceutical sciences*, 2019. 108(1): p. 178-186.
282. Wu, J. and G. Van den Mooter, The influence of hydrogen bonding between different crystallization tendency drugs and PVPVA on the stability of amorphous solid dispersions. *International Journal of Pharmaceutics*, 2023. 646: p. 123440.
283. Kestur, U.S., B. Van Eerdenbrugh, and L.S. Taylor, Influence of polymer chemistry on crystal growth inhibition of two chemically diverse organic molecules. *CrystEngComm*, 2011. 13(22): p. 6712-6718.
284. Caron, G., et al., Flexibility in early drug discovery: focus on the beyond-Rule-of-5 chemical space. *Drug Discovery Today*, 2020. 25(4): p. 621-627.
285. Moore, M.D. and P.L. Wildfong, Informatics calibration of a molecular descriptors database to predict solid dispersion potential of small molecule organic solids. *International journal of pharmaceutics*, 2011. 418(2): p. 217-226.
286. Trenfield, S.J., et al., The shape of things to come: Emerging applications of 3D printing in healthcare. *3D printing of pharmaceuticals*, 2018: p. 1-19.
287. Vaz, V.M. and L. Kumar, 3D printing as a promising tool in personalized medicine. *Aaps Pharmscitech*, 2021. 22: p. 1-20.
288. Günther, D., et al., Continuous 3D-printing for additive manufacturing. *Rapid Prototyping Journal*, 2014. 20(4): p. 320-327.
289. Jacob, S., et al., 3D printing technologies: recent development and emerging applications in various drug delivery systems. *AAPS PharmSciTech*, 2020. 21: p. 1-16.
290. Trenfield, S.J., et al., Shaping the future: recent advances of 3D printing in drug delivery and healthcare. *Expert opinion on drug delivery*, 2019. 16(10): p. 1081-1094.
291. Jamróz, W., et al., 3D printing in pharmaceutical and medical applications—recent achievements and challenges. *Pharmaceutical research*, 2018. 35: p. 1-22.
292. Gross, B.C., et al., Evaluation of 3D printing and its potential impact on biotechnology and the chemical sciences. 2014, ACS Publications.
293. Belhabib, S. and S. Guessasma, Compression performance of hollow structures: From topology optimisation to design 3D printing. *International Journal of Mechanical Sciences*, 2017. 133: p. 728-739.
294. Matai, I., et al., Progress in 3D bioprinting technology for tissue/organ regenerative engineering. *Biomaterials*, 2020. 226: p. 119536.

295. Jiménez, M., et al., Additive manufacturing technologies: an overview about 3D printing methods and future prospects. *Complexity*, 2019. 2019.
296. Cader, H.K., et al., Water-based 3D inkjet printing of an oral pharmaceutical dosage form. *International journal of pharmaceutics*, 2019. 564: p. 359-368.
297. Wang, S., et al., A Review of 3D Printing Technology in Pharmaceutics: Technology and Applications, Now and Future. *Pharmaceutics*, 2023. 15(2): p. 416.
298. Strutt, J.W. and L. Rayleigh, On the instability of jets. *Proc. London Math. Soc*, 1878. 10(4).
299. Derby, B., Inkjet printing of functional and structural materials: fluid property requirements, feature stability, and resolution. *Annual Review of Materials Research*, 2010. 40: p. 395-414.
300. Sumerel, J., et al., Piezoelectric ink jet processing of materials for medical and biological applications. *Biotechnology Journal: Healthcare Nutrition Technology*, 2006. 1(9): p. 976-987.
301. Prasad, L.K. and H. Smyth, 3D Printing technologies for drug delivery: a review. *Drug development and industrial pharmacy*, 2016. 42(7): p. 1019-1031.
302. Holman, R.K., et al., Spreading and infiltration of inkjet-printed polymer solution droplets on a porous substrate. *Journal of colloid and interface science*, 2002. 249(2): p. 432-440.
303. Roulon, S., et al., Production of reproducible filament batches for the fabrication of 3D printed oral forms. *Pharmaceutics*, 2021. 13(4): p. 472.
304. Jingwen, L., et al., 3D printing of bioinspired compartmentalized capsular structure for controlled drug release. *Journal of Zhejiang University. Science. B*, 2021. 22(12): p. 1022.
305. Smith, D.M., et al., Pharmaceutical 3D printing: Design and qualification of a single step print and fill capsule. *International journal of pharmaceutics*, 2018. 544(1): p. 21-30.
306. Scoutaris, N., S.A. Ross, and D. Douroumis, 3D printed “Starmix” drug loaded dosage forms for paediatric applications. *Pharmaceutical research*, 2018. 35: p. 1-11.
307. Tabriz, A.G., et al., Personalised tasted masked chewable 3D printed fruit-chews for paediatric patients. *Pharmaceutics*, 2021. 13(8): p. 1301.
308. Tabriz, A.G., et al., Personalised paediatric chewable Ibuprofen tablets fabricated using 3D micro-extrusion printing technology. *International Journal of Pharmaceutics*, 2022. 626: p. 122135.
309. Preis, M. and H. Öblom, 3D-printed drugs for children—are we ready yet? *AAPS PharmSciTech*, 2017. 18: p. 303-308.
310. Lafeber, I., et al., 3D printing of pediatric medication: the end of bad tasting oral liquids—a scoping review. *Pharmaceutics*, 2022. 14(2): p. 416.
311. van Kampen, E.E., L. Willemsteijn, and E.J. Ruijgrok, 3D printing of drugs: Expanding the options for child-tailored pharmacotherapy. *Archives of Disease in Childhood*, 2022. 107(10): p. 859-860.
312. Ma, X. and R.O. Williams III, Characterization of amorphous solid dispersions: An update. *Journal of Drug Delivery Science and Technology*, 2019. 50: p. 113-124.
313. Thabet, Y., D. Lunter, and J. Breitreutz, Continuous inkjet printing of enalapril maleate onto orodispersible film formulations. *International journal of pharmaceutics*, 2018. 546(1-2): p. 180-187.
314. Farhan, A.B., et al., An investigation into the factors governing the degree of dissolution enhancement of solid dispersion for poorly soluble drugs. *GSTF Journal of Advances in Medical Research (JAMR)*, 2015. 2: p. 1-7.

8 Appendix: Supporting Information (SI)

1) Stability data of printed microarrays of APIs within the PVPVA matrix

Microarrays of APIs/PVPVA depicted by PLM at 6 months of storage in accelerated conditions

APIs/PVPVA blends

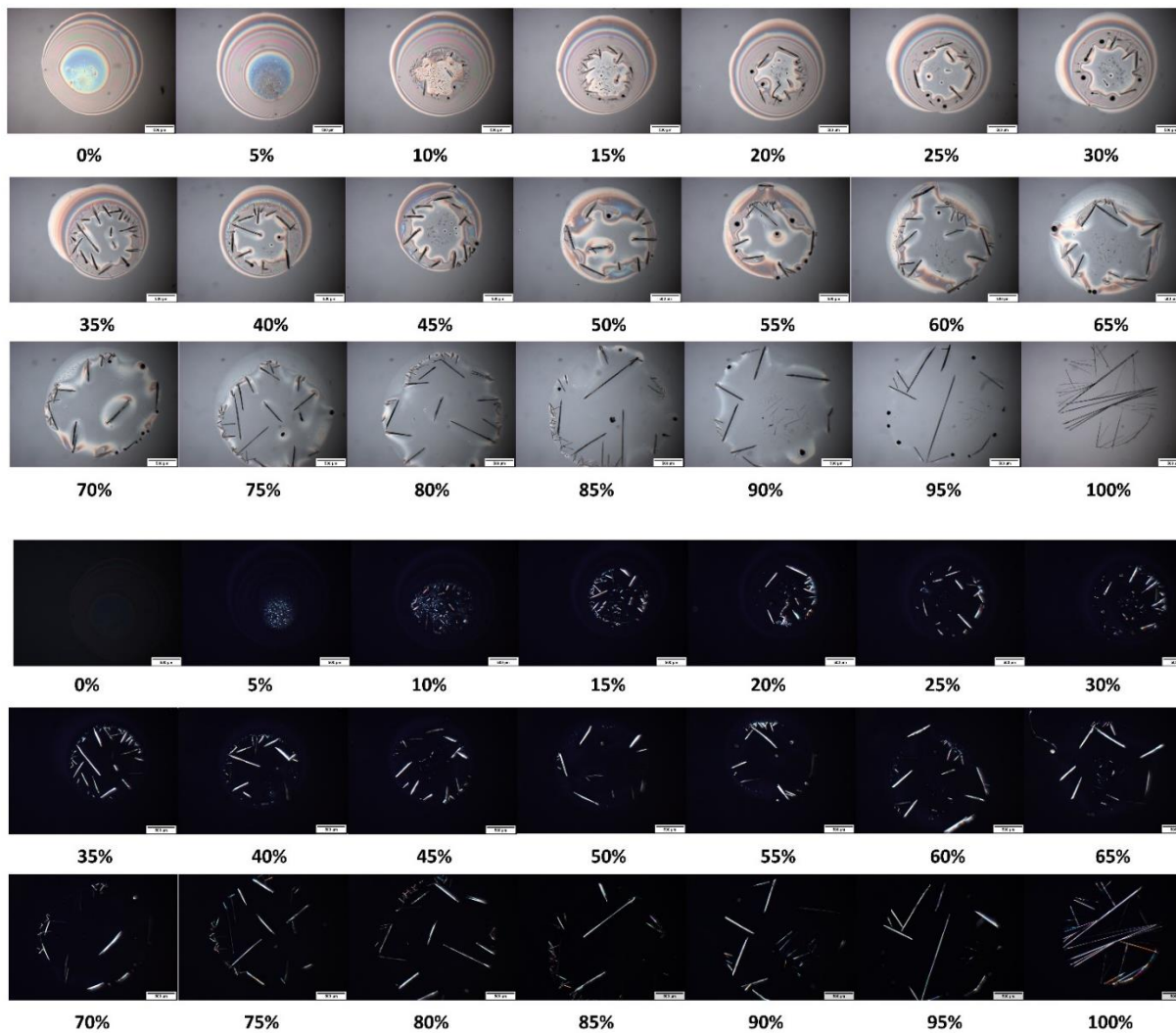


Figure S1. Microarray of Caffeine/PVPVA depicted by PLM. All the spots are reported with the bright field in the upper part of the figure and cross-polarised filters in the lower part of the figure. The images show all different ratios of Caffeine/PVPVA starting from 0% to 100% with a 5% Caffeine increment. The final mass of individual spots is 1000-1100 ng. The scale bar represents 500 μ m.

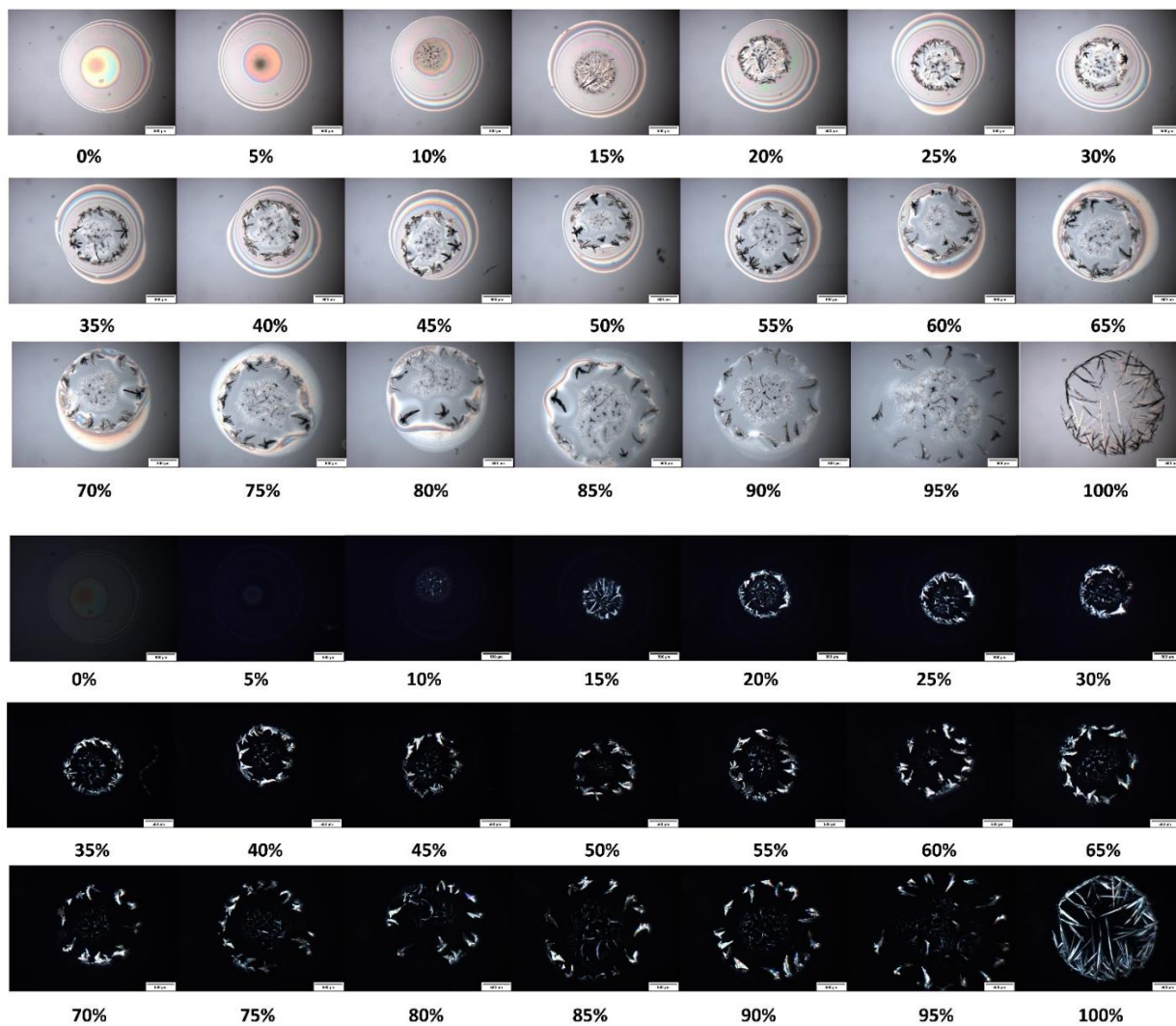


Figure S2. Microarray of Theophylline/PVPVA depicted by PLM. All the spots are reported with the bright field in the upper part of the figure and cross-polarised filters in the lower part of the figure. The images show all different ratios of Theophylline/PVPVA starting from 0% to 100% with a 5% Theophylline increment. The final mass of individual spots is 1000-1100 ng. The scale bar represents 500 μm.

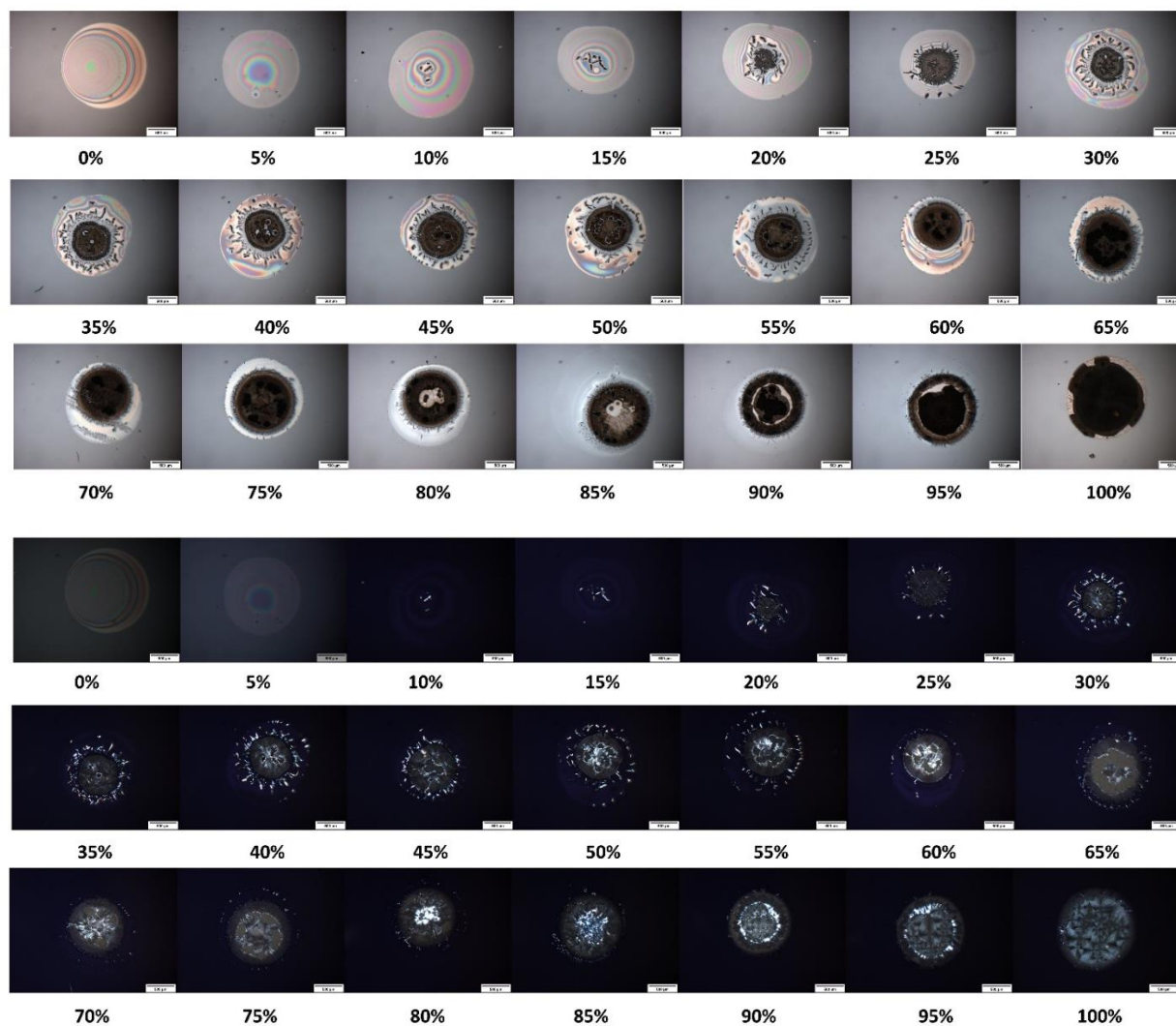


Figure S3. Microarray of Carbamazepine/PVPVA depicted by PLM. All the spots are reported with the bright field in the upper part of the figure and cross-polarised filters in the lower part of the figure. The images show all different ratios of Carbamazepine/PVPVA starting from 0% to 100% with a 5% Carbamazepine increment. The final mass of individual spots is 1000-1100 ng. The scale bar represents 500µm.

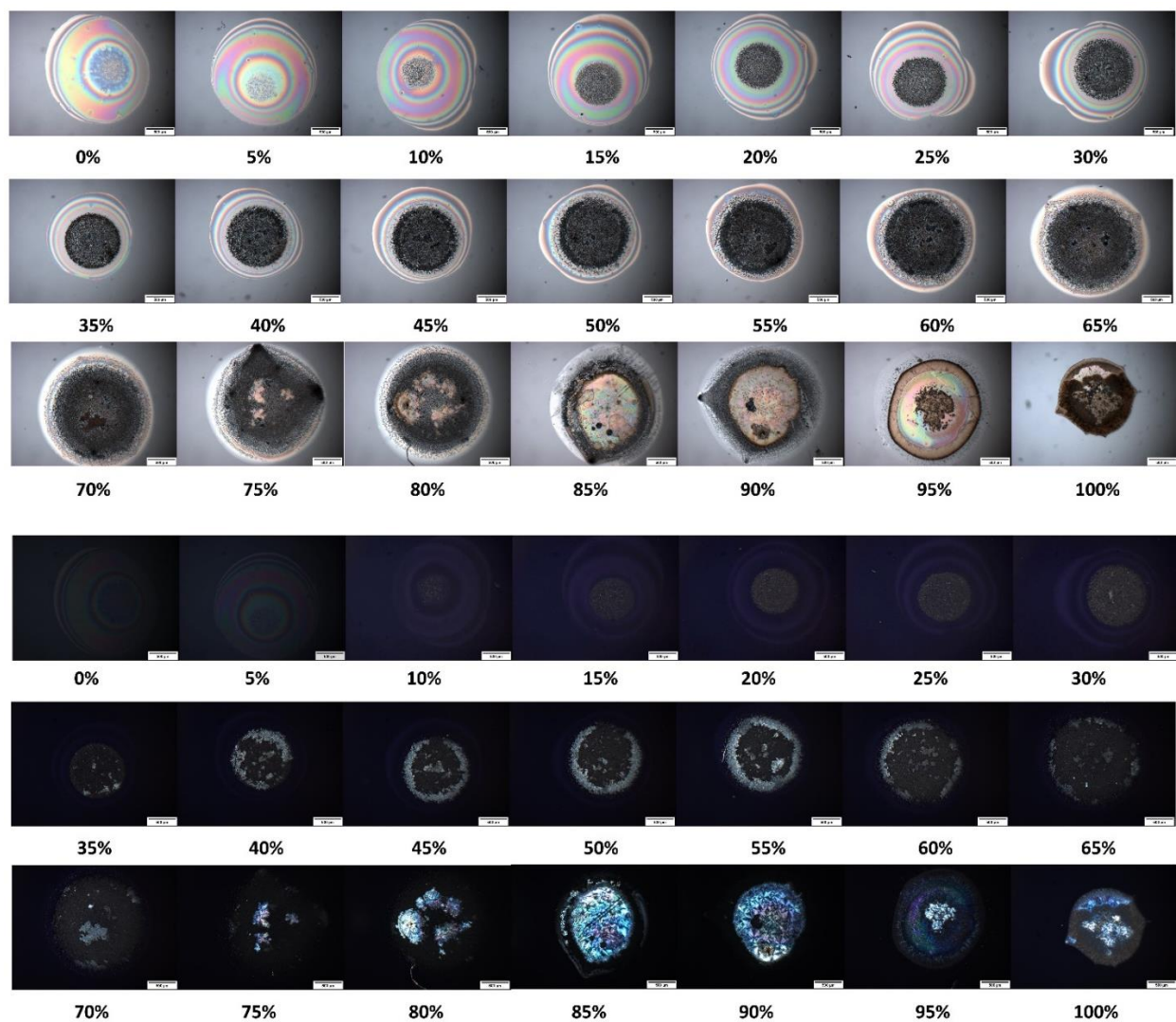


Figure S4. Microarray of Piroxicam/PVPVA depicted by PLM. All the spots are reported with the bright field in the upper part of the figure and cross-polarised filters in the lower part of the figure. The images show all different ratios of Piroxicam/PVPVA starting from 0% to 100% with a 5% Piroxicam increment. The final mass of individual spots is 1000-1100 ng. The scale bar represents 500 μ m.

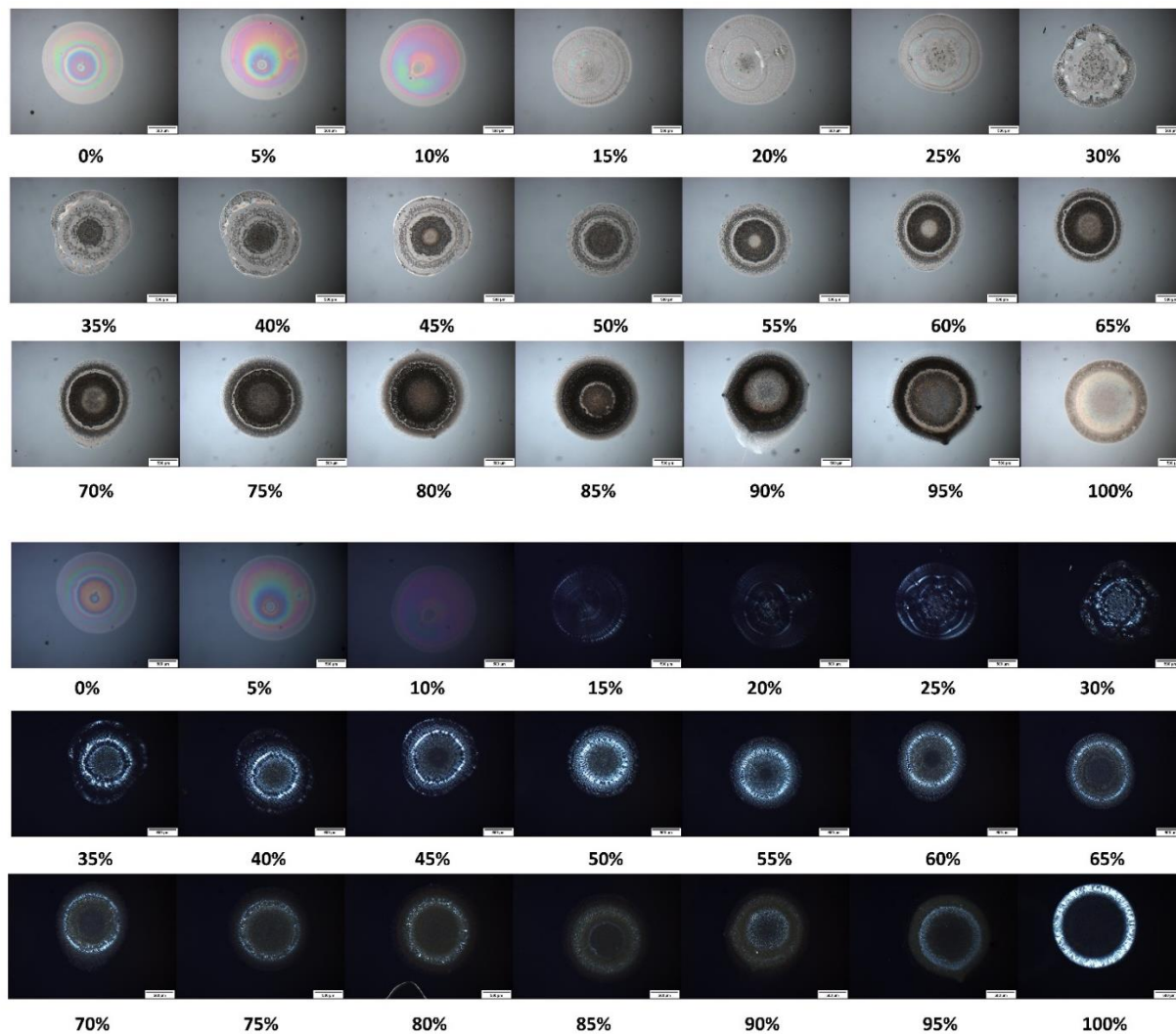


Figure S5. Microarray of Corticosterone/PVPVA depicted by PLM. All the spots are reported with the bright field in the upper part of the figure and cross-polarised filters in the lower part of the figure. The images show all different ratios of Corticosterone/PVPVA starting from 0% to 100% with a 5% Corticosterone increment. The final mass of individual spots is 1000-1100 ng. The scale bar represents 500 μ m.

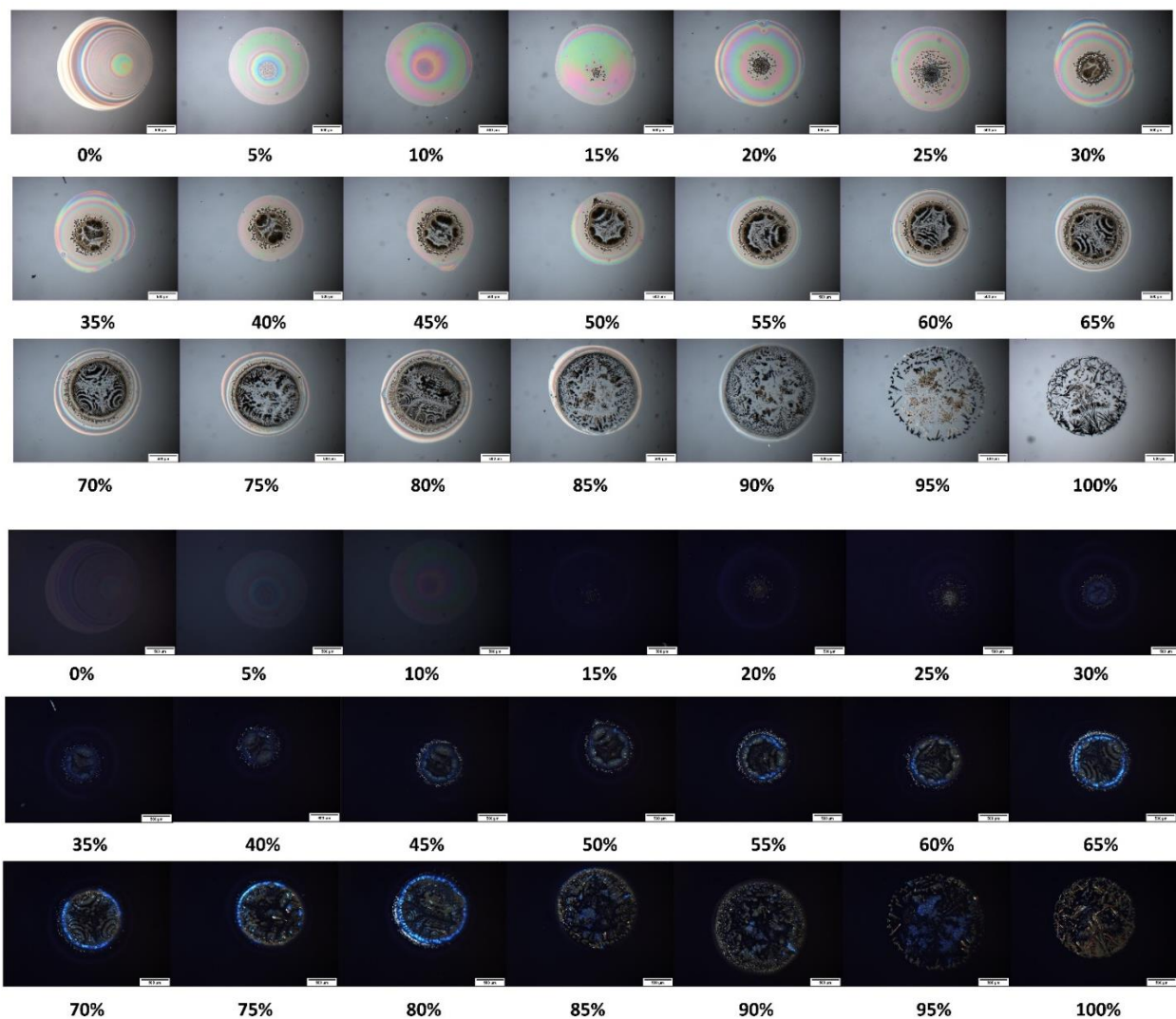


Figure S6. Microarray of Nitrofurantoin/PVPVA depicted by PLM. All the spots are reported with the bright field in the upper part of the figure and cross-polarised filters in the lower part of the figure. The images show all different ratios of Nitrofurantoin/PVPVA starting from 0% to 100% with a 5% Nitrofurantoin increment. The final mass of individual spots is 1000-1100 ng. The scale bar represents 500 μ m.

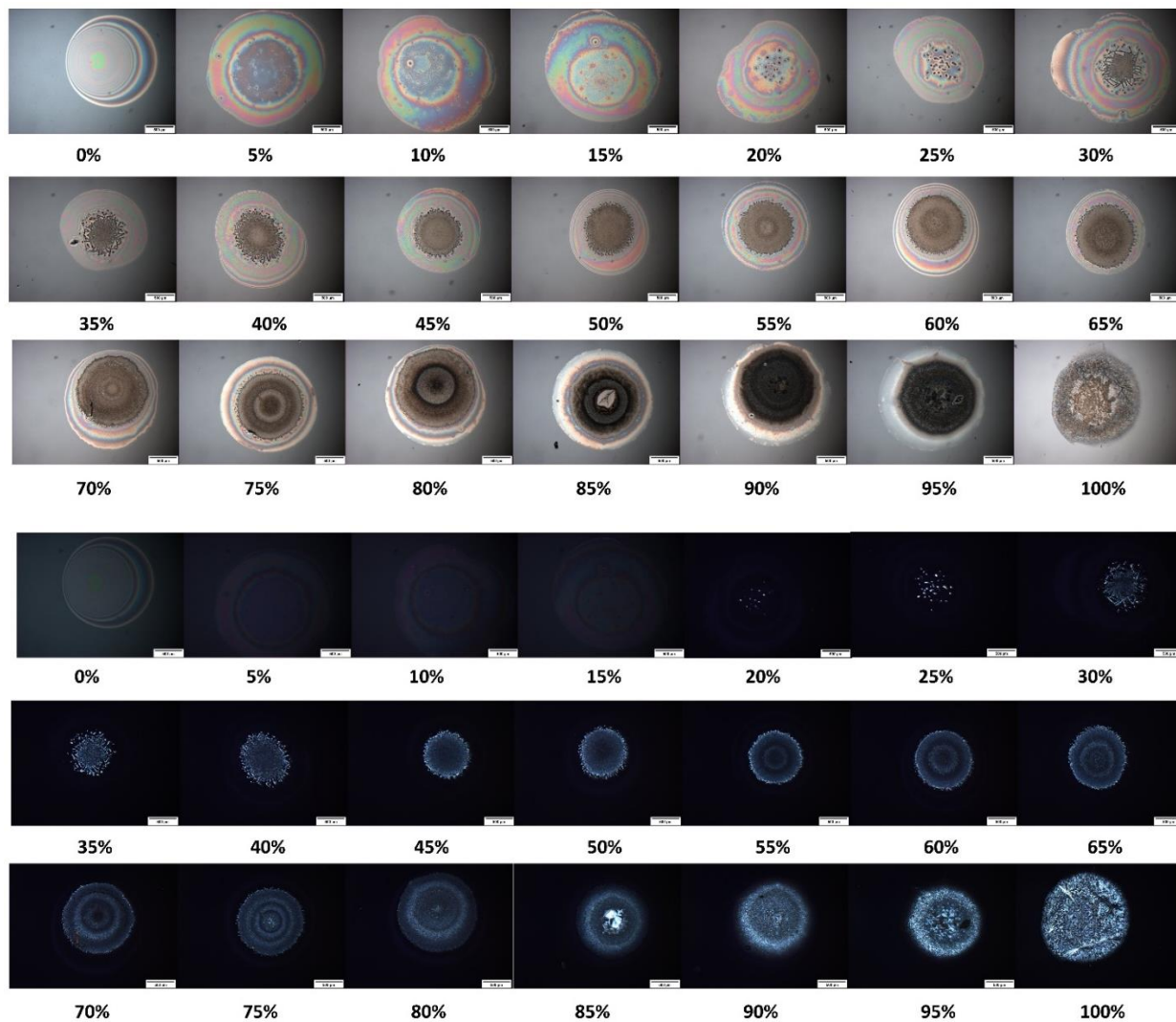


Figure S7. Microarray of Diclofenac sodium/PVPVA depicted by PLM. All the spots are reported with the bright field in the upper part of the figure and cross-polarised filters in the lower part of the figure. The images show all different ratios of Diclofenac sodium/PVPVA starting from 0% to 100% with a 5% Diclofenac sodium increment. The final mass of individual spots is 1000-1100 ng. The scale bar represents 500µm.

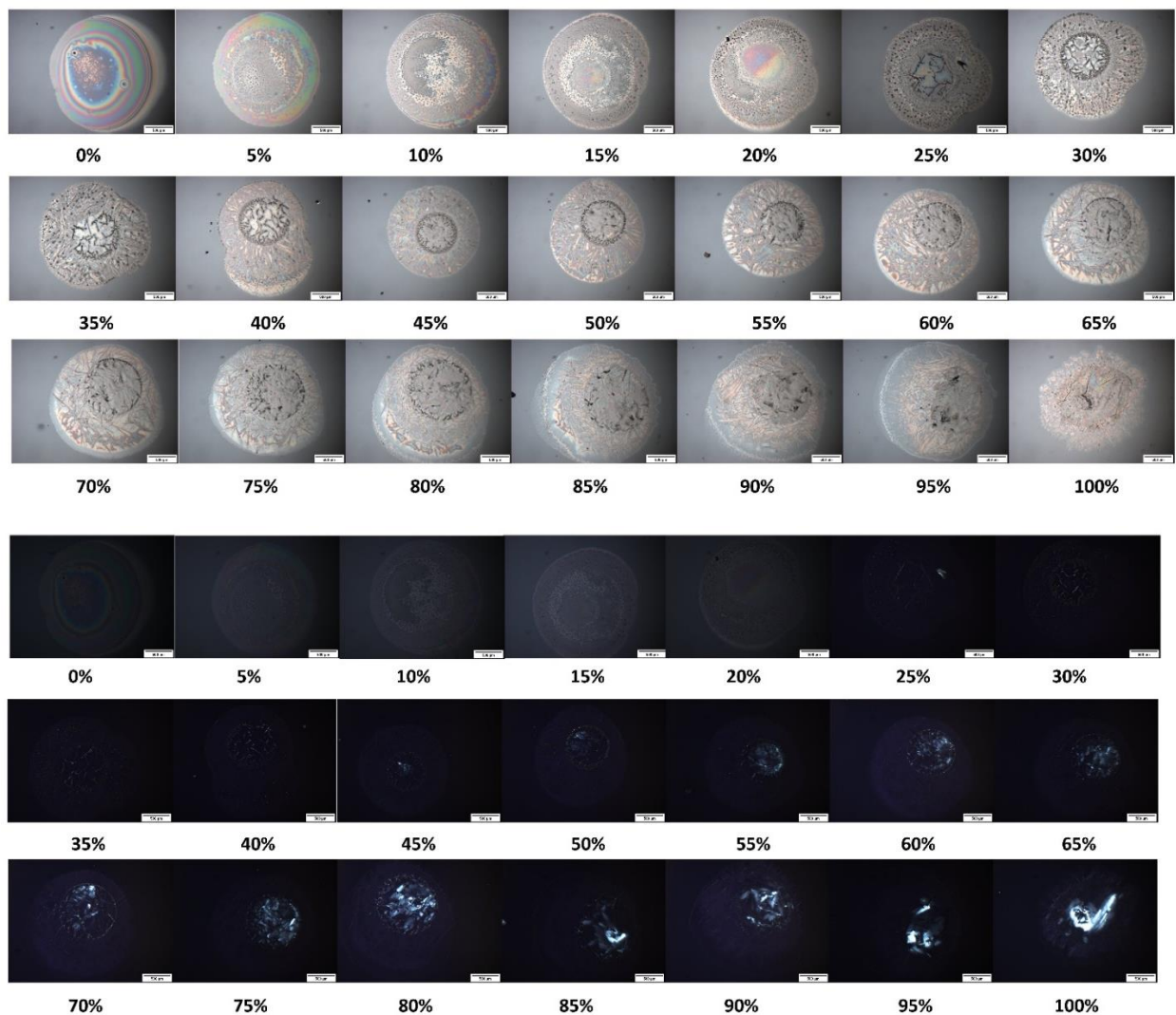


Figure S8. Microarray of Atenolol/PVPVA depicted by PLM. All the spots are reported with the bright field in the upper part of the figure and cross-polarised filters in the lower part of the figure. The images show all ratios of Atenolol/PVPVA, starting from 0% to 100% with a 5% Atenolol increment. The final mass of individual spots is 1000-1100 ng. The scale bar represents 500µm.

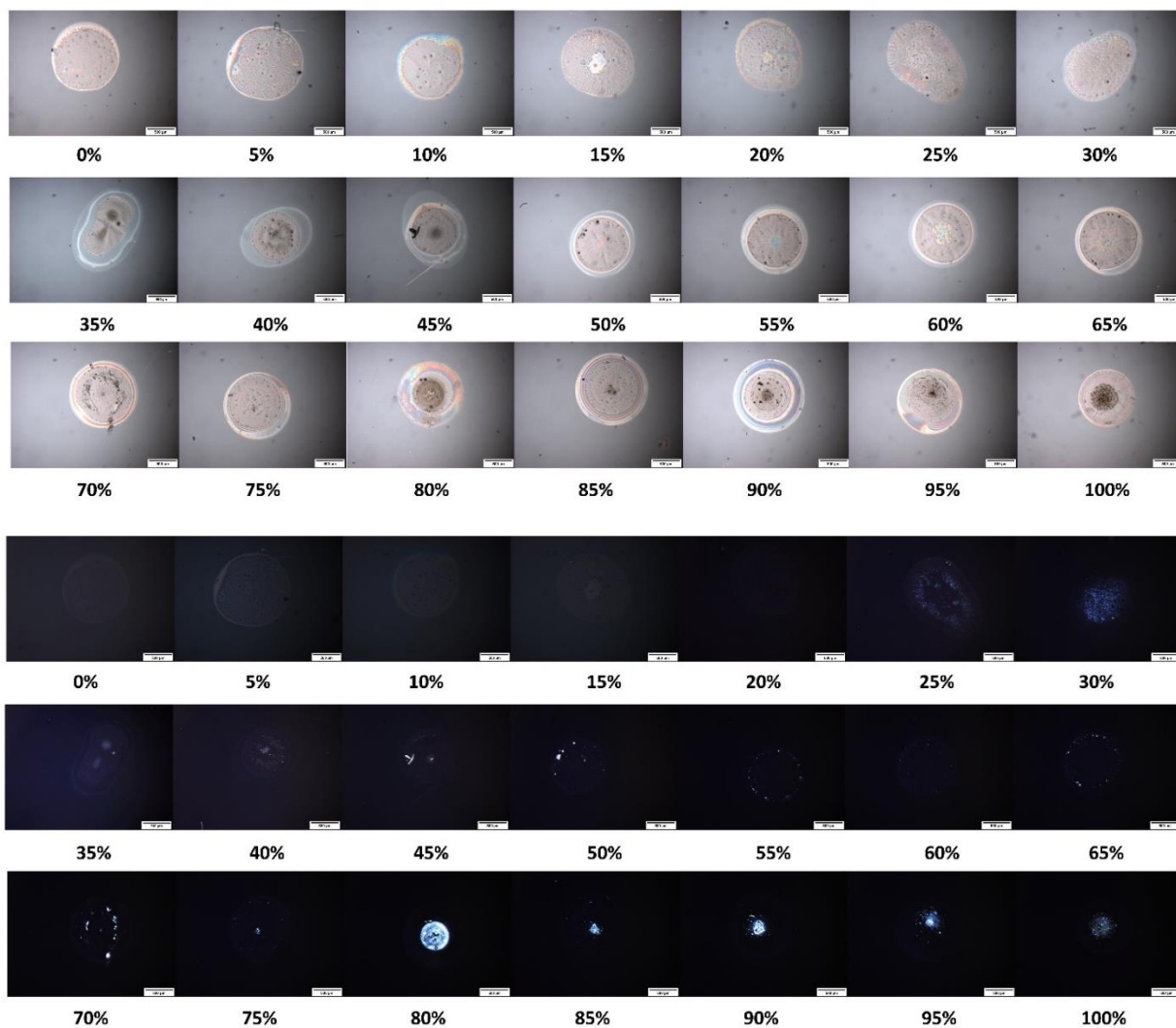


Figure S9. Microarray of Itraconazole/PVPVA depicted by PLM. All the spots are reported with the bright field in the upper part of the figure and cross-polarised filters in the lower part of the figure. The images show all different ratios of Itraconazole/PVPVA starting from 0% to 100% with a 5% Itraconazole increment. The final mass of individual spots is 1000-1100 ng. The scale bar represents 500µm.

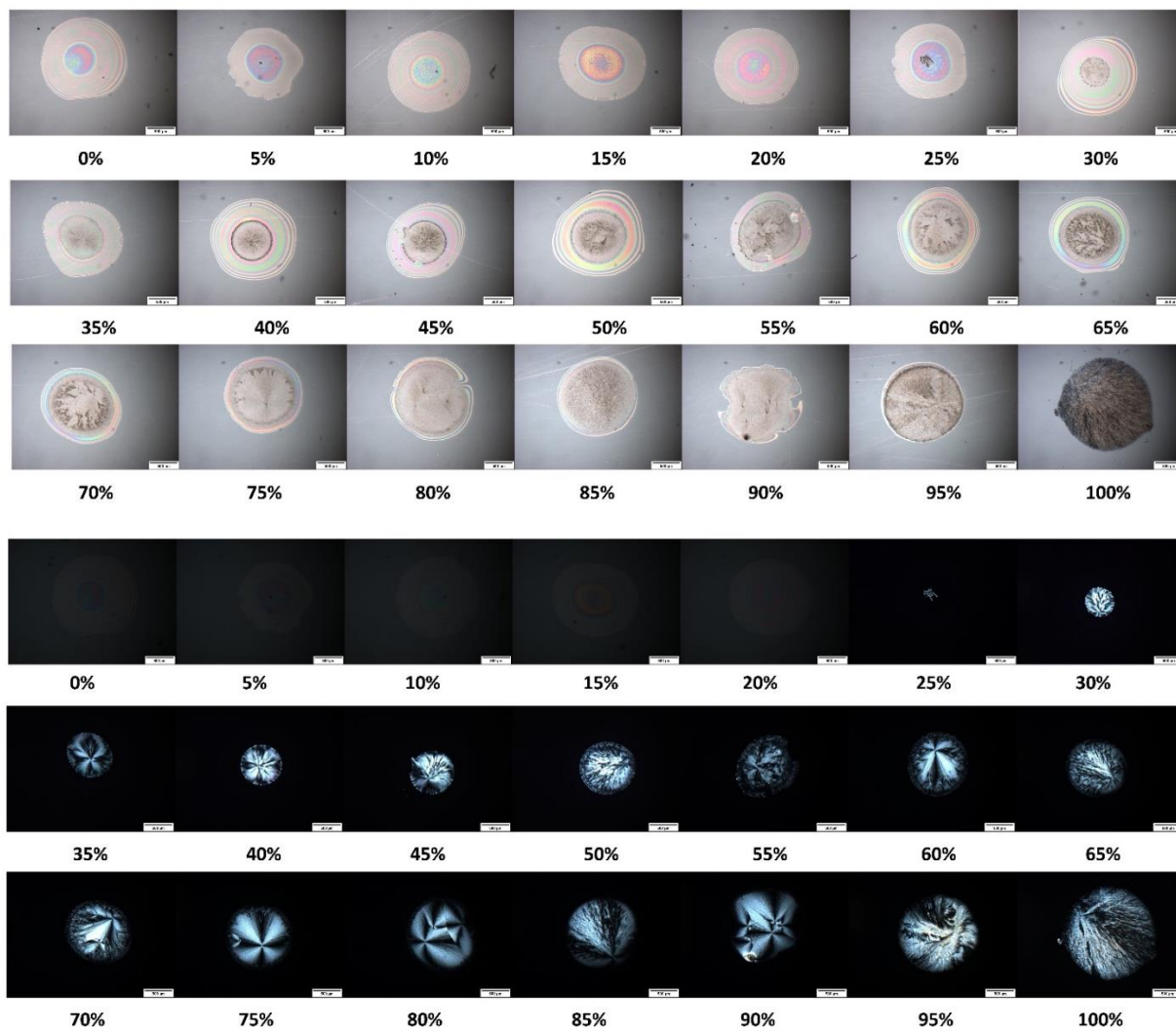


Figure S10. Microarray of Nicotinamide/PVPVA depicted by PLM. All the spots are reported with the bright field in the upper part of the figure and cross-polarised filters in the lower part of the figure. The images show all different ratios of Nicotinamide/PVPVA starting from 0% to 100% with a 5% Nicotinamide increment. The final mass of individual spots is 1000-1100 ng. The scale bar represents 500 μ m.

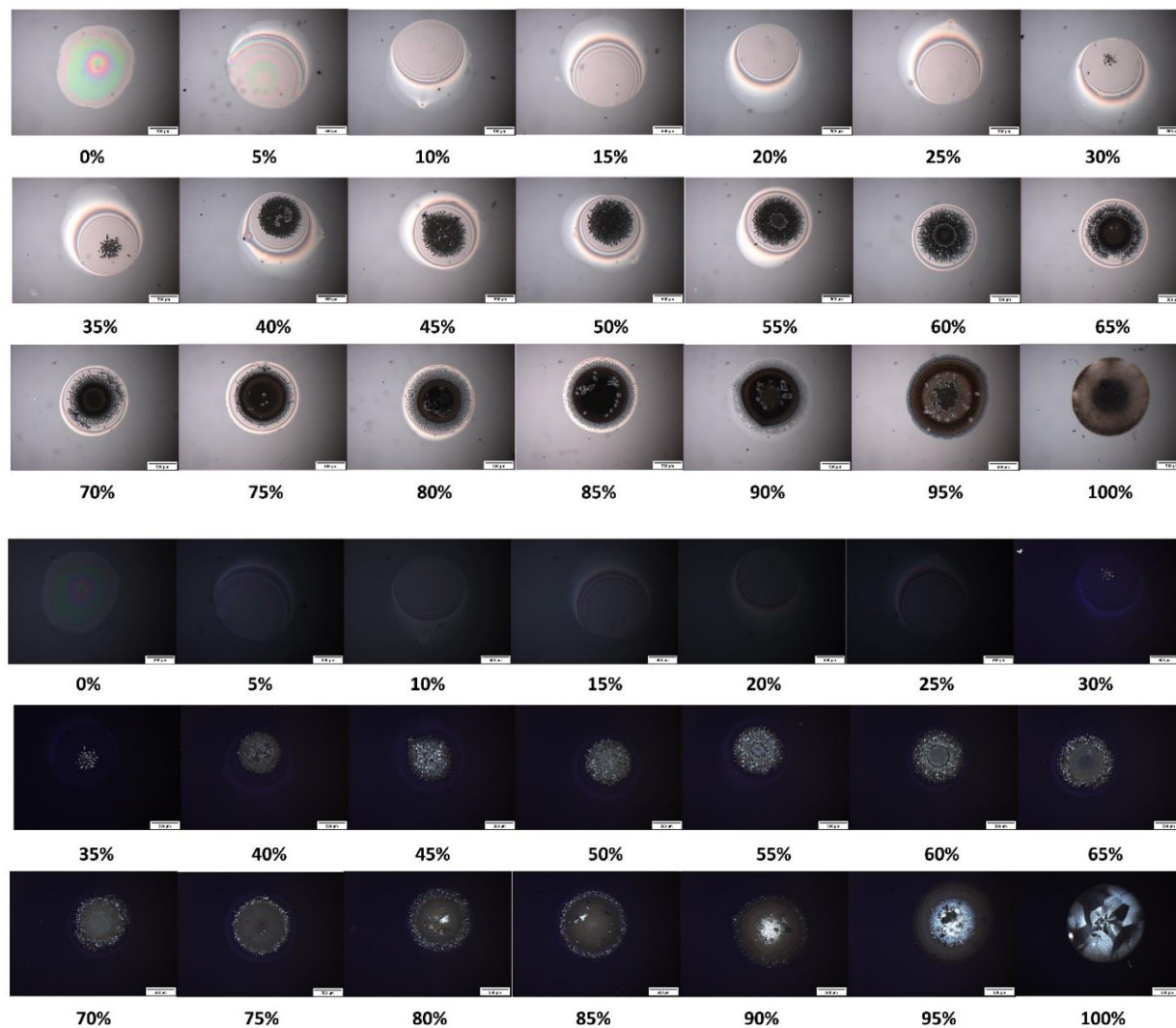


Figure S11. Microarray of β -Estradiol/PVPVA depicted by PLM. All the spots are reported with the bright field in the upper part of the figure and cross-polarised filters in the lower part of the figure. The images show all different ratios of β -Estradiol/PVPVA starting from 0% to 100% with a 5% β -Estradiol increment. The final mass of individual spots is 1000-1100 ng. The scale bar represents 500 μm .

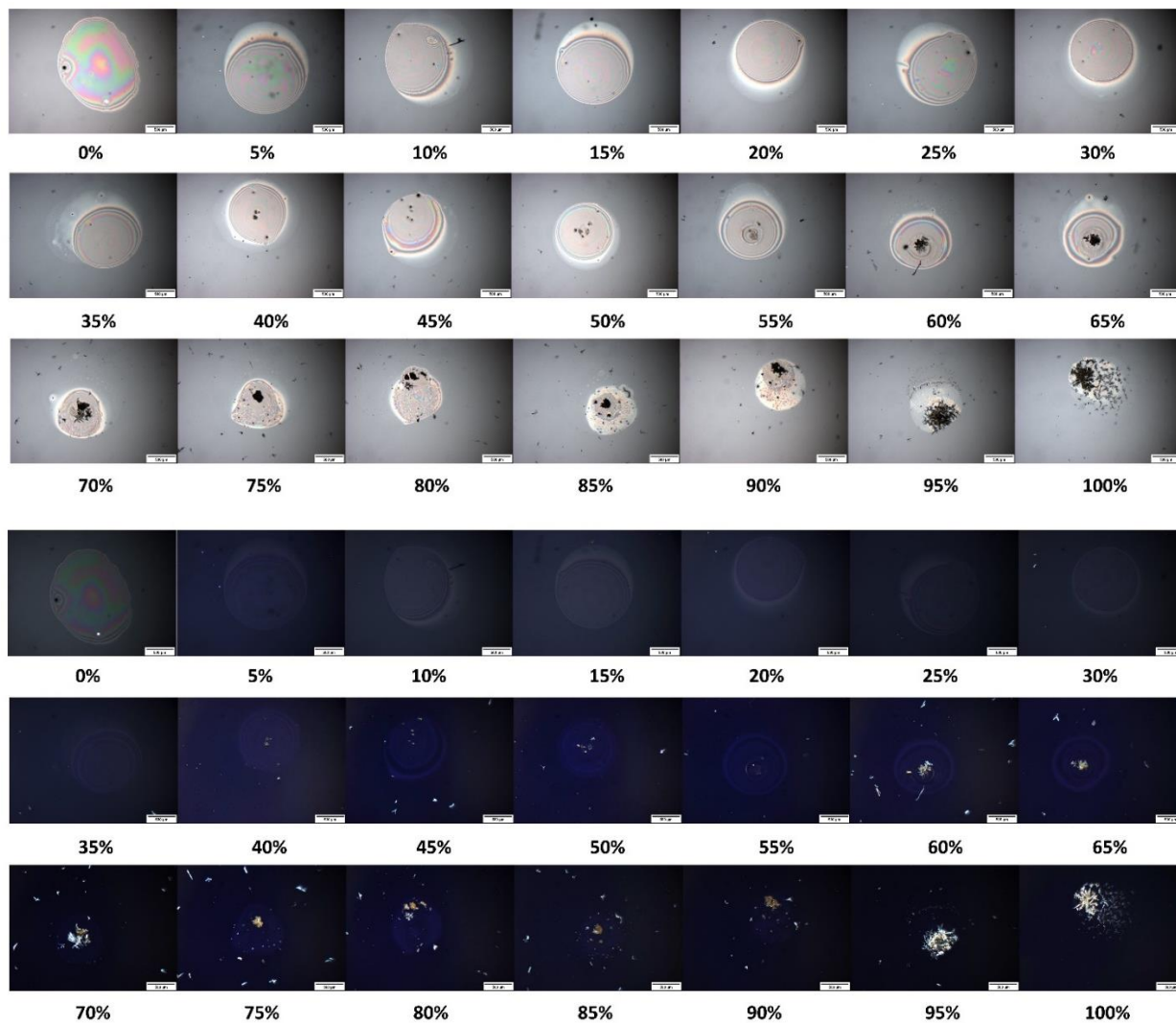


Figure S12. Microarray of Nifedipine/PVPVA depicted by PLM. All the spots are reported with the bright field in the upper part of the figure and cross-polarised filters in the lower part of the figure. The images show all different ratios of Nifedipine/PVPVA starting from 0% 100% with a 5% Nifedipine increment. The final mass of individual spots is 1000-1100 ng. The scale bar represents 500 μ m.

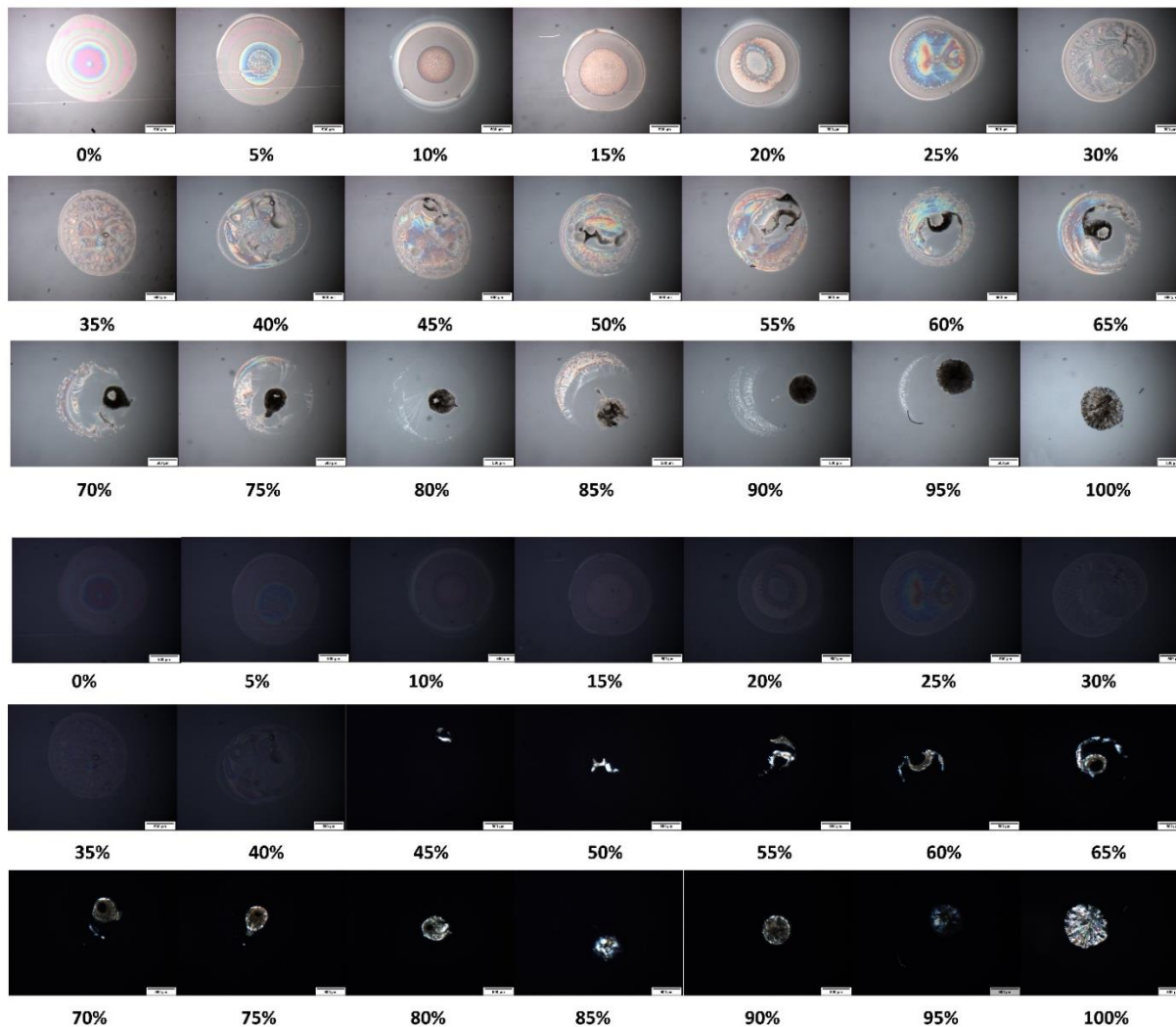


Figure S13. Microarray of Flufenamic acid/PVPVA depicted by PLM. All the spots are reported with the bright field in the upper part of the figure and cross-polarised filters in the lower part of the figure. The images show all different ratios of Flufenamic acid/PVPVA starting from 0% to 100% with a 5% Flufenamic acid increment. The final mass of individual spots is 1000-1100 ng. The scale bar represents 500 μ m.

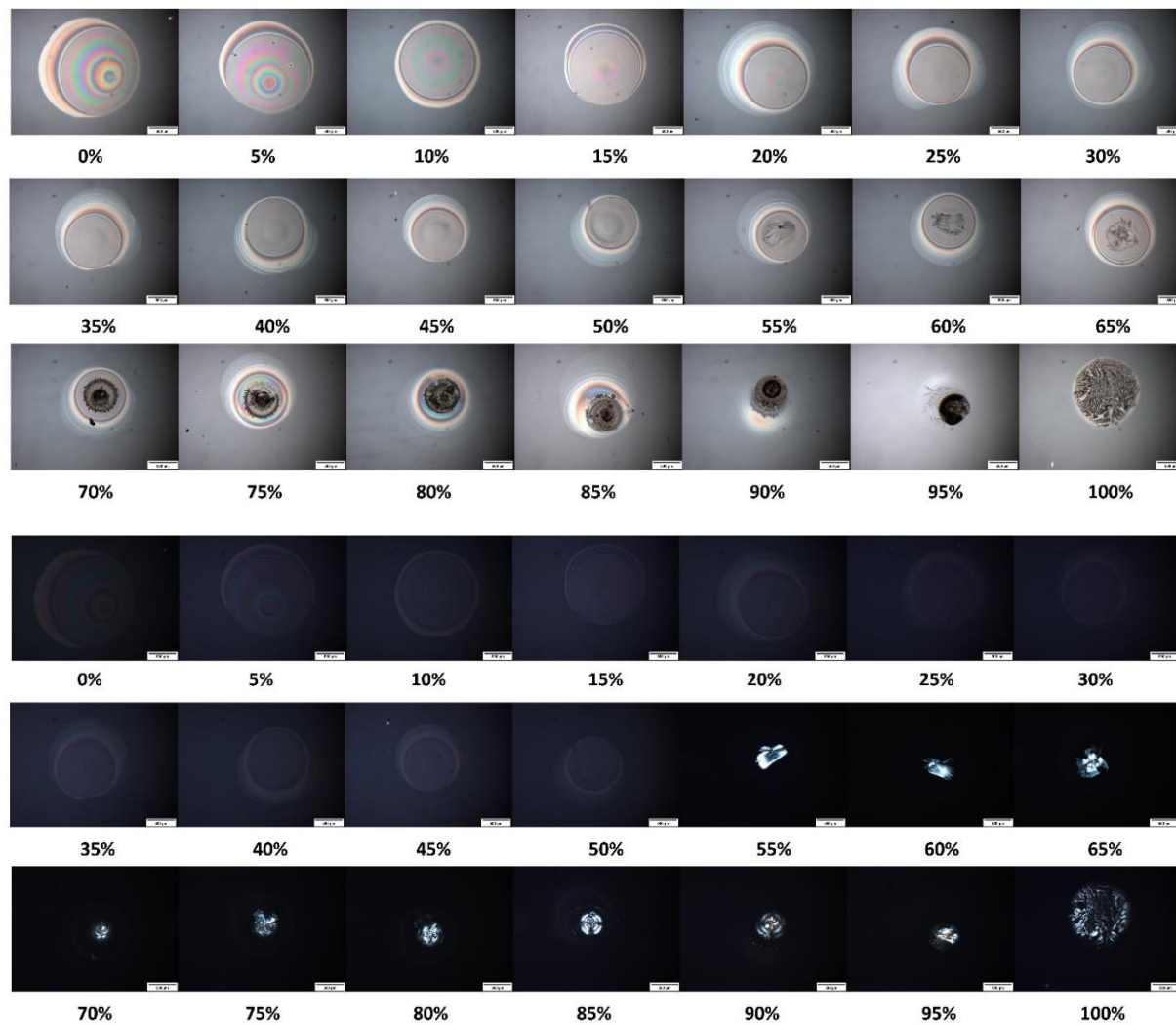


Figure S14. Microarray of Tolbutamide/PVPVA depicted by PLM. All the spots are reported with the bright field in the upper part of the figure and cross-polarised filters in the lower part of the figure. The images show all different ratios of Tolbutamide/PVPVA starting from 0% to 100% with a 5% Tolbutamide increment. The final mass of individual spots is 1000-1100 ng. The scale bar represents 500 μ m.

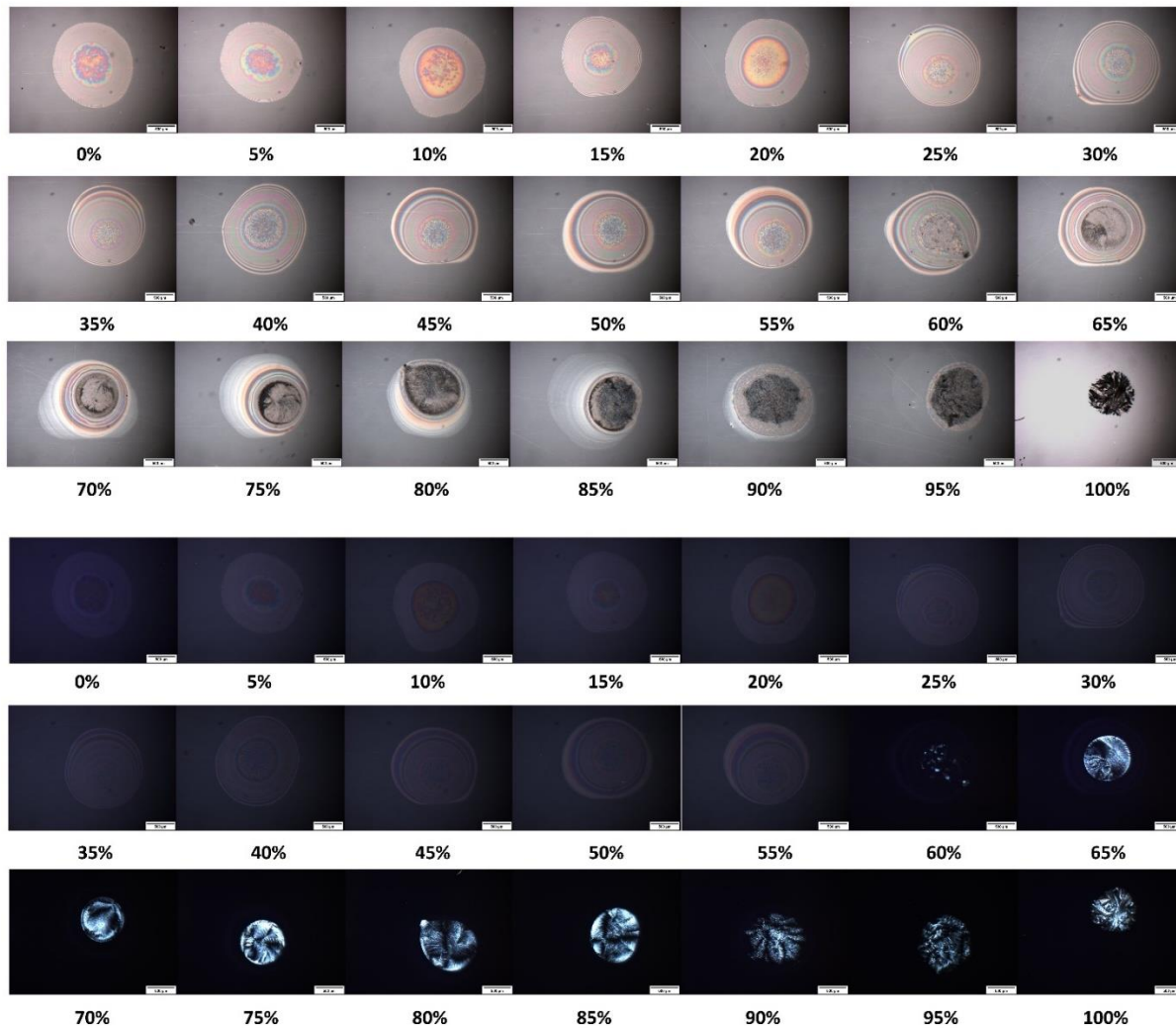


Figure S15. Microarray of Acetylsalicylic acid (Aspirin)/PVPVA depicted by PLM. All the spots are reported with the bright field in the upper part of the figure and cross-polarised filters in the lower part of the figure. The images show all different ratios of Aspirin/PVPVA starting from 0% to 100% with a 5% Aspirin increment. The final mass of individual spots is 1000-1100 ng. The scale bar represents 500 μm.

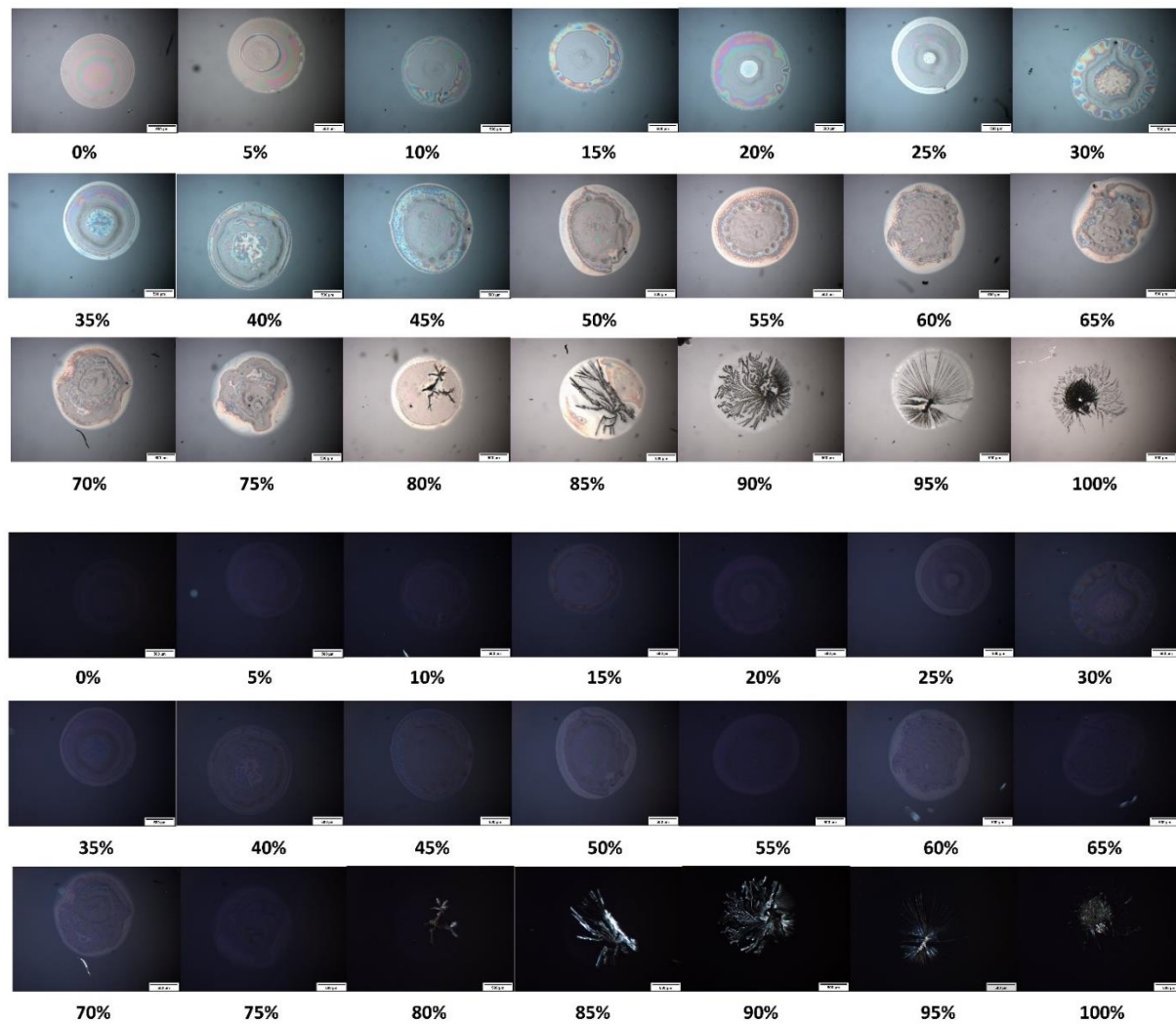


Figure S16. Microarray of Probuco/PVPVA depicted by PLM. All the spots are reported with the bright field in the upper part of the figure and cross-polarised filters in the lower part of the figure. The images show all different ratios of Probuco/PVPVA starting from 0% to 100% with a 5% Probuco increment. The final mass of individual spots is 1000-1100 ng. The scale bar represents 500 μ m.

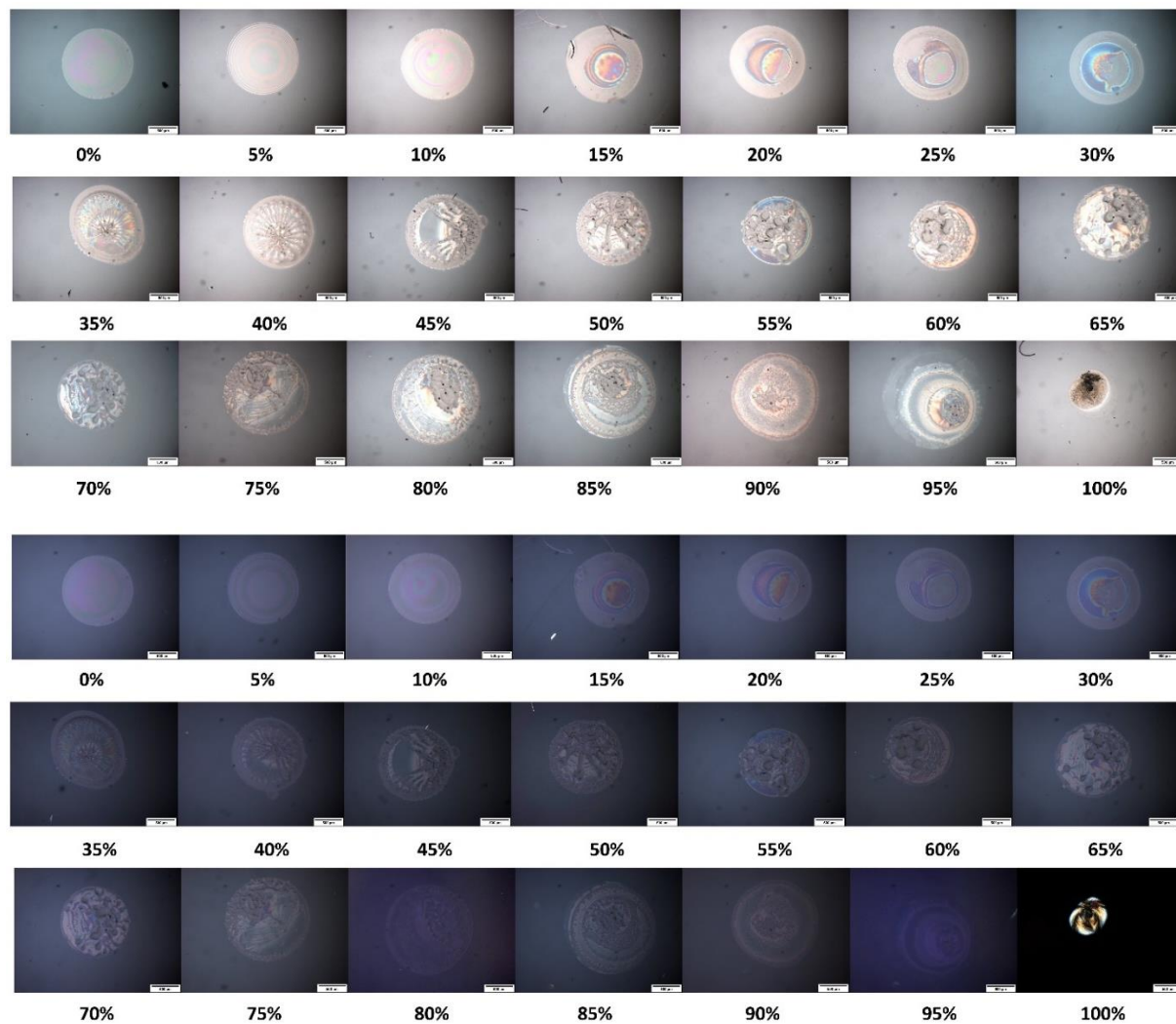


Figure S17. Microarray of Celecoxib/PVPVA depicted by PLM. All the spots are reported with the bright field in the upper part of the figure and cross-polarised filters in the lower part of the figure. The images show all different ratios of Celecoxib/PVPVA starting from 0% to 100% with a 5% Celecoxib increment. The final mass of individual spots is 1000-1100 ng. The scale bar represents 500 μ m.

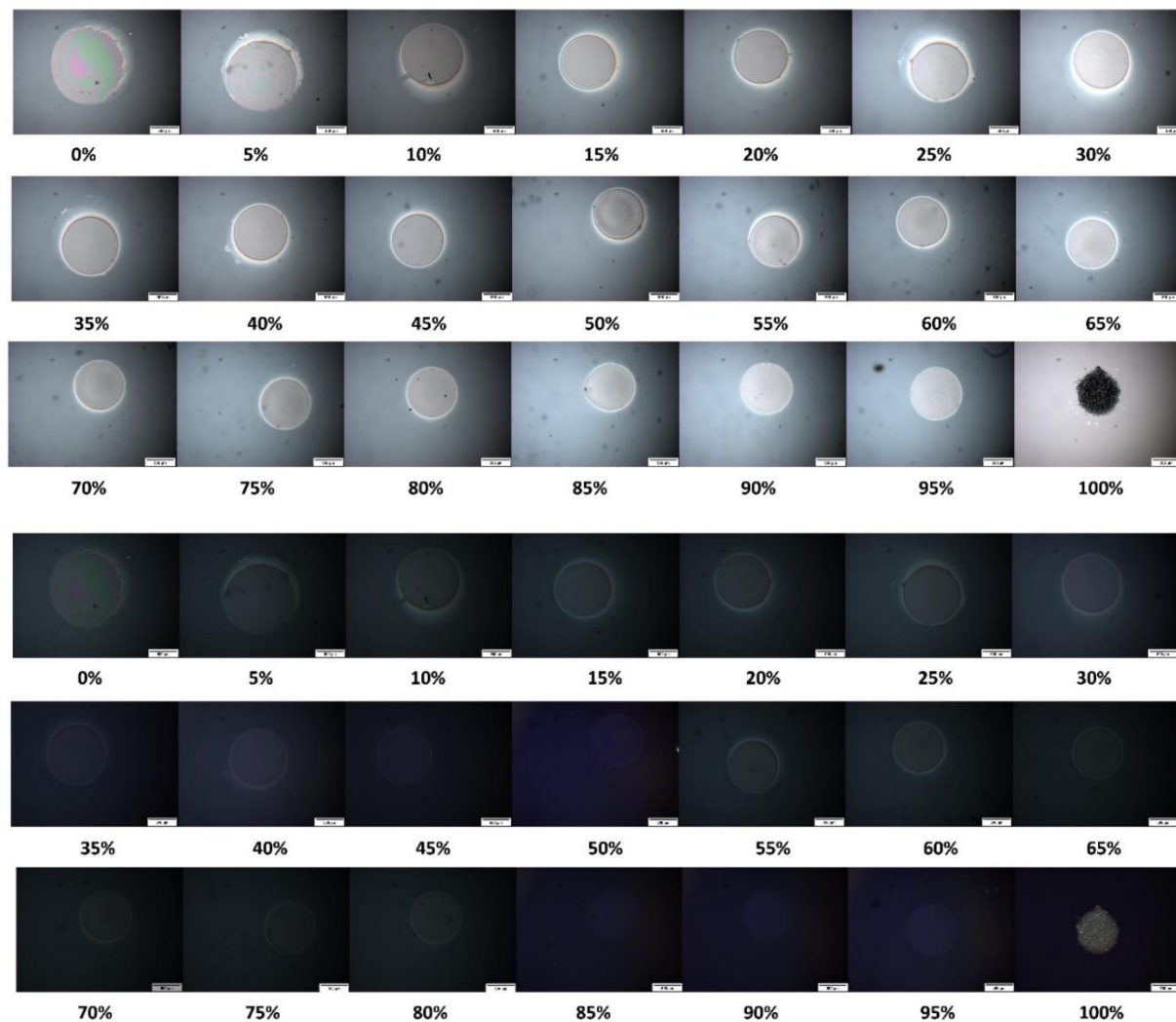


Figure S18. Microarray of Felodipine/PVPVA depicted by PLM. All the spots are reported with the bright field in the upper part of the figure and cross-polarised filters in the lower part of the figure. The images show all different ratios of Felodipine/PVPVA starting from 0% to 100% with a 5% Felodipine increment. The final mass of individual spots is 1000-1100 ng. The scale bar represents 500 μ m.

2) Stability data of printed microarrays of APIs within the Soluplus matrix

Microarrays of APIs/Soluplus depicted by PLM at 6 months of storage in accelerated conditions

APIs/ Soluplus blends

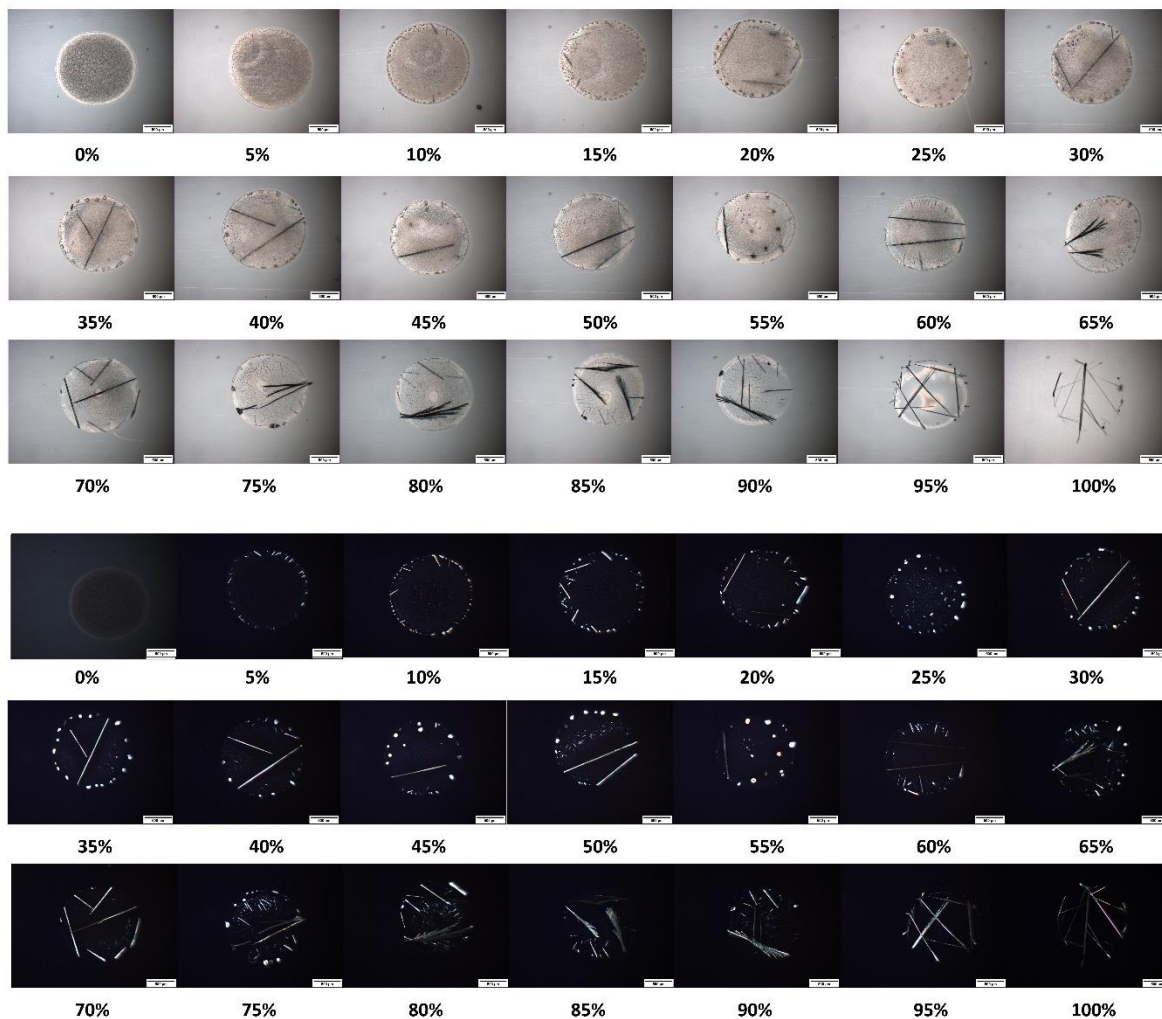


Figure S19. Microarray of Caffeine/Soluplus depicted by PLM. All the spots are reported with the bright field in the upper part of the figure and cross-polarised filters in the lower part of the figure. The images show all different ratios of Caffeine/Soluplus starting from 0% to 100% with a 5% API increment. The final mass of individual spots is 1000-1100 ng. The scale bar represents 500 μ m.

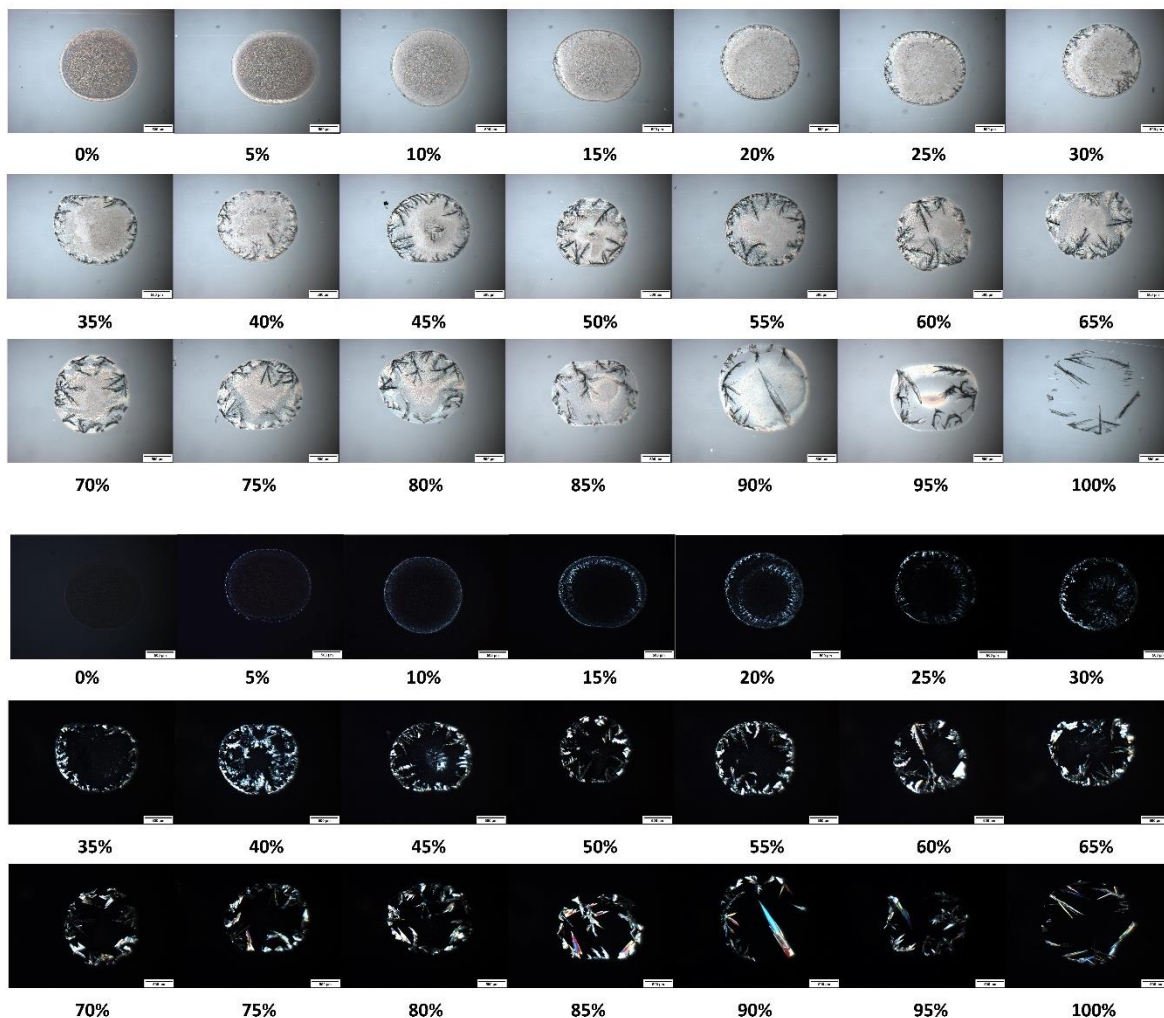


Figure S20. Microarray of Theophylline/Soluplus depicted by PLM. All the spots are reported with the bright field in the upper part of the figure and cross-polarised filters in the lower part of the figure. The images show all different ratios of Theophylline/Soluplus starting from 0% to 100% with a 5% API increment. The final mass of individual spots is 1000-1100 ng. The scale bar represents 500 μ m.

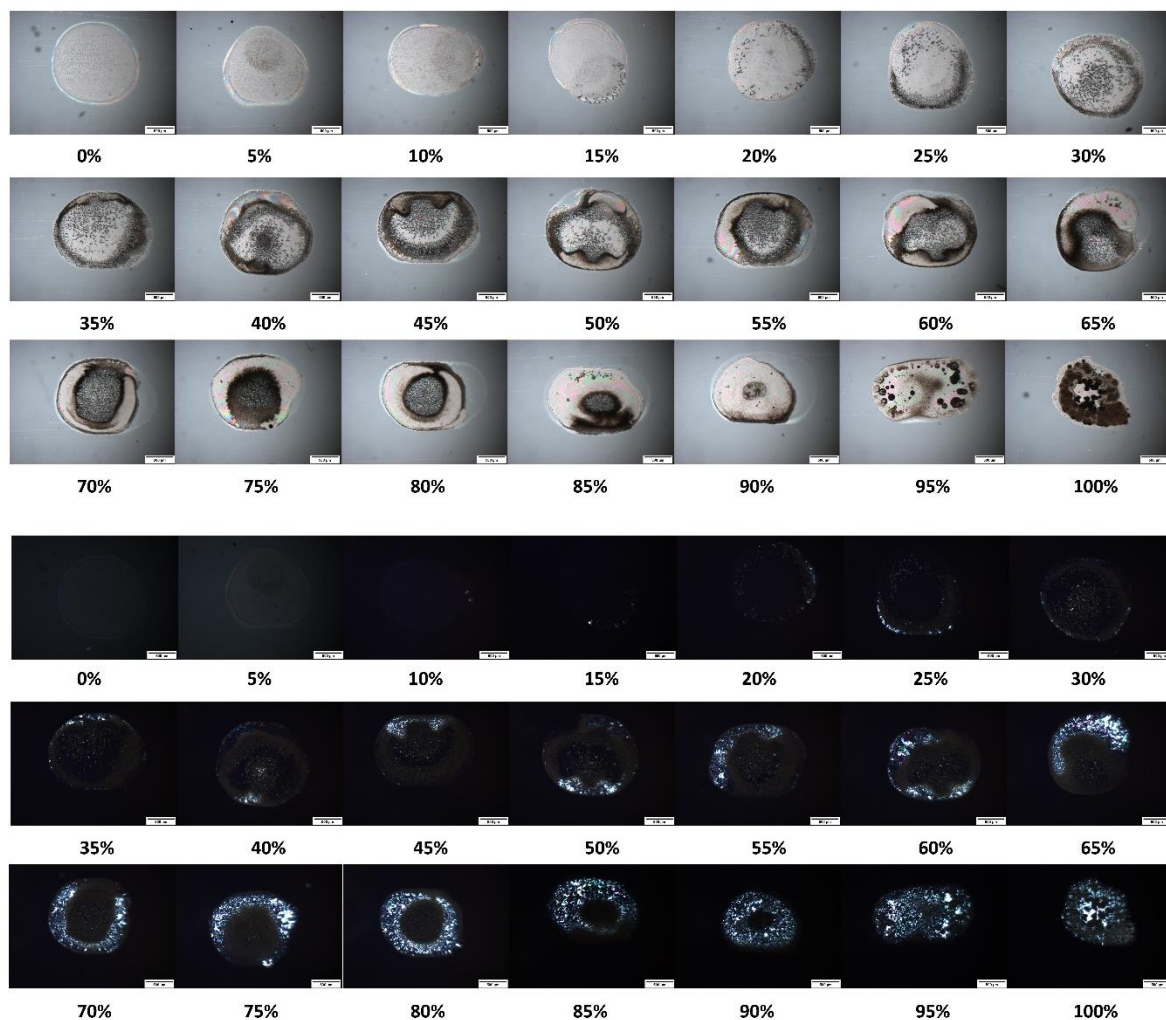


Figure S21. Microarray of Carbamazepine/Soluplus depicted by PLM. All the spots are reported with the bright field in the upper part of the figure and cross-polarised filters in the lower part of the figure. The images show all different ratios of Carbamazepine/Soluplus starting from 0% to 100% with a 5% API increment. The final mass of individual spots is 1000-1100 ng. The scale bar represents 500 μ m.

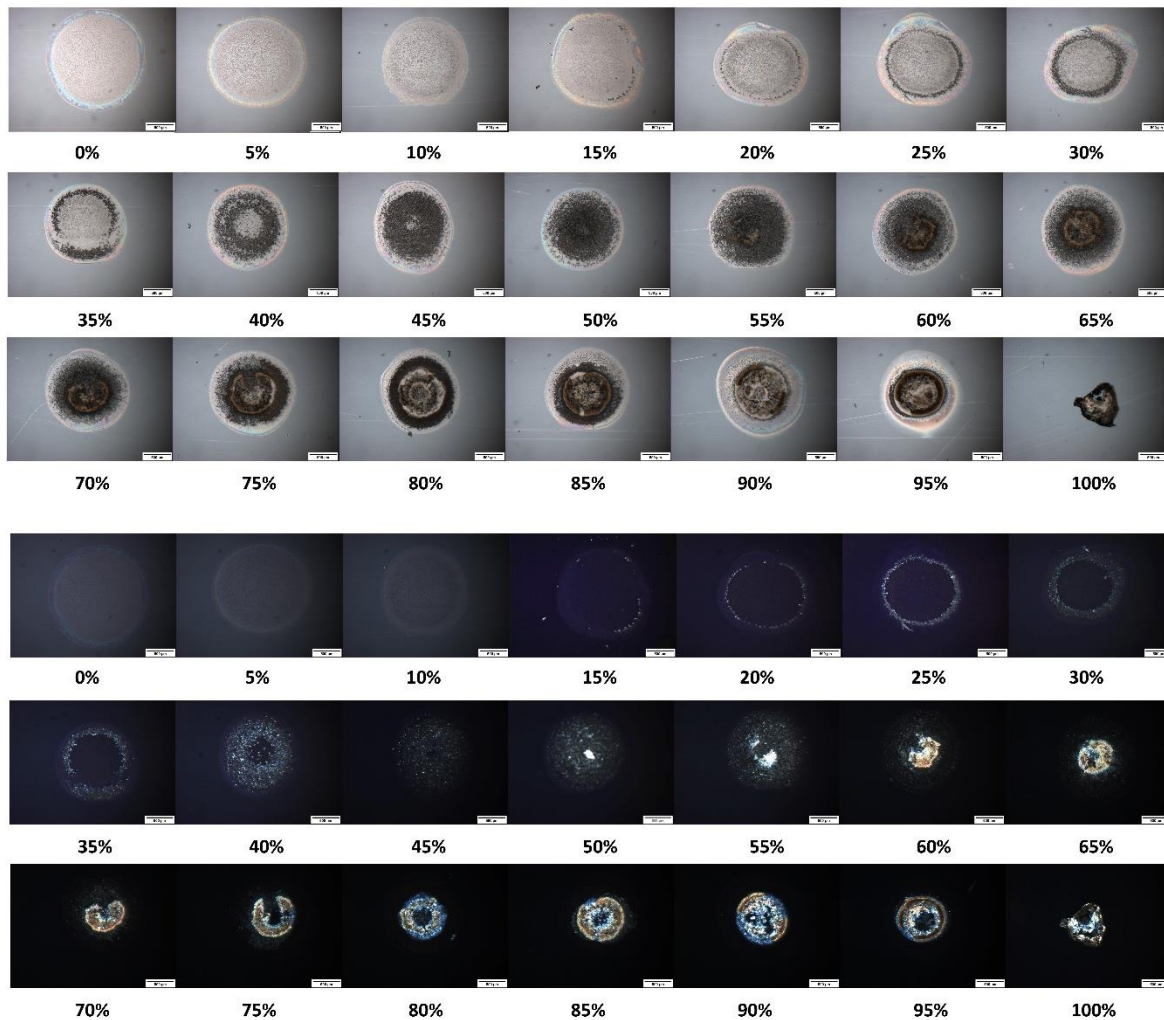


Figure S22. Microarray of Piroxicam/Soluplus depicted by PLM. All the spots are reported with the bright field in the upper part of the figure and cross-polarised filters in the lower part of the figure. The images show all different ratios of Piroxicam/Soluplus starting from 0% to 100% with a 5% API increment. The final mass of individual spots is 1000-1100 ng. The scale bar represents 500 μ m.

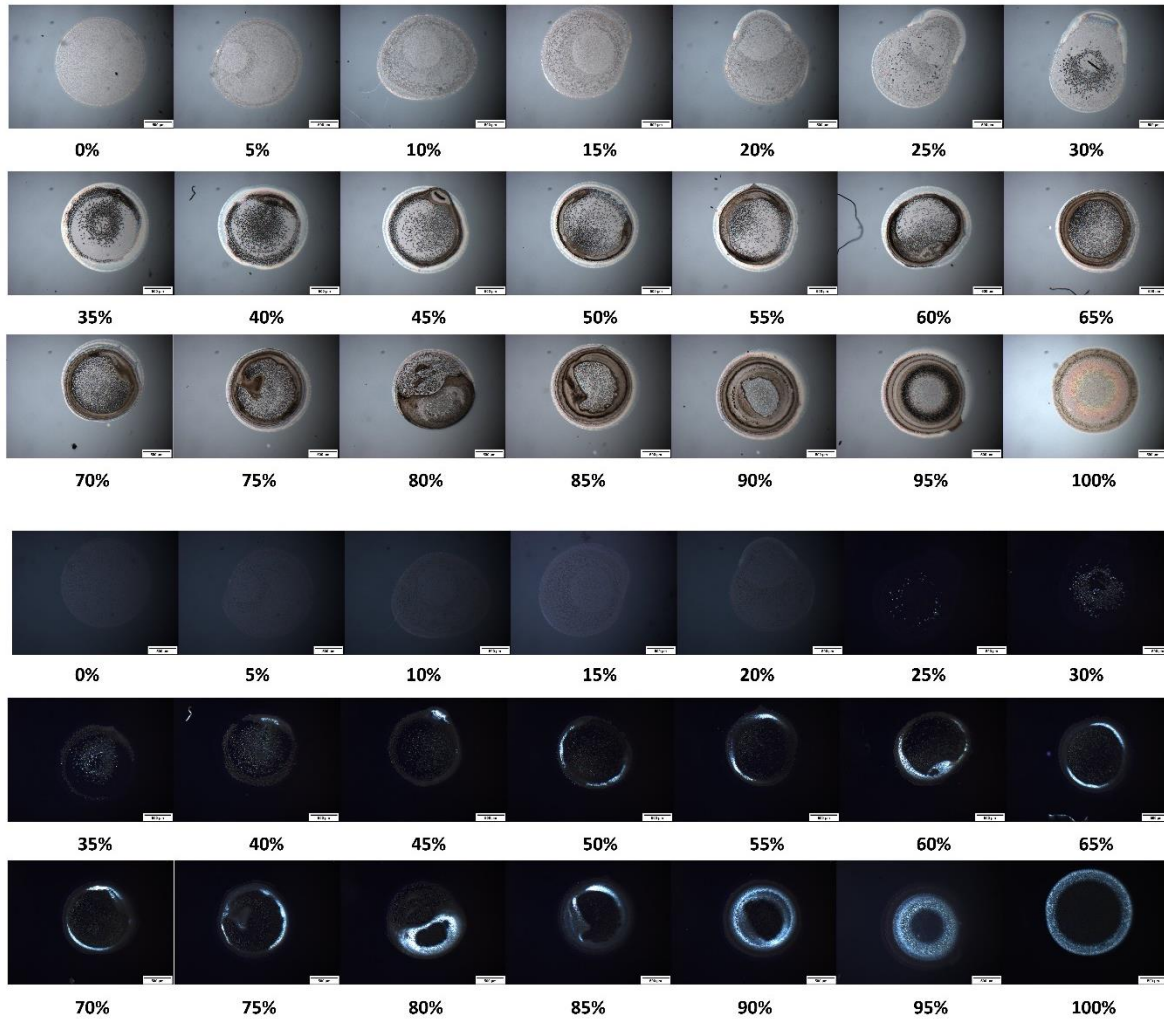


Figure S23. Microarray of Corticosterone/Soluplus depicted by PLM. All the spots are reported with the bright field in the upper part of the figure and cross-polarised filters in the lower part of the figure. The images show all different ratios of Corticosterone/Soluplus starting from 0% to 100% with a 5% API increment. The final mass of individual spots is 1000-1100 ng. The scale bar represents 500 μ m.

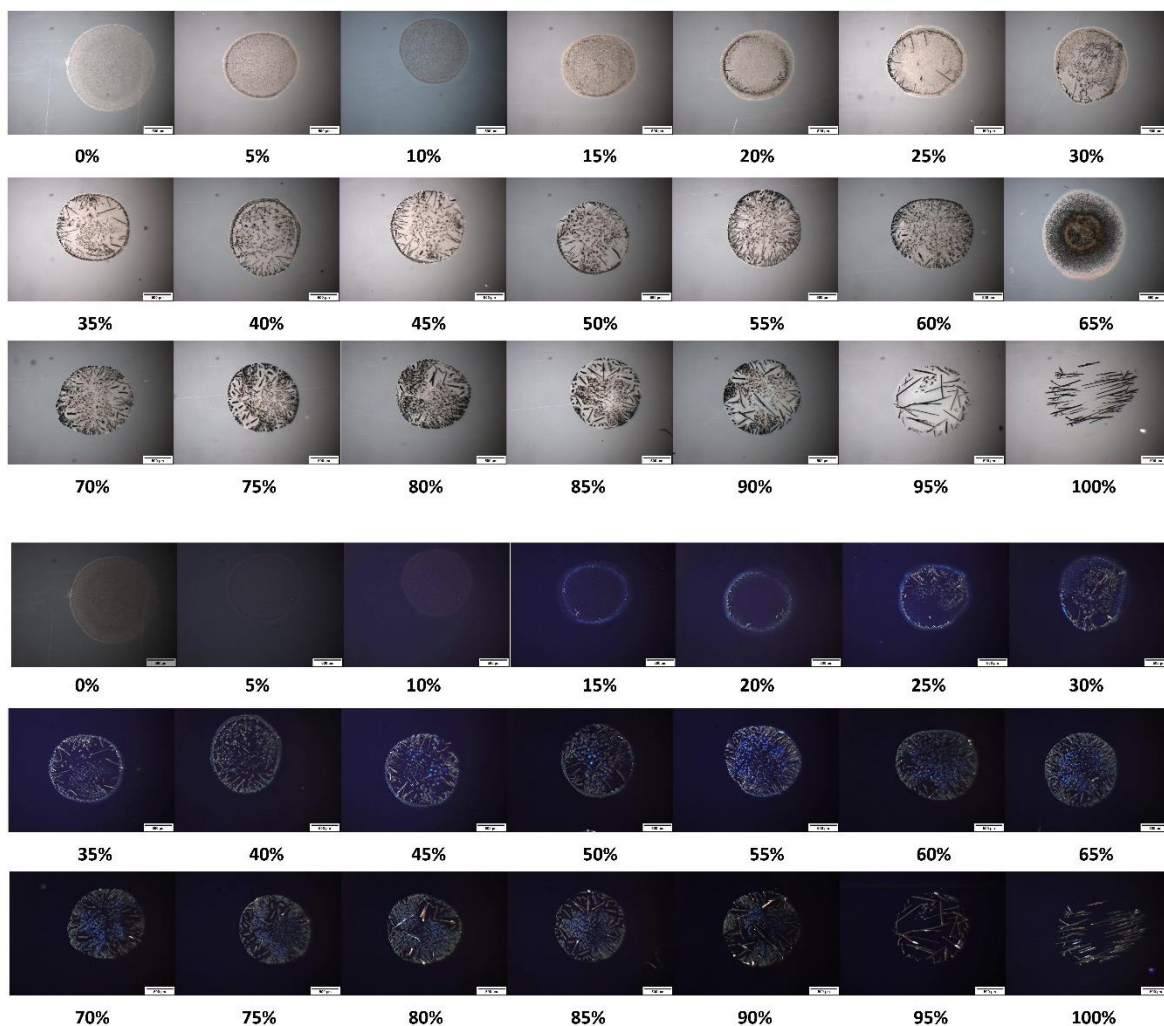


Figure S24. Microarray of Nitrofurantoin/Soluplus depicted by PLM. All the spots are reported with the bright field in the upper part of the figure and cross-polarised filters in the lower part of the figure. The images show all different ratios of Nitrofurantoin/Soluplus starting from 0% to 100% with a 5% API increment. The final mass of individual spots is 1000-1100 ng. The scale bar represents 500µm.

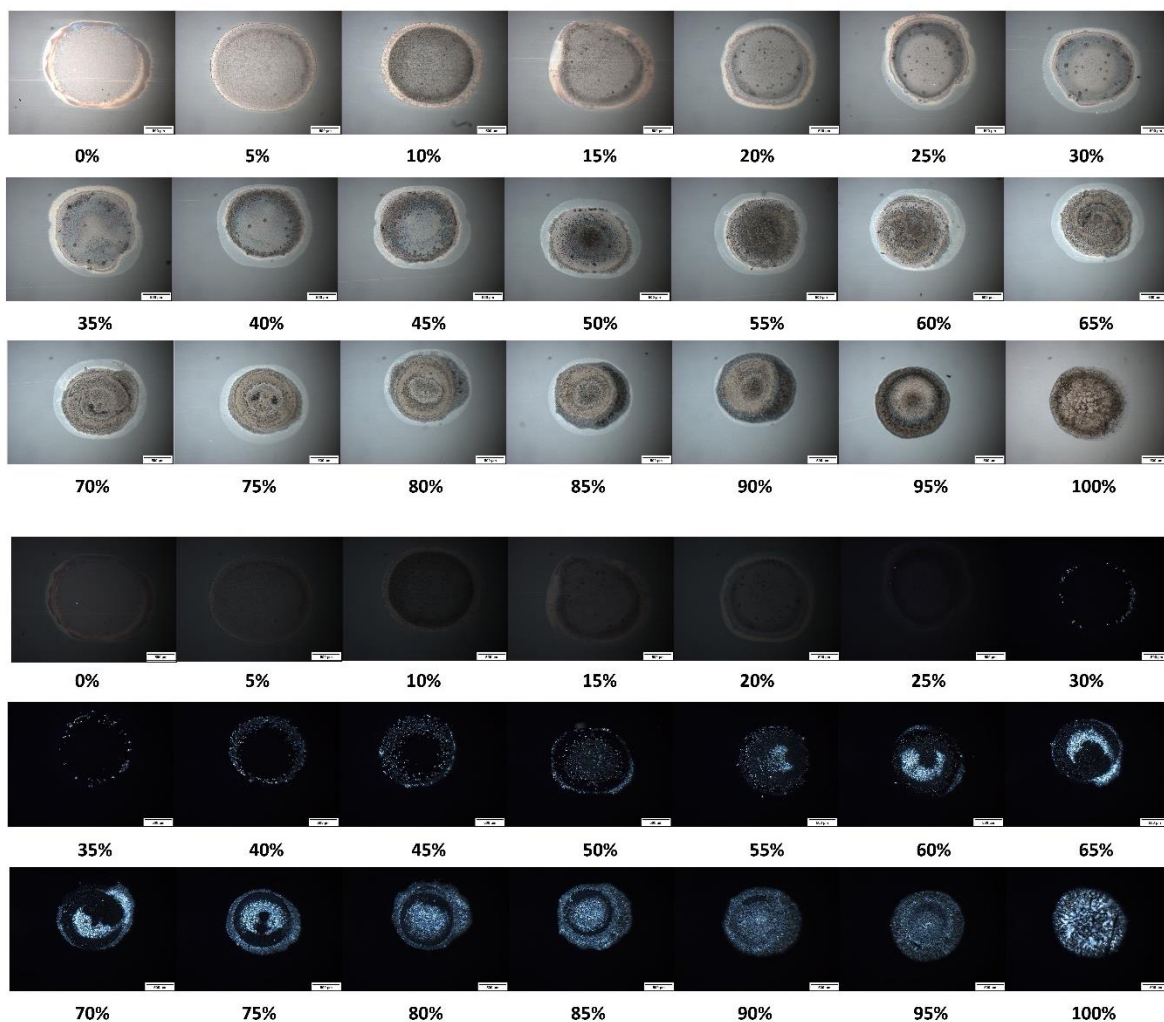


Figure S25. Microarray of Diclofenac sodium./Soluplus depicted by PLM. All the spots are reported with the bright field in the upper part of the figure and cross-polarised filters in the lower part of the figure. The images show all different ratios of Diclofenac sodium/Soluplus starting from 0% to 100% with a 5% API increment. The final mass of individual spots is 1000-1100 ng. The scale bar represents 500µm.

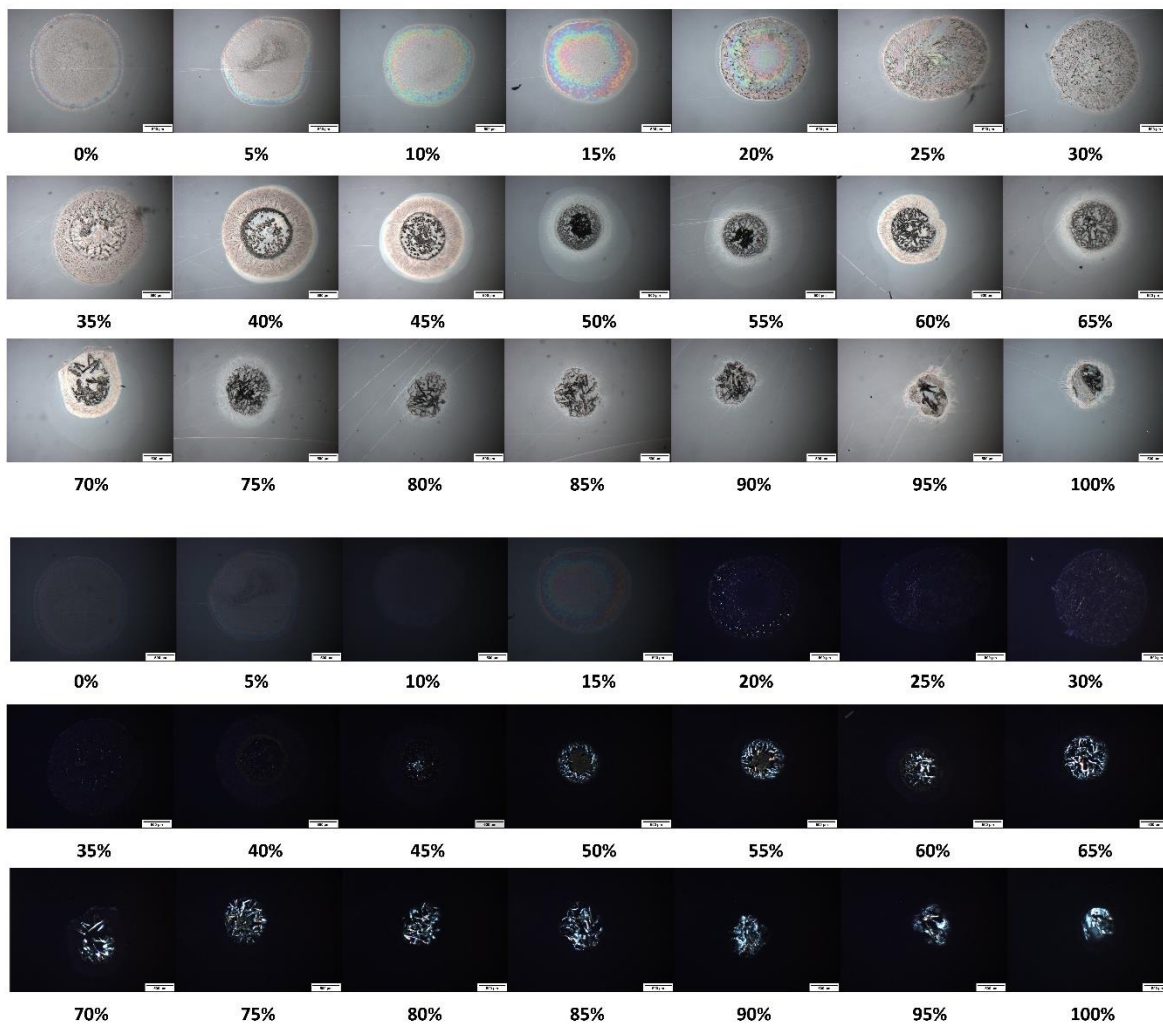


Figure S26. Microarray of Atenolol/Soluplus depicted by PLM. All the spots are reported with the bright field in the upper part of the figure and cross-polarised filters in the lower part of the figure. The images show all different ratios of Atenolol/Soluplus starting from 0% to 100% with a 5% API increment. The final mass of individual spots is 1000-1100 ng. The scale bar represents 500 μ m.

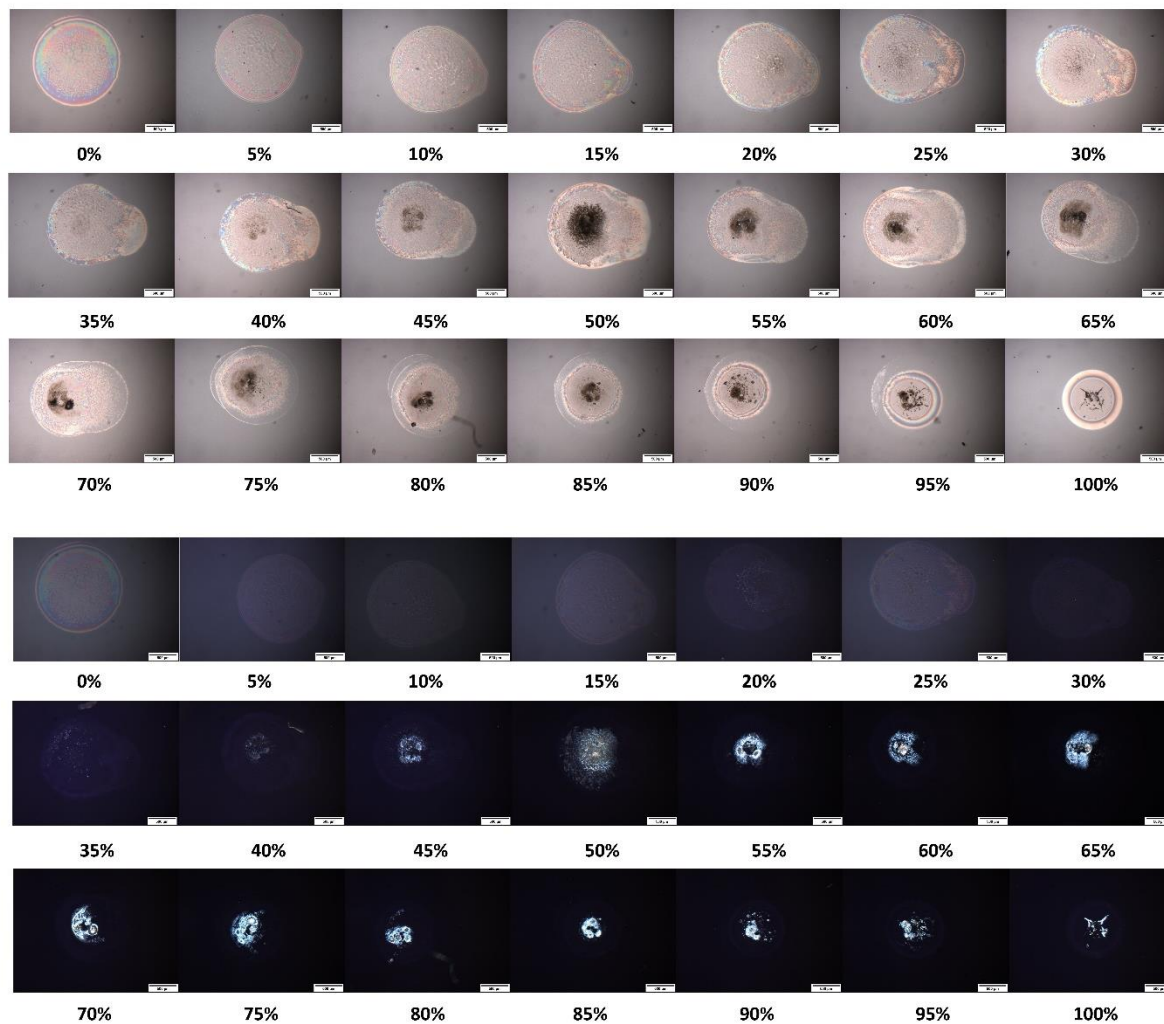


Figure S27. Microarray of Itraconazole/Soluplus depicted by PLM. All the spots are reported with the bright field in the upper part of the figure and cross-polarised filters in the lower part of the figure. The images show all different ratios of Itraconazole/Soluplus starting from 0% to 100% with a 5% API increment. The final mass of individual spots is 1000-1100 ng. The scale bar represents 500 μ m.

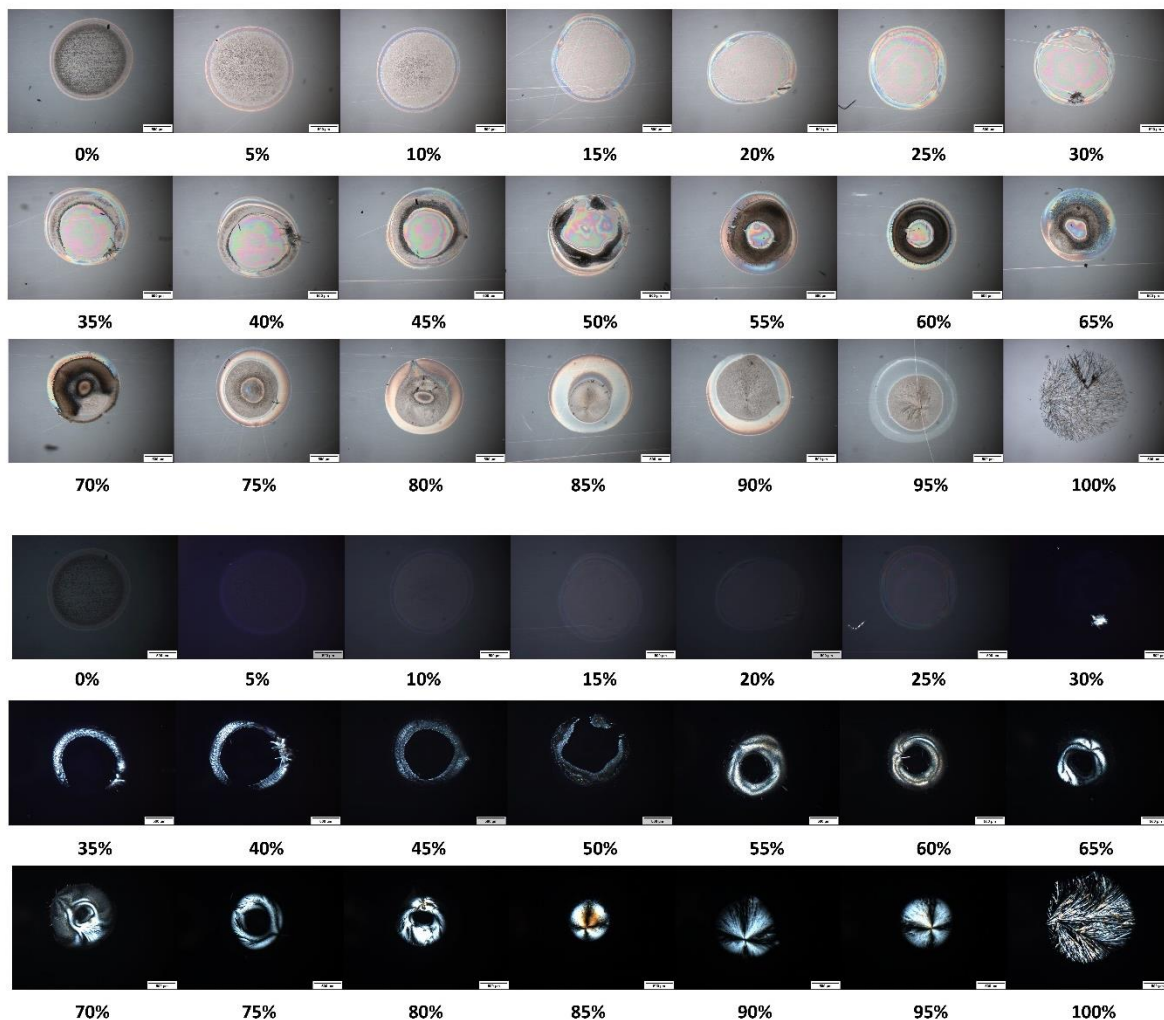


Figure S28. Microarray of Nicotinamide/Soluplus depicted by PLM. All the spots are reported with the bright field in the upper part of the figure and cross-polarised filters in the lower part of the figure. The images show all different ratios of Nicotinamide/Soluplus starting from 0% to 100% with a 5% API increment. The final mass of individual spots is 1000-1100 ng. The scale bar represents 500 μ m.

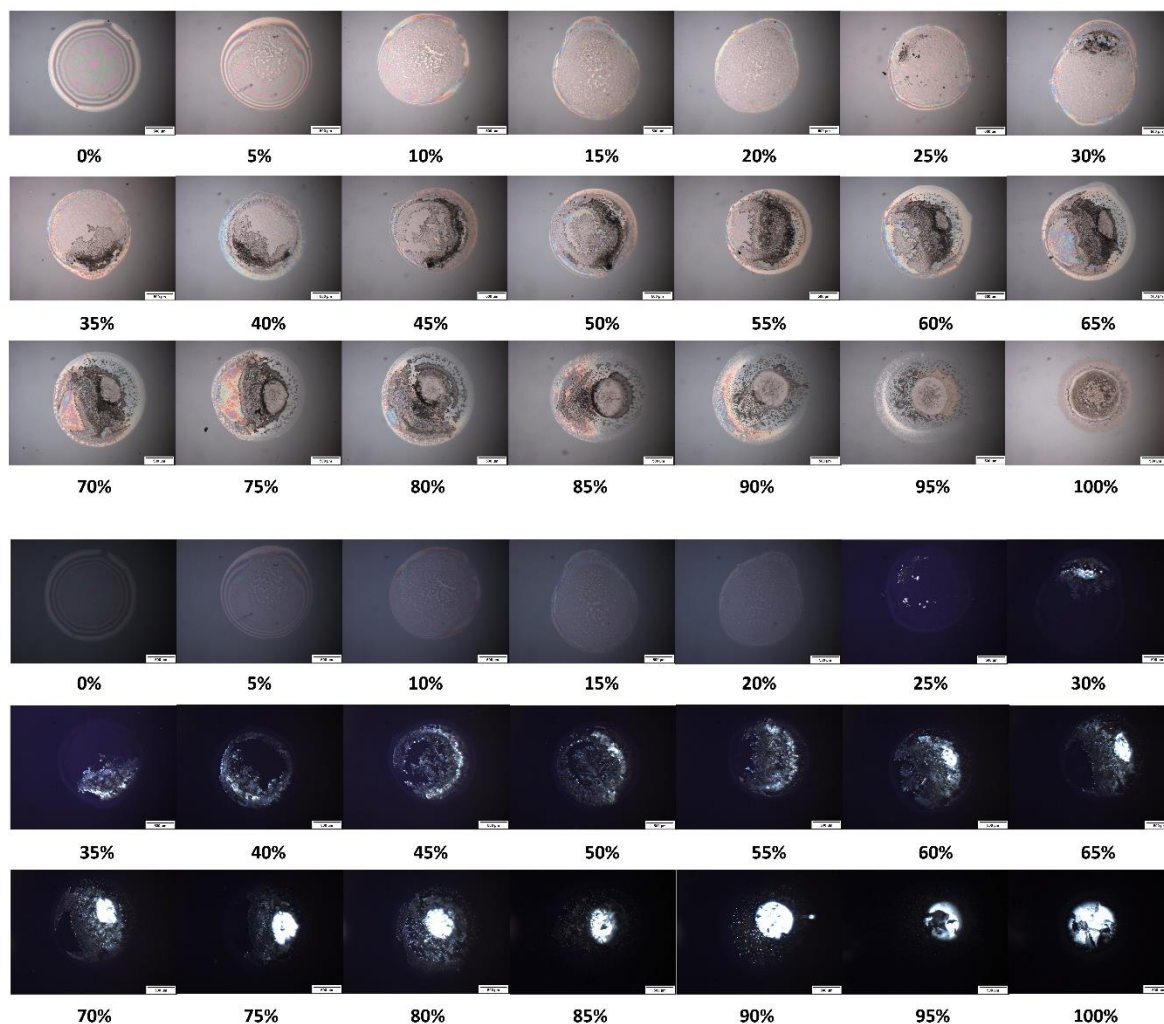


Figure S29. Microarray of Estradiol/Soluplus depicted by PLM. All the spots are reported with the bright field in the upper part of the figure and cross-polarised filters in the lower part of the figure. The images show all different ratios of Estradiol/Soluplus starting from 0% to 100% with a 5% API increment. The final mass of individual spots is 1000-1100 ng. The scale bar represents 500µm.

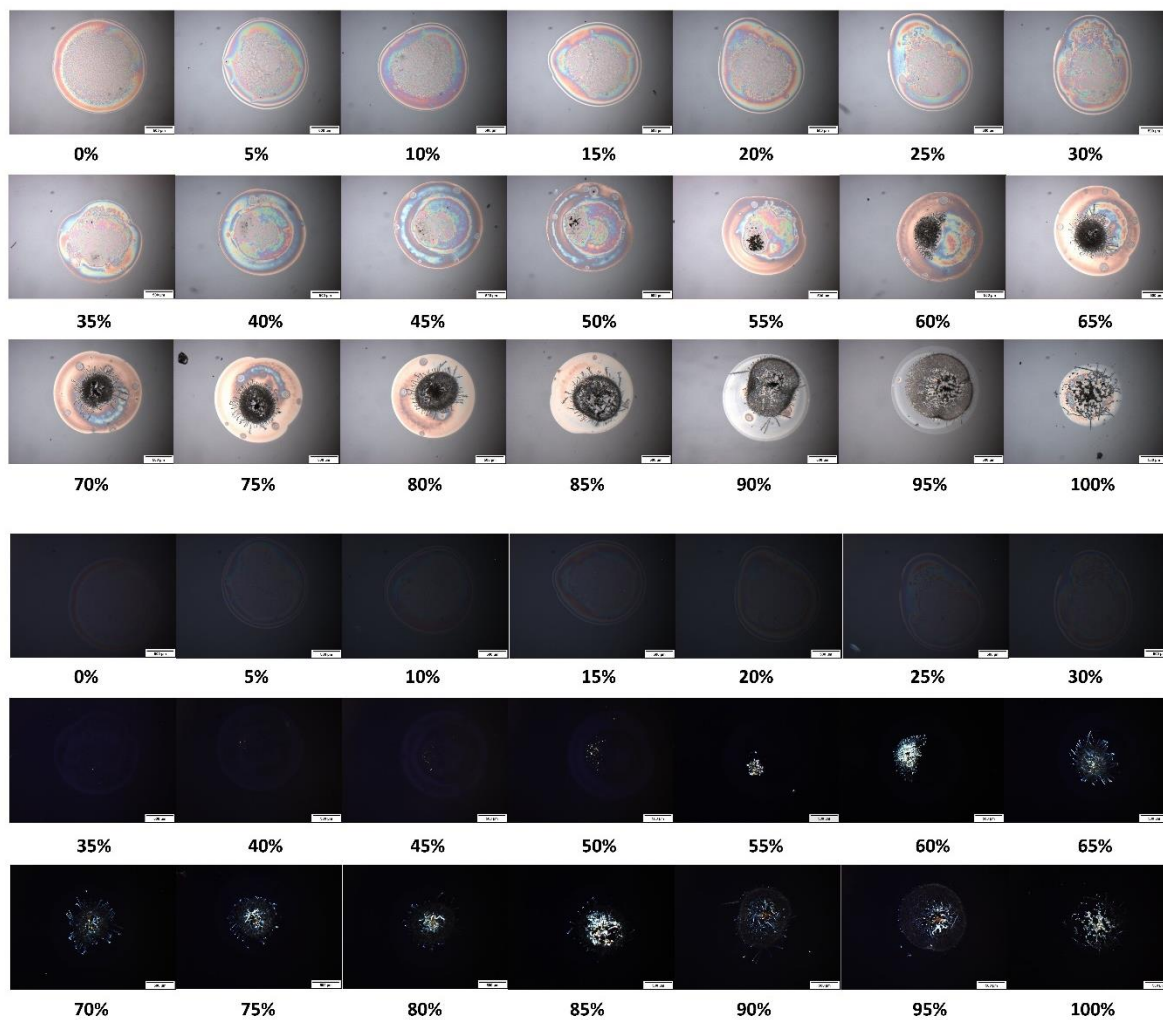


Figure S30. Microarray of Nifedipine/Soluplus depicted by PLM. All the spots are reported with the bright field in the upper part of the figure and cross-polarised filters in the lower part of the figure. The images show all different ratios of Nifedipine/Soluplus starting from 0% to 100% with a 5% API increment. The final mass of individual spots is 1000-1100 ng. The scale bar represents 500 μ m.

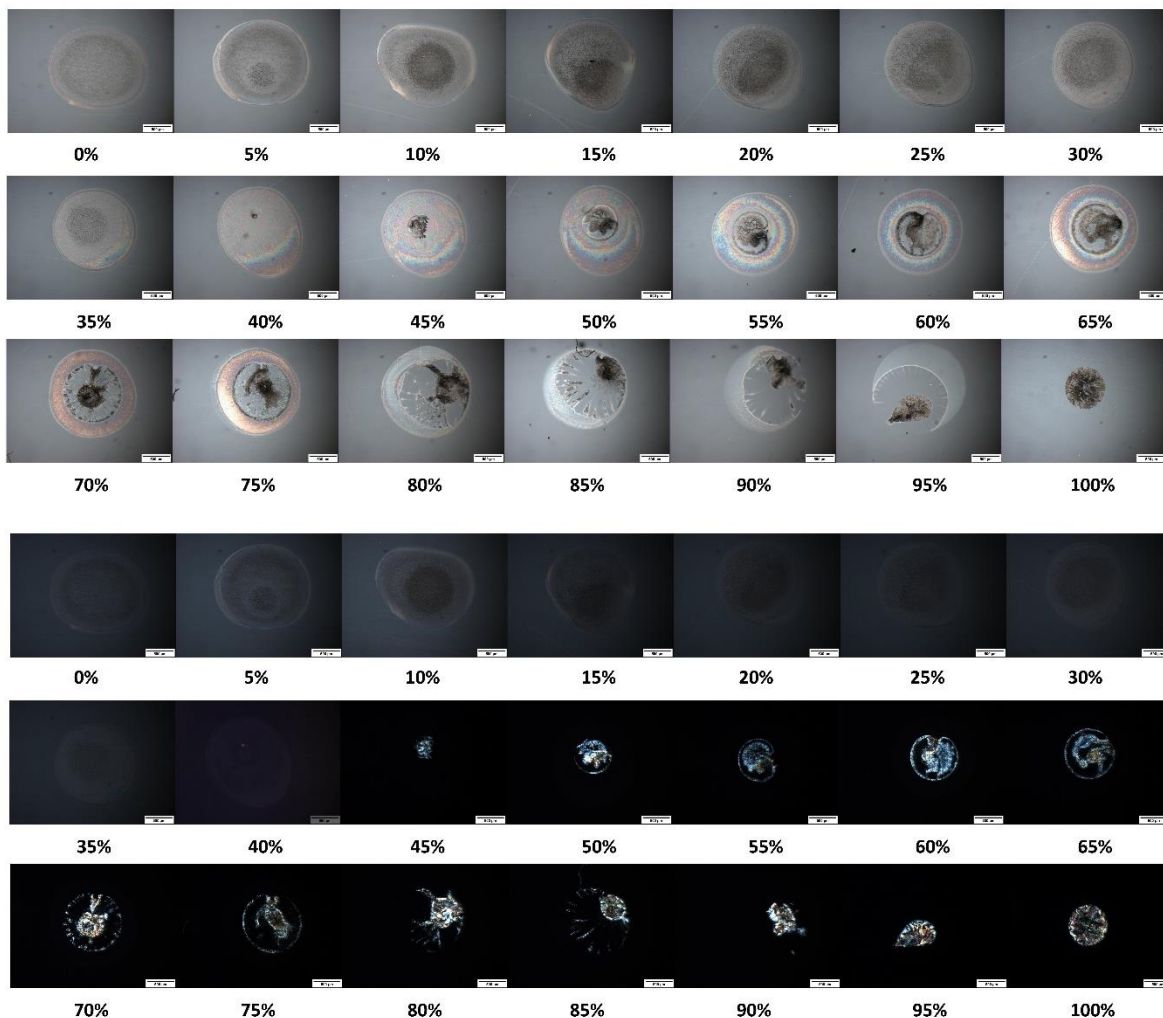


Figure S31. Microarray of Flufenamic acid/Soluplus depicted by PLM. All the spots are reported with the bright field in the upper part of the figure and cross-polarised filters in the lower part of the figure. The images show all different ratios of Flufenamic acid/Soluplus starting from 0% to 100% with a 5% API increment. The final mass of individual spots is 1000-1100 ng. The scale bar represents 500 μ m.

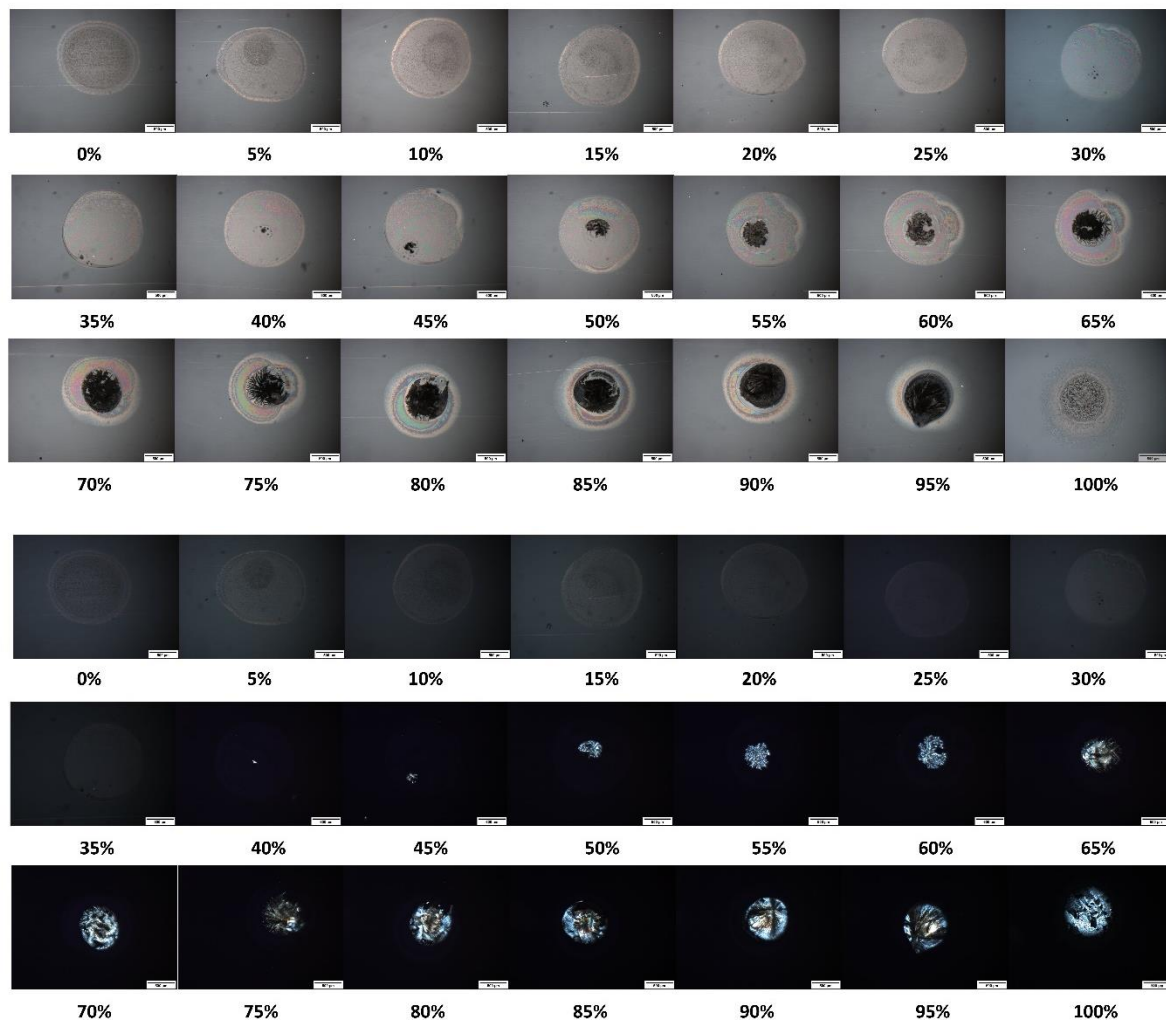


Figure S32. Microarray of Flurbiprofen/Soluplus depicted by PLM. All the spots are reported with the bright field in the upper part of the figure and cross-polarised filters in the lower part of the figure. The images show all different ratios of Flurbiprofen/Soluplus starting from 0% to 100% with a 5% API increment. The final mass of individual spots is 1000-1100 ng. The scale bar represents 500 μ m.

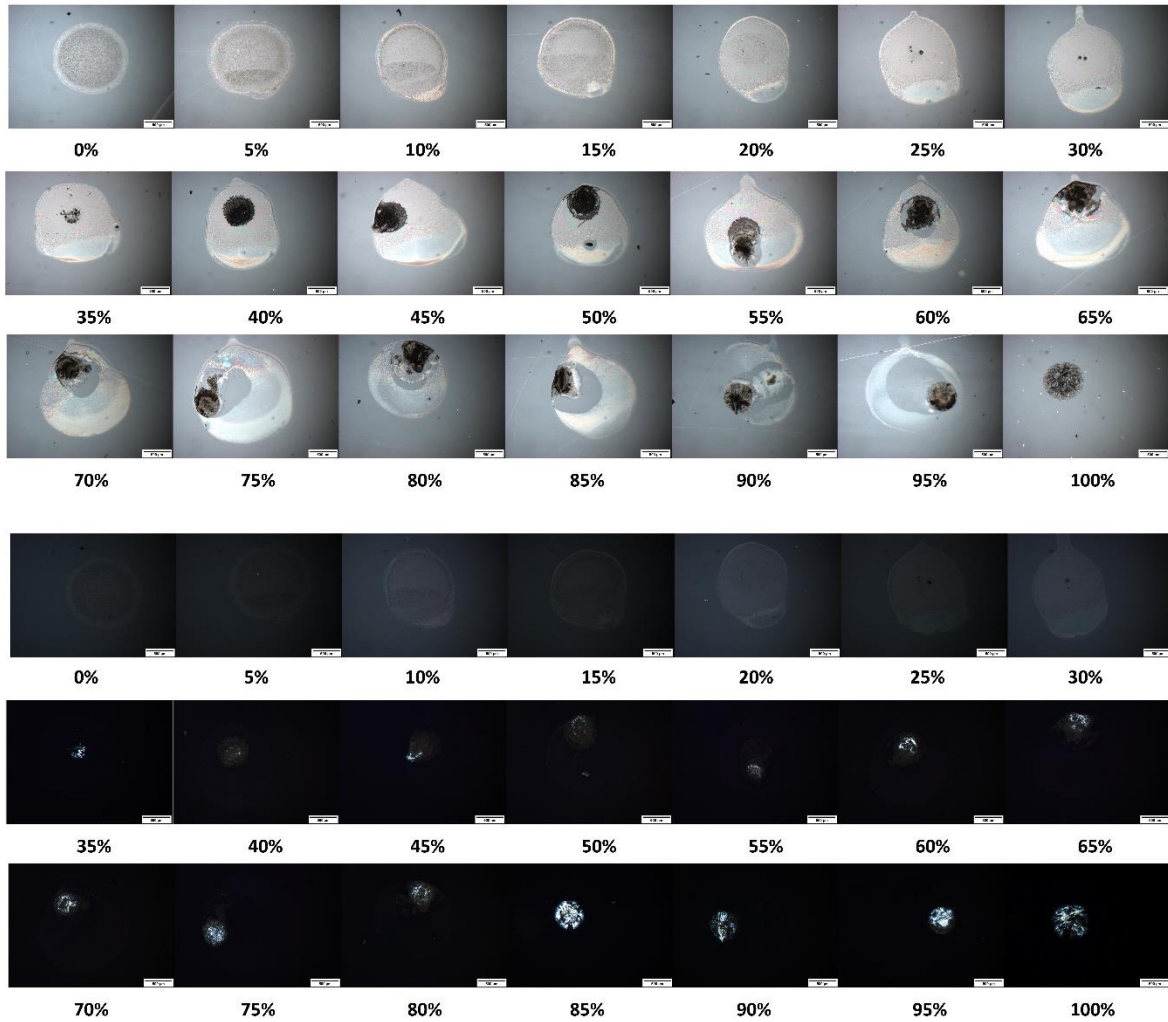


Figure S33. Microarray of Tolbutamide/Soluplus depicted by PLM. All the spots are reported with the bright field in the upper part of the figure and cross-polarised filters in the lower part of the figure. The images show all different ratios of Tolbutamide/Soluplus starting from 0% to 100% with a 5% API increment. The final mass of individual spots is 1000-1100 ng. The scale bar represents 500µm.

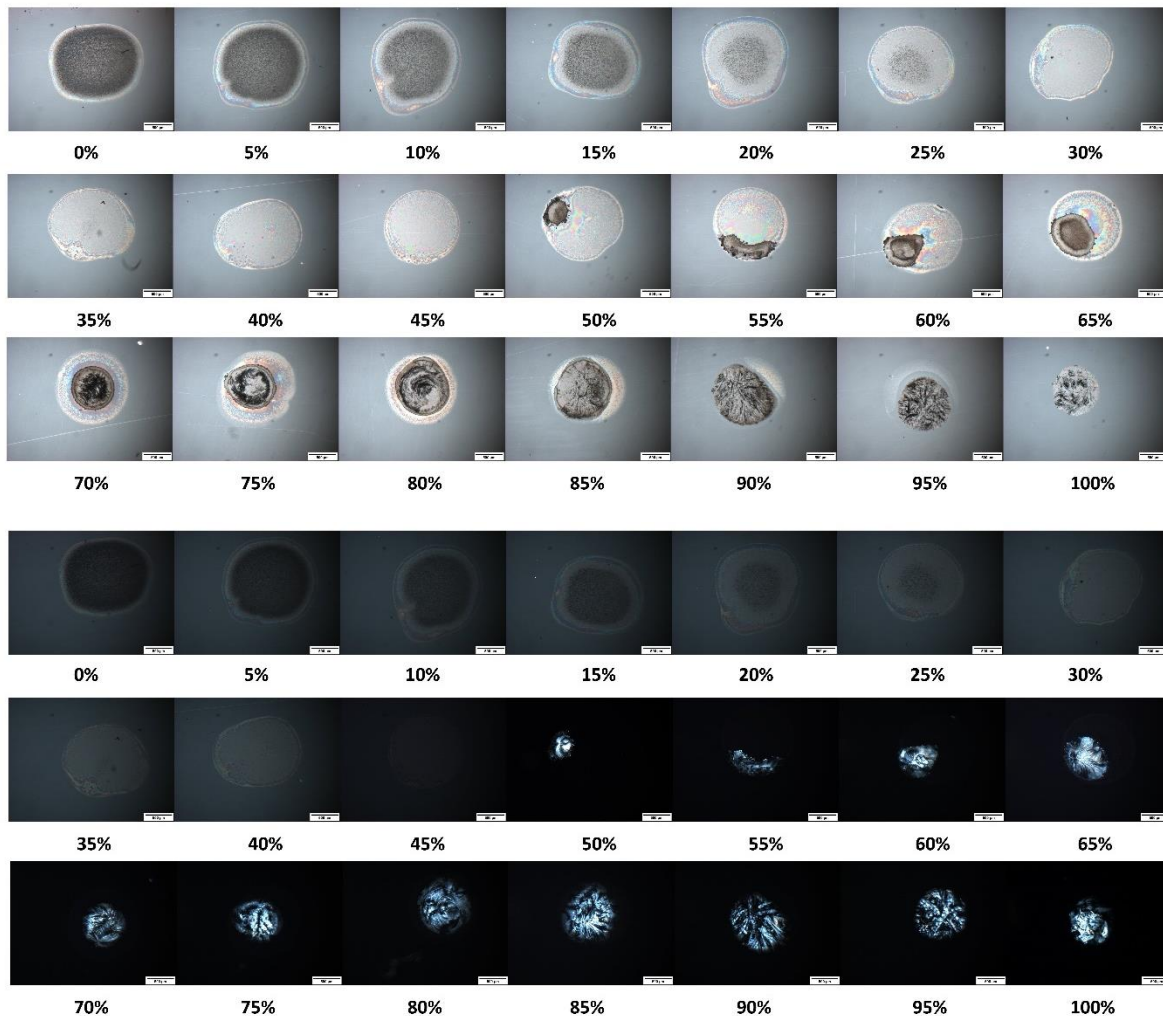


Figure S34. Microarray of Aspirin/Soluplus depicted by PLM. All the spots are reported with the bright field in the upper part of the figure and cross-polarised filters in the lower part of the figure. The images show all different ratios of Aspirin/Soluplus starting from 0% to 100% with a 5% API increment. The final mass of individual spots is 1000-1100 ng. The scale bar represents 500 μ m.

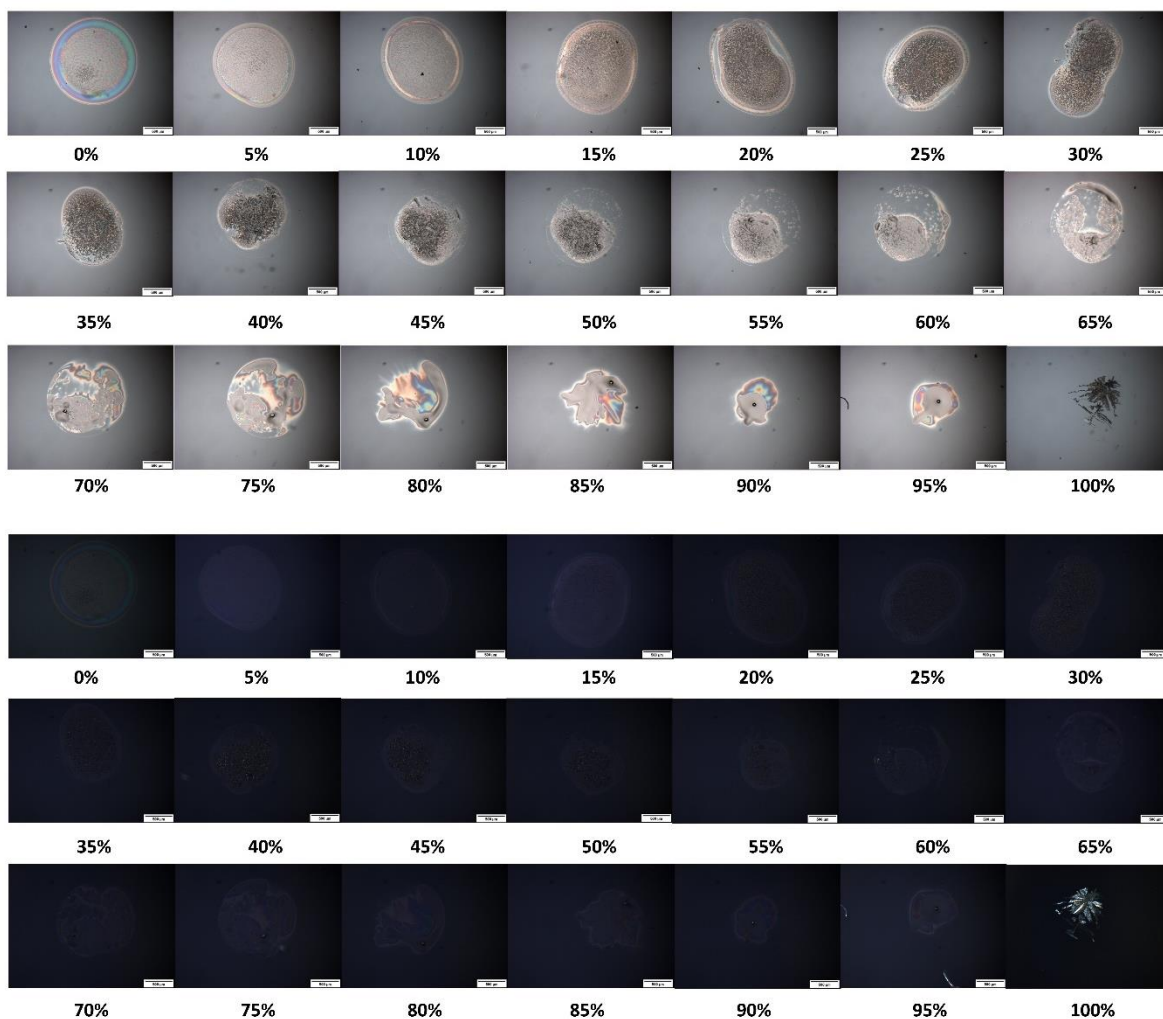


Figure S35. Microarray of Probutcol/Soluplus depicted by PLM. All the spots are reported with the bright field in the upper part of the figure and cross-polarised filters in the lower part of the figure. The images show all different ratios of Probutcol/Soluplus starting from 0% to 100% with a 5% API increment. The final mass of individual spots is 1000-1100 ng. The scale bar represents 500 μ m.

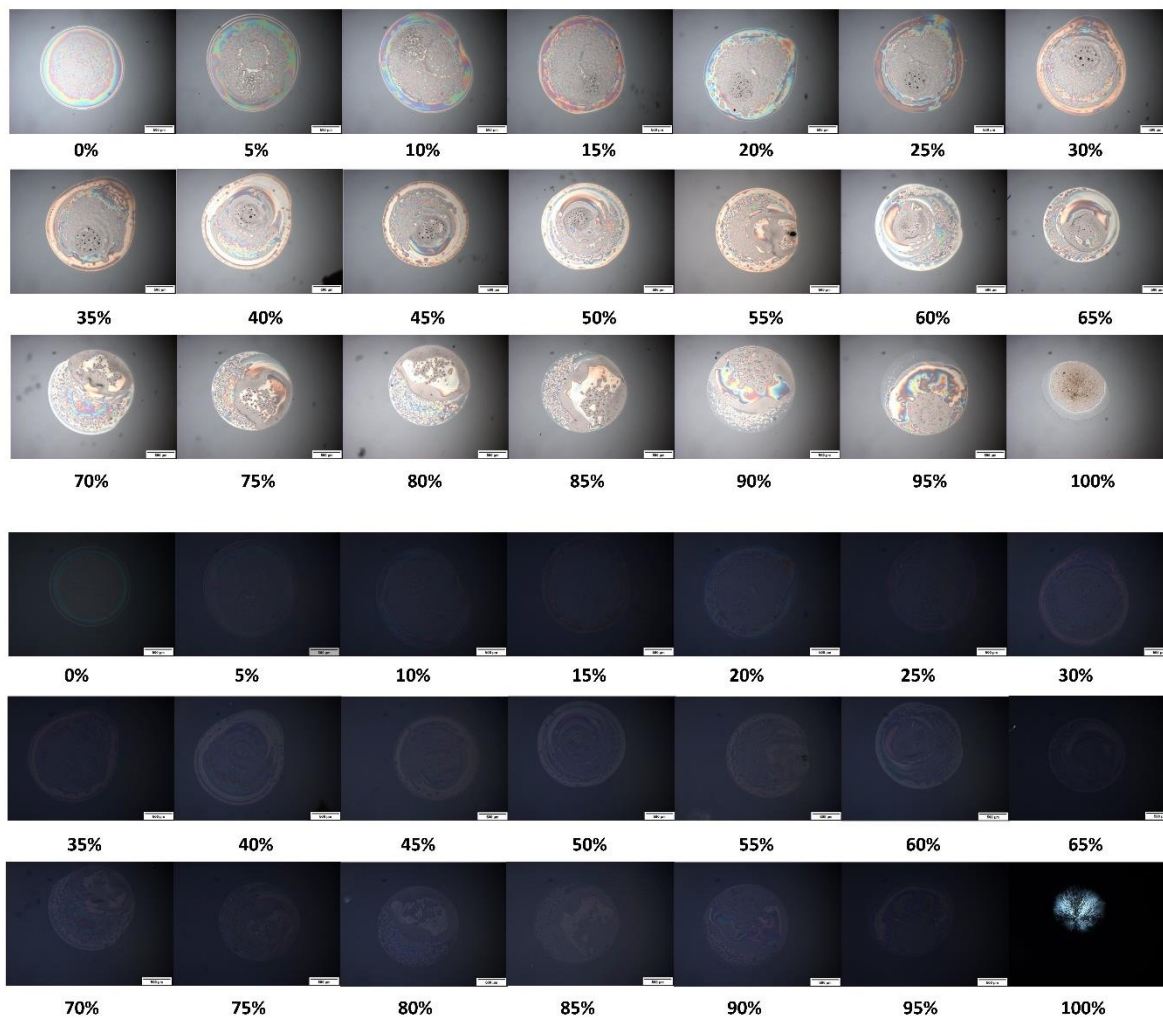


Figure S36. Microarray of Celecoxib/Soluplus depicted by PLM. All the spots are reported with the bright field in the upper part of the figure and cross-polarised filters in the lower part of the figure. The images show all different ratios of Celecoxib/Soluplus starting from 0% to 100% with a 5% API increment. The final mass of individual spots is 1000-1100 ng. The scale bar represents 500 μ m.

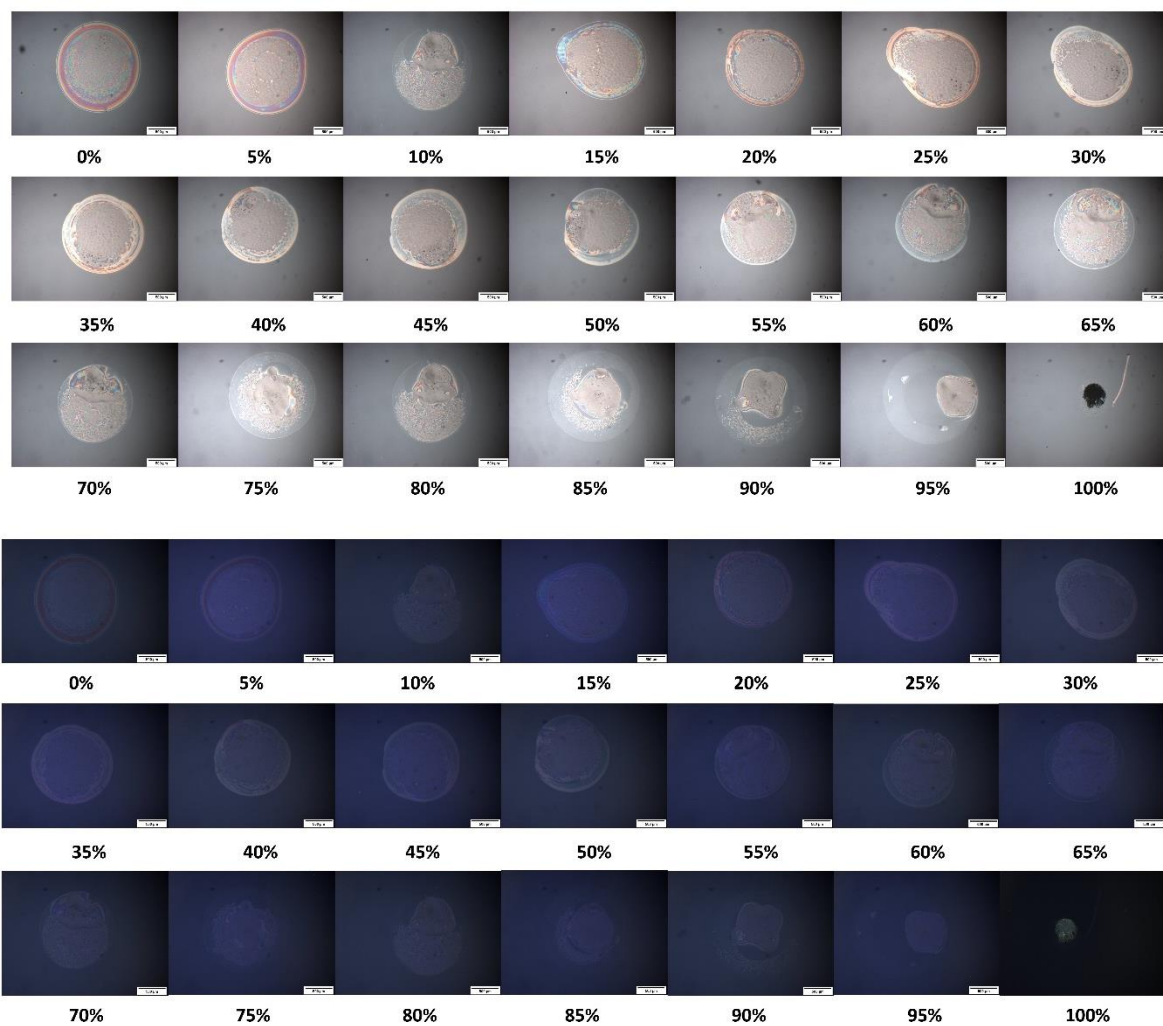


Figure S37. Microarray of Felodipine/Soluplus depicted by PLM. All the spots are reported with the bright field in the upper part of the figure and cross-polarised filters in the lower part of the figure. The images show all different ratios of Felodipine/Soluplus starting from 0% to 100% with a 5% API increment. The final mass of individual spots is 1000-1100 ng. The scale bar represents 500 μ m.

Stability data of printed microarrays of APIs within the HPMCAS matrix

Microarrays of APIs/HPMCAS depicted by PLM at 6 months of storage in accelerated conditions

APIs/HPMCAS blends

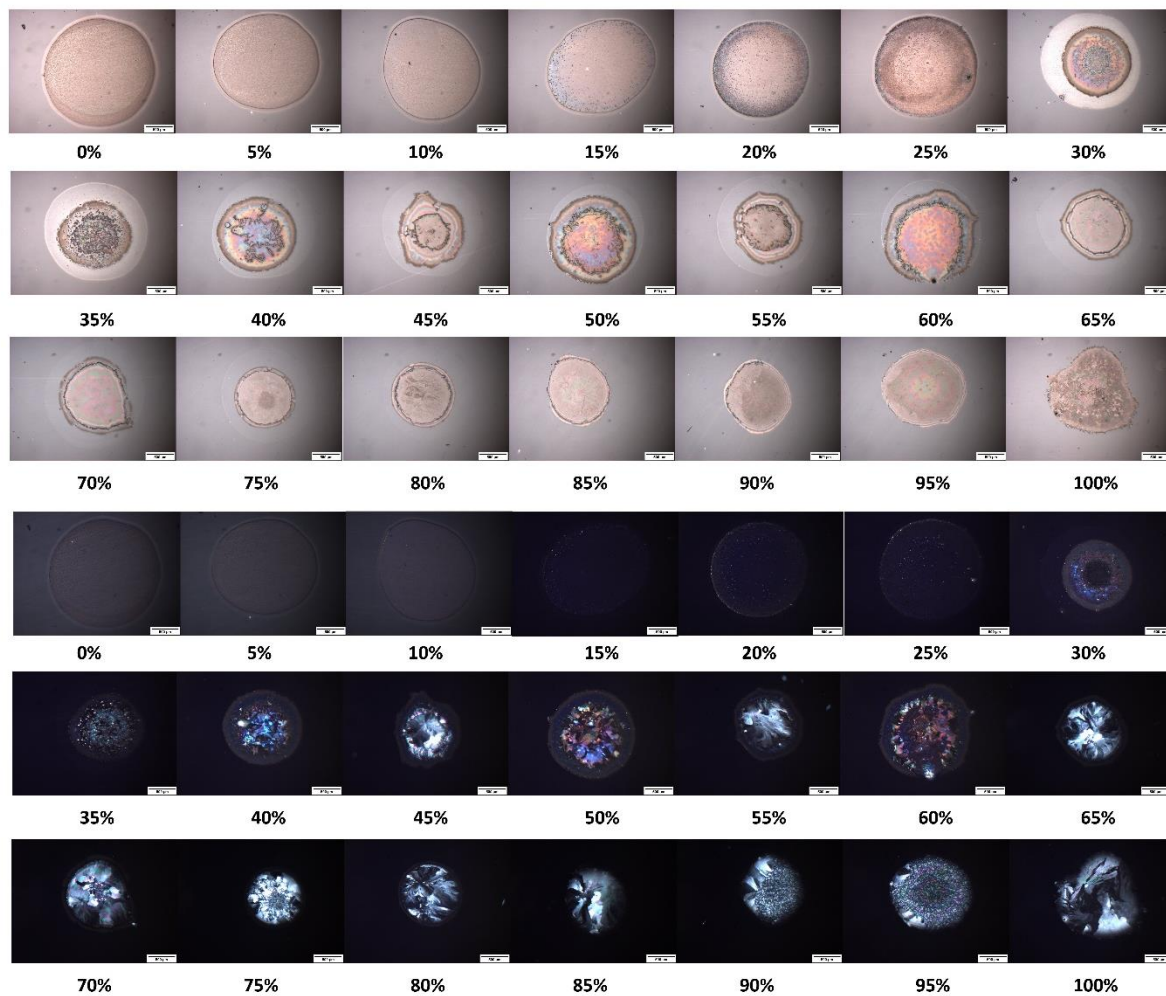


Figure S38. Microarray of Estradiol/HPMCAS depicted by PLM. All the spots are reported with the bright field in the upper part of the figure and cross-polarised filters in the lower part of the figure. The images show all different ratios of Estradiol/HPMCAS starting from 0% to 100% with a 5% API increment. The final mass of individual spots is 1000-1100 ng. The scale bar represents 500 μ m.

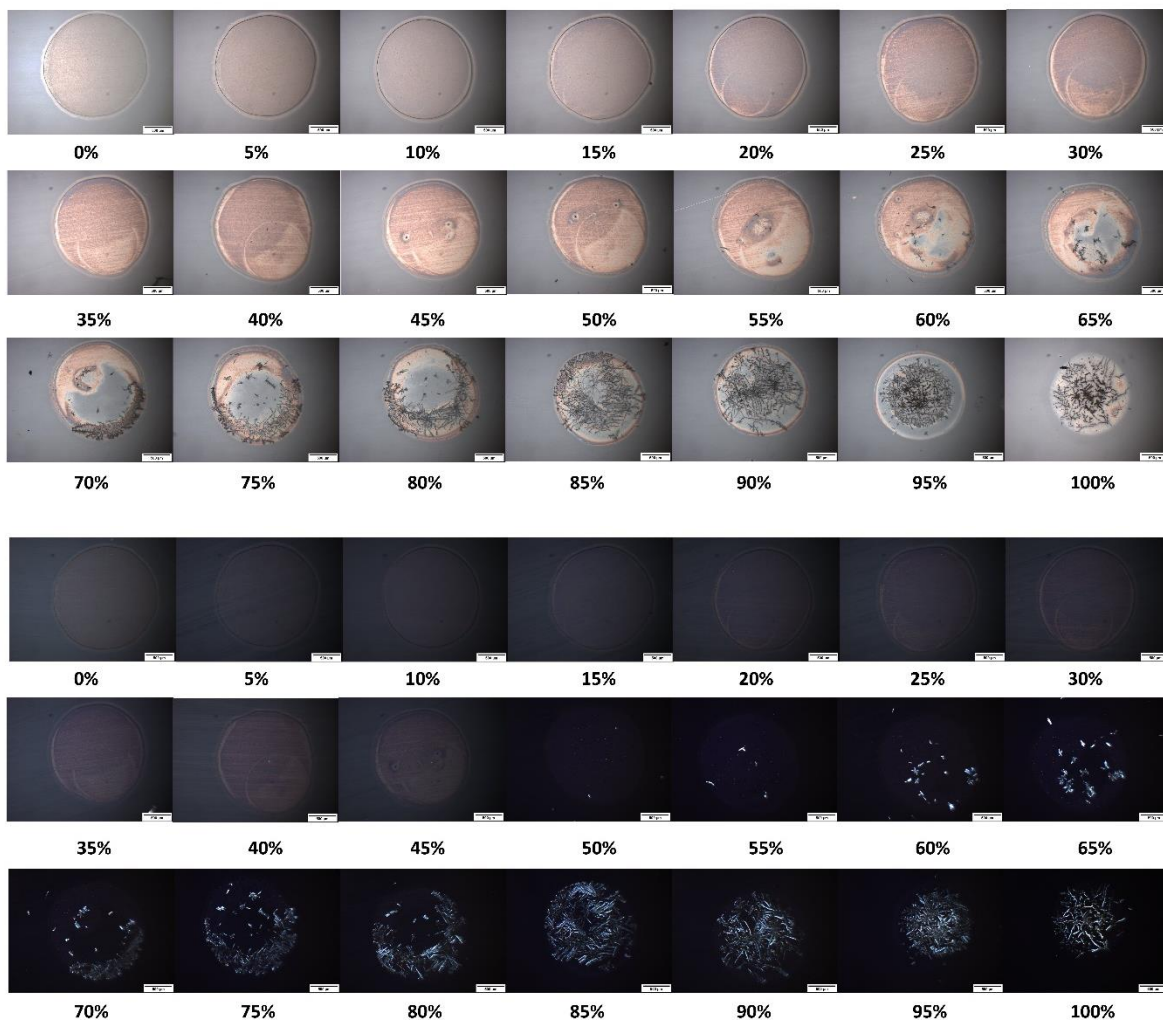


Figure S39. Microarray of Nifedipine/HPMCAS depicted by PLM. All the spots are reported with the bright field in the upper part of the figure and cross-polarised filters in the lower part of the figure. The images show all different ratios of Nifedipine/HPMCAS starting from 0% to 100% with a 5% API increment. The final mass of individual spots is 1000-1100 ng. The scale bar represents 500 μ m.

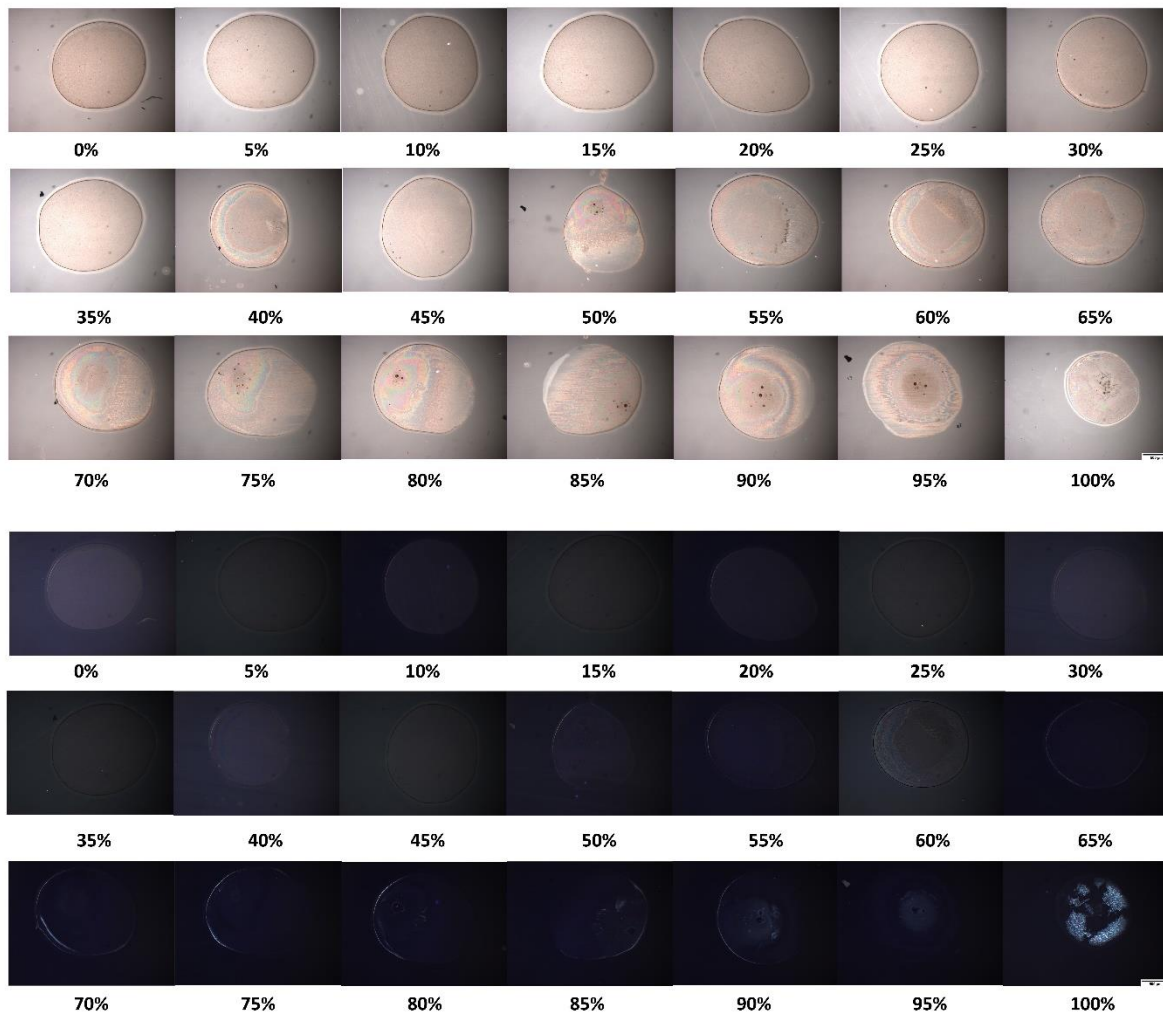


Figure S40. Microarray of Itraconazole/HPMCAS depicted by PLM. All the spots are reported with the bright field in the upper part of the figure and cross-polarised filters in the lower part of the figure. The images show all different ratios of Itraconazole/HPMCAS starting from 0% to 100% with a 5% API increment. The final mass of individual spots is 1000-1100 ng. The scale bar represents 500 μ m.

Comparison of predicted log stability, determined using the LOOCV method based on the multiple linear regression model, versus measured log stability from experimental microarray data across a range of drug loadings within the PVPVA polymeric matrix

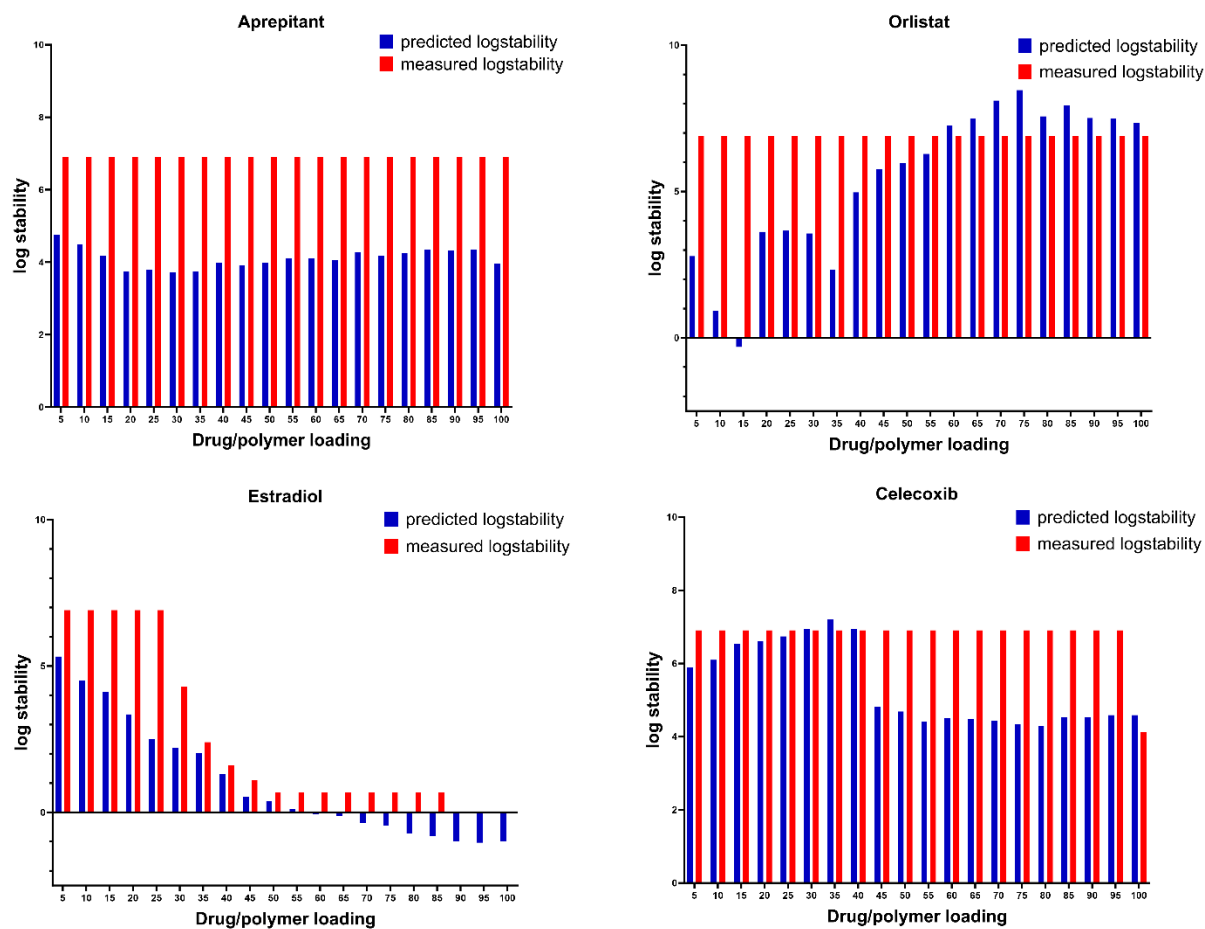


Figure S41. Comparison of predicted log stability, determined using the LOOCV method based on the multiple linear regression model, versus measured log stability from experimental microarray data for Aprepitant Orlistat, Estradiol, and Celecoxib across a range of drug loadings within the PVPVA polymeric matrix. The blue bars indicate the predicted stability, while the red bars show the measured stability, allowing for an evaluation of the predictive model's accuracy at different drug loadings.

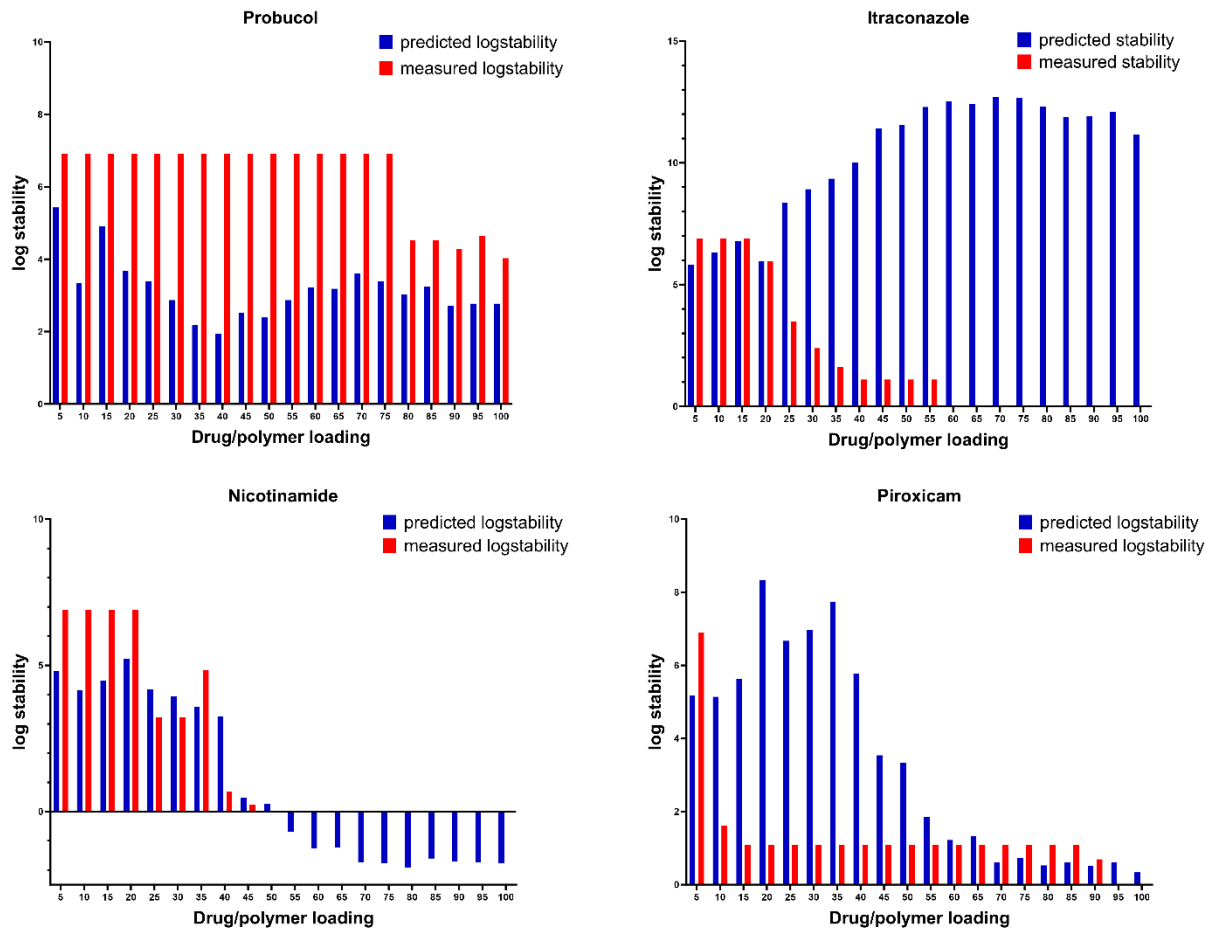


Figure S42. Comparison of predicted log stability, determined using the LOOCV method based on the multiple linear regression model, versus measured log stability from experimental microarray data for Probuco, Itraconazole, Nicotinamide, and Piroxicam across a range of drug loadings within the PVPVA polymeric matrix. The blue bars indicate the predicted stability, while the red bars show the measured stability, allowing for an evaluation of the predictive model's accuracy at different drug loadings.

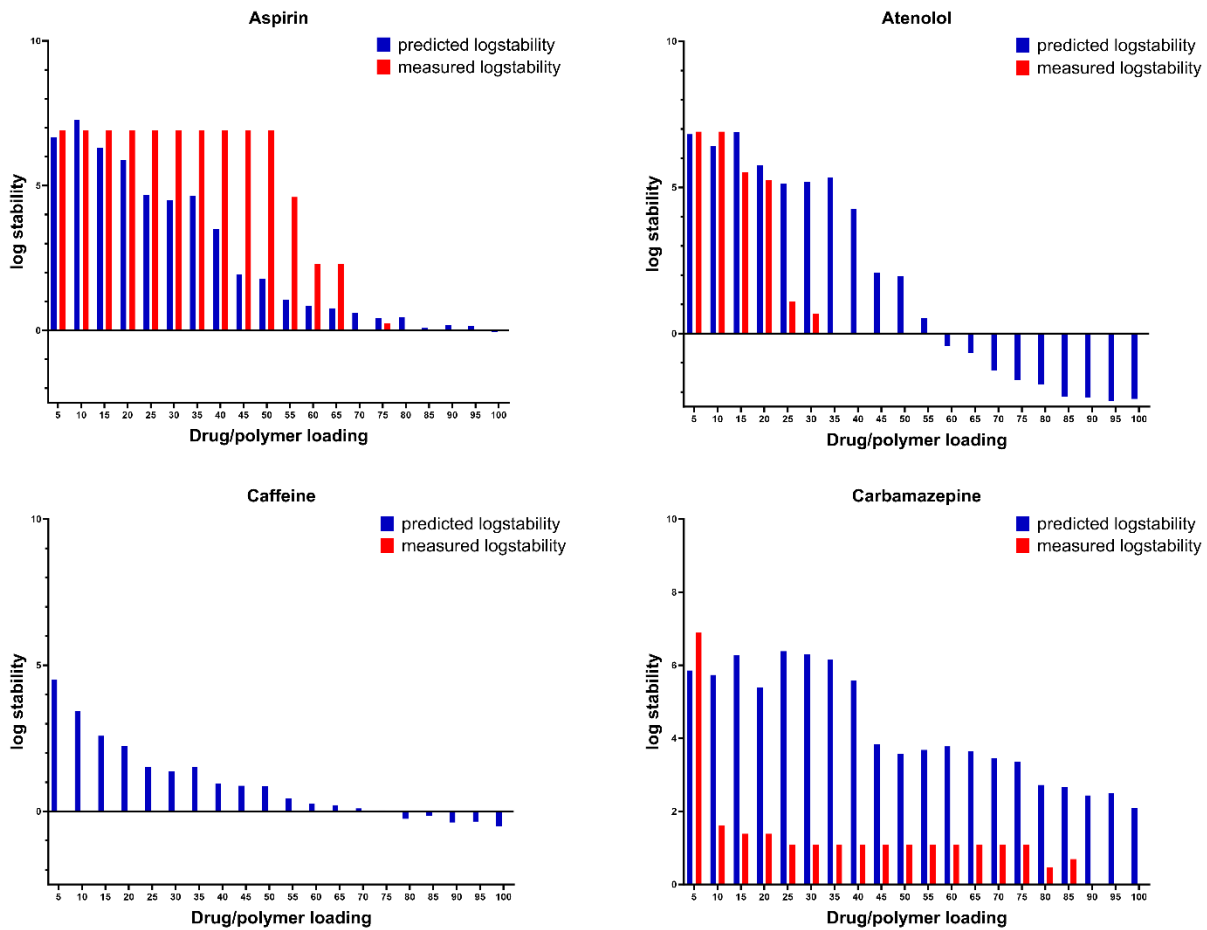


Figure S43. Comparison of predicted log stability, determined using the LOOCV method based on the multiple linear regression model, versus measured log stability from experimental microarray data for Aspirin, Atenolol, Caffeine, and Carbamazepine across a range of drug loadings within the PVPVA polymeric matrix. The blue bars indicate the predicted stability, while the red bars show the measured stability, allowing for an evaluation of the predictive model's accuracy at different drug loadings.

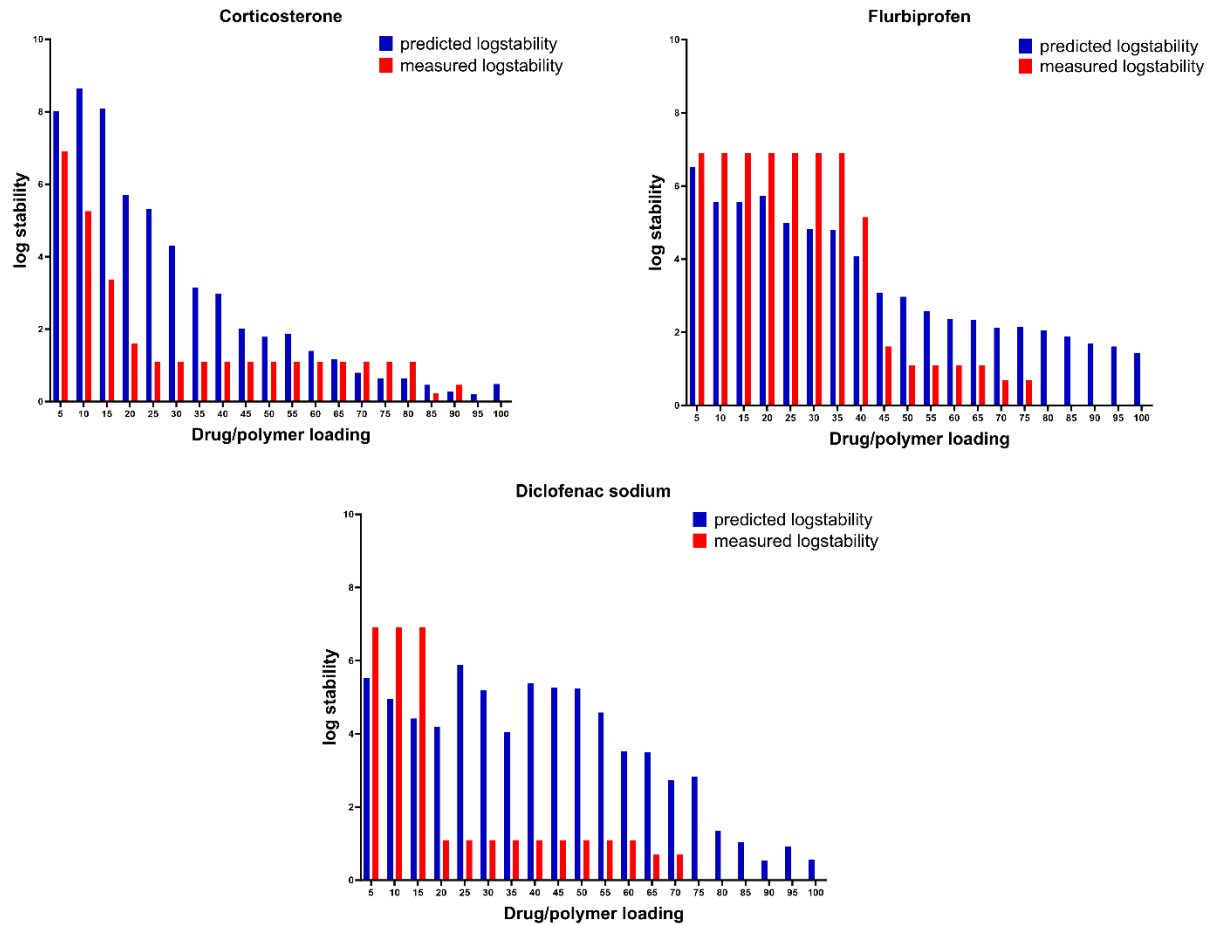


Figure S44. Comparison of predicted log stability, determined using the LOOCV method based on the multiple linear regression model, versus measured log stability from experimental microarray data for Corticosterone, Flurbiprofen and Diclofenac Sodium across a range of drug loadings within the PVPVA polymeric matrix. The blue bars indicate the predicted stability, while the red bars show the measured stability, allowing for an evaluation of the predictive model's accuracy at different drug loadings.

Comparison of predicted log stability, determined using the LOOCV method based on the multiple linear regression model, versus measured log stability from experimental microarray data across a range of drug loadings within the Soluplus polymeric matrix

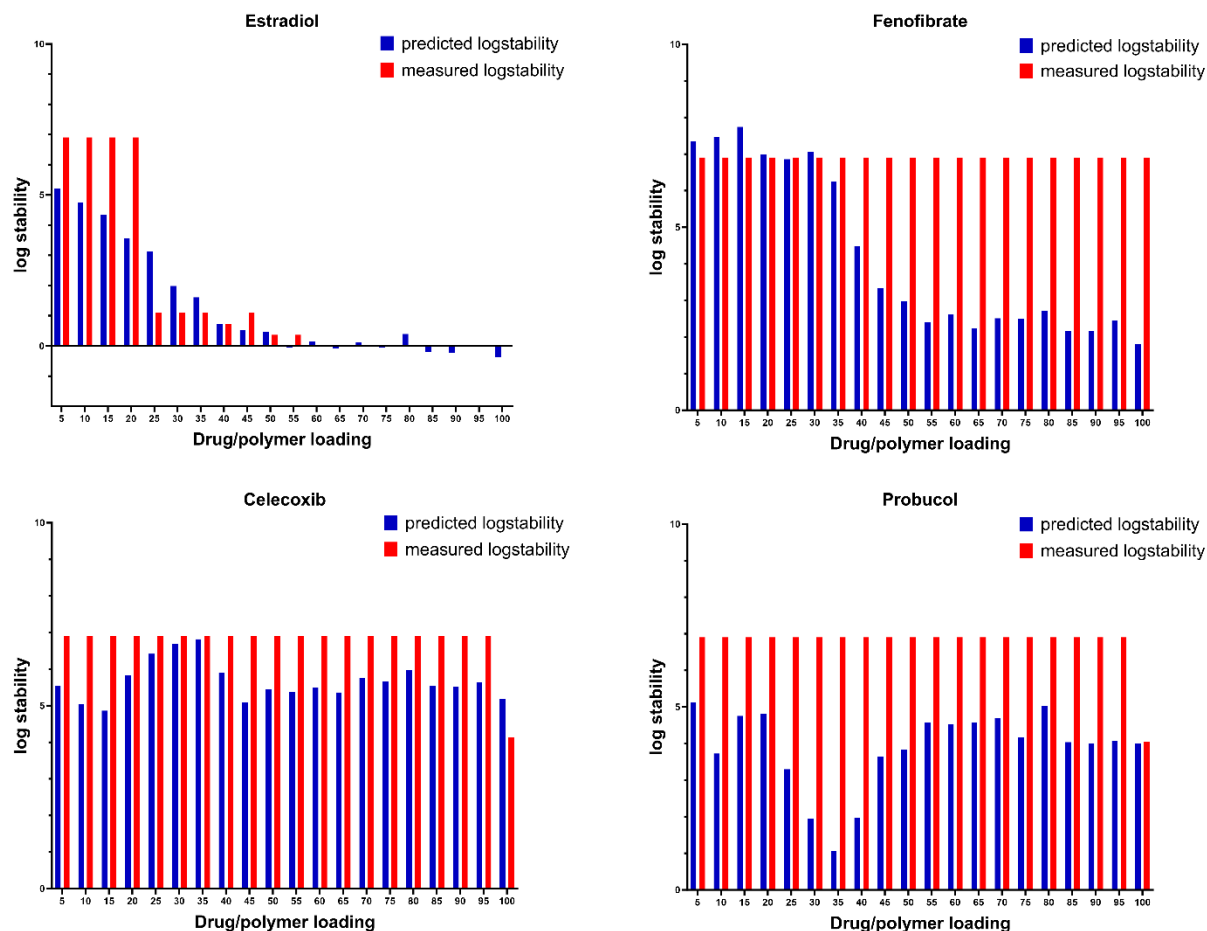


Figure S45. Comparison of predicted log stability, determined using the LOOCV method based on the multiple linear regression model, versus measured log stability from experimental microarray data for Estradiol, Fenofibrate, Celecoxib, and Probuocol across a range of drug loadings within the Soluplus polymeric matrix. The blue bars indicate the predicted stability, while the red bars show the measured stability, allowing for an evaluation of the predictive model's accuracy at different drug loadings.

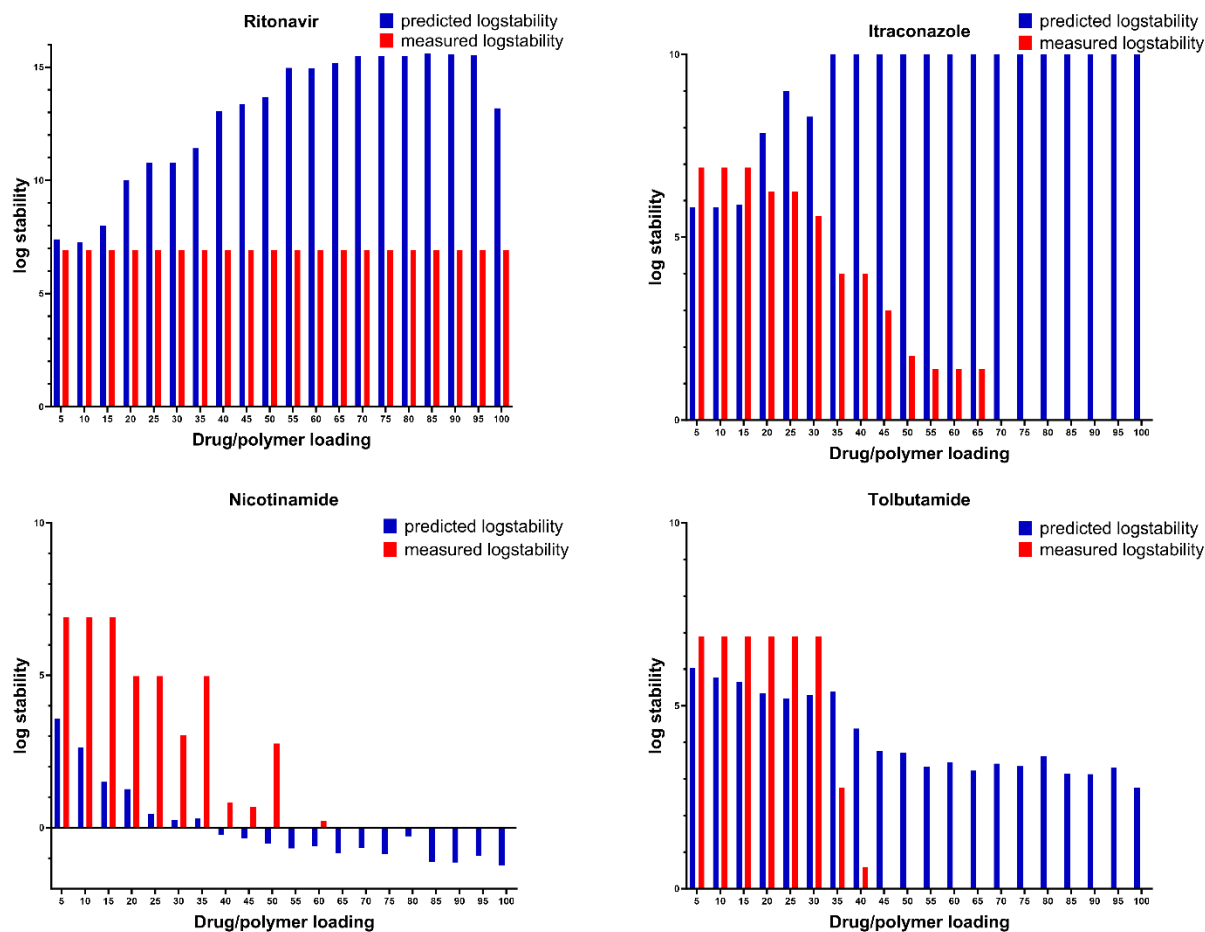


Figure S46. Comparison of predicted log stability, determined using the LOOCV method based on the multiple linear regression model, versus measured log stability from experimental microarray data for Ritonavir, Itraconazole, Nicotinamide, and Tolbutamide across a range of drug loadings within the Soluplus polymeric matrix. The blue bars indicate the predicted stability, while the red bars show the measured stability, allowing for an evaluation of the predictive model's accuracy at different drug loadings.

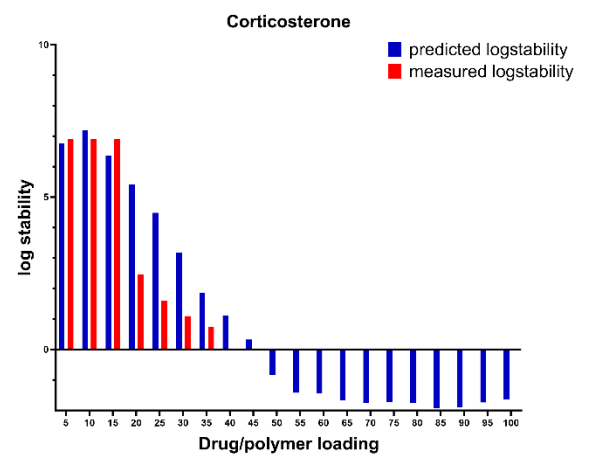
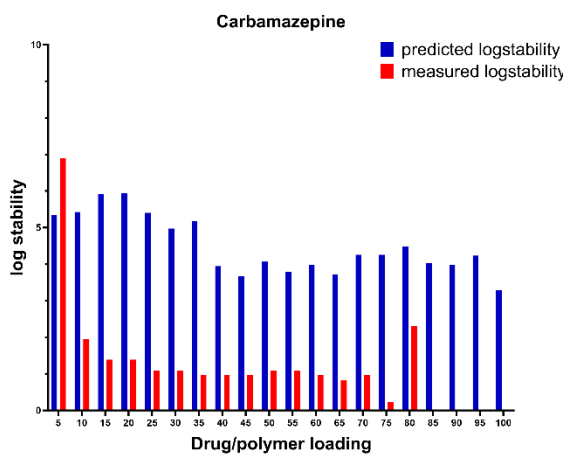
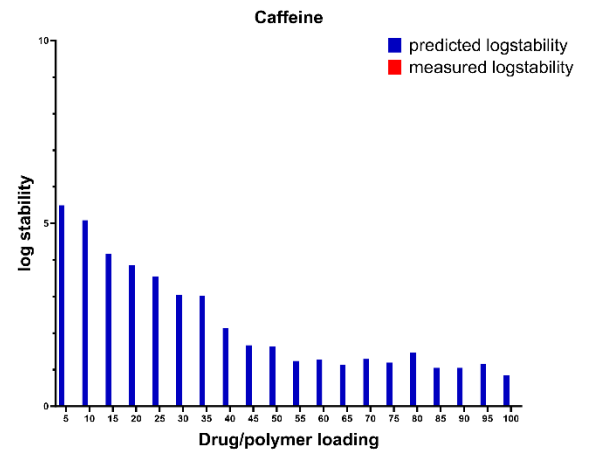
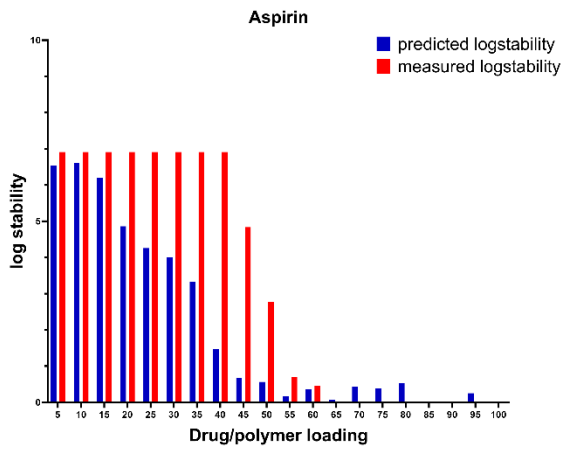


Figure S47. Comparison of predicted log stability, determined using the LOOCV method based on the multiple linear regression model, versus measured log stability from experimental microarray data for Aspirin, Caffeine, Carbamazepine, and Corticosterone across a range of drug loadings within the Soluplus polymeric matrix. The blue bars indicate the predicted stability, while the red bars show the measured stability, allowing for an evaluation of the predictive model's accuracy at different drug loadings.

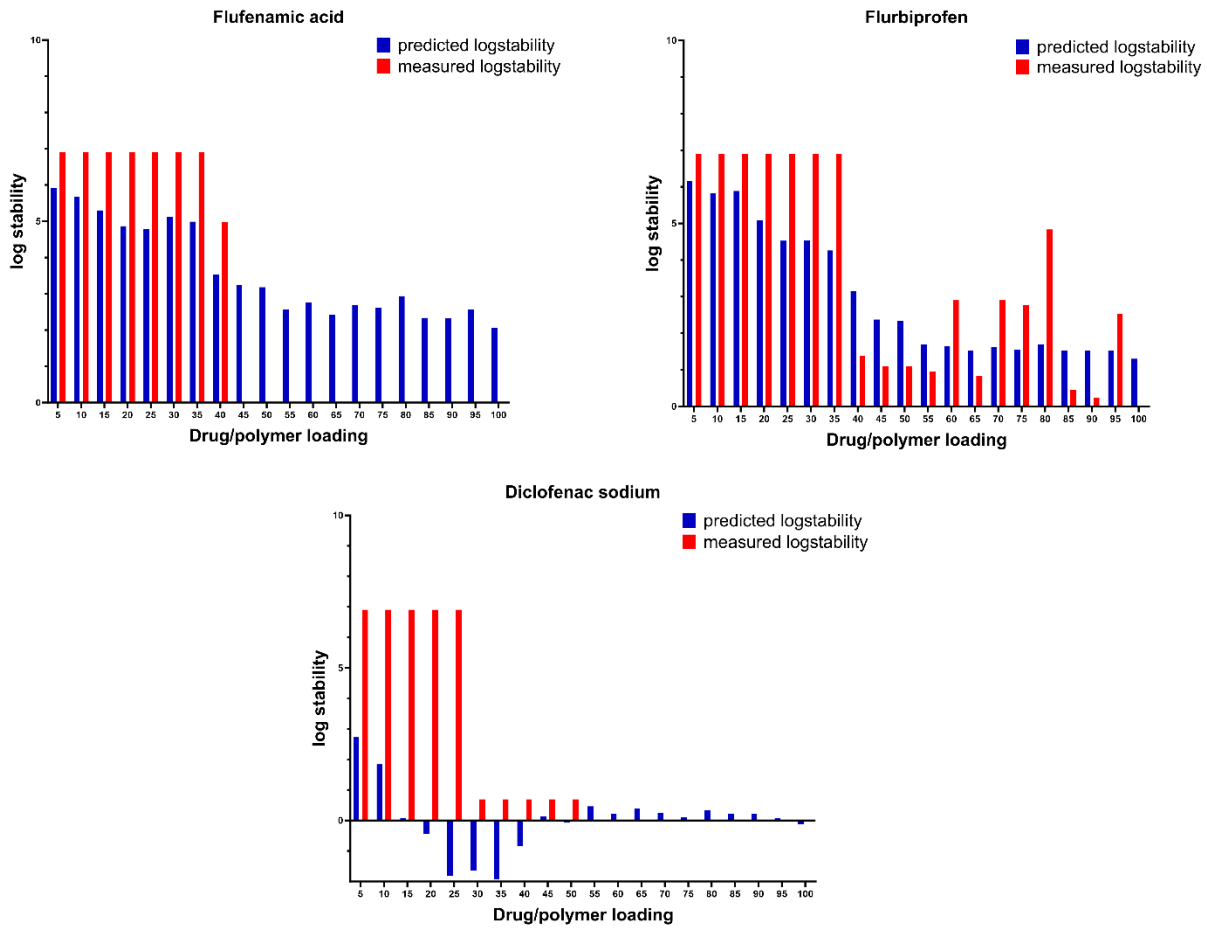


Figure S48. Comparison of predicted log stability, determined using the LOOCV method based on the multiple linear regression model, versus measured log stability from experimental microarray data for Flufenamic acid, Flurbiprofen, and Diclofenac Sodium across a range of drug loadings within the Soluplus polymeric matrix. The blue bars indicate the predicted stability, while the red bars show the measured stability, allowing for an evaluation of the predictive model's accuracy at different drug loadings.